

*DT*  
Bulletin 42

(Part 2 of 5 Parts)



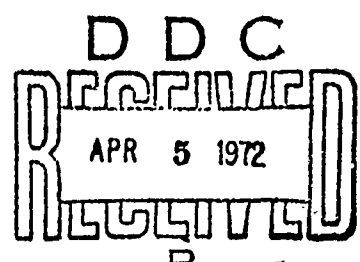
AD 739575

# THE SHOCK AND VIBRATION BULLETIN

Part 2  
Ground Motion,  
Dynamic Analysis

JANUARY 1972

A Publication of  
**THE SHOCK AND VIBRATION  
INFORMATION CENTER**  
Naval Research Laboratory, Washington, D.C.



Office of  
The Director of Defense  
Research and Engineering

Reproduced by  
**NATIONAL TECHNICAL  
INFORMATION SERVICE**  
Springfield, Va. 22151

This document has been approved for public release and sale; its distribution is unlimited.

SEE AD 739574

**Best  
Available  
Copy**

## **SYMPOSIUM MANAGEMENT**

### **THE SHOCK AND VIBRATION INFORMATION CENTER**

William W. Mutch, Director  
Henry C. Pusey, Coordinator  
Rudolph H. Volin, Coordinator  
Edward H. Schell, Coordinator

#### **Bulletin Production**

Graphic Arts Branch, Technical Information Division,  
Naval Research Laboratory

STUN for	
STI	WHITE SECTION <input checked="" type="checkbox"/>
DC	BUFF SECTION <input type="checkbox"/>
REPRODUCED	
SPECIFICATION	
BY	
DISTRIBUTION/AVAILABILITY CODES	
DIST.	AVAIL. AREA OR SPECIAL
A	21

*[Handwritten signature over the form]*

*40-16-52*

**Bulletin 42**  
**(Part 2 of 5 Parts)**

# **THE SHOCK AND VIBRATION BULLETIN**

**JANUARY 1972**

A Publication of  
**THE SHOCK AND VIBRATION  
INFORMATION CENTER**  
Naval Research Laboratory, Washington, D.C.

The 42nd Symposium on Shock and Vibration was held at the U.S. Naval Station, Key West, Florida, on 2-4 November 1971. The U.S. Navy was host.

Office of  
The Director of Defense  
Research and Engineering

*Details of illustrations in  
this document may be better  
studied on microfiche*

## CONTENTS

### PAPERS APPEARING IN PART 2

#### Ground Motion

SINE BEAT VIBRATION TESTING RELATED TO EARTHQUAKE RESPONSE SPECTRA .....	1
E. G. Fischer, Westinghouse Research Laboratories, Pittsburgh, Pennsylvania	
SEISMIC EVALUATION OF ELECTRICAL EQUIPMENT FOR NUCLEAR POWER STATIONS ...	11
R. H. Prause and D. R. Ahlbeck, BATTELLE, Columbus Laboratories, Columbus, Ohio	
SHOCK INPUT FOR EARTHQUAKE STUDIES USING GROUND MOTION FROM UNDERGROUND NUCLEAR EXPLOSIONS .....	21
D. L. Bernreuter, D. M. Norris, Jr., and F. J. Tokarz, Lawrence Livermore Laboratory, University of California, Livermore, California	
ROCKING OF A RIGID, UNDERWATER BOTTOM-FOUNDED STRUCTURE SUBJECTED TO SEISMIC SEAFLOOR EXCITATION .....	33
J. G. Hammer and H. S. Zwibel, Naval Civil Engineering Laboratory, Port Hueneme, California	
DEVELOPMENT OF A WAVEFORM SYNTHESIS TECHNIQUE-A SUPPLEMENT TO RESPONSE SPECTRUM AS A DEFINITION OF SHOCK ENVIRONMENT .....	45
R. C. Yang and H. R. Saffell, The Ralph M. Parsons Company, Los Angeles, California	
THE RESPONSE OF AN ISOLATED FLOOR SLAB-RESULTS OF AN EXPERIMENT IN EVENT DIAL PACK .....	55
J. M. Ferritto, Naval Civil Engineering Laboratory, Port Hueneme, California	
A SHOCK-ISOLATION SYSTEM FOR 22 FEET OF VERTICAL GROUND MOTION .....	67
E. C. Jackson, A. B. Miller and D. L. Bernreuter, Lawrence Livermore Laboratory, University of California, Livermore, California	
THE COMPARISON OF THE RESPONSE OF A HIGHWAY BRIDGE TO UNIFORM GROUND SHOCK AND MOVING GROUND EXCITATION .....	75
N. E. Johnson and R. D. Galletly, Mechanics Research, Inc., Los Angeles, California	
DEFORMATION AND FRACTURE OF TANK BOTTOM HULL PLATES SUBJECTED TO MINE BLAST .....	87
D. F. Haskell, Vulnerability Laboratory, U.S. Army Ballistic Research Laboratories, Aberdeen Proving Ground, Md.	
THE IMPULSE IMPARTED TO TARGETS BY THE DETONATION OF LAND MINES .....	97
P. S. Westine, Southwest Research Institute, San Antonio, Texas	
CIRCULAR CANTILEVER BEAM ELASTIC RESPONSE TO AN EXPLOSION .....	109
Y. S. Kim and P. R. Ukrainianetz, Department of Mechanical Engineering, University of Saskatchewan, Saskatoon, Canada	
MEASUREMENT OF IMPULSE FROM SCALED BURIED EXPLOSIVES.....	123
B. L. Morris, U.S. Army Mobility Equipment Research and Development Center, Fort Belvoir, Virginia	

### Dynamic Analysis

THE EFFECTS OF MOMENTUM WHEELS ON THE FREQUENCY RESPONSE CHARACTERISTICS OF LARGE FLEXIBLE STRUCTURES . . . . .	129
F. D. Day III and S. R. Tomer, Martin Marietta Corporation, Denver, Colorado	
INTEGRATED DYNAMIC ANALYSIS OF A SPACE STATION WITH CONTROLLABLE SOLAR ARRAYS . . . . .	137
J. A. Heinrichs and A. L. Weinberger, Fairchild Industries, Inc., Germantown, Maryland, and M. D. Rhodes, NASA Langley Research Center, Hampton, Virginia	
PARAMETRICALLY-EXCITED COLUMN WITH HYSTERETIC MATERIAL PROPERTIES . . . . .	153
D. T. Mozer, IBM Corporation, East Fishkill, New York, and R. M. Evan-Iwanowski, Professor, Syracuse University, Syracuse, New York	
DYNAMIC INTERACTION BETWEEN VIBRATING CONVEYORS AND SUPPORTING STRUCTURE . . . . .	163
M. Paz, Professor, Civil Engineering Department, University of Louisville, Louisville, Kentucky, and O. Mathis, Design Engineer, Rex Chainbelt Inc., Louisville, Kentucky	
RESPONSE OF A SIMPLY SUPPORTED CIRCULAR PLATE EXPOSED TO THERMAL AND PRESSURE LOADING . . . . .	171
J. E. Koch, North Eastern Research Associates, Upper Montclair, N.J., and M. L. Cohen, North Eastern Research Associates, Upper Montclair, N.J., and Stevens Institute of Technology, Hoboken, N.J.	
WHIRL FLUTTER ANALYSIS OF PROPELLER-NACELLE-PYLON SYSTEM ON LARGE SURFACE EFFECT VEHICLES . . . . .	181
Yuan-Ning Liu, Naval Ship Research and Development Center, Washington, D.C.	
THE DYNAMIC RESPONSE OF STRUCTURES SUBJECTED TO TIME-DEPENDENT BOUNDARY CONDITIONS USING THE FINITE ELEMENT METHOD . . . . .	195
G. H. Workman, Battelle, Columbus Laboratories, Columbus, Ohio	
VIBRATION ANALYSIS AND TEST OF THE EARTH RESOURCES TECHNOLOGY SATELLITE . . . . .	203
T. J. Cokonis and G. Sardella, General Electric Company, Space Division, Philadelphia, Pennsylvania	
FINITE AMPLITUDE SHOCK WAVES IN INTERVERTEBRAL DISCS . . . . .	213
W. F. Hartman, The Johns Hopkins University, Baltimore, Maryland	
ACCELERATION RESPONSE OF A BLAST-LOADED PLATE . . . . .	221
L. W. Fagel, Bell Telephone Laboratories, Inc., Whippany, New Jersey	
EFFECT OF CORRELATION IN HIGH-INTENSITY NOISE TESTING AS INDICATED BY THE RESPONSE OF AN INFINITE STRIP . . . . .	235
C. T. Morrow, Advanced Technology Center, Inc., Dallas, Texas	

### PAPERS APPEARING IN PART 1

#### Invited Papers

SMALL SHIPS-HIGH PERFORMANCE	
Rear Admiral H. C. Mason, Commander, Naval Ship Engineering Center, Washington, D.C.	

### Specifications

**SURVEY OF VIBRATION TEST PROCEDURES IN USE BY THE AIR FORCE**  
W. B. Yarchò, Air Force Flight Dynamics Laboratory, Wright-Patterson Air Force  
Base, Ohio

#### **SPECIFICATIONS - A PANEL SESSION**

**SOME ADMINISTRATIVE FACTORS WHICH INFLUENCE TECHNICAL APPROACHES  
TO SHIP SHOCK HARDENING**  
D. M. Lund, Naval Ship Engineering Center, Hyattsville, Maryland

### Measurement and Application of Mechanical Impedance

#### **FORCE TRANSDUCER CALIBRATIONS RELATED TO MECHANICAL IMPEDANCE MEASUREMENTS**

E. F. Ludwig, Assistant Project Engineer, and N. D. Taylor, Senior Engineer, Pratt & Whitney  
Aircraft, Florida Research & Development Center, West Palm Beach, Florida

**THE MEASUREMENT OF MECHANICAL IMPEDANCE AND ITS USE IN  
VIBRATION TESTING**  
N. F. Hunter, Jr., and J. V. Otts, Sandia Corporation, Albuquerque, New Mexico

**TRANSIENT TEST TECHNIQUES FOR MECHANICAL IMPEDANCE AND MODAL  
SURVEY TESTING**  
J. D. Favour, M. C. Mitchell, N. L. Olson, The Boeing Company, Seattle, Washington

**PREDICTION OF FORCE SPECTRA BY MECHANICAL IMPEDANCE AND ACOUSTIC  
MOBILITY MEASUREMENT TECHNIQUES**  
R. W. Shock, NASA/Marshall Space Flight Center, Huntsville, Alabama and G. C. Kao,  
Wyle Laboratories, Huntsville, Alabama

**DYNAMIC DESIGN ANALYSIS VIA THE BUILDING BLOCK APPROACH**  
A. L. Klosterman, Ph.D. and J. R. Lemon, Ph.D., Structural Dynamics Research  
Corporation Cincinnati, Ohio

**MOBILITY MEASUREMENTS FOR THE VIBRATION ANALYSIS OF CONNECTED  
STRUCTURES**  
D. J. Ewins and M. G. Sainsbury, Imperial College of Science and Technology,  
London, England

**Liquid-Structure Coupling in Curved Pipes - II**  
L. C. Davidson and D. R. Samsbury, Machinery Dynamics Division, Naval Ship Research and  
Development Center, Annapolis, Maryland

### Transportation and Packaging

**A SURVEY OF THE TRANSPORTATION SHOCK AND VIBRATION INPUT TO CARGO**  
F. E. Ostrem, General American Research Division, General American Transportation  
Corporation Niles, Illinois

**THE DYNAMIC ENVIRONMENT OF SELECTED MILITARY HELICOPTERS**  
M. B. Gens, Sandia Laboratories, Albuquerque, New Mexico

**HIGHWAY SHOCK INDEX**  
R. Kennedy, U. S. Army Transportation Engineering Agency, Military Traffic Management  
and Terminal Service, Newport News, Virginia

**DEVELOPMENT OF A ROUGH ROAD SIMULATOR AND SPECIFICATION FOR TESTING  
OF EQUIPMENT TRANSPORTED IN WHEELED VEHICLES**

H. M. Forkois and E. W. Clements, Naval Research Laboratory, Washington, D.C.

**LABORATORY CONTROL OF DYNAMIC VEHICLE TESTING**

J. W. Grant, U. S. Army Tank-Automotive Command, Warren, Michigan

**IMPACT VULNERABILITY OF TANK CAR HEADS**

J. C. Shang and J. E. Everett, General American Research Division,  
General American Transportation Corporation, Niles, Illinois

**A STUDY OF IMPACT TEST EFFECTS UPON FOAMED PLASTIC CONTAINERS**

D. McDaniel, Ground Equipment and Materials Directorate, Directorate for Research,  
Development, Engineering and Missile Systems Laboratory, U. S. Army Missile Command  
Redstone Arsenal, Alabama, and R. M. Wykoff, Industrial and Systems Engineering  
Department, The University of Alabama in Huntsville, Huntsville, Alabama

**DEVELOPMENT OF A PRODUCT PROTECTION SYSTEM**

D. E. Yound, IBM General Systems Division, Rochester, Minnesota, and  
S. R. Pierce, Michigan State University, East Lansing, Michigan

**MOTION OF FREELY SUSPENDED LOADS DUE TO HORIZONTAL SHIP MOTION IN  
RANDOM HEAD SEAS**

H. S. Zwibel, Naval Civil Engineering Laboratory, Port Hueneme, California

**PAPERS APPEARING IN PART 3**

Test Control

**ON THE PERFORMANCE OF TDM AVERAGERS IN RANDOM VIBRATION TESTS**

A. J. Curtis, Hughes Aircraft Company, Culver City, California

**A MULTIPLE DRIVER ADMITTANCE TECHNIQUE FOR VIBRATION TESTING OF  
COMPLEX STRUCTURES**

S. Smith, Lockheed Missiles & Space Company, Palo Alto Research Laboratory,  
Palo Alto, California, and A. A. Woods, Jr., Lockheed Missiles & Space Company,  
Sunnyvale, California

**EQUIPMENT CONSIDERATIONS FOR ULTRA LOW FREQUENCY MODAL TESTS**

R. G. Shoulberg and R. H. Tuft, General Electric Company, Valley Forge,  
Pennsylvania

**COMBINED-AXIS VIBRATION TESTING OF THE SRAM MISSILE**

W. D. Trotter and D. V. Muth, The Boeing Company, Aerospace Group,  
Seattle, Washington

**SHOCK TESTING UTILIZING A TIME SHARING DIGITAL COMPUTER**

R. W. Canon, Naval Missile Center, Point Mugu, California

**A TECHNIQUE FOR CLOSED-LOOP COMPUTER-CONTROLLED REVERSED-BENDING FATIGUE TESTS OF ACOUSTIC TREATMENT MATERIAL**

C. E. Rucker and R. E. Grandle, NASA Langley Research Center,  
Hampton, Virginia

**PROGRAMMING AND CONTROL OF LARGE VIBRATION TABLES IN UNIAXIAL  
AND BIAXIAL MOTIONS**

R. L. Larson, MTS Systems Corporation, Minneapolis, Minnesota

**A DATA AMPLIFIER GAIN-CODE RECORDING SYSTEM**  
J. R. Olbert and T. H. Hammond, Hughes Aircraft Company, Culver City, California

**STABILITY OF AN AUTOMATIC NOTCH CONTROL SYSTEM IN SPACECRAFT TESTING**  
B. N. Agrawal, COMSAT Laboratories, Clarksburg, Maryland

**Test Facilities and Techniques**

**SINUSOIDAL VIBRATION OF POSEIDON SOLID PROPELLANT MOTORS**  
L. R. Pendleton, Research Specialist, Lockheed Missiles & Space Company, Sunnyvale, California

**CONFIDENCE IN PRODUCTION UNITS BASED ON QUALIFICATION VIBRATION**  
R. E. Deltrick, Hughes Aircraft Company, Space and Communications Group, El Segundo, California

**SIMULATION TECHNIQUES IN DEVELOPMENT TESTING**  
A. Hammer, Weapons Laboratory, U. S. Army Weapons Command, Rock Island, Illinois

**A ROTATIONAL SHOCK AND VIBRATION FACILITY**  
R. T. Fandrich, Jr., Radiation Incorporated, Melbourne, Florida

**THE EFFECTS OF VARIOUS PARAMETERS ON SPACECRAFT SEPARATION SHOCK**  
W. B. Keegan and W. F. Bangs, NASA, Goddard Space Flight Center, Greenbelt, Maryland

**NON-DESTRUCTIVE TESTING OF WEAPONS EFFECTS ON COMBAT AND LOGISTICAL VEHICLES**  
R. L. Johnson, J. H. Leete, and J. D. O'Keefe, TRW Systems Group, Redondo Beach, California, and A. N. Tedesco, Advanced Research Projects Agency, Department of Defense, Washington, D.C.

**THE EFFECT OF THE FIN-OPENING SHOCK ENVIRONMENT ON GUIDED MODULAR DISPENSER WEAPONS**  
K. D. Denton and K. A. Herzing, Honeywell Inc., Government and Aeronautical Products Division Hopkins, Minnesota

**DEVELOPMENT OF A FLUIDIC HIGH-INTENSITY SOUND GENERATOR**  
H. F. Wolfe, Air Force Flight Dynamics Laboratory, Wright-Patterson Air Force Base, Ohio

**DEVELOPMENT OF A LIGHTWEIGHT, LINEAR MECHANICAL SPRING ELEMENT**  
R. E. Keefe, Kaman Sciences Corporation, Colorado Springs, Colorado

**TECHNIQUES FOR IMPULSE AND SHOCK TUBE TESTING OF SIMULATED REENTRY VEHICLES**  
N. K. Jamison, McDonnell Douglas Astronautics Company, Huntington Beach, California

**VIBRATION FIXTURING - NEW CELLULAR DESIGN, SATURN AND ORBITAL WORKSHOP PROGRAMS**  
R. L. Stafford, McDonnell Douglas Astronautics Company, Huntington Beach, California

**WALL FLOW NOISE IN A SUBSONIC DIFFUSER**  
E. F. Timpke, California State College, Long Beach, California, and R. C. Binder, University of Southern California, Los Angeles, California

PAPERS APPEARING IN PART 4

Isolation and Damping

TRANSIENT RESPONSE OF REAL DISSIPATIVE STRUCTURES  
R. Plunkett, University of Minnesota, Minneapolis, Minnesota

DYNAMIC RESPONSE OF A RING SPRING  
R. L. Eshleman, IIT Research Institute, Chicago, Illinois

SHOCK MOUNTING SYSTEM FOR ELECTRONIC CABINETS  
W. D. Delany, Admiralty Surface Weapons Establishment, Portsmouth, U.K.

METHODS OF ATTENUATING PYROTECHNIC SHOCK  
S. Barrett and W. J. Kacena, Martin Marietta Corporation, Denver, Colorado

ENERGY ABSORPTION CAPACITY OF A SANDWICH PLATE WITH  
CRUSHABLE CORE  
D. Krnjcinovic, Argonne National Laboratory, Argonne, Illinois

ON THE DAMPING OF TRANSVERSE MOTION OF FREE-FREE BEAMS IN  
DENSE, STAGNANT FLUIDS  
W. K. Blake, Naval Ship Research and Development Center, Bethesda, Maryland

OPTIMUM DAMPING DISTRIBUTION FOR STRUCTURAL VIBRATION  
R. Plunkett, University of Minnesota, Minneapolis, Minnesota

A LAYERED VISCOELASTIC EPOXY RIGID FOAM MATERIAL FOR  
VIBRATION CONTROL  
C. V. Stahle and Dr. A. T. Tweedie, General Electric Company, Space  
Division, Valley Forge, Pa.

OPTIMIZATION OF A COMBINED RUZICKA AND SNOWDON VIBRATION  
ISOLATION SYSTEM  
D. E. Zeidler, Medtronic, Inc., Minneapolis, Minnesota, and D. A. Frohrib,  
University of Minnesota, Minneapolis, Minnesota

TRANSIENT RESPONSE OF PASSIVE PNEUMATIC ISOLATORS  
G. L. Fox, and E. Steiner, Barry Division of Barry Wright Corporation,  
Burbank, California

EXPERIMENTAL DETERMINATION OF STRUCTURAL AND STILL WATER DAMPING  
AND VIRTUAL MASS OF CONTROL SURFACES  
R. C. Leibowitz and A. Kilcullen, Naval Ship Research and Development Center,  
Washington, D.C.

DAMPING OF A CIRCULAR RING SEGMENT BY A CONSTRAINED  
VISCOELASTIC LAYER  
Cpt. C. R. Almy, U.S. Army Electronics Command, Ft. Monmouth, New Jersey,  
and F. C. Nelson, Department of Mechanical Engineering, Tufts University,  
Medford, Mass.

DYNAMIC ANALYSIS OF THE RUNAWAY ESCAPEMENT MECHANISM  
G. W. Hemp, Department of Engineering, Science and Mechanics, University  
of Florida, Gainesville, Florida

Prediction and Experimental Techniques

A METHOD FOR PREDICTING BLAST LOADS DURING THE DIFFRACTION PHASE  
W. J. Taylor, Ballistic Research Laboratories, Aberdeen Proving Ground, Maryland

**DRAG MEASUREMENTS ON CYLINDERS IN EVENT DIAL PACK**

S. B. Melszen, Defence Research Establishment Suffield, Ralston, Alberta, Canada

**DIAL PACK BLAST DIRECTING EXPERIMENT**

L. E. Fugeiso, S. F. Fields, and W. J. Byrne, General American Research Division, Niles, Illinois

**BLAST FIELDS ABOUT ROCKETS AND RECOILLESS RIFLES**

W. E. Baker, P. S. Westine, and R. L. Bessey, Southwest Research Institute, San Antonio, Texas

**TRANSONIC ROCKET-SLED STUDY OF FLUCTUATING SURFACE-PRESSES  
AND PANEL RESPONSES**

E. E. Ungar, Bolt Beranek and Newman Inc., Cambridge, Massachusetts, and H. J. Bandgren, Jr. and R. Erwin, National Aeronautics and Space Administration, George C. Marshall Space Flight Center Huntsville, Alabama

**SUPPRESSION OF FLOW-INDUCED VIBRATIONS BY MEANS OF BODY  
SURFACE MODIFICATIONS**

D. W. Sallet and J. Berezow, Naval Ordnance Laboratory, Silver Spring, Maryland

**AN EXPERIMENTAL TECHNIQUE FOR DETERMINING VIBRATION MODES OF  
STRUCTURES WITH A QUASI-STATIONARY RANDOM FORCING FUNCTION**

R. G. Christiansen and W. W. Parmenter, Naval Weapons Center, China Lake, California

**RESPONSE OF AIR FILTERS TO BLAST**

E. F. Witt, C. J. Arroyo, and W. N. Butler, Bell Laboratories, Whippny, N.J.

**PAPERS APPEARING IN PART 5**

Shock and Vibration Analysis

**BANDWIDTH-TIME CONSIDERATIONS IN AUTOMATIC EQUALIZATION**

C. T. Morrow, Advanced Technology Center, Inc., Dallas, Texas

**A REGRESSION STUDY OF THE VIBRATION RESPONSE OF AN  
EXTERNAL STORE**

C. A. Golueke, Air Force Flight Dynamics Laboratory, Wright-Patterson Air Force Base, Ohio

**FACTOR ANALYSIS OF VIBRATION SPECTRAL DATA FROM MULTI-LOCATION  
MEASUREMENT**

R. G. Merkle, Air Force Flight Dynamics Laboratory, Wright-Patterson Air Force Base, Ohio

**RESPONSES OF A MULTI-LAYER PLATE TO RANDOM EXCITATION**

H. Saunders, General Electric Company, Aircraft Engine Group, Cincinnati, Ohio

**RESPONSE OF HELICOPTER ROTOR BLADES TO RANDOM LOADS  
NEAR HOVER**

C. Lakshmikantham and C. V. Joga Rao, Army Materials and Mechanics Research Center, Watertown, Massachusetts

**INSTRUMENTATION TECHNIQUES AND THE APPLICATION OF SPECTRAL  
ANALYSIS AND LABORATORY SIMULATION TO GUN SHOCK PROBLEMS**

D. W. Culbertson, Naval Weapons Laboratory, Dahlgren, Virginia, and V. F. DeVost, Naval Ordnance Laboratory, White Oak, Silver Spring, Maryland

**THE EFFECT OF "Q" VARIATIONS IN SHOCK SPECTRUM ANALYSIS**

M. B. McGrath, Martin Marietta Corporation, Denver, Colorado, and W. F. Bangs,  
National Aeronautics and Space Administration, Goddard Space Flight Center, Maryland

**RAPID FREQUENCY AND CORRELATION ANALYSIS USING AN ANALOG COMPUTER**

J. G. Parks, Research, Development and Engineering Directorate, U.S. Army Tank-Automotive Command, Warren, Michigan

**INVESTIGATION OF LAUNCH TOWER MOTION DURING AEROBEE 350 LAUNCH**

R. L. Kinsley and W. R. Case, NASA, Goddard Space Flight Center, Greenbelt, Maryland

**ON THE USE OF FOURIER TRANSFORMS OF MECHANICAL SHOCK DATA**

H. A. Gaberson and D. Pal, Naval Civil Engineering Laboratory, Port Hueneme, California

**WAVE ANALYSIS OF SHOCK EFFECTS IN COMPOSITE ARMOR**

G. L. Filbey, Jr., USAARDC Ballistic Research Laboratories, Aberdeen Proving Ground, Maryland

**STATISTICAL LOADS ANALYSIS TECHNIQUE FOR SHOCK AND HIGH-FREQUENCY EXCITED ELASTODYNAMIC CONFIGURATIONS**

K. J. Saczalski and K. C. Park, Clarkson College of Technology, Potsdam, New York

**Structural Analysis**

**NASTRAN OVERVIEW: DEVELOPMENT, DYNAMICS APPLICATION, MAINTENANCE, ACCEPTANCE**

J. P. Raney, Head, NASTRAN Systems Management Office and D. J. Weidman, Aerospace Engineer, NASA Langley Research Center, Hampton, Virginia

**EXPERIENCE WITH NASTRAN AT THE NAVAL SHIP R&D CENTER AND OTHER NAVY LABORATORIES**

P. Matula, Naval Ship Research & Development Center, Bethesda, Maryland

**RESULTS OF COMPARATIVE STUDIES ON REDUCTION OF SIZE PROBLEM**

R. M. Mains, Department of Civil and Environmental Engineering, Washington University, St. Louis, Missouri

**STRUCTURAL DYNAMICS OF FLEXIBLE RIB DEPLOYABLE SPACECRAFT ANTENNAS**

B. G. Wrenn, W. B. Haile, Jr. and J. F. Hedges, Lockheed Missiles and Space Company, Sunnyvale, California

**INFLUENCE OF ASCENT HEATING ON THE SEPARATION DYNAMICS OF A SPACECRAFT FAIRING**

C. W. Coale, T. J. Kertesz, Lockheed Missiles & Space Company, Inc., Sunnyvale, California

**DYNAMIC WAVE PROPAGATION IN TRANSVERSE LAYERED COMPOSITES**

C. A. Ross, J. E. Cunningham, and R. L. Sierakowski, Aerospace Engineering Department, University of Florida, Gainesville, Florida

**R-W PLANE ANALYSIS FOR VULNERABILITY OF TARGETS TO AIR BLAST**

P. S. Westine, Southwest Research Institute, San Antonio, Texas

**PERFORM: A COMPUTER PROGRAM TO DETERMINE THE LIMITING PERFORMANCE OF PHYSICAL SYSTEMS SUBJECT TO TRANSIENT INPUTS**

W. D. Pilkey and Bo Ping Wang, Department of Aerospace Engineering and Engineering Physics, University of Virginia, Charlottesville, Virginia

**STRUCTURAL DYNAMIC ANALYSIS AND TESTING OF A SPACECRAFT DUAL TRACKING  
ANTENNA**

D. D. Walters, R. F. Heidenreich, A. A. Woods and B. G. Wrenn, Lockheed Missiles  
and Space Company, Sunnyvale, California

**Ship's Problems**

**DETERMINATION OF FIXED-BASE NATURAL FREQUENCIES OF A COMPOSITE  
STRUCTURE OR SUBSTRUCTURES**

C. Ni, R. Skop, and J. P. Layher, Naval Research Laboratory, Washington, D.C.

**EQUIVALENT SPRING-MASS SYSTEM: A PHYSICAL INTERPRETATION**

B. K. Wada, L. Bamford, and J. A. Garba, Jet Propulsion Laboratory,  
Pasadena, California

**LONGITUDINAL VIBRATION OF COMPOSITE BODIES OF VARYING AREA**

D. J. Guzy, J.C.S. Yang, and W. H. Walston, Jr., Mechanical Engineering  
Department, University of Maryland, College Park, Maryland

**SIMPLIFIED METHOD FOR THE EVALUATION OF STRUCTUREBORNE VIBRATION  
TRANSMISSION THROUGH COMPLEX SHIP STRUCTURES**

M. Chernjawski and C. Arcidiacono, Gibbs & Cox, Inc., New York, New York

## **GROUND MOTION**

### **SINE BEAT VIBRATION TESTING RELATED TO EARTHQUAKE RESPONSE SPECTRA**

**E. G. FISCHER**  
**WESTINGHOUSE RESEARCH LABORATORIES**  
**PITTSBURGH, PENNSYLVANIA**

Vibration test criteria are developed for evaluating the earthquake resistance and reliability of electrical switchgear, including sensitive control devices. A series of sine beat vibrations applied at experimentally determined, natural frequencies of the equipment is potentially more damaging than the original seismic motion. The test table input can be related to the floor response spectra as calculated for a particular power plant structure and location in an active earthquake zone.

#### **INTRODUCTION**

It is customary to develop mathematical models of building structures [1] and then make computer-aided analyses of their dynamic response to seismic disturbances. Similarly, mechanical equipments located in such structures may require dynamic seismic analyses, although they become more complicated and difficult to model [2]. In the special case of sensitive electrical control devices subject to possible malfunction during earthquakes (for example, the safeguards equipment required for nuclear power plants), it becomes more practical to rely upon a conservative method of environmental testing. Experience indicates that the inadvertent loss of principle function under shock can pose more of a design problem than an obvious strength failure.

To obviate either difficult or questionable analyses, earthquake vibration test criteria have been developed for evaluating and demonstrating the reliability of electrical control devices for Electric Utility Systems. In particular, a series of sine beat vibrations are applied at experimentally determined natural frequencies of the equipment. This means that the equipment is conservatively tested by a procedure which makes it most vulnerable.

In addition, sine beat vibration inputs during test can be related to foundation or building floor shock response spectra for computer-simulated earthquakes. The test results provide data on natural frequencies and

damping for typical nonlinear systems, and such information can be used to authenticate parallel computer-aided dynamic analyses.

#### **RANDOM MOTION THEORY**

Random motion is non-periodic and, therefore, unpredictable with time. However, it can be described in statistical terms based upon "the analysis of noise in communication circuits" as pioneered by Rice [3].

Figure 1a illustrates a random vibration excitation which is characterized as broadband in the sense that it appears to include all frequencies in addition to its large fluctuations in amplitude. (Earthquake accelerographs of free-field ground motions usually exhibit such characteristics.)

By way of contrast, Fig. 1b illustrates the corresponding narrow-band vibration response of a simple (mass-spring-damper) oscillator wherein the frequency is restricted to the system natural frequency, although the amplitude fluctuations persist. As judged by the envelope of the peak magnitudes, this more-or-less harmonic motion is referred to as a random sine wave. (Building floor seismic response records exhibit similar sine beat characteristics.)

In general, the original seismic disturbance can be generated in terms of a non-stationary random process involving damped sinusoids with random frequencies as well as

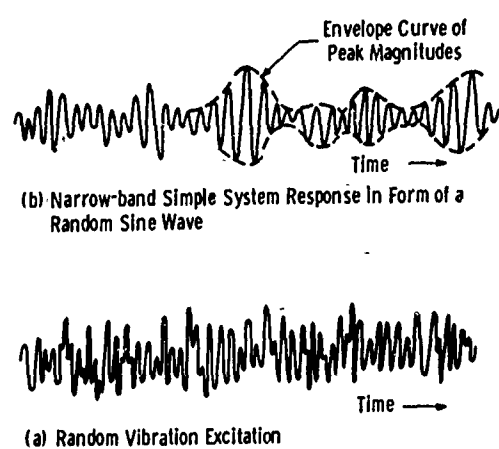


Fig. 1 - Acceleration-time history records of broadband excitation and narrow-band response

random phase relationships[4]. However, the present discussion can be simplified if limited to a "stationary random process" consisting of an ensemble of motion-time histories, the latter considered to be stationary if the statistical properties are not affected by a translation of the origin of time. Consequently, by means of the ergodic hypothesis, the required assembly-averaging of random data can be replaced by the more simple task of time-averaging over a single record of long duration.

Because resonant vibration buildup is an important engineering phenomenon, it is essential to evaluate the frequency content of seismic vibration excitation. For this purpose the quantity "power spectral density" (PSD) is used as a measure of frequency content of random-type functions. (Important frequency effects in earthquake free-field accelerographs appear to be limited to a range from 1 to 25 Hz.)

Figure 2 shows the frequency spectra chart of PSD for a random broadband excitation and a narrow-band response, the latter demonstrating the filter action of a simple oscillator. Hence, the acceleration-time histories shown in Figs. 1a, b have now been characterized by means of a statistical analysis as plotted in Fig. 2. (Earthquake ground motion response spectra usually appear as broadband excitation, whereas building floor response spectra correspond to narrow-band quasi-resonance buildup at one or more natural frequencies of the building)

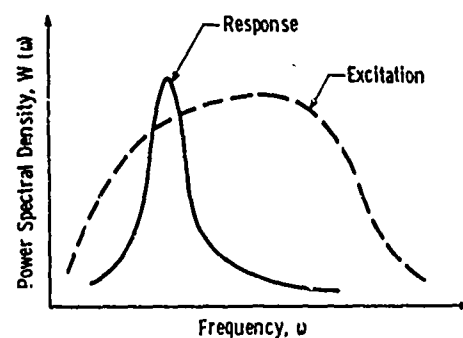


Fig. 2 - Frequency spectra showing the output response of a simple oscillator for a random vibration excitation

#### SINE BEAT VIBRATION

In general, when a random excitation is put through a lightly-damped, narrow-band-pass filter, the output response usually appears to be a harmonic signal with a slowly varying amplitude. The energy is transmitted primarily in the neighborhood of the natural frequency of the system filter. The vibration response wave (see Fig. 1b) appears to be a sine wave at a single frequency but with pulsating amplitude; hence the so-called sine beat vibration. The probability density of the instantaneous values of the filtered response tends to be normal, or Gaussian (symmetrical)[5].

On the other hand, the density distribution function of the amplitude variation of the envelope of the random sine wave (see Fig. 1b) tends to be skewed. It can be expressed explicitly by means of the well-known Rayleigh distribution curve, which is employed in studies of cumulative vibration fatigue. It is also called the two-dimensional error distribution with reference to the "random walk" problem, which was first solved by Lord Rayleigh[6]. Strength failures caused by random seismic disturbances involve a relatively few load cycles, but they can work the material in the elasto-plastic range of cumulative fatigue.

A special case of the fluctuating sine wave is, of course, the true sine beat vibration which can be expressed in terms of two rotating (acceleration) vectors as follows:

$$\ddot{x} = \frac{G}{2} [\cos 2\pi F_1 t - \cos 2\pi F_2 t],$$

$$= -G [\sin 2\pi \frac{F_1 + F_2}{2} t \cdot \sin 2\pi \frac{F_1 - F_2}{2} t]$$

where  $\frac{F_1 + F_2}{2}$  = natural (test) freq. of equipment, Hz  
 $\frac{F_1 - F_2}{2}$  = freq. of envelope, Hz (2 beat pulses)  
 $= \frac{\text{test frequency, Hz}}{2 \text{ (no. of cyc/beat)}}$   
 $G$  = peak accel. (386 in/sec<sup>2</sup>)

In actual testing, the frequency of the sine beat vibration of the test machine mounting plate corresponds to each natural frequency in the equipment as determined by a continuous sweep frequency search from 1 to 25 Hz. Hence, the equipment's capabilities are evaluated where it is most vulnerable.

In general, environmental testing techniques are well-established and several machines are available for reproducing actual earthquake motion-time histories [7], or test

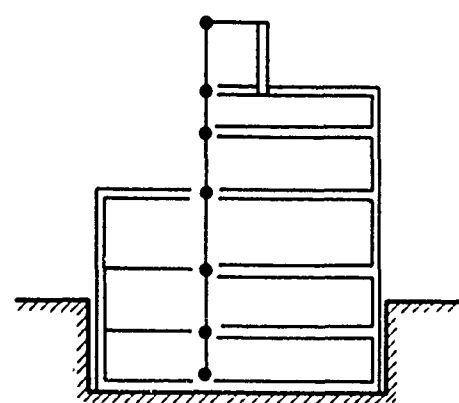
table motions which, in turn, develop specified shock response spectra in the mounted equipment [8, 9].

Also, steady-state vibration testing at equipment natural frequencies is well-known in terms of the Navy MIL-S-167 for shipboard environment. However, for seismic test criteria the sine beat motion input is much preferred because it produces only a limited quasi-resonance magnification and less cumulative fatigue.

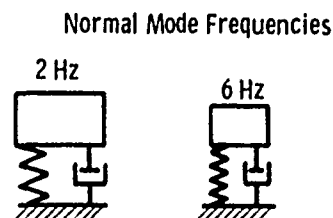
A novel feature introduced by this proposed sine beat vibration testing is that the test results and parallel design calculations for the equipment can be related to the peculiarities of the foundation or building seismic response spectra as supplied by the Electric Utility System for their installations.

#### TRANSIENT ANALYSIS OF BUILDINGS AND EQUIPMENT

The well-known normal-mode method can be applied specifically to mathematical models of buildings and equipment in order to determine a dynamically equivalent series of simple oscillators in terms of the uncoupled normal-mode shapes and fixed-base natural frequencies. In turn, the motion-time history of the earthquake disturbance can be applied to each oscillator and a summation obtained of the total transient response of the building or equipment.



(a) Dynamic Model of Building



(b) Equivalent Simple Oscillators

Fig. 3 - Computer-aided dynamic analysis of building subject to seismic disturbance

However, a distinction must be made between the broadband seismic excitation at ground level and the narrow-band floor motion at the various building elevations—the latter resulting from the filtering action of the mechanical-soil-structure system. Also, in the following discussion an essential distinction must be made between the customary shock response spectra used in design, and the original motion-time history used as the basis for the equivalent sine beat vibration testing.

Figure 3 shows (a) a typical mathematical model of a nuclear power plant building, and (b) the dynamically equivalent series of simple oscillators. Only the three lowest modes of vibration with natural frequencies of 2, 6 and 22 Hz need be considered, since they are the only ones calculated within the most important earthquake hazard range for vibration buildup from about 1 to 25 Hz. (Similar frequencies found in the equipment model are not necessarily coincident with those in the building.)

It is appreciated that in complex structures there may be important cross-coupling effects and fluctuating response motions when natural frequencies are close together. However, this situation is usually covered by specifying an envelope-type of building floor response spectra. (Similarly, when there is interaction of two or more equipment modes, then a more severe response condition might have to be recognized.)

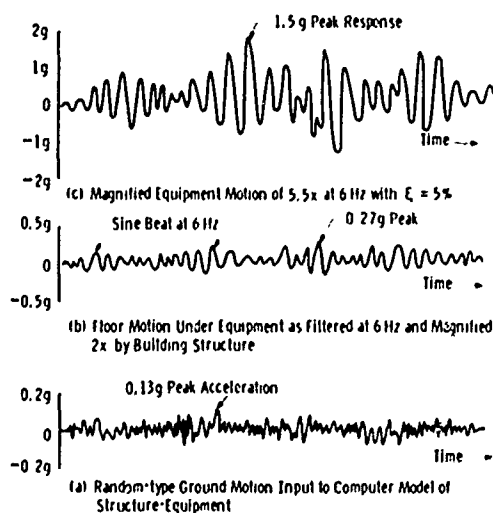


Fig. 4 — Typical accelerograms of OBE horizontal motion as transmitted by dynamic model

## FILTER ACTION OF THE BUILDING STRUCTURE

Figure 4 illustrates how (a) the broadband seismic excitation at the base of the building can be (b) filtered and magnified by the building structure, and (c) amplified by the equipment response at the coincident building natural frequency of 6 Hz.

The resulting floor motion shown in Fig. 4b consists of various harmonic oscillations depending upon the different paths along which the ground disturbance has been propagated. Essentially, this motion under the equipment has been filtered at 6 Hz and magnified 2.0 times by the building structure. In other words, it now approximates a random sine wave as shown in Fig. 1b, and in the form of an equivalent sine beat vibration can be applied to the test machine mounting plate in order to evaluate the seismic capabilities of the equipment.

In turn, the test machine will duplicate (or exceed) the resulting equipment response motion shown in Fig. 4c, which occurs when a natural frequency of the equipment coincides with a natural frequency of the building structure. At 6 Hz with 5 percent damping, the magnification of the floor motion in the equipment amounts to 5.5 times. (An equivalent sine beat vibration test using 5 cycles/beat at 6 Hz will produce this same magnification in equipment having 5 percent damping.)

It should be recognized that when a natural frequency of the equipment does not coincide with a natural frequency of the building structure then the quasi-resonance motion buildup in the equipment will be much less evident than as shown by Fig. 4c. (In turn, although a sine beat vibration test would be applied at the equipment natural frequency, the input amplitude should be reduced to produce only the floor response specified at the test frequency, which no longer coincides with a building structure natural frequency. The net result is a somewhat conservative sine beat test compared to using actual floor motion inputs.)

## BUILDING EQUIPMENT "DESIGN" PROCEDURE

Figure 5 shows a semi-log plot of typical floor response spectra as supplied by the Architect-Engineer of the building. It is information derived from a transient analysis of a pertinent building structure model with a base acceleration input corresponding to a

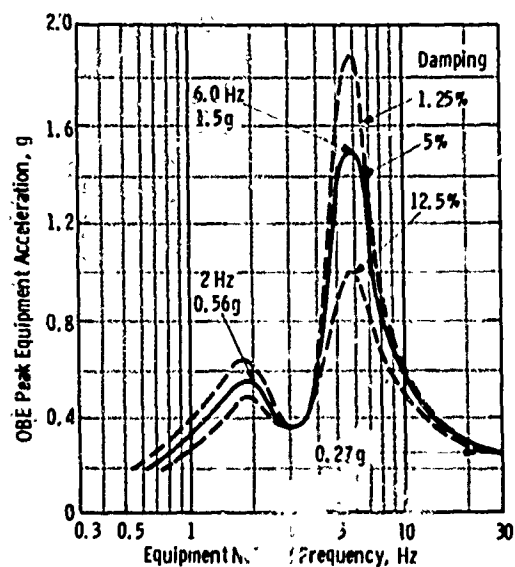


Fig. 5 - OBE horizontal floor response spectra at equipment location in building

horizontal motion-time history for an Operating Basis Earthquake (OBE). Presumably the model includes a soil-structure interaction factor, and the OBE has been established on the basis of the seismic history of a specific power plant site.

The filtering action of the building, as previously illustrated by Fig. 4, was based upon the data to be found and interpreted from Fig. 5. In other words, the ground motion is random with a peak value of 0.13 g. At an upper floor level where the equipment might be located, the input motion has been magnified 2 times to give a peak value of 0.27 g corresponding to the horizontal asymptote for frequencies above 30 Hz. (Compare Fig. 4b with Fig. 5). Finally, for 5 percent damping in the equipment at 6 Hz, which is the coincident building-equipment natural frequency, the maximum equipment response acceleration becomes 1.5 g. (Compare Fig. 4c with Fig. 5.)

Figure 5 also gives floor motion response spectra (actually the peak acceleration measured on the equipment at each of its natural frequencies) for several values of percent critical damping, which can be determined for the equipment from the motion buildup during the continuous sweep frequency test. The

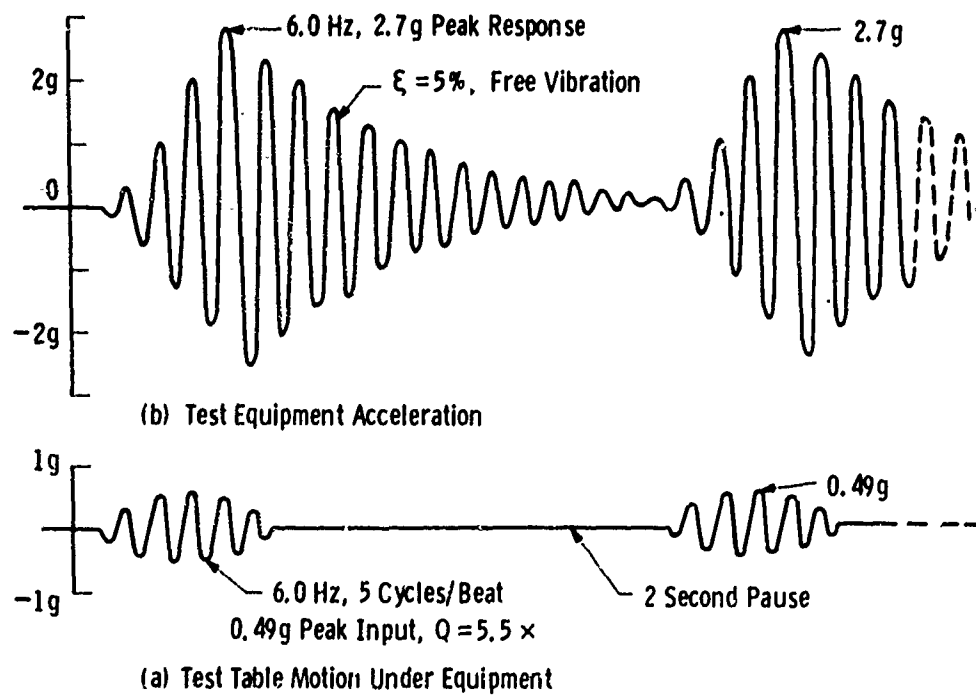


Fig. 6 - Sine beat motion test for DBE = 1.8 x OBE

maximum overall magnification of the ground motion into the equipment at 5 percent damping is  $1.5 \text{ g}/0.13 \text{ g} = 11.5$  times, which shows that the selective filtering action of the building structure can be quite influential. (For the El Centro earthquake at 5 percent damping the shock response spectra magnification is only  $0.55 \text{ g}/0.33 \text{ g} = 1.7$  times).

The floor response spectra shown in Fig. 5 can be used for equipment design purposes as follows. The peak horizontal response acceleration at the equipment cg will be  $1.5 \text{ g}$  at  $6 \text{ Hz}$  and  $5$  percent damping. This means that  $1.5$  times the weight of the equipment should be applied as an equivalent static horizontal load at the cg in order to verify that stressed members are below the yield point. Also, if the equipment natural frequency is  $30 \text{ Hz}$  or greater, there is no further magnification of the basic floor motion which is only  $0.27 \text{ g}$ .

#### BUILDING EQUIPMENT "TEST" PROCEDURE

For seismic testing of equipment, the vibration machine input is intended to simulate the worst aspects of the motion of the building floor at the attachment of the equipment. A conservative approximation of the earthquake-induced floor motion is applied by means of the sine beat vibration motion.

In addition, since the probability of an earthquake worse than the OBE is difficult to agree upon, the intensity multiplier is used to achieve a more safe Design Basis Earthquake, whereby  $\text{DBE} = 1.8$  (OBE). (In practice, the Electric Utility Company and the Architect-Engineer supply the foundation and floor response spectra with a statement regarding OBE and DBE.)

Finally, Fig. 6a shows that a sine beat vibration input consisting of  $5$  cycles/beat at  $6 \text{ Hz}$  and a peak amplitude of  $0.49 \text{ g}$  is the appropriate test machine input to represent the damaging effects of the floor motion under the equipment as shown in Fig. 4b, since  $1.8 (0.27\text{g}) = 0.49 \text{ g}$ . Fig. 6b shows that the equipment response amplitude reaches a peak of  $2.7 \text{ g}$  and then gradually decays as a free vibration at  $6 \text{ Hz}$  before the next sine beat vibration is applied.

The total number of successive beat effects applied to the equipment depends upon the earthquake magnitude, hence the time duration of the corresponding strong motion accelerograph. As many as  $5$  successive sine beats have been used in actual testing at each

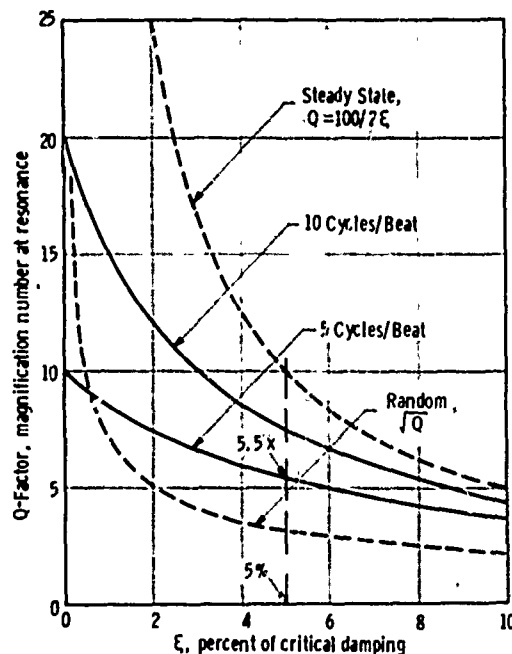


Fig. 7 - Vibration magnification at quasi-resonance

equipment natural frequency. In view of the cumulative fatigue effects associated with testing the equipment in three directions (East-West, North-South and vertical), it becomes apparent that sine beat vibration testing can be made very conservative with regard to probable local seismic activity.

In summary, it is important to recognize that for design purposes the floor response spectra of Fig. 5 can be applied directly. However, for test purposes it is necessary to apply the actual floor motion shown by Fig. 4b, or else apply the conservative substitute shown by Fig. 6a.

#### SINE BEAT VIBRATION TEST METHOD

Figure 7 provides the theoretical data needed for the correlation of floor response spectra (Fig. 5) and test table input (Fig. 6a). Based upon the transient analysis of a linear mass-spring-damper model with a sine beat base motion excitation, the vibration magnification curves (so-called Q-factor at resonance) are calculated for both  $5$  cycles/beat and  $10$  cycles/beat over a range of damping values ( $\xi$ , percent of critical). This elementary computer-aided analysis is equivalent to the normal-mode evaluation of the equipment response (see Fig. 4c and 6b).

Figure 7 also shows the Q-factors for steady-state vibration resonance ( $Q = 100/2g$ ) and for random (white noise) excitation equal to the square root of  $Q$ . The quasi-resonance buildups produced by the sine beat vibrations fall in between the latter two extremes. By comparison, seismic-motion response magnification factors fall somewhat below the random excitation values. The most damaging sections of earthquake oscillographs usually correspond to a sine beat vibration excitation of about 3 cycles/beat at various preferred frequencies from about 1 to 10 Hz.

The previous example for selecting a sine beat vibration test corresponding to building floor response spectra can be summarized as follows. At each experimentally determined natural frequency of the equipment, the ordinates for the OBE response spectra curve should be increased by the DBE factor (1.8 times) and then reduced by the Q-factor (5.5 times at 5 percent damping) in order to get the peak value of the sine beat input acceleration (0.49 g at 6 Hz), in this example for 5 cycles/beat. Notice that at equipment natural frequencies of approximately 4.2 and 8.4 Hz, which are non-coincident with the building structure natural frequency at 6 Hz, the response at 5 percent equipment damping is only 0.75 g instead of 1.5 g maximum at 6 Hz. Hence, the sine beat input acceleration peak should be only 0.245 g at 4.2 and 8.4 Hz instead of the 0.49 g at 6 Hz. This example shows the need for adjusting both building and equipment designs to avoid coincident natural frequencies.

It should be emphasized that in the example of Fig. 4a, the peak acceleration of 0.13 g corresponds to an earthquake characterized as VII on the Modified Mercalli Intensity Scale (6.5 Richter Scale), meaning damage "slight to moderate in well-built, ordinary structures." However, as shown by Fig. 6b the peak acceleration of 2.7 g in the power plant equipment under test amounts to an overall magnification of 21 times, indicating that sine beat vibration testing can be made quite severe.

This proposed test method is conservative in that should either the damping of the equipment be evaluated on the high side, or the input "cycles/beat" selected on the low side, the net result in both cases would be a smaller Q-factor and a larger test machine acceleration. Also, compared to steady-state vibration testing, the Q-factor near zero damping means only a limited resonance buildup. In other words, when testing unknown systems there will be no destructive buildup produced inadvertently. In addition, since equipment fragility levels are

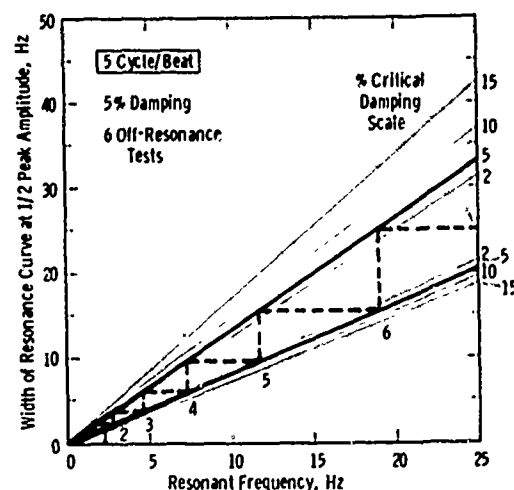


Fig. 8 - Chart for determining number of off-resonance tests at 1/2 peak amplitude

usually evaluated by testing at successively larger g-levels, the danger of fatigue failures is reduced because of lower average stressing.

#### OFF-RESONANCE SINE BEAT TESTS

The computer-aided analysis used to obtain the Q-factor curves of Fig. 7 has also supplied data for plotting resonance curves of magnification versus frequency from 1 to 25 Hz. Somewhat arbitrarily at the 1/2 peak amplitude ordinate, the corresponding (2) sideband frequencies can be determined along the abscissa for resonance curves at various values of damping in the simple oscillator system.

Figure 8 shows the above information plotted as a family of fan-shaped curves for a sine beat excitation at 5 cycles/beat. The upper and lower sideband frequency ordinates correspond to the intersections of a vertical line at a resonant (test) frequency abscissa with the two radial lines drawn for some value of percent critical damping. (Similar curves can be plotted at 10 cycles/beat and steady-state, wherein the sideband widths becomes increasingly smaller.)

The stair-step construction shown by the dashed-lines gives the maximum spacing between "off-resonance" test frequencies, together with the assurance that at least 1/2 peak amplitude will be excited.

Of course, when there are many equipment natural frequencies distributed over the range from 1 to 25 Hz, the stair-step construction may indicate that additional off-resonance tests are unwarranted. On the otherhand, when there are only one or two obvious equipment natural frequencies, or only building structure natural frequencies to consider, then they can be used to start the stair-step construction in both directions to establish additional off-resonance test points.

The primary purpose of the previous development is to avoid unwarranted cumulative fatigue and wear of equipment being tested for earthquake resistance. (As a practical matter, typical complex electrical switchgear systems usually introduce nonlinear effects in terms of snubber springs, clearances, friction, cross-coupling, etc. Equipment resonances appear heavily damped, but persist over a relatively wide frequency range and they can be excited in all three directions of testing.)

## CONCLUSIONS

In general, there are insufficient strong-motion earthquake accelerograms available for power plant structures, let alone specific types of equipment, to establish "an acceptable seismic risk". Also, it is generally agreed that an isolated peak acceleration response is not a reliable indication of damage. In switchgear equipment, where possible loss of principle function is a more important consideration, there does not appear to be any obvious correlation with field service reports.

The use of computer-aided analyses of buildings and equipment, and the specification of earthquake response spectra, all emphasize the importance of quasi-resonance phenomena as the source of damage or malfunction. Hence, sine beat vibration testing appears appropriate for evaluating complex equipment where it is most vulnerable—at its natural frequencies as determined by a vibration sweep at a reduced acceleration input from 1 to 25 Hz.

Sine beat vibration testing produces only a limited quasi-resonance buildup and avoids excessive fatigue in the equipment, both of which conditions appear typical of seismic disturbances. Also, sine beat test inputs and subsequent equipment responses can be directly related to the foundation or building floor seismic response spectra as supplied by the Electric Utility Company. In general, the severity of the test can be simply adjusted and the test results can be made conservative with respect to any specified seismic environment.

## REFERENCES

1. John A. Blume, et al, *Design of Multistory Reinforced Concrete Buildings for Earthquake Motions*, Portland Cement Assoc., 1961.
2. E. G. Fischer, et al, "Mathematical Model Analysis for the Dynamic Design of Machinery", SESA, Experimental Mechanics, October 1967.
3. S. O. Rice, *Bell Sys. Tech. J.*, 23, 282 (1944) and 24, 46 (1945).
4. J. W. Miles and W. T. Thompson: "Statistical Concepts in Vibration," Chapter 11, *Shock & Vibration Handbook*, McGraw-Hill, New York, 1961.
5. J. L. Bogdanoff, et al, "Response of a Simple Structure to a Random Earthquake-Type Disturbance," *Bull. SSA*, 51, 2 April 1961.
6. G. S. Mustin, "Theory and Practice of Cushion Design," Shock & Vibration Info. Center, U. S. Dept. of Defense, 1968.
7. J. Penzien, "Design and Research Potential of Two Earthquake Simulator Facilities," Richmond Field Station, University of California in Berkeley.
8. G. Shipway, "A New Technique for Seismic Shock Simulation," Wyle Labs; Norco, Cal. and Huntsville, Ala.
9. E. G. Fischer, "Design of Equipment to Withstand Underground (Nuclear Weapon) Shock Environment," 28th Shock and Vibration Symposium, U. S. Dept. of Defense, July 1960.

## DISCUSSION

Mr. Gaynes (Gaynes Testing Laboratories): How did you monitor the relays and switches to determine whether they were functioning or not functioning?

Mr. Fischer: Usually we had an electrical hook-up to an oscilloscope element. The definition of malfunction is quite a touchy point. In some applications, such as computers for the Safeguard system, any kind of relay flutter is not allowed at all, so one practically has to use solid state circuitry. Again, depending on the application, somebody gives you a definition of what constitutes a malfunction. There are accelerometers located on the structure etc, but as far as malfunctioning, it seems to be the electrical operation that is the most significant. Of course if the circuit breaker pops open it is pretty obvious that you are in trouble.

Mr. Haag (MTS Systems Corporation): We have been performing several tests in the seismic shock area including the sine beat, and we pretty much confirm your approach. We feel it is a severe test. To find the resonances, we do pretty much the same as required in MIL-STD-167, where you sweep the fre-

quencies, and determine the resonance modes by monitoring the displacement of the specimen. We also have gone quite a bit further. We have gone into the shock spectrum approach by using random transients in determining the ability of the product to withstand vibration. We will be presenting a paper in the near future on that particular comparison, and I think you will find that your feelings are correct. Using the sine beat seems to be a more severe test than using random transients, but if the shock spectrum can be adequately defined, I think that random transients would be superior way to go.

Mr. Fischer: Well it could be more authentic. I agree, but I started out by saying: "In the interests of simplicity we pretty much stuck to the sine beat." We justify the simplicity by saying it is a conservative test. Frankly, I will take testing with simultaneous input anytime. With actual earthquake records, as I believe Dr. Plunkett pointed out this morning, you just think you are pushing something in a certain direction. It can always escape at right angles. When you use three dimensional testing you never test nearly as severely as we are suggesting with sine beat testing.

## SEISMIC EVALUATION OF ELECTRICAL EQUIPMENT FOR NUCLEAR POWER STATIONS

Robert H. Prause and Donald R. Ahlbeck  
BATTELLE, Columbus Laboratories  
Columbus, Ohio

A review of current seismic specifications for electrical equipment and the different types of vibration excitation that might be used to satisfy these specifications led to the design and construction of a seismic vibration facility with the capability of reproducing typical building floor earthquake acceleration time histories. The design of the vibration table and control system and the development of the acceleration time-history command signal are discussed. A comparison of the acceleration response spectra for the table motion and a typical command signal demonstrates the feasibility of using this type of realistic simulation of earthquake motions for evaluating electrical equipment performance. Significant results from this work are included to provide equipment designers with some typical experience.

### INTRODUCTION

The design of nuclear power generating stations requires the consideration of many types of possible accident situations in order to insure that the public is protected from potential exposure to nuclear radiation. The consideration of earthquake effects is particularly important because the forces can be extremely large and all parts of a nuclear station could be affected simultaneously. Contrary to popular opinion, nearly all locations in the United States have a history of earthquakes, although the frequency of occurrence and severity vary considerably. As a result, all nuclear power generating stations being built in this country are designed to withstand earthquake motions even though they may be located in regions where earthquakes are ignored for other types of structures.

Modern dynamic analysis techniques have proved to be valuable tools for predicting the response to earthquake excitation of building structures, piping systems, and many types of mechanical equipment [1]. Electrical equipment, however, often consists of a light frame structure supporting flexible racks and panels to which a variety of components such as transformers, relays, switches and meters are mounted. Analytical techniques can be used to determine the adequacy of the basic structure of an electrical equipment cabinet to survive an earthquake; however, it is considered impractical, if not impossible, to determine by

analysis whether the electrical components will perform reliably without damage or temporary interruption of operation during a seismic disturbance. As a result of this conclusion, a laboratory facility for the seismic evaluation of Class I electrical equipment was designed and installed early in 1971 at the Battelle-Columbus Laboratories. The design of this facility was based on the desire to achieve a realistic simulation of the earthquake vibration environment.

### SEISMIC REQUIREMENTS FOR ELECTRICAL EQUIPMENT

The components and structures of a nuclear plant that are critical to the shutdown and maintenance of the reactor in a safe condition are designated as "Class I". These must be designed to remain functional when subjected to the Design Basis Earthquake (DBE), sometimes referred to as the Maximum Credible Earthquake, that has been selected for the particular plant location. Structures and components whose failure would not interfere with a controlled shutdown of the reactor or contribute to an excessive release of radiation are generally designated as "Class II", and these are subject to less severe seismic design requirements.

Manufacturers of Class I electrical equipment are now being required to verify that their equipment is capable of acceptable performance during a seismic disturbance.

Preceding page blank

A basic problem faced by these manufacturers is that only rarely are those persons responsible for the design of this type of electrical equipment also knowledgeable in earthquake engineering technology. Adding to this problem is the fact that there are no standard requirements for seismic evaluation, so a manufacturer receives a different set of seismic specifications for each new nuclear power generating station. While it is expected that the severity of the DBE will vary for different locations in the country, there is also considerable difference in the type of specifications being used to assure compliance with seismic requirements. The greatest source of confusion from nearly all types of seismic specifications is the use of response spectra as the principal means of describing the earthquake vibration environment. Therefore, a brief review of the development and implications of earthquake response spectra for earthquake engineering seems justified, since experience has shown that this type of description often confuses even specialists in other areas of structural dynamics and vibrations.

#### EARTHQUAKE RESPONSE SPECTRA

The design of each Class I building for a nuclear power generating station requires a detailed analysis of the response of that building (deflections, accelerations, stresses, etc.) to a typical earthquake ground motion selected for that location. The earthquake ground motion will have acceleration components in two orthogonal horizontal directions of about equal intensity and a vertical component that usually has lower peak accelerations, although the energy is concentrated at higher frequencies. Fig. 1 shows the component of ground acceleration recorded at El Centro, California, during the earthquake of May 18, 1940. Although the ground motion lasted for about 45 seconds, the most severe part of the earthquake occurred during an interval of only 10-15 seconds. The maximum acceleration of 0.33 g measured at El Centro is the strongest ground motion that has been recorded (the authors have no information on very recent earthquakes such as the one in Los Angeles in 1971). Data of this type are often used to establish the DBE ground motion at nuclear plant sites by retaining the time history and by linearly scaling the amplitudes to achieve a desired maximum acceleration.

The earthquake analysis of a Class I building requires a detailed mathematical model of the building's stiffness and mass distributions. The predictions of the building floor motions in response to the DBE ground motion are then used to establish the seismic requirements for equipment that will be located in that building. Fig. 2, for example, shows a typical 5-second record from the most severe part of the acceleration time history predicted for the floor of the auxiliary building of a nuclear power station. While

the acceleration time histories of the floor response could be included directly in equipment specifications, it has been customary in earthquake engineering to describe the equipment vibration environment by a response spectrum. The use of a response spectrum has particular significance as a method of characterizing a complex transient vibration in a way that is useful for determining how a simple structure will respond to that vibration. In particular, the earthquake response spectrum for a building floor is the maximum response of a series of single-degree-of-freedom oscillators that are excited by the floor motion. Each oscillator has a fixed percent of critical damping, but a different natural frequency, so the series of maximum responses gives a good representation of the frequency content of the floor motion. The floor response spectrum does not describe the acceleration versus frequency characteristic of the floor motion directly, and this is the principal source of misunderstanding by those who are familiar with the use of the Fourier spectrum or Fourier series to describe complex signals.

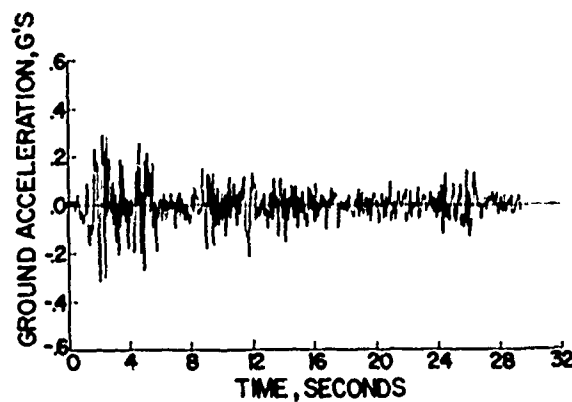


Fig. 1 - Ground acceleration record of North-South component of El Centro, California Earthquake, May 18, 1940

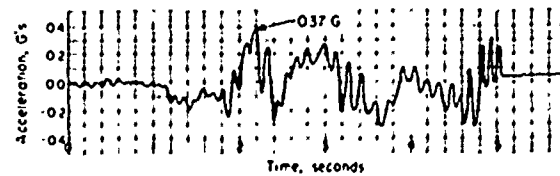


Fig. 2 - Typical horizontal building floor acceleration for DBE

The diagram shown in Fig. 3 of a series of mechanical oscillators resting on a building floor has proved useful for explaining the response spectrum. The floor acceleration time history,  $\ddot{y}(t)$ , would be predicted from a structural dynamics analysis of the building response to the DBE. The equation of motion for any one of the mechanical oscillators is

$$\ddot{z}_n(t) + 2\zeta\omega_n \dot{z}_n(t) + \omega_n^2 z_n(t) = -\ddot{y}(t) \quad (1)$$

where

$$z_n(t) = x_n(t) - y_n(t) \quad (2)$$

is the relative displacement between the mass and the floor,  $\omega_n$  is the undamped natural frequency of the  $n$ th oscillator, and  $\zeta$  is a selected value of critical damping ratio. There are many techniques available for calculating the displacement response time history,  $z_n(t)$ , and the maximum absolute value of the response,  $|z_n|_{\max}$ , can be obtained for each oscillator. The process can be repeated to determine a family of curves of  $|z_n|_{\max}$  versus natural frequency,  $\omega_n$ , for different values of damping, and this is the displacement response spectrum for the floor acceleration,  $\ddot{y}(t)$ . It is a matter of choice whether the maximum response parameter of relative displacement  $|z_n|_{\max}$ , relative velocity  $|\dot{z}_n|_{\max}$ , or absolute acceleration  $|\ddot{z}_n + \ddot{y}|_{\max}$  is plotted, because they are related for zero damping by the following equations:

$$|\dot{z}_n|_{\max} = \omega_n |z_n|_{\max} \quad (3)$$

$$|\ddot{z}_n + \ddot{y}|_{\max} = \omega_n^2 |z_n|_{\max} \quad (4)$$

A detailed discussion of the approximations involved for small damping can be found in Reference [2].

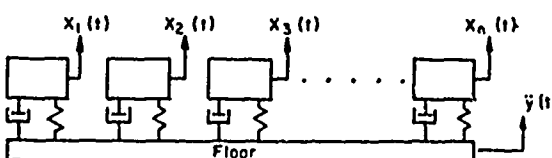


Fig. 3 - Series of mechanical oscillators used to determine floor motion response spectrum

Fig. 4 shows an acceleration response spectrum for the horizontal floor acceleration time history shown in Fig. 2. Most of the horizontal vibratory energy from earthquakes occurs at frequencies below 10 to 15 Hz, and the largest response of the building occurs at its natural frequencies. Therefore, the most severe vibrations will be experienced by floor-mounted equipment with natural frequencies close to those of the building. Equipment which is quite rigid (natural frequencies above about 30 Hz) will follow the floor motion exactly. Therefore, the acceleration amplitude which is approached asymptotically at high natural frequencies on the response spectrum is identical to the maximum floor acceleration that would be observed from the floor acceleration time history (see Fig. 2).

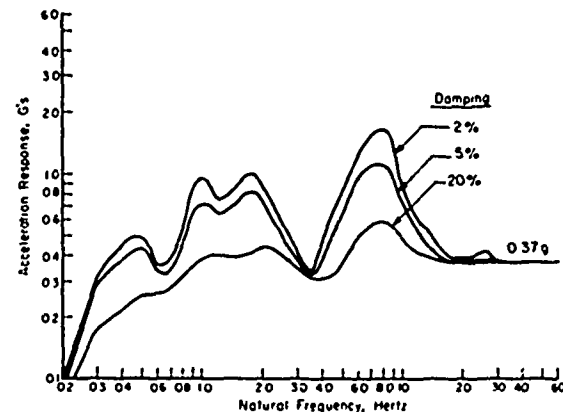


Fig. 4 - Floor horizontal acceleration response spectrum for DBE

#### SEISMIC VIBRATION STUDIES

The use of the response spectrum has some important advantages for designing structures to withstand earthquakes. However, its use as a specification of the earthquake vibration environment for equipment evaluation has some significant limitations resulting from the absence of all phase angle information. This makes it possible to devise any number of vibratory motions that will satisfy the response spectrum for a selected value of damping, many of which will have little resemblance to a typical earthquake floor acceleration time history.

Some of the different types of vibration currently being used to evaluate electrical equipment are decaying sinusoidal excitation, sine beat excitation, and constant amplitude sinusoidal excitation. All of these employ single frequency excitation so that a number of evaluations at different frequencies are required to cover the response spectrum.

Also, the response spectrum amplitudes for these motions vary more than the earthquake response spectrum for changes in damping. For example, the peak response spectrum amplitude of 1.1 g at 8 Hz for 5 percent damping shown in Fig. 4 can be satisfied by using a 0.11 g, constant-amplitude ( $Q = 1/2\zeta = 10$ ), sinusoidal vibration at the equipment base. However, if the equipment being evaluated has its lowest resonance at 8 Hz with only 2 percent damping ( $Q = 25$ ), the sinusoidal excitation would produce a peak acceleration of 2.75 g compared with about 1.6 g's for the floor earthquake motion--an "overtest" of 70 percent. The use of sine beat excitation is preferable to constant-amplitude sinusoidal excitation because the variation in the response spectrum amplitude with damping is less, but it is still different from that of an earthquake motion. This requires making conservative estimates of the expected equipment damping or measuring equipment damping at resonances--a procedure which is both expensive and possibly inaccurate because of nonlinearities.

The alternative of using the maximum floor acceleration amplitude to test at all frequencies may also severely overtest equipment. Furthermore, equipment with several resonant frequencies below 30 Hz will not respond to single frequency excitation in the same way it would respond to an earthquake motion, and the large number of evaluations required might produce fatigue failures that would never occur during an earthquake.

For these reasons, it seemed desirable to develop a more realistic simulation of the earthquake vibration environment. The principal goal was to be able to evaluate equipment efficiently while reducing the possibilities of subjecting it to vibration which might be considerably less severe or more severe than necessary. It would be quite dangerous to "undertest" the equipment, while overtesting might result in an unnecessary increase in the equipment cost.

#### SEISMIC VIBRATION FACILITY DESIGN

The first task in designing the Battelle-Columbus seismic vibration facility was to define the amplitude and frequency response requirements needed to reproduce the typical floor acceleration time history shown in Fig. 2. Preliminary processing of the acceleration data consisted of numerical integration to obtain velocity and displacement signals. The horizontal displacement reached a peak amplitude of 12 inches, with a predominant 0.3-Hz frequency plus some additional lower frequency component (the displacement did not return to the initial position within 5 seconds). Acceleration power spectral density curves for the 5-second signals were generated by Fast Fourier Transform techniques to provide some idea of frequency content. Large peaks were found at 0.3 and 0.9 Hz in

the spectrum of horizontal acceleration, with minor peaks at 1.5, 2.2, and 6.5 Hz. Negligible response was found above 10 Hz. The vertical acceleration power spectrum showed a predominant peak at 1.0 Hz, with lower amplitude peaks from 7 to 11 Hz and from 17 to 21 Hz. These amplitude and frequency requirements led to the selection of a servovalve-controlled hydraulic actuator to power the vibration table.

Since the type of equipment to be evaluated by this seismic vibration simulator was not expected to respond to large displacement components at low frequencies (below 1 Hz), one of the first design decisions was to limit the total actuator stroke to 6 inches (peak-to-peak). This was done in order to minimize the entrapped oil in the hydraulic actuator, thereby keeping the oil-column stiffness high and maximizing the high-frequency response capability. To keep the commanded displacement within this 6-inch limit, a high-pass filter was used in series with the acceleration command signal to attenuate frequency components below 1.5 Hz. Analog acceleration signals were recorded on FM tape by digital-to-analog conversion of the original digital computer data for use as simulator command signals. Command accelerations and the resulting filtered displacements used as a basis for the facility design are shown in Fig. 5. Peak accelerations of 0.37 g in the horizontal and 0.25 g in the vertical direction were recorded during five seconds of the floor vibration response data for the DBE.

The design of the seismic vibration facility included consideration of several tradeoffs necessary to achieve a "cost-effective" facility. Simultaneous vibration in vertical and horizontal directions, while desirable for achieving the most realistic simulation, was not incorporated because of its considerably greater cost and complexity. The coupling effects of simultaneous vertical and horizontal floor motions during an actual earthquake are reduced in importance by their considerable difference in both amplitude and frequency content. It is quite unlikely that the maximum accelerations will occur simultaneously in time for the two directions.

Physical size of the simulator was based on an estimate of equipment sizes to be evaluated in the foreseeable future. This limit was chosen to be about 3000 pounds in weight with maximum base dimensions of about 80 by 48 inches.

To provide a table with minimum weight and maximum stiffness, a equilateral triangle of steel I-beams with three angle-bisecting beams in the center was designed. The single hydraulic actuator is attached below the table centroid, and the actuator can be rotated 90 degrees to provide motion in either vertical or horizontal directions. Normal

modes of vibration of the table when actuated at the centroid were calculated by means of a finite-element digital computer program, and all natural frequencies were predicted to exceed 50 Hz. Support and guidance of the table in the horizontal mode are provided by Thomson "Roundways", while in the vertical mode a combination of Roundways and linear ball bushings is used for guidance at the three corners of the table. Three Firestone "Aride" springs connected through a pressure regulator to shop air are used to support the static weight of the table and equipment for excitation in the vertical direction. Fig. 6 shows the seismic vibration table positioned for vertical motion.

Reproduced from  
best available copy.

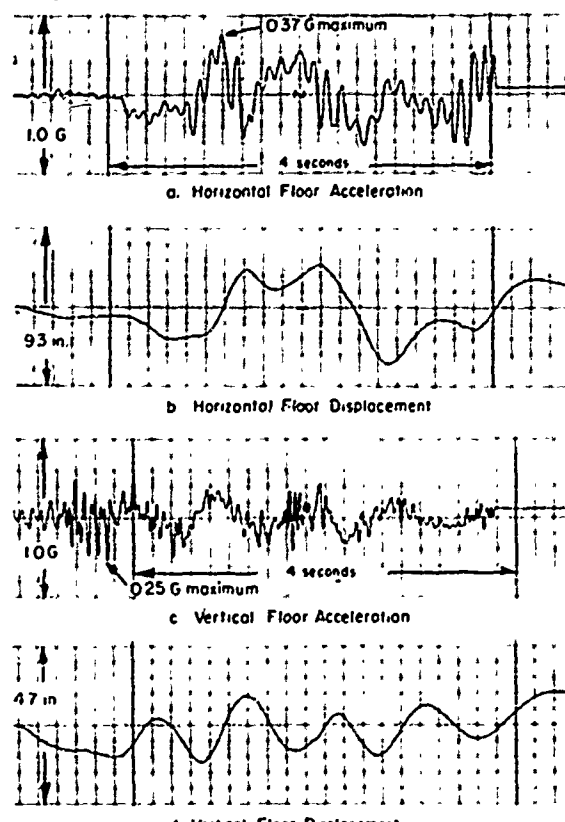


Fig. 5 - Acceleration and filtered displacement time histories of building floor response

An I-beam frame is used to provide a base for accurate alignment of the guideways and actuator. This base is fastened to a heavy "strongback" formed of 36-inch-deep I-beams located beneath the floor level of the laboratory. The strongback, fastened to a heavy concrete slab, provides the necessary seismic mass against which the simulator can react.

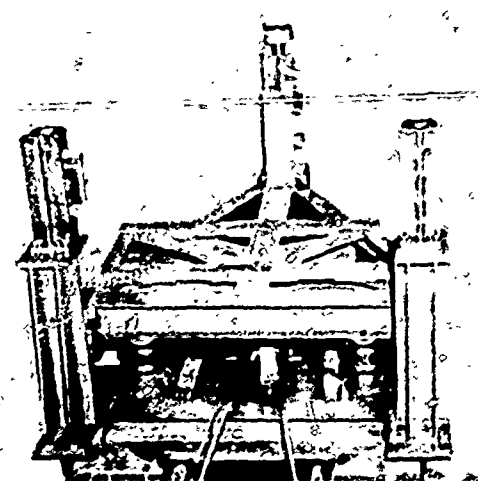


Fig. 6 - Battelle Seismic Vibration Table in vertical mode

Conflicting requirements of stiffness (oil-column resonance) and maximum oil flow rate at peak velocity dictated the choice of actuator size. A 2-1/2-inch bore, 1-inch rod, double rod-end cylinder was chosen to mate with an available 3000-psi, 25-gpm hydraulic supply and Moog 76-104 (15-gpm) flow control servovalve. For this size of actuator, a minimum oil-column resonant frequency of 22 Hz was estimated based on an assumed effective oil bulk modulus of 100,000 psi (in tests this resonance was found to be about 25 Hz).

Since the hydraulic power supply is located some distance from the simulator, a 1-gallon bladder accumulator, 10-micron filter, and solenoid shut-off valve are located at the base of the vibration table, with short lengths of hose supplying fluid to an actuator-mounted manifold. The servovalve and crossover relief valve are attached directly to this manifold to provide minimum entrapped oil on the "active" side of the servovalve. Safety functions (over-travel limit switches and servo over-command voltage level) deenergize the shut-off valve in the event of a system failure and stop the table with a maximum acceleration of about 0.75 g.

Design of the servo controller was based on the salient fact of life of a hydraulically actuated inertial load: the oil-column resonance [3]. This resonance results from the mass of the table and equipment oscillating on the effective stiffness of the entrapped oil, piston rod, and actuator support structure. Without compensation, the oil-column resonance adds a pair of lightly damped complex poles to the root locus plot. Several methods can be employed to control the

effects of oil-column resonance [4]: acceleration feedback, pressure feedback (in conjunction with a pressure control servovalve), or controlled bypass flow, for example.

Adjustable bypass flow using a needle valve and small tube across the actuator is an effective, yet inexpensive, method of controlling the resonance. The effects of introducing bypass flow (based on a linear estimate of system response) are sketched in the root loci of Fig. 7. For comparable values of forward-loop gain (the parameter  $K_a$  represents servo amplifier gain in amps per volt), the system with bypass flow is far more stable--this is shown by the reduced angle of a vector from the origin to the gain-dependent root. One disadvantage of bypass flow is the lower frequency of the resonant peak for desirable levels of damping.

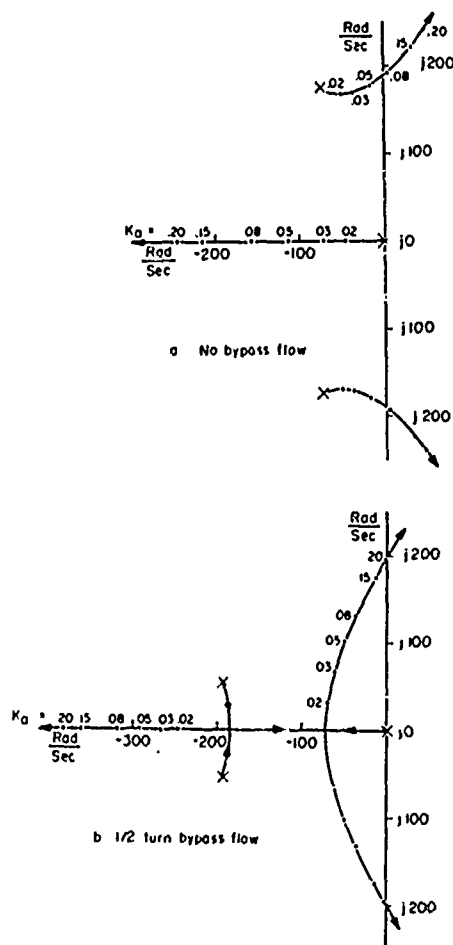


Fig. 7 - The effect of actuator bypass flow on root loci of the lower-frequency terms, hydraulic system with inertial load

Fig. 8 shows the control system in block-diagram form with linearized transfer functions for the major components. Primary servo-system feedback is derived from a position transducer (DCDT) mounted on the actuator. The position feedback signal is subtracted from the filtered, double-integrated acceleration command signal to provide the error signal to the servovalve. A modified acceleration feedback signal from a strain-gage accelerometer mounted on the table is also summed with the error signal to improve system response in the 10 to 20-Hz range.

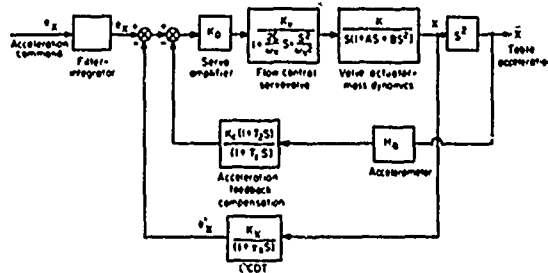


Fig. 8 - Seismic vibration facility control system

#### SEISMIC VIBRATION FACILITY PERFORMANCE

Closed-loop frequency response evaluations were conducted with a 1500-pound dummy equipment load on the table at normal acceleration amplitudes. A constant-amplitude voltage command to the double integration circuit was varied from 1 to 40 Hz, and the resulting table acceleration was monitored using a Quan-Tech Model 304TD wave analyzer to track the fundamental component of acceleration with a 1-Hz bandwidth filter. The results of the sinusoidal closed-loop frequency response evaluation are shown in Fig. 9. A second-order resonance with a +3-dB peak is evident at 10 Hz, and the effective system bandwidth (-3 dB point) is about 14 Hz for the command signal amplitude of 0.2 g.

While the closed-loop frequency response of the control system determines the capability of accurately reproducing a complex acceleration time history, the maximum acceleration determined by the actuator stroke, flow rate, and force limitation is the most significant parameter for any type of sinusoidal testing. Fig. 10 shows the maximum table accelerations that have been measured for the frequency range of 1 to 25 Hz. Accelerations are limited by the maximum flow rate of the servovalve at frequencies from about 1 to 10 Hz and by the maximum actuator force of about 7500 pounds at higher frequencies. Since the maximum floor accelerations seldom exceed 0.5 g for a DBE, the acceleration capability is adequate for frequencies above 2 Hz. Lower frequencies are of little practical interest because the lowest equipment resonant frequencies are seldom below 5 Hz.

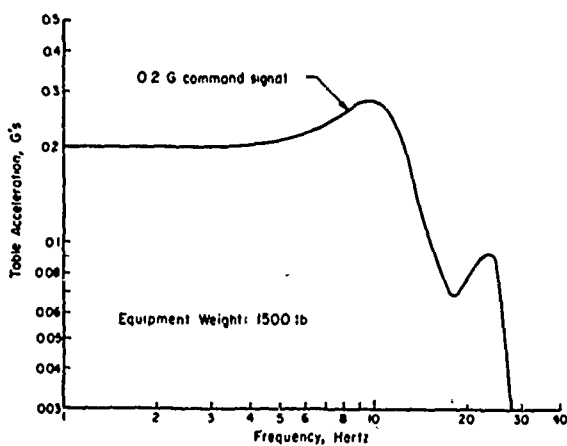


Fig. 9 - Table acceleration response to sinusoidal, constant-amplitude acceleration command signal

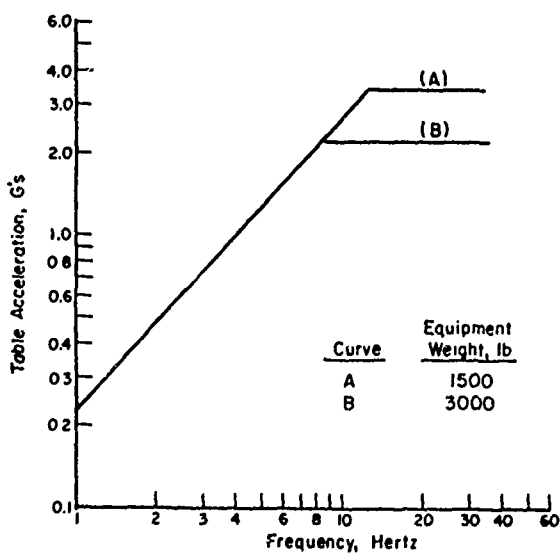


Fig. 10 - Maximum acceleration capability of seismic vibration table for sinusoidal excitation

Figures 11 and 12 show the capability of the vibration table to reproduce a floor-acceleration time history. The results in Fig. 11 show that the use of a high-pass filter to attenuate low-frequency components and the presence of some high-frequency noise makes it difficult to evaluate control system performance by comparing the time histories of the command and output signals. However, a comparison of the response spectra, Fig. 12, for the floor-acceleration command signal and the resulting table acceleration indicates acceptable agreement. The amplitude of the table acceleration can be increased above the 0.37-g maximum acceleration for the DBE so that the response spectrum of the table motion exceeds the required spectrum at all frequencies where any type of equipment resonance might occur (i.e., above 4 to 5 Hz). The increase in amplitude required to compensate for filter characteristics can be reduced by using an increased rate of filter attenuation (sharper filter) in the control system or by preprocessing the original floor-acceleration time histories with digital computer filter algorithms prior to obtaining an analog signal. High-frequency noise can be reduced by using an actuator with low-friction seals and extending the control system bandwidth by improved compensation for the oil-column resonance.

Fig. 11 consists of two time-history plots, (a) and (b), showing horizontal floor acceleration and horizontal table acceleration respectively over a period of 5 seconds. Both plots show a complex waveform with high-frequency noise superimposed on a lower-frequency oscillation. The x-axis is labeled 'Time, seconds'.

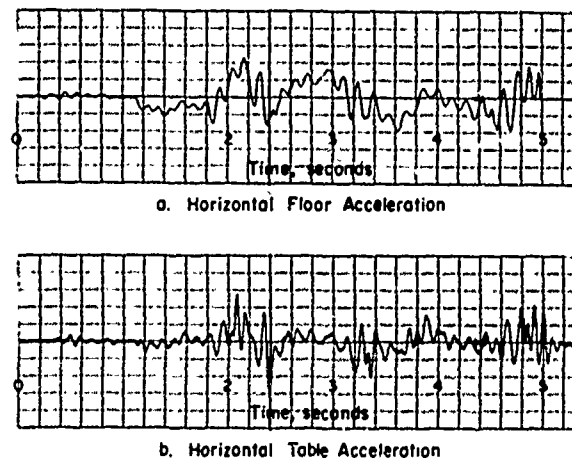


Fig. 11 - Comparison of horizontal table acceleration with DBE floor acceleration command signal

#### SEISMIC EVALUATION RESULTS

The seismic vibration facility has been in operation at Battelle-Columbus since February, 1971, and seismic evaluation programs have been completed for a variety of Class I electrical equipment. Results from this work are summarized briefly to provide equipment designers with some typical data on the natural frequencies, damping factors, and electrical performance of this type of equipment. Fig. 13 shows a typical electrical equipment cabinet mounted to the seismic vibration table and being subjected to earthquake excitation in the front-to-back horizontal direction. The equipment is energized electrically during the seismic evaluation and all critical electrical performance parameters are monitored continuously.

## VIBRATION CHARACTERISTICS

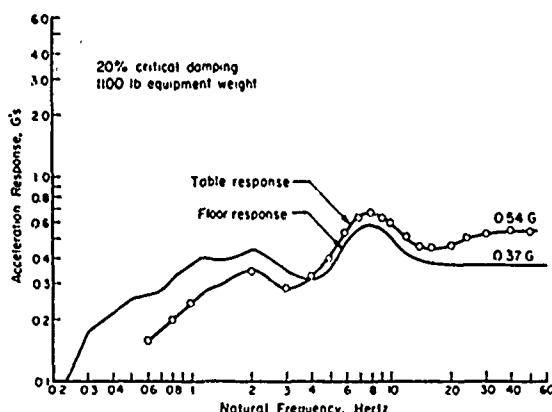


Fig. 12 - Comparison of vibration table horizontal acceleration response spectrum with floor response spectrum for DBE



Fig. 13 - Time exposure of typical equipment during horizontal vibrations

It is a general practice to conduct a brief vibration survey of each equipment unit in order to identify major natural frequencies prior to evaluating its electrical performance under specified seismic conditions. Table 1 lists the natural frequencies which have been measured for a variety of electrical equipment. These natural frequencies were determined by comparing the acceleration amplitudes from accelerometers located at the base and near the top of the equipment cabinet. While this procedure is satisfactory for determining the major structural natural frequencies of the cabinets, the identification of local panel resonances and resonances of components mounted inside the cabinet requires more extensive measurements than are practical. Therefore, an evaluation procedure which is based on exciting the equipment cabinet with sinusoidal vibration only at natural frequencies has the risk of missing a resonance of some small component that could cause an electrical failure.

TABLE 1

Typical Natural Frequencies of Electrical Equipment Cabinets

Item No.	Equipment Size, in.	Equip. Wt., lb	Natural Frequencies, Hz		
	W	D	H	Horiz.	Vert.
1	36	24	90	2350	4.5, 5.0 ---
2	36	24	90	700	9.5, 10 ---
3	60	20	90	1500	7.5, 7.5 ---
4	36	24	56	1200	11, 12.5 20
5	30	30	75	800	10.5, 11.5 ---
6	60	30	75	2000	9.5, 10.5 ---

The data in Table 1 indicate that it is unrealistic to expect equipment of this type to be designed to have horizontal natural frequencies above the maximum excitation frequency for earthquakes (about 20 Hz). Natural frequencies should be increased as much as possible during design by locating heavy components near the cabinet base and sizing the structural members at the cabinet base to transmit the inertial loads to the mounting bolts without excessive deflections. However, experience indicates that it is even more important for designers to consider the details of the mountings used for the components inside the cabinets. A broken mounting bracket for a transformer weighing about 100 pounds is the only structural failure of any type that

has been observed. However, even this failure occurred only after extensive exposure to sinusoidal excitation at resonance caused a fatigue condition that would not be expected from an earthquake.

The data in Table 2 show the apparent magnification factors and corresponding critical damping ratios measured while a typical equipment cabinet was excited at resonance at different acceleration amplitudes. The selection of an appropriate damping factor is one of the most difficult and important judgments that must be made for any type of dynamics study. This type of equipment usually has damping factors no lower than about 3 percent, and in most cases the damping is in the range of 5 to 10 percent of critical. However, the increase in damping with vibration amplitude shown in Table 2 can be expected for this type of equipment, indicating that nonlinear effects are quite significant.

TABLE 2 Effect of Acceleration Amplitude On Damping For A Typical Electrical Equipment Performance				
Equip. Base Accel., g's*	Equip. Top Accel., g's	Magnifi- cation Factor	Damping, Percent Critical	
0.11	1.2	11	4.5	
0.25	2.1	8.4	6.0	
0.39	2.6	6.7	7.5	
0.67	2.9	4.3	11.6	

\* - Constant-amplitude horizontal sinusoidal vibration at 8 Hz natural frequency.

#### EQUIPMENT PERFORMANCE

It is encouraging to report that most of the electrical equipment that has been subjected to vibration simulating the DBE for nuclear power generating stations has performed satisfactorily without any significant design changes. No examples of cabinet structural damage to the main structural members or hold-down bolts have been observed. The few electrical failures that have occurred were usually caused by high-voltage arcing or relays which malfunction. Failures have been observed in some meters which are often mounted on a flexible door panel, but a failure in this type of component seldom affects the primary functional performance of the equipment.

#### CONCLUSIONS

The results which have been achieved to date indicate the feasibility of using the actual floor-acceleration time histories predicted for a DBE to evaluate electrical equipment performance. The use of this type of realistic excitation substantially reduces the possibility of overtesting or undertesting the equipment. Furthermore, the vibration evaluation portion of a seismic evaluation program can be reduced substantially, since a preliminary survey for natural frequencies is unnecessary and the total exposure to the earthquake environment can be limited to about 60 seconds in each direction.

It is expected that the appropriate acceleration time histories can be supplied by the nuclear utilities once the advantages of using a more realistic earthquake simulation are recognized. However, there are some cases in which the use of an artificial earthquake signal has some important advantages. This type of signal can be generated using digital or analog techniques to modify wide-band noise with appropriate filters to produce a time-history signal having any desired response spectrum characteristic. Battelle's digital computer facility has been used to generate an artificial signal having a relatively flat (constant amplitude) acceleration response spectrum over the frequency range of 2 to 20 Hz. This type of excitation is desirable for evaluating equipment that will be installed in several different nuclear power generating stations where the seismic requirements are similar but where the particular time histories and response spectra depend on the different building natural frequencies and location of the equipment in the building.

#### ACKNOWLEDGMENT

The authors are grateful to the assistance of Mr. Charles Rodman and the other members of the Mechanical Dynamics Division at Battelle who have contributed to the design and operation of the seismic vibration facility. They also wish to express their appreciation for the cooperation and encouragement of Mr. Julius Tangel of the Public Service Electric and Gas Company.

#### REFERENCES

1. John A. Blume & Associates, "Summary of Current Seismic Design Practice for Nuclear Reactor Facilities", United States Atomic Energy Report TID-25021, Sept. 1967.
2. R.D. Kelly and C. Richman, "Principles and Techniques of Shock Data Analysis", SVM-5, The Shock and Vibration Information Center, Naval Research Laboratory, Washington, D.C., 1969.

3. V.H. Larson, "The Control of Acceleration by Electrohydraulic Shaker Systems", MTS Systems Corp., Technical Bulletin 840.00-1.
4. L.H. Geyer, "Controlled Damping Through Dynamic Pressure Feedback", Moog, Inc. Technical Bulletin 101.

## SHOCK INPUT FOR EARTHQUAKE STUDIES USING GROUND MOTION FROM UNDERGROUND NUCLEAR EXPLOSIONS\*

D. L. Bernreuter, D. M. Norris, Jr., and F. J. Tokarz  
Lawrence Livermore Laboratory, University of California  
Livermore, California

Comparisons are made between the ground motion from earthquakes (EQs) and underground nuclear explosions (UNEs). It is shown that peak g-levels and response spectra form a reasonable basis for comparison. Several approaches which attempt to characterize the time history are also discussed. It is shown that (1) the peak g-levels from UNEs have magnitudes comparable to those estimated for the strongest EQs, (2) the spectra from UNEs are similar to those from EQs, and (3) a time history comparison shows that both the duration of strong motion and the number of near-peak g-level cycles for UNEs fall within the range established for strong EQs. Based on these results it is concluded that ground motion from UNEs can provide an EQ-like environment for testing full-scale structures.

### INTRODUCTION

The recent San Fernando earthquake ( $M = 6.3$ ) provided the first real test of earthquake-resistant design as practiced in California. Many structures failed the test. This earthquake caused 64 deaths and an estimated \$553 million damage. The major cause of death was catastrophic collapse of multi-story buildings.

Earthquake-resistant design criteria used in California building codes are based on static approximation of the dynamic loads produced by earthquakes. These criteria require that the structure be capable of carrying a set of static lateral loads whose magnitudes and distribution are chosen so as to approximate the effects of the dynamic loads an earthquake might be expected to produce. In view of the damage caused by the San Fernando earthquake, it is clear that this static approximation method is inadequate.

The design of structures to withstand EQ (earthquake) forces requires a more detailed theoretical approach—one involving thorough dynamic analysis—to guarantee basic survivability. Significant capability for such analysis now exists with the computers and software presently available. Computer methods produce a dynamic analysis by idealizing the real structure into a mathematical model and then determining the response of the model to some prescribed ground motion. However, due to the lack of sufficient experimental data, cur-

rent methods of formulating mathematical models of real structures are not yet developed to the point where they can readily produce accurate models for most structures. This is true even for very low level seismic input, as shown by Tokarz and Bernreuter [1]. It has been very difficult to correlate results obtained from analysis with actual dynamic behavior of full-scale structures, principally because not much detailed data exists on actual dynamic behavior of structures during earthquakes.

Dynamic tests have been conducted on some large-scale structures in order to develop more accurate mathematical models [2]. However, because of the power and mass limitations of existing vibration generators, the amplitudes of vibration in these tests have not been large enough to cause substantial inelastic deformation. The dynamic response information is therefore valid only for small amplitudes of vibration. Since substantial inelastic deformation usually occurs prior to catastrophic failure, it is most important to treat the vibration problem at the relevant amplitudes. This highly nonlinear behavior makes it extremely difficult to apply the data that can be obtained from model tests [2]. The cost of building a shaker facility large enough to test full-scale structures has been estimated to be approximately \$20 million [3]. Even then the size and type of structure would be severely limited.

An alternative approach would be to use the ground motion from an underground nuclear

\*Work performed under the auspices of the U. S. Atomic Energy Commission.

explosion (UNE) to excite properly located structures to EQ-like ground motion. Several major advantages of using the ground motion from UNEs are: (1) the ground motion is available free as a by-product from nuclear tests, (2) there is no limit on the size or type of structure that could be tested, and (3) true soil-structure interaction would be achieved.

The ability to test any type of structure and the achievement of true soil-structure interaction are important. For example, underground nuclear reactors and storage containers can be tested. In fact, for many types of large structures this technique of subjecting the full-scale structure to ground motion from a UNE seems to be the only practical way to investigate the structure's response to an EQ.

#### CHARACTERIZATION OF EQ GROUND MOTION

The feasibility of simulating EQ ground motion with UNE-induced ground motion depends on the similarity of the two phenomena. The mechanism of energy release is much different in a UNE than in an EQ. There are considerable similarities and also considerable differences between the induced ground motions depending on the criteria of comparison. The choice of criteria will depend upon the purpose for making the comparison. For example, criteria used by seismologists to compare UNE and EQ ground motion from the viewpoint of seismic detection of underground testing [4] are quite different from criteria used by structural engineers whose basic concern is the response of structures.

In order to show that UNE-induced ground motion is similar to that from EQs it is necessary to establish a means of properly characterizing EQs from the point of view of structural response. Many studies have been made to develop the best means of characterizing EQ ground motion [5-10]. However, this has proved difficult to accomplish, one reason being that only a few records of strong-motion EQs exist (here strong motion is arbitrarily taken to be a peak g-level greater than 0.1 g). These records show a large variation in pulse shape, time of duration, peak g-level, and number of cycles. Some of the complex causes of these variations are discussed in a paper by Trifunac [8].

The most generally used criteria to characterize EQs for structural studies are (1) peak g-level, (2) response spectra, (3) Fourier spectra, (4) power spectral density, and (5) time history comparisons. None of these criteria are completely satisfactory.

Peak g-level has the advantage of being extremely simple to compare. It is also physically meaningful. Nevertheless, peak g-level alone is not adequate to characterize EQs [7].

In addition, no clear relation between EQ magnitude and peak g-level has been established. This is shown in Figs. 1 and 2. Figure 1 gives a correlation of g-level vs distance from the closest point of observed faulting. The EQ magnitudes range from 5.5 to 8.3. It should be noted that the peak g-level from the San Fernando EQ was around 1 g. Figure 2 gives a correlation by Housner [11] relating EQ magnitude to peak g-level and range. Also shown in this figure are the Parkfield EQ ( $M = 5.7$ ) and the San Fernando EQ ( $M = 6.3$ ). As can be seen, these clearly do not fit Housner's projected correlation.

The response spectrum has been preferred for structural engineering studies of strong-motion earthquakes, because it combines both the representation of the exciting force and the response calculations. It thus lumps together under one representation the major parameters of interest to the structural engineer. The major disadvantage of the response spectrum is that only peak response is determined. The number of near-peak response cycles, which are important for studying post-yield behavior of structures, is lost.

The Fourier spectrum of an input function shows directly the significant frequency characteristics of the function, and from it the time-history response of the system can be computed. However, in the study by Jenschke et al. [5] it was found that results obtained using the Fourier spectral method were not satisfactory: the sine and cosine Fourier transforms showed high irregularities of the same order as the ground acceleration function, and no correlated characteristics could be found. These high irregularities make it difficult to use the sine and cosine Fourier spectra for comparison purposes. Hudson [6] showed that the Fourier amplitude spectrum is much more regular and is very closely related to the relative velocity spectrum. It has no advantage over the relative velocity spectrum and in fact is inferior in that the peak levels may be lost; time-history aspects are also lost.

The power spectral density approach is attractive in that it allows a probabilistic approach to be used. However, Jenschke et al. [5] found that this approach was inadequate since ground motions produced by EQs and UNEs are essentially nonstationary phenomena, even for dynamic systems having natural periods considerably shorter than the duration of the ground motion. This is a serious problem when dealing with the ground motion from UNEs because the duration of shaking is quite short—about 5 to 15 sec as compared to 30 sec for the El Centro EQ.

Several investigators have made attempts to generate artificial accelerograms using various nonstationary processes. But as pointed out by Trifunac [8] the models generally

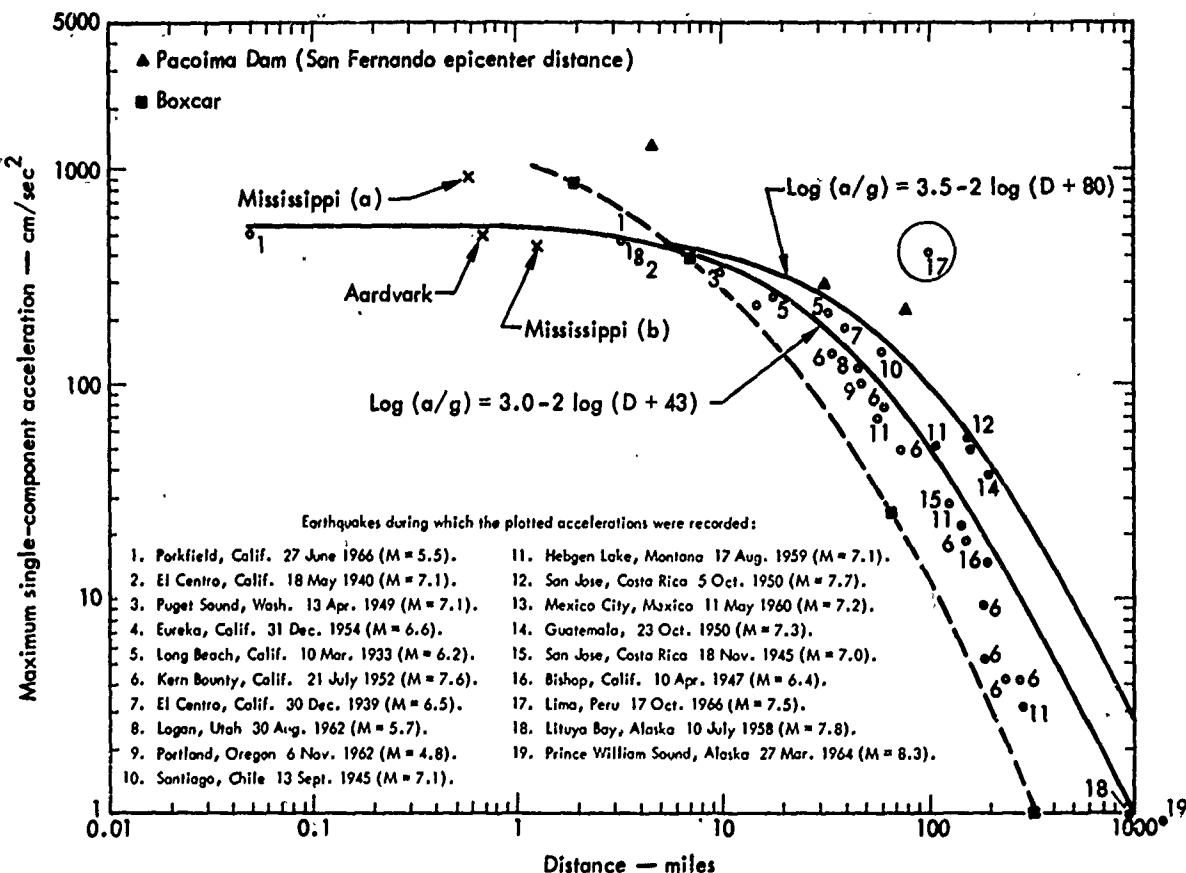


Fig. 1 - Plots of g-level vs distance from closest point of observed faulting. From Cloud and Perez [10]

used are too simple. This results from a lack of knowledge of the actual character of strong motion accelerograms. At the present time these investigations have not progressed far enough to make use of here.

Direct time-history comparisons are usually not made except to obtain qualitative insight into the nature of the ground motion. Some generalized time-history characterization of EQ ground motion is needed to study the post-yield behavior of structures. No such characterization exists. Cloud and Perez [10] suggested comparing total time the acceleration was above a certain g-level. Figure 3 shows such a comparison for the Parkfield and El Centro EQs. It is not at all evident from this figure that the El Centro EQ was by far the more damaging.

Other investigators suggest counting the number of cycles of a given g-level. Both this suggestion and the previous one (total time above a certain g-level) give some useful information, but they do not properly characterize

the time histories relative to post-yield behavior of structures.

Trifunac [8] suggests using the response envelope spectrum which is a three-dimensional plot of magnitude of response of one-degree-of-freedom oscillators vs time and frequency. Only some accelerograms from the 1940 El Centro EQ have been studied in this way; hence at the present time this approach—while interesting—does not offer a meaningful characterization of EQs.

The above discussion summarizes the approaches generally suggested to characterize EQ ground motion for structural response studies. It is clear that no adequate single characterization exists. Based on this discussion we plan to establish a similarity between EQ and UNE ground motion by showing that (1) the peak g-levels from UNEs are within the range estimated for the strongest EQs, (2) the response spectra from typical UNEs are similar to those of strong EQs, and (3) the duration of

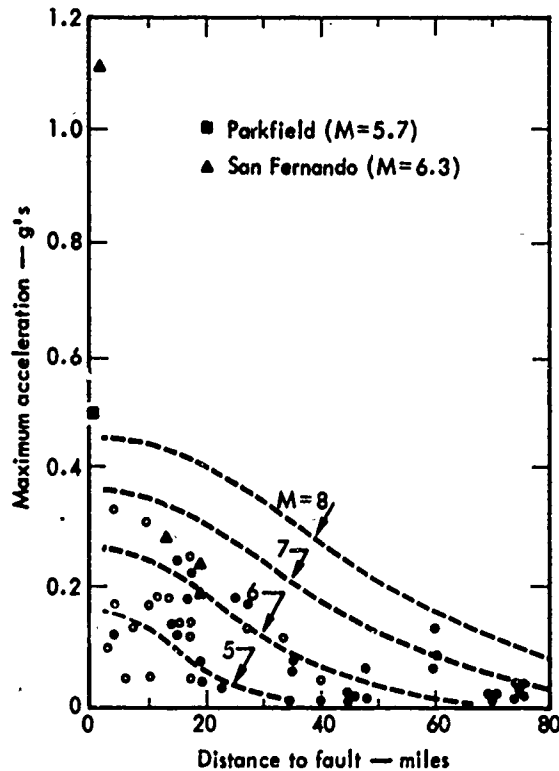


Fig. 2 - Plots of earthquake magnitude and peak g-levels vs range. From Housner [11]

the pulse and the number of cycles of peak g-levels fall within the range established by major EQs.

#### COMPARISONS OF UNE AND EQ GROUND MOTION

##### Peak g-Level Comparison

Most of the published correlations of UNE ground motion data deal with peak g-levels below those of interest [13,14]. To extrapolate this data to close-in distances leads to gross errors. The most comprehensive discussion of surface ground motion from UNEs in the strong motion regime is that by Bernreuter et al. [12].

The magnitude of the peak g-level at the ground surface from a UNE depends on several factors [12]. These include (1) yield, (2) the depth of burial (DOB), (3) distance from surface ground zero (range), (4) geology around the explosive, and (5) geology through which the wave is transmitted. For a given yield the peak surface ground motion can vary by a factor of 20. But since devices of a given yield are usually buried in similar geologies (and at similar depths) it becomes more meaningful to talk about general curves of peak g-level versus yield and range.

Figure 4 is a plot of peak g-level versus range for "typical" nuclear explosive yields of 10, 100, and 1000 kt (kilotons). For ranges less than 1 DOB the value plotted is the initial acceleration. In this regime, the motion is such that the top several hundred feet of earth spalls away from the lower layers, often causing a larger peak g-level when the spall gap closes. It would be undesirable to locate test structures within this spall regime.

It is clear from this figure that the peak g-level of the strongest EQ can be easily duplicated, or exceeded (if desired), by a UNE. See Fig. 1 for estimated EQ peak g-levels.

##### Response Spectra Comparisons

Various types of response spectra can be generated. These include relative displacement, relative velocity, and absolute acceleration spectra. For low assumed values of viscous damping (less than 10% critical) all of the above spectra are related [6]. Since all of the spectra to be considered for comparison have low values of damping, only the velocity spectrum will be used.

No standard EQ spectrum has been generally accepted for comparison purposes [7]

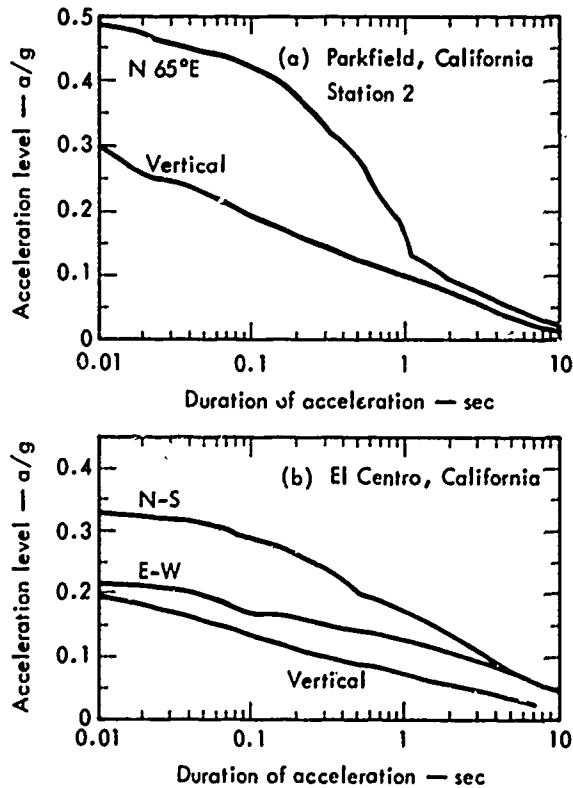


Fig. 3 - Comparison of Parkfield and El Centro earthquakes

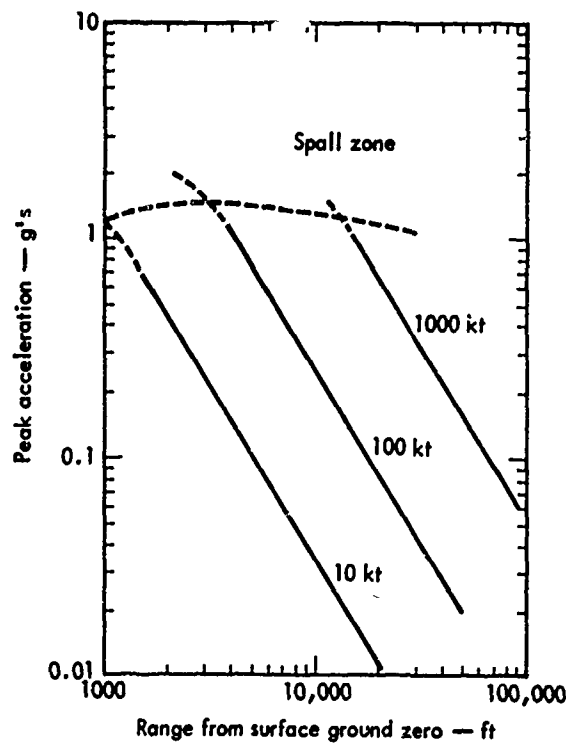


Fig. 4 - Peak radial acceleration for typical UNEs as a function of range for several yields

(although several have been proposed). Comparison herein will be made relative to the El Centro (1950, NS), Olympia (1949, N80E), and Taft (1952, N21E) spectra; these are the spectra most used for design studies.

There is substantial variation in spectra between different EQs and between the same EQ recorded at different stations. Figure 5 shows a comparison of the above-mentioned EQs. Figure 6 shows two stations from the Parkfield EQ, both having a peak acceleration level of 0.5 g. A comparison of Figs. 5 and 6 shows even greater differences between the same EQ at different stations than between different EQs.

Spectra of the UNE ground motion recorded off NTS have been extensively studied [15,16]. However, extrapolation of these studies to locations much closer to ground zero is not valid.

Spectra of the close-in ground motion from UNEs have not been extensively computed or studied. This is because most permanent NTS structures are simple, one-story, strongly built field-type structures located out of the very strong motion regime. Also, for close-in survivability, the peak g-level and change in kinetic energy are the important parameters. This limits (at this time) our choice of UNE ground motion for comparison.

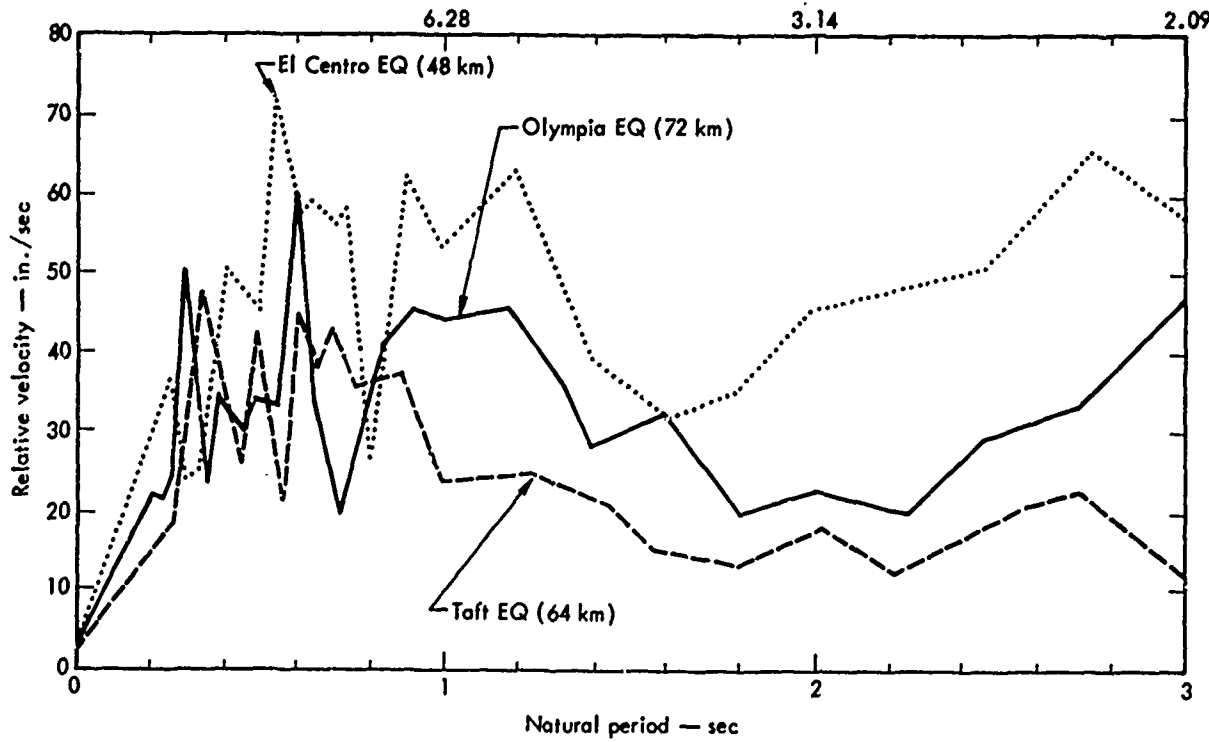


Fig. 5 - Comparison of El Centro, Olympia, and Taft EQs

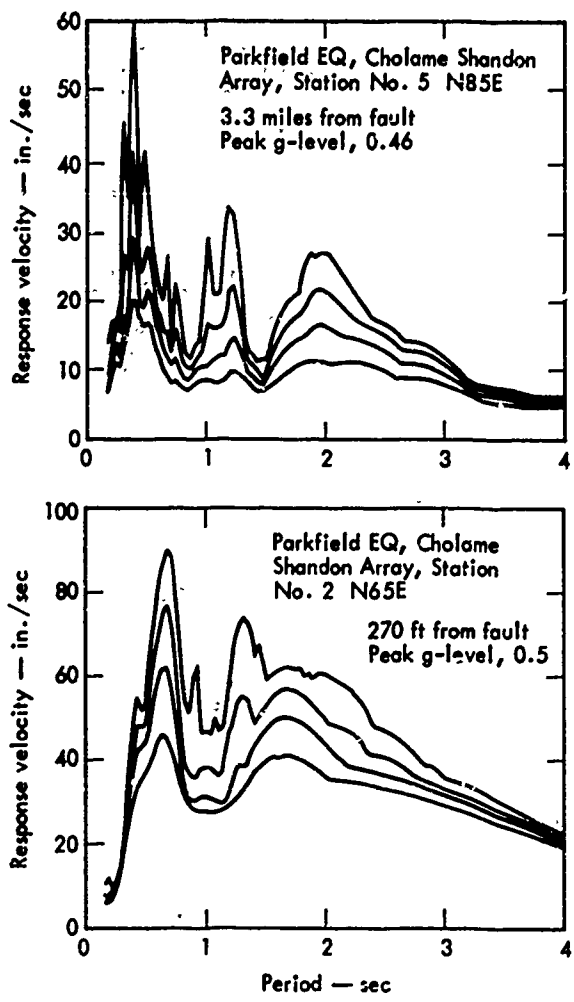


Fig. 6 - Response spectrum from Parkfield EQ (June 1966) at two stations

Table 1 lists four events for comparison purposes. These events were chosen since they cover a wide range in yield and geological conditions. Figure 7 compares Mississippi (a) and El Centro. Figure 8 compares Mississippi (b), Aardvark, and Olympia. Figure 9 compares Blanca and Taft, and Fig. 10 compares Halfbeak and El Centro.

A study of Figs. 7-10 shows that the response spectra from typical UNEs are similar to those from strong EQs. Furthermore, the variations between the UNEs and EQs are no greater than the variations between the EQs themselves, as shown in Figs. 5 and 6. Carder and Cloud [17] also noted this similarity between EQ spectra and UNE spectra.

#### Time-History Comparisons

Figure 11 shows accelerograms from three UNEs, namely Aardvark, Mississippi, and Boxcar (1.2 Mt). (No accelerogram was available for Halfbeak; the spectrum was computed from a velocity transducer.) The duration of strong phase motion (peak g-level greater than 0.1 g) is approximately 2 sec for Aardvark and over 7 sec for Boxcar. This figure shows in addition that the duration of strong motion from a UNE increases with larger yield and also with increased distance from ground zero.

Figure 12 shows the accelerograms from the El Centro, San Fernando, and Parkfield EQs. The duration of strong shaking for these EQs was 20, 10, and 1.5 sec, respectively. The number of near-peak g-level cycles of ground motion ranged from 3 for the Parkfield EQ to over 10 for El Centro.

The accelerograms of the EQs and UNEs shown are quite different. Nevertheless, the duration of strong motion and the number of cycles of near-peak g-level for the UNEs fall

TABLE 1  
Sources of UNE Spectra

Event	Yield (kt)	Geology	Recording Range (ft)	Peak g-Level	Ref.
Mississippi (a)	20-200	Tuff overlaid with deep alluvium	3280	0.98	[5]
Mississippi (b)	—	—	6560	0.45	[5]
Halfbeak	300	Saturated tuff overlaid with dry tuff	7000	—	[19]
Blanca	19	Tuff	5310	0.5	[17]
Aardvark	38	Tuff overlaid with deep alluvium	3600	.74	[5]

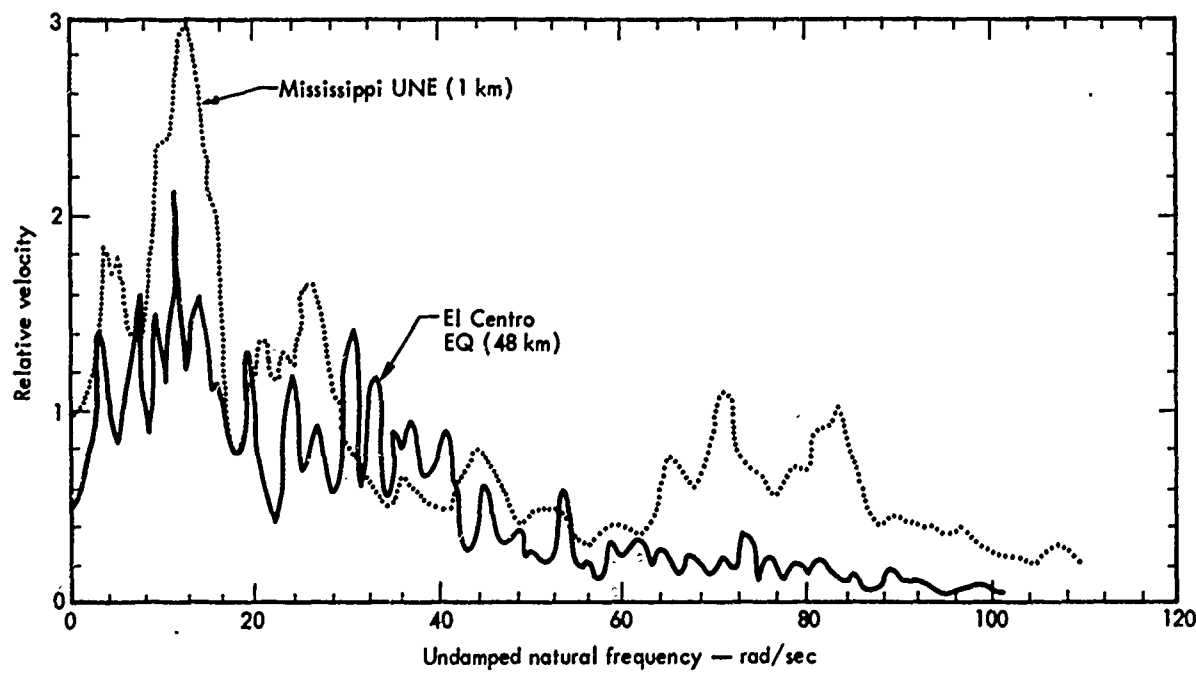


Fig. 7 - Mississippi UNE vs El Centro EQ. Relative velocities normalized by dividing original velocities by 0.1 g

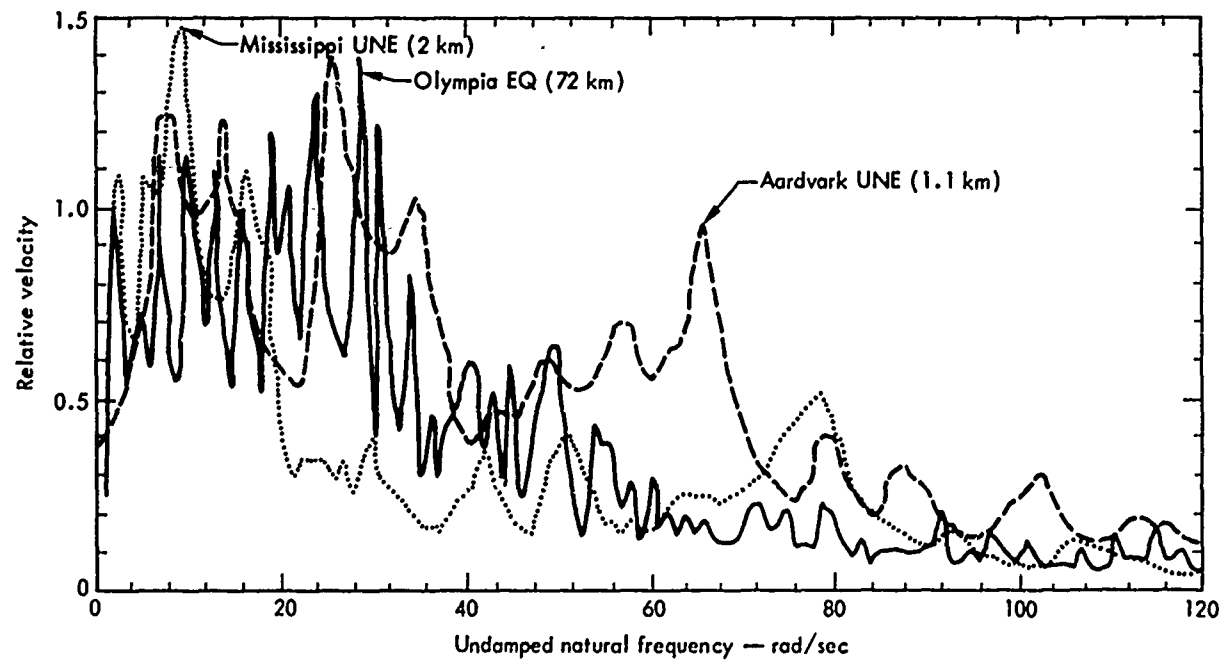


Fig. 8 - Mississippi and Aardvark UNEs vs Olympia EQ. Relative velocities normalized by dividing original velocities by 0.1 g

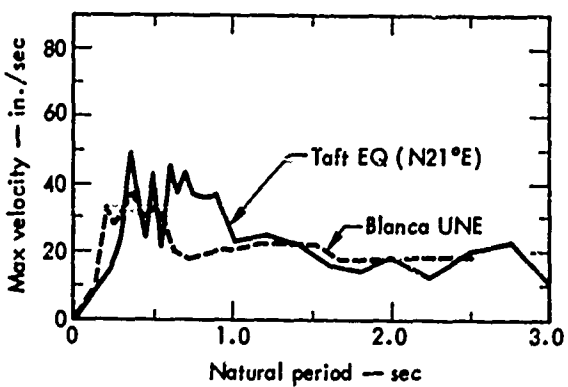


Fig. 9 - Blanca UNE vs Taft EQ

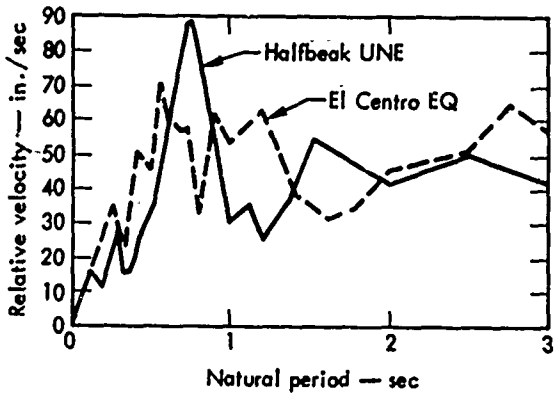


Fig. 10 - Halfbeak UNE vs El Centro EQ

within the range established by the EQs. It is therefore concluded that from the standpoint of a time history comparison, the ground motion from any of these UNEs could be considered as being representative of a future major EQ.

#### SUMMARY

The foregoing comparisons show that from the structural engineer's viewpoint, close-in ground motions from UNEs are similar to those produced by major EQs. More specifically:

- (1) The peak g-levels from UNEs are comparable to those estimated for the strongest EQs.
- (2) The spectra from typical UNEs are similar to those from EQs (i.e., the envelope developed for typical UNE spectra would match an envelope from strong EQs).
- (3) A time history comparison of ground motion from typical UNEs shows that both the duration of strong motion and the number of

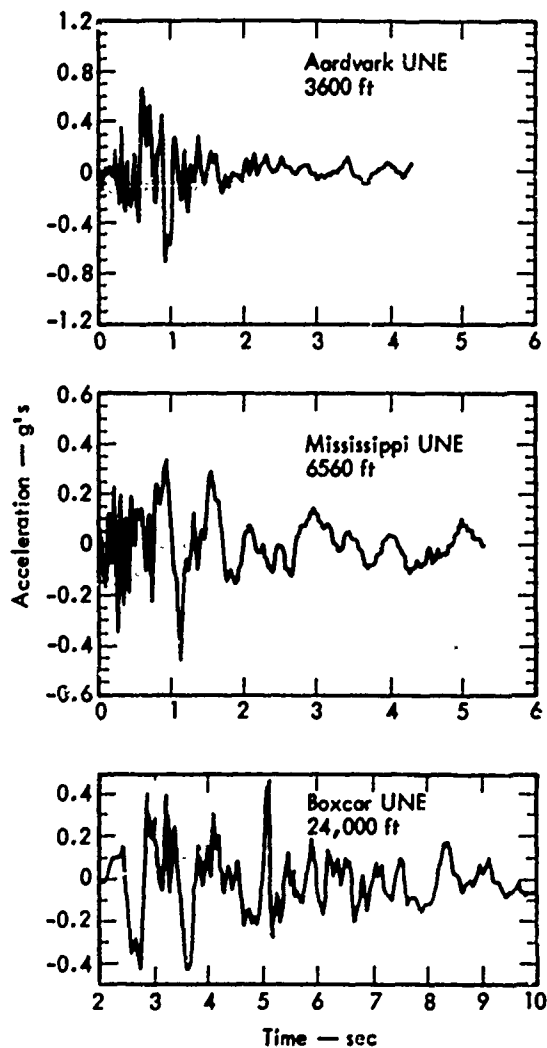


Fig. 11 - Accelerograms from Aardvark, Mississippi, and Boxcar UNEs.

near-peak g-level cycles for UNEs fall within the range established by strong EQs.

From these results it is concluded that typical UNEs generate ground motion equivalent to that of a possible future major EQ. Therefore, by predetermining the yield and location of UNEs (relative to the location of a test structure), a test structure can be excited by ground motion comparable to that of a future major EQ.

However, to study post-yield behavior of structures it will be necessary to generate UNE ground motion with longer pulse durations and also more cycles of near-peak g-level. This can be accomplished by sequentially firing UNEs or by subjecting test structures to ground motions from UNEs fired over a large time

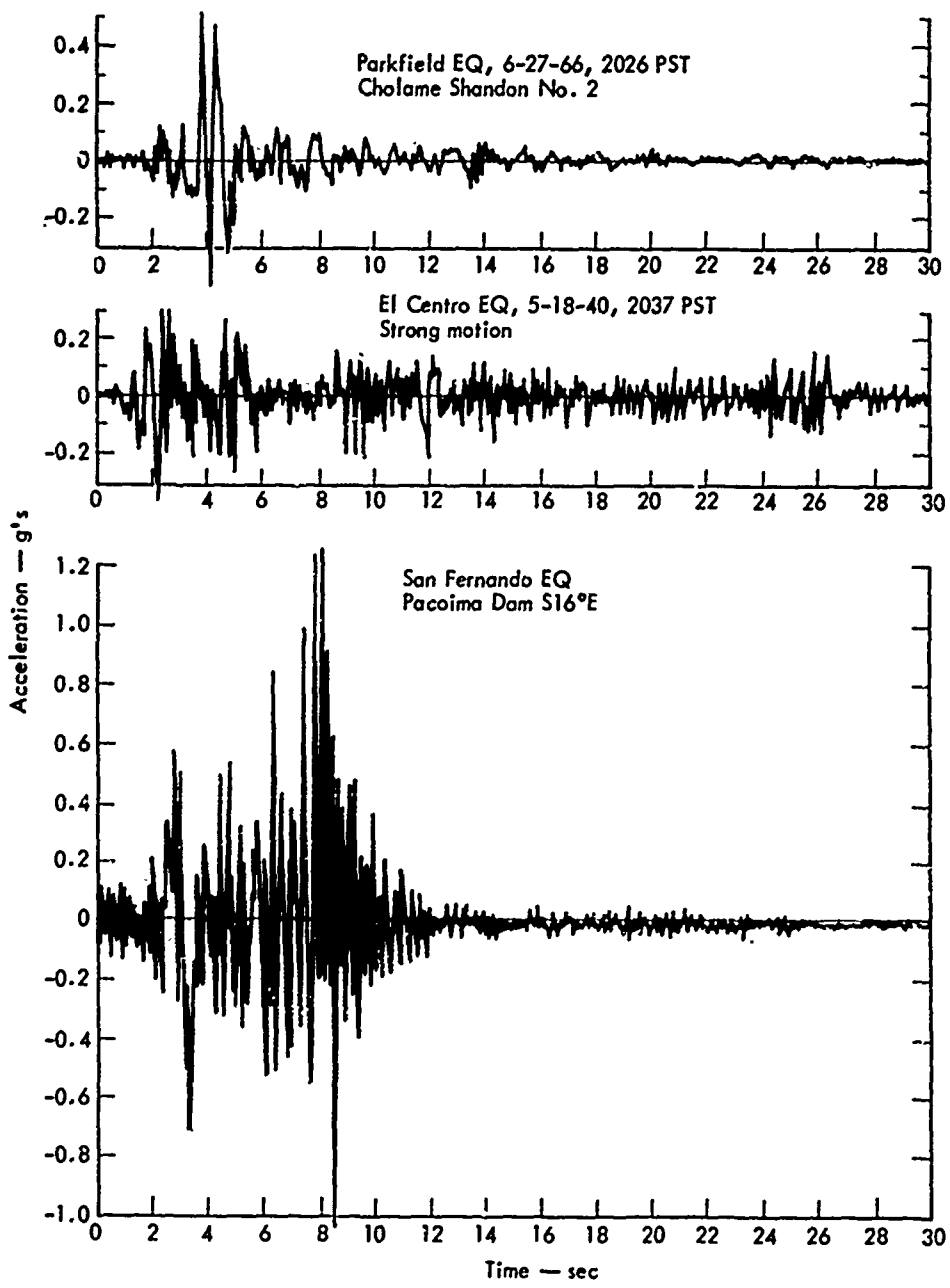


Fig. 12 - Accelerograms from Parkfield, El Centro, and San Fernando EQs.

span. Both of these possibilities need much further study.

In order to properly locate structures a study must be made to correlate the ground motion spectra from UNEs with yield, geology, and depth of burial of the explosive. Once this is accomplished it would be possible to subject test structures to increasingly strong motion ranging from elastic response to finally severe damage.

One important fact to note is that lower yield explosives can be used. The only reason for using very large yield explosives is to increase the duration of shaking. This is of some importance since a large number of lower yield explosives are detonated as compared to the very high-yield explosives. Springer and Kinnaman [18] give a list of U. S. UNEs. This list indicates that more than a sufficient number of UNEs are exploded every year to supply the required ground motion for any type of test program.

## REFERENCES

1. F. Tokarz and D. L. Bernreuter, "Comparison of Calculated and Measured Response of a High-Rise Building to Ground Motions Produced by Underground Nuclear Detonations," Lawrence Livermore Laboratory Rept. UCRL-50977, Dec. 23, 1970
2. D. E. Hudson, "Dynamic Tests of Full Scale Structures," pp. 127-149 in Earthquake Engineering (R. Wiegel, editor), Prentice-Hall, Englewood Cliffs, N.J., 1970
3. J. Penzien, J. G. Bouwkamp, R. W. Clough, and D. Rea, "Feasibility Study of Large-Scale Earthquake Simulator Facility," Earthquake Engineering Research Center, University of California, Berkeley, Rept. EERC-67-1, Sept. 1967
4. J. R. Evernden, "Identification of Earthquakes and Explosions by Use of Teleseismic Data," J. Geophys. Res., Vol. 74, No. 15, pp. 3828-3856, 1969
5. V. A. Jenschke, R. W. Clough, and J. Penzien, "Characteristics of Strong Ground Motions," Proc. 3rd World Conf. Earthquake Eng., Vol. I, pp. III-125-III-142, 1965
6. D. E. Hudson, "Some Problems in the Application of Spectrum Techniques to Strong-Motion Earthquake Analysis," Bull. Seism. Soc. Am., Vol. 52, pp. 417-430, 1962
7. D. E. Hudson, "Design Spectrum," pp. 93-106 in Earthquake Engineering (R. Wiegel, editor), Prentice-Hall, Englewood Cliffs, N.J., 1970
8. M. D. Trifunac, "Response Envelope Spectrum and Interpretation of Strong Earthquake Ground Motion," Bull. Seism. Soc. Am., Vol. 61, pp. 343-356, 1971
9. S. C. Liu and D. P. Jhaveri, "Spectral and Correlation Analysis of Ground-Motion Accelerograms," Bull. Seism. Soc. Am., Vol. 59, pp. 1517-1534, 1969
10. W. K. Cloud and V. Perez, "Strong-Motion Records and Acceleration," Proc. 4th World Conf. Earthquake Eng., Vol. I, pp. A2-119-A2-132, 1969
11. G. W. Housner, "Intensity of Earthquake Ground Shaking Near the Causative Fault," Proc. 3rd World Conf. Earthquake Eng., Vol. I, pp. III-94-III-115, 1965
12. D. L. Bernreuter, E. C. Jackson, and A. B. Miller, "Control of the Dynamic Environment Produced by Underground Nuclear Explosives," in Proc. Symp. on Eng. With Nuclear Explosives (Las Vegas, Nev., 1970), U.S. Atomic Energy Commission Rept. CONF-700101, Vol. 2, pp. 979-993, May 1970
13. J. R. Murphy and J. A. Lahoud, "Analysis of Seismic Peak Amplitudes from Underground Nuclear Explosions," Bull. Seism. Soc. Am., Vol. 59, pp. 2325-2341, 1969
14. W. V. Mickey, "Seismic Wave Propagation," in Proc. 3rd Plowshare Symposium (Davis, California, 1964), U.S. Atomic Energy Commission Rept. TID-7695, pp. 181-194, 1964
15. R. D. Lynch, "Response Spectrum for Pahute Mesa Nuclear Events," Bull. Seism. Soc. Am., Vol. 59, pp. 2295-2309, 1969
16. R. A. Mueller and J. R. Murphy, "Seismic Spectrum Scaling of Underground Detonations," Environmental Research Corp. Rept. NVO-1163-195, 1970
17. W. K. Cloud and D. S. Carder, "Ground Motions Generated by Underground Nuclear Explosions," in Proc. 2nd World Conf. Earthquake Eng., Vol. III, pp. 1609-1632, 1960
18. D. Springer and R. Kinnaman, "Seismic Source Summary for U.S. Underground Nuclear Explosions 1961-1970," to be published in Bull. Seism. Soc. Am. See also Lawrence Livermore Laboratory Rept. UCRL-73036, February 1971
19. H. F. Stevenson, "Structural Response to Close-in Horizontal Ground Motion from Underground Nuclear Tests at Pahute Mesa," Holmes and Narver, Inc., Las Vegas, Nev., Rept. HN-20-1039, 1969

## DISCUSSION

Voice: In terms of the duration at certain amplitudes in those plots that you showed, what was the origin of that data?

Mr. Bernreuter: That was from a paper by Cloud and a coauthor in the fourth world earthquake conference. He was looking at how long the level remained above a certain value; for example, how many seconds it remained above 1/2 g or 1/4 g for different earthquakes.

Voice: Then this was not the actual time he dwelled at any particular level?

Mr. Bernreuter: No.

Voice: Was it the time after the initiation of the event?

Mr. Bernreuter: Yes.

Mr. Haag (MTS Systems Corporation): I am interested in knowing if any one has done any work in relating the earthquake accelerations to the type of

soil conditions in the surrounding areas. For instance, the acceleration levels in a particular earthquake may vary from place to place depending on the type of soil or rock encountered. Are you aware of any studies that have been done?

Mr Bernreuter: Yes, there have been quite a few studies. Harry Seed, University of Southern California has made studies trying to relate amplifications of base rock motions to soil structure. There are also several other papers on the subject.

Mr. Haag: Have they been conclusive in any way?

Mr. Bernreuter: I do not really feel that they have been conclusive. One main reason being simply the lack of recorded motion. Once the San Fernando records are studied in detail, one might be able to understand this better. This is the first time we have had so many recording stations for a given earthquake over varied geologies. So there is some hope that this may be clarified.

ROCKING OF A RIGID, UNDERWATER BOTTOM-FOUNDED  
STRUCTURE SUBJECTED TO SEISMIC SEAFLOOR EXCITATION

J. G. Hammer and H. S. Zwibel  
Naval Civil Engineering Laboratory  
Port Hueneme, California

This paper describes an analytical study of an early-generation seafloor structure subjected to severe seismic excitation. The structure is assumed to consist of a spherical pressure hull supported on legs, which in turn rest on pads on the sea floor. Friction between the pads and the underlying soil and the shear resistance of the soil prevent sliding of the structure, but the structure tends to rock rigidly in a manner that compresses the soil beneath it and may cause lifting off.

The problem is formulated by second order differential equations containing non-linear terms. Effects of drag, added mass, and foundation reaction are considered. A numerical method of solution is followed that generates solutions at successive time intervals that are automatically adjusted to conform with preestablished accuracy criteria. The behavior of the foundation depends on the vertical forces and the load history. The ground excitation is a simulated earthquake motion generated from a random process of prescribed power spectral density, multiplied by appropriate envelope factors.

An example structure is analyzed and its response computed for three different support conditions. The results are shown in terms of displacement and accelerations of the structure and shearing force and vertical reactions of the supporting medium.

#### INTRODUCTION

A structure placed on the floor of the ocean must be adequate for the loading conditions expected during its useful lifetime. One of the most severe conditions, and one that is not too well understood, would occur when there were heavy seismic disturbances in the ocean floor. This paper describes a study and analysis of the behavior of a particular kind of structure under such loading.

The structure considered is an early-generation type that would be constructed out of the water and lowered into position on the ocean floor. It might be a self-contained, unmanned scientific or observation station; or it could be a manned station complete with life support systems and means for ingress-egress. As envisioned, it would consist of a negatively buoyant spherical pressure hull supported by framed legs, which in turn rest on footings. The footings would rest on or in the bottom material, possibly with additional fasteners to prevent sliding. The structure could look like the simplified model shown in Fig. 1.

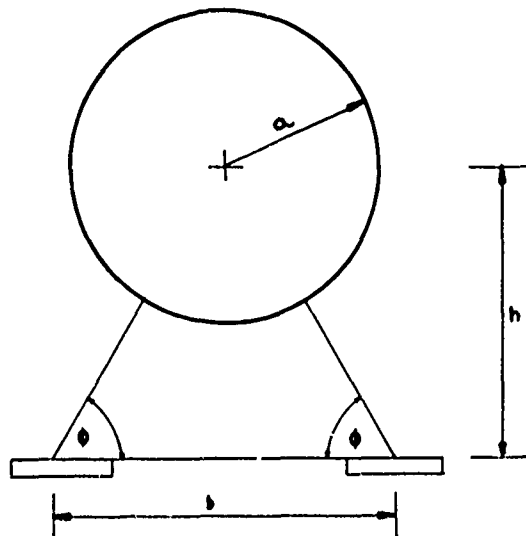


Fig. 1 - Simplified structure

The structure is assumed to be in moderate to deep water. The spherical pressure hull is designed for the hydrostatic pressure at that depth. The footings are proportioned so as to support the weight of the submerged structure without exceeding the bearing strength of the bottom material. The mass of the structure is assumed to be concentrated at the center of the spherical hull. The main drag effects of the water are assumed to be those acting on the spherical hull. The position of the structure at any time is given by two coordinates as shown in Fig. 2.

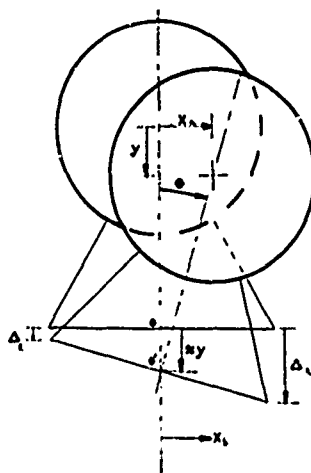


Fig. 2 - Coordinate system

The rotation clockwise from its initial position is given by  $\theta$ , and the vertical downward displacement of the center of mass is given by  $y$ . The horizontal position of the center of mass relative to the base of the structure is proportional to  $\theta$  for small rotations since the structure moves as a rigid body. Its total displacements are the sum of the relative movements and the movements of the supporting medium.

The loading situation is as follows. The ocean floor undergoes a violent horizontal shaking, which in turn shakes the footings and the rigid structure that they support. The system moves in a combination of rocking, horizontal translation, and vertical settlement of the footings. Forces acting on the structure are the inertia of its mass and the added mass of the water, the drag forces caused by the motion of the water relative to the structure, gravity forces due to the submerged weight of the structure, and the reactive forces of the ocean floor material on the footings. All of the motion is assumed to occur in the single vertical plane that contains the horizontal axis of movement of the base excitation. The response of the structure is described by time records of accelerations, velocities, and displacements. The foundation requirements are

described by the holding forces to prevent sliding relative to the ocean floor and by the vertical forces acting on the footings.

#### PROPERTIES OF THE OCEAN FLOOR

Probably the largest unknown factor in the problem being considered is the nature of the material on which the structure is likely to be placed. Submarine soils apparently vary as widely as do terrestrial soils. One of the most complete surveys of available data is Ref. [1], which considered about 250 reports and abstracted data from the most relevant of them. The actual samples taken from the deep ocean floor are very few. Ref. [1] reported that only 300 or so cores have been obtained from the North Atlantic, for example, which averages only one sample for each 30,000 square miles. The quantity of data from Pacific Ocean sampling is even less representative.

What is believed, however, is that the floor of the Pacific Ocean is covered chiefly with clastic, red clay deposits consisting of volcanic and terrigenous colloidal matter. The predominant sediments of the Atlantic and Indian Oceans are calcareous oozes, with an ooze being defined as a material containing greater than 30% organic material. Closer to the land masses, terrigenic deposits that have come from rivers and currents cover the ocean floor on the continental shelves. The portion of the ocean floor that is solid rock is believed to be a very small percentage.

Ref. [1] gives the following estimates as to the composition of the ocean floor. About 8% of the area of the sea floor is terrigenic shelf sediment in an average water depth of 100 meters. About 46% is an ooze and 28% is a red clay. These latter two compositions occur in the deep ocean and are pelagic sediments. The remaining part of the ocean floor is believed to be hemipelagic muds, plus the small amount of rock outcropping previously mentioned.

These ocean bottom sediments have accumulated over long periods of time. The rates of deposit are of the order of a centimeter or less per thousand years. Based on this kind of rate, the total depth of sediment would be expected to be a few kilometers. However, seismic surveys indicate a sediment thickness of only 0.1 to 0.5 kilometers. It is believed that below this depth gradual hardening of the sediment has taken place so that the layers are intermediate in composition between the upper sediment and the basaltic bedrock underlying it.

The core samples that have been taken of the uppermost few feet of the ocean bottom sediment indicate very low shear strengths. These range from 0.5 psi to 2.5 psi. The water content varies from 80% to 150% in the majority of samples. The porosity was in the range 60% to 80%.

The shear strength seems to increase almost linearly with depth below the water-sediment interface. The void ratio apparently does not decrease with depth. This might indicate that the older, lower deposits have become stronger through age rather than by consolidation. At the soil-water interface, however, one can conclude that the material supporting the structure will be very soft with a low shearing and bearing. In fact 89% of the samples reported in Ref.[1] had bearing strengths in the range 0.5 to 2.5 psi.

When a negatively buoyant structure is placed on the ocean floor, there will be some immediate settlement due to an almost elastic distortion of the bottom material. Following this, there will be a much slower, and greater, settlement due to consolidation of the material under the additional weight of the structure. An equilibrium is eventually reached, and this condition is assumed at the time the seismic disturbance occurs.

If a footing has settled into the sediment it will resist being pulled out because of suction formed beneath it. These break-cut forces are commonly experienced in anchor and salvage work. It is believed that pullout finally results when a failure mechanism occurs in the soil material surrounding the footings. It is sometimes considered that the average foundation stress resisting pullout of a footing is comparable to the ultimate bearing capacity of the soil material. This was assumed in Ref.[2], and was substantiated by actual experience reported in that study.

It is believed that the rate of loading has an effect on the static resistance of the soil mass. There are several studies (Ref.[3], [4]) that have looked at the dynamic properties of soil under footings of structures on land. Ref.[5] assumes a homogeneous, isotropic, elastic medium and derives expressions for a soil resistance function involving a linear combination of the deformation and the velocity of deformation. The deformation is multiplied by a coefficient K, and the velocity by a coefficient C. K and C are functions of the shearing modulus of the soil, its mass density, the size of the footing, Poisson's ratio of the soil, and the frequency of the periodic force that is loading the soil. Ref.[6] uses a similar soil resistance function to study dynamic field tests on a soil-pile system, with the additional assumption that C is also proportional to the depth of the hole.

Another possible motion of the footing (assumed to rest on or in a horizontal ocean floor) is horizontal sliding. Sliding motion would be resisted by friction and by the shearing resistance of the sediment material. It is believed that the shearing resistance manifests itself in a way that offers passive resistance to slipping within the soil along some interior surface outward from the footing. This kind of passive resistance has been studied in a

classical way, and solutions usually used are those due to Rankine and to Coulomb (Ref.[7]). It would be possible, therefore, to make a rough estimate of the horizontal restraint on a sunken footing, given the properties of the soil material and the structural forces and geometry. Lacking specific information about the sediment properties, it is convenient to assume that sliding is prevented, and to compute the horizontal restraint required during the response. In a specific location the capabilities of the bottom material could be compared with what is needed to prevent sliding.

The thick layer of soft material overlying the bedrock will tend to alter the nature of seismic disturbances occurring in the bedrock as they are transferred up to the sediment-water interface. Studies have been made of layered soil masses to show the effect on a seismic disturbance applied at the lowest layer and transmitted by shear from horizontal layer to layer until it reaches the uppermost layer (Ref.[8]). These studies seem to show that an input earthquake such as that recorded at El Centro in 1940 will emerge with similar low frequency components but with attenuated high frequency components. Of interest is the fact that the peak accelerations of the movement do not change appreciably since they seem to be associated with the lower frequencies. The particular structural size and type that is of interest here responds primarily to the lower frequencies, and it is therefore assumed that ignoring the moderating effect of the layers of sediment would not alter the structural response significantly if the bedrock input resembled a large land earthquake. The problem, of course, is that one cannot predict what the disturbance will be, even in the bedrock.

What can be done is to take a record of a strong typical earthquake and use it for study purposes as though it were applied to the footings of the structure. The analytical procedure established for this can be refined as information concerning sediment properties and depths and bedrock motions becomes available.

#### EQUATIONS

Fig. 3 shows the system of forces acting on the structure when it is displaced so that  $\theta$ ,  $y$  and  $x_b$  are all positive and the motion is such that the three accelerations  $\ddot{\theta}$ ,  $\ddot{y}$  and  $\ddot{x}_b$  are also positive.

The center of mass is accelerated horizontally by the combination of two motions: a motion relative to the base as the rigid structure rotates, and the motion of the base itself. The total horizontal acceleration of the mass is thus  $\ddot{h}\dot{\theta} + \ddot{x}_b$ , and the inertia force is

$$F_{Hf} = BM(h\ddot{\theta} + \ddot{x}_b)$$

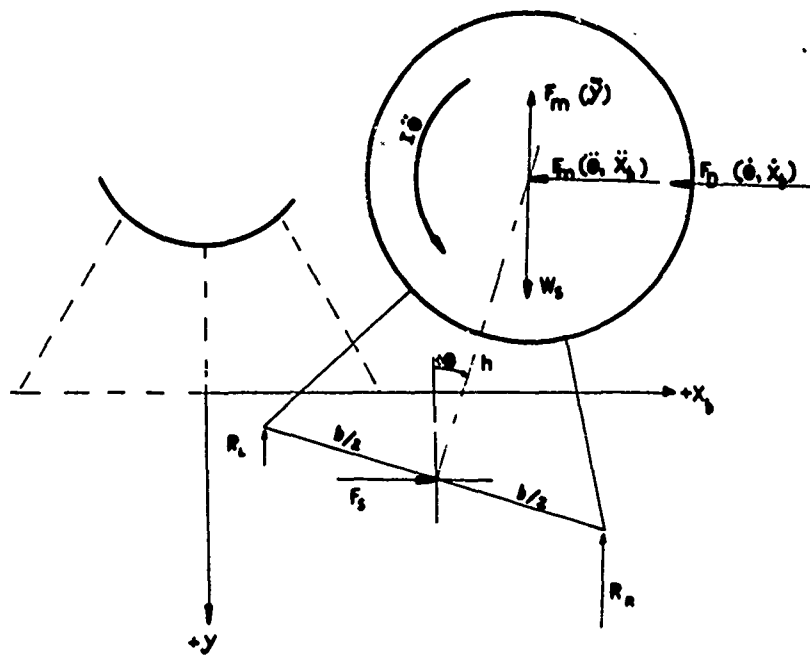


Fig. 3 - Force system ( $\theta, y, x_b, \dot{\theta}, \dot{y}, \dot{x}_b$  positive)

where  $M$  is the mass of the structure and  $\beta$  is a multiplier that incorporates the added mass of the water.

The structure is considered to move through the water with a velocity resulting from the same two motions: A horizontal component of the rotation about the base, plus the base motion. The total velocity of the structure through the stationary water is then  $h\dot{\theta} + \dot{x}_b$ , and the drag force acting on the sphere is

$$F_D = 1/2 C_D \pi a^2 \rho (h\dot{\theta} + \dot{x}_b) (|h\dot{\theta} + \dot{x}_b|)$$

where  $C_D$  is a drag coefficient,  $\pi a^2$  is the cross section presented to the flow, and  $\rho$  is the mass density of the water. The quantity in the second parentheses is shown as an absolute value so that the velocity squared will have the same algebraic sign as the velocity; and the drag force will have a direction consistent with the direction of the flow.

These horizontal drag and inertia forces acting through the center of mass are opposed by a force  $F_S$  acting through the base in a horizontal direction opposite to the algebraic sum of the inertia and drag forces.

There is an inertial resistance to rotation of the sphere about its own diameter. This resistive torque is

$$\tau_{\theta} = \gamma M a^2 \dot{\theta}$$

with  $M$  the mass,  $a$  the radius, and  $\gamma$  the proper coefficient so that  $\gamma Ma^2$  is the mass moment of inertia of the spherical structure about its own diameter.

$R_L$  and  $R_R$  describe the static and dynamic resistance of the soil beneath the footings. They are assumed to have the following form

$$R_L = R_S(\Delta_L) + R_D(\Delta_L, \dot{\Delta}_L)$$

$$R_R = R_S(\Delta_R) + R_D(\Delta_R, \dot{\Delta}_R)$$

where  $\Delta_L$  and  $\Delta_R$  are the vertical movement of the footings and  $\dot{\Delta}_L$  and  $\dot{\Delta}_R$  are the accompanying velocities. From the geometry of Fig. 3

$$\Delta_L = y - \frac{b}{2} \theta$$

$$\Delta_R = y + \frac{b}{2} \theta$$

The static resistance of the soil material is given by  $R_S(\Delta)$ , in which the resistive force depends on the vertical compression; and  $R_D(\Delta, \dot{\Delta})$  is the additional effect caused by the rate of loading  $\dot{\Delta}$  and the depth of the hole  $\Delta$ .

The other vertical forces act through the center of mass. They are the inertia force

$$F_M = \gamma M \ddot{\theta}$$

and the submerged weight

$$W_S = \alpha Mg$$

where  $Mg$  is the weight in air and  $\alpha$  is a multiplier to give the weight in water.

From the force system shown in Fig. 3 equilibrium equations can be written. Summing the moments about the center of mass

$$\gamma Ma^2\ddot{\theta} = - BMh(\dot{h}\dot{\theta} + \ddot{x}_b) + R_L\left(\frac{b}{2} + h\dot{\theta}\right) - R_R\left(\frac{b}{2} - h\dot{\theta}\right) \\ - 1/2 C_D \pi a^2 \rho h (\dot{h}\dot{\theta} + \ddot{x}_b) (|\dot{h}\dot{\theta} + \ddot{x}_b|) \quad (1)$$

and summing the vertical forces

$$BM\ddot{y} = \alpha Mg - R_L - R_R \quad (2)$$

where  $R_L$  and  $R_R$  are functions of  $\theta, y, \dot{\theta}$  and  $\dot{y}$  as previously explained.

Eqs.(1) and (2) can be transformed into four first order equations by making the following substitutions

$$X_1 = y/h$$

$$X_2 = \theta$$

$$X_3 = \dot{y}/\sqrt{gh}$$

$$X_4 = \sqrt{\frac{h}{g}} \dot{\theta}$$

These equations can then be arranged in the form

$$\begin{aligned} \dot{X}_1 &= f_1(X_3) \\ \dot{X}_2 &= f_2(X_4) \\ \dot{X}_3 &= f_3(X_1, X_2, X_3, X_4) \\ \dot{X}_4 &= f_4(X_3, X_4, \dot{x}_b/\sqrt{gh}, \ddot{x}_b/g) \end{aligned} \quad (3)$$

where  $\ddot{x}_b$  and  $\dot{x}_b$  are the acceleration and velocity of the support medium, and  $g$  is the acceleration of gravity.

Eq. (3) is a set of simultaneous nonlinear first order differential equations. The initial conditions at time zero are

$$X_1(t_0) = X_2(t_0) = X_3(t_0) = X_4(t_0) = 0 \quad (4)$$

While Eqs.(3) and (4) cannot be solved directly, they can be handled readily by numerical methods. The procedure used here is to begin a step-by-step solution using the Runge-Kutta method to predict values of each of the  $X_n$  coordinates at the end of successive time intervals. The values for any given time are substituted into Eq. (3) to find the time derivatives.

After the Runge-Kutta procedure has given points for four times and the corresponding first derivatives have been obtained, Hamming's modified predictor-corrector method is used to advance through succeeding intervals of time. This method is a stable fourth order integration procedure that requires approximately half the calculations per step than other methods of comparable accuracy require. It has the additional advantage that at each step the calculation procedure gives an estimate of the local truncation error. The procedure is therefore able to choose and change the size of the time interval based upon a pre-established accuracy criterion. The particular subroutine used is given in Ref.[9].

#### AN EXAMPLE STRUCTURE

In order to demonstrate the application of the procedure, a number of assumptions were made as to values of the parameters, and a particular structure was analyzed. As far as possible the assumptions relating to the properties of the soil media are consistent with the reported data of Refs.[1], [2] and [7]. No attempt was made to make a detailed design of a structure, nor was an optimum configuration sought.

It is assumed that a steel structure is to be placed on the level ocean floor at a depth of 6,000 feet. The structure resembles that shown in Fig. 1, with a radius  $a$  of 10 feet, a base dimension  $b$  of 30 feet, and angle  $\phi$  of  $60^\circ$ . If the spherical hull is designed for the hydrostatic pressure at 6,000 feet and an estimate made for the weight of the legs, footings and interior loads, the whole structure is assumed to weigh 418,000 pounds in air and 148,000 pounds in the water. For symmetry, it is assumed that the structure has four legs and four footings, with each footing about 12 feet square and having a bearing pressure of about 1.8 psi when resting in the static position.

The added mass of the water is assumed to be one-half the mass of the volume of water displaced by the spherical hull. The drag

coefficient is assumed to be unity. The mass moment of inertia of the structure about a horizontal diameter of the spherical hull was assumed to be  $2/3 Ma^2$  with no added mass effect when the sphere rotates.

Three types of support media were considered. The first was an almost rigid rock-like surface that has the static resistance function shown in Fig. 4(a). The second was a

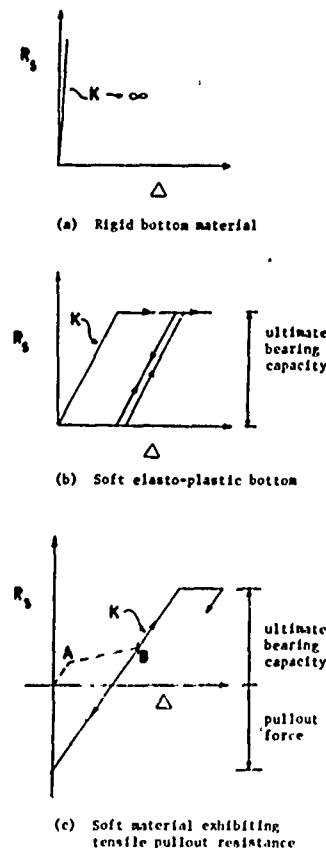


Fig. 4 - Static resistance functions assumed for seafloor material

soft material that deformed elastically under the dead load of the structure but did not consolidate. When loaded further it followed the pattern shown in Fig. 4(b). The third type deformed initially under the dead load both by distortion and consolidation. It follows the pattern of Fig. 4(c). An additional property of type (c) material is that it offers a tensile type resistance to having the footing lift out.

The type (a) bottom material does not change with rate of loading so its resistance does not depend upon  $\dot{\Delta}$ . Types (b) and (c) are assumed to be velocity dependent and to have a resistance function of the form  $R = k\Delta + c\dot{\Delta}$ . The coefficient  $c$  was assumed to have a value

numerically equal to one-tenth the slope  $k$  of the static resistance. This static slope was assumed to be 6,000 lb/in. for both types (b) and (c); and the coefficient  $c$  was therefore taken as 600 lb-sec/in.<sup>2</sup>.

The above assumptions imply that the structure placed on type (a) material will not settle. When the seismic loading occurs, the footings will tend to rock or slide, but will not depress the supporting medium.

In type (c) material an initial settlement of

$$(W_s/4)(1/k) = \left(\frac{148,000 \text{ lb}}{4}\right)\left(\frac{1}{6,000 \text{ lb/in.}}\right) \approx 6 \text{ in.}$$

was assumed under each footing. In type (c) material an initial settlement of 6 inches was assumed due to elastic distortion, and an additional settlement of 18 inches was assumed due to consolidation.

Type (a) material was assumed to have unlimited bearing strength. Types (b) and (c) were assumed to have an ultimate bearing strength three times the static bearing pressure. The pullout strength of type (c) material then becomes the force necessary to lift the footing a distance equal to the consolidation settlement against a resistance of 6,000 lb/in. plus the addition velocity dependent viscous force.

The structure-soil-water system is then assumed to be excited by a horizontal motion of the base resembling a strong earthquake on land. This obviously will not be the same motion as occurs in the bedrock below the supporting material, except perhaps for material type (a); but indications are that the layers of sediment will have a small effect on the frequency components that affect this structure the most. Using the base motion as though it were applied to the base of the structure is therefore not considered unconservative; and of course one is not sure anyway of the nature of the movement in the bedrock. It is possible to model the effects of the sediment layers on the motion passing through them, but this could be done if more specific information were available about a particular structural site.

The input used in this example is an artificial accelerogram, taken from Ref.[10], that is believed to contain all the characteristics of a very strong earthquake, stronger than that for which recorded data exist. The earthquake is of 120 seconds total duration and is designed to represent an upper bound for the ground motions to be expected in the vicinity of the causative fault during an earthquake of magnitude 8 or greater.

Ref.[10] followed the following procedure. An approximation to white noise was passed through a filter to give the process the desired frequency content as determined by the power spectral density. The resulting stationary Gaussian process was then given the desired non-stationary properties by multiplying by a suitably chosen envelope. The record was then processed and corrected to filter the spurious long period components. Response spectra were then calculated and compared to those of recorded motions. Undesirable frequency components were removed by filtering again. Finally the accelerograms were scaled to the appropriate intensities of shaking. Fig. 5 shows the resulting simulated records, which are used as the input for this structure.

having the same support material, did not lift off at all. It instead moved horizontally with the ground.

In Fig. 6(b) a departure from  $\theta = 0$  does not necessarily mean that lift-off has occurred because the rotation may be due to vertical movement of the footings. Lift-off did occur, however, for this case on both sides. This can be seen from Figs. 7(a) and 7(b), which are plots of the force exerted by the left and right footings as a function of time. It is interesting to note that the reaction force can momentarily exceed the static bearing capacity because of the dynamic effect. Comparing the final portions of the curves in Fig. 6(b) and Fig. 7 shows that the structure is settling into a

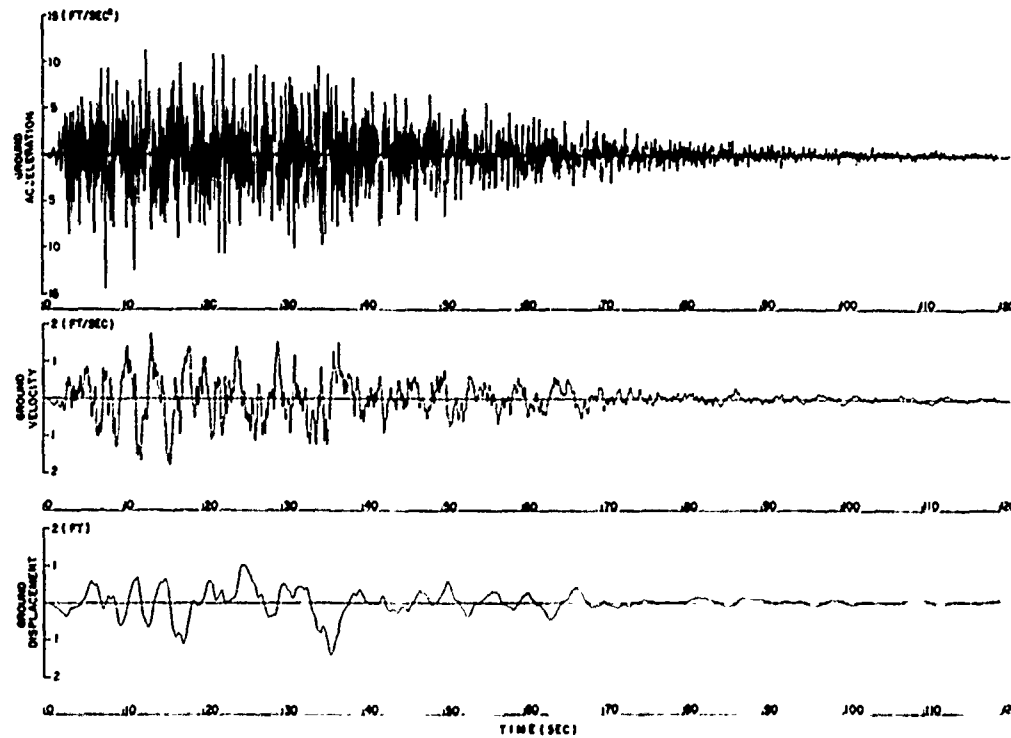


Fig. 5 - Assumed base excitation

## RESULTS

Fig. 6 shows the displacement  $x_r$  of the center of mass of the structure relative to its base and the angle of rotation in degrees, both as a function of time for the first 80 or 100 seconds of the earthquake. Fig. 6(a) is the response if the supporting material is type (a), Fig. 6(b) is for type (b), and Fig. 6(c) is for type (c).

In Fig. 6(a) any departure from  $\theta = 0$  means a footing has lifted off. The maximum lift at  $\theta = 7^\circ$  is about 3-1/2 feet. The same structure responding in air to the same excitation, and

canted position even though the foundation reactions are fairly balanced.

In Fig. 7(c) the response is less because of the resistance to uplift of the footings. In this particular case, none of the footings broke loose to lift off.

In computing the response the assumption was made that the structure was restrained from horizontal sliding. The results in Figs. 6 and 7 do not include any sliding relative to the support material. The total horizontal

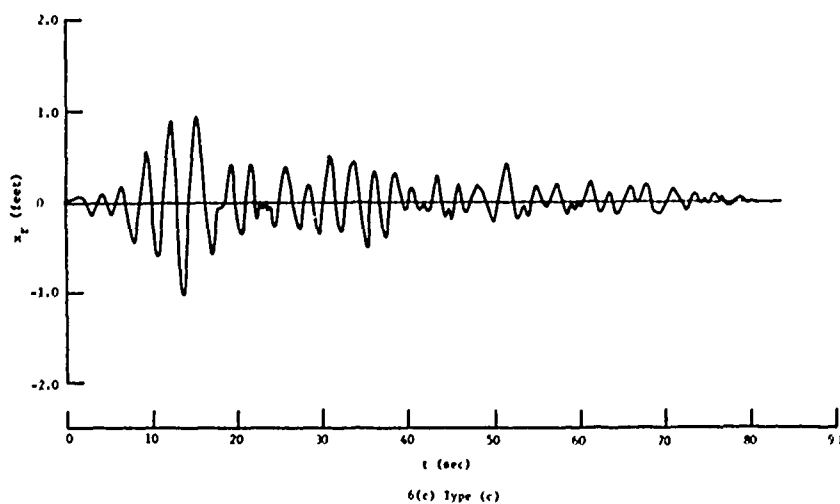
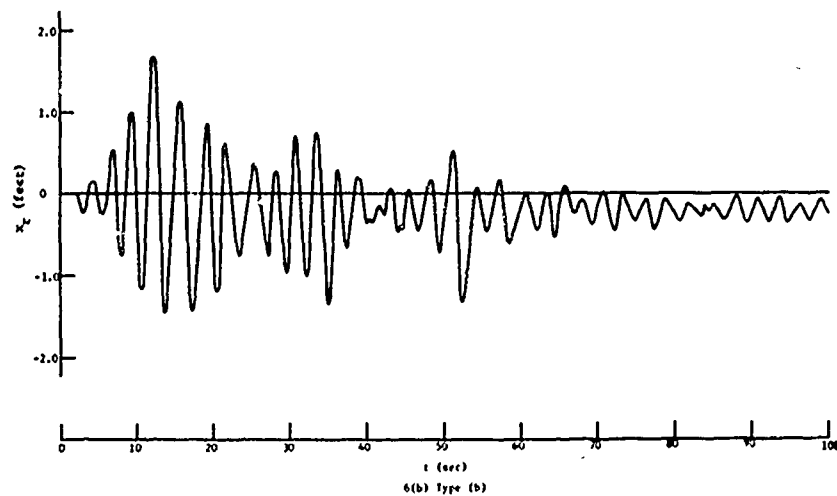
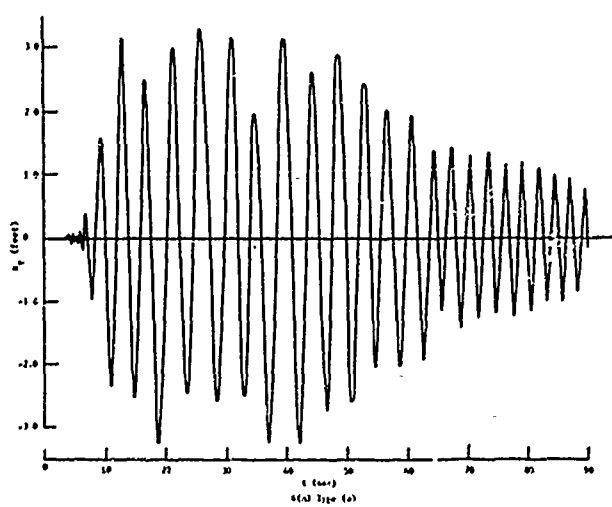


Fig. 6 - Response of sample structure

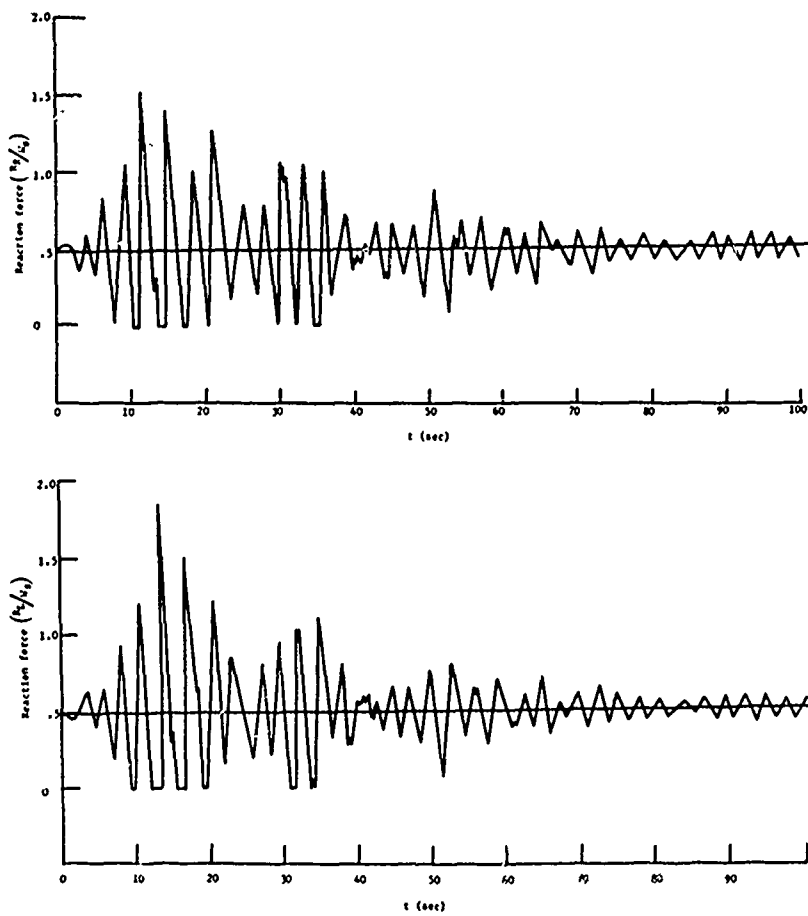


Fig. 7 - Vertical reactions on footings

restraining force required to prevent sliding was calculated, however, and the values were as follows:

Table 1

Type of Bottom Material	Maximum $F_g$ if no Sliding
(a)	130,000 lb
(b)	111,400
(c)	104,600

These horizontal forces must be resisted by friction between the footings and the bottom material, and by the dynamic shearing resistance of the material. The horizontal force would probably be shared unequally by the four footings if none lifted off; and by perhaps two of them if lift-off occurred. Whether or not horizontal resistances of the magnitude shown in Table 1 could be developed is not certain. It is certain that materials of type (b) and

(c) would have a very low static shearing strength, possibly not exceeding 1 psi. It would appear that types (b) and (c) might develop these forces under the footings assumed if all the footings were acting. The structure on the type (a) material would have to develop its horizontal restraint principally through friction between footings and support material. The force required would be nearly equal to the submerged weight of the structure, so it appears doubtful that the required frictional force could develop. Some kind of shear fasteners might be used to hold the footings against shear. These fasteners would of course affect the tendency toward lifting off, so the problem would require re-analysis.

Finally, the peak values of absolute acceleration of the center of mass of the sphere were computed during the response time in each of the three cases. The peak acceleration was 0.250 g for the structure on type (a) material, 0.202 g for type (b), and 0.189 g for type (c). The input acceleration of the base had a peak value of about 0.44 g that did not coincide with the peak responses of the structure.

## CONCLUSIONS

The kind of approach and solution described here could be extended and applied to the analysis of a great number of situations. The method itself is not limited to simplified abstractions, and if more accurate information were known about a particular structure and location, a more realistic analysis could be made. The purpose of this paper has been to discuss some of the problem elements and to demonstrate a method of solution.

Even such a simplified analysis, however, should be useful. It can permit a rapid preliminary analysis of any structure being planned for the ocean floor. From the analysis rough design criteria can be formulated for the strengths required in the various structural components. The possibility of a failure of a footing in bearing or shear might be predicted and avoided. In some cases, failure by gross movement in overturning or sliding might be indicated if additional restraints were not provided. The predictions of peak accelerations might show the need for shock mounting delicate equipment. The maximum displacement and final displacement might be useful if precise positioning were a requirement for the structure.

Continuing the approach described here to study structures of varying size and mass ought to provide considerable additional insight into the behavior of ocean floor structures in general when they are subjected to earthquake forces.

## REFERENCES

- [6] K. W. Korb and H. M. Coyle, "Dynamic and Static Field Tests on a Small Instrumented Pile," Research Report No. 125-2, Texas Transportation Institute, Texas A&M Univ., Feb. 1969.
  - [7] K. Terzaghi and R. H. Peck, Soil Mechanics in Engineering Practice, John Wiley & Sons, 1948.
  - [8] I. M. Idriss and H. B. Seed, "Seismic Response of Horizontal Soil Layers," J. of Soil Mechanics and Foundation Div., Proceedings of the ASCE, Vol. 94, Jul. 1968.
  - [9] IBM System/360 Scientific Subroutine Package (360A-CM-03X) Version III, Programmers Manual, p. 337, Fourth Ed. 1968.
  - [10] P. C. Jennings, G. W. Housner and N. C. Tsai, "Simulated Earthquake Motions," Earthquake Engineering Research Laboratory, California Inst. of Technology, Apr. 1968.
- [1] W. E. Schmid, "Penetration of Objects Into the Ocean Bottom," Final Report, Contract N62399-68-C-0044 for Naval Civil Engineering Laboratory, Mar. 1969.
  - [2] W. D. Liam Finn and P. M. Byrne, "Analysis of Ocean Bottom Sediments," 1971 Offshore Technology Conference Paper No. OTC 1471, Apr. 1971.
  - [3] R. V. Whitman and F. E. Richart, "Design Procedures for Dynamically Loaded Foundations," J. of Soil Mechanics and Foundation Div., Proceedings of the ASCE, Vol. 93, Nov. 1967.
  - [4] R. T. Ratay, "Sliding-Rocking Vibration of a Body on Elastic Medium," J. of Soil Mechanics and Foundation Div., Proceedings of the ASCE, Vol. 97, Jan. 1971.
  - [5] T. K. Hsiech, "Foundation Vibrations," Proceedings of the Institution of Civil Engineers, Vol. 22, May 1962.

## NOTATION

Symbol	Meaning
a	radius of spherical hull
b	base dimension of structure
c	velocity coefficient in soil resistance
g	acceleration of gravity ( $32.2 \text{ ft/sec}^2$ )
h	height of center of mass above base of structure
k	displacement coefficient in soil resistance
q	ultimate bearing stress of soil
t	time
$x_r$	motion of center of mass relative to base
$\dot{x}_b, \ddot{x}_b$	displacement, velocity, and acceleration of base excitation
$y, \dot{y}, \ddot{y}$	vertical displacement, velocity and acceleration of center mass
$C_D$	drag coefficient
$F_D$	drag force
$F_M$	inertia force
$F_S$	composite force acting horizontally through base of structure
M	mass of structure
$R_L, R_R$	left and right vertical reaction forces on footings
$W_s$	submerged weight of structure
$X_1, \dot{X}_n$	coordinates of transformed equations
$\alpha$	ratio of weight of structure in water to that in air
$\beta$	ratio of effective mass of structure and water to the mass of structure
$\gamma$	coefficient of $Ma^2$ in expression for mass moment of inertia
$\Delta_L, \Delta_R$	vertical displacement of left and right footings
$\dot{\Delta}_L, \dot{\Delta}_R$	vertical velocity of left and right footings
$\theta, \dot{\theta}, \ddot{\theta}$	angular displacement, velocity, and acceleration of rigid structure
$\rho$	mass density
$\delta$	base angle of structural configuration

## DISCUSSION

Voice: Did you include any kind of damping to account for the soil radiation?

Mr. Hammer: We have run cases where we coupled the damping of the soil with equivalent structural damping to get a new equivalent factor, but in this study we just assume 5% critical damping for each mode.

Mr. Zudans (Franklin Institute): The model looked to me like you had a weightless type of foundation at each support. You did not have any coupling between different support points. Is that correct?

Mr. Hammer: No. There were only soil springs to ground and not soil springs from support to support.

DEVELOPMENT OF A WAVEFORM SYNTHESIS TECHNIQUE -  
A SUPPLEMENT TO RESPONSE SPECTRUM AS A

DEFINITION OF SHOCK ENVIRONMENT

Robert C. Yang and Herbert R. Saffell  
The Ralph M. Parsons Company  
Los Angeles, California

A procedure is developed for synthesizing a time-history to describe a transient disturbance such that the response spectrum of the disturbance matches a given spectrum and the amplitude ratios and phase relationships of its frequency components remain within assigned ranges.

INTRODUCTION

Analyses and tests to determine the responses of systems exposed to transient disturbances often employ a response spectrum as a means for bounding the severity of all probable disturbances. As the response spectrum describes only peak responses to the disturbance of linear, undamped oscillators expressed as a function of their natural frequencies, the spectrum does not define unique amplitudes and phase angles of the frequency components of the disturbance itself. An infinite number of disturbances, each with different component amplitudes and phase angles, can generate peak responses in the linear undamped oscillators which are essentially identical. Indeed, as transient disturbances are rarely unique, this generality of the response spectrum has been one of the factors which has prompted its extensive use as a means for defining shock severity.

The response spectrum alone as a criterion of input motion in analyses or tests of many practical systems, however, may not be sufficient to properly define system responses. First, as the spectrum bounds the peak motions only of linear, undamped systems, responses of systems with other characteristics may be significantly different. Second, while in some respects the generality of the spectrum may be desirable, in others it may be too broad in that other information concerning the disturbance may be available which might be employed to reduce the size and perhaps the severity of the family of possible disturbances. Third, of course, shock test machines must generate motions which are describable in time rather than in frequency.

In most analyses and in all tests, therefore, the disturbance must be described by time-histories. If the strength of the disturbance is bounded by a spectrum, however, spectra of the synthesized time-histories must closely approximate the design spectrum.

Peak responses of any system except an undamped single degree-of-freedom linear system to a motion time-history whose spectrum matches the design spectrum may differ significantly from those bounded by the spectrum. The magnitude of these differences will depend both on the characteristics of the system and on the amplification ratios and phase relationships of the frequency components of the disturbance. If all responses bounded by the spectrum are the result of disturbances which must be considered in design, strict compliance with the spectrum would require that an infinite number of time-histories be considered in analyses and tests, each with frequency components whose amplitudes and phases were different.

Practical considerations, however, limit to a very few the number of time-histories which can be considered in analyses or tests, sometimes to only a single one. Thus, in selecting a few specific time-histories to represent the entire family bounded by the spectrum, the characteristics of the system which will be exposed to the motions must be examined and the parameters of the frequency components of the time-histories chosen so that, hopefully, critical responses of the system will be generated.

The family of motions bounded by a spectrum can be reduced in size if an

examination of the basic phenomenon which resulted in the spectrum indicates that limits can be established, even grossly, for the ranges of possible amplification ratios and phase relationships. For example, all possible disturbances might be describable as "pulse-like" or as "oscillatory" implying that the amplification ratios for the former will be low while for the latter they will be higher. Or, perhaps, it may be known that all the energy is introduced at essentially the same time, such as might occur in impact, thus providing some insight into the phase relationships.

Synthesis of a time-history of a realistic disturbance thus involves not only matching the design response spectrum but also incorporating specified amplification ratios and phase relationships for each frequency component. Response spectra, in nondimensional form, for pulses, such as a sine, versed sine, ramp, terminal peak, square, and others have been treated extensively in the literature, and little problem is usually encountered in synthesizing a family of such pulses which will satisfy these three requirements. Where the disturbance is more oscillatory, however, the problem of matching closely not only a response spectrum but also the amplification ratios and phase relationships of the original disturbance is more difficult.

This paper describes a technique for synthesizing oscillatory waveforms such that their response spectra closely match a given spectrum and the amplification ratio and phase relationship of each of its frequency components approximate specified values.

#### THEORETICAL FORMULATION

Principles. The equation of motion of a simple linear oscillator subjected to base excitation is:

$$\frac{d^2y}{dt^2} + \omega_n^2 y = \omega_n^2 W(t) \quad (1)$$

where  $y$  is the absolute acceleration of the mass,  $\omega_n$  is the natural frequency of the system,  $t$  is time, and  $W(t)$  is the base acceleration. The response spectrum of the excitation function  $W(t)$  is a plot of the maximum responses of the system defined by Equation 1, as a continuous function of  $\omega_n$ .

$W(t)$  can be expressed as a linear combination of acceleration functions  $f_m(t)$ , such that

$$W(t) = \sum_{m=1}^M A_m f_m(t) \quad (2)$$

where  $A_m$  are constant coefficients defining the amplitude of the function  $f_m(t)$ . In synthesizing a time-history the problem is to select a sequence of  $M$  functions,  $f_m(t)$ , ( $m = 1, 2, \dots, M$ ), with associated coefficients  $A_m$  so that the response spectrum of the composite waveform not only matches  $M$  points on a given response spectrum but at intermediate frequencies as well. To match a spectrum exactly at all frequencies, an infinite number of terms would be required. However, as the response spectrum to be matched usually involves some measure of uncertainty, small deviations may be acceptable in frequency regions lying between the selected frequencies  $\omega_n$  so long as they do not exceed prescribed bounds.

An analytical solution of Equation 1 for the forcing function  $f_m(t)$  which would reduce the problem to an explicit solution of a set of  $M$  simultaneous algebraic equations for  $M$  unknown values of  $A_m$  is not possible since an infinite number of such functions can be found whose spectra will closely match the required spectrum.

Forcing Function. If a unique forcing function is to be defined, therefore, it is necessary to postulate a function  $f_m(t)$  such that its amplification ratio and component frequencies may be varied to satisfy the equation. Further, since the function will be used to represent a real transient event, its initial conditions must be zero and its terminal values of both acceleration and velocity must vanish. For some phenomena, displacements must also terminate at zero.

In constructing such a function, consider first the case where all frequency components are in phase. Equation 3 describes one forcing function which satisfies all specified conditions whenever  $N$ , the number of half-cycles, is any odd integer except unity.

$$f_m(t) = \begin{cases} \sin 2\pi b_m t \sin 2\pi N_m b_m t & 0 \leq t \leq T_m \\ = 0 & t > T_m \end{cases} \quad (3)$$

The frequency of each component of the forcing function is  $N_m b_m$  and the frequency of its envelope  $b_m$ , where  $b_m$  is expressed in Hz. Then  $T_m$ , the duration of the forcing function, is  $T_m = 1/(2b_m)$ . This forcing function where  $N = 5$  is shown in Figure 1.

Solution of Equations. The solution of Equation 1 (Reference 1), substituting Equations 2 and 3, is

$$y(t, \bar{\omega}_n, b_m) = \sum_{m=1}^M A_m Q_m(t, \bar{\omega}_n, b_m) \quad (4)$$

where

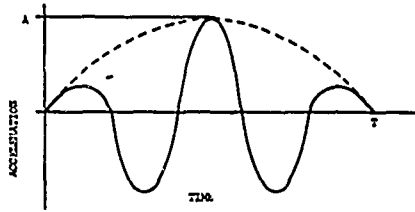


Figure 1. Selected Acceleration Forcing Function,  $N = 5$

$$Q_m = \frac{1}{2} \bar{\omega}_n^2 \left\{ \frac{\cos 2\pi\bar{\omega}_n t - \cos [2\pi(1-N_m)b_m t]}{(1-N_m)^2 b_m^2 - \bar{\omega}_n^2} - \frac{\cos 2\pi\bar{\omega}_n t - \cos [2\pi(1+N_m)b_m t]}{(1+N_m)^2 b_m^2 - \bar{\omega}_n^2} \right\} H(T_m - t) \quad (5)$$

$$+ 2N_m \bar{\omega}_n^2 b_m^2 \left\{ \frac{\cos 2\pi\bar{\omega}_n t - \cos [2\pi\bar{\omega}_n (t - T_m)]}{[(1-N_m)^2 b_m^2 - \bar{\omega}_n^2][(1+N_m)^2 b_m^2 - \bar{\omega}_n^2]} \right\} H(t - T_m)$$

$\omega_n = 2\pi\bar{\omega}_n$ , and  $H$  is the Heaviside function. The first term of Equation 5 defines the principal responses of the oscillator to the forcing function while the second term defines its residual responses.

Equation 5 is determinate for all values of  $t, \bar{\omega}_n$ , and  $b_m$  except when  $b_m = \bar{\omega}_n/(1 - N_m)$  and  $b_m = \bar{\omega}_n/(1 + N_m)$ . As  $b_m$  approaches either of these values, however, the limit of  $Q_m$  can be obtained by applying L'Hospital's rule. Thus, Equation 5 may be rearranged

$$Q_m = \left\{ \begin{aligned} & \frac{1}{2} \bar{\omega}_n \pi t \left[ \pi \delta(N_m - 1) \bar{\omega}_n t \cos 2\pi\bar{\omega}_n t + \sin 2\pi\bar{\omega}_n t \right] \\ & - \frac{(N_m - 1)^2 \left[ \cos 2\pi\bar{\omega}_n t - \cos 2\pi \frac{N_m}{N_m - 1} [1 + \delta(N_m - 1)] \bar{\omega}_n t \right]}{4[2N_m + \delta(N_m + 1)^2(N_m - 1)]} H(T_m - t) \\ & + \frac{N_m(N_m - 1) \pi \left[ 1 + 2\delta(N_m - 1) \right] [\delta \pi(N_m - 1)^2 \cos 2\pi\bar{\omega}_n t + 2 \sin 2\pi\bar{\omega}_n t]}{4[2N_m + \delta(N_m + 1)^2(N_m - 1)]} H(t - T_m) \end{aligned} \right\} \quad (6)$$

where  $\delta = \frac{1}{\bar{\omega}_n} \left( \frac{\bar{\omega}_n}{1 - N_m} - b_m \right)$  and  $|\delta| \ll 1$ , and

$$Q_m = \left\{ \begin{aligned} & (N_m + 1)^2 \left[ \cos 2\pi\bar{\omega}_n t - \cos 2\pi \frac{N_m - 1}{N_m + 1} [1 + \delta(N_m + 1)] \bar{\omega}_n t \right] \\ & - \frac{4[-2N_m + \delta(N_m - 1)^2(N_m + 1)]}{\pi t \bar{\omega}_n \left[ \pi \delta \bar{\omega}_n (N_m + 1) t \cos 2\pi\bar{\omega}_n t + \sin 2\pi\bar{\omega}_n t \right]} H(T_m - t) \\ & + \frac{N_m(N_m + 1) \pi \left[ 1 + 2\delta(N_m + 1) \right] [\delta \pi(N_m + 1)^2 \cos 2\pi\bar{\omega}_n t + 2 \sin 2\pi\bar{\omega}_n t]}{4[-2N_m + \delta(N_m - 1)^2(N_m + 1)]} H(t - T_m) \end{aligned} \right\} \quad (7)$$

where  $\delta = \frac{1}{\bar{\omega}_n} \left( \frac{\bar{\omega}_n}{1 + N_m} - b_m \right)$  and  $|\delta| \ll 1$ .

Amplitude Coefficients. From the response spectrum to be matched,  $M$  numbers of  $y_k$  maximum responses corresponding to frequencies  $\bar{\omega}_k$  ( $k = 1, 2, \dots, M$ ) can be selected. If the response spectrum is to be matched closely at intermediate frequencies, the choice of the number and relative values of the frequencies is not completely arbitrary nor is the selection of component frequencies  $b_m$ . Procedures for establishing these parameters are discussed later.

Assume that values have been assigned to  $y_k$ ,  $\bar{\omega}_k$ , and  $b_m$  and that a trial set of amplitude coefficients  $\bar{A}_1, \bar{A}_2, \dots, \bar{A}_M$  based on the desired amplification ratio, have been selected. Either Equation 5, 6, or 7 may be searched numerically for the maximum response occurring during the time period  $0 \leq t \leq (T_m + 1/2\bar{\omega}_k)$  and for the time  $t_k$  at which the maximum response occurred.

A set of matrix equations can be written

$$\{\bar{y}_k\} = [Q_{km}] \{\bar{A}_m\} \quad k, m = 1, 2, 3, \dots, M \quad (8)$$

where  $\bar{y}_k$  is the maximum value of  $\sum_{m=1}^M A_m Q_{km}$  corresponding to  $\bar{\omega}_k$ , and  $Q_{km}$  is evaluated at  $t = t_k$ .

Usually, the maximum response  $\bar{y}_k$  at frequency  $\bar{\omega}_k$  calculated from the first trial values of  $\bar{A}_m$  will not coincide with the maximum responses indicated on given spectrum at the corresponding frequency. A new set of  $A_m$  values can then be calculated as

$$\{A_m\} = [Q_{km}]^{-1} \{\bar{y}_k\} \quad k, m = 1, 2, 3, \dots, M \quad (9)$$

Using the modified coefficients, a new set of values for  $\bar{y}_k$  and  $t_k$  can be determined. This process may then be repeated until the calculated maximum responses are approximately equal to the response values indicated on the response spectrum; or  $|\bar{y}_k - \bar{y}_k| < \delta$ , where  $\delta$  is an arbitrarily small number.

The iteration procedure employed to obtain coefficients  $A_m$  is not necessarily convergent for any value of waveform component frequency  $b_m$ . From Equation 8 it may be noted that if the diagonal terms of the square matrix  $[Q_{km}]$  are large compared to the off diagonal terms of the same row, the diagonal terms of the inverse matrix  $[Q_{km}]^{-1}$  will also be relatively large. At each iteration step the new value of coefficient  $A_m$  of each row is influenced principally by the required maximum response value  $y_k$  where  $m$  and  $k$  have identical index numbers and correspond to one system frequency  $\bar{\omega}_k$  on the given spectrum.

Thus, at each iteration step, the variation of  $A_m$  is a single valued function of  $y_k$  and the process converges. To generate large diagonal elements in  $[Q_{km}]$ , the value of  $b_m$  for a given  $N$  must be selected so as to produce a near resonant response; that is, the maximum response at a selected system frequency should be dominated by one frequency component of the forcing function and none of the other frequency components should contribute substantially to it.

Amplification Ratio. The amplification ratio of each individual frequency component of the waveform can be determined from its normalized response spectrum (Figure 2). Maximax responses are indicated by the solid lines while the residual responses are shown by the dotted and dashed lines.

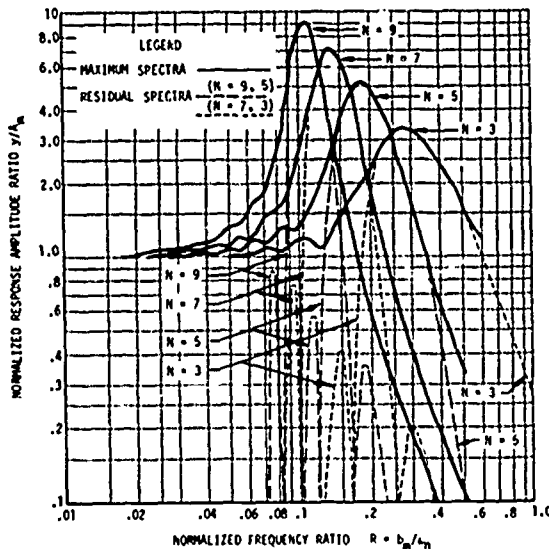


Figure 2. Normalized Maximax and Residual Response Spectra of the Selected Waveform Component for  $N = 3, 5, 7$ , and  $9$

It may be noted from Figure 2 that the maximum normalized response amplitude ratios for components where  $N$  is 3, 5, 7, or 9 are very nearly equal to the value of  $N$  for that component. Where  $N$  is equal to 3 or 5, the value of the normalized frequency parameter  $b_m/\bar{\omega}_n$  is equal to 0.28 and 0.19 respectively. For  $N = 7$  and  $N = 9$ , the normalized frequency at which maximum response occurs is even closer to  $1/N$ . Thus, if the forcing function frequency  $N_m b_m$  is selected to correspond to a proper ratio of the selected system frequency  $\omega_n$  the amplification ratio at the frequency  $\omega_n$

is equal approximately to the selected number of half-cycle oscillations  $N$ .

As an example, assume that it is desired to match a given spectrum at a frequency of 10 Hz with a single frequency component with an amplification ratio of 7. The selected component should have  $N = 7$  half-cycle oscillations at a frequency of  $b_m = 10/7 = 1.43$  Hz. However, if the forcing function is to include components at other frequencies, convergence of the iteration procedure can be assured only so long as the response of any single frequency component is not influenced substantially by those due to the remaining components. Note also, that the amplification ratio of a single component can only be an odd integer and that the minimum amplification ratio is 3 in order to satisfy the requirement that all motions vanish at  $t = T_m$ .

Selection of Frequencies. If the iteration procedure converges, the spectrum of a waveform synthesized as described above will match  $M$  points on the given spectrum and the specified amplification ratios will be approximated at these points. The problem which remains is that of selecting frequencies  $\bar{\omega}_k$  such that they are sufficiently separated to ensure convergence of the solution but not separated so far that at intermediate frequencies a close match between the two spectra cannot be obtained.

The complexity of the equations describing the response motions precludes the use of a closed form solution to identify optimum match points. However, a semi-empirical approach has been developed which, although perhaps not yielding optimum values, has been found to give good results and is simple to apply.

Frequently a design response spectrum, when plotted on four coordinate paper (such as shown later in Figure 4) is trapezoidal with a low-frequency range of constant relative displacement, a mid-frequency range of constant pseudo-velocity, and a high-frequency region of constant absolute acceleration. While spectra of few, if any, physical phenomena are of this exact shape, spectra of many occurrences of a phenomenon are frequently bounded in this manner. While this spectrum shape is not essential to the technique for selecting appropriate frequencies, it does simplify the selection.

To demonstrate the method consider the trapezoidal spectrum shown in Figure 3 and the three collinear points which are to be matched. The problem is to select the three frequencies,  $\bar{\omega}_1$ ,  $\bar{\omega}_2$ , and  $\bar{\omega}_3$  such that both the solution will converge and, in the region of the spectrum between these frequencies, the spectrum of the synthesized wave will lie close to the line which includes the three points.

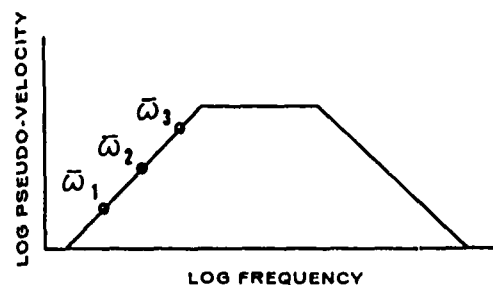


Figure 3. Three Selected Match Points on a Trapezoidal Response Spectrum

In determining the frequencies, two adjacent match points are considered at a time. In the region between two match points, the spectrum is influenced more by the component at the higher frequency. Thus, in the procedure, if the components for the two match points do not have the same value for  $N$ , the value corresponding to the higher frequency component should be assumed to be applicable to both points.

If the match points lie on a line of constant relative displacement, the stipulation can be made

$$\frac{y_k}{y_{k-1}} = \left( \frac{\bar{\omega}_k}{\bar{\omega}_{k-1}} \right)^2$$

While if they lie in a line of constant pseudo-velocity

$$\frac{y_k}{y_{k-1}} = \frac{\bar{\omega}_k}{\bar{\omega}_{k-1}}$$

If they lie in a line of constant acceleration, of course  $y_k = y_{k-1}$ .

Using these relationships, a large number of cases were calculated in which the separation ratio  $a$ , where  $a = \bar{\omega}_k/\bar{\omega}_{k-1}$ , and the parameter  $N_m$  were varied. Optimum separation ratios for different values of  $N$  are shown in Table 1.

TABLE 1 (Reference 1)

## OPTIMUM SYSTEM FREQUENCY RATIOS FOR DIFFERENT VALUES OF N

N	3	5	7	9	11	13
$\alpha = \frac{\bar{\omega}_k}{\bar{\omega}_{k-1}}$	1.3	1.35	1.6	1.45	1.35	1.3

Thus, in the example, if  $N_1 = 5$ ,  $N_2 = 7$ , and  $N_3 = 5$ , and assuming  $\bar{\omega}_1 = 1.0$  Hz,  $\bar{\omega}_2$  should be 1.6 Hz and  $\bar{\omega}_3 = 1.6 \times 1.35 = 2.16$  Hz.

Phasing of Waveform Components. Phasing of the waveform components can be represented by specifying a delay in the starting time of each waveform component. Mathematically, the waveform with phased components can be written similar to Equation 3. Thus

$$W(t) = \sum_{m=1}^M A_m f_m$$

$$f_m = 0 \quad 0 \leq t \leq t_{dm}$$

$$= \sin 2\pi b_m(t-t_{dm}) \sin 2\pi N_m b_m(t-t_{dm}) \quad (10)$$

$$t_{dm} \leq t \leq t_{dm} + T_m$$

$$= 0 \quad t \geq t_{dm} + T_m$$

where  $t_{dm}$  is the time of initiation of the  $m$ th waveform component from time zero.

Equations 4 thru 7 remain valid even when the time delay is included in them. Thus, the time delay term will have little effect on the responses at the spectrum match points. In the range between the match points, however, the effect of the time delay can be much more pronounced and match points selected to minimize error in the intermediate range are no longer valid for all time delays.

Using the separation frequencies ratios shown in Table 1, responses at the intermediate frequencies were calculated for various time delays of any three adjacent frequency components and the ranges of time delays were identified in which deviation was found to be a minimum. If  $t_{dm}$  is the time delay of the  $m$ th frequency component measured from time zero, the time delay between the  $(M+1)$ th and the  $M$ th components is  $t_d, (M+1), M$ . The time delay ratio  $D_r$  is defined as the ratio of the time delay of two adjacent components to the period of a half-cycle of the component at frequency  $N_m b_m$ . Thus

$$D_r = (2N_m b_m) t_d, (M+1), M$$

Note that when  $D_r \leq N$ , the time-histories of the two frequency components occur consecutively. For match point frequency ratios shown in Table 1, a close correlation with the design spectrum in the region between these frequencies cannot be achieved where the time delay ratio exceeds  $N$ .

Ranges of time delay ratios for values of  $N$  from 3 thru 13 which will minimize deviations from the design spectrum in the region between match point frequencies are shown in Table 2. These ranges were calculated for three frequency components whose frequency ratios were as indicated in Table 1, and whose values of  $N$  were equal. For other frequency ratios and combinations of  $N$ , of course, other ranges of time delays might yield equally acceptable correlations with the design spectrum.

TABLE 2

RANGE OF ACCEPTABLE TIME DELAY RATIOS FOR DIFFERENT VALUES OF N RANGES OF TIME DELAY RATIOS,  $D_r$ 

$N = 3$	$N = 5$	$N = 7$	$N = 9$	$N = 11$	$N = 13$
0.15-0.45	0.1-0.14 1.7-2.1	0.8-1.2 2.7-3.0 4.6-4.9 7.3-7.6	0.4-1.3 2.5-3.0 4.6-5.0 7.3-7.6	0.1-1.3 1.1-3.0 4.1-5.3 7.1-7.5	0.0-1.45 2.7-3.2 4.5-4.9 6.3-6.7 10.1-10.5

MWAVSYN Computer Program. A computer program, designated MWAVSYN, was developed to solve Equations 5, 6, and 7 for amplitudes  $A_m$  and to perform the iterations necessary to ensure that the response spectrum of the composite time-history match the design spectrum within an assigned tolerance  $\pm$ .

Input data for the program consists of a definition of the required trapezoidal response spectrum, amplification ratios and time delays as functions of frequency, and the accuracy tolerance imposed on the spectrum of the synthesized waveform. Using the optimum system ratios given in Table 1, the program selects the system frequency match points on the spectrum. An interpolation subroutine then establishes the required response amplitude, amplification ratio, and time delay for each frequency component. Amplification ratios are reduced to integers which are nearest to the odd-numbered half-cycle oscillations. Based on the half-cycle oscillations at the selected system frequency points,

the time delays are forced to stay within the ranges shown in Table 2. A minimum accuracy tolerance of 15 percent has usually been found to be easily achievable.

Output data consists of time-motion histories of the composite waveform expressed in terms of acceleration, velocity, and displacement. Time-motion histories can be punched on cards and/or plotted by a CALCOMP machine. A detailed description of the program is presented in Reference 1.

#### EXAMPLE

Dynamic analyses of structures subjected to earthquake or nuclear weapons effects involve the calculation of time-motion histories at many interior locations. Owing to the many assumptions involved in these analyses, such as the detail nature of the external loads, the soil and site properties, and the dynamic characteristics of the structures themselves, responses calculated at any given location can be regarded as only one of a large number of possible responses. To account for possible differences in the details of the responses due to possible variations in the parameters, the shock environment within various zones of structures are frequently bounded by spectra enveloping the spectra of the calculated responses of all points lying within that zone.

For example, an envelope of spectra of predicted vertical responses of a typical structure is shown in Figure 4 by the dotted lines. In the design of shock isolation systems supported by the third floor, time-histories of the disturbance were required. As no single time-history of the predicted responses had a spectrum which matched the envelope, and as it was not feasible to investigate the behavior of the shock isolation system to all time-histories whose spectra were included in the envelope, it was desirable to synthesize a time-history which would incorporate "worst" conditions.

Based on a consideration of the frequencies of the modes of the shock isolation system, it was concluded that it would be necessary to match the design spectrum only within the range of frequencies from 0.1 to 20 Hz. Time-histories of the calculated structural responses were then filtered within this frequency bandwidth to determine their amplification ratios (Figure 5). Phase relationships were estimated from an examination of the predicted time-histories and the loading phenomena which produced them. It was noted that

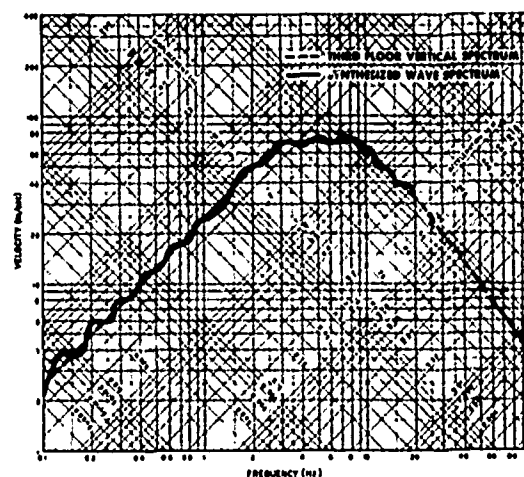


Figure 4. Comparison of the Vertical Spectrum of a Typical Structure and the Spectrum Generated by the Synthesized Waveform

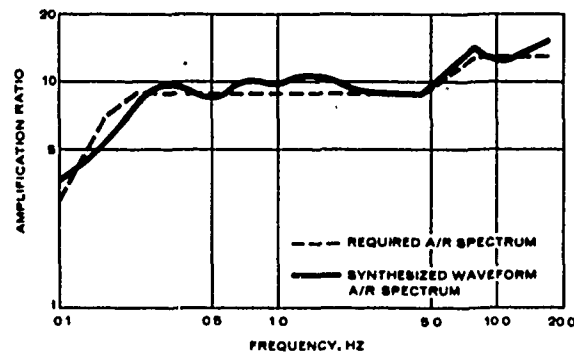


Figure 5. Comparison of the Required Amplification Ratio Spectrum and the Amplification Ratio Spectrum of the Synthesized Waveform

the low-frequency responses of the structure were the first to be energized by their exposure to an outrunning ground motion, that as the airblast pressure wave approached closer to the structure higher-frequency modes were energized, and that the arrival airblast pressure wave at the structure was accompanied by the highest-frequency responses.

Input requirements based on these estimates and the calculated amplitude coefficients of the synthesized waveform are summarized in Table 3. The response spectrum, generated from the synthesized waveform is shown by the solid line in

Figure 4. As noted, the accuracy is within  $\pm 15$  percent at frequencies of lower than 0.3 Hz and better than  $\pm 10$  percent at higher frequencies. The required amplification ratio spectrum and the amplification ratio spectrum of the synthesized waveform are compared in Figure 5. Acceleration, velocity, and displacement time-histories are shown, in Figures 6 thru 8.

#### SUMMARY

A technique has been developed which simplifies the synthesis of an oscillatory waveform incorporating specified amplification ratios and time delays and matching a given response spectrum. The nature of the basic synthesized waveform limits the frequency components which can be included in the waveform and requires that their amplification ratios be equal to odd integers greater than unity.

Despite these restrictions, however, the technique is a significant improvement over the older cut-and-try methods and, in addition, has the important advantage of permitting the systematic variation of amplification ratio and phase, two parameters of vital importance to the responses of most practical systems.

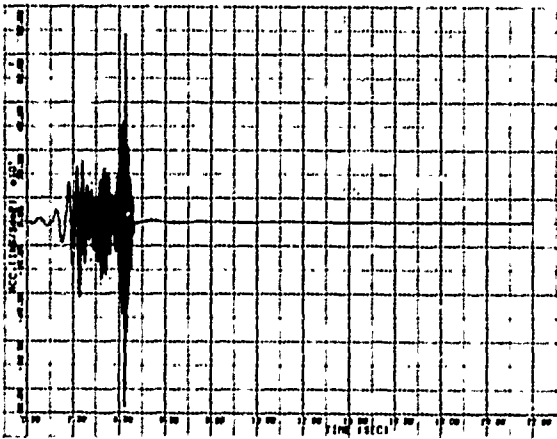


Figure 6. Acceleration-Time Function of the Synthesized Waveform

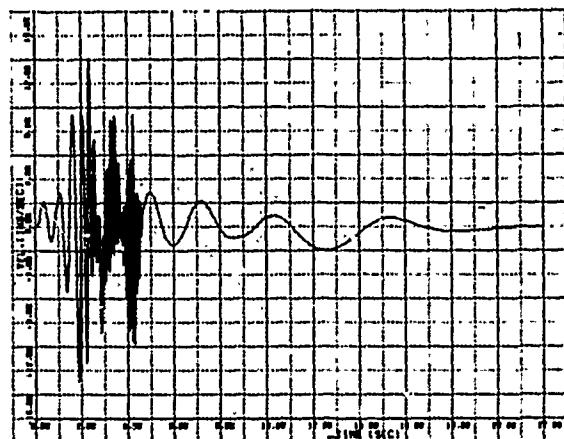


Figure 7. Velocity-Time Function of the Synthesized Waveform

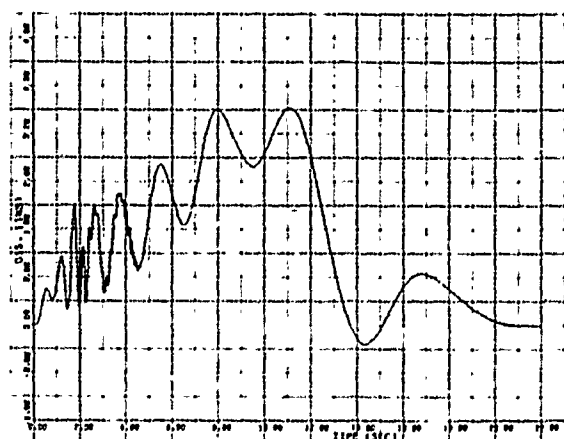


Figure 8. Displacement-Time Function of the Synthesized Waveform

TABLE 3

SYSTEM FREQUENCIES, COMPONENT FREQUENCIES, TIME DELAYS, AND  
CALCULATED AMPLITUDE COEFFICIENTS OF THE SYNTHESIZED WAVEFORM

NUMBER OF FREQUENCY COMPONENT $m$	SELECTED SYSTEM FREQUENCY $\omega_m$ , Hz	COMPONENT FREQUENCY $b_m$ , Hz	NUMBER OF HALF-CYCLE OSCILLATIONS $N_m$	TIME DELAY $t_{dm}$ , sec	AMPLITUDE COEFFICIENT $A_m$ , in./sec <sup>2</sup>
1	0.100	0.028	3	0	0.37
2	0.160	0.023	7	0	0.64
3	0.232	0.026	9	0	1.02
4	0.336	0.037	9	0	1.71
5	0.488	0.054	9	0	4.43
6	0.706	0.078	9	0	7.51
7	1.025	0.114	9	0	16.42
8	1.487	0.165	9	0	31.90
9	2.152	0.239	9	0.925	76.70
10	3.120	0.347	9	1.563	153.41
11	4.530	0.503	9	2.005	219.45
12	6.110	0.555	11	2.889	232.05
13	7.950	0.612	13	3.707	246.13
14	10.310	0.793	13	4.006	312.37
15	13.430	1.033	13	4.006	280.70
16	17.48	1.345	13	4.006	250.35

## REFERENCES

1. R. C. Yang, Modification of the WAVSYN Computer Program, Document No. SAF-82, The Ralph M. Parsons Company, 30 April 1971

## THE RESPONSE OF AN ISOLATED FLOOR SLAB—RESULTS OF AN EXPERIMENT IN EVENT DIAL PACK (U)

J. M. Ferritto  
Naval Civil Engineering Laboratory  
Port Hueneme, California

This paper outlines a test of a horizontal cylinder covered with an earth berm subjected to the pressure and drag forces in the 300-psi overpressure region from the detonation of the 500-ton high-explosive shot of Event DIAL PACK. The objective of this test was to obtain information on the response of an isolated floor slab placed on a soil fill inside the concrete cylinder. Data from seventeen channels of active instrumentation, composed of a pressure cell, velocity gages and accelerometers, were recorded. Reduction of the data was made.

### INTRODUCTION

#### Objective

The prime objective of this project was to obtain information on the response of an isolated floor slab inside a horizontal cylinder covered with soil and subjected to pressure and drag forces in the 300-psi overpressure region. The specific objectives were:

1. Determine the absolute motions of the floor slab caused by the blast loading.
2. Determine the motions of the slab relative to the cylinder.
3. Evaluate the survivability of the structure including the performance of the retaining wall.

#### Background

There is a requirement to store sensitive equipment in aboveground hardened shelters. The equipment must be shock isolated from the shelter. It is important to limit the blast induced motions transmitted to the floor slab to reduce the shock isolation requirements. The concept of the concrete slab on a soil fill inside a horizontal concrete cylinder is being considered as a possible means for diminishing the shock motion. This structure, if satisfactory, will provide simple, inexpensive shelters which can be rapidly constructed and will eliminate the cost of providing expensive shock isolation platforms.

#### Shock Isolation

An essential element in the design of protective structures is the provision of a reliable shock isolation system for personnel and equipment. The levels of shock to which a system acting at its designed structural capacity may be exposed can be very high, with ground accelerations over a hundred g's and ground displacements over two feet. Very few devices are capable of withstanding shocks of this magnitude without serious damage. A more serious limitation is the peak shock which an unsupported human being can tolerate. Yet the unimpaired functioning of both personnel and equipment immediately following an attack must be preserved if the facility is to fulfill its intended mission.

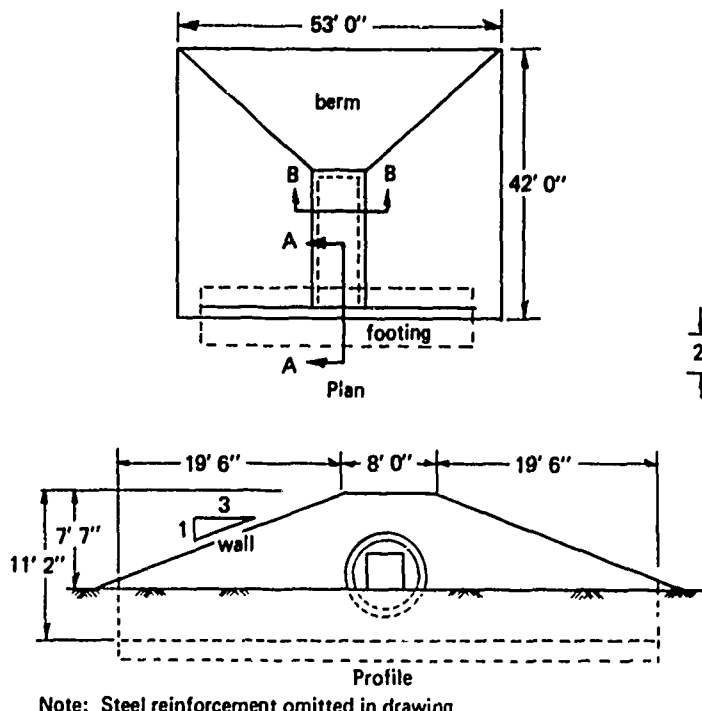
In the design of shock resistant equipment, the required strength of the equipment is controlled by its response to the shock produced by the dynamic loads on the structure. Expensive conventional shock isolators could increase the cost of the structure to an extent that might be unacceptable. An alternate approach is to isolate the floor slab by "floating" it on a layer of soil within the cylinder. The cylinder is a closed structure capable of being constructed economically and supporting high overpressures with minimum disturbance. The floor slab must be strong enough to carry the equipment load and resist the longitudinal and torsional motions from the shock. The motions of the floor slab are related to the motions of the surrounding concrete cylinder transmitted through the soil fill. However, as the cylinder is displaced downward, the inertia of the isolated floor slab tends to reduce the peak accelerations felt on the floor.

Preceding page blank

## EXPERIMENTAL PROGRAM

### Test Structure

The isolated floor slab test was planned as part of Event DIAL PACK [1], a high explosive field test of 500 tons conducted at the Defence Research Establishment Suffield (DRES), Ralston, Alberta, Canada. The test structure, located at an azimuth of 120 degrees 270 feet from ground zero, was at an anticipated side-on pressure range of 300 psi. The structure location and construction details are shown in Figures 1 and 2. It consisted of a 6-foot-inner-diameter 7-inch-thick horizontal right-circular cylinder aligned perpendicular to the direction of propagation of the blast wave. The invert of the cylinder was 1 1/2 feet below the natural grade. The cylinder was covered with 2 1/2 feet of compacted fill forming a tapered earth berm extending along the sides of the cylinder and one end at a 3:1 slope. A 2-foot-thick retaining wall held the other end of the earth berm in place; a bolt-on steel closure plate was incorporated in the retaining wall to provide access into the cylinder. One and one-half feet of compacted soil was placed inside the cylinder, and a 6-inch concrete slab was cast over the soil. A spring-mass system, Figure 3, was installed 4 feet from the rear end of the slab to simulate equipment on the slab. Figure 4 shows the structure under construction, and Figure 5 shows the completed structure.



### Instrumentation

Seventeen channels of active instrumentation consisting of eight structure velocity gages, eight accelerometers, and one pressure cell were used. The layout of the instrumentation is shown in Figures 6 and 7. The first letter, A or V, indicates an accelerometer or a velocity gage; the second letter, V or H, indicates vertical or horizontal orientation. The data were conditioned, amplified, and recorded on 32-track tape recorders located in a bunker 2,700 feet from ground zero. An inter-range instrumentation group timing system was recorded on one track of each tape recorder and later used in the data reduction. Timing from an NCEL-designed timing generator was also recorded on one track of all recorders. A detonation zero pulse provided by DRES was recorded as received directly onto the last track of each tape recorder to provide a reference for data located on different tape recorders.

The gages were mounted on steel plates cast in or bolted to the structure. The pressure cell was installed in a specially designed concrete mount which was cast in the wall with the heat shield flush with the face of the wall. Passive instrumentation consisted of three orthogonally oriented reed gages mounted on the slab and a scratch gage (Figure 7) mounted between the retaining wall and the cylinder.

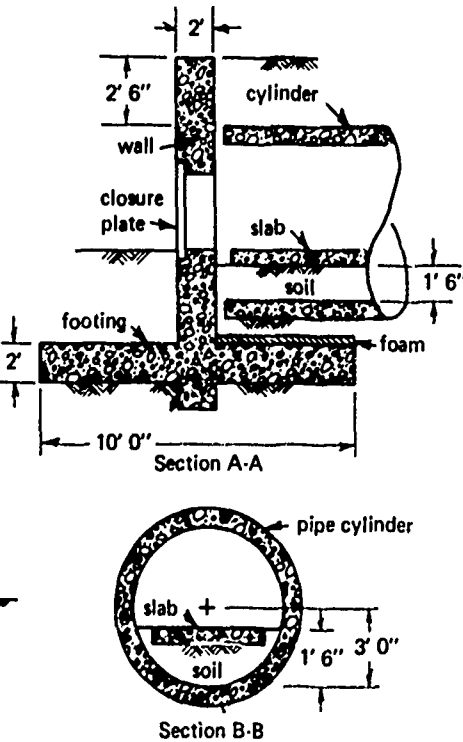


Figure 1. Construction plan.

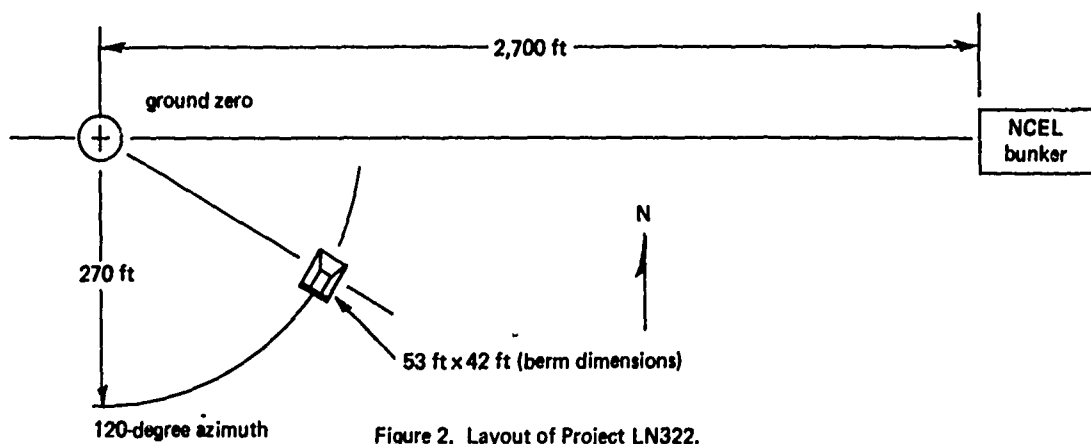
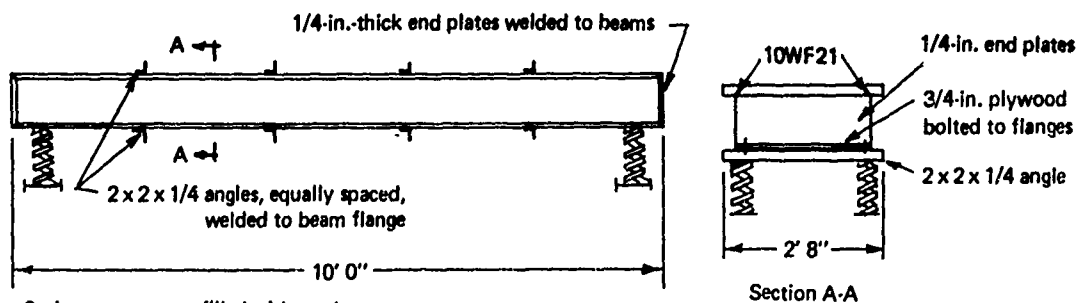


Figure 2. Layout of Project LN322.



Spring-mass system filled with sand bags to a total weight of 4,000 lb.

Figure 3. Spring-mass load system.

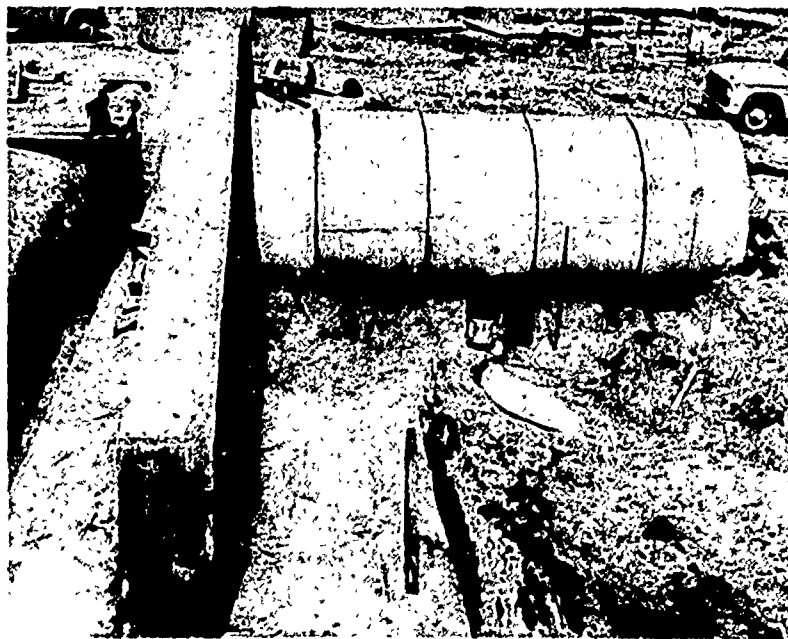


Figure 4. Test structure under construction.

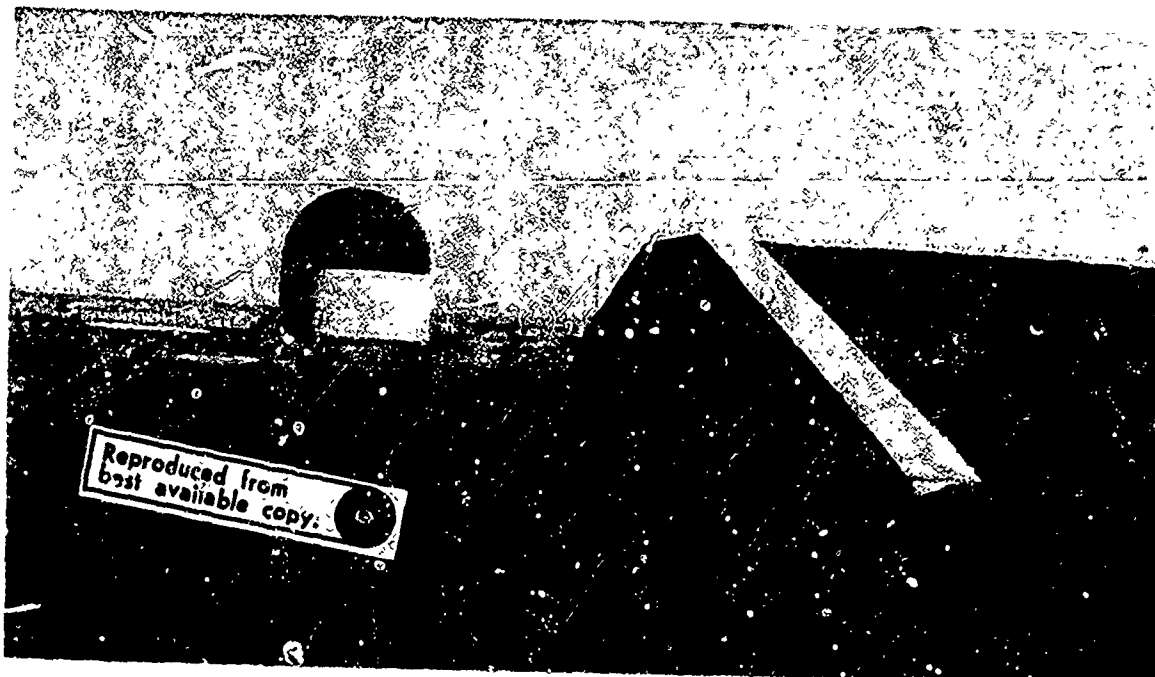


Figure 5. Completed test structure prior to test.

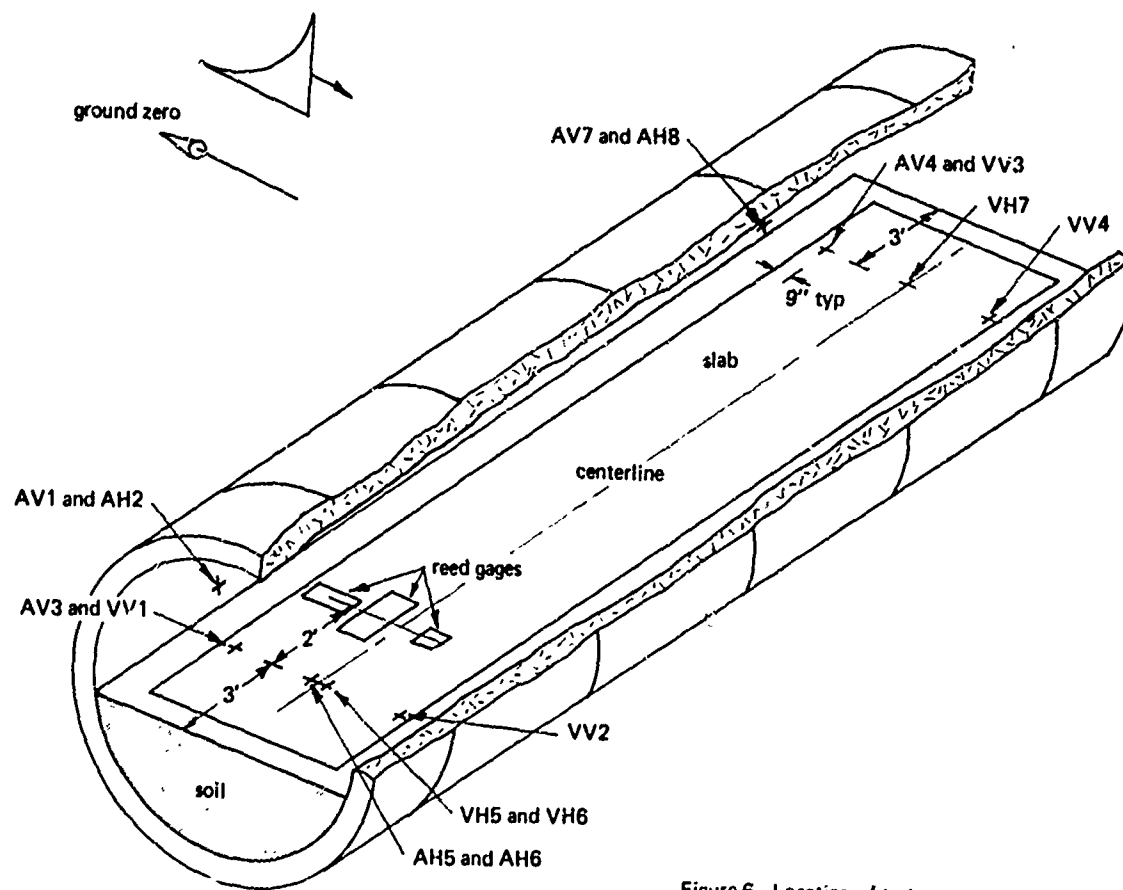


Figure 6. Location of test gages.

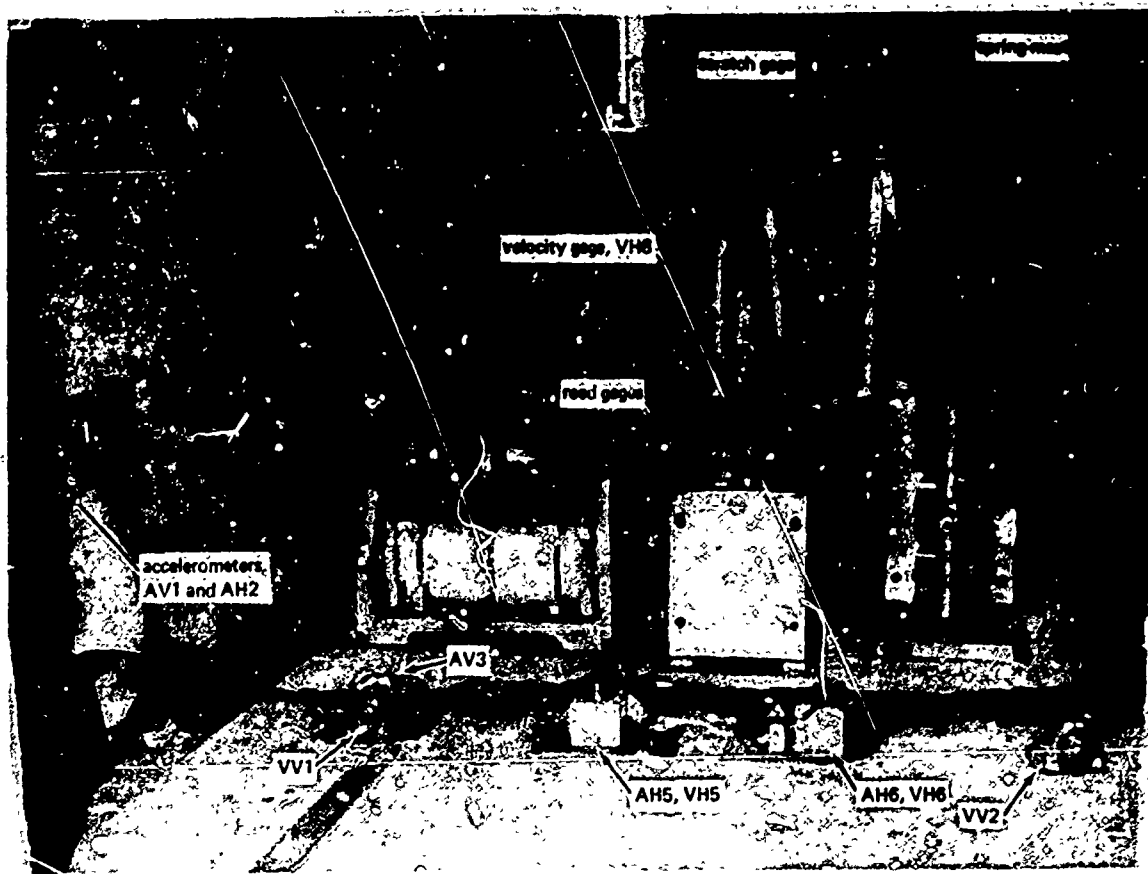


Figure 7. Test gages.

The pressure gage was set in the outside face of the retaining wall to measure the free-field side-on overpressure. Horizontal and vertical accelerometers were set on the cylinder near each end to measure the horizontal and vertical components of the cylinder motion. The slab instrumentation was placed in the same cross-sectional planes as the cylinder instrumentation to evaluate the relative motions of the slab with respect to the cylinder. A vertical and two horizontal accelerometers were set at the center of the floor slab to record floor accelerations in three orthogonal directions. The two vertical velocity gages at each end were installed near opposite edges of the floor slab to record rotational motions of the floor slab. The three orthogonal reed gages were used to provide records of horizontal and vertical shock spectra. The scratch gage was used to record relative motion between the retaining wall and the cylinder.

## RESULTS AND DISCUSSION

### Observed Damage

The detonation of the 500-ton high-explosive charge occurred on 23 July 1970. At D+1 hour project personnel returned to the LN322 site. The fireball had blackened the retaining wall and the berm with a layer of carbon dust. Twelve inches of crater ejecta were deposited in front of the ground zero end of the retaining wall. This level was reduced to about 2 inches in front of the closure plate. The maximum size of the ejecta was estimated to be 8 inches. Approximately 18 inches of the berm on the ground zero side were compressed and/or blown away.

A pattern of major diagonal cracks was noted on the wall. Several of these cracks were observed on the top surface of the wall and extended completely through the wall. The wall had about 1-degree permanent rotation into the berm. Some cracks in the concrete were noted around the closure plate. At D+1 day the closure plate was removed revealing additional cracking in the wall. These cracks appeared to go completely through the wall.

The concrete cylinder sections suffered significant damage. A horizontal line of compressive failure was located at about 30 degrees from the top of the cylinder on the leeward side of all the sections. A region of major spalling and tensile cracking was noted at about 90 degrees from the compression zone (60 degrees from the top of the cylinder) on the windward side of all of the sections (Figure 8). The first three sections had been unintentionally oriented so that the splice in the circular reinforcing steel was located in the region of the tension failure. The splice appeared to have failed, and a section of the pipe was pushed inward approximately 4 inches along this line. The floor slab was littered with spalled concrete and sand.

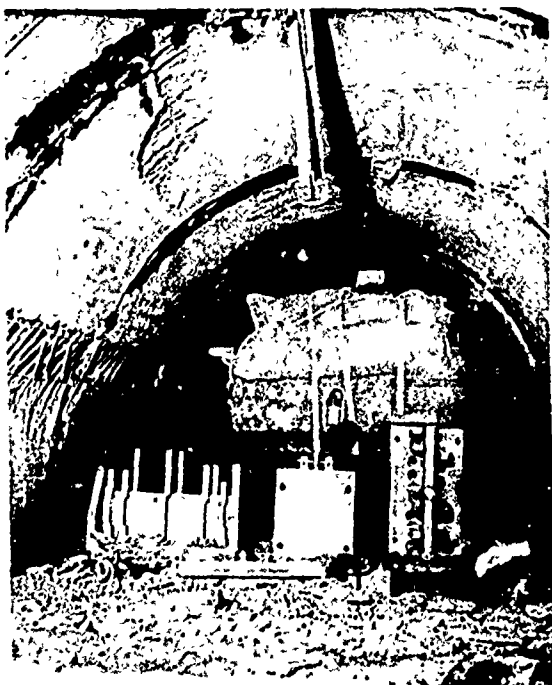


Figure 8. Postshot view of interior of structure.

Postshot measurements revealed that the slab rotated clockwise approximately 3 degrees. The permanent relative horizontal translation of the slab was 1/2 inch away from the ground zero side of the cylinder. The center of the slab remained at the same elevation relative to the cylinder. The permanent horizontal translation of the cylinder with respect to the retaining wall was 3-5/16 inches away from ground zero.

#### Reed Gages

The plates from the reed gages were removed, and measurements of the traces were taken and converted to displacements. These values, plotted in Figure 9, give the shock frequency spectra of the slab.

The reed gage consists of a number of masses on a rigid base. The response of equipment mounted on the slab to a given shock can be determined from the measured response of a reed having the same frequency and damping as the equipment to the shock. Thus, the shock spectra diagram can be used to determine the shock isolation requirements of the equipment.

#### Active Instrumentation

All of the active channels of instrumentation functioned satisfactorily. The analog data tape was returned to NCEL where the data were converted to digital form using the NCEL Analog-to-Digital Converter. Accelerations were sampled at increments of 0.1 msec for 200 msec, and velocities were sampled at increments of 1 msec for 2,000 msec. No filtering was used. The data were automatically plotted using a CDC 6600 computer.

Figure 10 is a plot of the side-on pressure data recorded at the midpoint of the retaining wall above the closure plate. The peak pressure recorded was 317 psi. The shock wave had an arrival time of 32 msec and a total duration of the positive phase of 103 msec. The actual duration of the positive phase was longer than the expected value of 60 msec.

In several radial horizontal velocity plots, the velocity at late time did not return to zero, indicating permanent tilting had occurred. Visual measurement made after the shot indicated a permanent tilting of the slab of about 3 degrees clockwise when viewed from the retaining wall looking into the structure. Correction factors were subtracted in an attempt to remove the tilting effect. The accelerations and velocities were integrated. A summary of the peak values is presented in Table 1. Positive values indicate motions down, away from ground zero, and to the right looking at ground zero.

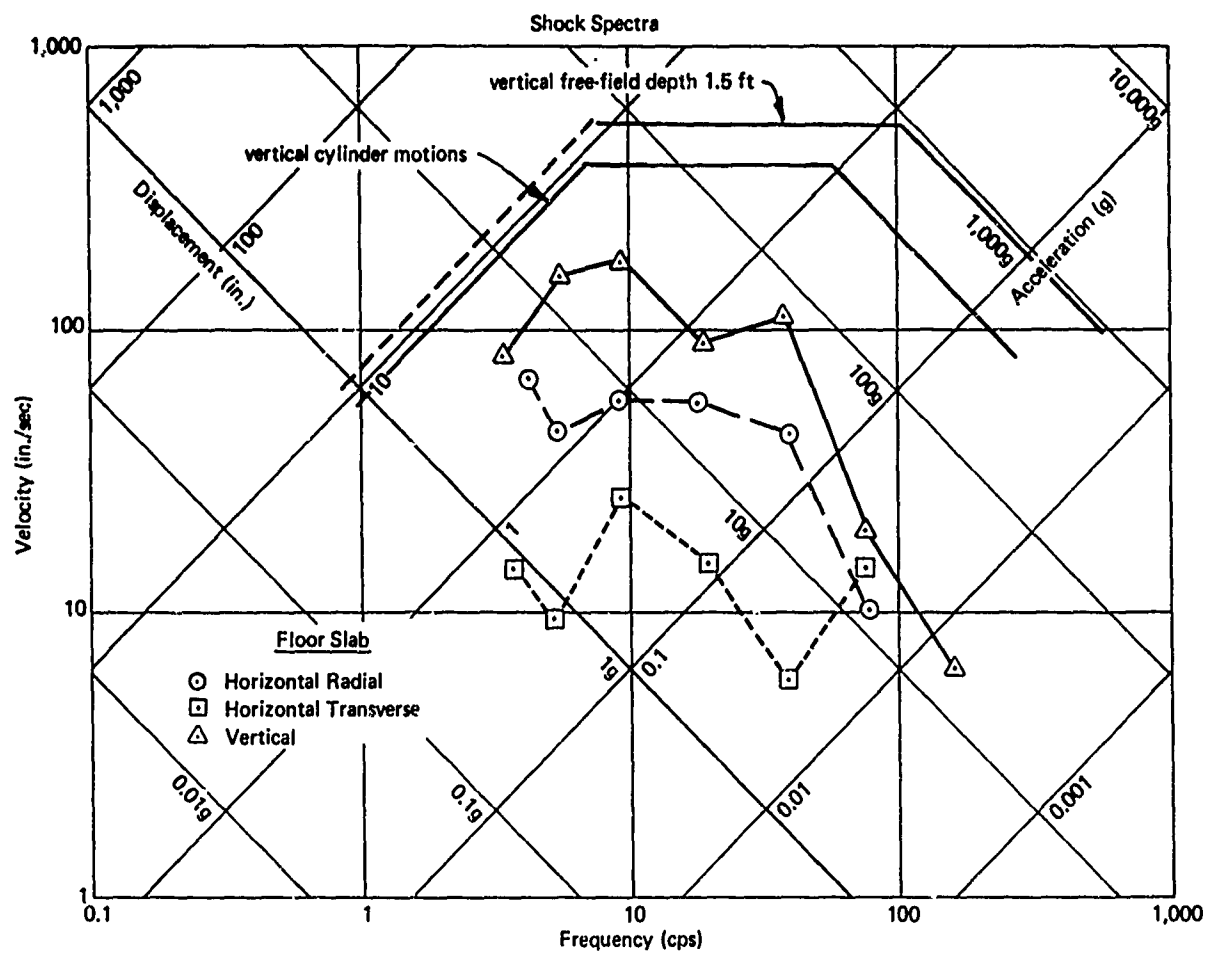


Figure 9. Shock spectra of floor slab.

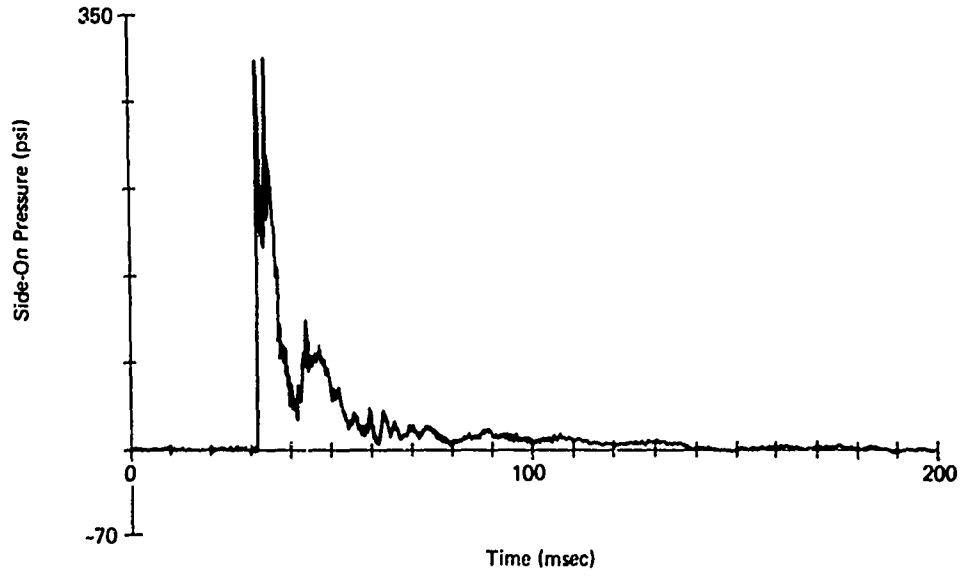


Figure 10. Pressure--time curve, gage PS1.

Table 1. Peak Instrumentation Values

Type of Instrumentation	Gage No.	Peak Acceleration (g)		Peak Velocity (fps)		Peak Displacement (in.)	
		Negative	Positive	Negative	Positive	Negative	Positive
Cylinder							
Vertical accelerometer	AV1	19.6	146.8	2.3	20.1	0.0	8.5
Vertical accelerometer	AV7	112.8	173.9	7.6	22.4	2.4	5.6
Horizontal accelerometer	AH2	90.2	52.6	9.9	5.0	2.3	3.2
Horizontal accelerometer	AH8	72.4	86.0	6.3	11.2	0.4	13.9
Floor Slab							
Vertical accelerometer	AV3	23.7	28.5	4.8	10.7	0.0	4.9
Vertical accelerometer	AV4	15.5	11.3	1.1	10.5	0.0	5.5
Vertical velocity	VV1			5.4	11.3	0.0	5.3
Vertical velocity	VV2			2.0	9.2	0.0	5.4
Vertical velocity	VV3			1.0	9.1	0.0	4.8
Vertical velocity	VV4			2.0	7.4	0.0	6.6
Horizontal transverse accelerometer	AH6	3.0	2.2	0.0	.5	0.0	.4
Horizontal transverse velocity	VH6			0.7	.9	0.4	.6
Horizontal radial accelerometer	AH5	13.5	19.4	0.0	3.8	0.0	2.8
Horizontal radial velocity	VH5			1.0	3.4	0.6	3.8
Horizontal radial velocity	VH7			1.3	3.9	0.3	4.0
Spring-Mass							
Horizontal radial velocity	VH8			0.7	3.2		

Note: 1. Accelerometer data taken for 200 msec, and velocity gage data taken for 2,000 msec.  
 2. Positive direction is downward, away from ground zero, and to the right facing ground zero.

The horizontal and vertical displacements obtained from double integrations of cylinder accelerations were used to produce a plot of cylinder movement (Figure 11). Although there may be some error associated with this procedure, it is believed to be accurate enough to relate direction of motion and approximate orders of magnitude of movement. Similar plots, Figures 12 and 13, were made for the slab movement using the horizontal and vertical displacements obtained from the integration of the velocities.

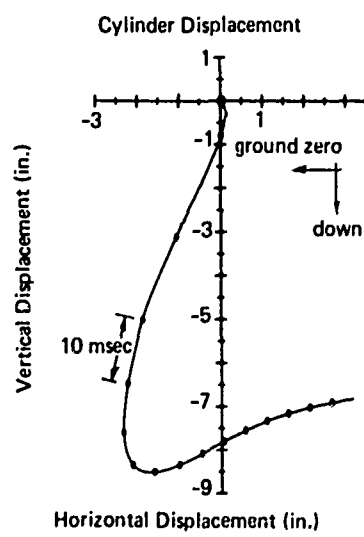


Figure 11. Displacement of cylinder.

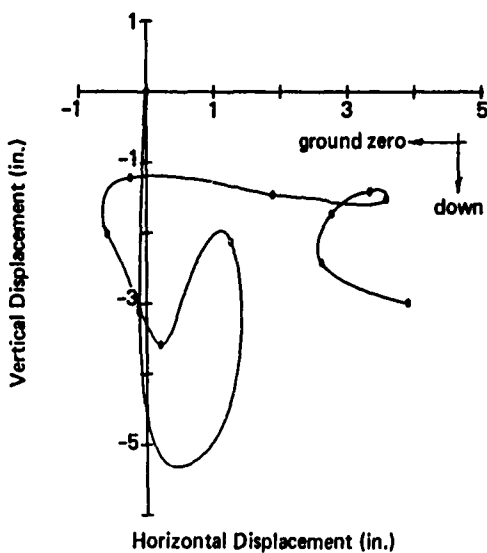


Figure 12. Displacement of floor slab, windward side.

Figures 11, 12, and 13 indicate the motion of the structure was initially downward and away from ground zero, then downward and toward ground zero. Subsequent motion at about  $D+100$  msec was upward and away from ground zero. The motion toward ground zero is quite unusual and unexpected, but is believed to be valid. Possible sources of error such as gage rotation, reversed calibration, or an erroneous gage were considered and found not to have been present. This effect was observed on four independent sets of instrumentation. Ovaling of the cylinder was also dismissed as a possible explanation because the direction of ovaling near the gage location was inward rather than outward. The initial downward movement was caused by the direct compressive wave. A possible explanation of the horizontal movement toward ground zero is the reaction to the magnitude shear wave which enveloped the berm producing planes of opposing shear forces. These forces gave rise to motion as slippage occurred. The reverse movement of the structure was caused by a combination of rebound and direct induced ground shock arriving about 100 msec after detonation.

The time to peak positive accelerations of the cylinder was about 12 msec after the arrival of the blast wave; however, the time to peak positive acceleration of the floor slab was about 110 msec after the arrival of the blast wave. The magnitude of the floor slab accelerations was substantially reduced compared to that of the cylinder. Once set in motion, the movement of the floor slab was independent of the cylinder. The slab appears to have remained stationary during the initial movements of the cylinder, and then moved downward until coming to rest on the soil.

Figure 14 shows the relative vertical displacement of two velocity gages located on the slab and separated by 36

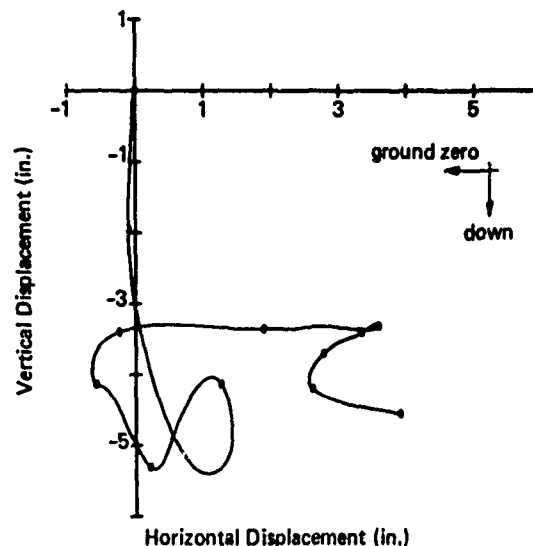


Figure 13. Displacement of floor slab, leeward side.

inches. The amount of rotation shown is about 3 degrees, confirming the field measurement. From Figure 14, the rotation of the slab began at about 125 msec and rotated the full amount at about 200 msec.

Generally the data obtained in the first few hundred milliseconds are very reliable. After this period secondary effects may adversely affect the data. The peak values and wave shapes in early time (several hundred milliseconds) are quite reliable and are relatively the most important. Accelerometers are usually more reliable than velocity gages when rotation of the gage is suspected. Velocity gages experiencing rotation as slight as three degrees may erroneously indicate apparent motion of 100 percent of the anticipated value in magnitude. Evidence that this has occurred is noted when velocities at late times (2 seconds) fail to return to zero. Accelerometers are relatively insensitive to rotation and are influenced only by the product of the sine of the angle of rotation and the component of acceleration in the perpendicular direction. Thus, for small rotations the influence is negligible.

Integrations of acceleration data give reasonable indications of wave shape and velocity. Displacements from integration of accelerations should be capable of giving an order of magnitude of movement and direction. The integration of data represents a second level of confidence.

#### Shock Isolation

Using an isolated concrete slab "floating" on sand within a horizontal cylinder reduced the peak acceleration of 174g's on the cylinder to about 28g's on the floor slab. The 22-fps peak vertical velocity of the cylinder was reduced to about 11 fps. Table 2 compares the peak motions and shows the

shock isolation of the isolated floor slab.

#### CONCLUSIONS

The objectives of this project were satisfied. The motions of the floor slab were determined, and the survivability of the structure evaluated. All of the instrumentation functioned satisfactorily. Data were obtained to compute the shock isolation requirements for equipment to be stored in the shelter. The significant findings and conclusions are:

1. The isolated floor slab significantly reduced the transmitted motion.
2. Shock spectra data for designing the required shock isolation system has been determined.

Table 2. Comparison of Peak Motions

	Velocity (fps)	Acceleration (g's)
<b>Vertical</b>		
Cylinder	22	174
Floor slab	11	28
<b>Horizontal</b>		
Cylinder	11	90
Floor slab	4	19

#### REFERENCES

1. NCEL Technical Report R-726, "Dynamic Response of an Isolated Floor Slab—Results of an Experimental Test in Event DIAL PACK," by J. M. Ferritto, May 1971, Port Hueneme, California.

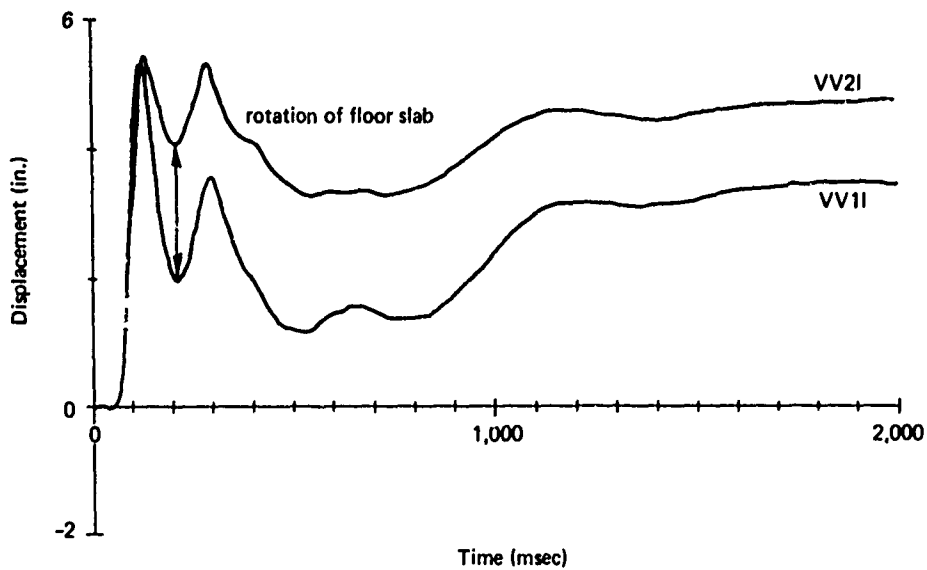


Figure 14. Rotation of floor slab.

## DISCUSSION

Voice: Concerning the measurement on the floor slab, does this refer to the isolated mass sitting on top of the springs, or is the slab sitting on top of the soil?

Mr. Ferritto: All the measurements were made on the actual concrete floor slab. The spring mass system shown in the slides is simply used to provide an equivalent equipment on the floor slab.

Voice: Is it correct that you were not trying to establish the effect of isolation using a layer of soil?

Mr. Ferritto: Basically that is correct. The springs of the mass and the weight of the mass were selected to provide the frequency that we would expect from a typical piece of equipment placed on the slab. It actually represented what we tried to approximate in the model.

Mr. Koen (Bell Telephone Laboratories): The high accelerations in your last slide would indicate the presence of very high frequency data. You also mentioned that you planned to use nonlinear finite element analysis techniques. Would this predict any of the high frequency phenomena which I assume to be present?

Mr. Ferritto: To this date we have been running a structural analysis primarily interested in the optimization of the structure itself without looking at the isolation characteristics. We have made several runs. The time step and other information we have used in sizing the finite element mesh has been selected, basically, to satisfy the structural characteristics. The structure, as we are now looking at it, has

about 4,800 degrees of freedom, so it is quite a large problem. We are attempting first to look at it structurally, and the time step is made as large as possible keeping the economics in mind in order to be able to run the problem.

Voice: Do you solve 4,000 dynamic degrees of freedom?

Mr. Ferritto: Yes, We are running approximately 300 time increments to approximate about 100 milliseconds, I believe.

Voice: What is the highest frequency of the model you are putting together?

Mr. Ferritto: It is a very complex problem because the loading is quite complicated. We have a traveling wave. We have a very complex soil-structure interaction. The extent to which the berm participates in the problem still remains an unknown. This is one reason we are using a plane strain, finite element analysis with a quadrilateral element rather than another type of modeling procedure. The period of the cylinder by itself in compression is about 2 milliseconds. The period of the cylinder in flexure is about 11 milliseconds.

Mr. Zudans (Franklin Institute): I am interested in your 4,000 dynamic degrees of freedom. Are you modeling it as a two-dimensional infinitely long type of strip?

Mr. Ferritto: Yes, it is a plane strain model. The quadrilateral element that we are using has 12 degrees of freedom and approximately 400 elements.

## A SHOCK-ISOLATION SYSTEM FOR 22 FEET OF VERTICAL GROUND MOTION\*

E. C. Jackson, A. B. Miller and D. L. Bernreuter  
Lawrence Livermore Laboratory, University of California  
Livermore, California

Shock isolation of fragile equipment from severe ground motion induced by underground nuclear detonations requires special techniques for inexpensive, reliable performance. Two shock-mitigation systems that have been used successfully for the past several years are described. These systems have allowed equipment to be located closer to the explosive source, resulting in considerable savings in diagnostic cable costs. A new system has been designed for even more severe ground motion. The new design, the instrumented testing program, and test results are discussed in this paper.

### INTRODUCTION

Experimental data from underground nuclear detonations are conditioned and recorded by sensitive electronic equipment. Normally, the experiment requires the equipment to be located relatively close to the explosive source. In many cases, ground motion induced by these nuclear explosions requires shock-isolation systems capable of supporting heavy instrumentation vans and isolating them from a very severe three-dimensional dynamic environment.

During the past several years we have designed, developed, and fielded several different shock-mitigation systems. Two basic systems have been standardized and are discussed in this paper. These standard designs have allowed us to reduce signal attenuation and to reduce very large cable costs by locating equipment close to the source. Shock-isolation costs themselves have also been reduced, and overall reliability has been increased by this standardization.

To meet requirements for even more severe ground motion, we have designed a shock-mitigation system to withstand vertical ground motion up to 32 ft/sec, or about 22 ft displacement. The new system is a modification of one of our standard designs, with the usual crushable materials replaced by a columnar energy absorber. This energy absorber allows a longer stroke without an increase in payload initial height.

In this paper, we discuss the new design, the instrumented testing program, and the test results.

### REQUIREMENTS AND ENVIRONMENT

For maximum utilization and mobility, most electronic equipment is housed in truck-trailer vans or portable buildings on skids. Most trailers are conventional highway type, but a few have been fabricated for higher shock requirements (7 g vertical). Loaded weights vary from less than 10,000 lb to 72,000 lbs for trailers and up to 140,000 lb for skid buildings. There is a large variety of electronic equipment and accessories. Shock fragility levels vary from 1/2 g to more than 50 g. When properly mounted, most equipment falls within our medium fragility range - 6 g vertical.

The ground motion induced by an underground nuclear detonation varies considerably, depending upon yield of device, geology, and location of interest. The optimum location, with respect to reliability and overall costs for diagnostic and other portable instrumentation bunkers located on the surface, regardless of yield, is safely outside the subsidence crater, but not more than half the depth of burial from surface ground zero. In this area the surface usually spalls and follows a ballistic path. Figure 1 is a time history curve of surface ground motion for a large event, but the characteristics are typical of the spall region. The vertical slapdown acceleration pulse is usually followed by a horizontal radial pulse, which can be either away from or toward surface ground zero. Horizontal tangential pulses are also occasionally significant.

\* Work performed under the auspices of the U.S. Atomic Energy Commission.

Preceding page blank

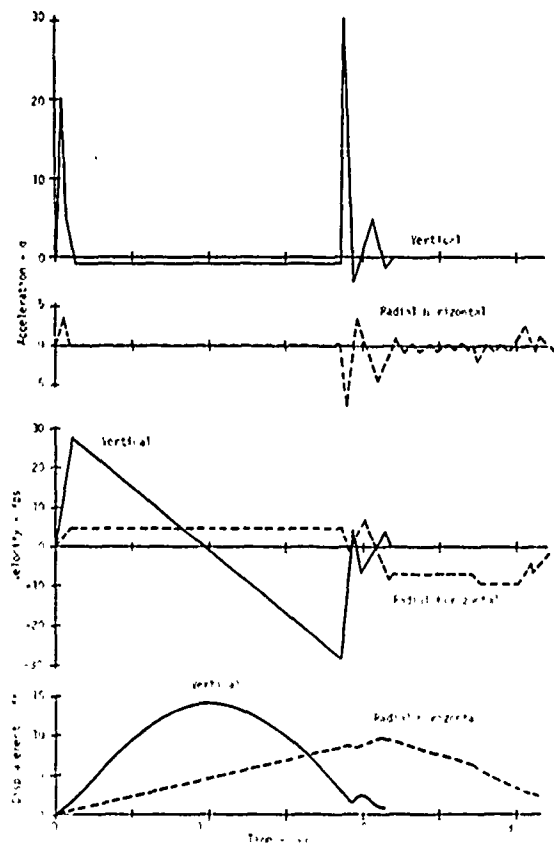


Fig. 1 Typical time history of ground motion within the spall region.

#### DESIGN METHODS

The overall problem blends together: (1) definition of input, i.e., ground shock parameters; (2) fragility level or shock sensitivity of equipment to the input and response (i.e., does it record or transmit through shock arrival time?); and (3) design of a fail-safe shock mount system to modify the shock environment when required.

The reliability of a system is strongly dependent on a foreknowledge of the input conditions. Prediction of surface ground motion for our purposes relies heavily on empirical data and methods (see Ref. 1). The shock-isolation design for a given event is based on nominal and maximum ground motion estimates in order to obtain a factor of safety based on energy. The maximum estimates are based on maximum credible yield and maximum scatter of applicable empirical ground-motion data. Whenever possible, the design is based only on peak input parameters since detailed time histories of ground motions are very difficult to predict.

The basic requirement of all shock-mitigation systems is controlled relative displacement and force transmission between the shock input and the package or system to be isolated. The fundamental classification of shock and vibration systems is the manner in which it stores, absorbs, or dissipates energy. A great many different materials and methods are used in shock and vibration isolation. A complete discussion of all parameters involved in shock mounting items for underground detonations would be quite long; therefore, in this paper we will describe only a few methods that we have been using.

In some cases, accurate final position or alignment of the equipment with respect to the ground is important and must be considered in the overall design. However, in most cases position and alignment are not important. This paper concerns only these cases. This variance allows us to design around the three-dimensional ground-motion environment by decoupling the horizontal shock components. Decoupling is achieved by placing the system on surfaces with very low friction. Vertical accelerations are isolated by constant force vs displacement energy absorbers. Ideally, these absorbers should have negligible rebound characteristics. With this condition the conventional analysis is relatively simple (see Ref. 1). Accurate measurement of the payload weight and center of gravity and the appropriate sizing of the energy absorbers minimize the amount of differential vertical displacements (tilting) of the system. When required, excessive horizontal displacements are controlled by nylon tethers. Energy-absorber deceleration set values are based on equipment fragility levels and a structural amplification factor of 1.75. This factor accounts for the elasticity of the shock mount structures, equipment mounting brackets and the trailer structure. Dynamic effects of impact velocity on energy absorber forces are considered separately.

We have developed several shock mount systems varying in complexity and cost. The selection of a system for a given event depends primarily on the estimated maximum vertical ground motion as shown in Table 1. The energy-absorber system does not necessarily have a factor of safety greater than unity with these maximum estimated input conditions, except for the incorporation of fail-safe features. The respective nominal ground motion values are much less.

#### FOAM AND REUSABLE CRIBBING SYSTEM

For many events the estimated maximum ground motion is less than 10 ft/sec and we use the foam and reusable cribbing (F&RC) system for trailers and vans. It includes permanent reusable wood cribbing with an angle iron base

TABLE 1  
Shock-Mitigation System Limits

System	Maximum Vertical Ground Motion	
	Velocity, ft/sec	Displacement, ft
Foam and reusable cribbing	10	~ 2-1/3
Universal guided column	24	~ 12
Full-stroke guided column	32	~ 22

tied to the trailer (Fig. 2). This forms a solid extension of the trailer structure to the normal suspension height and is capable of withstanding the horizontal loads. A simple foam and plywood crush pad is bolted under the cribbing. Styrofoam is used because for the required heights and surface areas, it is strong enough to withstand the horizontal shear forces without additional guide structures. The crush strength of the polystyrene foam is constant for the first 35% of deflection and increases gradually to about 140% at 65% deflection. Because very-low-friction surfaces are not required, the crush pads sit directly on plywood ground pads.

#### UNIVERSAL GUIDED-COLUMN SYSTEM

The universal guided-column (UGC) system was designed for ground motions exceeding the F&RC system capabilities and up to a maximum of 24 ft/sec or about 12-ft displacement. A typical installation is shown in Fig. 3. It is an energy-absorption system that can use almost any crushable material. Commercially available polystyrene rigid foam has been the most inexpensive reliable material. The vertically controlled crush load is transferred to the trailer via a cross beam. Each end of this beam contains a guide in which a column is inserted. This column extends through the crushable material down to the surface pad.

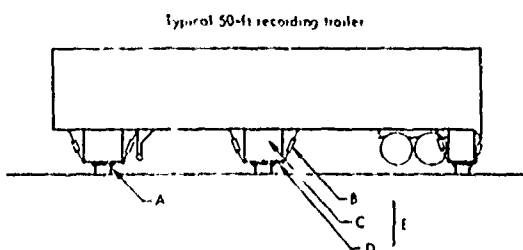


Fig. 2 F&RC shock-mitigation systems: (A) replaceable foam pad bolted to cribbing, (B) turnbuckle tie, (C) wood cribbing with plywood scabbing, (D) angle iron frame, (E) reusable cribbing assembly.



Fig. 3 Typical installation of Universal Guided Column (UGC) system.

The bottom of the column is attached to a metal disk by means of a pivot joint. The crushable material sits between the metal disk and the beam as shown in Fig. 4. All horizontal loads are transferred to the metal disk and therefore into the metal guide column. Horizontal loads into the disk are controlled by antifriction surface pads made of properly sized Teflon, grease, and acrylic. The pad design is based on many laboratory friction tests and field experience. Measurements of the actual full-size system have consistently indicated a 0.06 coefficient of friction. The horizontal force is transferred to the beam by means of the metal column, which imposes a twisting moment on the beam. Because the beam is a box-type structure, it can withstand the torsional loads. The magnitude of this twisting moment is a function of the coefficient of friction for the surface pad and crushable material height and crush load.

We have found that the maximum horizontal displacements occur after slapdown and after the crushable material has compressed; therefore, the surface pad is designed to have very low friction for a limited horizontal displacement while the structure is mounted high and then after slap-down the column moment arm is smaller and the system is allowed to slide onto higher friction

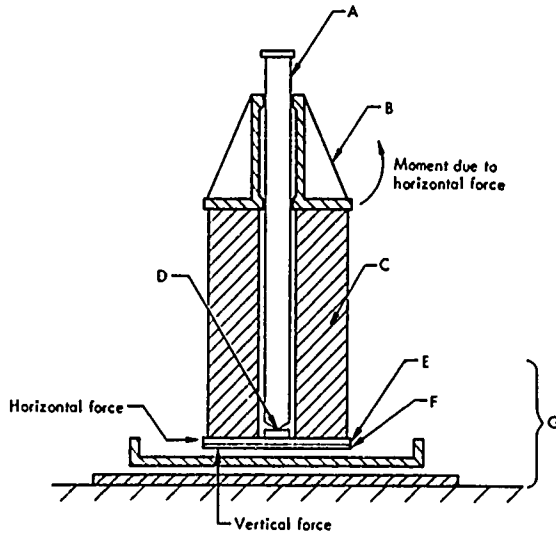


Fig. 4 UGC characteristics: (A) column, (B) crossbeam, (C) crushable material, (D) pivot joint, (E) metal disc, (F) Teflon, (G) anti-friction surface pad, exploded for clarity.

surfaces. Nylon rope tie downs are also used to prevent excessive horizontal displacement and to absorb some of the energy.

This system has been used reliably on more than twenty occasions with actual ground motions exceeding 12 ft/sec or 36 in. displacement. Vertical energy-absorption strokes have reached 40 in. and horizontal displacements up to 8 ft have occurred.

#### FULL-STROKE, GUIDED-COLUMN SYSTEM

A new shock-mounting system has recently been designed to meet requirements for very severe vertical ground motion up to 32 ft/sec or about 22-ft displacement. This design is a modification of the UGC system, with the crush materials replaced by a full-stroke, constant-force proprietary energy absorber. For crush materials (honeycomb, Styrofoam, etc.) the energy-absorption stroke relative to the original height is designed to be about 35% for nominal design conditions and/or 65% for maximum credible conditions, depending upon which case prevails. The crush materials bottom out at 65 to 75% deflection. The full-stroke system allows the original height to be reduced by one third, and therefore the structural requirements for some of the basic components are also reduced by one third.

The structures for the full-stroke, guided-column (FSGC) system are similar to the UGC system except that they are stronger. The

primary difference in the system is the type and location of the energy absorber (see Fig. 5). All remaining components function the same as the UGC system.

The constant-force columnar energy absorber is called a TOR-SHOK and is manufactured by A. R. A. Products, Inc. A single stage of this device consists of two concentric tubes with a coil of ductile wire forced between them. The interference fit between the wire and the tubes is sufficient to prevent sliding and to force the wires to rotate. Rotation of the wires is similar to rotating the ring of a torus inside out. The resulting tensile and compressive strains are in the plastic range. Contracting or extending the

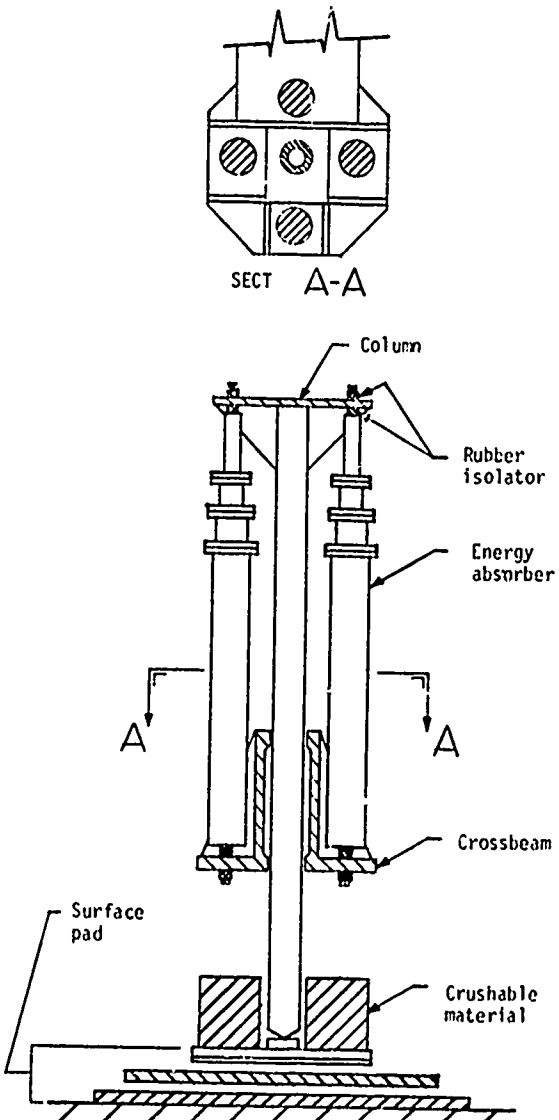


Fig. 5 Characteristics of FSGC system.

tubes apart axially forces the wires to rotate many times. The repeated cyclic plastic straining results in almost constant energy absorption per cycle of rotation (or inch of linear stroke) until eventual fatigue failure.

Before incorporating TOR-SHOKs into a shock-mounting system we purchased some for static and dynamic tests of individual units in both the extension and contraction directions. During the static tests loads were uniform and increased breakaway loads occurred only a few times. Impact acceleration pulses (three times the average deceleration values) were measured on the payload in about half of the extension and compression drop tests. The axial component of the lateral resonant vibration was quite apparent during the compression drop tests. In one case, this was a function of two stages and not the overall length of the column. In all tests drop height, stroke, and the average deceleration values agreed very well. There were no changes in load during the tests, even though one unit experienced five complete strokes.

In order to use the full-stroke capability of the guided-column system, we attach the energy absorber between the top of the column and the beam, as shown in Fig. 5. We are using three-stage energy absorbers with a compressed length of 58.5 in. and 8-ft stroke capability with capacities up to 12,000 lb. Each column can accommodate up to four energy absorbers with a total deceleration load capacity of 48,000 lb. Rubber isolators are used in mounting to insure that no bending moments are transferred into the energy absorber.

#### DROP TESTS

A series of full-scale drop tests using a 30,000 lb trailer was conducted. Various load

ratings and cluster arrays of energy absorbers were tested. At some locations the clusters were arranged to impart very high eccentric loadings into the columns. The FSGC system set up before drop testing is shown in Fig. 6.

Test instrumentation consisted of accelerometers and high-speed movies. Thirteen accelerometers were placed on the top of the columns, on the FSGC beams and on the equipment inside the trailer. All channels were recorded on magnetic tape, with seven selected channels on oscilloscopes for quick evaluation.

The drop tests are summarized in Table 2. Tilting occurred during the first three tests, but averaged deceleration strokes agreed with test parameters. An erroneous center of gravity location, which was discovered before testing began, caused the tilting. After the

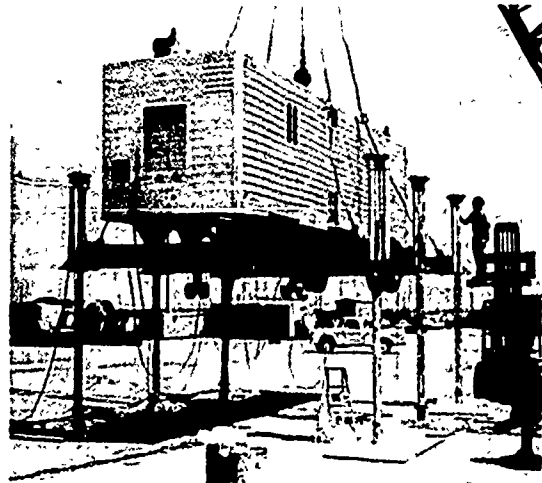


Fig. 6 Prototype FSGC system before testing.

TABLE 2  
Drop-Test Results - Average Values

Test No.	Drop Height (in.)	Velocity at Impact (ft/sec)	Deceleration Design Conditions		Actual Stroke (in.)
			Force <sup>†</sup>	Stroke (in.)	
1	21.5	10.7	2.7	7.9	7.62
2	38	14.3	2.7	14	13.5
3	74	19.9	2.8	26.4	26.9
4	12	8.0	3.0	4	4
5	180	31.0	3.17	57	55 - left side 77 - right side*

<sup>†</sup> Gravity force not included

\* Three energy absorbers failed and system bottomed out on right side.

third test the energy absorbers were reset (compressed) and redistributed in accordance with the correct center of gravity location. Figure 7 shows the trailer after the fourth test during preparation for the 15-ft drop of the fifth test. Fifteen energy absorbers were used during the fifth test, and three of them failed. They represented 26.6% of the total deceleration force. Two failed on the side that bottomed (see Fig. 8). They represented 34% of the deceleration force on that side. Peak accelerations inside the trailer, when the system bottomed, were 12 g (see Fig. 9). None of the equipment inside the trailer was damaged (including the fluorescent lights) and the only damage to the trailer was a wrinkled skin in one area requiring replacement of a few rivets. Motion of the trailer during the third, fourth, and fifth tests is shown in the movies.

Typical unfiltered acceleration response of equipment inside the trailer is shown in Fig. 9. Transducers 12 and 13 are at opposite ends of the trailer. An initial peak pulse occurred only at one end during the second test and at both ends during the fifth test. These initial peaks occurred randomly during the testing. Impact acceleration at the top of the columns was 100 to 300 g.

Failure of the three energy absorbers during the fifth test occurred when individual stages reached the end of their stroke and the spot-welded bands failed to retain the wires (see Fig. 10). Modified energy absorbers were then successfully tested. Several units were statically loaded to 25,000 lb (twice the maximum absorption load), and one unit was

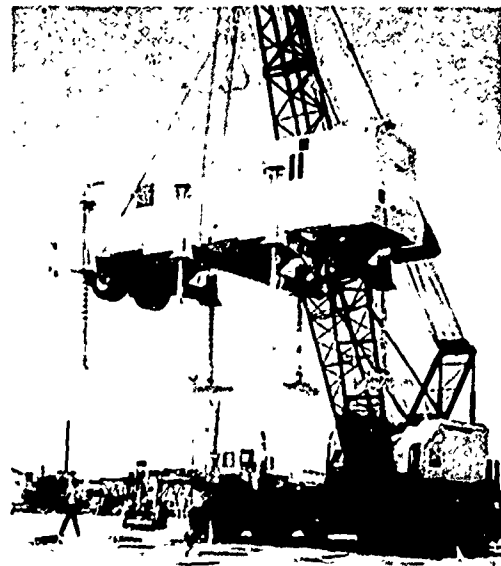


Fig. 7 Prototype FSGC system ready for 15-ft drop test.



Fig. 8 Right side of FSGC system after 15-ft drop test, showing two separated energy absorbers.

Reproduced from  
best available copy.

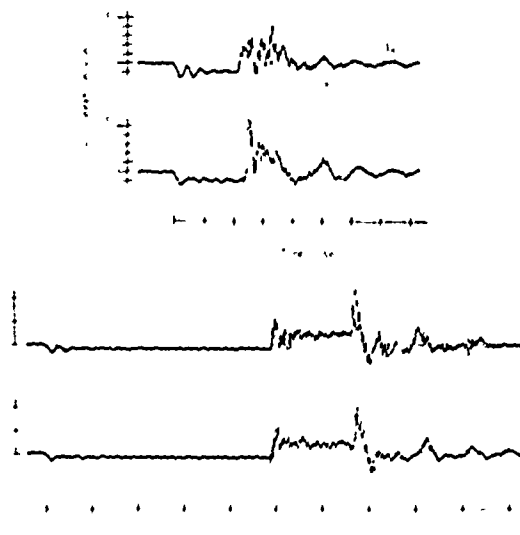


Fig. 9 Response of equipment inside trailer during tests 2 and 5.

impact-tested to failure. This unit finally failed at a swaged tubing flange.

Our comprehensive test program identified discrepancies in the as-built FSGC system. These were corrected before using the system under actual severe ground-motion conditions. Normally we desire fail-safe shock-mitigation systems. In actual field applications of this system, we have installed rigid-foam backup

pads. These are under the protective polyethylene covers at the base of each column in Fig. 11.

#### ACKNOWLEDGMENT

The authors would like to acknowledge the cooperation and assistance provided by Holmes & Narver, Inc., (Nevada Test Site) in connection with the F&RC and UGC systems and EG&G, Inc., (Las Vegas) in the drop test portion of this program. In particular, the efforts of Mr. E. Fuller and Mr. H. Montalvo of H&N and Mr. P. Mulhall and Mr. R. Nakanishi of EG&G are gratefully acknowledged.

#### REFERENCE

1. D. L. Bernreuter, E. C. Jackson, and A. B. Miller, "Control of the Dynamic Environment Produced by Underground Nuclear Explosives," in Proc. Symp. on Eng. With Nuclear Explosives (Las Vegas, Nev., 1970), U.S. Atomic Energy Commission Rept. CONF-700101, Vol. 2, pp. 979-993, May 1970

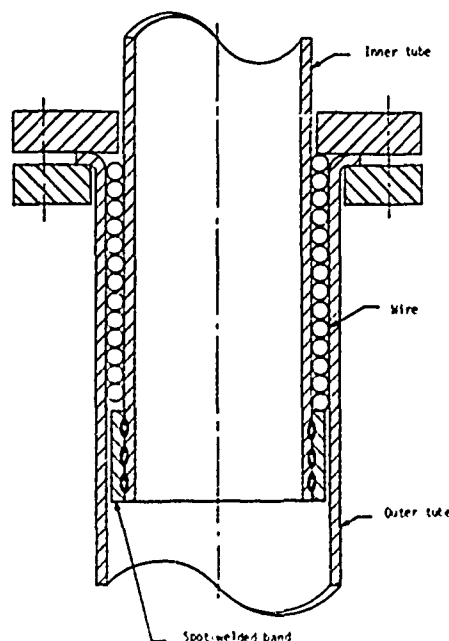


Fig. 10 Cross section of energy absorber at end of extension stroke.



Fig. 11 Field installation of FSGC system.

## DISCUSSION

Mr. Fox (Barry Wright Corporation): How much deflection did you get out of the foam itself? Was most of the deflection taken up under the shock?

Mr. Bernreuter: Yes, the actual extension of the TOP SHOCKS themselves took up most of the shock.

Mr. Fox: Was that fifteen feet?

Mr. Bernreuter: No, I think their stroke was designed to be twelve feet capacity. In this case they stroked 12 feet because they bottomed out. In fact, a couple of the units failed. We picked the trailer up 15 feet off the ground and dropped it, so it had a velocity of about 28 feet per second when it struck the ground.

Mr. Fox: You were only concerned about the initial shock blast. You did not care what happened after the initial blast? Is that correct?

Mr. Bernreuter: Yes.

Mr. Peralta (Bell Telephone Laboratories): In sizing the shock absorbers, do you do any kind of calculation as to how much energy they should be able to absorb?

Mr. Bernreuter: Yes we do quite a bit of calculation based on the weight of the trailer, the expected level, etc. The formulas are worked out, and we have performed a computer analysis.

THE COMPARISON OF THE RESPONSE  
OF A HIGHWAY BRIDGE TO UNIFORM GROUND SHOCK  
AND MOVING GROUND EXCITATION (U)

Neil E. Johnson and Robert D. Galletly  
Mechanics Research, Inc.  
Los Angeles, California

This paper compares the dynamic response of a highway bridge structure subjected to:

- The Uniform Ground Acceleration Time History for the May 18, 1940 El Centro Earthquake
- Moving Ground Acceleration
- An Average Acceleration Shock Spectrum for Strong Ground Motion

An analytical procedure is outlined for predicting the response of a highway bridge structure whose ground motion varies between its supports and is dependent upon seismic wave propagation characteristics.

A typical six span highway bridge is presented. A finite element model of this bridge is developed including representation of soil/foundation stiffness and damping characteristics. The response of this structure is evaluated for the various ground motion conditions using normal mode techniques. The dynamic analysis of this structure was predicted using the MRI/STARDYNE Structural Analysis System.

#### INTRODUCTION

Considerable interest is currently being expressed as to the behavior of civil structures under the effects of seismic excitation. Traditional analysis techniques applied to such structures include the use of quasi-static load factors, shock spectra and, in some cases, acceleration time histories. This paper addresses a special case of time history analysis wherein the propagation velocity of a seismic wave moving longitudinally along the structure is considered. Results from this moving ground motion analysis technique are compared with more traditional time history and shock spectra techniques through the application of all three techniques to an idealized highway bridge.

For structural analysis the assumed ground motion is often given in the form of an acceleration time history recorded during a seismic event [1] or an artificially generated time history with certain numerical and statistical quantities retained [2]. For purposes of structural evaluation this ground motion is generally applied to the foundation and ground supports in a uniform manner, that is with the disturbance of the ground exactly the same at each ground point for each time.

When the characteristic length of a structure is large enough that the propagation time of the

seismic wave train must be considered as it traverses the structure the assumption of uniform ground motion for the structural assembly can no longer be justified. If it can be anticipated that the ground motion may differ in phase and magnitude among several structural supports then the resulting structural response must be reviewed carefully. This paper addresses a hypothetical case where a strong seismic disturbance propagates along the ground supporting a typical two lane, six span, single pedestal support highway bridge structure at a relatively slow, uniform velocity.

The method of analysis utilized for attacking the problem of the dynamic response of a structural system to moving ground motion is outlined in detail. Particular emphasis is placed upon utilizing standard structural commodities and analytical techniques. The results of this effort were then compared to results considering uniform ground motion for the same seismic disturbance and to results considering a typical average shock spectrum for strong ground motion. A discussion of the bridge model is given. This includes the geometry and design description of the bridge assembly. A brief summary of the assumed soil properties is indicated. The structure was assumed to be supported on foundations with linear characteristics associated with soft soil. The results of the modal vibration analysis are provided.

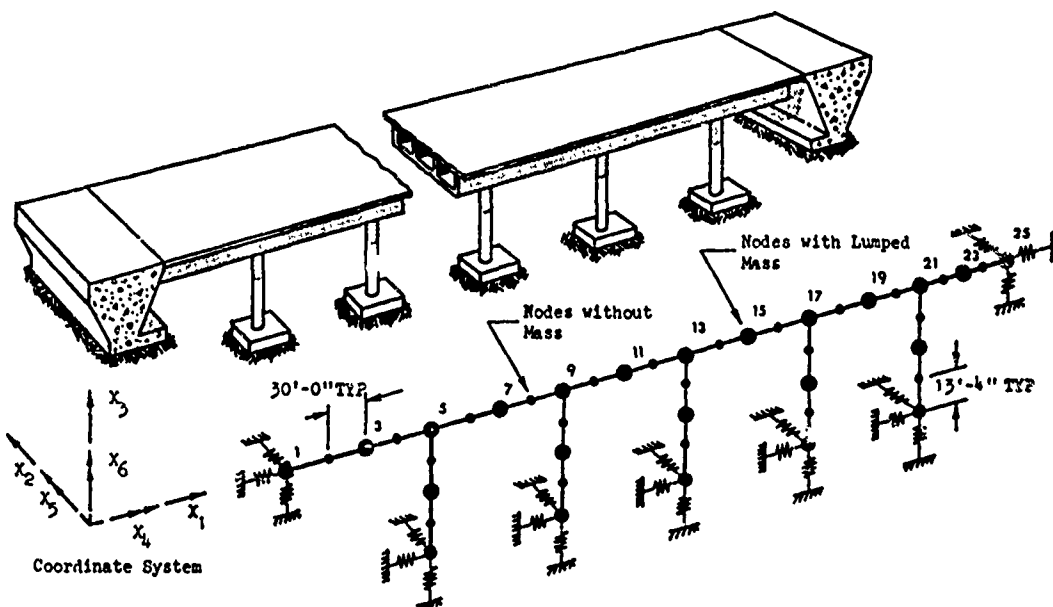


Fig. 1 - Bridge Physical Characteristics and Idealized Mathematical Model

A finite element model of the bridge structural system was developed. The natural frequencies, mode shapes and related properties are identified. Normal mode techniques were utilized in the problem formulation. The STARDYNE Structural Analysis System and its auxiliary subroutines were used exclusively for the modal vibration analysis and the dynamic response computations.

#### BRIDGE MODEL

A mathematical model of a typical six-span, single pedestal support highway bridge was developed to illustrate the analysis techniques described herein. The bridge, which is shown in Fig. 1 and Fig. 2, is an idealization of a typical structure and is patterned after typical two-lane highway bridge designs.

The idealized bridge consists of six 120 foot long two-lane spans with the roadway superstructure placed approximately 50 feet above the ground surface. Reinforced concrete construction was assumed. Support columns and bridge ends are assumed to be supported on massive pad-type foundations.

Foundation/soil interaction was idealized as a series of linear support springs. These springs have been designed to give reasonable translational and rotational stiffness properties to the assumed type of bridge. The soil spring rates are shown in Table 1.

The example bridge was modeled as a lumped mass, finite element model as shown in Fig. 1. This model consists of 45 unconstrained nodes each having 6 degrees of freedom. Only 25 nodes were selected as mass point locations in order

to minimize the number of dynamic degrees of freedom for the problem. Note that a much more detailed model might be desired if an actual highway bridge were to be analyzed using the techniques described herein. Such a model would probably include a more extensive three-dimensional model considering both beam and plate finite elements and a more detailed description of soil/structure interaction including pile foundations, if used. The assumed mass distribution is summarized in Table 2.

The roadway superstructure and support columns were modeled as a series of beam members. Section properties evaluated for these beams are given in Table 3. These section properties assume concrete as the basic material with appropriate modifications for reinforcing steel.

Using the finite element model described above, the natural frequencies and normal modes of the bridge were determined through the use of the STARDYNE Structural Analysis System computer program. The STARDYNE program, developed by MRI and in use by a large number of engineering firms worldwide through Control Data Corporation Data Centers, is a large (up to 6000 DOF) static and dynamic analysis system based on the finite element, normal mode method of analysis.

The lowest sixty (60) normal modes were determined. These modes, which can be generally classed as either horizontal bending, vertical bending or longitudinal are summarized in Table 4. The generalized weight and modal participation factors corresponding to each of these modes are also given in Table 4. A brief description of the normal mode method and the terms in Table 4 is given in Appendix A.

Due to the symmetry properties of the idealized structural system, it should be noted that only a portion of the normal modes listed in

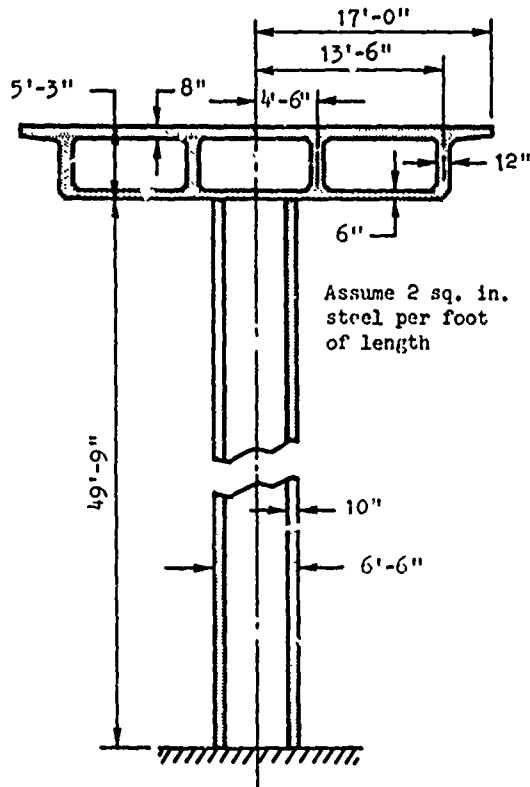


Fig. 2 - Typical Cross-Section

Table 4 were used in the various dynamic response analyses described below. A modal damping factor of .05 was used for all response analyses.

TABLE 1  
SUMMARY OF SOIL SPRING CONSTANTS

Direction	Soil Spring Rate
X1	$1.215 \times 10^6$ lb/in
X2	$1.215 \times 10^6$ lb/in
X3	$2.430 \times 10^6$ lb/in
X4	$9.475 \times 10^9$ in/lb
X5	$9.475 \times 10^9$ in/lb
X6	$9.475 \times 10^9$ in/lb

TABLE 2

SUMMARY OF MASS PROPERTIES

Element	Mass Property
Roadway Superstructure	8476.32 lbs/ft
Support Columns	2344.8 lbs/ft
Pad Foundations	204,282 lbs Each

TABLE 3

BEAM PROPERTIES

Beam Type	Area in <sup>2</sup>	J in <sup>4</sup>	I <sub>2</sub> in <sup>4</sup>	I <sub>3</sub> in <sup>4</sup>	Shear Shape Factors	
					SF <sub>2</sub>	SF <sub>3</sub>
Roadway	8410	12,711,655	4,371,662	170,156,240	0.350	0.411
Support Column	2314	2,522,483	1,201,474	1,201,474	0.5	.5

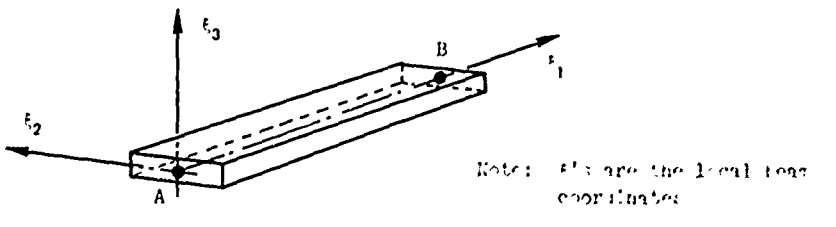


TABLE 4  
RESULTS OF THE MODAL ANALYSIS

Mode No.	Frequency (cps)	Generalized Weight (kips)	Modal Participation Factors			Mode Description
			X <sub>1</sub>	X <sub>2</sub>	X <sub>3</sub>	
1	0.577	3360	0	1.2473	0	Horizontal Bending
2	1.419	3427	0	0	0	Horizontal Bending
3	2.005	6557	1.0414	0	0	Longitudinal
4	2.717	3570	0	0.5015	0	Horizontal Bending
5	3.021	1724	-0.1081	0	0	Vertical Bending
6	3.037	1396	0	0	0.6009	Vertical Bending
7	3.185	1651	0.0588	0	0	Vertical Bending
8	3.319	2669	0	0	0.4782	Vertical Bending
9	3.431	1958	0.0249	0	0	Vertical Bending
10	3.502	2284	0	0	1.5701	Vertical Bending
11	3.597	2557	0	0	0	Horizontal Bending
12	4.152	4360	0	0.3618	0	Horizontal
13	4.454	3204	0	0	0	Horizontal Rotation
14	5.058	1544	0	0.5317	0	Horizontal Bending
15	5.406	1849	0	0.1843	0	Horizontal Bending
16	5.731	2588	0	0	0.0111	Vertical Bending
17	6.058	3412	0.170	0	0	Vertical Bending
18	6.449	1773	0	0	0	Horizontal Bending
19	6.486	827	0	0	0	Horizontal Bending
20	6.532	3207	0	0	-0.0062	Vertical Bending
21	6.984	580	0	-0.2120	0	Vertical Bending
22	7.013	3582	0.0333	0	0	Longitudinal
23	7.190	753	0	0	-0.0382	Vertical
24	7.209	585	0	0.6433	0	Horizontal
25	7.241	1227	0.8915	0	0	Longitudinal
26	7.256	620	0.0100	0	0	Longitudinal
27	7.259	52	0	0	0	Horizontal
28	7.259	701	0	0	-0.0183	Longitudinal
29	7.278	761	-0.0444	0	0	Longitudinal
30	7.434	1512	0	0	0.2482	Vertical Bending
31	7.492	54	0	1.0036	0	Horizontal
32	7.572	1250	0.0374	0	0	Vertical Bending
33	7.676	3178	0	0	0.1235	Vertical Bending
34	7.703	827	0	0	0	Torsion
35	8.448	389	0	-0.0744	0	Horizontal
36	8.54	312	0	0	0.1000	Longitudinal
37	8.731	862	0	-0.072	0	Horizontal Bending
38	9.51	1023	0	0	0	Horizontal
39	11.723	225	0	-0.0103	0	Horizontal
40	11.736	3190	0	0	0	Horizontal Bending
41	12.332	1782	0	0	0	Torsion
42	13.176	1188	0	0.0173	0	Horizontal
43	13.886	1053	0	0	0	Horizontal
44	14.395	1405	0	-0.0300	0	Horizontal Bending
45	14.445	155	0	0.0156	0	Horizontal Bending
46	14.77	1500	0	0	0	Horizontal
47	14.815	162	0	-0.0027	0	Horizontal
48	15.11	643	-0.0647	0	0	Longitudinal
49	17.197	212	0	0	0	Horizontal Bending
50	18.55	157	0	0	0.001	Horizontal
51	18.713	218	-0.0433	0	0	Horizontal
52	18.776	133	-0.077	0	0	Horizontal
53	18.785	134	0	0	0.0011	Horizontal
54	19.13	111	-0.045	0	0	Horizontal
55	19.22	261	0	0.0044	0	Horizontal Bending
56	20.50	513	0	0	0	Horizontal
57	20.90	440	0	-0.0170	0	Horizontal Bending
58	21.63	117	0	-0.0085	0	Horizontal
59	22.057	114	0	0	0	Horizontal Bending
60	23.541	77	0	0.0121	0	Horizontal

## PRESENTATION OF THE METHOD OF ANALYSIS

The earthquake response of structures is described in many sources [3, 4]. A variety of computational tools are available to the structural analyst. Both transient response techniques [5] and shock spectra methods [6] have achieved wide acceptance in predicting the behavior of structural systems subjected to ground motion. This paper addresses the problem of the response of structures with large characteristic length and considers the case where unattenuated strong ground motion traverses the supports of a structure at a uniform velocity. The method is developed in a straightforward manner and is outlined below.

Consider a system with  $n$  degrees of freedom and  $r$  resilient supports to ground. Fig. 1 shows a typical system. Assume that the equations of motion are to be written in center-of-mass coordinates and the mass matrix of the system  $[M]$  is diagonal. For simplicity, assume the damping is small and proportional to the stiffness. This is done for ease of the present analysis; other restricted types of damping could be considered. Modal techniques will be introduced, modal damping will be utilized and modal coupling due to damping will be neglected.

In the absence of ground motion the equations of motion are:

$$[M]\{\ddot{x}\} + [C]\{\dot{x}\} + [K]\{x\} = 0 \quad (1)$$

where

$\overset{n}{[M]}$  is the diagonal mass matrix of the system;

$\overset{n}{[C]}$  is the damping matrix of the system;

$\overset{n}{[K]}$  is the stiffness matrix of the system;

$\overset{n}{[x]}$  describes the absolute motion of the mass elements of the system.

For ground motion of the supports the forces induced upon the system are described in terms of relative motion between the mass elements and the support elements. Considering this effect, the equations of motion can be written

$$[M]\{\ddot{x}\} + [C]\{\dot{x}\} - [c']\{\dot{y}\} + [K]\{x\} - [k']\{y\} = 0 \quad (2)$$

where

$\overset{r}{[k']}$  is a rectangular array of stiffness coefficients relating ground attach nodes to adjacent internal nodes of the system;

$\overset{r}{[c']}$  is a rectangular array of damping coefficients relating ground attach nodes to adjacent internal nodes of the system;

$\overset{r}{\{y\}}$  describes the absolute ground motions (displacements) at each of the  $r$  supports.

Rearranging Eq. (2), the equations of motion become

$$[M]\{\ddot{x}\} + [C]\{\dot{x}\} + [K]\{x\} = [k']\{y\} + [c']\{\dot{y}\} \quad (3)$$

Just as the terms on the left hand side of the equations can be considered as the forces acting upon the system in the absence of ground motion ( $\{y\} = \{\dot{y}\} = \{\ddot{y}\} = 0$ ), the terms of the right hand side can be viewed as those forces induced upon the system by the ground motions  $\{y\}$  when the mass points are constrained ( $\{x\} = \{\dot{x}\} = \{\ddot{x}\} = 0$ ). This provides a straightforward way for constructing  $[c']$  and  $[k']$ .

For seismic analysis the ground motion is often described in terms of ground acceleration. Eq. (3) may be rewritten in the following manner to accommodate these terms.

Introducing a new set of auxiliary coordinates  $\{z\}$ , the forces induced by ground motion on the constrained system (right hand side of Eq. (3)) may be written

$$[K]\{z\} + [C]\{\dot{z}\} = [k']\{y\} + [c']\{\dot{y}\} \quad (4)$$

Substituting the transformation

$$\{z\} = [T]\{y\} \quad (5)$$

where

$\overset{n}{[T]}$  is a transformation of constant coefficients;

$\overset{n}{[z]}$  is an auxiliary set of coordinates into Eq. (4), it is seen that

$$[K][T]\{y\} + [C][T]\{\dot{y}\} = [k']\{y\} + [c']\{\dot{y}\} \quad (6)$$

Comparing like coefficients in Eq. (6) it may be written that

$$[K][T] = [k'] \quad (7)$$

and

$$[C][T] = [c'] \quad (8)$$

Eqs. (7) may be rewritten to give

$$[T] = [K]^{-1}[k'] = [C]^{-1}[c'] \quad (9)$$

The two right hand portions of Eq. (9) are identical expressions since it was previously assumed that

$$[C] = \sigma[K] \quad \text{and} \quad [c'] = \alpha[k'] \quad (9)$$

Furthermore, the existence of  $[K]^{-1}$  is assured since  $[K]$  represents the stiffness matrix of a constrained system.

Next, using Eq. (4), Eq. (1) may be written

$$[M]\{\ddot{x}\} + [C]\{\dot{x}\} + [K]\{x\} = [K]\{z\} + [C]\{\dot{z}\} \quad (10)$$

Rearranging terms, Eq. (10) becomes

$$[M]\{x\} + [C](\{\dot{x}\} - \{\dot{z}\}) + [K](\{x\} - \{z\}) = 0 \quad (11)$$

Then

Defining

$$\{\beta\} = \{x\} - \{z\} \quad (12)$$

and subtracting  $[M]\{\dot{z}\}$  from both sides, Eq. (11) may be written

$$[M]\{\ddot{\beta}\} + [C]\{\dot{\beta}\} + [K]\{\beta\} = -[M]\{\ddot{z}\} \quad (13)$$

Noting that

$$\{\ddot{z}\} = [T]\{\ddot{y}\} = [K]^{-1}[k']\{\ddot{y}\} \quad (14)$$

Eq. (13) may be written

$$[M]\{\ddot{\beta}\} + [C]\{\dot{\beta}\} + [K]\{\beta\} = -[M][K]^{-1}[k']\{\ddot{y}\} \quad (15)$$

or

$$[M]\{\ddot{\beta}\} + [C]\{\dot{\beta}\} + [K]\{\beta\} = -[D][k']\{\ddot{y}\} \quad (16)$$

where  $[D] = [M][K]^{-1}$  is the dynamical matrix for the constrained system.

For the case of moving ground motion, it can be assumed that the basic ground disturbance has a plane wave front and a time history given by  $\ddot{y}(t)$ . Further, let the velocity of propagation for the disturbance be  $v$  and the time the disturbance encounters the first ground point be  $t = 0$ . Then, the disturbance will arrive at successive ground points at a time

$$t_i = \frac{d_i \cos \theta_i}{v} \quad (\text{see Fig. 3}) \quad (17)$$

where

- $t_i$  is the time of arrival of the disturbance at the  $i$ th ground point;
- $d_i$  is the distance from the first ground point to the  $i$ th ground point;
- $\theta_i$  is the angle between a line adjoining the first ground point and the  $i$ th ground point and the direction of wave propagation;
- $v$  is the velocity of propagation.

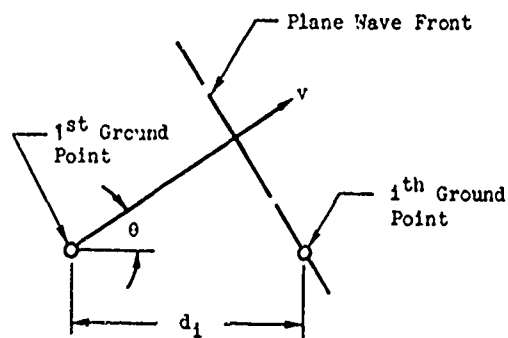


Fig. 3 - Wave Train Propagation

$$\{\ddot{y}\} = \begin{Bmatrix} \ddot{y}_1(t) \\ \ddot{y}_2(t) \\ \vdots \\ \ddot{y}_i(t) \\ \vdots \\ \ddot{y}_r(t) \end{Bmatrix} = \begin{Bmatrix} \ddot{y}(t) \\ \ddot{y}(t - t_2) \\ \vdots \\ \ddot{y}(t - t_1) \\ \vdots \\ \ddot{y}(t - t_r) \end{Bmatrix} \quad (18)$$

Fig. 4 shows the time histories of a ground disturbance for the special case of several evenly spaced colinear ground points.

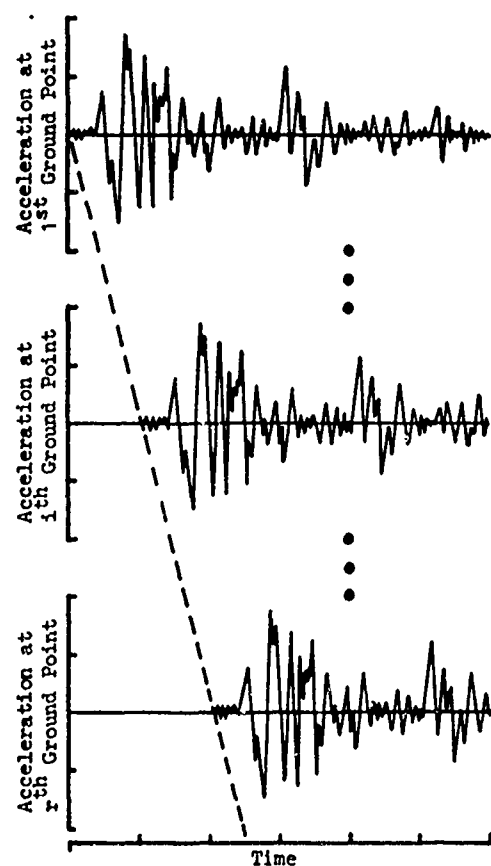


Fig. 4 - Time History for Moving Ground Motion

Consider a solution to Eq. (16) of the form

$$\{\beta\} = \{\phi\}\{\eta\} \quad (19)$$

where

- $\{\phi\}$  is an array of mode shapes of the undamped constrained system;
- $\{\eta\}$  is a set of generalized (modal) coordinates.

Substituting and premultiplying by  $[\phi]^T$ , Eq. (16) becomes

$$[\phi]^T [M] [\phi] \{\ddot{\eta}\} + [\phi]^T [C] [\phi] \{\dot{\eta}\} + [\phi]^T [K] [\phi] \{\eta\} = -[\phi]^T [D] [k^1] \{y\} \quad (20)$$

On defining, in the usual manner, the generalized parameters

$$\begin{aligned} [\phi]^T [M] [\phi] &= [M] \\ [\phi]^T [C] [\phi] &= [C] \\ [\phi]^T [K] [\phi] &= [K] \\ [\phi]^T [D] [k^1] \{y\} &= [F] \end{aligned}$$

The equations of motion become

$$[M] \{\ddot{\eta}\} + [C] \{\dot{\eta}\} + [K] \{\eta\} = [F] \quad (21)$$

After solving Eq. (21) for  $\{\ddot{\eta}\}$ , the absolute accelerations of the system become

$$\{\ddot{x}\} = [\phi] \{\ddot{\eta}\} = \{x\} - \{z\} = \{x\} - [T] \{y\}$$

and

$$\{x\} = [\phi] \{\eta\} + [T] \{y\}$$

#### INPUT DATA

For this study three methods for solving the dynamic response of a structural system to seismic inputs were used. For each method, three loading conditions were considered. The methods were:

- Transient response of the structural system subjected to the uniform ground acceleration time history for the May 18, 1940 El Centro earthquake (North-South component);
- Transient response of the structural system subjected to moving ground motion with a constant propagation velocity of 400 ft/sec and an acceleration time history given by the May 18, 1940 El Centro earthquake (North-South component);
- Response of the structural system subjected to the average acceleration shock spectrum for strong ground motion [3].

The time history of the May 18, 1940 El Centro earthquake (North-South component) is shown in Fig. 5. The average acceleration shock spectrum for strong ground motion is shown in Fig. 6.

The loading conditions considered were:

- The horizontal component of the ground acceleration in the lateral direction of the bridge with a magnitude equal to that for the May 18, 1940 El Centro earthquake. The vertical component of ground acceleration equal to 0.6 times the horizontal component (Case 1);
- The horizontal component of the ground acceleration in the longitudinal direction of the bridge with a magnitude equal to

that for the May 18, 1940 El Centro earthquake. The vertical component of ground acceleration equal to 0.6 times the horizontal component (Case 2);

- The horizontal component of the ground acceleration in a direction 45° to the longitudinal direction of the bridge with a magnitude equal to that for the May 18, 1940 El Centro earthquake. The vertical component of ground acceleration equal to 0.6 times the horizontal component (Case 3).

#### RESULTS

Using the loading conditions described above, a series of nine independent analyses were performed. Each of these analyses resulted in the computation of displacements, velocities and accelerations at the various nodes on the idealized bridge structure. These results can be further extended to include equivalent nodal forces and internal member loads and stresses.

To briefly illustrate some the results obtained and to provide a basis for comparing the three methods used, the following representative data are presented.

Acceleration responses of a point on the roadway at the midspan of the bridge are presented in Fig. 7 through 12. Figs. 7, 9 and 11 show representative acceleration time histories using the Uniform Ground Motion (UGM) method for each of the three load cases. Figs. 8, 10 and 12 show similar acceleration time histories using the Moving Ground Motion (MGM) method.

Figs. 13, 14 and 15 show the distribution of maximum values of acceleration for each load condition as a function of bridge span (see Fig. 1 for span locations). Shown on each figure are results from the Uniform Ground Motion, Moving Ground Motion and Shock Spectra (SS) analysis methods. It should be noted that the acceleration values shown on these figures for various span locations do not necessarily occur at the same point in time. Consequently, some care should be used when interpreting these analysis results.

#### CONCLUSION

A number of conclusions may be drawn from a review of the analysis results presented above. Some of the more significant of these are described below.

It is seen from Figs. 7 through 12 that the time range of peak response of the bridge is generally of longer duration for the Moving Ground Motion cases than for the Uniform Ground Motion cases. This phenomena would increase the probability of achieving an extreme peak response due to a fortuitous combination of modal responses.

An examination of Fig. 14 shows that for Uniform Ground Motion, the longitudinal response is significantly higher than for Moving Ground Motion. This is due to very large modal participation of the first longitudinal mode of the system when both end supports have the identical ground excitation. For the Moving Ground case, a reduct-

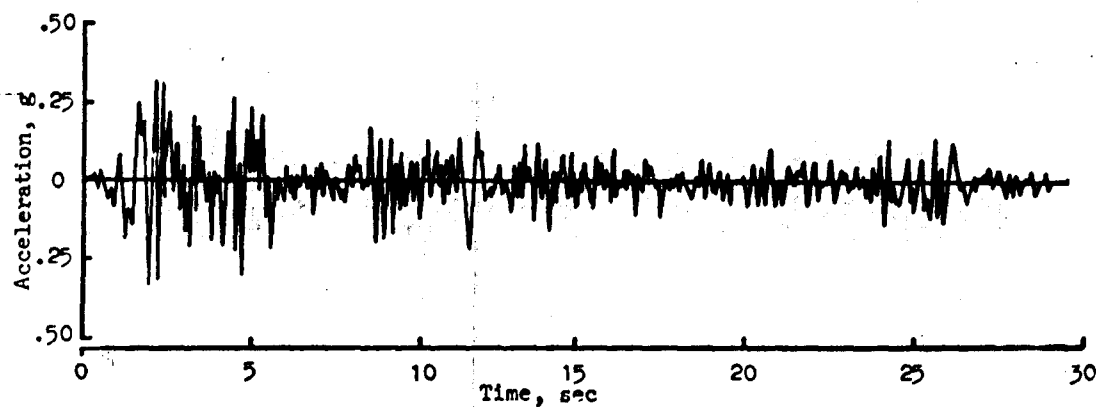


Fig. 5 - North-South Component of Horizontal Ground Acceleration of El Centro Earthquake May 18, 1940.

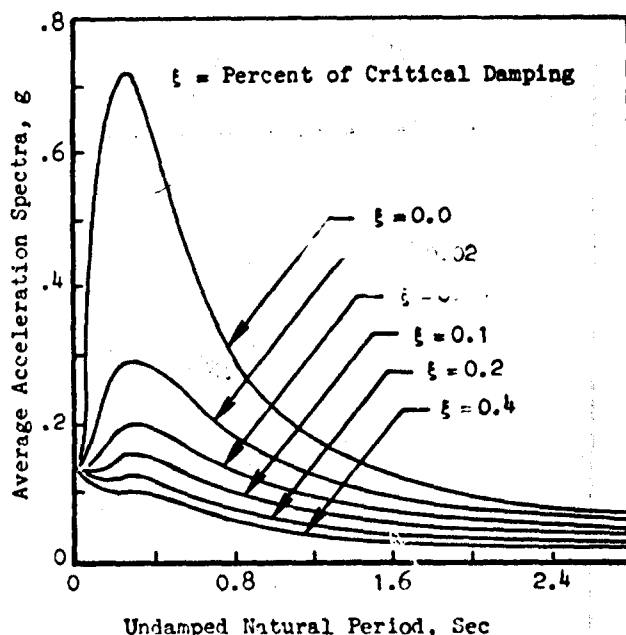


Fig. 6 - Average Acceleration Spectrum Curves

tion in the participation of the first longitudinal mode was observed when the ground excitation of each end support was distinctly different.

Due to the bridge symmetry, the responses to the Uniform Ground Motion exhibit symmetry properties about the midspan of the bridge. This property of the response results does not occur for the Moving Ground Motion method. This is due to the variation in ground motion at the bridge supports as the seismic disturbance traverses the structure. Generally, the response for the two methods differ and the method producing the higher response depends upon both the loading condition and location considered.

The response spectrum selected for this comparison was a composite average of acceleration shock spectra for several strong ground motion events [3]. Since this spectrum does not bound that derived from the ground motion time history utilized for this problem the resulting response does not necessarily encompass the results obtained from time history studies. For a shock spectra analysis the phase relationships are lost and a pessimistic summation of modal response is assumed. For a given ground motion time history a response derived from shock spectra analysis will bound the response developed from a time history analysis for either the Uniform or Moving Ground Motion method.

In summary, it can generally be concluded that an evaluation of Moving Ground Motion effects result in different structural response than would be computed from a Uniform Ground Motion analysis. The probability of higher responses tends to increase as the number of supports increases. Consequently, it can be recommended that Moving Ground Motion should be considered in the seismic design of multiple support bridges.

It can be further concluded that time history response analysis of either the Moving or Uniform Ground Motion types will give more meaningful response predictions than those obtained from Shock Spectra analysis when many modes contribute to the response of the system. For this reason, realistic and economical highway bridge design practice should consider time history effects.

#### REFERENCES

1. Robert L. Wiegel, *Earthquake Engineering*, Prentice-Hall, New Jersey, 1970
2. M. Amin and A. Ang, "Nonstationary Stochastic Models of Earthquake Motion", Journal of the Applied Mechanics Division, ASCE, Vol. 94 No. EM2, Procurement Paper 3205, April 1968
3. Cyril M. Harris and Charles E. Crede, *Shock and Vibration Handbook*, Vol. 1, McGraw-Hill, New York, 1941
4. Walter C. Hurty and Moshe F. Rubinstein, *Dynamics of Structures*, Prentice-Hall, New Jersey, 1967

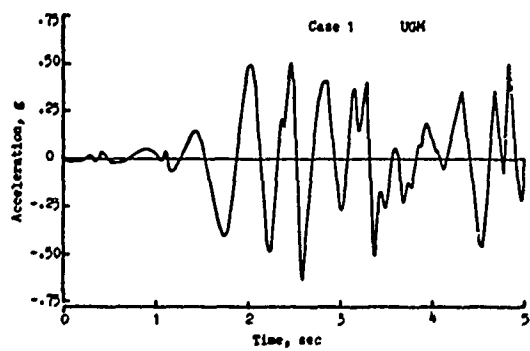


Fig. 7 - Mid Span Horizontal Acceleration History  
Uniform Ground Motion

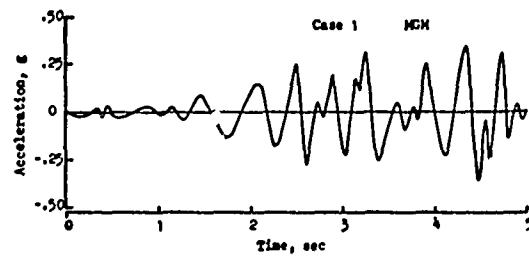


Fig. 8 - Mid Span Horizontal Acceleration History  
Moving Ground Motion

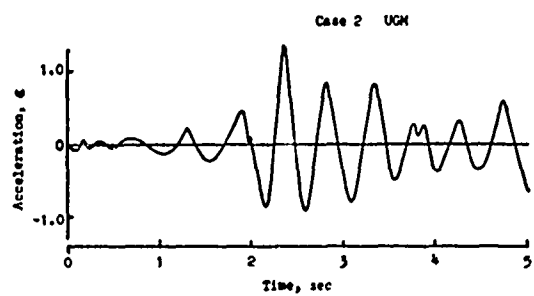


Fig. 9 - Mid Span Longitudinal Acceleration History  
Uniform Ground Motion

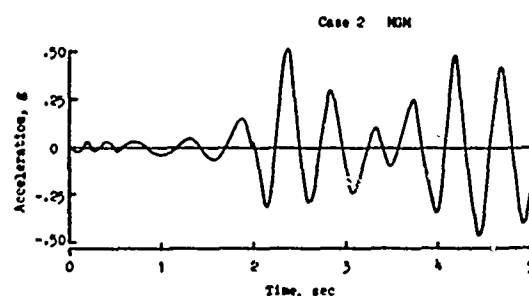


Fig. 10 - Mid Span Longitudinal Acceleration History  
Moving Ground Motion

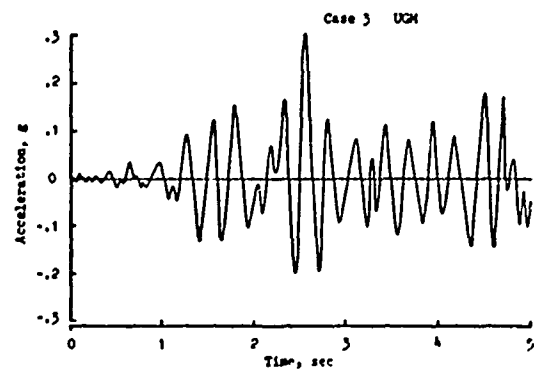


Fig. 11 - Mid Span Vertical Acceleration History  
Uniform Ground Motion

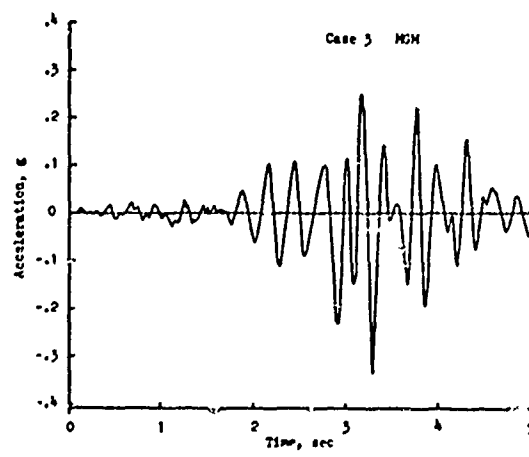


Fig. 12 - Mid Span Vertical Acceleration History  
Moving Ground Motion



Fig. 13 - Maximum Horizontal Acceleration Distribution  
(Case 1)

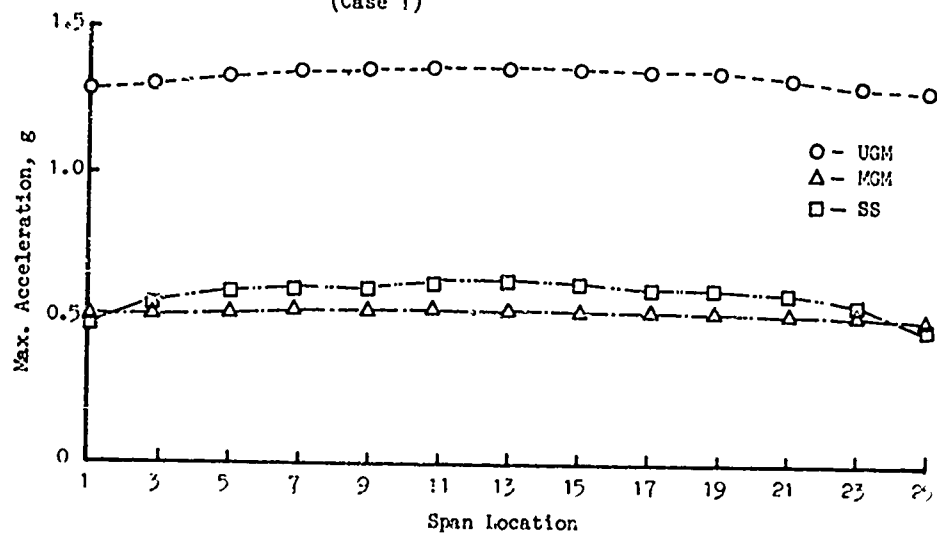


Fig. 14 - Maximum Longitudinal Acceleration Distribution  
(Case 2)

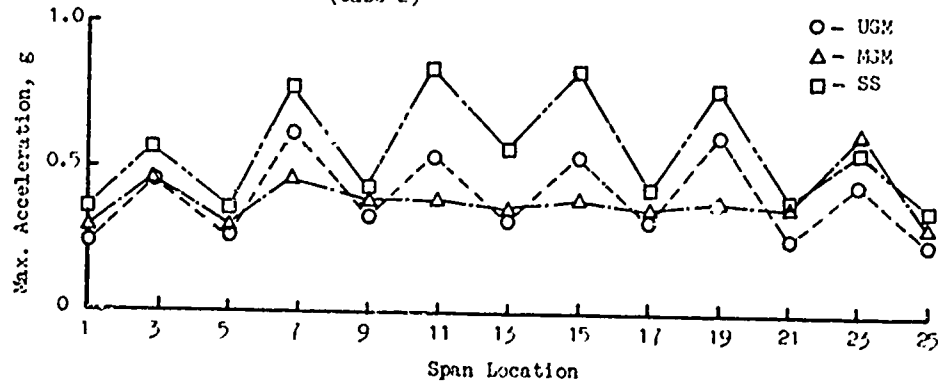


Fig. 15 - Maximum Vertical Acceleration Distribution  
(Case 3)

5. Richard Rosen, et al, STARDYNE: User's Manual, Mechanics Research, Inc. and Control Data Corporation, 1971
6. Richard T. Haelsig, DYNRE IV User's Guide, Mechanics Research, Inc., 1968

Note that modal participation factors are computed for each of the three translational degrees of freedom.

#### APPENDIX A: DEFINITION OF ANALYSIS TERMS

The STARDYNE System is formulated around the "Stiffness" or "Displacement" method of structural analysis. In using this method, the structural system can be represented by the following equations of motion (for free vibration):

$$[\mathbf{M}]\{\ddot{x}\} + [\mathbf{K}]\{x\} = 0 \quad (1)$$

where

$[\mathbf{M}]$  is the diagonal mass matrix;

$[\mathbf{K}]$  is the stiffness matrix;

$\{x\}$  is the system coordinate.

The eigenvalues (natural frequencies) and eigenvectors (normal modes) of the system can be extracted from the following reformulated version of Eq. (1)

$$([\mathbf{K}] - \omega_r^2 [\mathbf{M}])\{\phi^{(r)}\} = 0 \quad (2)$$

where

$\omega_r^2$  is the  $r$ th eigenvalue;

$\phi^{(r)}$  is the  $r$ th eigenvector.

The generalized mass of the structure is given by

$$[\bar{\mathbf{M}}] = |\phi|^\text{T} [\mathbf{M}] |\phi| \quad (3)$$

The generalized weight is given by

$$[\bar{\mathbf{M}}_g] = [\bar{\mathbf{M}}] g \quad (4)$$

where

$g$  is the Gravitational constant.

The modal participation factors  $\beta_j(r)$  are defined to be

$$\beta_j(r) = \frac{\sum m_i \phi_{ir}}{M_r}$$

where

$\beta_j(r)$  is the modal participation factor for the  $r$ th mode in  $j$ th translational direction;

$m_i$  is the element of mass associated with  $i$ th degree of freedom;

$\phi_{ir}$  is the component of  $r$ th modal vector associated with  $i$ th degree of freedom;

$M_r$  is the generalized mass for  $r$ th mode.

DEFORMATION AND FRACTURE OF TANK BOTTOM  
HULL PLATES SUBJECTED TO MINE BLAST

Donald F. Haskell  
Vulnerability Laboratory  
U.S. Army Ballistic Research Laboratories  
Aberdeen Proving Ground, Md.

An analytical study has been performed to develop a method for predicting the deformation and fracture characteristics of flat rectangular tank bottom hull plates subjected to blast attack from shallow buried mines located under the plate's center. The analytical method developed does not require electronic digital computers in its application, and is an easy to use, accurate, and directly applicable tool for vulnerability assessments and engineering design. The method of analysis is based on large structural plastic deformation, a semi-inverse energy method and a reasonable description of material behavior including a static stress-strain curve and strength failure criterion. Blast loading is characterized by the energy associated with the blast wave. Plate deformation is calculated by equating blast energy imparted to the plate to the strain energy absorbed by the plate in reaching its final deformed shape. These formulations developed correlate within an average error of 7% with available aluminum and steel plate mine blast test results.

The results of the effort are presented in simple graph and nomogram format for rapid armor areal weight determinations and mine blast-tank bottom plate evaluations. This method of analysis will facilitate vulnerability assessments and engineering design of armor subjected to mine blast attack.

**LIST OF SYMBOLS**

$\Delta$	maximum transverse plate deformation i.e. amplitude of displacement $w$ (see Fig 1), in	$\bar{U}$	plate strain energy, in-lb
$E_m$	reflected mine blast energy flux density, in-lb/in <sup>2</sup>	$S$	mine explosive charge weight, lb
$F_y$	plate tensile yield strength, psi	$a, b$	width and length respectively of rectangular plate (see Fig 1), in
$K$	plate fracture criterion constant with the following values: 1.315 - mean fracture; 0.835 - sure fracture (95% probability of fracture); 1.791 - no fracture (95% probability that fracture will not occur)	$e$	base of the natural system of logarithms
$M$	typical measurement	$e_F$	plate tensile normal fracture strain.
$\bar{M}$	mean value of typical measurement.	$h$	plate thickness, in
$R$	standoff (plate-bottom to mine-top distance i.e., see Fig 1), in	$h_{NF}$	no-fracture thickness i.e., plate thickness with a 95% probability that fracture will not occur upon mine blast attack, in
$S = \frac{4}{\pi^2} h_F (1 + \frac{a}{b}) F_y e_F$	plate strain energy absorbed to fracture per unit plate area, in-lb/in <sup>2</sup>	$h_{SF}$	sure-fracture thickness i.e., thickness with 95% probability of fracture, in
$U$	plate strain energy of deformation, in-lb/in <sup>3</sup>	$h_F$	mean thickness at which fracture occurs, in
		$n$	number of measurements
		$p$	normally reflected pressure from the blast wave, psi
		$\sigma$	$\sigma = \sqrt{\frac{1}{n} \sum_{i=1}^n \left[ \frac{M_i - \bar{M}}{h_F} \right]^2}$ standard deviation of the average relative error.

**Preceding page blank**

## INTRODUCTION

The vulnerability analyst, munitions designer, and armored vehicle designer need a methodology for determining the effects of mine blast attack on the integrity of armored vehicle hull bottom plates. To be efficient and effective, this methodology should be reasonably accurate and account for the various factors that influence tank bottom plate integrity in actual mine blast encounters. In addition, it should be simple in form so practical answers can be easily obtained in a short time. Such a methodology has been unavailable up to the present time. In the past the information required to assess mine-tank bottom encounters had to be obtained by rather expensive and time consuming test programs - analytical methods to develop this information were not available. This situation was caused by the very complicated nature of the problem.

To avoid these complications, an approximate method of analysis was selected to treat the subject problem. The result of this treatment is a simple method for rapidly predicting, with reasonable accuracy and without recourse to a high speed electronic digital computer, the deformation and fracture characteristics of armored vehicle hull bottom plates attacked by blast type mines. The particular equations developed are applicable to flat rectangular plates of uniform thickness with fully clamped, or built-in, edges that are subjected to blast from shallow buried mines centrally located under the plate (see Figure 1). These equations should be particularly useful for quick vulnerability estimates and in the initial design phases of land mines and most armored vehicle design projects.

## TEST DESCRIPTION

All the data presented in this report was obtained from available test results and battle damage records. The data consist of results from armor plate - mine blast tests performed at Aberdeen Proving Ground as well as combat damage data collected by the BDARP (Battle Damage Assessment and Reporting Program) teams operating in South Vietnam.

In the APG tests the mines included pancake-type service and experimental cased mines as well as experimental bare pancake charges. The test procedure was as follows. A test plate as shown in Figure 2 was placed on top of two steel beams measuring approximately twelve inches square by sixty inches in length with the beams resting on the ground. A rectangular steel frame weighing three and a half tons and an 8 ton plate for a total hold-down-to-test plate weight ratio of 28 were then placed on top of the test plate. (This hold-down-to-test plate weight ratio may be compared to the typical tank-to-bottom plate weight ratio of 24.) This fixture provided essentially clamped (fixed) boundary conditions all around the plate. A mine was then positioned centrally

under the test plate in a predrilled hole leaving a distance of 17 inches between the top surface of the mine and bottom surface of the test plate. The mine was then covered with approximately 3 inches of loosely packed soil. After detonation of the mine, deformation and the extent of cracking, if any, were recorded.

The Army BDARP mine category data collected described damage to the equipment including such factors as damage location, systems affected and threat involved.

Tables I and II list the deformation and fracture test results of rolled homogeneous armor steel plates and 5083 aluminum plates. Charge weight ranged from 2.5 to 24 lbs with a constant stand-off and burial depth of 17 inches and 3 inches, respectively. Since mechanical properties test results for each of the plates tested were not available, estimates of the necessary parameters were obtained from the material specifications. Yield strength and failure strain for the 5083 aluminum alloy plates were obtained from MIL HDBK 23 specifications. In regard to the steel armor plate, measured or specified hardness values were converted to yield strength and failure strain by means of well known relations (Ref. 1).

The steel plates ranged in thickness from 3/4 in. to 1 1/2 in. while thickness of the aluminum plates ranged from 3/4 in. to 3 inches. All plates were essentially the same size - either 40 in. by 65 in. or 44 in. by 75 in. All the aluminum plates were apparently of the same strength and ductility whereas the steel plates ranged in strength and ductility from 90,000 psi to 172,000 psi and 0.15 in/in. to 0.23 in/in. respectively. Correlation between these test results and predictions of the analysis is discussed in the next section.

## CORRELATION OF ANALYSIS AND TEST RESULTS

Deformation and Fracture Relations. The deformation and fracture analysis developed yields the following relations for plate deformation and fracture thickness:

$$A = \frac{1}{2} \left( \frac{a^2 b^2}{a^2 + b^2} \frac{E_m}{F_y h} \right)^{1/2} \quad (1)$$

$$h_f = \frac{K L_m}{(1 + \frac{a}{b}) F_y c_p} \quad (2)$$

where

$$L_m = 117435 K^{-1/3} e^{0.23 - 0.544 R_k^{-1/3}} \quad (3)$$

$$K = \begin{cases} 1.315 & \text{for the median fracture thickness} \\ 0.835 & \text{for sure fracture, i.e., 95\% probability of fracture} \\ 1.791 & \text{for no fracture, that is, 95\% probability that fracture will not occur} \end{cases}$$

**Deformation Correlation.** Table I lists theoretical results for plate deformation calculated by use of Eq. 1 as well as the deviation of these predictions from the test results. As indicated, the average positive error is 14% and the negative error is 18.1% with the overall average error -6.4%. The average absolute error is 16.6%. These test and analytical results are plotted in Figure 3. In this figure the test data has been plotted as reduced deformation amplitude  $\bar{A}$  defined by:

$$\bar{A} = 2A \left( \frac{a^2+b^2}{a^2b^2} F_y h \right)^{1/2}$$

versus mine blast energy flux density  $E_m$ . The test data is as follows: circles represent 5083 aluminum and the squares class 2 rolled homogeneous steel armor. Each data point represents a single test plate or the average of either two or three tests. A least squares fit of the data is shown as the solid (—) line with the  $2\sigma$ , or 95% probability of occurrence, limits as the dotted (---) lines. The dashed line is the theoretical curve. As indicated, the theoretical curve is slightly below the least squares curve. Consequently, plate deformation predicted by the present theory is, on the average, 6.4% lower than would be obtained in practice. If a conservative method for predicting deformation is desired, the equation corresponding to either of the  $2\sigma$  limits could be employed. For example, use of the upper  $2\sigma$  curve to predict deformation would yield results that 95% of the time are higher than would be obtained in actual practice.

**Fracture Correlation.** Plate fracture data listed in Table II is plotted in Figure 4. In this figure plate strain energy absorbed to the point of fracture per unit plate area  $S$  is plotted versus mine blast energy flux density  $E_m$  according to Eq. 2. Along with the test data points this figure shows the least squares fit curve of the test data (equation 2 with  $k = 1.315$ ),  $2\sigma$  probability limits (equation 2 with  $k$  equal to 0.835 and 1.791) and the theoretical fracture line. As in Figure 3 the circles and squares represent 5083 aluminum and class 2 rolled homogeneous armor steel plates respectively. The triangles correspond to actual tank damage from mine blast in South Vietnam.

The theoretical criterion for fracture is essentially

$$S = C_m$$

whereas the least squares fit equation for the test data is

$$S = 0.533 E_m$$

That is, the slope of the least squares data fit is slightly higher than half that of the theoretical plate fracture criterion. There may be two possible reasons for this discrepancy between theory and test results, namely, inadequacy of the fracture criterion and neglect of bending

action. However, until this analysis is improved to bring the theory into closer agreement with test, adequate fracture predictions may be made by using the least squares data fit equation as the fracture criterion. The average absolute error between this least squares fit equation and the plate test data is 13.2%. Besides, as indicated by Figure 4, the actual tank mine damage data points which were not used in arriving at the least squares equation and its  $2\sigma$  limits fall well within the  $2\sigma$  probability limits of the least squares fit equation.

## DISCUSSION

**General.** The deformation relation, Eq. 1, was derived from first principles without making use of test data to develop the equation. First principles were also used in developing the form of the fracture relation, Eq. 2, although the exact value of the fracture criterion constant  $K$  was obtained from a least squares fit of test data.

A relatively simple and straightforward means for calculating the thickness of a given plate that will fracture when attacked by mine blast is presented by the nomograms of Figures 5 through 7. These nomograms have been prepared from the fracture thickness equation (Eq. 2). Figure 5 is a nomogram for mean fracture thickness based on Eq. 2 with  $K = 1.315$  where this value of  $K$  has been determined by a least squares fit of the plate fracture data. As indicated previously, the average error of this relation is -0.6% and the average absolute error is 13.2%.

Figure 6 presents the conditions for plate thickness with a 95% (or  $+2\sigma$ ) probability of no fracture,  $h_{NF}$ . That is, plates of this thickness have a 95% probability of retaining their integrity after a mine attack. This nomogram is based on Equation 2 with  $K = 1.791$ .

Plate thickness that will be breached by 95% of the mine attacks may be obtained from Figure 7. This figure is a nomogram for sure fracture thickness,  $h_{SF}$ , i.e., it represents 95% probability of fracture. It is based on Eq. 2 with  $K = 0.835$ , the equation for the  $-2\sigma$  limit curve of Figure 4.

Through five scales, these nomograms in Figures 5, 6 and 7 relate plate shape  $\frac{a}{b}$ , toughness  $U$ , fracture thickness  $h_f$ , scaled standoff  $R/K^{1/3}$ , and mine charge weight  $W$ . In addition there are two unlabeled scales used in the calculations.

The procedure for using the fracture nomograms is as follows. The sure-fracture nomogram, Figure 7, will be used as an example. To calculate the thickness  $h_{SF}$  at which a plate of width-to-length aspect ratio  $\frac{a}{b}$  with strain energy absorption capacity (toughness)  $U_{RP}$  will fracture

with 95% certainty under attack from a mine of charge weight  $W$  at a standoff  $R$ :

1. Locate the aspect ratio on the  $\frac{a}{b}$  scale, point 1, the plate toughness on the  $U_{RP}$  scale, point 2, and draw a straight line through these points intersecting line a at point 3.

2. Similarly, locate the charge weight on the  $W$  scale, point 4, and the scaled standoff on the  $R/W^{1/3}$  scale, point 5. Draw a straight line through points 4 and 5 intersecting line b at point 6.

3. Draw a straight line through points 3 and 6 intersecting the sure fracture thickness scale  $h_{SP}$  at point 7. This value is the thickness which fracture occurs.

#### SUMMARY

Two equations have been developed, one for deformation and one for fracture of flat, rectangular, clamped plates subjected to blast attack from shallow buried mines. The average error between predictions of these equations and test results, including both plate and tank data, is less than 7% with the average absolute error less than 17%. From the fracture criterion a set of plate fracture nomograms have been prepared that yield plate thickness for 95% probability of fracture under mine blast attack, 95% probability that the plate will not fracture, and mean fracture thickness. Fracture thickness and areal weight can be determined from these nomographs in little more than the time it takes to draw three straight lines on the nomograph.

#### REFERENCES

1. T. Lyman, Ed., Metals Handbook, pp. 108-110, 8th Ed. Vol. 1, Properties and Selection of Metals. American Society for Metals, 1961.

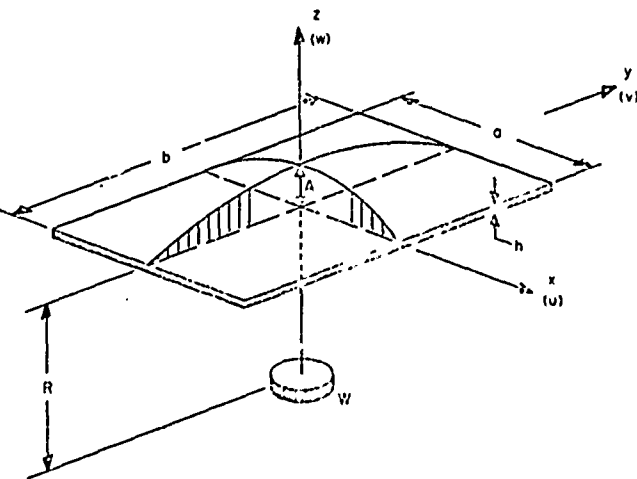


Figure 1 - Mine-Rectangular Plate Configuration

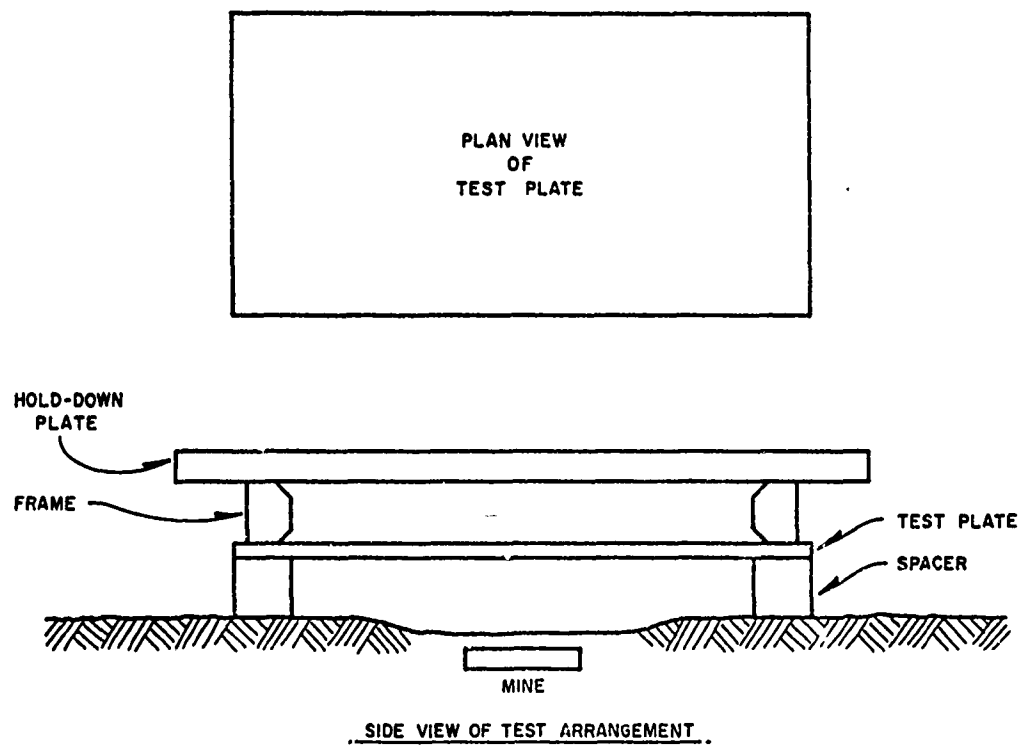


Figure 2 -Typical Plate Test Arrangement.

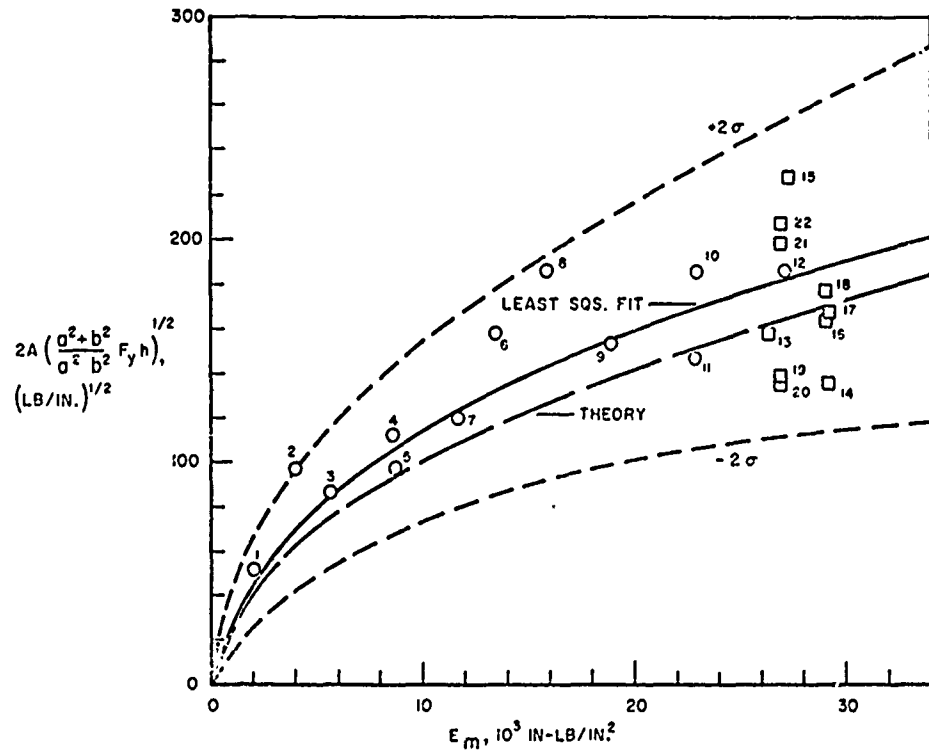


Figure 3 -Plate Deformation; O: 5083 Aluminum Test Data, □: Rolled Homogeneous Armor Steel Test Data, —: Least Squares Fit of Data, ---: Theory

Table I. Deformation Data  
Stand-Off = 17 In. (Includes 3 In. Mine Burial Depth)

Test Case No.	Material	W Charge Weight lb	h Plate Thickness in	a Plate Width in	b Plate Length in	F <sub>y</sub> Yield Strength KSI	A <sub>s</sub> Test Plate Deformation in	A <sub>s</sub> Theory Plate Deformation in	Deviation From Test %
1	5083 Al.	2.5	0.75	44	65	33	6.0	5.18	-8.2 -13.7
2		4.0	0.75	44	65	33	11.25	7.32	-3.93 -34.9
3		5.0	1.25	44	65	33	7.75	6.71	-1.04 -13.4
4		7.0	1.25	44	65	33	10.0	8.52	-1.68 -16.8
5		7.0	1.75	44	65	33	6.875	7.07	+.95 +2.8
6		10.0	1.75	44	65	33	12.0	8.79	-3.21 -26.7
7		9.0	2.00	44	65	33	8.5	7.24	-.85 -9.8
8		12.0	2.00	44	65	33	13.25	8.95	-4.3 -32.4
9		14.0	2.50	44	65	33	9.75	8.72	-1.03 -10.6
10		17.0	2.50	44	65	33	11.75	9.61	-2.14 -18.2
11		17.0	5.00	44	65	33	8.5	8.76	+.26 +30.6
12		20.0	3.00	44	65	33	10.75	9.51	-1.24 -11.5
13	Steel	19.41	1.0	40	65	160	6.750	6.9	+.15 +2.2
14		21.5	1.25	40	65	150	5.125	6.7	+1.575 +30.7
15		20.2	1.0	40	65	163	9.625	6.97	-2.655 -27.6
16		21.2	1.0	40	65	116	8.208	8.52	+.312 +3.8
17		21.5	1.0	40	65	137	7.58	7.85	+.27 +3.6
18		20.0	1.0	40	65	161	7.25	7.24	-.01 -0.1
19		19.9	1.0	44	65	164	6.25	7.38	+1.13 +18.1
20		19.9	1.0	44	65	126	7.0	8.42	+1.42 +20.3
21		19.9	1.0	44	65	96	11.63	9.61	-2.02 -17.3
22		19.9	1.0	44	65	143	10.0	7.91	-2.09 -20.9

Average Error = -6.4%  
 Average + Error = 14.0%  
 Average Absolute Error = 16.6%

Table II. Fracture Data  
Stand-Off = 17 In. (This Includes 3 In. Mine Burial Depth)

Test Case No	Material	W Charge Weight lb	h Plate Thickness in	a Plate Width in	a Plate Length in	F <sub>y</sub> Yield Strength KSI	e <sub>f</sub> Failure Strain in/in	Deviation From Least Squs %
1	5083 Al.	4.0	0.75	44	65	33	.16	+25.7
2		6.5	1.25	44	65	33	.16	-0.2
3		12.0	2.0	44	65	33	.16	+15.6
4		11.9	2.0	44	65	33	.16	-14.6
5		11.0	2.0	44	65	33	.16	-6.2
6		15.9	2.5	44	65	33	.16	-21.7
7		19.9	3.0	44	65	33	.16	-25.2
8		14.5	2.5	44	65	33	.16	-10.6
9		17.5	2.5	44	65	33	.16	-27.0
10		Steel	20	0.75	44	60	135	.17
11		20.7	1.50	44	60	112	.20	+55.8
12		20.2	1.0	40	65	137	.175	+7.6
13		20.2	1.0	40	65	116	.22	+14.4
14		21.4	1.0	40	65	161	.155	+5.5
15		20.1	1.0	40	65	163	.15	-0.1
16		21.9	1.0	40	65	137	.17	-4.6
17		20.8	1.0	40	65	160	.16	+11.5
18		17.6	0.75	40	65	172	.13	-14.0
19		24	1.25	40	65	150	.16	+13.6
20		19.9	1.0	44	65	90	.225	-4.0
21		19.9	1.0	44	65	90	.23	-2.4
22		19.9	1.0	44	65	114	.20	+7.8
23		19.7	1.0	44	65	137	.17	+10.2
24		19.9	1.0	44	65	110	.21	-2.8

Average = -0.6%  
Error

Average  
Absolute = 13.2%  
Error

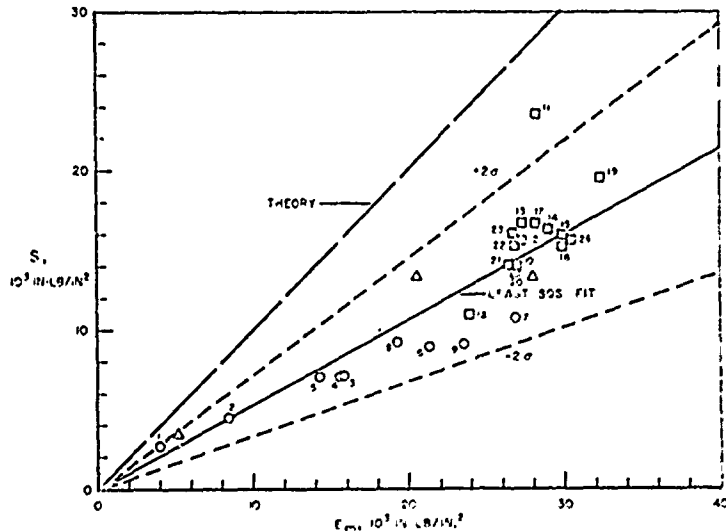


Figure 4 - Plate Fracture. 5083 Aluminum Test Data: O, Rolled Homogeneous Armor Steel Test Data: □, Tank Test Data: Δ, Least Squares Fit of Data: —, Theory: —

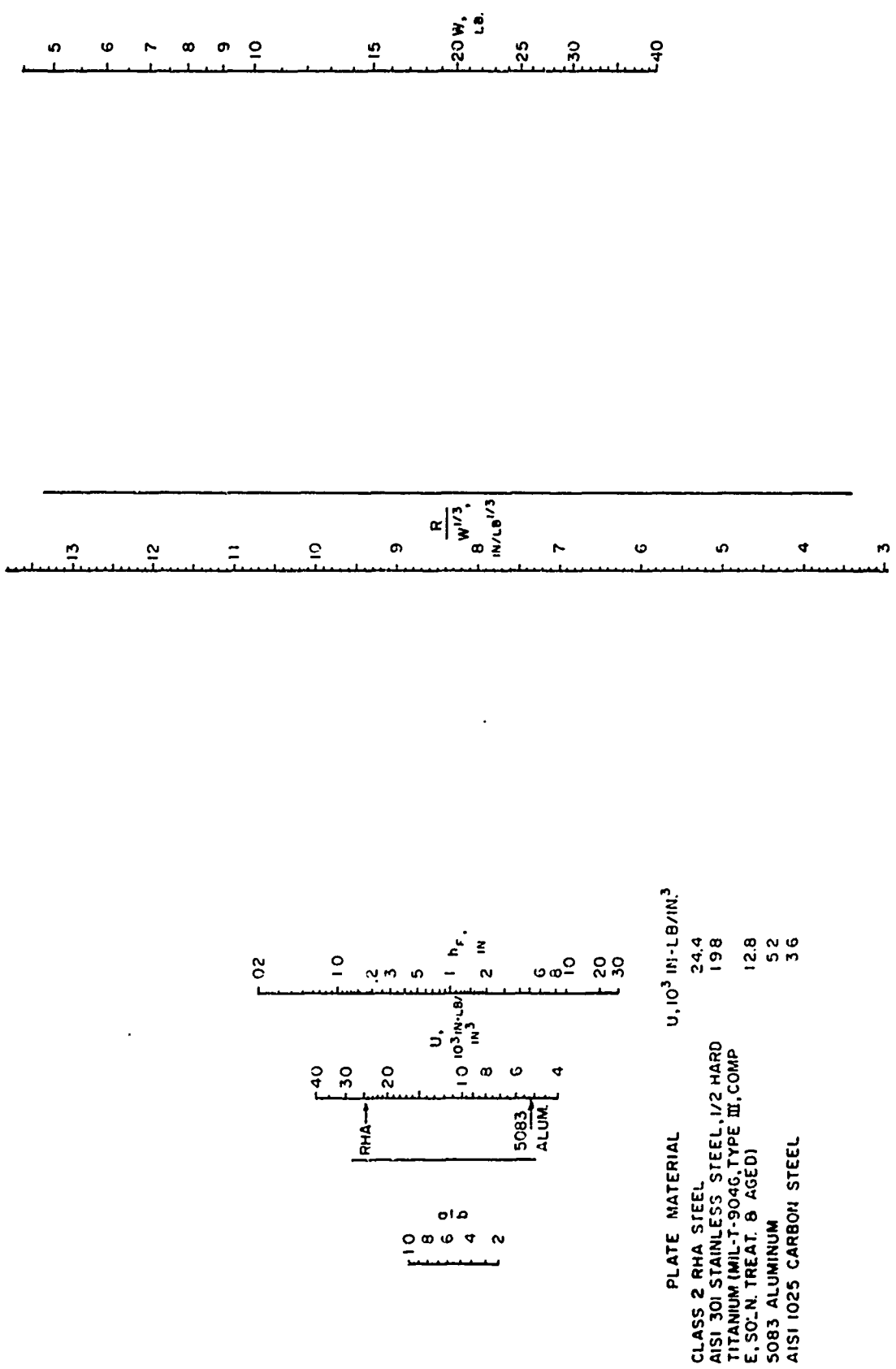


Figure 5 Mean Fracture Thickness Nomogram

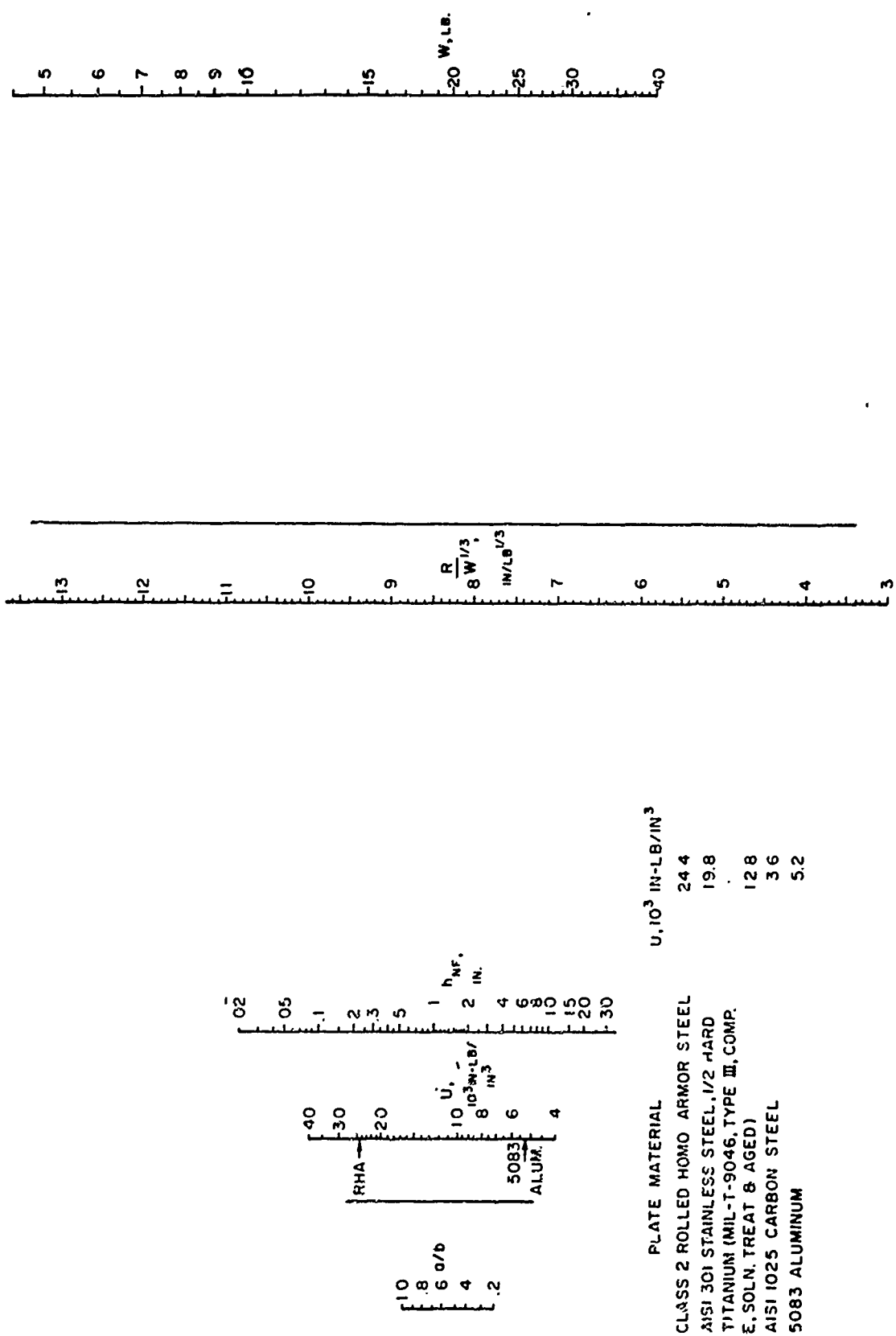


Figure 6 Nomogram for 95% Probability of No Fracture.

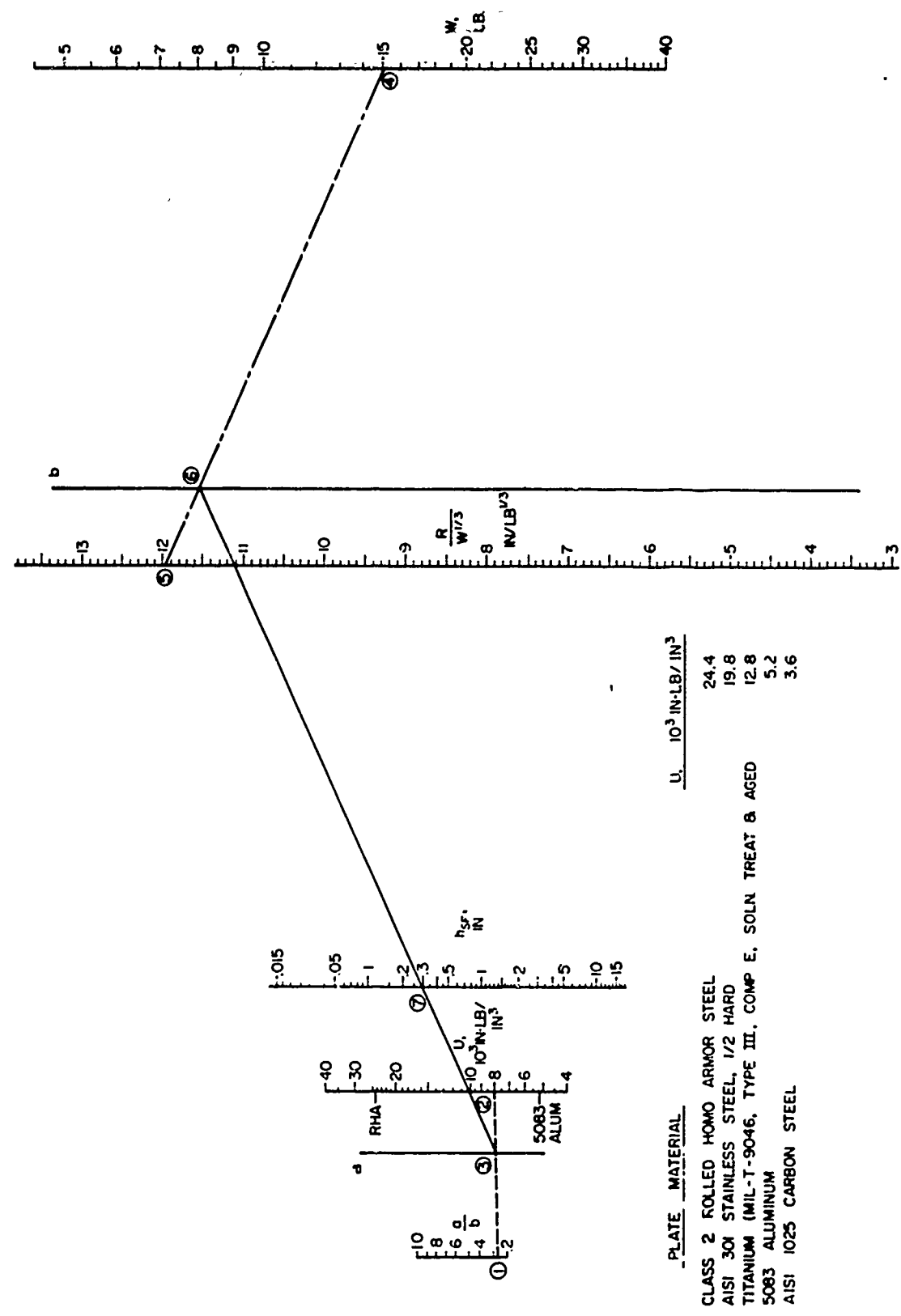


Figure 7 95% Probability of Fracture Nomogram

## THE IMPULSE IMPARTED TO TARGETS BY THE DETONATION OF LAND MINES

Peter S. Westine  
Southwest Research Institute  
San Antonio, Texas

Numerous expensive testing programs have been conducted to determine how land mines damage vehicles or armor plates; however, very few analytical studies have been conducted because the load imparted to a structure from a land mine explosion has never been determined. The few analytical calculations which have been made assumed that the target was loaded by an air blast. In this paper, the writer shows that the impulse imparted to the target is not entirely an air blast phenomenon. The impulse is caused principally by the momentum in the soil particles surrounding the buried explosive. A technique is developed for predicting the impulse imparted to targets such as wheels and armor plates. Several illustrative calculations are compared with experimental test results to establish the validity of this procedure for estimating the impulse imparted to a target from a land mine explosion.

### INTRODUCTION

Although the effects of land mines on combat vehicles have constituted a serious problem for a long time, very few theoretical or careful experimental studies have been made of this problem in the past. Almost all past efforts have been purely empirical; that is, one simply blew up vehicles or armor plates with land mines, and determined what thicknesses of various armor materials would be necessary to "defeat" given mines. Numerous testing programs of this nature are listed in a recent bibliography [1].

All of the analytical studies which have been conducted assumed that the loading is an air blast phenomena. Personnel at Cornell Aeronautical Laboratories [2] used BRL data on reflected impulses and pressures from explosive charges in air to estimate loads on tank hull bottoms from mine detonation. These air blast data were applied without considering ground reflection factors or accounting for the effects of burial. In another study conducted at the Cleveland Army Tank Automotive Plant, Allison Division of General Motors [3], the same BRL data for impulsive loads from air blast were not properly used as in the Cornell

study; however, the authors did recognize the limitations of using air blast data directly and attempted to account for the effects of shock wave reflections from the ground plane by doubling the explosive charge weight. A limited set of experiments measuring blast loads from buried 5-lb TNT explosive charges was conducted by Aerojet General Corporation [4] and compared with air blast data. The conclusions made from these experiments were:

- 1) The impulse from an explosive charge in the ground is a function of charge weight, stand-off distance, and depth of burial.
- 2) Buried charges demonstrate a greater efficiency in transmitting impulse to a target than does a blast wave from a spherical charge in air.

In this paper, the author will demonstrate that the impulse imparted to a target by detonating a land mine is not an air blast phenomenon. The basic premise behind these earlier studies, chiefly that the loading was caused by a shock wave propagated through air, was incorrect. Aerojet General's conclusion that buried charges are more efficient was a correct observation; however, they were

incorrect in comparing the loads to air blast ones. The impulse imparted to a target from a land mine explosion is caused by the momentum in the explosive products from the charge and primarily from the soil encasing the charge. This paper considers only the impulse, i.e., the area under the positive pressure history of the load imparted to a target from a land mine explosion. Peak pressures and transient loading histories are not included, and cannot be discussed until direct measurements are made of these effects. These limitations will not affect structural studies of hull plate response or vehicle overturning provided the response of the system being studied falls within the impulsive loading realm. This paper will indicate how specific impulse is distributed over the surface of several targets, particularly wheels and flat plates.

#### LOADING FROM A MINE BLAST

The nature of the loading applied to a structure such as the hull of a combat vehicle from a land mine explosion involves very complex phenomena. A shock wave propagated through air is only a minor cause of loading and not the principal one. Rudimentary calculations indicate that the mass of earth and explosive products impinging upon the floor plate contribute considerably to the loading. Therefore, the loading is a very complex wave form that differs considerably from the classical, exponentially-decaying wave that is usually associated with blasts.

Baker [5] has shown that very close to the charge the normally-reflected specific impulse from a spherical charge detonated in air equals:

$$i_R = \frac{(2 ME)^{1/2}}{4\pi S^2} \quad (1)$$

where  $M$  = total mass of explosive and engulfed air  
 $E$  = energy release in explosive  
 $S$  = stand-off distance from center of charge  
 $i_R$  = reflected specific impulse.

This equation is applicable whenever the mass of the engulfed air is less than approximately one-tenth the mass of the explosive products. If the explosive charge represented by Eq. (1) is encased, the mass,  $M$ , represents the mass of the case and explosive. Observe that no parameters defining ambient atmospheric conditions, such as ratio of specific heats, atmo-

spheric density, or velocity of sound in air, can be found in Eq. (1). The specific impulse imparted to the body being loaded is caused primarily by the momentum of the explosive products rather than being caused by a shock wave propagated through air. Although this equation is for a spherical explosive charge in air, a land mine represents a very similar circumstance. One can think of the ground which surrounds the mine as a charge surrounded by a weak case of soil. The mass term,  $M$ , is thus the mass of the mine and an equivalent mass of soil. The philosophy represented by Eq. (1) is applicable to a land mine explosion because the mass of the engulfed air at standoffs typical of mine attacks is very small relative to the mass of the explosive products. If we assume that a 20-lb land mine is covered by 3 in. of earth and that the hull of a structure is 17 in. above the center of the mine, then we can demonstrate the validity of this claim. The density of air under ambient sea-level atmospheric conditions is 0.0765 lb/ft<sup>3</sup> and the volume of this air enclosed within a sphere 17 in. in diameter is 11.9 ft<sup>3</sup>. Thus, the weight of an equivalent amount of engulfed air is 0.0765 times 11.9 or 0.91 lb, which is very small relative to 20 lb of high explosive. Actually this ratio of air mass relative to mass of explosive products is smaller than 0.91 to 20.0, because the effective weight of soil (approximately 100 lb) is 5 times greater than the weight of the charge in this illustrative example. Later discussions will show how to estimate the effective mass term,  $M$ , in Eq. (1).

Jack and Armendt [6] have measured transient pressures at the surface of a plate from spherical pentolite charges detonated in a vacuum. This loading is believed to be somewhat analogous to loads caused by land mines because the pressures are primarily caused by the explosive products. A typical pressure trace as recorded by Jack and Armendt may be seen in Fig. 1. Observe that this normally-reflected pressure history differs markedly from conventional air blast waves. Two shock fronts may be seen at A and B in the pressure history in Fig. 1. The rest of the wave has a gradual rise time and a rounded shape. The gradual rise time and rounded shape are caused by the mass of the explosive products impinging upon the plate and the pressure transducer in it. Theoretical studies such as those by Lutzky [7] indicate that explosions in an absolute vacuum would have these characteristics. Jack and Armendt feel that the initial, sharp-rising shock front at point A is an initial reflected air blast wave that would disappear entirely were they to have had a complete rather than partial vacuum. They offer

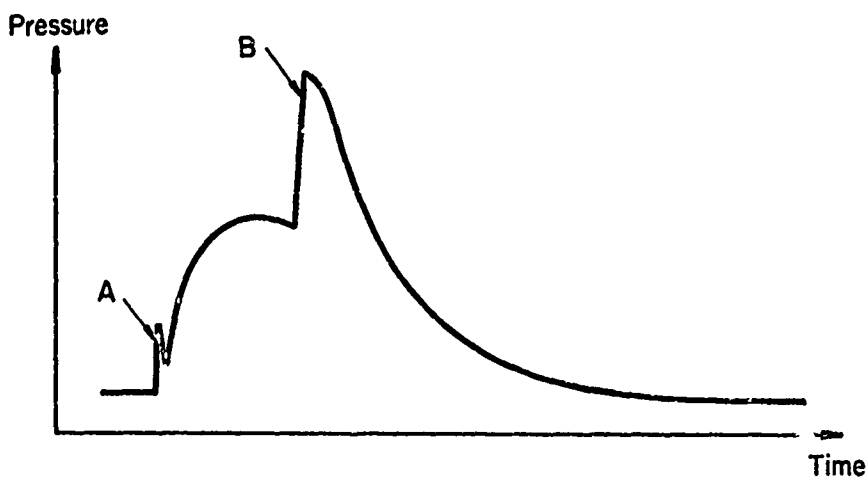


Fig. 1. Normally-Reflected Pressure History Taken In Vacuum Near a Spherical Pentolite Charge

no opinion as to the cause of the second shock front at location B in Fig. 1. The second shock front may be a secondary shock (sometimes called a "pete" wave by other investigators). Ordinarily, these shocks are less intense than the first shock; however, under these circumstances the wave has an atmosphere of gases from the explosive products through which it can expand; whereas, the incident wave has almost no medium through which it can be conducted. A land mine blast will probably give a loading somewhat similar to that seen in Fig. 1; however, the relative magnitude of first shock, explosive products, and second shock wave pressures will vary considerably. One can observe in Fig. 1 that the impulse (area under the pressure history) is principally caused by the explosive products and that air shocks produce very little impulse. Probably in a land mine explosion, the initial peak would be larger because of the presence of an atmosphere, but the secondary shock would be greatly diminished, because of reflections being transmitted far into the earth and because the cylindrical shape of a land mine would disperse reflections rather than focus them as in a spherical charge. A strong possibility exists that a peak pressure will occur which is a shock rather than being caused by momentum from soil flung upward by a land mine explosion; however, the vast majority of the impulse is caused by momentum in soil products.

#### LOADING IMPARTED TO COMPLEX TARGETS

Before discussing what numerical value should be assigned to the mass,  $M$ , in Eq. (1)

so that the specific normally reflected pulse,  $i_R$ , can be computed, we will consider how Eq. (1) can be applied to real targets which possess complex configurations. Eq. (1) allows one to compute the normally reflected impulse per unit area at various standoff distances. This equation does not tell one how to calculate the total impulse,  $I$ , imparted to a wheel or to a plate where the impulses imparted to differential areas on these targets are not normally reflected. Total impulse can be determined by knowing the projected area of a target and the peak normally reflected impulse imparted to this area by using Eq. (2).

$$I_R = i_R A \Phi \quad (2)$$

The term  $\Phi$  in Eq. (2) is a shape factor which is a function of target shape and standoff conditions. This shape factor will be calculated for wheels and rectangular plates, both of which are common targets.

#### SHAPE FACTOR FOR A WHEEL

To calculate the shape factor for a wheel, consider encounter conditions as presented in Fig. 2a. The wheel being considered is located directly over the center of the explosive charge. We determine the total vertical impulse imparted to the wheel by considering the specific impulse imparted to a differential area located on the rim of the wheel. The total impulse is then computed by integrating the differential areas around that portion of the rim being loaded. Fig. 2b shows the specific impulse being applied to a differential area,  $dA$ .

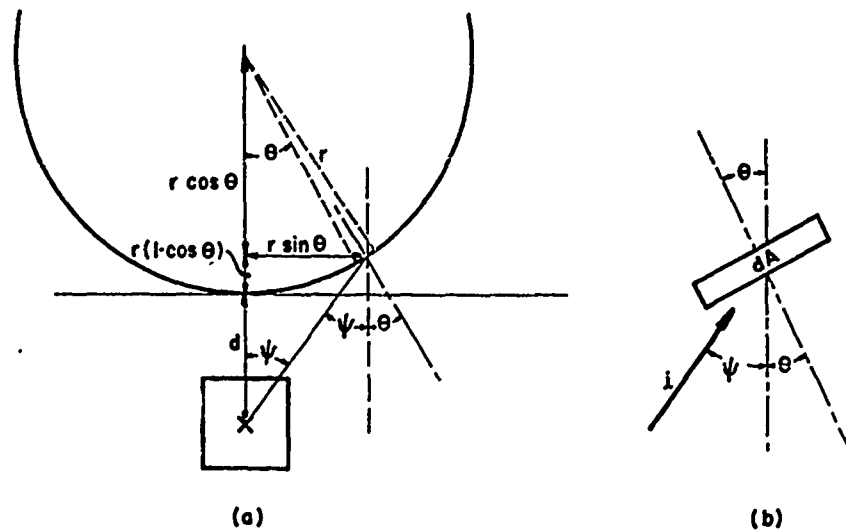


Fig. 2. Wheel Traversing a Land Mine

If the wheel is a thin strip of thickness,  $h$ , then the differential area,  $dA$ , equals:

$$dA = hr d\theta \quad (3)$$

The specific impulse,  $i$ , as shown in Fig. 2b at the location of the differential area equals after substituting for  $S$  in Eq. (1):

$$i = \frac{(2ME)^{1/2}}{4\pi \left[ \frac{r(1-\cos\theta)+d}{\cos\psi} \right]^2} \quad (4)$$

Geometric considerations which are seen in Fig. 2a indicate:

$$\tan\psi = \frac{r \sin\theta}{r(1-\cos\theta)+d} \quad (5)$$

The  $\cos\psi$  can be calculated from the  $\tan\psi$  and equals after substituting Eq. (5) for  $\tan\psi$ :

$$\cos\psi = \frac{r(1-\cos\theta)+d}{\sqrt{r^2 \sin^2\theta + [r(1-\cos\theta)+d]^2}} \quad (6)$$

We will assume that only that component of the specific impulse which is perpendicular to the differential area imparts momentum to the target. This assumption would be invalid were this to be an air shock; however, it is valid because we are considering momentum from moving particles of soil. The impulse which is applied to the differential area equals:

$$di_A = i \cos(\psi + \xi) dA \quad (7)$$

This impulse may be divided into its vertical and horizontal components. We are only interested in the vertical component as all horizontal components cancel because of symmetry. The vertical component,  $di$ , of the impulse equals:

$$di = i \cos(\psi + \xi) \cos\theta dA \quad (8)$$

The total impulse imparted to the wheel is obtained if one integrates Eq. (8) over the loaded segment of the wheel. Because this loading is caused by soil particles impacting the wheel, all segments of the wheel are loaded until the impulse vector,  $i$ , becomes tangent to the wheel. The impulse vector which is parallel to a line from the center of the charge to the differential area becomes parallel to the wheel when  $\tan\psi$  is a maximum. This occurs at:

$$\frac{d}{d\theta} (\tan\psi) = 0$$

$$-r \cos\theta (d + r - r \cos\theta) + r^2 \sin^2\theta = 0$$

or at

$$\cos\theta = \frac{r}{r+d} \quad (9)$$

Let us define a nondimensional quantity,  $\delta$ , such that

$$\delta = \left( 1 + \frac{d}{r} \right) \quad (10)$$

Substituting for  $\frac{d}{r}$  in Eq. (9) and rearranging terms indicates that the limits of integration are:

$$\theta = \arccos\left(\frac{1}{\delta}\right) \quad (11)$$

Because of symmetry, the total impulse may be obtained by multiplying Eq. (8) by 2.0 and integrating the resulting expression from  $\theta$  equal to zero to the limit expressed by Eq. (11). This integration gives:

$$I = \int_0^\theta 2i \cos(\psi + \theta) \cos \theta dA \quad (12)$$

Substituting Eqs. (3) and (4) into Eq. (12) and recognizing that  $2rh$  equals the projected area,  $A$ , of the wheel yields:

$$I = \frac{(2ME)^{1/2} A}{4\pi S^2} (r+d)^2 \int_0^\theta \frac{\cos^2 \psi \cos(\psi + \theta) \cos \theta d\theta}{(d+r-r \cos \theta)^2} \quad (13)$$

But Eq. (13) is Eq. (2) provided the shape factor,  $\psi$ , for a wheel equals:

$$\psi = (r+d)^2 \int_0^\theta \frac{\cos^2 \psi \cos \theta \cos(\psi + \theta) d\theta}{(d+r-r \cos \theta)^2} \quad (14)$$

Eq. (14) for the shape factor may be simplified further if the appropriate substitutions from Eqs. (5) and (6) are made into Eq. (14). Making these substitutions and gathering terms yields:

$$\psi = \delta^2 \int_0^\theta \frac{(\delta \cos \theta - 1) \cos \theta d\theta}{[\delta^2 + 1 - 2\delta \cos \theta]^{3/2}} \quad (15)$$

Although this integral is a very difficult one to compute in closed form, a numerical solution is easily obtained on a computer. The results from a numerical investigation are presented in Fig. 3 where shape factor  $\psi$  for a wheel is presented as a function of  $\delta$ .

#### SHAPE FACTOR FOR RECTANGULAR PLATES

To calculate the shape factor for a rectangular plate, consider a plate with a rectangular x-y coordinate system having an origin at the center of the plate. Because of the symmetry which exists when the charge is buried directly under the center of the plate, we will consider the vertical impulse imparted to a differential area located in only one quadrant of the plate. The plate will have half spans of  $X$  and  $Y$ . The slant range,  $R$ , from the center of the charge to the differential area equals:

$$R = \sqrt{x^2 + y^2 + S^2} \quad (16)$$

The differential area,  $dA$ , equals:

$$dA \approx dy dx \quad (17)$$

Eq. (1) indicates that the specific impulse directed at the differential area is:

$$i = \frac{(2ME)^{1/2}}{4\pi R^2} \quad (18)$$

Once again we assume that the component of this impulse which is tangential to the differential area does not load the differential area, and that all of the impulse imparted to this differential area is caused by the normal component of the impulse,  $i$ , expressed in Eq. (18). The impulse imparted to the differential area equals:

$$i_A = i \frac{S}{\sqrt{x^2 + y^2 + S^2}} \quad (19)$$

One calculates the total impulse imparted to the entire plate by substituting into Eq. (20).

$$I = 4 \int_0^X \int_0^Y i_A dA \quad (20)$$

Substituting Eq. (16) into Eq. (18), Eq. (18) into Eq. (19), and Eq. (19) and (17) into Eq. (20) yields:

$$I = \int_0^X \int_0^Y \frac{(2ME)^{1/2} 4S dx dy}{4\pi(x^2 + y^2 + S^2)^{3/2}} \quad (21)$$

If one multiplies and divides Eq. (21) by  $S^2 XY$  and recognizes that  $4XY$  equals the projected area,  $A$ , then:

$$I = \frac{(2ME)^{1/2} A}{4\pi S^2} \int_0^X \int_0^Y \frac{S dx dy}{(x^2 + y^2 + S^2)^{3/2}} \quad (22)$$

But Eq. (22) is Eq. (2) provided the shape factor,  $\psi$ , for a rectangular plate equals:

$$\psi = \left[ \frac{S^3}{XY} \right] \int_0^X \int_0^Y \frac{dx dy}{(x^2 + y^2 + S^2)^{3/2}} \quad (23)$$

After performing this integration, one obtains for the shape factor of a rectangular plate:

$$\psi = \frac{1}{(X/S)(Y/S)} \arctan \left[ \frac{(Y/S)(X/S)}{\sqrt{(Y/S)^2 + (X/S)^2 + 1}} \right] \quad (24)$$

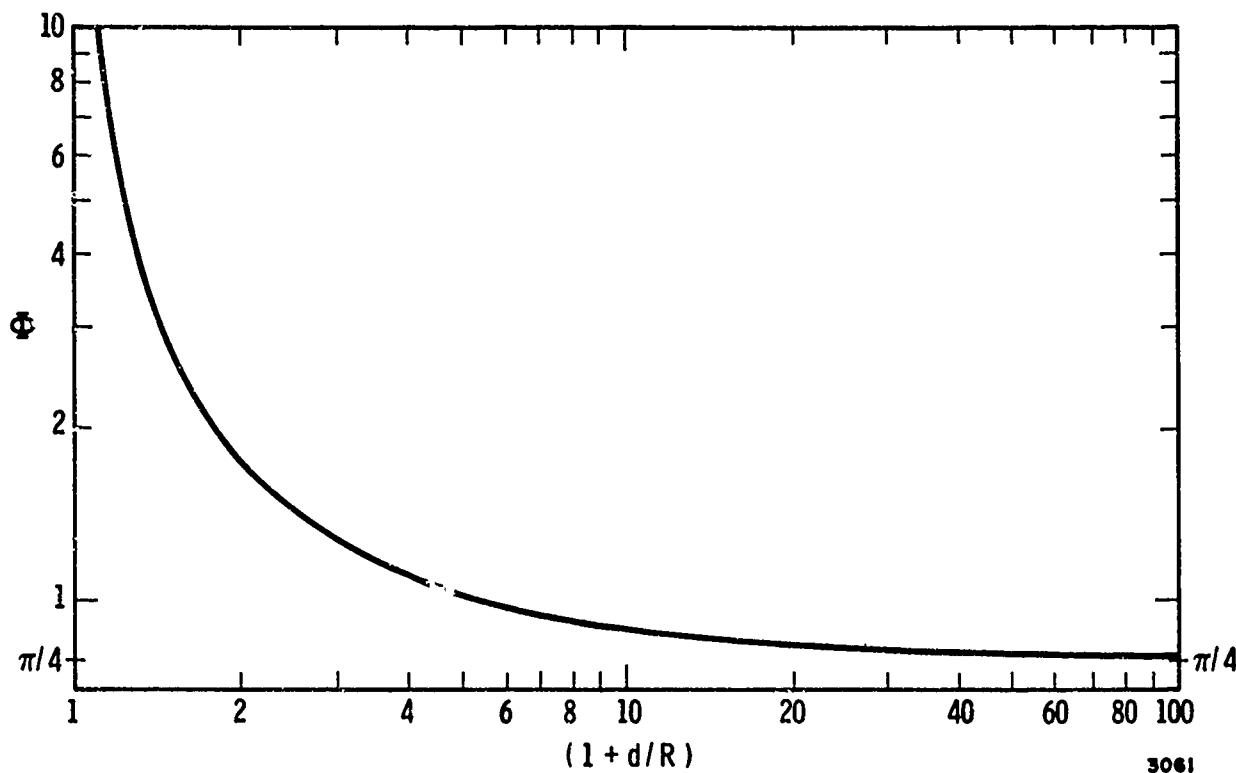


Fig. 3. Shape Factor For a Wheel

#### MODEL ANALYSIS TO DETERMINE EFFECTIVE MASS

If one knows that value of effective mass is appropriate for a given size of explosive charge and depth of burial, he can compute either specific impulse or total impulse by selecting the appropriate shape factor and substituting in Eqs.(1) and (2). Effective mass,  $M$ , will be determined by using the analytical results expressed by Eqs.(1) and (2), conducting a similitude analysis to interrelate charge weight and depth of burial, and applying some experimental results to devise a numerical relationship between the various parameters.

To conduct a similitude analysis, one begins by listing the relevant parameters. We wish to measure specific impulse,  $i$ ; this parameter is our response parameter. The impulse is created by detonating an explosive charge of weight,  $W$ , which was buried at some depth,  $d$ , from the surface of the soil to the center of the charge. Impulse is to be measured at some standoff distance,  $S$ , from the center of the charge. The most difficult aspect in conducting this similitude analysis is the selection of appropriate parameters for characterizing the soil. Fortunately, a recent analysis [8] of a similar problem, the size of

crater produced by detonating a buried explosive, indicates what soil properties should be selected. In order to determine the impulse from the detonation of a buried explosive, we are interested in the momentum imparted to soil particles. The explosive cratering analysis must concern itself with both the momentum imparted to soil particles and the influence of gravity on the trajectory of these particles. Reference [8] uses the bulk density of the soil,  $\rho$ , the seismic velocity of the soil,  $c$ , and the acceleration of gravity,  $g$ , to characterize soil properties. In this study, we will use two of these three parameters, the density,  $\rho$ , and the seismic velocity,  $c$ ; however, we will delete the acceleration of gravity,  $g$ , from our analysis. Deleting this term from the analysis is equivalent to assuming that gravitational effects are insignificant. Such an assumption is appropriate as the gravitational field of the earth is not strong enough to appreciably reduce the momentum in soil particles in the relatively small distance between most land mines and targets. The six parameters which have just been presented as defining this problem of the impulse from the detonation of a land mine are summarized in Table A together with their fundamental dimensions in the engineering system of force,  $F$ ; length,  $L$ ; and time,  $T$ .

TABLE A  
Parameters For Determining Impulse  
From A Land Mine Explosion

Symbol	Parameter	Fundamental Dimensions
i	specific impulse	FT/L <sup>2</sup>
W	charge weight	FL
d	depth of burial	L
S	standoff distance	L
$\rho$	density of soil	FT <sup>2</sup> /L <sup>4</sup>
c	seismic velocity	L/T

Many different textbooks present several different procedures for developing the three nondimensional ratios called pi terms from the six parameters listed in Table A. In this paper, we will omit the algebraic procedures and present the results. Table B lists three pi terms which can be obtained.

TABLE B  
Pi Terms - Impulse From  
Land Mine Explosion

$\pi_1 = \frac{i}{\rho c d}$	Scaled impulse
$\pi_2 = \frac{S}{d}$	Geometric similarity
$\pi_3 = \frac{W}{\rho c^2 d^3}$	Scaled charge weight

The first pi term is normalized or scaled impulse. This pi term is a unique function of the other two pi terms, a statement of geometric similarity and scaled charge weight. We write this functional relationship as Eq.(25).

$$\frac{i}{\rho c d} = f \left( \frac{S}{d}, \frac{W}{\rho c^2 d^3} \right) \quad (25)$$

The soil parameters  $\rho$  and  $c$  can be deleted from Eq.(25), because they are essentially constants. Soil density varies very little over a wide range of soil conditions. Seismic velocity for soil in a solid state does vary over a limited range; however, the soil which provides most of the impulse from a land mine explosion acts more like a fluid than a solid. We will assume that the seismic velocity of all soil "fluids" is constant. A careful perusal of Reference [8] would show that relatively accurate predictions of crater size can be made when  $\rho$  and  $c$  are treated as constants. Deleting  $\rho$  and  $c$  from Eq.(25) because they are constants yields Eq.(26).

$$\frac{i}{d} = f' \left( \frac{S}{d}, \frac{W}{d^3} \right) \quad (26)$$

Eq. (26) defines a three-dimensional space. This space can be reduced in a two-dimensional space by squaring the second pi term and multiplying the result by the first pi term to form a new dependent parameter. After performing this operation, Eq.(26) may be rewritten as Eq.(27).

$$\frac{i S^2}{d^3} = f'' \left( \frac{W}{d^3} \right) \quad (27)$$

Eq. (27) is Eq. (1) without an explicit expression for the appropriate functional format. Eq.(1) states that impulse varies inversely as the square of the standoff,  $S$ . Inasmuch as the effective mass,  $M$ , in Eq.(1) cannot possibly be a function of  $S$ , Eq.(1) indicated that the three-dimensional space expressed by Eq.(25) should be rewritten as the two-dimensional space, Eq.(27).

Eq. (1) does not tell us how effective mass,  $M$ , relates to charge weight,  $W$ , and depth of burial,  $d$ ; thus, it does not furnish the desired functional format for predicting impulse from a land mine explosion. Eq.(27) which is Eq.(1) expressed in a slightly different form does not provide the desired functional form either. The functional format relating scaled charge weight,  $W/d^3$ , to scaled impulse,  $(i S^2)/(d^3)$ , must be obtained from experimental test data. Experiments must be conducted so the measured scaled impulse,  $(i S^2)/(d^3)$  can be plotted as a function of scaled charge weight,  $W/d^3$ . Before making this plot, Eq.(27) will be modified by substituting Eq.(2) to form Eq.(28) which is an expression for total impulse rather than for specific impulse. Analyzing test data in terms of total impulse rather than in terms of specific impulse is more convenient.

$$\frac{i S^2}{A \cdot d^3} = f'' \left( \frac{W}{d^3} \right) \quad (28)$$

#### SCALED IMPULSE AS FUNCTION OF SCALED CHARGE WEIGHT

Reference [4] describes a limited series of tests in which 5.0 lb charges were buried at various depths and a rigid mass with an exposed surface area of 50 in.<sup>2</sup> suspended at various heights directly over these charges. The masses were not constrained or prevented from moving vertically; however, they could not rotate or translate horizontally. By measuring the displacement of the mass for different depths of burial and standoff distances,

normally reflected total impulse could be easily calculated from Eq. (29).

$$\left(\frac{I}{M}\right)^2 = V^2 = 2gh \quad (29)$$

Table C contains the test number, depth of burial, air gap between ground and bottom of the mass, and the calculated total impulse for these tests. The depth of burial was measured from the ground to the top of the charge rather than to the center of the charge. By assuming that the 5.0 lb charges were cylinders with diameters of twice their thicknesses, depths of burial and standoff distances from the center of the charge were estimated. Because the masses being loaded by the explosive charge and soil products are very small, the shape factor  $\Phi$  is essentially equal to 1.0 in these tests. The final two columns in Table C present scaled impulse and scaled charge weight. In subsequent discussion, these two quantities will be plotted to determine the functional format for Eq. (28). The quantities  $(IS^2)/(A \cdot d^3)$  and  $W/d^3$  are dimensional because the soil constants have been deleted from this analysis. Throughout the rest of this paper, the units for I will be (lb-sec), A will be ( $in^2$ ), S will be (ft), d will be (ft), and i will be (psi-sec).

The wheels were held by a yoke whose other end was attached by means of a torsion spring to a rigid wall. This test configuration is effectively a spring-loaded pendulum with a wheel as the ball of the pendulum. By measuring the maximum rotation of the yoke and wheel system as a result of the detonation of various size explosive charges, the impulse imparted to a wheel could be calculated. The explosive charges used in this test varied from 0.106 lb to 0.468 lb of pentolite. The charges were rectangular parallelepipeds with a constant surface area of 2" by 2" and a thickness that depended upon the size of the explosive charge. 1/2" of soil was placed over the charges. Steel wheels which were 7" in diameter and 1" thick were in direct contact with the ground. On a few occasions the yoke held only one wheel which was centered directly over the mine; however, most experiments were conducted on a 3-wheel array with a 1.75" center-to-center spacing between successive wheels. The middle wheel in any array was always over the center of the land mine. In a 3-wheel array, the impulse was applied to all 3 wheels. To estimate the impulse imparted to the center wheel only, the following equation was applied and solved for the impulse imparted

TABLE C

$\frac{IS^2}{A \cdot d^3}$  Versus  $\frac{W}{d^3}$  Using Rigid Mass Test Data

Test No.	Soil Cover To Top Of Charge (in)	Air Gap (in)	Total Impulse (lb-sec)	d (ft)	S (ft)	$\frac{IS^2}{A \cdot d^3}$ (psi-sec ft)	$\frac{W}{d^3}$ (lb ft <sup>3</sup> )
101	12	4	123.5	1.125	1.46	3.68	3.51
102	12	0	166.0	1.125	1.125	2.95	3.51
105	4	12	80.3	0.458	1.46	35.5	51.8
106	8	8	118.3	0.791	1.46	10.2	10.1
107	12	4	154.2	1.125	1.46	4.60	3.51
108	12	8	90.9	1.125	1.79	4.07	3.51
109	12	0	198.9	1.125	1.125	3.54	3.51
111	4	16	39.5	0.458	1.79	26.3	51.8
113	8	12	75.5	0.791	1.79	9.68	10.1
114	4	8	177.5	0.458	1.125	46.6	51.8
115	8	4	202.9	0.791	1.125	10.3	10.1
117	4	8	170.7	0.458	1.125	44.6	51.8

A second group of experiments which measured impulse imparted to targets from land mine explosions are from a series of unreported model tests conducted by Mr. Bruce Morris at MERDC, Fort Belvoir. In these experiments, wheels were placed over buried charges

$$i_c + 2i_c \sin\theta = i_3 \quad (30)$$

$$\text{where } \tan\theta = \left(\frac{12d}{1.75}\right)$$

to the center wheel,  $i_c$ . The experimental

data indicate that Eq. (30) proportions the impulse appropriately. In developing Eq. (30), we assume that the impulse imparted to the outside wheels is applied parallel to a line from the center of the charge to the bottom of the wheel, and that the upward momentum of outside wheels is caused by the vertical component of this impulse. Table D contains the total impulse measured by this test arrangement, the number of wheels in the test array, the equivalent impulse imparted to the center wheel only, the charge weight, depth of burial, and standoff distance. Before computing the total impulse imparted to a center wheel, one must look up the shape factor for the wheel in Fig. 3. Both  $\delta$  and  $\Phi$  are listed in Table D for each test configuration. The dependent quantity,  $(IS^2)/(A \cdot d^3)$ , and independent quantity,  $W/d^3$ , are computed from this information and listed in the last two columns of Table D.

A straight line fits the experimental data presented in Fig. 4 very accurately. The equation of this line as obtained by a least-squares fit to the data in Fig. 4 gives Eq. (31).

$$\frac{1}{A} = 1.725 \frac{W^{0.72} d^{0.84}}{S^2} \quad (31)$$

Eq. (31) is the explicit expression for either Eq. (27) or Eq. (1). If one substitutes  $1.4 \times 10^{16}$  W for E in Eq. (1) and equates the left hand side of Eqs. (1) and (31) after making the expressions dimensionally consistent, he obtains the effective mass term, M. M when expressed in slugs is given by Eq. (32).

$$M(\text{slugs}) = 3.49 W^{0.44} d^{1.68} \quad (32)$$

Usually the reader prefers to think of mass in units of pounds. Mass in pounds is given by Eq. (33).

TABLE D

$\frac{IS^2}{A \cdot d^3}$  Versus  $\frac{W}{d^3}$  Using Wheel Data

Test No.	Total Impulse (lb-sec)	No. Wheels	Impulse on Center Wheel	d (ft)	S (ft)	$\delta$	$\Phi$	$\frac{IS^2}{A \cdot d^3}$ (psi-sec ft)	$\frac{W}{d^3}$ ( $\frac{\text{lb}}{\text{ft}^3}$ )
2	23.5	3	12.1	.0832	.3749	1.285	4.3	98.3	400.
3	32.6	3	16.1	.0930	.3847	1.319	4.0	105.5	353.
4	18.6	3	10.7	.0607	.3524	1.208	5.45	155.	475.
5	27.7	3	14.6	.0778	.3695	1.266	4.55	131.5	425.
6	28.5	3	14.1	.0930	.3847	1.319	4.0	92.6	353.
8	53.3	3	24.2	.117	.4084	1.402	3.25	110.5	261.
9	28.1	3	13.9	.0930	.3847	1.319	4.0	91.2	353.
10	43.2	3	20.1	.110	.4017	1.378	3.4	102.	286.
11	47.1	3	21.4	.117	.4087	1.402	3.25	97.5	261.
13	71.4	3	31.7	.125	.4167	1.430	3.1	130.	240.
14	13.7	1	13.7	.0930	.3847	1.275	4.0	90.	353.
15	15.9	1	15.9	.103	.3947	1.354	3.6	90.	311.
16	23.9	1	23.9	.113	.4047	1.387	3.4	113.5	274.

Tables C and D contain all of the measurements of impulse imparted to objects from land mine explosions that are known to this writer. In spite of spending many years and dollars on explosive plate bulge tests, no one has measured the impulse imparted to the plates in such experiments. In Fig. 4, one sees a plot of scaled impulse,  $(IS^2)/(A \cdot d^3)$ , as a function of  $W/d^3$  for the data contained in Tables C and D. These experimental data appear to collapse into a unique function as predicted by Eq. (28).

$$M(\text{lbs}) = 112.5 W^{0.44} d^{1.68} \quad (33)$$

The author had substituted into Eq. (33) before making his earlier statement that the most significant mass in the explosive products from a land mine explosion was the mass of the soil products.

Fig. 4 also shows that experimental results agree well with Eq. (31). The scatter is small considering the inherent scatter in experimental test results. Although data from

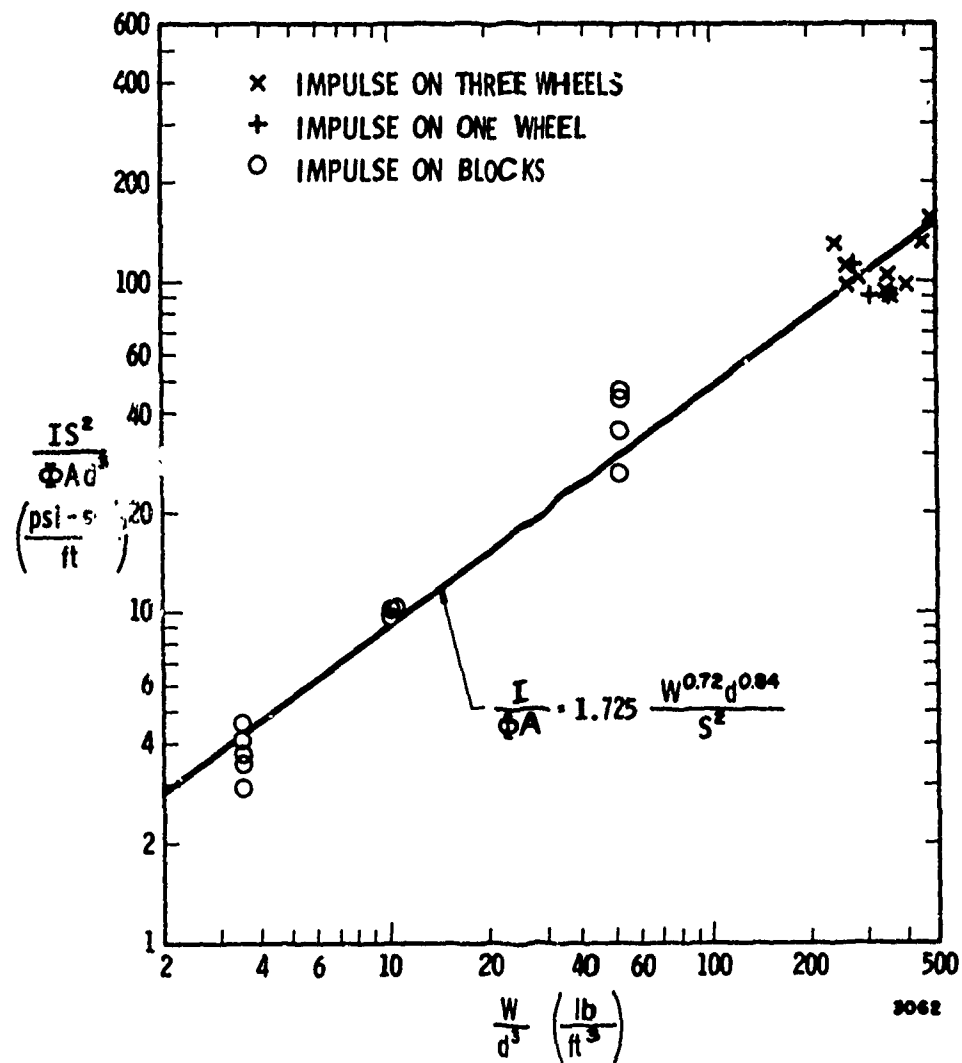


Fig. 4. Scaled Impulse Versus Scaled Charge Weight

only two types of experiments are used in developing Fig. 4, a significant number of data points (25 points) from a variety of test conditions is used to develop this curve. The charge weights in the wheel experiments were varied by a factor of 4.0. Depths of burial on the rigid mass tests ranged from 4" to 12" of soil cover, and the air gap varied from zero to 16". By combining these facts with the observation that these data involve two different types of targets, one can see that  $\frac{I}{\Phi A}$ ,  $W$ ,  $d$ , and  $S$  have all been varied in Eq. (31).

#### SUMMARY

Fig. 4 and Eq. (31) do have limits of  $W/d^3$  for which they apply. Obviously, if the depth of burial is too great, the detonation of a buried explosive will not disturb the surface of

the ground. On the other hand, if the charge is located at the surface with no cover over it, the impulse begins to be an air blast phenomenon. Three data points were not included in Table C, because in those rigid mass tests the top of the charge was flush with the surface of the ground, and no soil covered the charge. Because the center of the charge was below the surface of the ground,  $W/d^3$  equaled a finite value of 2570. Extending the least-squares fit in Fig. 4 would predict that scaled impulse,  $(IS^2)/(d^3)$ , should equal 490. Using Eq. (1) as applied to air blast with a ground reflection factor of 2.0 predicts that scaled impulse,  $(IS^2)/(d^3)$ , would equal 4745. The average of the three tests on the rigid masses was a scaled impulse,  $(IS^2)/(d^3)$ , of 3227. Obviously this test was in a transition range where the impulse was changing from being

caused by momentum in soil particles to being caused by momentum in the explosive products from the charge. Some finite soil cover is required for Eq. (31) to be valid. Provided scaled charge weight,  $W/d^3$ , falls between 1 and 1000, the analysis procedure recommended in this report should be valid.

The other major restrictions to this analysis procedure is that the standoff distance to the target must be sufficiently small so that the weight of an equivalent sphere of air must be less than 0.1 times the weight of the explosive products given by Eq. (33). For a 20 lb charge buried 3 in. deep, this observation means that the standoff distance must be less than 38 in. for this approach to be strictly valid. Probably this standoff distance can be doubled without causing serious error. Most targets are much closer to the ground than several feet. This final restriction does not appear to be very restrictive.

In this paper a procedure has been developed for predicting either the specific impulse or the total impulse imparted to any target exposed to a land mine explosion. We have seen that the impulse is not primarily an air blast phenomenon. The loading is caused by momentum in the explosive soil products. To calculate the impulse imparted to complex targets, one must determine a shape factor which is a function of the geometry associated with encounter conditions. The shape factor for a wheel may be obtained from Fig. 3 and the shape factor for rectangular objects such as plates may be calculated using Eq. (24). These shape factors are substituted into Eq. (31) to compute the total impulse imparted to any target. The specific impulse at any location on a target may be estimated by substituting Eq. (33) into Eq. (1) and taking the appropriate component of the resulting specific impulse.

#### ACKNOWLEDGMENTS

This paper is a direct outgrowth of contract DAAK 02-70-C-0579 between the U. S. Army Mobility Equipment Research and Development Center, Fort Belvoir, Virginia, and Southwest Research Institute, San Antonio, Texas. Under the terms of this contract, Southwest Research Institute is to design, develop, and test a new mine clearing roller system. A rational design of a new roller system required that we determine the nature and magnitude of the loads from a land mine explosion.

The author is indebted to Mr. Bruce Morris, the Army's technical monitor on this project and Mr. Alexander Wenzel, SwRI project leader, for being given the opportunity of probing into this problem. In addition, Dr. Wilfred E. Baker of SwRI is hereby thanked for reviewing this text and making several helpful suggestions.

#### REFERENCES

1. J. Sova, "Summary of Armor Materials and Configuration Tests at Aberdeen Proving Ground," *Combat Vehicle Mine Protection Conference (U)*, U. S. Army Weapons Command, 28 June 1967 (Confidential Report).
2. J. K. Cockrell, R. Anderson, et al., "Phase III Parametric Design/Cost Effectiveness Study for a Mechanical Infantry Combat Vehicle (MICV)," Cornell Aeronautical Labs., Report 6M-2144-H-4, 20 February 1968 (Confidential Report).
3. A. B. Wenzel, R. C. Young, and C. R. Russell, "Structural Response and Human Protection From Land Mines (U)," Allison Division of General Motors Corp., Cleveland Army Tank-Automotive Plant, TR 3481, June 1968 (Secret Report).
4. W. L. Kincheloe, "Reduction of Blast Effects," Final Quarterly Report, 0477-01 (04)FP, Contract DA-44-009-ENG-4780, May 1962.
5. W. E. Baker, "Prediction and Scaling of Reflected Impulse From Strong Blast Waves," *Int. Jour. Mech. Sci.*, 9, pp. 45-51, (1967).
6. W. H. Jack, Jr., and B. F. Armendt, Jr., "Measurements of Normally Reflected Shock Parameters From Explosive Charges Under Simulated High Altitude Conditions," BRL Report No. 1280, Aberdeen Proving Ground, Maryland, April, 1965.
7. M. Lutzky, "Explosions in Vacuum," NOLTR 62-19, White Oaks, Maryland, November 1962.
8. P. S. Westine, "Explosive Cratering," *Journal of Terramechanics*, Vol. 7, No. 2, 1970, pp. 9-19.

## CIRCULAR CANTILEVER BEAM ELASTIC RESPONSE TO AN EXPLOSION

Y.S. Kim and P.R. Ukrainetz  
Department of Mechanical Engineering  
University of Saskatchewan  
Saskatoon, Canada

The response of a circular cantilever beam subjected to a plane transverse air blast was obtained. From this response, the drag coefficients of the circular cylinder under the unsteady flow conditions of an air blast wave were determined using the domain conversion method. Using this method, a conversion of the response was made from the time domain into the frequency domain and then from the frequency domain back to the time domain.

Two circular aluminum cantilever beams of lengths 5 ft. and  $2\frac{1}{4}$  ft., and diameters 3 in. and 2 in., respectively, were tested at the 11 psi nominal overpressure location in a 500 ton TNT field explosion (Dial Pack). From the measured response, the drag force was obtained, and using the empirical equation for dynamic pressure, the drag coefficients were obtained in the region of Reynolds number  $7.81 \times 10^5$  to  $3.7 \times 10^5$  and Mach number 0.41 to 0.23.

### INTRODUCTION

Baker [1] obtained maximum responses of rectangular cantilever beams subjected to an air blast wave. The loading was separated into a diffraction phase and a drag phase, each having pressure decreasing linearly with time to zero. In considering the drag phase, a mean drag coefficient was used for its duration. This duration was determined from the linearly decaying time function which maintained the same drag impulse as that obtained from the Brode [2] empirical relation for dynamic pressure. For a stiff beam, the predicted and the experimental results showed good agreement. However, for slender beams, poor agreement was obtained.

The elastic response of a circular cantilever beam subjected to a transverse plane air blast wave was studied in this investigation. The loading was separated into two phases as was done by Baker. However, the drag phase analysis considered the actual drag loading which was expressed in polynomial form. Drag loading is drag pressure times projected area and drag pressure is drag coefficient times dynamic pressure.

The drag coefficient will be a function of time due to a continuously changing Reynolds number and Mach number during the air blast loading. The drag coefficients of a circular cylinder under steady-state conditions are already well known. However, the drag co-

efficients under unsteady-state conditions such as those from the air blast wave have only recently begun to be investigated [3][4]. Bishop [3] obtained drag coefficients of a circular cylinder and pressure coefficients around the cylinder when subjected to an air blast wave of nominal pressure 20.7 psi. The obtained drag coefficients were in the range of Reynolds number (Mach number) from  $3.75 \times 10^6$  (0.6) to  $1 \times 10^6$  (0.25). The results agreed roughly with steady state values. Meilisen [4] measured drag coefficients of circular cylinders by the free flight method at 12 psi and 8.5 psi nominal pressure locations. The blast wave source was a 500 ton TNT field explosion. The obtained drag coefficients were in the range of Reynolds number (Mach number) from  $1 \times 10^6$  (0.433) to  $0.44 \times 10^6$  (0.205). The drag coefficients oscillated about the mean values of 0.67 and 0.48 for the 12 psi and 8.5 psi locations, respectively. It was mentioned that Reynolds number and Mach number appeared to vary jointly in such a way that the drag coefficient did not change with the time varying flow of the blast wave.

In this work, the drag loading (drag coefficients) from an air blast wave was obtained using the elastic response record of a circular cantilever beam subjected to the air blast wave. To obtain the actual drag loading, the elastic response of the beam was separated into a quasi-static response and a sinusoidal response. By expressing the drag loading (forcing function)

in a polynomial form, the relation between the forcing function and the quasi-static response was obtained. Thus the forcing function was determined from the "known" quasi-static response. The quasi-static response was obtained by converting the time domain response into the frequency domain and then from the frequency domain back to the time domain.

#### BLAST LOADING

The overpressure-time record at some distance from an open air explosion source can be represented by Friedlander type decay [5] which is given by

$$p(t) = P_0 \left(1 - \frac{t}{T_+}\right) e^{-Kt/T_+} \quad (1)$$

where  $P_0$  is peak overpressure,  $T_+$  is the positive duration of the overpressure and  $K$  is a decaying constant. For low values of  $P_0$  (about 10 psi), the overpressure can be represented with reasonable accuracy by setting  $K = 1$ .

The dynamic pressure in the air blast wave is given by the empirical relation [2]

$$q(t) = q_0 \left(1 - \frac{t}{T_d}\right)^2 e^{-\beta t/T_d} \quad (2)$$

where  $q_0$  is peak dynamic pressure which can be obtained from the Rankine-Hugoniot relation

$$q_0 = P_0 \left(2.5 - \frac{17.5}{r+7}\right) \quad (3)$$

where  $r$  is the ratio of the peak overpressure to the ambient pressure. In (2),  $T_d$  is the duration of the dynamic pressure and is usually slightly larger than  $T_+$  due to the inertia of moving air. For low values of  $q_0$ , the dynamic pressure can be expressed with reasonable accuracy using  $\beta = 2$ .

When the shock front hits the leading edge (stagnation point) of a circular cylinder, the pressure rises instantaneously to the normal reflected pressure. As the shock front passes over the cylinder, regular reflections occur until the angle between the shock front and the interacting surface reaches a critical value which depends on the shock strength and the radius of curvature. At this stage, Mach stems arising from the incident and reflected waves begin to form at each side of the cylinder. These Mach stems continue to envelope the surface until they cross over at the trailing edge and start to go back around the cylinder. For small shock strengths up to about 5 psi peak overpressure, the waves continue right back to the front of the cylinder and cross over once again at the leading edge. After this, the waves become very weak and are rapidly dissipated. In the case of stronger shocks (for example about 20 psi), the waves, on passing back across the cylinder, form their own complex Mach stems. These never really reach the front of the cylinder because they break up and are dissipated

in the wake flow.

Melissen and Naylor [6] arrived at a non-dimensionalized time for double vortices to fully form and start shedding. It was photographically obtained from the interaction of the air blast waves (of peak overpressures 10 to 17 psi) with circular cylinders. This time is given by

$$\frac{UT_1}{D} \approx 2.5 \quad (4)$$

where  $U$  is shock front velocity,  $D$  is diameter of the cylinder, and  $T_1$  is the time for double vortices to fully form and start shedding. This is then the start of steadily decaying flow.

As already mentioned, the net transverse loading on a circular cylinder as a result of the air blast wave is separated into the diffraction phase and the drag phase. Fig. 1 shows this type of loading. In the approximate procedure for determining the net transverse loading during the diffraction phase, the net transverse overpressure is considered as a pressure decaying linearly from the normal reflected peak overpressure at time  $t = 0$  to the drag pressure at time  $t = T_1$ . The time  $T_1$  is obtained from (4). The drag phase then follows the diffraction phase.

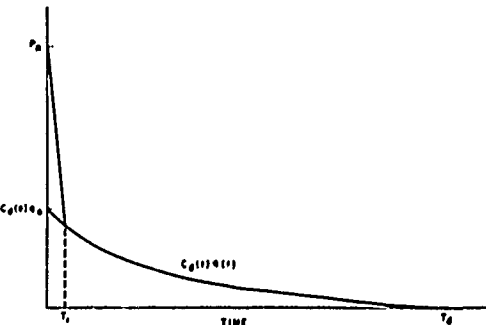


Fig. 1

#### Net Transverse Pressure on Circular Cylinder RESPONSE IN TIME DOMAIN

Small deflection, linear elastic theory (the Euler beam equation) will be used for predicting the response of a circular cantilever beam subjected to a transverse plane air blast wave.

The solution of the Euler beam equation with respect to deflection is represented by

$$y(x,t) = \sum_{n=1}^{\infty} X_n(x) g_n(t) \quad (5)$$

where  $X_n(x)$  are normal mode functions and  $g_n(t)$  are time functions which can be determined from Lagrange's equation. When the beam is subjected to a uniformly distributed forcing function

$p(t) = P \cdot f(t)$ , the time function equation becomes

$$\ddot{g}_n(t) + (\omega_n)^2 g_n(t) = \frac{P\phi_n}{M_n} f(t) \quad (6)$$

where  $\omega_n$  are natural frequencies,  $\phi_n$  are modal participation factors, and  $M_n$  are generalized masses. Dots in the expression represent time differentiation.

The solution of (6) with nonvanishing initial conditions becomes

$$g_n(t) = \frac{P\phi_n}{(\omega_n)^2 M_n} \omega_n \int_0^t f(\tau) \sin \omega_n(t-\tau) d\tau + g_n(0) \cos \omega_n t + \frac{\dot{g}_n(0)}{\omega_n} \sin \omega_n t \quad (7)$$

where  $\tau$  is a dummy variable.

The strain (for zero initial conditions) at the stagnation point at distance  $x$  from the root of the beam becomes

$$e(x,t) = P \sum_{n=1}^{\infty} E_n(x) \cdot G_n(t) \quad (8)$$

$$\text{where } E_n(x) = \frac{4D^2}{EI} \frac{\nu_n}{(K_n)^5} \frac{x^5}{X_n(L)^2} \frac{d^2 X_n}{dx^2} \quad (9)$$

In (8),  $G_n(t)$  is the nth mode response time function; in (9),  $D$  is diameter,  $E$  is modulus of elasticity,  $I$  is moment of inertia,  $L$  is length of the beam,  $\nu_n$  are constants of the normal modes  $X_n(x)$ , and  $K_n$  are related to the roots  $\lambda_n (= K_n L)$  of the frequency equation.

The normalized (in magnitude at  $t = 0$ ) forcing function  $f(t)$  is a polynomial of the  $M$ th order in time.

$$f(t) = a_0 + a_1 t + a_2 t^2 + \dots + a_M t^M$$

$$= 0 \quad \text{for } 0 \leq t \leq T$$

$$= 0 \quad \text{for } t > T \quad (10)$$

For this forcing function, the nth mode response time function  $G_n(t)$  for  $0 \leq t \leq T$  becomes

$$G_n(t) = \omega_n \int_0^t f(\tau) \sin \omega_n(t-\tau) d\tau$$

$$= C_n^0 + C_n^1 t + C_n^2 t^2 + \dots + C_n^{M-1} t^{M-1}$$

$$- C_n^0 \cos \omega_n t - \frac{C_n^1}{\omega_n} \sin \omega_n t \quad (11)$$

where the coefficients are given by

$$C_n^m = \sum_{i=0,2,4,\dots}^M (-1)^{i/2} \frac{(m+i)!}{m!} \cdot \frac{a_{m+i}}{(\omega_n)^i} \quad (12)$$

$$m = 0, 1, 2, \dots, M$$

In (12)

$$c_M = M - m \quad \text{if } (M-m) \text{ is even}$$

$$= M - m - 1 \quad \text{if } (M-m) \text{ is odd.}$$

(12) can also be expressed as

$$C_n^m = \frac{1}{m!} \sum_{i=0,2,4,\dots}^M c_M (-1)^{i/2} \frac{f^{(m+i)}(0)}{(\omega_n)^i} \quad (13)$$

$$m = 0, 1, 2, \dots, M$$

Rewriting  $G_n(t)$  of (11) gives

$$G_n(t) = g_n^*(t) - g_n^*(0) \cos \omega_n t - \frac{\dot{g}_n^*(0)}{\omega_n} \sin \omega_n t \quad (14)$$

$$= g_n^*(t) - A_n \sin(\omega_n t + \phi_n) \quad (15)$$

where

$$g_n^*(t) = C_n^0 + C_n^1 t + C_n^2 t^2 + \dots + C_n^{M-1} t^{M-1} \quad (16)$$

$$= f(t) - \frac{1}{(\omega_n)^2} f''(t) + \frac{1}{(\omega_n)^4} f''''(t) - \dots + (-1)^{M/2} \frac{f^{(M)}(t)}{(\omega_n)^M}$$

$$A_n = \left( [g_n^*(0)]^2 + \left[ \frac{\dot{g}_n^*(0)}{\omega_n} \right]^2 \right)^{1/2}$$

$$\phi_n = \tan^{-1} \frac{\omega_n g_n^*(0)}{\dot{g}_n^*(0)} \quad (17)$$

In (15),  $G_n(t)$  was separated into two parts which are  $g_n^*(t)$  and a sinusoidal response.  $g_n^*(t)$  will be called the nth mode quasi-static response time function. This quasi-static response is different from the static response which can be obtained from the Euler beam equation by setting the inertia term equal to zero.

The strain corresponding to  $g_n^*(t)$  becomes

$$e^*(x,t) = P \sum_{n=1}^{\infty} E_n(x) g_n^*(t) \quad (18)$$

$g_n^*(t)$  can be expressed in matrix form as

$$g_n^*(t) = \{t\}^T \{C_n\} \quad (19)$$

$$\text{where } \{t\}^T = [1, t, t^2, \dots, t^M]$$

$$\{C_n\} = \begin{Bmatrix} C_n^0 \\ C_n^1 \\ C_n^2 \\ \vdots \\ C_n^M \end{Bmatrix}$$

The constant column vector  $\{C_n\}$  can be expressed

by

$$\{C_n\} = [S_n] \cdot \{A\} \quad (20)$$

where  $\{A\}$  is a constant column vector of the forcing function  $f(t)$  and  $[S_n]$  is a  $M \times M$  upper triangular square matrix which can be obtained from (12). Then substituting (19) and (20) into (18) gives

$$e^*(x,t) = P(t)^T \sum_{n=1}^M E_n(x) [S_n] \cdot \{A\} \quad (21)$$

In (21),  $P(t)^T \{A\}$  is the forcing function  $P(t)$ . Thus if  $e^*(x,t)$  is known, the forcing function  $P(t)$  can be obtained from (21) by expressing  $e^*(x,t)$  in polynomial form.

So far damping has not been considered. However, in the actual case there is a slight damping in the response due mainly to internal damping and aerial damping. When damping is considered, the strain becomes

$$e_d(x,t) = P(t)^T \sum_{n=1}^M E_{nd}(t) G_{nd}(t) \quad (22)$$

where  $E_{nd}(x) = E_n(x)/[1 - (\zeta_n)^2]$

In (22),  $G_{nd}(t)$  is the damped nth mode response time function which corresponds to  $G_n(t)$  in the case of no damping.

$$G_{nd}(t) = \omega_{nd} \int_0^t f(\tau) e^{-\zeta_n \omega_n(t-\tau)} \sin \omega_{nd}(t-\tau) d\tau \quad (23)$$

$$= [g_{nd}^*(t) - g_{nd}^*(0) \cos \omega_{nd} t - \frac{\dot{g}_{nd}^*(0)}{\omega_{nd}} \cdot$$

$$\sin \omega_{nd} t] e^{-\zeta_n \omega_n t} \quad (24)$$

$$= g_{nd}^*(t) e^{-\zeta_n \omega_n t} - A_{nd} \sin(\omega_{nd} t + \phi_{nd}) \cdot$$

$$e^{-\zeta_n \omega_n t} \quad .$$

$$= g_{nd}^*(t) e^{-\zeta_n \omega_n t} - A_{nd} \cos(\omega_{nd} t + \phi_{nd}^c) \cdot$$

$$e^{-\zeta_n \omega_n t} \quad (25)$$

$$\text{where } \omega_{nd} = \omega_n [1 - (\zeta_n)^2]^{\frac{1}{2}} \quad (26)$$

$$g_{nd}^*(t) = C_{nd}^0 + C_{nd}^1 t + C_{nd}^2 t^2 + \dots \quad (27)$$

$$A_{nd} = ([g_{nd}^*(0)]^2 + [\frac{\dot{g}_{nd}^*(0)}{\omega_{nd}}]^2)^{\frac{1}{2}}$$

$$\phi_{nd} = \tan^{-1} \frac{\omega_{nd} g_{nd}^*(0)}{\dot{g}_{nd}^*(0)}, \quad \phi_{nd}^c = \tan^{-1} (1/\tan \phi_{nd}) \quad (28)$$

Coefficients  $C_{nd}^0, C_{nd}^1, C_{nd}^2, \dots$  are obtained by

substituting  $f(t)$  of (10) and the infinite series expansion of  $e^{i\omega_n t}$  into (23). The coefficients are thus

$$C_{nd}^m = \sum_{i=0,2,4,\dots} (-1)^{i/2} \frac{(m+i)!}{m!} \frac{A_{m+i}}{(\omega_{nd})^i} \quad (29)$$

In (29),  $A_{m+i}$  are the constants of  $f(t) e^{i\omega_n t}$  expanded in an infinite series. These are given by

$$A_{m+i} = \sum_{j=0}^m \frac{(-\zeta_n \omega_n)^{(m+i-j)}}{(m+i-j)!} a_j \quad (30)$$

where  $a_j = 0$  for  $j > M$ .

With the consideration of damping, the nth mode quasi-static response time function,  $g_{nd}^*(t) e^{-\zeta_n \omega_n t}$ , can be expressed in an infinite series as

$$g_{nd}^*(t) e^{-\zeta_n \omega_n t} = C_{ne}^0 + C_{ne}^1 t + C_{ne}^2 t^2 + \dots + C_{ne}^m t^m + \dots \quad (31)$$

where

$$C_{ne}^m = \sum_{j=0}^m \frac{(-\zeta_n \omega_n)^{(m-j)}}{(m-j)!} C_{nd}^j \quad (32)$$

By taking terms up to the  $M$ 'th order ( $M' \geq M$ ) in (31),  $g_{nd}^*(t) e^{-\zeta_n \omega_n t}$  can be expressed in matrix form as

$$g_{nd}^*(t) e^{-\zeta_n \omega_n t} = \{t\}^T \{C_{ne}\} \quad (33)$$

$$\text{In (33), } \{C_{ne}\} = [B_n] \{C_{nd}\} \quad (34)$$

where  $[B_n]$  is a  $M' \times M'$  lower triangular square matrix which can be obtained from (32) and  $\{C_{nd}\}$  is a constant column vector of  $C_{nd}^j$  ( $j = 0, 1, 2, \dots, M'$ ).  $\{C_{nd}\}$  can be expressed as

$$\{C_{nd}\} = [S_{nd}] \{D_n\} \{A\} \quad (35)$$

where  $[S_{nd}]$  is an upper triangular square matrix which can be obtained from (29), and  $\{D_n\}$  is a lower triangular square matrix which can be obtained from (30).

Then the strain corresponding to  $g_{nd}^*(t) e^{-\zeta_n \omega_n t}$  becomes

$$e_d^*(x,t) = P(t)^T \sum_{n=1}^M E_{nd}(x) [B_n] \{S_{nd}\} \{D_n\} \{A\} \quad (36)$$

Thus if the quasi-static response  $e_d^*(x,t)$  and the damping ratios  $\zeta_n$  are known, the forcing function  $P(t)$  can be obtained from (36) by

expressing  $e_d^*(x,t)$  in polynomial form. For this case, an error will result due to truncation of the infinite series when taking terms up to the  $M'$ th order only. However, if  $M'$  is taken sufficiently large, the error can be minimized.

#### RESPONSE IN FREQUENCY DOMAIN

Taking Fourier Transform (FT) of (7) with zero initial conditions gives

$$\tilde{G}_n(\omega) = \frac{P\phi_n}{(\omega_n)^2 M_n} \omega_n \tilde{H}_n(\omega) \cdot \tilde{F}(\omega) \quad (37)$$

Substituting (37) into FT of (5) yields

$$\tilde{Y}(x,\omega) = \sum_{n=1}^{\infty} \frac{P\phi_n}{(\omega_n)^2 M_n} \omega_n X_n(x) \tilde{H}_n(\omega) \cdot \tilde{F}(\omega) \quad (38)$$

where  $\tilde{H}_n(\omega)$  is FT of impulse response function  $\sin \omega_n t$  of the beam. This impulse response function is causal, i.e.  $\sin \omega_n t$  is zero for  $t < 0$ . Thus

$$\tilde{H}_n(\omega) = F(\sin \omega_n t u(t)) = \frac{\omega_n}{(\omega_n)^2 - \omega^2} - j \frac{\pi}{2} \cdot$$

$$[\delta(\omega + \omega_n) - \delta(\omega - \omega_n)] \quad (39)$$

where  $\delta(\omega)$  is the delta function.

Forcing function  $f(t)$  is also zero for  $t < 0$ . Let FT of  $f(t)$  be

$$\tilde{F}(\omega) = \tilde{R}_f(\omega) + j\tilde{X}_f(\omega) \quad (40)$$

Substituting (39) and (40) into (37) will give  $\tilde{G}_n(\omega)$  which has real and imaginary parts.

FT of a real causal time function  $h(t)$  [7] is

$$\tilde{h}(\omega) = \tilde{R}(\omega) + j\tilde{X}(\omega) \quad (41)$$

where

$$\tilde{R}(\omega) = \int_0^\infty h(t) \cos \omega t dt$$

$$\tilde{X}(\omega) = - \int_0^\infty h(t) \sin \omega t dt \quad (42)$$

Inverse Fourier Transform (IFT) of  $\tilde{h}(\omega)$  is

$$h(t) = \frac{2}{\pi} \int_0^\infty \tilde{R}(\omega) \cos \omega t dt$$

$$= - \frac{2}{\pi} \int_0^\infty \tilde{X}(\omega) \sin \omega t dt \quad (43)$$

As indicated by (43), the causal time function can be obtained using only the real or the imaginary part of FT.

The real part of  $\tilde{G}_n(\omega)$  is

$$R\{\tilde{G}_n(\omega)\} = \frac{P\phi_n}{(\omega_n)^2 M_n} \omega_n [\tilde{G}_n^1(\omega) + \tilde{G}_n^2(\omega)] \quad (44)$$

where

$$\tilde{G}_n^1(\omega) = \frac{\omega_n}{(\omega_n)^2 - \omega^2} \tilde{R}_f(\omega) \quad (45)$$

$$\tilde{G}_n^2(\omega) = \frac{\pi}{2} [\tilde{X}_f(\omega) \delta(\omega - \omega_n) - \tilde{X}_f(\omega) \delta(\omega + \omega_n)] \quad (46)$$

Taking IFT of  $\tilde{G}_n(\omega)$  using the real part only as given in (44) yields

$$g_n(t) = \frac{P\phi_n}{(\omega_n)^2 M_n} \omega_n [g_n^1(t) + g_n^2(t)] \quad (47)$$

$g_n^1(t)$  and  $g_n^2(t)$  are time functions obtained from  $\tilde{G}_n^1(\omega)$  and  $\tilde{G}_n^2(\omega)$ , respectively.

$$g_n^1(t) = \frac{2}{\pi} \int_0^\infty \tilde{G}_n^1(\omega) \cos \omega t d\omega \quad (48)$$

$$g_n^2(t) = \int_0^\infty [\tilde{X}_f(\omega) \delta(\omega - \omega_n) - \tilde{X}_f(\omega) \delta(\omega + \omega_n)] \cdot$$

$$\cos \omega t d\omega$$

$$= \tilde{X}_f(\omega_n) \cos \omega_n t \quad (49)$$

If the response in the frequency domain  $\tilde{G}_n(\omega)$  is known, the response in the time domain can be obtained from (48) and (49). Also, if the response in the frequency domain is known,  $\tilde{G}_n^2(\omega)$  can be readily obtained because  $\tilde{G}_n^2(\omega)$  has delta functions only. Knowing  $\tilde{G}_n^1(\omega)$ ,  $\tilde{R}_f(\omega)$  can be obtained from (45). Then by taking IFT of  $\tilde{R}_f(\omega)$ , the forcing function  $f(t)$  can be obtained. If the imaginary part of  $\tilde{G}_n(\omega)$  rather than the real part is used, a parallel analysis will give the same result.

The domain conversion is made possible using the Fast Fourier Transform (FFT). However, FFT does not have the characteristic property of FT of a causal time function. Thus the response, likewise the forcing function, in the frequency domain obtained from the above analysis and that obtained using FFT will be different. Actually, obtaining the forcing function directly from (45) is possible in theory only. In practice, the quasi-static response can be obtained using the characteristics of FFT. The forcing function can then be obtained from the derived relation between the quasi-static response and the forcing function. FFT is simply an efficient method of computing the Discrete Fourier Transform (DFT) [8].

As shown in the Appendix, a sinusoidal function (sine and/or cosine) can be represented by impulses in the frequency domain. This is accomplished by taking the sampling duration as an integer number of periods corresponding to the frequency of the function. Impulses on the imaginary axis correspond to a sine function and impulses on the real axis correspond to a cosine function.

Cutting (or smoothing) these impulses in the frequency domain corresponds to removing the sinusoidal function in the time domain. This "cutting impulse technique" can thus be used to obtain the quasi-static response of the beam. The sinusoidal response is removed by making use of this domain conversion method.

A slightly damped sine function can still be represented by impulses at the corresponding frequency on the imaginary axis, except that there will now be a small side lobe across the impulses. The sampling duration must be the same as for the case of no damping. Thus, using the imaginary part of FT only (refer to the Appendix), the cutting impulse technique can still be used to remove the damped sine function. In this case an error due to the existing small side lobe will result. However, the error is quite small as shown in the Appendix.

A slightly damped cosine function will have impulses and small side lobes on the real axis in the frequency domain. The cutting impulse technique can also be used to remove this function, this time by using the real part of FT only.

Thus, when slight damping exists in the response, the sinusoidal function must be made a sine or a cosine function only with a zero phase angle in order to use the cutting impulse technique. This is possible by starting the sampling at time

$$T_s = \frac{\phi_{nd}}{\omega_{nd}} \quad \text{or} \quad T_s = \frac{C}{\omega_{nd}} \quad \text{in (25)}$$

In Fig. 2 the response (strain) of an aluminum cantilever beam of length 5 ft. and diameter 3 in. (which was also tested in a field explosion) subjected to a uniformly distributed exponential forcing function is shown. Here modes up to the 2nd were taken into account and damping was neglected. The units of the response are psi, which is the result of dividing the strain by  $\sum_{n=1}^{\infty} E_n(x)$ .

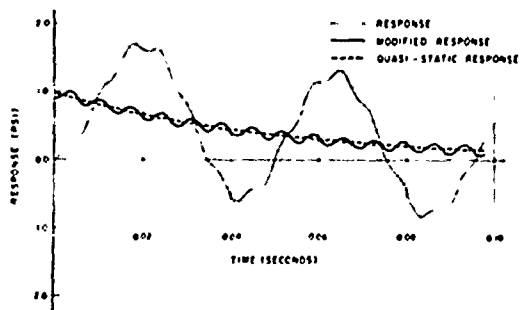


Fig. 2 Responses of Circular Aluminum Cantilever Beam Subjected to Uniformly Distributed Exponential Forcing Function  $e^{-kt}$  ( $k = 20$ ,  $L = 5$  ft.,  $D = 3$  in.)

The FT of this response was obtained using 1024 sampling points ( $N$ ) for the duration of eight times the fundamental period (the same sampling duration which was used for the compilation of experimental results for the 5 ft. - 3 in beam). Since no damping was considered, sampling was started at  $t = 0$  (with sample interval being  $\Delta t$ ). The result is shown in Fig. 3. (FT is shown for positive  $\omega$  only in all Figures). In Fig. 3, an impulse at  $\omega_1$  on the imaginary axis corresponds to the sine function and an impulse at  $\omega_1$  on the real axis corresponds to the cosine function. Since the sampling duration is not an integer multiple of the period corresponding to  $\omega_2$ , the response in the frequency domain at  $\omega_2$  is not of impulse form.

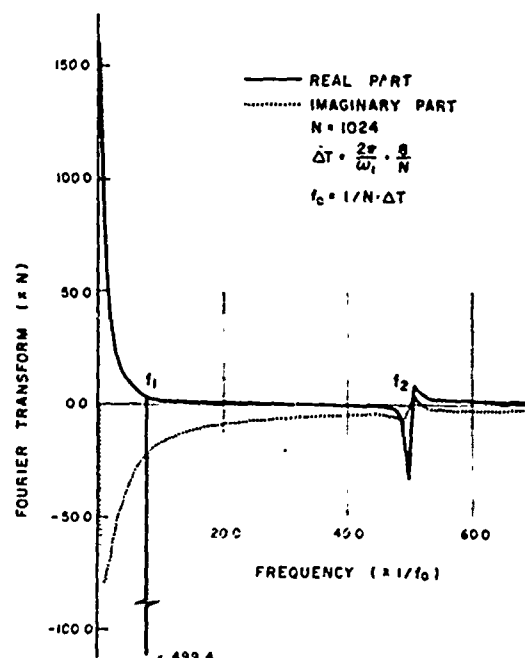


Fig. 3 Response in Frequency Domain of Circular Aluminum Cantilever Beam Subjected to Uniformly Distributed Exponential Forcing Function  $e^{-kt}$  ( $\omega_1 = 145.5$  rad/sec.,  $k = 20$ ,  $L = 5$  ft.,  $D = 3$  in.)

Cutting the impulses at  $\omega_1$  by linear interpolation using adjacent points implies removing the sinusoidal response corresponding to  $\omega_1$  in the time domain and also implies that the quasi-static response in the frequency domain has a value at  $\omega_1$  which is the average of the two adjacent point values. After cutting the impulses, IFT was taken using both real and imaginary parts. The result is shown in Fig. 2 and is called the modified response. As shown in Fig. 2, the fundamental mode is absent from this response. From this modified response the quasi-static response can be readily obtained and is also shown in Fig. 2. If the sampling is taken fine enough such that an integer number of periods corresponding to  $\omega_2$  can be obtained for another sampling duration from this IFT, the

sinusoidal response corresponding to  $\omega_2$  can also be removed if needed.

Instead of using both real and imaginary parts for the IFT, the real part or imaginary part only can be used. After cutting the impulses, IFT was taken using only the imaginary part of FT. The modified response is shown in Fig. 4. This modified response is different from the modified response shown in Fig. 2 due to the folding effect (refer to the Appendix). The forcing function  $e^{-kt}$  is around 0.001 at the end of the sampling duration. Thus at  $t = 0$ , the error in the quasi-static response due to the folding effect is around 0.1%.

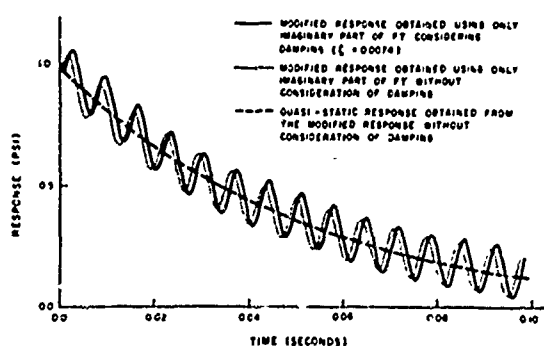


Fig. 4 Responses of Circular Aluminum Cantilever Beam Subjected to Uniformly Distributed Exponential Forcing Function  $e^{-kt}$  ( $L = 5$  ft.,  $D = 3$  in.,  $k = 20$ )

For the 5 ft.-3 in. beam, a damping ratio of 0.0074 for the fundamental mode was observed from initial laboratory tests. The beam response was obtained again, this time taking the damping into account. To make the sinusoidal function a sine function (with zero phase angle) only, sampling was started at time  $T_s = 0.96$  ms. The FT is shown in Fig. 5. After cutting the impulses at  $\omega_1$  (of the imaginary part), IFT was taken using the imaginary part only. The result is shown in Fig. 4. The differences between the two modified responses of Fig. 4 are due to:

1. Sampling starting time  $T_s$ .
2. Existing damping effect on the modified response. Damping effect on the quasi-static response is very small and the difference due to damping was estimated to be only about 0.3%.
3. The remaining sinusoidal difference corresponding to  $\omega_1$ . This is due to the existing side lobe in the frequency domain when damping is considered. The maximum difference is about 2% (refer to the Appendix).

The similarity between the exponential forcing function used and the quasi-static response was examined. The quasi-static response was smaller than the forcing function by approxi-

mately 1.5%.

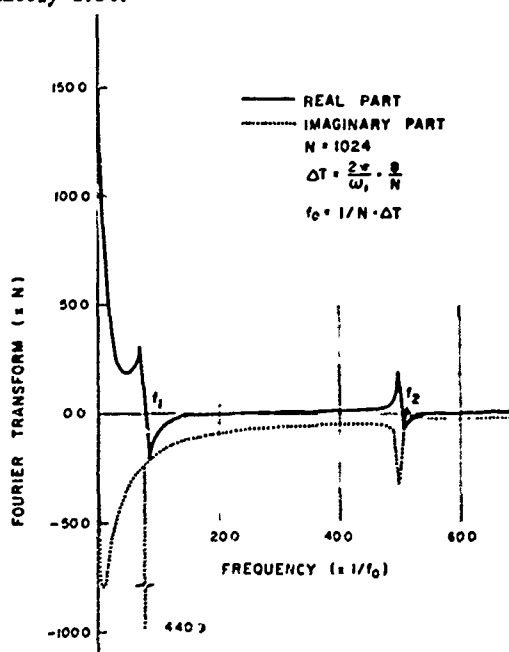


Fig. 5 Damped Response in Frequency Domain of Circular Aluminum Cantilever Beam Subjected to Uniformly Distributed Exponential Forcing Function  $e^{-kt}$  ( $\omega_1 = 145.5$  rad./sec.,  $k = 20$ ,  $\zeta_1 = 0.0074$ ,  $L = 5$  ft.,  $D = 3$  in.)

To avoid ambiguity, the exponential forcing function and the quasi-static response obtained from the modified response considering damping were not shown in Fig. 4.

#### EXPERIMENT AND EXPERIMENTAL RESULTS

Two aluminum cantilever beams, one of length 5 ft. and diameter 3 in. and the other of length 2.5 ft. and diameter 2 in., were tested at the expected 12 psi nominal overpressure location in a field explosion of 500 tons of TNT. This test was conducted on July 23, 1970 at Defence Research Establishment Suffield, Ralston Alberta. Circular aluminum rods of smooth surface were fixed to steel bases using a shrink fit method. The steel bases were then fixed in the field by bolting them to concrete bases. Four strain gauges (one facing charge one on the opposite side, and the other two similarly located, but higher on the beam) were installed on each beam. Two strain gauges were used for each strain output. The strain gauges were connected through bridges to a magnetic tape recorder which was located in a bunker.

An overpressure record obtained from a piezo-electric gauge at the expected 12 psi nominal overpressure location is shown in Fig. 6. From this record it can be seen that the actual peak overpressure is approximately 11 psi and the duration is about 0.23 sec.

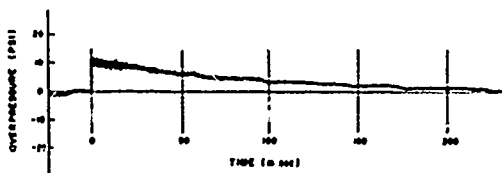


Fig. 6 Overpressure Obtained from 500 Ton TNT Field Explosion at the Location of Expected 12 psi Nominal Overpressure

Strain outputs from the 5 ft.- 3 in. beam at the location 1.0 in. from the root and from the 2.5 ft.- 2 in. beam at the location 0.75 in. from the root are shown in Fig. 7. The responses show that the ground shock arrives at the beam before the air blast wave. Due to the excitation of the beam base from the ground shock, a small free oscillation of the beam, mainly of fundamental mode type, is initiated. When the shock front of the air blast wave arrives at the beam, the initial conditions of the beam response are no longer zero because of these small free oscillations.

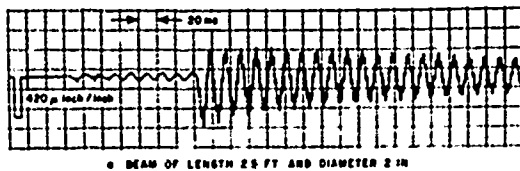


Fig. 7 Response (Strain Output) of Circular Aluminum Cantilever Beams Subjected to Air Blast Wave of Peak Overpressure 11 psi

The beam response from the air blast wave consisted of a slightly damped sinusoidal response (mainly of fundamental and 2nd mode type) superimposed on the quasi-static response. The domain conversion method and the cutting impulse technique can be used to remove the sinusoidal response and so yield the quasi-static response.

The response was sampled by digitizing using a sample interval ( $\Delta T$ ) of 0.125 ms. The time  $t = 0$  was set to be the time when the shock front arrived at the beam. Fundamental frequencies ( $\omega_1$ ) of both beams were obtained by taking FT of the responses after 0.23 sec. (slightly damped free vibrations now exist). The actual fundamental frequencies obtained, as well as predicted values, are shown in Table 1.

	Predicted(rad/sec)	Actual(rad/sec)
5 ft.- 3 in.	145.5	144.0
2.5 ft.- 2 in.	388.1	395.5

TABLE 1 Fundamental Frequencies

To make the fundamental mode of the sinusoidal response a sine function only, sampling was started for the 2.5 ft.- 2 in. beam at  $T_s = 16 \Delta T$  and was carried on for the duration of twenty-two times its actual fundamental period. For the 5 ft.- 3 in. beam, sampling was started at  $T_s = 33 \Delta T$  and continued for the duration of eight times its actual fundamental period. Then a conversion into the frequency domain was made using FFT. After cutting the impulses (on the imaginary axis) corresponding to the fundamental frequency  $\omega_1$ , IFT was taken using only the imaginary part to get the modified response. The result for the 5 ft.- 3 in. beam is shown in Fig. 8. The modified response is made up of a sinusoidal response (which has modes higher than 2nd) superimposed on the quasi-static response (dotted line). The actual quasi-static response (up to 65 ms) was obtained by eye from the quasi-static responses (which were obtained by taking two more and two less sample points at the beginning) using an "averaging" method (refer to the Appendix). This response is shown in Fig. 8 by a dashed line. The actual quasi-static response does not have any sinusoidal response remaining in it.

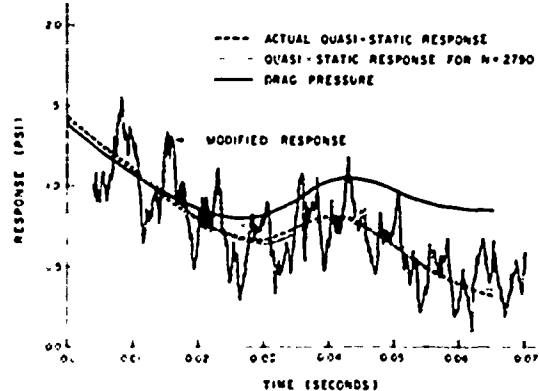


Fig. 8 Responses of Circular Aluminum Cantilever Beam of Length 5 ft. and Diameter 3 in. at 11 psi; Location ( $\Delta T = 0.125$  ms.,  $N = 2790$ )

The modified response and the actual quasi-static response for the 2.5 ft.- 2 in. beam were obtained using the same procedure and are shown in Fig. 9.

Several attempts were made to remove the sinusoidal response corresponding to the 2nd mode ( $\omega_2$ ) from the modified response using the technique described previously. However, due to the difficulty of fitting an integer number of

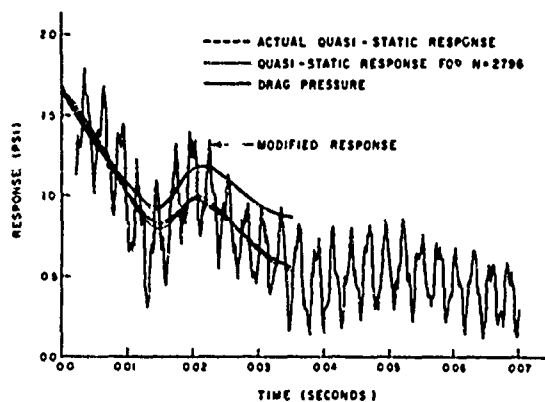


Fig. 9 Responses of Circular Aluminum Cantilever Beam of Length 2.5 ft. and Diameter 2 in. at 11 psi Location ( $\Delta t = 0.125$  ms.,  $N = 2796$ )

cycles of the 2nd mode from the modified response, it was not possible to construct an impulse at  $\omega_2$  in the frequency domain. This difficulty arose as a result of the relatively large sample interval for  $\omega_2$  and the accumulation of error in obtaining FT and IFT using FFT.

An empirical relationship was fitted to the actual quasi-static response time data (data were obtained using a time increment of 1.25 ms). The type of curve fitted was a polynomial obtained using polynomial regression. Due to the "bumps" (a fairly rapid rise followed by a gradual fall) in the responses, the relationship for each beam was obtained in parts as follows (actual quasi-static response  $P_s$  in psi and time  $t$  in sec):

5 ft.- 3 in. beam

$$0 - 35 \text{ ms: } P_s(t) = 1.446 - 31.643t - 587.10t^2 + 26127.7t^3 \quad (50)$$

$$35 - 65 \text{ ms: } P_s(t) = -5.369 + 392.87t - 7990.08t^2 + 50734.8t^3$$

2.5 ft.- 2 in. beam

$$0 - 15 \text{ ms: } P_s(t) = 1.687 - 53.006t - 4774.23t^2 + 299549.3t^3 \quad (51)$$

$$15 - 35 \text{ ms: } P_s(t) = -3.571 + 563.53t - 22080.6t^2 - 267967.9t^3$$

Expressing the actual quasi-static response in parts using polynomials gives rise to the difficulty in matching the magnitude and the slope (rate of change) of the responses at the points where two parts meet. With regard to (50) and (51), there is a slight difference in the slope at the point where the magnitude of the responses is made to coincide.

A smooth curve was drawn through the intersection point to connect the two parts for each case. The regions of inaccuracy resulting (intersection regions) are actually very short. The intersection regions cannot be expressed by

either of the two parts of (50) and (51) in each case. However, differences will be small because the slope differences at the intersection points are small.

Actual drag pressures were obtained from (50) and (51) using (21). In (21), modes up to the 6th were taken. Since slight damping exists in the actual response, (36) should have been used. However, because damping ratios of modes higher than the second were very hard to obtain and the damping effect was in fact very small, (21) was used instead of (36). The drag pressures obtained are shown in Figs. 8 and 9 and can be represented by the following:

5 ft.- 3 in. beam

$$0 - 35 \text{ ms: } P_d(t) = 1.396 - 24.986t - 587.10t^2 + 26127.7t^3 \quad (52)$$

$$35 - 65 \text{ ms: } P_d(t) = -5.625 - 404.82t - 7990.08t^2 + 50734.8t^3$$

2.5 ft.- 2 in. beam

$$0 - 15 \text{ ms: } P_d(t) = 1.630 - 42.55t - 4774.23t^2 + 299549.3t^3 \quad (53)$$

$$15 - 35 \text{ ms: } P_d(t) = -11.265 + 572.18t - 22080.6t^2 + 267967.9t^3$$

As mentioned when dealing with response, the existence of the intersection region introduces an error. The error will be small, however, because the intersection region is very short. Because this error will accumulate as more parts are taken into account, the drag pressures (and also the actual quasi-static responses) were not obtained after 65 ms for the 5 ft.- 3 in. beam nor after 35 ms for the 2.5 ft.- 2 in. beam.

Drag coefficients can then be obtained from

$$C_d(t) = \frac{P_d(t)}{q(t)}$$

For approximately the first 0.5 ms the flow is conditioned by reflection and diffraction of the incident shock and hence there is no true drag coefficient until a steadily decaying flow is established around the cylinder. However, the "equivalent" drag coefficient, as it may be termed, is useful for the purpose of constructing the loading configuration on the beam as shown in Fig. 1.

Drag coefficients obtained from the responses of the two beams as a function of Reynolds number and Mach number are shown in Figs. 10 and 11.

## DISCUSSION

### Drag Coefficients

Drag coefficients obtained from the response of the 5 ft.- 3 in. cantilever beam for the duration of the initial 65 ms are for Reynolds number  $7.81 \times 10^5$  and Mach number 0.41 (at time  $t = 0$ ) to Reynolds number  $4.1 \times 10^5$  and Mach number 0.23 (at time  $t = 65$  ms). Mach numbers

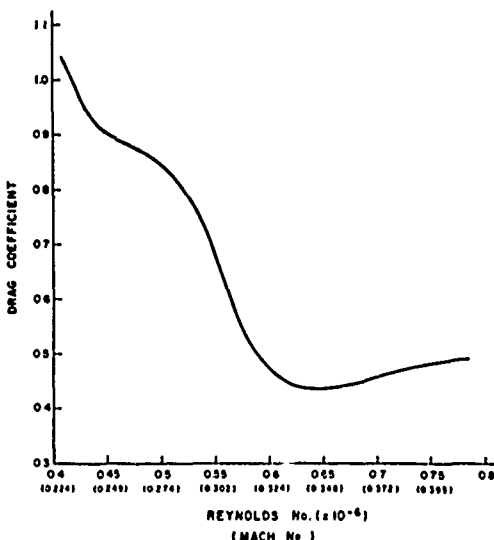


Fig. 10 Drag Coefficient vs Reynolds Number and Mach Number obtained from Elastic Response of Cantilever Beam of Length 5 ft. and Diameter 3 in. at 11 psi Location

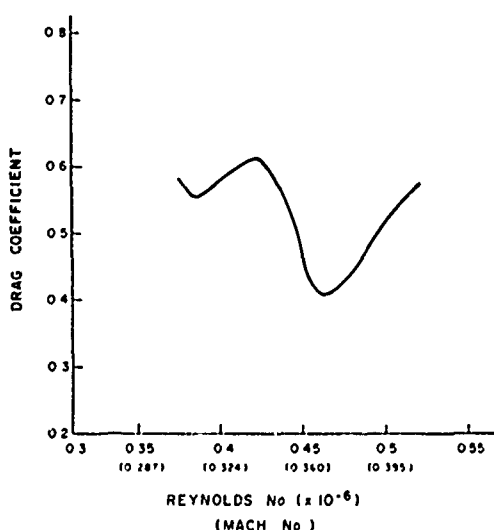


Fig. 11 Drag Coefficient vs Reynolds Number and Mach Number Obtained from the Elastic Response of Cantilever Beam of Length 2.5 ft. and Diameter 2 in. at 11 psi Location

are lower than the critical Mach number (which is approximately 0.41). Thus with regard to the steady state values of the drag coefficients, the Reynolds number effect on drag coefficients is expected to be dominant in this Mach number range.

Drag coefficients of a circular cylinder subjected to an air blast wave generally follow steady state values. However, the following

differences were observed:

1. The upper critical Reynolds number is higher in the case of air blast drag coefficient values.
2. The drag coefficients above the critical Reynolds number range are a little higher compared to the steady state values even considering the Mach number effect.
3. The levelling off of air blast drag coefficients at Reynolds number around  $5 \times 10^5$  was not expected. Of course this region is in the critical region where flow conditions vary continuously. Thus, any small shift in the flow conditions can cause considerable changes. This may be the explanation for the "levelling off" of the drag coefficient at Reynolds number around  $5 \times 10^5$ . Variations in the drag coefficient (the same kind of phenomenon as noted above) were also observed for the 2.5 ft.- 2 in. beam.

Drag coefficients obtained from the 2.5 ft.- 2 in. beam response for the duration of the initial 35 ms. are for Reynolds number  $5.2 \times 10^5$  and Mach number 0.41 (at time  $t = 0$ ) to Reynolds number  $3.7 \times 10^5$  and Mach number 0.3 (at time  $t = 35$  ms). Drag coefficients as a function of Reynolds number and Mach number varied between a maximum value of around 0.61 and a minimum value of around 0.41 for the range of Reynolds number and Mach number observed. It appears that the drag coefficient increases considerably before levelling off as Reynolds number decreases below  $3.7 \times 10^5$ .

#### Elastic Response and Maximum Strain

The response of a cantilever beam subjected to an air blast wave will exhibit a side oscillation perpendicular to the direction of blast wave travel due to vortex shedding. This side oscillation is very small compared to the response in the direction of the blast wave. Since the shear centre and centroid coincide, the bending vibrations about the two perpendicular axes are independent of each other. Thus, the obtained strain outputs from the strain gauges (placed in the direction of the blast wave) did not record any strain from the side oscillation.

The maximum displacements at the mid-sections of the two beams were:

5 ft.- 3 in. beam 0.01 ft.

2.5 ft.- 2 in. beam 0.004 ft.

As shown above, the displacements of the beams were very small and hence use of the Euler beam equation is justified.

Since the response was mainly of fundamental mode type, the maximum velocity at midsection was obtained using the maximum displacement at midsection and the fundamental frequency. Thus, the maximum velocities were:

5 ft.- 3 in. beam 1.55 ft/sec

2.5 ft.- 2 in. beam 1.45 ft/sec

The velocities of the beams are very small com-

pared to the air particle velocity during the blast loading (at  $t = 0$ , the air particle velocity was 504.5 ft/sec). Therefore, the effect of the velocity of the beams on Reynolds number of air flow around the beams can be neglected.

For both beams, maximum strains were obtained near the quarter point of the first cycle of each fundamental frequency. Analytically, maximum strains were computed using the loading configuration of Fig. 1 together with initial conditions. For the drag loading, mean drag coefficients of 0.48 and 0.562 for the 5 ft.-3 in. beam and the 2.5 ft.-2 in. beam, respectively, were used. Mean drag coefficients are the mean values of the drag coefficient for the duration of a quarter of the first fundamental period of each beam. Computed and measured maximum strains are shown in Table 2.

	Computed( $\mu\text{in/in}$ )	Measured( $\mu\text{in/in}$ )
5 ft.-3 in. beam	653	684
2.5 ft.-2 in. beam	490	510

TABLE 2

#### Experimental and Computed Maximum Strains

The computed maximum strains show close agreement with the experimental values. Instead of using mean drag coefficients with dynamic pressure of Friedlander decay type as was done above, maximum strains were also obtained using the actual drag pressures of (52) and (53). The maximum strains so found were very close to the strains determined using mean drag coefficients.

The good agreement between computed maximum strains and experimentally obtained maximum strains implies that the obtained drag coefficients up to at least  $\frac{1}{4}$  of the period of each fundamental frequency are correct. Also, the good agreement suggests that the loading configuration used is justified.

#### APPENDIX

The Fourier Transform pair for continuous signals can be written in the form

$$\begin{aligned}\bar{x}(\omega) &= \int_{-\infty}^{\infty} x(t) e^{-j\omega t} dt \\ x(t) &= \frac{1}{2\pi} \int_{-\infty}^{\infty} \bar{x}(\omega) e^{j\omega t} d\omega\end{aligned}\quad (\text{A.1})$$

The analogous Discrete Fourier Transform pair to (A.1) is

$$\begin{aligned}\bar{x}(i) &= \frac{1}{N} \sum_{k=0}^{N-1} x(k) e^{-j \frac{2\pi i}{N} k} \\ x(k) &= \sum_{i=0}^{N-1} \bar{x}(i) e^{j \frac{2\pi k}{N} i}\end{aligned}\quad (\text{A.2})$$

where  $N$  is number of sample points.

When  $\bar{x}(i)$  and  $x(k)$  of (A.2) are separated into real and imaginary parts, it can be shown that  $R(x(k))$  is composed of two parts,  $\sum_{i=0}^{N-1} R(\bar{x}(i)) \cos \frac{2\pi k}{N} i$  and  $\sum_{i=0}^{N-1} I(\bar{x}(i)) \sin \frac{2\pi k}{N} i$ .

The former is symmetric about the folding sampling duration  $t_f (k = \frac{N}{2})$  and the latter is antisymmetric about  $t_f$ .

Expanding  $R(x(k))$  for a point  $k^*$  ( $k^* \leq \frac{N}{2}$ ) gives

$$\begin{aligned}R(x(k^*)) &= \sum_{i=0}^{N-1} [R(\bar{x}(i)) \cos \frac{2\pi k^*}{N} i - I(\bar{x}(i)) \sin \frac{2\pi k^*}{N} i] \\ &= \frac{1}{N} \sum_{k=0}^{N-1} R(x(k)) \sum_{i=0}^{N-1} \cos \frac{2\pi k^*}{N} i \cdot \cos \frac{2\pi k}{N} i \\ &\quad + \frac{1}{N} \sum_{k=0}^{N-1} I(x(k)) \sum_{i=0}^{N-1} \cos \frac{2\pi k^*}{N} i \cdot \sin \frac{2\pi k}{N} i \\ &\quad + \frac{1}{N} \sum_{k=0}^{N-1} R(x(k)) \sum_{i=0}^{N-1} \sin \frac{2\pi k^*}{N} i \cdot \sin \frac{2\pi k}{N} i \\ &\quad - \frac{1}{N} \sum_{k=0}^{N-1} I(x(k)) \sum_{i=0}^{N-1} \sin \frac{2\pi k^*}{N} i \cdot \cos \frac{2\pi k}{N} i\end{aligned}\quad (\text{A.3})$$

In (A.3),  $\sum_{i=0}^{N-1} \cos \frac{2\pi k^*}{N} i \cdot \cos \frac{2\pi k}{N} i$ ,  $\sum_{i=0}^{N-1} \cos \frac{2\pi k^*}{N} i \cdot \sin \frac{2\pi k}{N} i$ ,

$\sin \frac{2\pi k}{N} i$ ,  $\sum_{i=0}^{N-1} \sin \frac{2\pi k^*}{N} i \cdot \sin \frac{2\pi k}{N} i$ , and  $\sum_{i=0}^{N-1} \sin \frac{2\pi k^*}{N} i \cdot \cos \frac{2\pi k}{N} i$  are analogous to the integral forms

$$\begin{aligned}\int_0^1 \cos 2\pi k^* y \cdot \cos 2\pi ky dy, \quad &\int_0^1 \cos 2\pi k^* y \cdot \sin 2\pi ky dy \\ \int_0^1 \sin 2\pi k^* y \cdot \sin 2\pi ky dy \quad &\text{and} \int_0^1 \sin 2\pi k^* y \cdot \cos 2\pi ky dy\end{aligned}$$

respectively. Thus  $R(x(k^*))$  becomes

$$\begin{aligned}R(x(k^*)) &= \frac{1}{2N} \sum_{k=0}^{N-1} R(x(k)) \delta_{kk^{**}} \\ &\quad + \frac{1}{2N} \sum_{k=0}^{N-1} R(x(k)) c_{k^{**}} \delta_{kk^{**}}\end{aligned}\quad (\text{A.4})$$

where  $\delta_{kk^{**}}$  is the Kronecker delta

$k^{**}$  is  $k^*$  and  $N - k^*$

$c_{k^{**}} = 1$  when  $k^{**}$  is  $k^*$

$= -1$  when  $k^{**}$  is  $N - k^*$

In (A.4), the first term resulted from

$\sum_{i=0}^{N-1} R(\bar{x}(i)) \cos \frac{2\pi k^*}{N} i$  and the second term from

$\sum_{i=0}^{N-1} I(\bar{x}(i)) \sin \frac{2\pi k^*}{N} i$ . For  $k^* > \frac{N}{2}$ , the same result will be obtained. Therefore, it can be seen that  $\sum_{i=0}^{N-1} R(\bar{x}(i)) \cos \frac{2\pi k}{N} i$  is a symmetric expression of  $\frac{1}{2}R(x(k))$  folded about the folding sample duration  $t_f$  and  $-\sum_{i=0}^{N-1} I(\bar{x}(i)) \sin \frac{2\pi k}{N} i$  is an antisymmetric expression of  $\frac{1}{2}R(x(k))$  folded

about  $t_f$ . Thus  $R\{x(k)\}$  can be obtained using only the real part or the imaginary part of  $\hat{x}(i)$  if  $R\{x(k)\}$  is finite up to  $t_f$ . The same is true for  $I\{x(k)\}$ .

Thus, when  $x(k)$  is real,  $R\{\hat{x}(i)\}$  is symmetric and  $I\{\hat{x}(i)\}$  is antisymmetric about the folding frequency  $f_f$  ( $i = \frac{N}{2}$ ).

By taking IFT using  $R\{\hat{x}(i)\}$  only (setting  $I\{\hat{x}(i)\}$  equal to zero), a modified  $\frac{1}{2}x(k)$  which is symmetrically folded about  $t_f$  in the real part will be obtained. Likewise, by taking IFT using  $I\{\hat{x}(i)\}$  only, the modified  $\frac{1}{2}x(k)$  which is antisymmetrically folded about  $t_f$  in the real part will be obtained. Since  $\hat{x}(i)$  is interpreted as being periodic from the sampling theorem, the Fourier coefficients between  $N/2$  and  $N-1$  can be viewed as the "negative frequency" harmonics between  $-N/2$  and  $-1$ . Likewise, the last half of the time function can be interpreted as negative time.

The DFT of a sinusoidal function depends upon the sampling duration taken. If the sampling duration is taken as an integer number of periods of the corresponding frequency, there will be impulses at the corresponding plus and minus frequency points in the frequency domain. Impulses will be obtained on the imaginary axis for a sine function and on the real axis for a cosine function. The magnitude of an impulse is  $\frac{1}{N}$ . If the sampling duration is not an integer number of periods, taking DFT will not produce impulses. The fact that the occurrence of impulses depends on the sampling duration of the DFT can be explained by the sampling theorem [7].

When damping exists, the sinusoidal function cannot be represented with impulses only in the frequency domain.  $\sin \omega_1 t e^{-\zeta_1 \omega_1 t}$  with  $\omega_1 = 145.5$  rad/sec and  $\zeta_1 = 0.0074$  is shown in Fig. A.1. There are impulses at  $\pm \omega_1$  and small side lobes around  $\pm \omega_1$  in the imaginary part while the real part is far different from that when there is no damping (the real part is zero when there is no damping).  $\cos \omega_1 t e^{-\zeta_1 \omega_1 t}$  will have the same FT as  $\sin \omega_1 t e^{-\zeta_1 \omega_1 t}$  except that the real part and imaginary part will be interchanged.

In Fig. A.2, the imaginary parts of  $\sin \omega_1 t e^{-\zeta_1 \omega_1 t}$  are shown for different sampling durations. The sampling duration of I is eight times the period of  $\omega_1$ , the sampling duration of II is shorter than that of I by  $\Delta T_{II}$ , and the sampling duration of III is longer than that of I by  $\Delta T_{III}$ . As shown in Fig. A.2, taking more or less sample points than the exact number makes the side lobe change sign across the corresponding frequency. After cutting the impulses, IFT was taken using only the imaginary part for each case. For I, a function very close to a slightly damped sine wave (with zero phase angle) of initial amplitude 0.02 was recovered. For II and III, functions very close to slightly damped plus and minus cosine waves (with zero phase angle) of initial amplitude 0.02 were recovered, respectively. Thus, for these cases, the error due to the existing side lobe was 2% at most. For

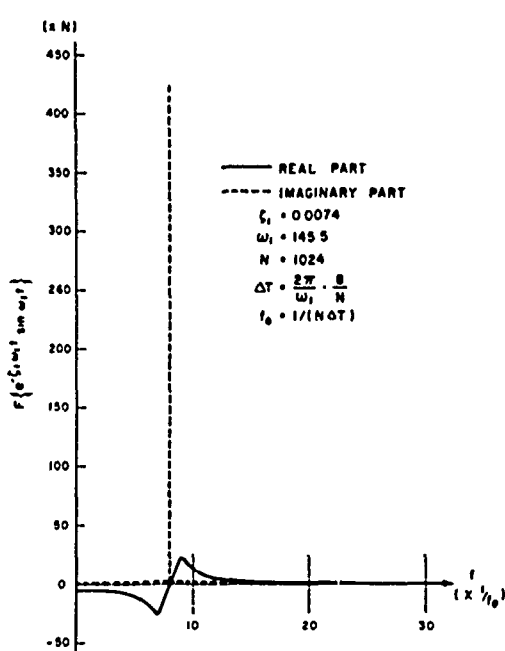


Fig. A.1 Slightly Damped Sine Function in Frequency Domain

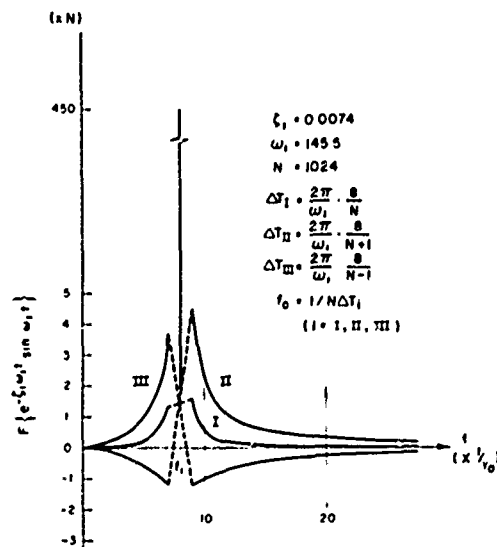


Fig. A.2 Imaginary Parts of Slightly Damped Sine Function Obtained with Different Sampling Duration

cases II and III, if the middle of the two recovered functions is taken (an "averaging" used), the error due to the existing damping can be minimized

From the above discussion, it is evident that when slight damping exists, the sinusoidal function must be a sine function only or a cosine function only to make use of the cutting impulse technique; while in the case of no damping, the sinusoidal function does not necessarily have to be a sine or a cosine function only.

#### REFERENCES

1. W.E. Baker, W.O. Ewing, Jr., J.W. Hanna, and G.W. Burnewitch, "The Elastic and Plastic Response of Cantilevers to Air Blast Loading", Proceedings of the second U.S. National Congress of Applied Mechanics, 1962, pp. 853-866.
2. N.L. Brode, "Numerical Solutions of Spherical Blast Wave", Journal of Applied Physics, June 1955.
3. V.J. Bishop and R.D. Rowe, "The Interaction of a Long Duration Friedlander Shaped Blast Wave with an Infinitely Long Right Circular Cylinder. Incident Blast Wave 20.7 psi, Positive Duration 50 ms, and a 16 cm Diameter Cylinder", AWRE Report No. O - 38/67, April, 1967.
4. S.B. Mollsen, "Drag Measurements on Cylinders by the Free Flight Method-Operation Prairie Flat", Suffield Technical Note No. 249, Jan. 1969.
5. S. Glasstone, "The Effects of Nuclear Weapons", Published by the United States Atomic Energy Commission, 1957, Revised in 1962.
6. S.B. Mollsen and R. Naylor, "Aerodynamic Drag Measurements and Flow Studies on a Circular Cylinder in a Shock Tube", Suffield Memorandum No. 7169, May 1969.
7. A. Papoulis, *The Fourier Integral and Its Application*, McGraw-Hill Book Co., Inc., New York, 1962.
8. G.D. Bergland, "A Guided Tour of the Fast Fourier Transform", IEEE Spectrum, July 1969

#### ACKNOWLEDGMENTS

The work reported herein was supported by the Defence Research Board (Grant No. 1678-09) and the National Research Council (Grant No. A-3384). The authors wish to thank Defence Research Establishment Suffield personnel for their helpful suggestions and for the opportunity to participate in event Dial Pack (500 ton TNT field explosion).

## MEASUREMENT OF IMPULSE FROM SCALED BURIED EXPLOSIVES

Bruce L. Morris  
U.S. Army Mobility Equipment Research and Development Center  
Fort Belvoir, Virginia 22060

A dimensional analysis was performed to determine the physical scaling parameters governing the response of wheels to blast loading. Hopkinson scaling was used to determine the proper charge size and location for one-quarter scale blast tests. The total energy imparted to the test wheels by the detonation was determined, and the scaled specific impulse was calculated. The test and calculation procedures are described.

### INTRODUCTION

The utilization of mine neutralization hardware require that this equipment operate under the intense pressure of near-field explosive detonations. Since accurate theoretical knowledge of this explosive-target interaction is limited, designers have had in the past to resort to full-scale explosive tests to evaluate and prove their designs. This process is expensive and time-consuming, so this Center elected to use scale models to evaluate materials and configurations for mine clearing roller wheels capable of withstanding the blast effects of 30 lbs of explosive.

### DERIVATION OF SCALING LAWS

In order to correctly interpret the experimental results, it was necessary to determine the dimensionless products, or  $\Pi$  terms, governing the interaction between explosive and target. Since the target wheels are in contact with the ground, parameters describing ambient air conditions were omitted from the analysis. It is believed that a major portion of the impulse imparted to the target is caused by the soil being thrown out of the crater and impacting on the target. Westine [1] concludes that density and seismic velocity, rather than a stress parameter, best describe the soil conditions. These parameters, along with others governing this phenomena, are listed in Table I along with their dimensions in a force-length-time (FLT) system.

Ten dimensionless products, or  $\Pi$  terms, can be formed from these 13 parameters. There are many techniques for creating this list of terms, and no matter which method is used, the analysis is not modified as only the algebra is deleted. Listed below is one set of dimensionless products or  $\Pi$  terms.

$$\begin{aligned}
 \Pi_1 &= \frac{tL^{1/2}p^{1/2}}{M^{1/2}} && \text{Time scaling} \\
 \Pi_2 &= \frac{\rho L^3}{Mp} \\
 \Pi_3 &= \frac{cm^{1/2}}{L^{3/2} p^{1/2}} && \text{Soil conditions} \\
 \Pi_4 &= r_i \\
 \Pi_5 &= \frac{aM}{L^2 p} && \text{Initial conditions and restraints} \\
 \Pi_6 &= \frac{f}{PL^2} \\
 \Pi_7 &= \frac{E}{PL^3} \\
 \Pi_8 &= \frac{aM}{L^2 p} \\
 \Pi_9 &= \frac{tL^{1/2}}{p^{1/2} M^{1/2}} && \text{Response scaling} \\
 \Pi_{10} &= \frac{\sigma}{p}
 \end{aligned}$$

For replica models,  $\frac{L_m}{L_p} = \lambda$ ,  $\lambda < 1$ , where  $m$  and  $p$  denote model and prototype respectively. If the same material is used in the model and prototype wheels,  $\frac{M_m}{M_p} = \lambda^3$ . We assume equality of blast pressure, ie,  $P_m = P_p$ . These constraints are then applied to the above  $\Pi$  terms to establish the scaling law below.

Table I. Physical Parameters Governing Explosive-Target Interaction

Symbol	Description	Units
P	Blast pressure	FL <sup>-2</sup>
t	Time	T
$\rho$	Mass density of soil	FL <sup>-4T<sup>-2</sup></sup>
c	Seismic velocity of soil	LT <sup>-1</sup>
L	Characteristic length	L
$r_i$	Shape of System	-----
M	Mass of target	FL <sup>-1T<sup>-2</sup></sup>
g	Acceleration of gravity	LT <sup>-2</sup>
f	Total load on wheel	F
E	Energy absorbed in wheel system	FL
a	Acceleration of wheel under blast load	LT <sup>-2</sup>
i	Impulse applied to wheel	FT
$\sigma$	Stress in target	FL <sup>-2</sup>

$\pi_1 \quad t_m = 2t_p$  Time scales as length ratio

#### TEST EQUIPMENT AND PROCEDURES

The test wheels were placed in a 3.5 by 2.5 by 2.5 foot dirt-filled test rig as seen in Figure 1. The wheels were connected with a common axle and secured to the test box by rubber torsion spring with a total calibrated rotational stiffness of 1180 inch-pounds per degree of rotation.

The explosive charges (2 inch square blocks of C-4 explosive cut to provide desired weight) were placed under the center wheel with one-half inch of soil cover over the charge. The charges were detonated by M-6 blasting caps, and the spring rotation was measured by the scribes in Figure 1.

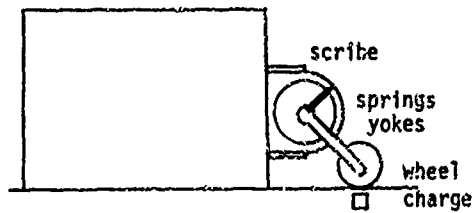
$\pi_2 \quad \rho_m = \rho_p$  Same soil for model and prototype

$\pi_3 \quad c_m = c_p$

$\pi_4 \quad (r_i)_m = (r_i)_p$  Geometric similarity

$\pi_5 \quad g_m = \frac{1}{\lambda} g_p$  Since model and prototype tests are conducted in same gravitational field, this term is distorted as an engineering judgement.

$\pi_6 \quad f_m = \lambda^2 f_p$  Loads scale as square of length ratio to provide equal stresses.



Hopkinson has shown that blast pressure is a function of stand-off distance R and charge weight W as  $P=f(R/W^{1/3})$ . Thus, if  $R_m = \lambda R_p$ ,  $W_m = \lambda^3 W_p$  to produce equalblast pressures.

Figure 1. Test box showing rubber torsion springs, scribes, and test yokes.

## IMPULSE CALCULATIONS

For computational purposes, the wheel torsion-spring system is as shown in Figure 2.

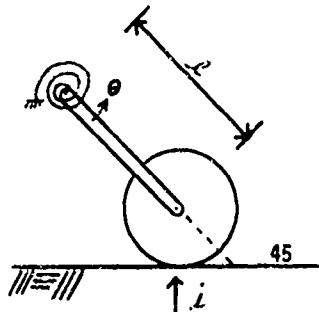


Figure 2.

Symbol	Description
$\theta_p$	precad angle
$\theta_{\max}$	maximum rotation
K	spring constant
i	total impulse
E	total energy
$M_0$	initial spring moment
$\ell$	length of yoke
I	mass moment of inertia
T	torque

Ignoring gravitational effects, the total energy absorbed in the test system is given by

$$E = \text{Force} \times \text{Distance} = \frac{k(\theta_p + \theta_{\max})}{2} \times [\theta_{\max} \ell] \\ E = K(\theta_p + \frac{\theta_{\max}}{2}). \quad (1)$$

From conservation of energy, K.E. = P.E. and  
 $V = 2E/M$  (2)

From the impulse-momentum relationship,

$$\frac{i}{\sqrt{2}} = mv = \sqrt{2Em}. \quad (3)$$

Substituting eq. (1) into eq. (3) and realizing that  $I=m\ell^2$  yields

$$i = \frac{\sqrt{2KI}}{\ell} \theta_{\max} \sqrt{1 + \frac{2\theta_p}{\theta_{\max}}} \quad (4)$$

Equation (4) can also be derived using a conservation of momentum approach. Here,

$T = I \ddot{\theta}$  where  $\dot{\theta}$  and  $\ddot{\theta}$  denote derivatives with respect to time.

$$-(M_0 + K\theta) = i\ddot{\theta}$$

$$\ddot{\theta} + (\frac{K}{I})\theta = -(\frac{M_0}{I}) \quad (5)$$

Boundary conditions on eq. (5) at  $t=0$  are  $\theta=0$  and  $\dot{\theta}=\dot{\theta}_{\text{orig}}$ . Thus,

$$I \dot{\theta}_{\text{orig}} = \frac{\theta_i}{\sqrt{2}}$$

$$\dot{\theta}_{\text{orig}} = \frac{\ell i}{\sqrt{2} I}$$

For small angles ( $\sin \theta = \theta$ ), the solution of eq. (5) is given by

$$\theta = A \cos \omega t + B \sin \omega t - \frac{M_0}{K} \quad (6)$$

$$\dot{\theta} = -A \omega \sin \omega t + B \omega \cos \omega t$$

$$\omega = \sqrt{\frac{K}{I}} \quad (7)$$

Substituting the boundary conditions into eqs. (6) and (7) yields

$$A = \frac{M_0}{K} \text{ and } B = \frac{\ell i}{\sqrt{2KI}}$$

$\theta_{\max}$  occurs at a time  $t_{\max}$  when  $\dot{\theta} = 0$ , or when  
 $\tan \omega t_{\max} = B/A$

$\sin \omega t_{\max}$  and  $\cos \omega t_{\max}$  are calculated from  
 $\tan \omega t_{\max}$ , and the results are substituted into  
eq. (6) to determine  $\theta_{\max}$ ,

$$\theta_{\max} = A \sqrt{\frac{I}{1+(B/A)^2}} + B \sqrt{\frac{(B/A)^2}{1+(B/A)^2}} - \frac{M_0}{K}$$

Substituting for A and B and solving for i yields

$$i = \frac{\sqrt{2KI}}{\ell} \theta_{\max} \sqrt{1 + \frac{2 M_0}{K \theta_{\max}}}$$

But  $M_0 = K \theta_p$  and the above equation reduces to eq. (4).

Equation (4) gives the impulse imparted to the three-wheel test rig, but the impulse on the center wheel alone is desired. This is approximated by

$$i_C + 2 i_C \sin \delta = i_{\text{wheel}}$$

where  $i_C$  = impulse on center wheel

$$\tan \delta = 12d/1.75$$

d = depth to center of charge in feet

Westine [2] has developed a method of calculating the impulse imparted to a target from a land mine detonation given by

$$I = i A \theta$$

where  $I$  = total impulse  
 $i$  = specific impulse  
 $A$  = projected area of target = 7 in<sup>2</sup> for these tests  
 $\theta$  = shape factor which is a function of target shape and standoff conditions

Shape factors are determined for the various configurations tested under this program. These shape factors, together with the total impulse as calculated from eq. (4), are used to calculate the specific impulse generated by the detonations. This impulse is transformed into scaled specific impulse by dividing by the cube root of the charge weight. These scaled specific impulses are presented in Table II along with the scaled distances and other data items and are compared to previous extrapolated data [3] for TNT in Figure 3. The TNT data has been adjusted to C-4 explosive. Data generated from these small charges is thus seen to fall within the limits of data generated using explosive charges of up to 550 lbs.

#### REFERENCES

- [1]. P.S. Westine, "Explosive Cratering," J. Terramechanics, Vol. 7, No. 2, pp. 9 to 19, 1970.
- [2]. P.S. Westine, "Impulse Imparted to Targets by Detonation of Land Mines," in Symposium on Mine Detection and Neutralization, March 24-25, 1971, Vol 1 of 2, Fort Mc Nair, Washington, D.C.
- [3]. W. D. Kennedy, "Explosions and Explosives in Air," in Effects of Impact and Explosions Volume I, Summary Technical Report, NDRC, Washington, 1946.

Table II. Scaled Specific Impulse

Shot Number	Charge wt. (lbs)	Scaled Dist. (ft/lb <sup>-3</sup> )	Impulse on 1 Wheel (lb-sec)	$\theta$	Specific Imp (psi-sec)	Scaled Specific Impulse psi-msec lb <sup>1/3</sup>
2	.229	.068	12.1	4.30	.402	656
3	.285	.062	16.1	4.00	.575	875
4	.106	.088	10.7	5.45	.281	594
5	.200	.072	14.6	4.55	.457	782
6	.285	.062	14.1	4.00	.504	766
8	.420	.056	24.2	3.25	1.063	1420
9	.285	.062	13.9	4.00	.496	755
10	.381	.058	20.1	3.40	.845	1165
11	.420	.056	21.4	3.25	.942	1260
13	.470	.054	31.7	3.10	1.460	1880
14	.285	.062	13.7	4.00	.489	744
15	.342	.060	15.9	3.60	.631	900
16	.395	.057	23.9	3.40	1.005	1370

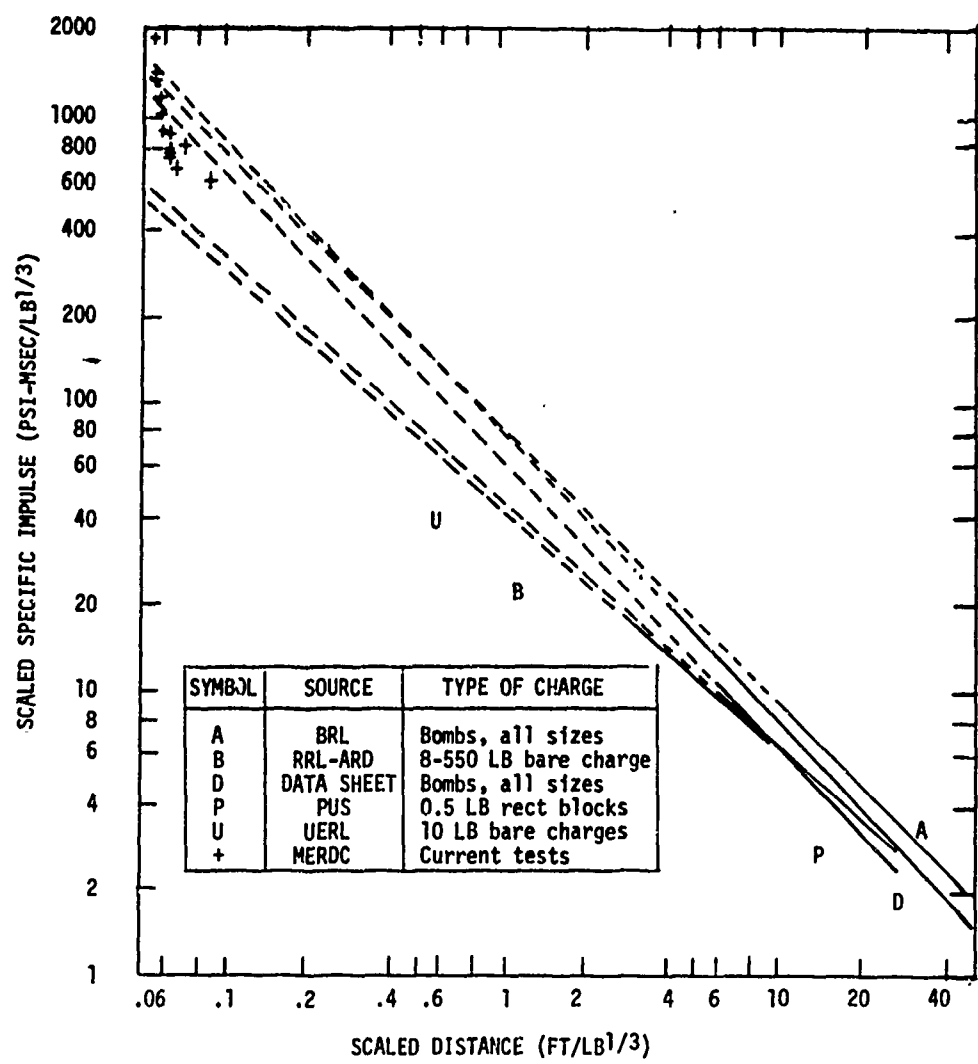


Figure 3. Scaled Specific Impulse vs Scaled Distance.

## DYNAMIC ANALYSIS

### THE EFFECTS OF MOMENTUM WHEELS ON THE FREQUENCY RESPONSE CHARACTERISTICS OF LARGE FLEXIBLE STRUCTURES

F. D. Day III and S. R. Tomer  
Martin Marietta Corporation  
Denver, Colorado

A computer program using existing mathematical techniques has been developed for use in performing linear frequency response analyses of large elastic systems that contain axisymmetric momentum wheels (gyros). The program incorporates the state vector form of the dynamic equations of motion, and uses complex eigenvalue/eigenvector transformations to yield a set of uncoupled equations that are easily solved for the steady-state responses of the system. The structural characteristics are input in the form of normal modes of the system with nonrotating momentum wheels (i.e., all translational inertias and the rotational inertias about the axes normal to the spin axis are included). These system modes may be derived directly from a finite-element model or through the modal coupling of a number of subsystems. The program was used to calculate transfer functions on the Skylab Apollo telescope mount both with and without the control moment gyros. A comparison of these transfer functions is presented.

#### INTRODUCTION

The generally accepted method for determining transfer functions on large systems is based on calculating the normal modes of the system and using them to uncouple the equations of motion. This method is based on the assumption that the modal damping matrix is diagonal. There are times, however, when the assumption of a diagonal damping matrix is not valid; for example, when a structure has gyros or momentum wheels. The introduction of the momentum term produces a skew-symmetric, rather than a diagonal, damping matrix. In the past, analyses of this type have neglected the effects of the momentum wheels. The purpose of this study is to include the momentum term and develop a method to facilitate the calculation of the transfer functions so that their effects on the structure can be evaluated.

The method makes use of existing mathematical techniques to develop the state vector form of the dynamic equations of motion. From these equations, complex eigenvalue/eigenvector transformations are then generated and used to uncouple the equations of motion. Once the equations are uncoupled, they are easily solved for the harmonic steady-state response.

Undamped normal modes are used to describe the characteristics of the flexible structure. These modes are sufficient to uncouple the

equations of motion only when modal damping or damping proportional to either the mass or stiffness matrix is assumed. The introduction of the momentum wheel terms, however, recouples the modal damping matrix, and a second eigenvalue solution must be determined. This is done using the state vector form of the equations of motion.

This method was used to calculate transfer functions for the Skylab Apollo telescope mount (ATM) in order to determine the effects of the control moment gyros (CMGs) on the structure's behavior. The importance of this example and the reason for choosing it lie in the fact that these same transfer functions are used in designing the experiment pointing control system (EPCS) for the ATM. Because of the proximity of the CMGs (which are used for overall cluster control) to the ATM, their effect on the EPCS sensors could be significant. Transfer functions with and without the CMGs were computed. The results are compared in this paper.

#### THEORETICAL DEVELOPMENT

The derivation of techniques used to generate acceleration responses or transfer functions for large flexible structures with momentum wheels will be developed in four parts:

Preceding page blank

1. A brief review of the equations of motion for the elastic structure without momentum wheels;
2. Equations of motion for a spinning rotor as a free body;
3. Equations of motion for a flexible structure with spinning momentum wheels or gyros;
4. Procedure used in the digital computer program for uncoupling and solving the response equations.

### 1. Equations of Motion for Large Flexible Structures

Response analyses of large flexible structures generally employ component modal substitution or modal coupling [Ref 1] techniques to reduce the number of equations required for the solution. These techniques rely on the orthogonality of the undamped normal modes of the structure or substructure to produce diagonal equivalent mass and stiffness matrices. In addition, modal damping is usually assumed so that the final equations are uncoupled and readily solved.

In terms of the generalized or modal coordinates, the uncoupled equations are of the form

$$\begin{bmatrix} m_{eq} \\ \ddot{q} \end{bmatrix} + \begin{bmatrix} 2\zeta\omega_0 m_{eq} \\ q \end{bmatrix} + \begin{bmatrix} \omega_0^2 m_{eq} \\ 0 \end{bmatrix} = \{F(t)\} \quad (1)$$

where

$$\begin{aligned} \{q\} &= \text{vector of modal coordinates;} \\ \begin{bmatrix} m_{eq} \end{bmatrix} &= [\phi]^T \{m\} [\phi] \\ &= \text{generalized mass matrix;} \\ \begin{bmatrix} \omega_0^2 m_{eq} \end{bmatrix} &= [\phi]^T \{k\} [\phi] \\ &= \text{generalized stiffness matrix;} \\ \begin{bmatrix} 2\zeta\omega_0 m_{eq} \end{bmatrix} &= [\phi]^T \{c\} [\phi] \\ &= \text{generalized damping matrix;} \\ \{F(t)\} &= [\phi]^T \{f(t)\} \\ &= \text{generalized force,} \end{aligned}$$

and the discrete coordinates,  $\{x\}$ , are related to  $\{q\}$  by the modal coordinate substitution

$$\{x\} = [\phi] \{q\}. \quad (2)$$

Now, for a harmonic forcing function,

$$\{f(t)\} = \{f_o\} e^{i\Omega t}; \quad (3)$$

and for steady-state responses,

$$\{q(t)\} = \{q_o\} e^{i\Omega t}, \quad (4)$$

where the modal coordinate vector  $\{q_o\}$  consists of complex numbers yielding magnitude and phase information.

Substituting Eq. 3 and 4 into Eq. 1 yields, when the normal modes are orthonormalized on the mass matrix,

$$\left( \begin{bmatrix} \omega_0^2 - \Omega^2 \\ 0 \end{bmatrix} + i \begin{bmatrix} 2\zeta\omega_0 \Omega \\ 0 \end{bmatrix} \right) \{q_o\} = [\phi]^T \{f_o\} \quad (5)$$

since

$$\begin{bmatrix} m_{eq} \end{bmatrix} = \begin{bmatrix} 1.0 \end{bmatrix}$$

when the modes are orthonormalized on the mass matrix. Solving for  $\{q_o\}$ ,

$$\{q_o\} = \left( \begin{bmatrix} \omega_0^2 - \Omega^2 \\ 0 \end{bmatrix} + i \begin{bmatrix} 2\zeta\omega_0 \Omega \\ 0 \end{bmatrix} \right)^{-1} [\phi]^T \{f_o\}. \quad (6)$$

Substituting Eq. 6 into Eq. 2 yields a matrix equation relating responses to forcing functions in discrete coordinates:

$$\{x_o\} = [\phi] \left( \begin{bmatrix} \omega_0^2 - \Omega^2 \\ 0 \end{bmatrix} + i \begin{bmatrix} 2\zeta\omega_0 \Omega \\ 0 \end{bmatrix} \right)^{-1} [\phi]^T \{f_o\}. \quad (7)$$

For single-unit input forces, Eq. 7 describes the steady-state transfer function.

The uncoupled set of equations formed by Eq. 6 and 7 can be solved quite efficiently by digital computers. The solution involves only matrix multiplication and the inversion of a diagonal complex matrix. As will be shown in the following sections, including rotating momentum wheels fully couples the modal equations of motion, greatly increasing the computer cost involved in determining responses from this formulation of the problem.

### 2. Equations of Motion for a Spinning Rotor as a Free Body

Consider a rigid body spinning about one of its principal axes of inertia. If the coordinate system is fixed in the body at the center of mass and aligned with the principal axes of inertia, Euler's moment equations can be expressed as follows:

$$M_x = I_x \ddot{\theta}_x + \dot{\theta}_y I_z \dot{\theta}_z - \dot{\theta}_z I_y \dot{\theta}_y;$$

$$\begin{aligned} M_y &= I_y \ddot{\theta}_y + \dot{\theta}_z I_x \dot{\theta}_x - \dot{\theta}_x I_z \dot{\theta}_z; \\ M_z &= I_z \ddot{\theta}_z + \dot{\theta}_x I_y \dot{\theta}_y - \dot{\theta}_y I_x \dot{\theta}_x. \end{aligned} \quad (8)$$

For an axisymmetric rotor ( $I_x = I_y = I_o$ ) with constant angular velocity  $\lambda$  about the  $z$  axis, Eq. 8 becomes

$$\begin{aligned} M_x &= I_x \ddot{\theta}_x + \dot{\theta}_y (I_z - I_o) \lambda; \\ M_y &= I_y \ddot{\theta}_y - \dot{\theta}_x (I_z - I_o) \lambda; \\ M_z &= 0. \end{aligned} \quad (9)$$

Since the inertias about any axes in the  $x$ - $y$  plane are the same, the coordinates can be fixed at the center of mass with the  $z$  axis coincident with the spin axis and the  $x$  and  $y$  axes nonrotating. The angular velocities and accelerations,  $\dot{\theta}_1$  and  $\ddot{\theta}_1$ , respectively, are then descriptive of the coordinate system's motion, while the spin rate,  $\lambda$ , relates the body motion to the coordinate system.

In matrix form, letting  $\gamma = (I_z - I_o) \lambda$ , Eq. 9 becomes

$$[M] = \begin{bmatrix} I_o & 0 & 0 \\ 0 & I_o & 0 \\ 0 & 0 & 0 \end{bmatrix} (\ddot{\theta}) + \begin{bmatrix} 0 & \gamma & 0 \\ -\gamma & 0 & 0 \\ 0 & 0 & 0 \end{bmatrix} (\dot{\theta}). \quad (10)$$

The acceleration coefficient matrix is independent of the spin rate and can be included in the system inertia matrix when the momentum wheels are coupled with the elastic structure. The velocity coefficient matrix, however, is dependent on the spin rate and will couple the system modal equations.

### 3. Equations of Motion for a Flexible Structure with Spinning Momentum Wheels

Writing the equations of motion for the combined system in discrete coordinates,

$$[m] \ddot{\{x\}} + (\{c\} + [\Gamma]) \dot{\{x\}} + [k] \{x\} = \{f(t)\} \quad (11)$$

where  $[m]$  now contains the rotor inertias about axes normal to the spin axis, and  $[\Gamma]$  contains the skew-symmetric rotational-dependent terms,  $\gamma$ , transformed to the system coordinates.

A coordinate transformation,  $\{x\} = [\phi] \{q\}$ , using the undamped normal modes yields

$$\begin{aligned} \ddot{\{q\}} + \left( \begin{bmatrix} 2\zeta\omega_o \\ \omega_o^2 \end{bmatrix} + [\phi]^T [\Gamma] [\phi] \right) \dot{\{q\}} + \\ \begin{bmatrix} 0 \\ \omega_o^2 \end{bmatrix} \{q\} = [\phi]^T \{f(t)\} = \{F(t)\}. \end{aligned} \quad (12)$$

In the previous section, the equations of motion in modal coordinates, Eq. 6, were uncoupled and could be readily solved for responses. Equation 12, however, is fully coupled in the velocity coefficients. If one proceeds as in section 1 and lets

$$\begin{aligned} \{f(t)\} &= \{f\} e^{i\Omega t}; \\ \{F(t)\} &= \{F_o\} e^{i\Omega t}; \\ \{q(t)\} &= \{q_o\} e^{i\Omega t} \end{aligned}$$

for steady-state response to a harmonic input, the solution to Eq. 12 would be in the form

$$\begin{aligned} \{q_o\} &= \left[ \begin{bmatrix} \omega_o^2 - \Omega^2 \\ 2\zeta\omega_o \Omega \end{bmatrix} + [\phi]^T \right. \\ &\quad \left. [\Gamma] [\phi] \Omega \right]^{-1} \{F_o\}. \end{aligned} \quad (13)$$

The solution then involves inverting a fully coupled matrix that is also dependent on the frequency of the forcing function. Since the inversion must be performed for each forcing frequency, the determination of responses from Eq. 13 is very time-consuming and costly. However, these equations can be uncoupled by rewriting them in state vector form and generating complex eigenvalues and eigenvectors. The procedure to be followed is outlined below.

### 4. Procedure Used to Uncouple the Combined System Equations of Motion

Rewriting Eq. 12 as

$$\ddot{\{q\}} + [B] \dot{\{q\}} + [E] \{q\} = \{F\} \quad (14)$$

where

$$\begin{aligned} [B] &= \begin{bmatrix} 2\zeta\omega_o \\ \omega_o^2 \end{bmatrix} + [\phi]^T [\Gamma] [\phi]; \\ [E] &= \begin{bmatrix} 0 \\ 1.0 \end{bmatrix}, \end{aligned}$$

the equations of motion can be expressed in terms of a state vector by making the following substitutions [Ref. 2]:

$$\begin{aligned} \{Z\} &= \begin{Bmatrix} q \\ \dot{q} \end{Bmatrix}; \\ [R] &= \begin{bmatrix} 0 & 1.0 \\ 1.0 & 0 \end{bmatrix}; \\ [H] &= \begin{bmatrix} 0 & 0 \\ 0 & -1.0 \end{bmatrix}; \\ [D] &= \begin{Bmatrix} F \\ 0 \end{Bmatrix}. \end{aligned} \quad (15)$$

The modal equations of motion can then be expressed as

$$[R] \{Z\} + [H] \{Z\} = \{D\}. \quad (16)$$

Premultiplying by  $-[R]^{-1}$  yields

$$-\{\dot{Z}\} - [R]^{-1} [H] \{Z\} = -[R]^{-1} \{D\}$$

or

$$[U] \{Z\} - \{\dot{Z}\} = \{J\}, \quad (17)$$

where

$$[R]^{-1} = \begin{bmatrix} 0 & 1.0 \\ -E & -B \end{bmatrix},$$

which must exist, and

$$\begin{aligned} [U] &= -[R]^{-1} [H] = \begin{bmatrix} 0 & 1.0 \\ -E & -B \end{bmatrix}; \\ \{J\} &= -[R]^{-1} \{D\} = \begin{bmatrix} 0 \\ -F \end{bmatrix}. \end{aligned}$$

The homogeneous form of Eq. 17 is the standard formulation for an eigenvalue problem. Now, letting

$$\{Z\} = \{\psi\} e^{at}, \quad (18)$$

the homogeneous form of Eq. 17 then becomes

$$([U] - a[-1.0]) \{\psi\} = \{0\}, \quad (19)$$

where the set of values  $a_j$  are complex eigenvalues with corresponding eigenvectors  $\{\psi_j\}$ .

Assembling the eigenvectors into a matrix  $[Y]$ , the coordinate substitution

$$\{Z\} = [Y] \{\xi\} \quad (20)$$

into Eq. 17 produces

$$[U] [Y] \{\xi\} - [Y] \{\dot{\xi}\} = \{J\}. \quad (21)$$

Since, for the eigenvector matrix  $[Y]$ ,

$$[U] [Y] = [Y] [-a],$$

premultiplying Eq. 21 by  $[Y]^{-1}$  uncouples the system of equations in the form

$$[-a] \{\xi\} - \{\dot{\xi}\} = [Y]^{-1} \{J\}. \quad (22)$$

For a harmonic input and steady-state responses

$$\begin{aligned} \{J\} &= \{J_0\} e^{iat}; \\ \{\xi\} &= \{\xi_0\} e^{iat}, \end{aligned} \quad (23)$$

so that Eq. 22 becomes

$$[-a - i\Omega] \{\xi_0\} = [Y]^{-1} \{J_0\}$$

or

$$\{\xi_0\} = [-a - i\Omega]^{-1} [Y]^{-1} \{J_0\}. \quad (24)$$

This formulation of the equations of motion involves the inversion of a forcing frequency-dependent matrix that is diagonal. If responses or transfer functions are to be generated for more than just a few forcing frequencies, it becomes much more efficient to generate the complex eigenvalues and eigenvectors once and to invert the diagonal matrix  $[-a - i\Omega]$  each time than to invert the coupled matrix in Eq. 13 for each forcing frequency.

Substituting back to discrete degrees of freedom from Eq. 12 and 17 into Eq. 24 yields

$$\{\xi_0\} = [-a - i\Omega]^{-1} [Y]^{-1} \begin{cases} 0 \\ -[\phi]^T \{f(t)\} \end{cases}$$

and, since

$$\{Z\} = \begin{bmatrix} q \\ \dot{q} \end{bmatrix} = [Y] \{\xi\}$$

and

$$\{\ddot{x}\} = [\phi] \{\ddot{q}\} = i\Omega [\phi] \{\dot{q}\},$$

the discrete coordinate accelerations can be expressed as functions of the discrete forces by

$$\begin{aligned} \{\ddot{x}\} &= i\Omega [\phi] \{f_2\} [-a - i\Omega]^{-1} \\ &= [Y]^{-1} \begin{cases} 0 \\ -[\phi]^T \{f(t)\} \end{cases}, \end{aligned} \quad (25)$$

where  $[Y_2]$  is the lower half of the matrix

$$[Y] = \begin{bmatrix} \gamma_1 \\ \gamma_2 \end{bmatrix}.$$

#### SAMPLE PROBLEM

The following example shows how the method was applied to include momentum wheels when determining the frequency response of the Skylab ATM and associated substructures pictured in Fig. 1. The ATM is the experiment portion of Skylab that houses the photographic and telescopic equipment.

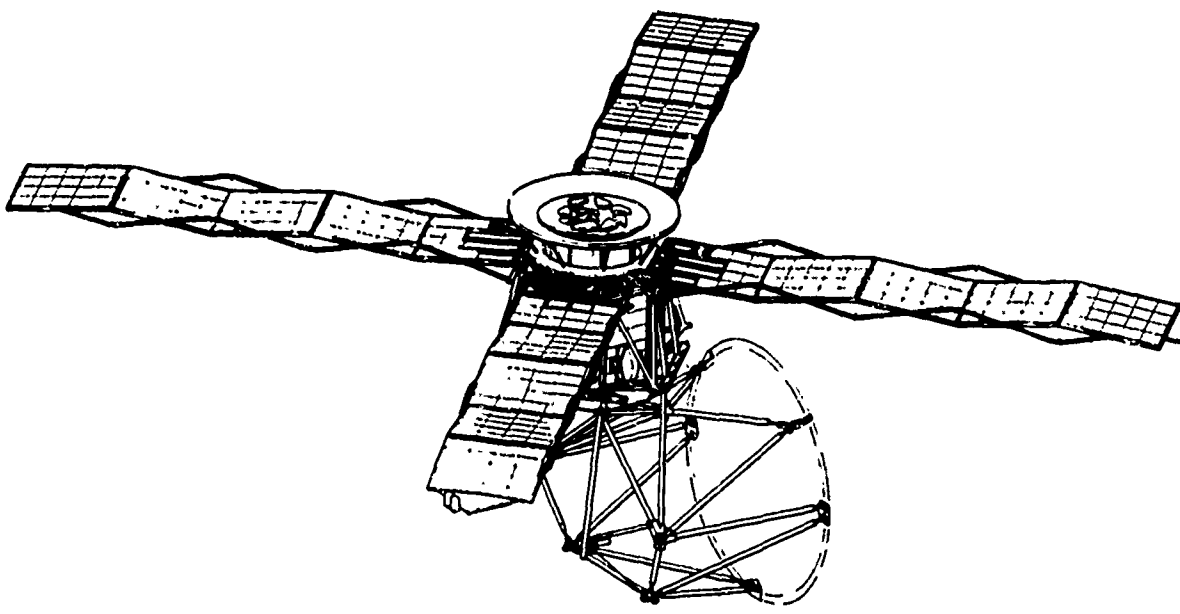


FIGURE 1. ATM RACK, DEPLOYMENT ASSEMBLY, SOLAR ARRAYS

Figure 1 shows the ATM rack, deployment assembly, and ATM solar arrays. The rack is the main support, and houses the structure containing the experiments; in addition, it houses the CMGs, which are used to stabilize the entire Skylab cluster in orbit. These three CMGs, which have a spin rate of 9300 rpm, are the momentum wheels considered in this analysis. Figure 2 shows the orientation of each of the three CMGs to the Skylab cluster.

Figure 3 shows the ATM spar, canister, and gimbal ring assembly (GRA). The spar is the structure on which the various experiment packages are mounted. The GRA is used to aim the various photographic experiments. The GRA is controlled by the EPCS, which has motion sensors on the spar.

The design of the EPCS depends on transfer functions calculated for various points on the ATM system. The goal of this task was to determine the effect of the spinning CMGs on the EPCS transfer functions. Although the cluster control system, of which the CMGs are a part, and the EPCS are independent control systems, the elastic motion of the CMG support structure will cause the wheel (gyro) to generate a torque that may be picked up by the EPCS sensors and cause the system to respond.

Using existing models of the various ATM substructures for the vibration analysis led to a total structural model with 1321 degrees of freedom. Two factors associated with this study dictated that the size of this model be reduced: first, the computer cost to obtain an eigenvalue

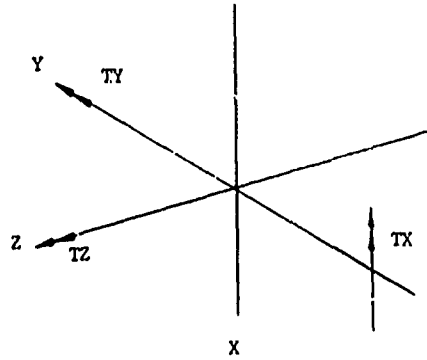


FIGURE 2. CMG SPIN AXES

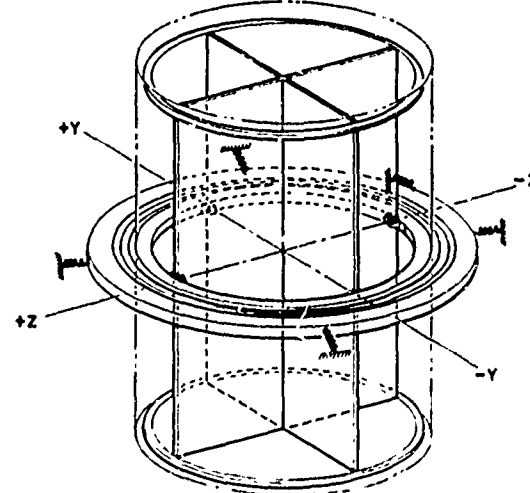
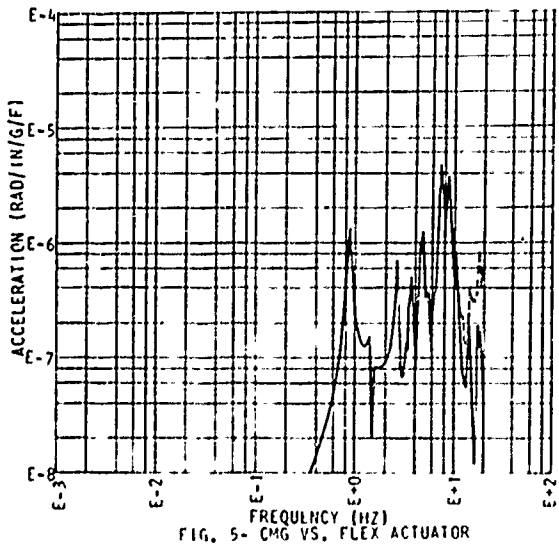
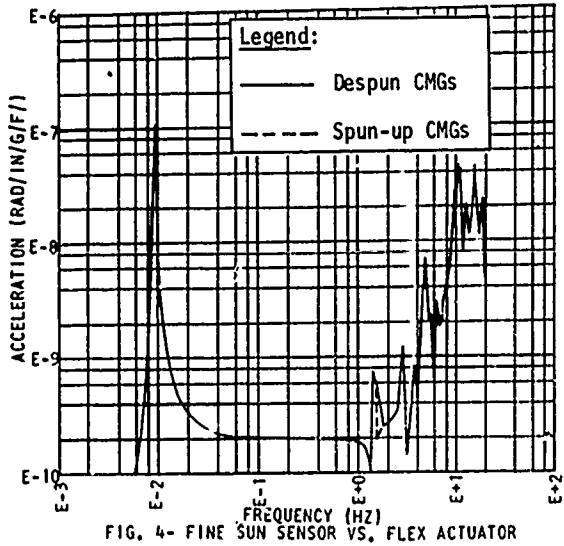


FIG. 3. SPAR/CANISTER/GRA

solution to this large a model was excessive, and second, the current transfer function program could only accommodate 50 modes due to computer storage limitations. In light of these two factors, we decided to use the constrained component mode substitution method [Ref. 3], or inertial modal coupling method, as it is more commonly called, to determine the modal properties. To use this method, the ATM system was broken into three substructures, consisting of the spar and GRA, the ATM rack, and the canister. For this analysis, the deployment assembly and ATM solar arrays are considered part of the rack.

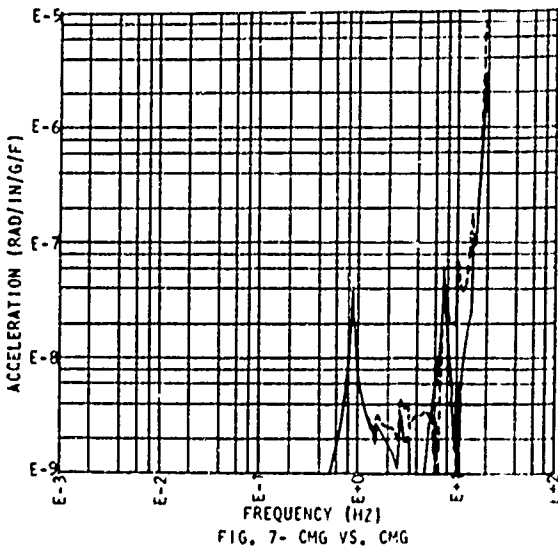
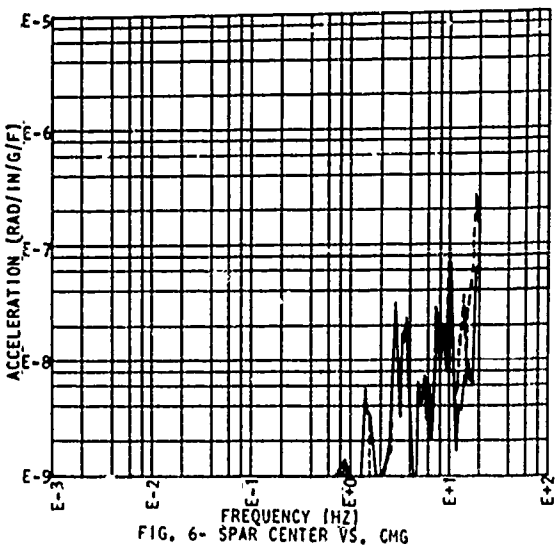
By using this method, the eigenvalue solution for the final modes and frequencies was performed on a 288-degree-of-freedom system, rather than on a 1321-degree-of-freedom system. These 288 degrees of freedom represent component modes of the various substructures selected with a frequency cutoff criterion. The frequency of the modes obtained ranged from 0.009 to 68 Hz.



To perform the transfer function analysis on the ATM, force input points and acceleration output points were selected on the basis of their effect on the EPCS. The input points selected were the GRA flex actuator torque motors and the rotor imbalance moments on the CMGs. The output points selected were the fine sun sensor and the EPCS rate gyros (both of which are on the spar), the flex actuators, and the CMGs.

#### RESULTS AND CONCLUSIONS

The results shown in Fig. 4 thru 7 indicate that the CMGs on the ATM have a distinct effect on the ATM transfer functions. In general, the effect is random: that is, the amplitude of the transfer function for a given input/output combination may remain unchanged, increase, or decrease, depending on the frequency range in question. Predictably, the greatest effect occurs when either the input or output point is near the CMGs, as can be seen in the figures.



Although the results of this study indicate that including momentum wheels or gyros in the calculation of transfer functions for structures containing them can influence the magnitude of the transfer functions, the governing factors on the magnitude of their effect are not clearly understood. Limitations on the scope of this study prevented investigation of some key factors, such as the proximity effect exhibited in the example and the effect of higher-mode truncation on the validity of the transfer functions near the truncation frequency.

#### NOMENCLATURE

##### Matrices

- $\{\phi\}$  = matrix of undamped normal modes, either generated directly from a discrete coordinate model or indirectly through component mode synthesis
- $[m]$  = mass matrix in discrete coordinates
- $[k]$  = stiffness matrix in discrete coordinates
- $[c]$  = damping matrix in discrete coordinates
- $\begin{bmatrix} m_{eq} \end{bmatrix}$  = diagonal generalized mass matrix  
=  $\begin{bmatrix} 1.0 \end{bmatrix}$  if the normal modes are orthonormalized on the mass matrix
- $\begin{bmatrix} \omega_m^2 \end{bmatrix}$  = diagonal generalized stiffness matrix
- $\begin{bmatrix} 2\zeta\omega_0 m_{eq} \end{bmatrix}$  = diagonal generalized damping matrix
- $[\Gamma]$  = matrix of assembled rotation-dependent terms
- No. of Rotors  
 $= \sum_{j=1}^{N_r} [T]_j^T$   
 $\begin{bmatrix} 0 & Y & 0 \\ -Y & 0 & 0 \\ 0 & 0 & 0 \end{bmatrix}_j [T]_j$
- $[T]$  = coordinate transformation matrix relating the rotor local coordinates  $\{\theta\}$  to the system coordinates  $\{x\}$
- $[B]$  = coupled velocity coefficient matrix for inclusion of momentum wheels  
 $= \begin{bmatrix} 2\zeta\omega_0 \end{bmatrix} + \{\phi\}^T [\Gamma] \{\phi\}$
- $[E] = \begin{bmatrix} \omega_0^2 \end{bmatrix}$  = generalized stiffness matrix

- $[R] = \begin{bmatrix} B & 1.0 \\ 1.0 & 0 \end{bmatrix}$  = state-vector velocity coefficient matrix
- $[H] = \begin{bmatrix} E & 0 \\ 0 & -1.0 \end{bmatrix}$  = state-vector displacement coefficient matrix
- $[U] = -[R]^{-1} [H]$  = state-vector characteristic matrix
- $\{\Psi\}$  = matrix of complex eigenvectors
- $\{\alpha\}$  = diagonal matrix of complex eigenvalues
- $\{\Psi_1\}$  = upper half of  $\{\Psi\}$
- $\{\Psi_2\}$  = lower half of  $\{\Psi\}$

##### Vectors

- $\{q\}$  = vector of normal mode coordinates
- $\{F(t)\}$  = vector of generalized forces in normal mode coordinates  
=  $\{\phi\}^T \{f(t)\}$
- $\{f(t)\}$  = vector of discrete forces
- $\{x\}$  = vector of discrete coordinates
- $\{f_o\}$  = vector of discrete force amplitudes
- $\{q_o\}$  = vector of modal coordinate amplitude/phase coefficients
- $\{x_o\}$  = vector of discrete coordinate amplitude/phase coefficients
- $\{M\}$  = vector of moments in rotor coordinates
- $\{\theta\}$  = vector of rotational degrees of freedom in rotor coordinates
- $\{F_o\}$  = vector of normal mode coordinate generalized force coefficients
- $\{Z\}$  = state vector  
=  $\begin{Bmatrix} q \\ \dot{q} \end{Bmatrix}$
- $\{D\}$  = generalized forces in state-vector formulation of the equations of motion  
 $= -[R]^{-1} \{D\} = \begin{Bmatrix} 0 \\ -\ddot{r} \end{Bmatrix}$
- $\{\Psi\}$  = complex eigenvector
- $\{\xi\}$  = vector of complex mode generalized coordinates
- $\{J_o\}$  = coefficient matrix in  $(J) = \{J_o\} e^{i\Omega t}$

##### Scalars

- $\Omega$  = circular frequency of forcing function
- $\omega_{o_j}$  = undamped natural circular frequency of  $j^{\text{th}}$  mode
- $m_j$  = moment about axis

$I_j$  = mass inertia about principal axis

$\theta_j$  = rotational degree of freedom about axis

$\lambda$  = constant angular velocity about rotor spin axis

$\gamma$  = angular momentum

$$= (I_z - I_o) \lambda$$

$\alpha$  = complex eigenvalue

$$i = \sqrt{-1}$$

#### Symbols

[ ] = diagonal matrix

[ ]<sup>T</sup> = transpose of matrix

[ ]<sup>-1</sup> = inverse of matrix

[---] = partitioned matrix

{---} = partitioned vector

#### REFERENCES

1. W. C. Hurty, "Dynamic Analysis of Structural Systems Using Component Modes," AIAA J., Vol. 3, No. 4, pp. 678-685, April 1965.
2. P. W. Likens, "Dynamics and Control of Space Vehicles," NASA TR 32-1329, Rev. 1, Jet Propulsion Laboratory, Pasadena, California, January 15, 1970.
3. W. A. Benfield and R. F. Hruda, "Vibration Analysis of Structures by Component Mode Substitution," AIAA/ASME 11th Structures, Structural Dynamics, and Materials Conference, Denver, Colorado, April 22-24, 1970.

#### ACKNOWLEDGEMENTS

The authors wish to acknowledge the efforts of Mr. Jack Nichols and Mr. Wayne Ivey, S&E - ASTN-ADS, Marshall Space Flight Center, for their aid in obtaining permission to use the Skylab ATM modal data obtained under Contract NAS8-24000.

## INTEGRATED DYNAMIC ANALYSIS OF A SPACE STATION WITH CONTROLLABLE SOLAR ARRAYS

Joseph A. Heinrichs and Alan L. Weinberger  
Fairchild Industries, Inc.  
Germantown, Maryland

Marvin D. Rhodes  
NASA Langley Research Center  
Hampton, Virginia

An integrated dynamic analysis and corresponding digital computer simulation for application to a space station with controllable solar arrays are presented. The analysis and simulation have been developed for the primary purpose of evaluating dynamic load interactions between the solar arrays and the space station which can result from orbital perturbations of the combined system. Integrated into the analytical formulation are the dynamics associated with the space station, the solar array flexibilities and their respective control systems. Application of the simulation is made utilizing present concepts of a space station with large area arrays and of typical control systems. A structural analysis of the flexible solar arrays is initially required to provide modal data for the simulation; and analytical results for an array concept are given.

A verification of the structural dynamic methods used in the simulation is presented. This verification is accomplished by the application of the simulation to a problem of known solution, a uniform beam subjected to a unit step load applied at mid-span.

### INTRODUCTION

The solar cell and battery system has been successfully used on many small spacecraft; however, space stations of the future will have power requirements which are much larger than those within the present design experience of solar cell systems. Therefore, the solar cell arrays used on future space stations must be relatively large and be capable of tracking the sun in a manner that does not restrict the desired space station orientation. This is usually accomplished through the use of an orientation control system (OCS) for the arrays. A potential problem exists due to undesirable interactions between the solar arrays and space station caused by required control and stabilization forces combined with external perturbations.

Spacecraft instabilities have been observed in the past when flexible appendages are part of the satellite structure. This past experience is summarized by Likins and Bouvier [1]. Because of the requirements imposed upon large area solar arrays, a weight-efficient design rather than a stiffness

design results, and the primary array frequencies may fall within the control system bandwidth. A digital computer simulation for evaluating the dynamic interactions of large solar cell arrays and orbiting space stations has been formulated and considers the dynamic characteristics of the array structure and the required systems for attitude and orientation control. The objectives of this simulation were to (1) provide an automated methodology of interaction loads analysis for use as a design tool, (2) analyze present array structural concepts which are to provide 100 KW of electrical power to future space stations and (3) obtain an indication of space station stability by its real time motions.

The equations of motion for an orbiting space station with attached controllable arrays have been generated and were digitally programmed for solution by numerical integration techniques. In the development of the system's motion equations, a modal synthesis technique was employed whereby the elastic characteristics of the arrays were described by a finite set of orthogonal cantilever modes. Only rigid body motions of the space station were

considered. The rigid body/flexible body interface was described by space station acceleration in terms of induced inertial loads forcing the flexible arrays; in like manner the flexible array root forces and moments acted as forcing functions on the space station. Structural mode descriptions of the arrays were required as input to the simulation; therefore, a structural analysis of the elastic system was required prior to the performance of this simulation. Provision was made in the simulation for closed loop attitude control system dynamics of the space station and OCS dynamics for the solar arrays. The latter control system provided the desired orientation of the arrays with the sun by controlling the rotation about the orbit-adjust and seasonal-adjust axes. Outputs of the simulation include interaction forces and moments, magnitudes of all motion variables and control parameters as functions of time.

The formulated simulation has been applied to an extendible solar array structural concept and space station which are presently undergoing separate engineering evaluations. Also, candidate array orientation control and space station attitude control systems have been mathematically described and digitally programmed for this application. Two attitude control systems were provided for the space station; they are the reaction jet and control moment gyro (CMG) systems. The necessary modal

synthesis analysis of the array structure was performed by a stiffness matrix method utilizing equivalent discrete element structural models representing 600 inertial degrees of freedom. The modes utilized in the simulation were chosen on the basis of a significant percentage of load participation in interface force and moment. Simulations were performed on the orbiting structural system perturbed by initial attitude errors and external forces representing docking.

To demonstrate the adequacy of the methodology which has been simulated, a problem of known solution was selected --- the uniform free-free beam planar response to a unit step load applied at mid-span. The flexible appendage solar arrays were represented as cantilever uniform beams, having the first five bending modes as flexible degrees of freedom. When coupled inertially with the rigid body translation mode, the cantilever mode solution yielded results for frequency and loads which compared favorably with the exact free-free beam solution.

#### CONSIDERED PARAMETERS

The presented analysis and corresponding simulation is intended to be applicable to future space stations with controllable solar arrays such as that shown in Figure 1. Structural concepts

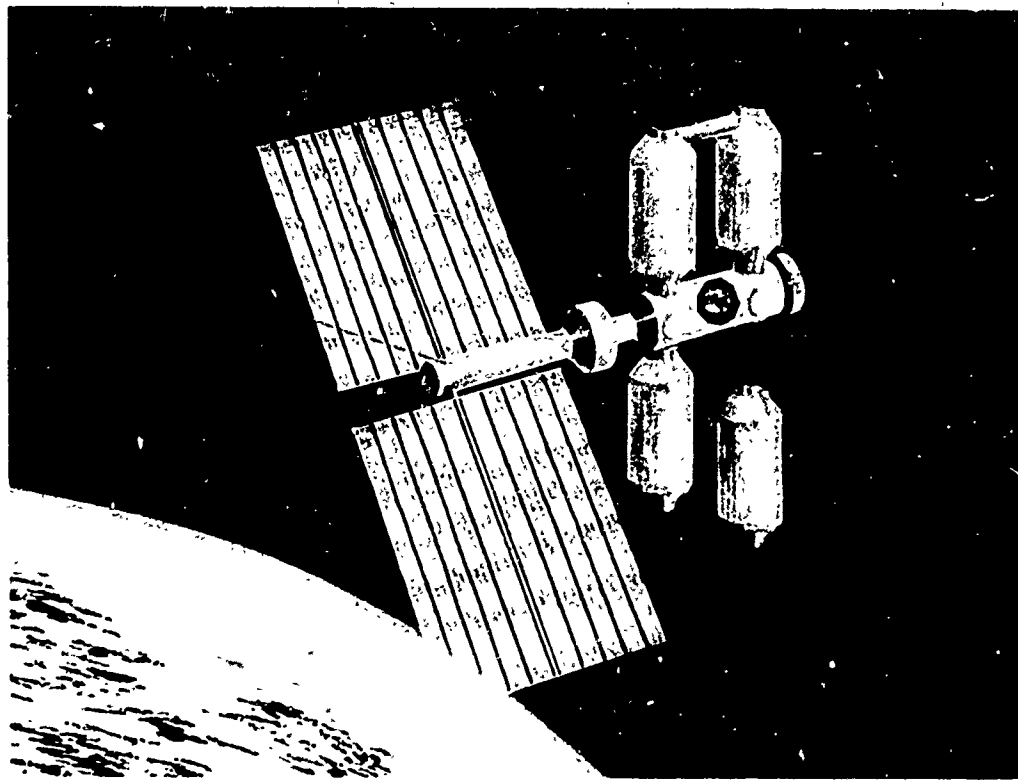


Fig. 1. Space Station and Solar Array Structural Concepts

of arrays and space stations as shown and associated control systems are presently undergoing separate engineering developments without regard to a total system dynamics criteria for minimizing interaction loads. One objective of the present analysis is to assist in the development of dynamics criteria for each of the component structures from analytical results of total system characteristics.

In order to account for all of the significant dynamic influences upon the space station and solar array load interactions, the following parameters were considered as basic and are accounted for in the simulation

- Solar array flexible body dynamics in terms of generalized modal coordinates.
- Space station rigid body dynamics.
- Space station control system dynamics including guidance and command.
- Solar array OCS dynamics including guidance and command.

It was assumed that the space station structural frequencies are significantly higher than the solar array frequencies and are decoupled from the control system. The analysis considerations can be best described by the block diagram shown in Figure 2. This illustration shows the breakdown of the basic parameters together with the considered coupling paths.

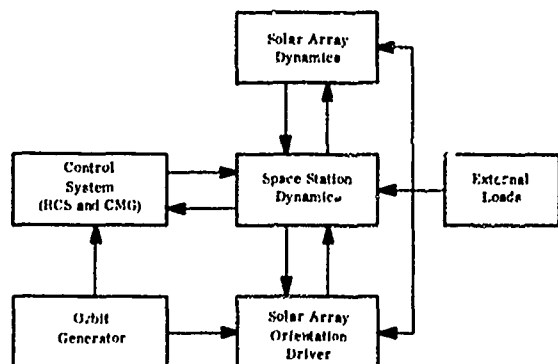
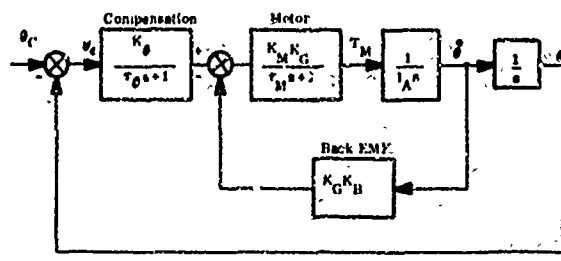


Fig. 2. Analysis Considerations

The constraint placed upon the representation of the array dynamics is that they be described in terms of their orthogonal cantilever modes. The orientation and space station control systems that have been incorporated into the simulation are those designed to complement the present space station and array configurations. The primary requirements of an OCS are maintaining a desired accuracy with the sun vector and

providing sun alignment within a specified time after leaving the earth's shadow. In addition, the OCS must meet accuracy requirements despite experienced space station disturbances and provide minimum dynamic excitation to the arrays. Two generic types of OCS drive systems have been considered in the simulation and are the continuous and non-linear drive systems. The continuous-type drive system employs either a DC torque motor or a variable-frequency synchronous motor as its drive element. A block diagram of the continuous-drive OCS model contained in the simulation is shown in Figure 3.



#### Legend

- $K_M$  - motor gain
- $T_M$  - motor time constant
- $K_B$  - back EMF coefficient
- $I_A$  - array inertia about rotation axis
- $K_g, T_g$  - gain and time constant for loop compensation
- $K_G$  - system gear ratio
- $A, B$  - same as figure 6

Fig. 3. Continuous Drive OCS Model

The non-linear drive OCS is similar to the continuous drive system with the exception that the control logic of the non-linear OCS is operated in an on-off manner. When the array error exceeds some preselected threshold value, the motor is turned on until the array is driven to a null position at which point the motor is switched off. This threshold value has been made a user option in the simulation so that its affect upon loads can be evaluated by parametric studies.

Two generic types of control laws/torques have been incorporated into the simulation for attitude control of the space station and are the CMG and the reaction jet control system (RCS). The CMG control system is used for precision attitude stabilization against cyclic disturbance torques without the need for propellant expenditure. It consists of three two-degree-of-freedom control moment gyros with parallel outer gimbals and with their momentum vectors initially equally spaced in the orbit plane (Figure 4.). This particular CMG configuration permits simple steering laws and a planar, rather than three dimensional, anti-hangup law. The CMG control dynamics included in the simulation [2] has a system frequency of 1.4 Hz and a damping ratio

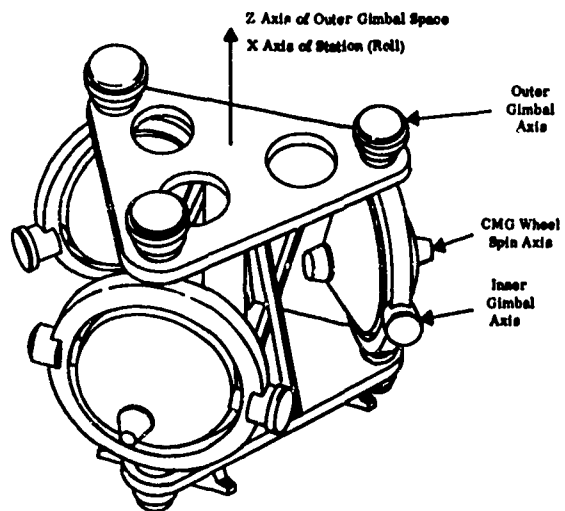


Fig. 4. 3 PM Control Moment Gyro Array

of 0.707. The RCS is primarily used for reference attitude acquisition maneuvers and the momentum desaturation of the CMG system. It is also an alternate to the CMG for controlling attitude of the space station. The RCS is depicted in the sketch of Figure 5. It is comprised of 4 sets of quad thrusters providing redundant control about the pitch, roll and yaw body axes. All maneuvers using the RCS are performed by firing the thrusters in pairs. The RCS model included in the simulation is depicted in Figure 6 and the corresponding control equations are given in Reference 3.

In order to account for space station disturbances such as crew motions and docking forces, provision has also been made in the simulation to allow for the application of time dependent forcing functions.

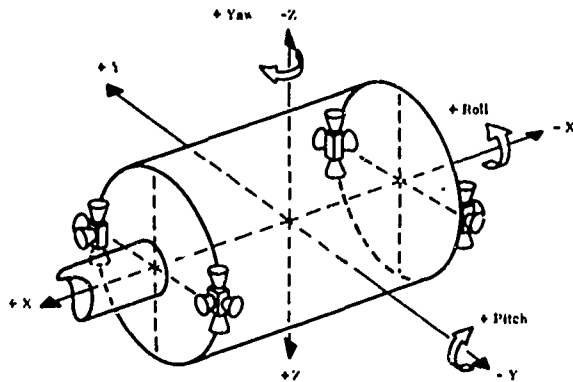
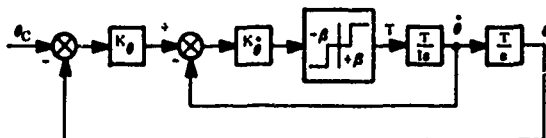


Fig. 5. RCS Jet Location/Function



#### Legend:

- $\theta_C$  = Commanded Attitude Angle
- $\dot{\theta}, \ddot{\theta}$  = Attitude Angle; Rate
- $K_g, K_d$  = Attitude Angle Gain, Rate Gain
- $\beta$  = Control Loop Deadband
- $T$  = RCS Torque Level
- $I$  = Space Station Moment of Inertia

Fig. 6. RCS Model

## ANALYTICAL FORMULATION

Space station and solar array motion equations were formulated together with the interactive dynamics provided by the respective attitude and orientation control systems. The method given by Likins [4] has been used as a basis for the methodology provided in the simulations. The simulation developed from the employed mathematical models has been successfully run on the CDC 6600 computer. The simulation model utilized for the mathematical system is described below.

- The space station and the two arrays are each modeled as interconnected bodies with each of the arrays permitted controlled rotations about the spacecraft attachment points. The allowed axes of rotation consist of those parallel to the space station roll axis and the array vane axis.
- The flexibility of the solar array is modeled by means of a truncated set of cantilever modes which is excited by the acceleration of the array support. A difference equation technique [5] is utilized to obtain the modal response.
- Maneuver and attitude control of the space station together with the solar array orientation control are modeled in terms of the transient forces and torques produced by closed loop guidance equations. Both the space station attitude and array orientation guidance commands are computed external to the structural dynamics section. These provide the space station with a fixed orientation relative to orbit coordinates and point the solar arrays at the sun.

- The array driver gear train for the axis parallel to the roll axis is modeled as an ideal mechanical transformer. The vane driver axis is directly driven, and either or both motions about these axes may be rigidly constrained.
- The simulation orbit generator uses Lyddane's method [6] for near earth orbits. The generator is included in the simulation to provide a reference for guidance commands. A block diagram representation of the simulation program is presented in Figure 7 where important logical switches and function interconnection have been clearly delineated.

#### RIGID BODY AND FLEXIBLE BODY DYNAMICS FORMULATIONS

Salient equations and techniques used in the simulation are shown below. A complete formulation of all equations may be found in Reference 7. The space station and array are modeled as a subsystem of interconnected bodies whose motion is described by the Newton-Euler equations of motion.

The connected space station and solar array bodies in the Earth Centered Inertial (ECI) coordinate frame are shown in Figure 8. The following three vector equations are utilized.

##### System Force

$$m_T \frac{d^2(\bar{R}_0 + \bar{C})}{dt^2} = \sum_J \bar{F}_{A_J} + \bar{F}_R \quad (1)$$

##### Space Station Moment

$$\begin{aligned} \frac{d}{dt} \cdot (\bar{L}_0) &= (-\bar{l}_R) \times \bar{F}_R + \sum_J \bar{r}'_J \times \bar{F}_{H_J} \\ &+ \sum_J \bar{T}_{A_J} - \sum_J \bar{r}'_J \times \bar{F}_{A_J} - \sum_J \bar{T}_J \quad (2) \\ &+ \bar{T}_{AC} + \bar{T}_{CMG} \end{aligned}$$

##### Jth Array Body Moment

$$\frac{d}{dt} (\bar{L}_J) = \bar{T}_J - \bar{r}_J \times \bar{F}_{H_J} \quad (3)$$

The following notation applies

$J$	- Index of solar array, J is equal to 1 or 2
$\bar{F}_{A_J}, \bar{T}_{A_J}$	- are the transient forces and torques produced by the flexible array dynamics
$\bar{T}_{AC}$	- torque exerted on space station by hinged body along constrained axes
$m_T$	- total system mass
$O_N$	- Newtonian reference point
$O_B$	- Spacecraft reference point
$CG_{S.S.}$	- Space station center of gravity
$CG_{SYS}$	- Center of gravity for the entire system
$CG_J$	- Center of gravity for the $J^{TH}$ hinged body
$\bar{R}_0$	- Radius vector in ECI
$\bar{F}_R$	- External force applied to space station
$\bar{L}_J$	- Angular momentum of $J^{TH}$ array body about its CG
$\bar{L}_0$	- Angular momentum of space station about its CG
$\bar{h}_J$	- Vector from space station reference point to space station/array interface
$\bar{r}_J$	- vector from the space station/array interface to the CG of the $J^{TH}$ array body (on space station)
$\bar{l}_R$	- vector from point of external force application to space station CG
$\bar{C}$	- vector from space station reference to system CG
$\bar{T}_J$	- Interface torque on $J^{TH}$ array body produced by OCS
$\bar{r}'_J$	- $(\bar{r}_0 - \bar{h}_J)$ force moment arm
$\bar{F}_{H_J}$	- Interface force exerted by space station on $J^{TH}$ array body

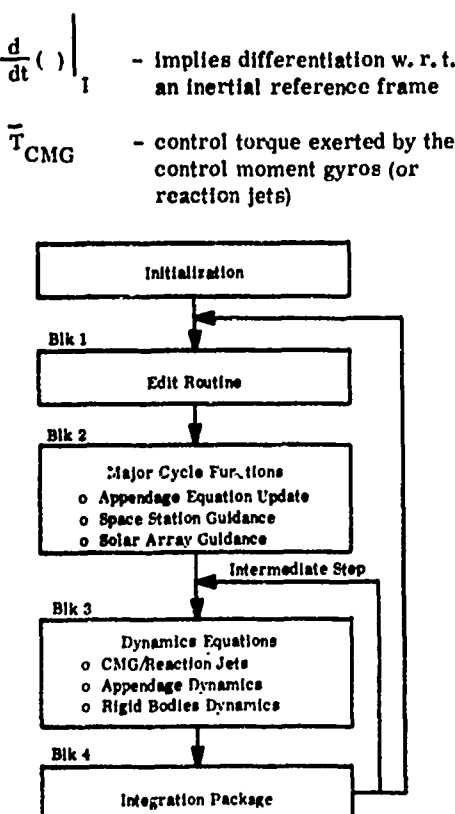


Fig. 7. Simulation Flow Chart

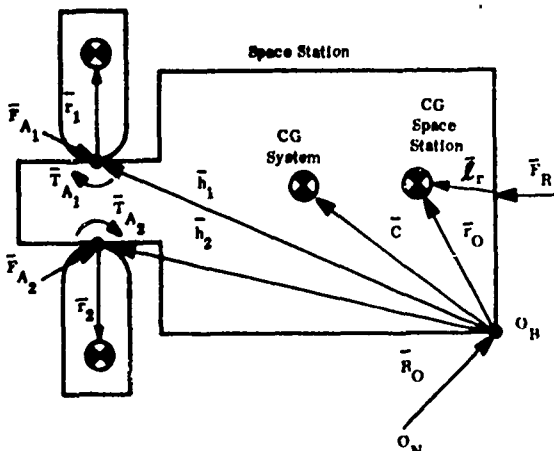


Fig. 8. Rigid Body System Geometry

Equations 1-3 were formulated into a set of matrix equations for the facilitation of digital computations. The system force and space station moment equations were formulated with respect to the space station reference frame and the array body equations were written in the array

reference frame. This requires the updating of specific direction cosine matrices during the simulation. The principal coordinate frames and direction cosine identities utilized are as follows:

$$\begin{aligned}\{X_s\} &= [C_o]^T \{X_I\} \quad \text{where } X_I \text{ is the vector} \\ &\text{in the (ECI) coordinates,} \\ \{X_{A_1}\} &= [C_1]^T \{X_s\} \quad X_s \text{ is the vector in space} \\ &\text{station coordinates, and} \\ \{X_{A_2}\} &= [C_2]^T \{X_s\} \quad X_A \text{ is the vector in solar} \\ &\text{array coordinates.}\end{aligned}$$

The direction cosine matrices are calculated in the simulation in terms of Euler angles and are updated periodically by the following equation:

$$\dot{[C_I]} = [C_I] \begin{bmatrix} 0 & -\omega_{i3} & \omega_{i2} \\ \omega_{i3} & 0 & -\omega_{i1} \\ -\omega_{i2} & \omega_{i1} & 0 \end{bmatrix} = C_I \dot{\tilde{\omega}}_i$$

where  $\omega_{i1}$ ,  $\omega_{i2}$ ,  $\omega_{i3}$  are the rotational rates about the  $i$ th coordinate frame axis. The rigid body scalar equations derived from those presented above reduce to the matrix form shown in Figure 9. The submatrices  $[A_i]$  represent the linear term coefficients,  $R_{0i}$  and  $\dot{R}_{0i}$  represent the rigid body translational and rotational accelerations respectively and  $\dot{\tilde{\omega}}_{A_i}$ , the rigid array rotational accelerations relative to the space station coordinates for the two unconstrained axes of rotation. The right hand side of the equations represent the applied forces, torques (control torques included) and all non-linear terms. Controlling torque profiles are computed in the simulation at designated time increments by the appropriate control equations and are used to force the above matrix equations. The array and space station attitudes are referenced to their respective coordinate systems and are periodically updated during the simulation.

The flexible array dynamics formulations are adapted from the flexible appendage equations developed by Likins [4]. Shown in Figure 10 is a sketch of the flexible array geometry utilized in the analysis. It is assumed that the particle masses of the array have negligible inertias and deflections are sufficiently small that linear structural analysis is valid. The force on the  $j$ th mass is given in Equation 5.

$$\bar{F}_j = m_j \frac{d^2}{dt^2} (\bar{R}_o + \bar{h}_j + \bar{r}_j + \bar{v}_j) \quad (5)$$

The terms used are defined in Figure 10.

$$\begin{bmatrix} A_1 \\ A_2 \\ A_3 \\ A_4 \end{bmatrix} \begin{bmatrix} A_5 \\ A_6 \\ A_7 \\ A_8 \end{bmatrix} \begin{bmatrix} A_9 \\ A_{10} \\ A_{11} \\ A_{12} \end{bmatrix} \begin{bmatrix} A_{13} \\ A_{14} \\ A_{15} \\ A_{16} \end{bmatrix} \begin{bmatrix} \bar{r}_{O_1} \\ \bar{r}_{O_2} \\ \bar{r}_{O_3} \\ \omega_{O_1} \\ \omega_{O_2} \\ \omega_{O_3} \\ \omega_{A_{11}} \\ \omega_{A_{12}} \\ \omega_{A_{21}} \\ \omega_{A_{22}} \end{bmatrix} = \begin{bmatrix} F_1 \\ F_2 \\ F_3 \\ F_4 \end{bmatrix} \quad (4)$$

Fig. 9. Rigid Body Matrix Equations

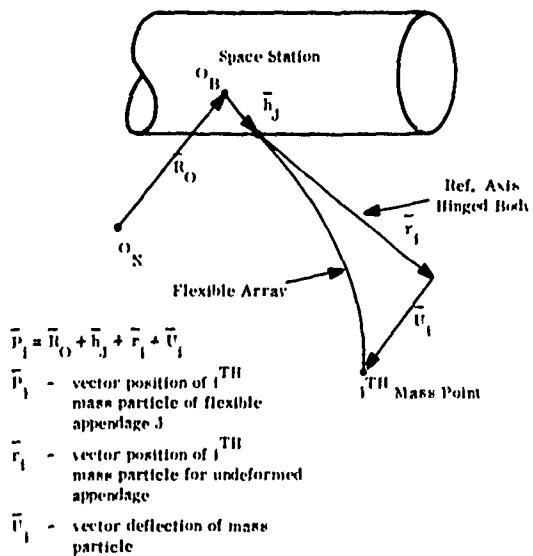


Fig. 10. Flexible Array Geometry

Substitution of the appropriate direction cosine matrices and consideration of the appropriate properties resulting from elastic deformation gives the following:

$$[M]\ddot{q} + [K]q = -[G]q - [B]\dot{q} + L \quad (6)$$

where  $q = \begin{bmatrix} U_1^1 & U_2^1 & U_3^1 & U_1^2 & U_2^2 & U_3^2 & \dots & U_1^N & U_2^N & U_3^N \end{bmatrix}$

$M$  is the mass matrix

$K$  is the symmetric stiffness matrix

$L$  is the matrix of rigid body inertial loads (Reference 4)

$B$  and  $G$  are force coefficient matrices which are dependent upon rotation rates (Reference 4)

The order of the above equations of motions are  $3N$  where  $N$  is the number of discrete masses comprising the dynamical system. Following the method of Reference 4, it is of convenience to transform Equation 6 into orthogonal coordinates representing cantilever modes of vibration. The system of equations in orthogonal coordinates can then be truncated on the basis of some chosen criteria or engineering experience. This procedure permits orders of magnitude reduction in the number of equations describing array flexibility. The discrete coordinate equations can be transformed to normal coordinates by orthogonal transformations produced by most automated matrix methods of structural dynamics analysis. The transformed equation then becomes

$$\begin{aligned}
 \ddot{\eta} + 2\xi\sigma\dot{\eta} + \sigma^2\eta &= \phi^T G \phi \eta - \phi^T B \phi \dot{\eta} \\
 &+ \phi^T L
 \end{aligned} \quad (7)$$

where  $\eta$ ,  $\dot{\eta}$ ,  $\ddot{\eta}$  are  $M \times 1$  matrices and  $M$  is the number of cantilevered modes utilized. Note that a modal damping term ( $2\xi\sigma$ ) has been arbitrarily inserted in the classic manner of structural analysis.

The assumption has been made in going from Equation 6 to Equation 7 that the motion dependent matrices which are functions of rigid body rotation rates, are small and have a negligible effect upon the resulting transformation procedure. Without this assumption the simulation would be required to be performed in discrete coupled coordinates with resulting manipulations of large order matrices.

The left hand sides of Equations 4 and 7 are constructed in the simulation from computed direction cosines, the rigid body inertia tensor, center of gravity and appendage attachment locations in the space station coordinate frame and modal properties of flexible appendages. The latter includes deflection coefficients, frequencies, damping coefficients and masses, for a chosen number of modes.

Both the rigid body and elastic equations are solved sequentially employing a finite difference method. A change to the integration procedure in the simulation is presently being

made and incorporates the simultaneous solution of the equations. Excitation of Equation 7 is accomplished by the internal loading acting on each of the discrete masses resulting from the translational and rotational accelerations of the rigid bodies. The rigid body equations are in turn forced by the application of the flexible body interaction loads, control system torques and external forces. The simulation computes interaction loads from the following definitions.

$$F_{A_j} = \sum_{i,j} m_j \phi_{ij} \ddot{\eta}_i \quad \text{Transient force}$$

$$T_{A_j} = \sum_{i,j} r_j m_j \phi_{ij} \ddot{\eta}_i \quad \text{Transient moment}$$

The total interaction forces and torques are defined by

$$F_{INT_j} = -F_{H_j} + C_j F_{A_j}$$

$$T_{INT_j} = -T_{H_j} + C_j T_{A_j} - (C_j \tilde{r}_j C^T_j) F_{H_j}$$

where

$F_{INT_j}$  is the total force exerted by the  $j^{th}$  flexible array/hinged body combination on the space station.

$T_{INT_j}$  total moment exerted by the  $j^{th}$  flexible array/hinged body combination on the space station.

$F_{H_j}, T_{H_j}$  are the hinge forces and moments on the  $j^{th}$  rigid hinged body.

and

$C_j$  is the appropriate direction cosine matrix (internally computed).

The above completes the outline description of the formulations and the computations used in the simulation. The simulation computes all transient variables at specified time increments with the option of automatically plotting these variables with the Calcomp plotter. As previously mentioned, a basic assumption of rigid space station dynamics is made in the mathematical development. Work is in progress for modifying the present simulation to include space station flexibility in terms of free-free modes of vibration.

#### SIMULATION VERIFICATION

Verification of the simulation program was accomplished in two distinct parts. Each functional subprogram --- Lyddane's orbit generator, CMG space station control, OCS linear and non-linear solar array drives --- was

exercised independently and the results correlated with known data. At that point, the complete program was checked for continuity and a problem of known solution was then executed to verify the structural dynamics methodology contained in the simulation. The problem --- a free-free beam with zero damping subjected to a concentrated force at mid-span --- was selected because it was considered to be a good test for solution convergence. It also provided information concerning the accuracy of the analytical approach and programming techniques. Closed form solutions for the modal response of free-free beams subjected to concentrated forces are provided by Leonard [8]. In addition, two other solutions for the response of a free-free beam were obtained using numerical integration methods. One solution was obtained by the method provided in Reference 5 and the other by an independently derived method using a variable order Adams integrator. These solutions provided a basis for verification of the simulations.

It was necessary to approximate the free-free beam configuration in the simulation by two cantilever beams, attached at their points of constraint. Figure 11 shows a sketch of the cantilever geometry and associated coordinates. The "space station" mass has been set to zero and the "solar arrays"

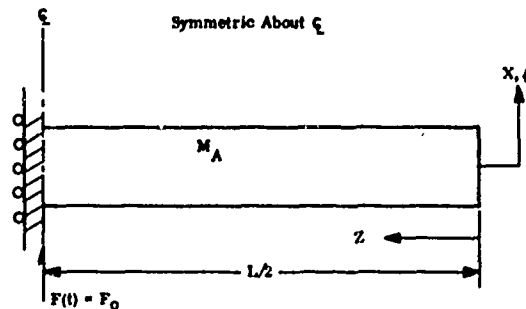


Fig. 11. Cantilever Beam Simulation of a Free-Free Beam

represented by cantilever-free beams. An analysis was initially made for system eigenvalues and eigenvectors of the two-cantilever arrangement in order that comparisons could be made with corresponding theoretical free-free modal properties. These comparisons were necessary to determine if cantilever beam modes could be used to accurately represent free-free beam modes. Motion equations for the system of two connected cantilevers were derived to facilitate the frequency analysis; these equations are presented below.

$$M_A \ddot{X}(t) + \sum_{i=1}^N \bar{V}_i \left( \frac{L}{2} \right) \ddot{\xi}_i(t) = F_0 \quad (8)$$

$$M_{EQ_i} \ddot{\xi}_i(t) + M_{EQ_i} \omega_i^2 \xi_i(t) \\ + \bar{V}_i \left( \frac{L}{2} \right) \ddot{x}(t) = 0 \quad (9)$$

where

$$\bar{V}_i \left( \frac{L}{2} \right) = V_i \left( \frac{L}{2} \right) / \omega_i^2 \quad i = 1, 2, 3 \dots N$$

and

- $M_A$  = Mass of the cantilevered beam
- $V_i \left( \frac{L}{2} \right)$  = Modal shear force coef. in the  $i^{TH}$  cantilever mode at mid-span of the simulated free-free beam
- $F_o$  = applied step load at mid-span
- $X(t)$  = coordinate for rigid body motion
- $M_{EQ_i}$  = generalized mass of the  $i^{TH}$  cantilever mode
- $\omega_i$  =  $i^{TH}$  cantilever mode natural frequency (uncoupled)
- $\xi_i(t)$  = generalized modal coordinate for the  $i^{TH}$  cantilever mode
- $\Omega_i$  = coupled frequency of vibration of the system, approximates the  $i^{TH}$  free-free frequency

The solutions of Equations 8 and 9, using only the fundamental cantilever mode, are given by the following:

$$\ddot{x}(t) = \frac{F_o}{M_A} + \frac{\bar{V}_1^2}{M_A (M_A M_{EQ_1} - \bar{V}_1^2)} \cos \Omega t \quad (10)$$

$$\ddot{\xi}_1(t) = -\frac{\bar{V}_1 F_o}{(M_A M_{EQ_1} - \bar{V}_1^2)} \cos \Omega t \quad (11)$$

$$\ddot{\xi}_1(t) = -\frac{\bar{V}_1 F_o}{\Omega^2 (M_A M_{EQ_1} - \bar{V}_1^2)} (1 - \cos \Omega t) \quad (12)$$

where

$$\Omega = \sqrt{\frac{M_A M_{EQ_1}}{(M_A M_{EQ_1} - \bar{V}_1^2)}} \omega_1 \quad (13)$$

Similarly, the corresponding analytical solutions for the perturbed free-free beam were

derived and are shown below. The subscript "F" refers to free-free in these equations.

$$\ddot{x}_F(t) = \frac{2F_o}{2M_A} \quad (14)$$

$$\ddot{\xi}_F(t) = \frac{2F_o \phi_{F1} \left( \frac{L}{2} \right)}{M_{EQ_F1}} \cos \Omega_{F1} t \quad (15)$$

$$\ddot{\xi}_{F1}(t) = \frac{2F_o \phi_{F1} \left( \frac{L}{2} \right)}{M_{EQ_F1} \Omega_{F1}^2} (1 - \cos \Omega_{F1} t) \quad (16)$$

It should be noted that anti-symmetric modes of the free-free beam were not excited due to the positioning of the disturbance force at mid-span.

Modal data for both the free-free and cantilever uniform beams were obtained from standard reference tables [9] in order to compare the cantilever and free-free beam formulations. Numerical data assumed for this comparison were:  $M_A = 5.0$  slugs,  $F_o = 0.5$  lb.,  $\omega_1 = 12,566$  rad/sec. The evaluation of the numerical coefficients of Equations 8-16 was based upon a 25 point discretized mass representation of both the cantilever and free-free beams. The frequencies obtained by an orthogonal coordinate transformation analysis of Equations 8 and 9, for the cantilever beams, are given in Table 1. These frequencies, along with corresponding free-free beam frequencies have been normalized with respect to the frequency of the fundamental free-free beam mode. The rate of convergence in this frequency comparison is demonstrated by the successive number of modes used. Similarly, the degree of correlation and convergence in the modal amplitude domain can be seen in Figure 12 which is based upon use of three cantilever modes. The comparisons show that the cantilever beam formulation can be used to accurately describe free-free beam modal properties if a sufficient number of cantilever modes are used.

Although motion histories of the flexible appendages were of interest, the primary objective of the simulation was to obtain interaction loads between the space station and solar array for design evaluation. Therefore, for purposes of verification with known solutions [5, 8] shear force histories at the one-quarter span beam location were obtained. Figure 13 compares the shear history obtained from the use of one cantilever mode in the simulation with the shear calculated using the natural acceleration method and one free-free mode. Excitation at the base of the cantilever beams by a zero mass space station posed no problem for the simulation.

TABLE 1

Frequency Comparison of (Uniform Beam) Cantilever + Rigid Body Mode Representation  
of a Free-Free Uniform Beam

Frequency Ratios:  $\frac{f_n}{f_{1,\text{free-free}}}$

Reference Frequency Ratios			Calculated Coupled Mode Frequency Ratios				
Symmetric Mode No., n	Free-Free Beam	Uncoupled Cantilever Beam	1 Mode Cantilever Beam + Rigid Body	2 Mode Cantilever Beam + Rigid Body	3 Mode Cantilever Beam + Rigid Body	4 Mode Cantilever Beam + Rigid Body	5 Mode Cantilever Beam + Rigid Body
1	1.000	0.632	1.0101	1.0006	1.0003	1.0000	1.0000
2	5.404	3.958	---	5.548	5.420	5.408	5.405
3	13.344	11.074	---	---	13.749	13.410	13.367
4	24.814	21.652	---	---	---	25.584	24.965
5	39.812	36.861	---	---	---	---	41.030

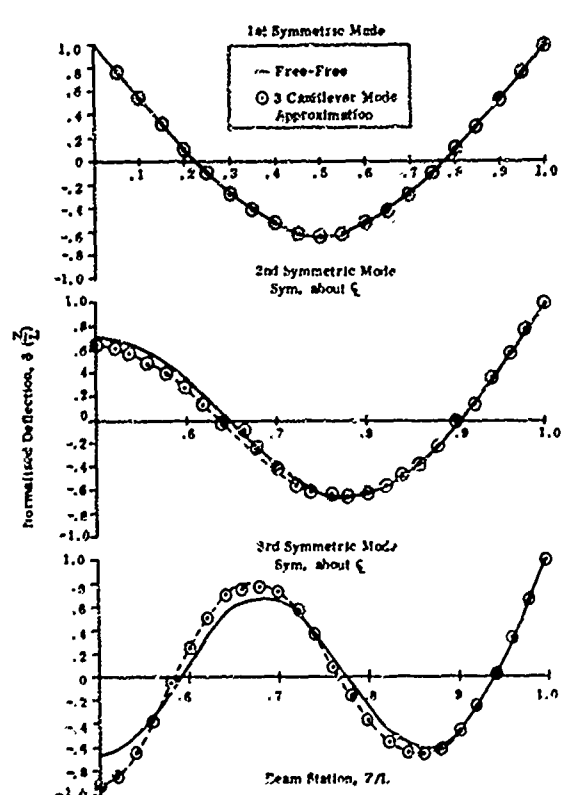


Fig. 12. Comparison of Mode Shapes for a Free-Free Uniform Beam and a 3 Cantilever Mode Approximation

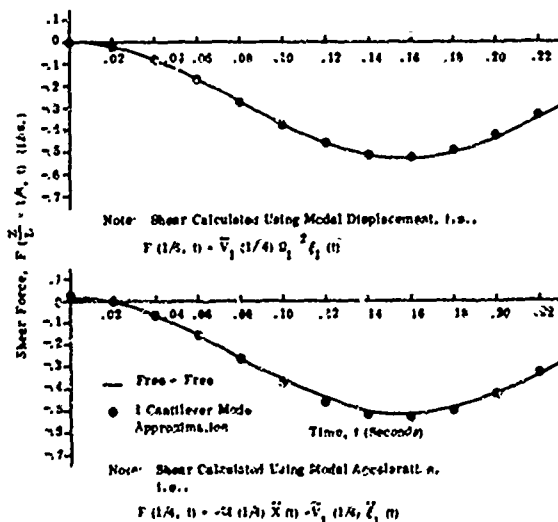


Fig. 13. Comparison of Cantilever & Free-Free Beam Shear at 1/2 Span vs. Time for a Unit Step Force Applied at Mid-Span.

Figure 13 also contrasts the modal acceleration and modal displacement methods of computing total load. The calculation of force history corresponding to the modal displacement method was made independently of the simulation. At the one-quarter span, the differences in loads from the two methods were not significant. With respect to computing total (quasi-steady plus dynamic) loads, Bisplinghoff [10] points out the desirability of the modal acceleration method

which is the method used in the simulation. The comparisons given by Figure 13 show an excellent agreement between the simulation results and those obtained by an independent method utilizing the variable order Adams numerical integration technique.

Figure 14 presents a comparison of simulation results using five cantilever modes with independently calculated results using free-free modes. The low frequency waveform and magnitude in both histories is seen to be in good agreement. The small differences in the high frequency content between the histories are attributable to the degree of convergence in approximating the given number of free-free modes by the same number of cantilever modes.

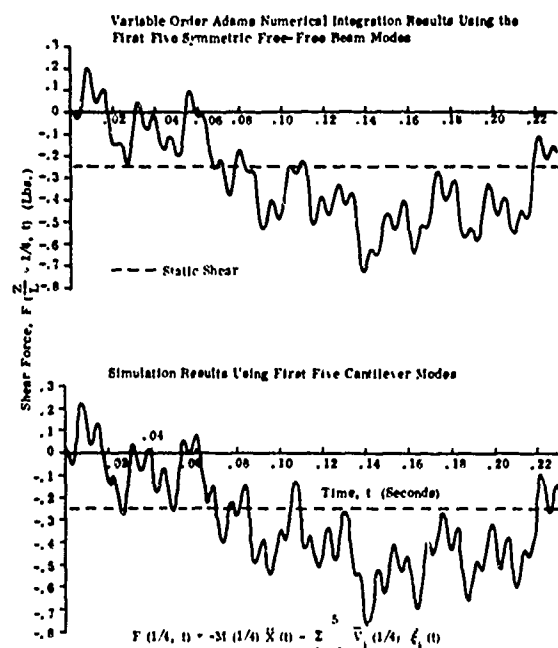


Fig. 14. Uniform Beam Comparisons of Shear Histories @ 1/4 Span for a Unit Step Force Applied at Mid-Span

Figure 15 presents a comparison of simulation results using five cantilever modes with results obtained using the Nastran "Direct Transient Response Method" [5]. The free-free beam representation was discretized into 40 masses for use in this method. Modal truncation was not considered in this method; each of the discrete masses was allowed two inertial degrees of freedom corresponding to planar bending of the beam. In general, good agreement exists between the frequency content of the two shear histories. Also, the maximum shear force given by the histories is in excellent agreement.

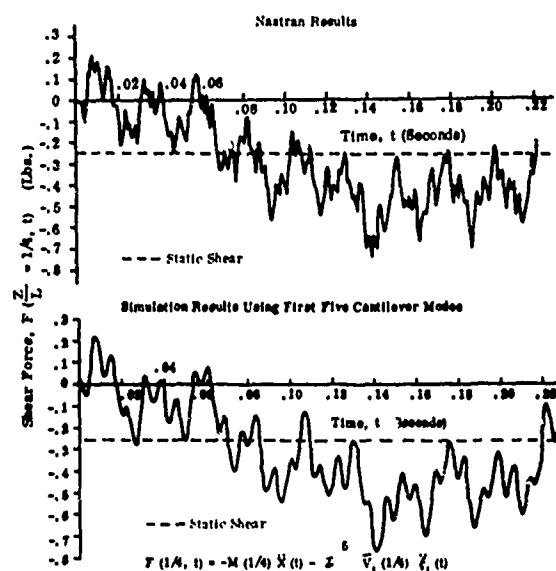


Fig. 15. Uniform Beam Comparisons of Shear History @ 1/4 Span for a Unit Step Force Applied at Mid-Span

A mode-by-mode comparison of the maxima shear force components derived from the simulation and those given in Reference 8 is presented in Figure 16. Again, the differences indicated are attributable to the degree of convergence in approximating the given number of free-free modes by the same number of cantilever modes.

The above presented comparisons between the cantilever and free-free beam response results demonstrated that the structural dynamics methodology contained in the simulation was sufficient for the accurate evaluation of interaction loads.

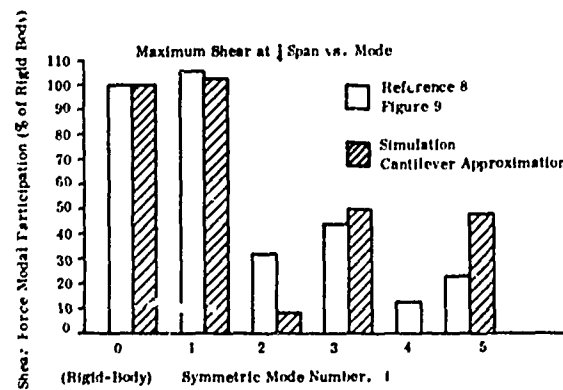


Fig. 16. Comparison of Modal Shear Force Participation for a Uniform Beam Subjected to a Unit Step Load Applied at Mid-Span

## TYPICAL SIMULATION RESULTS

An extensive analysis of the parameters that influence the structural dynamics of solar arrays is planned. This analysis will form the basis of a generalized dynamic design criterion for solar array structures. Although this analysis has not been completed, some preliminary results have been obtained.

The solar array/space station concept being evaluated is shown in Figure 17. The space station is a rather stiff structure (modeled as a rigid body) which contains 96.5% of the total mass. The solar array is a large flexible structure composed of membrane strips stretched between the inner and outer structural support members. An extendible boom in the center of each vane applies a tension load to the membrane strips. The solar cells and associated interconnects are cemented to the membrane substrate and generate the power required for space station operations. This array was designed by the Lockheed Company under Contract NAS9-11039 and is reported in Reference 11.

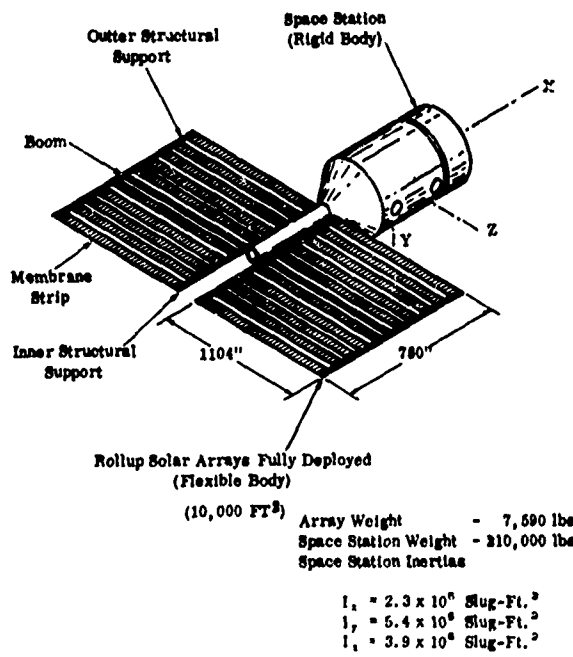


Fig. 17. Space Station/Solar Array Concept for Dynamic Interactions Study (Rollup Flexible Array)

A structural analysis was performed on these solar arrays prior to simulation to obtain required modal data. The matrix method of structural analysis considered in Reference 12 was utilized. The array was modeled using a discrete mass technique with 200 mass points, each mass having

3 degrees of freedom. The stiffness of the array membrane was considered as a function of applied tension loading, and the central boom was modeled as a beam column. A detailed description of the structural modeling and resultant modal data is reported in Reference 3. Selected frequencies are listed in Table 2 in terms of in-plane and out-of-plane modes.

The selections of modes to be used in the simulation was made on the basis of those contributing a large percentage of load participation. Load participation for symmetric modes is evaluated by calculating the shear at the array attachment point due to a base translational acceleration. The participation is equal to  $(\sum m_i \phi_i)^2 / R_n \sum m_i$  where  $m_i$  is the discrete mass,  $\phi_i$  is the modal deflection coefficient and  $R_n$  is the modal mass. Load participation for anti-symmetric modes is evaluated by calculating the moment at the array attachment point due to a base rotational acceleration. This participation function is equal to  $(\sum m_i \phi_i r_i)^2 / R_n \sum m_i r_i^2$  where  $r_i$  is the distance from the vane axis of the array to the mass point. A typical mode shape is shown in Figure 18 for an out-of-plane anti-symmetric mode. The load participation factor for this mode was 67.7%. The results of the analysis also indicate that modes with a significant load participation fall within the frequency bandwidth of the space station attitude control system. Therefore, coupling of the attitude control system with array modes can be expected.

Selected results from one simulation are presented and correspond to the configuration of Figure 17 with small initial attitude errors. The space station was perturbed by a force history representing the docking of an orbiting module. The disturbance force is directed along the X axis of the space station. The continuous OCS drive system was used in this simulation for array control.

Figure 19 is a graphical series of results from this simulation. The docking load profile and resulting roll axis acceleration, is given in Figure 19a. It is seen from Figure 19a that the magnitude of feedback force from the flexible arrays upon the space station is small because of the non-oscillatory nature of the acceleration history. Figure 19b shows the initial array orientation errors with respect to the sun vector as a function of time. Figure 19c shows the time variations of modal acceleration for two array modes - an out-of-plane mode forced primarily by OCS torque and an in-plane bending mode forced primarily by space station acceleration. Space station control torques were not initiated during this simulation since the angular dead-band contained within the reaction jet control system

TABLE 2  
Frequencies and Modal Participation Factors of Selected Rollup Array Modes

Out of Plane					
Symmetric			Antisymmetric		
Mode	Frequency (Hz)	Percent Participation	Mode	Frequency (Hz)	Percent Participation
6	.0734	50.4	6	.0557	67.7
36	.203	12.5	31	.162	5.4
56	.287	3.5	57	.318	7.3
			62	.340	7.7
In-Plane					
Symmetric			Antisymmetric		
Mode	Frequency (Hz)	Percent Participation	Mode	Frequency (Hz)	Percent Participation
2	2.26	57.0	1	.291	55.0
			2	1.94	3.1
			7	2.71	6.5
			8	4.12	2.7

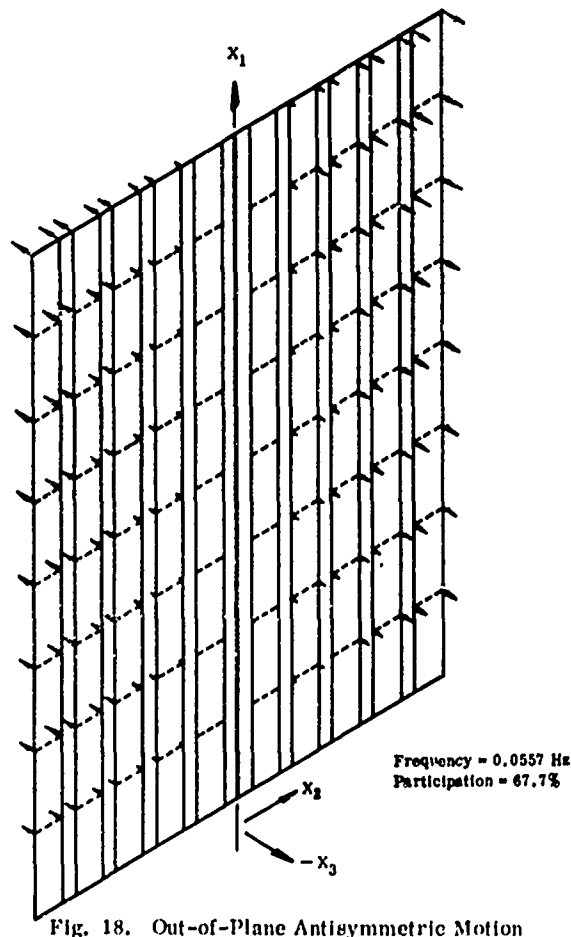


Fig. 18. Out-of-Plane Antisymmetric Motion

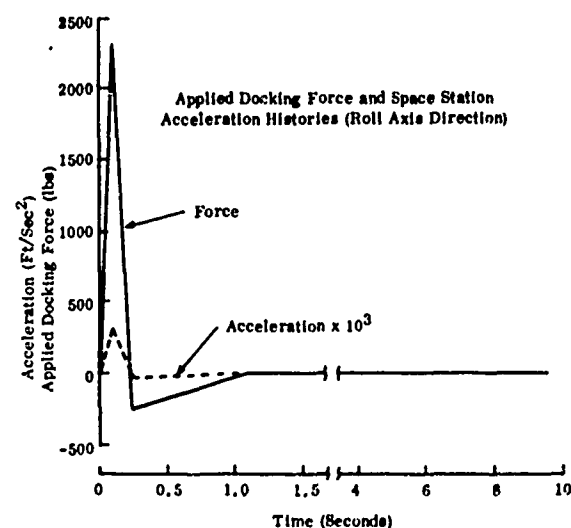


Fig. 19 (a). Simulation Results for an Externally Applied Docking Force

was not exceeded. Figure 19d presents the time variation of interaction force along the space station X axis and interaction moment about the space station Y axis. Initial high frequency transient loads are seen to decay rapidly. This is caused by a relatively high value (0.05) of the input modal damping parameter. These limited results which are presented show the type of design data that can be obtained from this digital simulation of the integrated dynamic analysis. A complete set of data, corresponding to variations

In initial parameters and basic structural data, will provide the basis for the derivation of a structural design criterion.

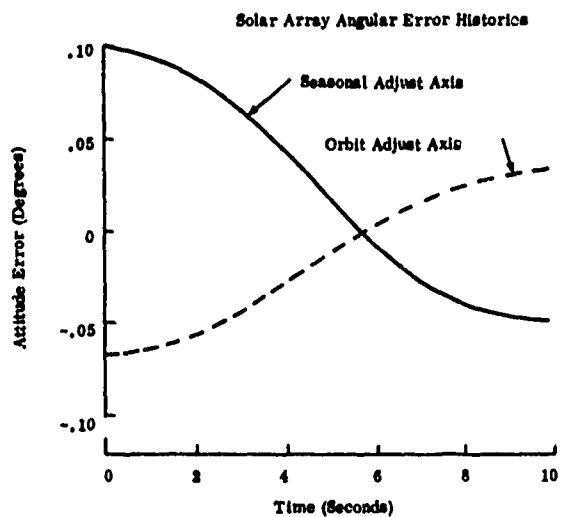


Fig. 19. (b)

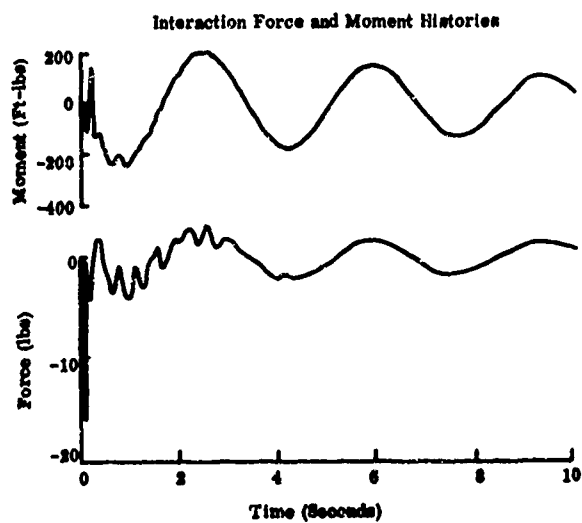


Fig. 19. (d)

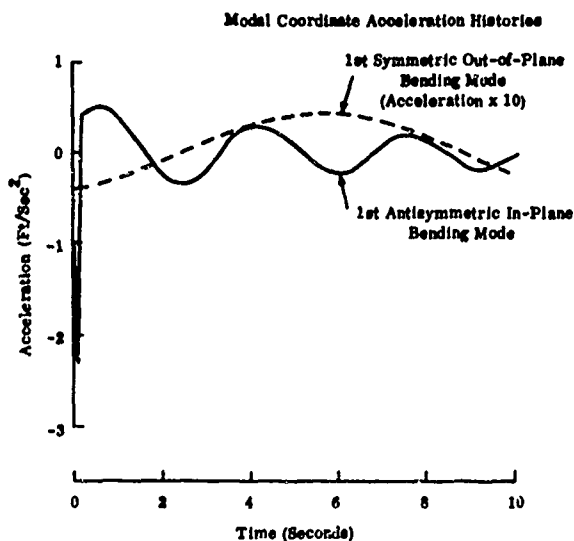


Fig. 19. (c)

## CONCLUSIONS

An integrated dynamic analysis method has been developed and implemented in a digital computer program for simulating the structural dynamic interactions between a space station and controllable solar arrays. Simulation verification studies demonstrated that the analytical formulation and the modal synthesization technique employed provide an accurate method for evaluation of dynamic interactions. In addition, the verification studies showed the programming of the simulation to be correct.

## REFERENCES

1. P. W. Likins and H. K. Bouvier, "Attitude Control of Non-rigid Spacecraft," *J. Astronautics and Aeronautics*, May 1971/Vol. 9 No. 5 Pg. 64-71.
2. "Preliminary Synthesis and Simulation of the Selected CMG Attitude Control System," General Electric Report EL-506-D, 5 March 1970, General Electric Company, Binghamton, New York.
3. "Interim Report, The Study of Dynamic Interactions of Solar Arrays with Space Stations and Development of Array Structural Requirements" Fairchild Industries Report 8581R-1, February 1971, Fairchild Industries, Germantown, Maryland.
4. P. W. Likins, "Dynamics and Control of Flexible Space Vehicles" Jet Propulsion Laboratory Technical Report 32-1329, Revision 1, January 15, 1970.
5. "The NASTRAN Theoretical Manual", NASA SP-221, Section 11.3, 1970, Office of Technology Utilization, NASA, Washington, D. C.
6. R. H. Lyddane, "Small Eccentricities or Inclinations in the Brouwer Theory of the Artificial Satellite," *Astronomical Journal*, Volume 68, No. 8, October 1963, p. 555.
7. "Structural Interaction Simulation System", Technical Report R104, Revision I, Wolf Research and Development Corporation, Riverdale, Maryland.
8. R. W. Leonard, "On Solutions for the Transient Response of Beams", NASA Technical Report R-21, 1959.
9. D. Young and R. P. Felgar, Jr., "Tables of Characteristic Functions Representing Normal Modes of Vibration of A Beam," University of Texas Publication No. 4913, 1 July 1949.
10. R. L. Bisplinghoff and H. Ashley, *Principles of Aeroelasticity*, pp. 344-350. John Wiley and Sons, Inc., 1962.
11. "Evaluation of Space Station Solar Array Technology and Recommended Advanced Development Programs", First Topical Report LMSC-A981486, Lockheed Missiles & Space Company, December 1970.
12. "Stardyne User's Manual", Mechanics Research Inc., Document, Los Angeles, California, January 1971.

## DISCUSSION

Mr. Zudans (Franklin Institute): When you indicated on one of these diagrams the docking force introduced into the system, how was it introduced relative to the mass-center of the system? You seem to be getting the moments, but there were no indications on the slide as to how this was done.

Mr. Weinberger: In this particular case the docking force was applied at the aft end of the space station along the axis of the space station. There were some out-of-plane motions. These motions were due primarily to a slight misalignment of the solar arrays that were active with a linear control system. This means that even 0.1 of a degree attitude error would cause some motion of the solar arrays, and hence some torques into the system. But the docking force was applied along the axis of the space station. There was no eccentric force or loading.

Mr. Mains (Washington University): You said at one step that you were using a 600 degree-of-freedom system for analysis. Is that correct?

Mr. Weinberger: That is correct.

Mr. Mains: Did you use a direct integration technique to get those response curves that you showed?

Mr. Weinberger: Yes we did.

Mr. Mains: How do you have any handle on the meaning, the reliability, of a solution of that size for this kind of problem?

## DISCUSSION

Mr. Weinberger: The 600 degrees of freedom simply referred to the structural analysis model that was developed. From the structural analysis model, the generalized mass and modal coordinates were used for the modes that were selected. In this case we used 12 modes, so the 12 elastic modes were used for the solar arrays plus the 6 rigid body degrees of freedom for the space station. We did not have a 600 degrees of freedom model for direct integration.

Mr. Mains: Did you then do an eigenvalue solution on the 600 degrees of freedom?

Mr. Weinberger: Yes. We did it to get the frequencies and the mode shapes and the generalized masses.

Mr. Mains: How do you have any handle on the reliability of an eigenvalue solution of that size?

Mr. Weinberger: I think the reliability of structural models of that size is fairly well documented, for example, in the NASTRAN program and users manual.

Mr. Mains: You might be surprised if you would check the orthogonality of the vectors sometime.

Mr. Zudans: I would like to comment more on these questions, because 600 degrees of freedom dynamically today is nothing. You can handle 3,000 and there is a perfect orthogonality. The NASTRAN program and many other programs use the inverse iteration routine with spectral shapes and it is very, very reliable. However, I wanted to ask a question. How did you account for obvious nonlinear attitudes in your solar array? It is such a flexible structure that it could not be handled as a linear one.

Mr. Weinberger: We are examining this problem in connection with the tension loads that are transmitted through the boom and so on. This is one of the areas in which we have made certain assumptions in linearizing. The validity of these assumptions has not been established at this point, although we do have some preliminary test data from Lockheed on the array of this type. This was a Lockheed array geometry that we were studying. From what we have been able to ascertain, we have chosen the model in such a way that the results agree fairly well with the test data. We get a correlation in that respect. This is the only way that we can have any confidence in the linearization of the array.

Mr. Clevensen (Langley Research Center): If I understood you correctly, you used NASTRAN for verifying some of your results?

Mr. Weinberger: That's right.

Mr. Clevensen: Why could not you have used NASTRAN exclusively and saved considerable work?

Mr. Weinberger: Of course one of the problems that we looked at was the coupling of the control system. I am not familiar with the NASTRAN program with regard to the demap instructions and the auxiliary usage of NASTRAN, other than for structural and vibration analysis. I assume that you might be able to code subroutines which represent the orientation control system and the rigid body mechanics. One thing that comes to mind immediately is the size of NASTRAN. We have been able to modularize this program in such a way that it uses much less digital computer time in core than the NASTRAN program would use. We felt it was more efficient in developing our own program, rather than to resort to the NASTRAN program.

## PARAMETRICALLY EXCITED COLUMN WITH HYSTERETIC MATERIAL PROPERTIES

D. T. Mozer  
IBM Corporation  
East Fishkill, New York

and

R. M. Evan-Iwanowski, Professor  
Syracuse University  
Syracuse, New York

An investigation is performed to determine the effects of hysteretic material properties on the dynamic response of parametrically excited systems. Expressions are developed for stress distributions, forces and moments for a parametrically excited column. Column response is determined for the stationary case with additional assumptions on material properties and stress distributions.

### INTRODUCTION

This paper is related to the description, simulation and means of minimizing the effects of mechanical vibration on technical hardware by means of a theoretical investigation of the effects of hysteretic material properties on the response of parametrically excited systems.

If an initially straight column, Fig. 1, is subjected to a periodic axial load,  $P(t) = P_0 + P_1(t) \cos\theta(t)$ , and if the maximum amplitude of the load is less than that of the static buckling (Euler) load,  $P_E$ , then the column experiences only longitudinal vibrations. There are, however, certain relationships between the disturbing frequency  $\delta(t) = v(t)$  and the natural frequency  $\Omega$  of transverse vibrations of the column for which the straight column becomes dynamically unstable and lateral vibrations occur. For a sufficiently small value of  $P_1(t)$  one such relationship between  $\delta(t)$  and  $\Omega$  is  $\delta = 2\Omega$ . The response which occurs under these conditions is called parametric resonance. This phenomenon of parametric resonance may be expressed more generally as  $v(t)/2\Omega = 1/m$  where  $m = 1, 2, 3, \dots$

For increasing values of  $P_1(t)$  the points of instability mentioned above cover instability regions. That is, there exist continuous ranges of the values of  $v(t)$  for which the column will be unstable, in  $\{v/2\Omega, P_1/2(P_E - P_0)\}$  space.

The largest of these instability regions, and thus the most important region, is the first region characterized by  $v = 2\Omega$ . Consequently this paper is concerned with the nature of vibratory motion of the column related to this region.

Our discussion thus far has implied, among other things, that the material of the column

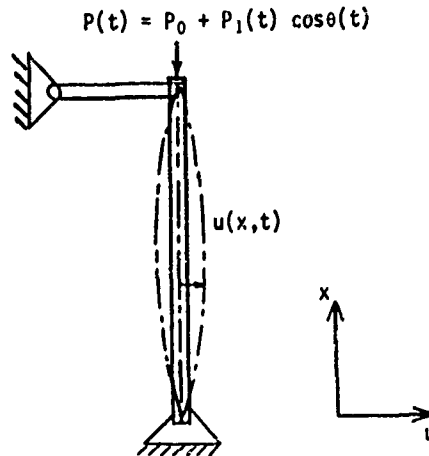


Fig. 1 - Column Configuration

obeys Hooke's law. It is well known that few solids actually obey Hooke's law very closely. Of these few solids, many are used in structural members. The principal reasons for their use are: (1) they display nearly Hookean behavior to a relatively high stress level, (2) over-all structure cost, (3) over-all structure weight.

In many instances, however, it is desired to have machine or structural members perform multiple functions. For example it may be desirable to have a column perform both as a column and as an electrical or thermal conductor. In this case the selection of the material will be based on some compromise between its load carrying capabilities and its electrical or

thermal conductivity. Such situations may present the necessity to use materials whose mechanical properties are non-Hookean over-all but the smallest stress levels. Once we leave the domain of the Hookean solid elastic column, a large field opens up even to the most casual observer. The number and complexity of the material properties, along with their relatively crude rheological models becomes overwhelming if one attempts to apply them with rigor to the problem of the parametrically excited column, (an exhaustive discussion is given in Ref. 1).

Several authors have considered material properties other than the simple Hookean case in the analysis of the parametrically excited column. K. K. Stevens [1], for example, solves for the cases of the Maxwell Element and the Three-Parameter Model as material properties for the stationary case. The case of a simple viscous damper in parallel with a spring (Voigt Element) is shown in references treated for stationary and nonstationary modes. Later K. K. Stevens and R. M. Evan-Iwanowski [2] introduced the complex modulus material property representation to the stationary response of the parametrically excited column. It is important to note here that in this analysis energy dissipation occurs only due to the bending of the column and not due to its axial compression. V. V. Bolotin [3] considers amplitude dependent damping forces due to viscous and dry friction at an end support of the column, but these forces do not arise from the material properties of the column itself. Detailed discussion is also given by Mozer [4].

This paper deals with determination of regions of stability and instability as well as the lateral amplitude response of the axially excited column whose material properties are of the pointed hysteresis loop variety. The Davidenkov model is used to represent this material property.

### 1. BASIC RELATIONSHIPS

Davidenkov [5] developed relations to represent the behavior of metals in the form

$$\dot{\sigma} = E(c \pm \frac{y}{n}[(\epsilon_0 \mp \epsilon)^n - 2^{n-1} \epsilon_0^n]) \quad (1.1)$$

These relations depend only on the amplitude of the strain. It is graphically represented in Fig. 2.

The Davidenkov expressions have been used extensively by many authors, e.g. [6] to solve several classes of problems in which the material is assumed to have hysteresis loops of the form represented by (1.1).

#### Stress Distributions in Parametrically Excited Column.

It is the objective of this section to develop stress or strain distributions for the parametrically excited column. In some instances the expression for the moment on any column

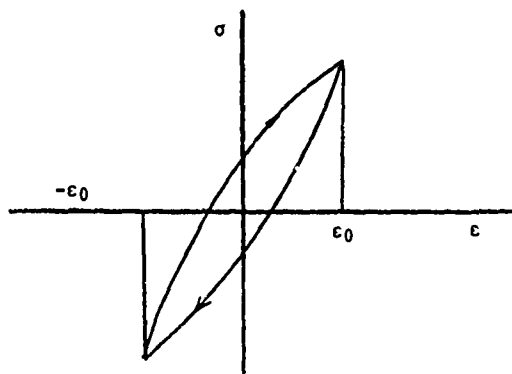


Fig. 2 - Davidenkov's Model

cross section at any time will be developed from the stress distributions. On other instances expressions for the temporal part of the motion of the column are derived.

Analysis of the system configuration yields the partial differential equation

$$\frac{\partial^2}{\partial x^2} [M] + P(t) \frac{\partial^2 u}{\partial x^2} + m \frac{\partial^2 u}{\partial t^2} = 0 \quad (1.2)$$

where  $M$  is the moment at any cross section and  $M = \int A \sigma y dA$ . We have made the usual Bernoulli-Euler assumptions, and the deflection  $u$  is regarded as small.

The strain at any point is

$$\epsilon = \epsilon_a + \frac{y}{\rho} c_a + y K = \epsilon_a + y \frac{\partial^2 u}{\partial x^2} \quad (1.3)$$

So far the treatment is for any material property.

Consider now the stresses in the column whose material property is such that it is characterized by a pointed hysteresis loop. We know already that in the principal region of instability the frequency of lateral response of the column is half that of the excitation frequency. Thus the period of the bending stresses will be twice the period of the periodic portion of the axial stresses. In addition these two stresses will in general be out of phase. A typical stress strain diagram for a fiber at some distance from the neutral axis is presented in Fig. 3.

In Fig. 3 the small loop is due to the periodic axial load and the larger loop is due to the slower periodic bending. The period of the total loop is the same as the period of lateral motion of the column. The loop contains four distinct branches. If the bending is reduced the picture is altered to look somewhat like that shown in Fig. 4. If the bending is removed completely, the two loops converge into a single two branch loop, the period of which is

the same as the period of  $P(t)$ .

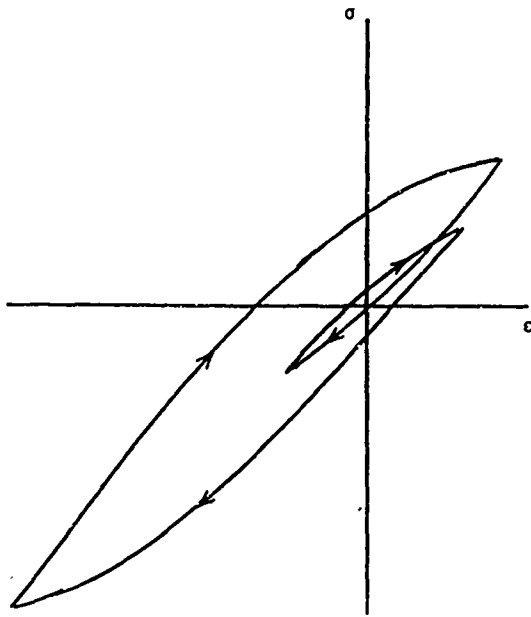


Fig. 3 - Stress strain in a fiber of a column with hysteretic material. Large moment.

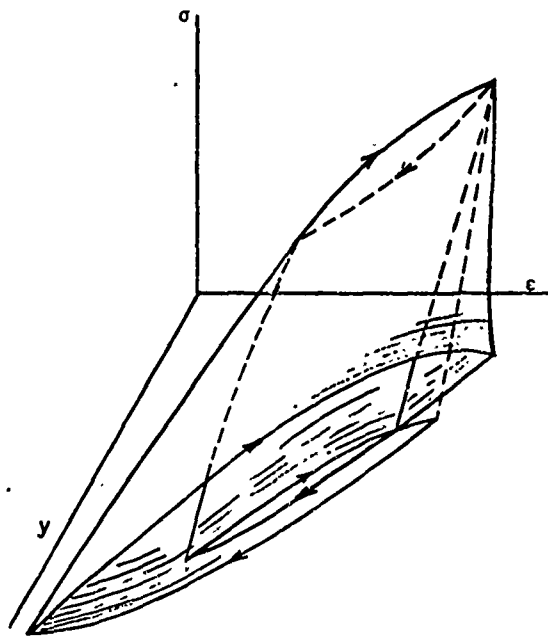


Fig. 5 - Stress strain in a cross section of a column with hysteretic material.

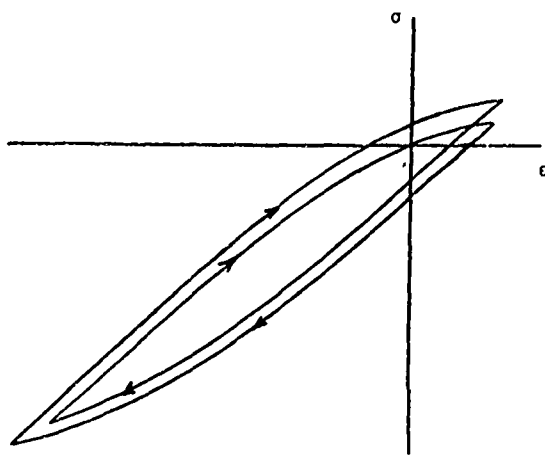


Fig. 4 - Stress strain in a fiber of a column with hysteretic material. Small moment.

The stress strain distribution at a cross section of the column will be somewhat like that shown in Fig. 5.

The stresses on a cross section of the column are such that at certain times three branches of the four branches of the loop are present. Thus for a material having a pointed hysteresis loop, we require several equations to represent the stress across the column at different times. Each equation contains two or three terms corresponding to the different branches of the hysteresis loop present in a cross section.

The use of the Davidenkov relations in the case of the parametrically excited column where axial stresses are taken into account is in general not possible since the constants in the relations will not always allow the loop to close after a complete cycle of the column. However, if one assumes that the strains due to bending and the strains due to the axial load are in phase, then it is possible to write equations for a four branch loop based on the Davidenkov relations. The evaluation of the constants in the resultant expressions is difficult since they depend on the distance from the neutral axis,  $y$ .

## 2. RESPONSE OF COLUMN WITH POINTED LOOP MATERIAL HYSTERESIS

We make the additional assumption that the axial stresses are small and will not contribute appreciably to the column response. This assumption is a fairly good one for the slender column. Under the assumptions made, moment acting on a cross-section is

$$M = E I \frac{\partial^2 u}{\partial x^2} + \bar{c} \frac{\partial}{\partial x} \left( \frac{\partial^2 u}{\partial x^2} \right) \quad (2.1)$$

where  $\bar{\epsilon}$  is a small parameter such that  $\bar{\epsilon} > 0$ ,  $\bar{\epsilon} \ll 1$  and where

$$\hat{\phi} \left( \frac{\partial^2 u}{\partial x^2} \right)$$

is the dissipation functional depending only on the curvature and material constants. The arrows above  $\hat{\phi}$  represent the branches corresponding to increasing and decreasing curvature. Substituting (2.1) into (1.2), we get

$$EI \frac{\partial^4 u}{\partial x^4} + \bar{\epsilon} \frac{\partial^2}{\partial x^2} [\hat{\phi} \left( \frac{\partial^2 u}{\partial x^2} \right)] + P(t) \frac{\partial^2 u}{\partial x^2} + m \frac{\partial^2 u}{\partial t^2} = 0 \quad (2.2)$$

We seek a solution to equation (2.2) of the form

$$u(x,t) = f(t) \sin \frac{\pi x}{L} \quad (2.3)$$

Substituting these values into (2.2) we get

$$EI \frac{\pi^4}{L^4} \sin \frac{\pi x}{L} f(t) + \bar{\epsilon} \frac{\partial^2}{\partial x^2} [\hat{\phi} \left( \frac{\partial^2 u}{\partial x^2} \right)] - P(t) f(t) \frac{\pi^2}{L^2} \sin \frac{\pi x}{L} + m \ddot{f}(t) \sin \frac{\pi x}{L} = 0 \quad (2.4)$$

In order to make any headway toward solving (2.4) we need to know more about the functional  $\hat{\phi}$ . We rewrite the equation for Davidenkov's model

$$\hat{\sigma} = E[\epsilon \mp \frac{y}{n} [(c_0 \pm \epsilon)^n - 2^{n-1} c_0^n]] \quad (2.5)$$

and the definition for the moment

$$\hat{M} = \int_A \hat{\sigma} y dA$$

and also noting that

$$\epsilon = y \frac{\partial^2 u}{\partial x^2}$$

in the case where the axial strains are neglected. We may now substitute the above value for  $\epsilon$  from (2.5) and substitute the resulting expression for the stress into  $M$  we get

$$\begin{aligned} \hat{M} = EI \int_A y^2 \frac{\partial^2 u}{\partial x^2} dA \mp \frac{EY}{n} \int_A \left[ \left( \frac{\partial^2 u}{\partial x^2} \right)_{\max} \pm \right. \\ \left. \pm \frac{\partial^2 u}{\partial x^2} \right]^n - 2^{n-1} \left( \frac{\partial^2 u}{\partial x^2} \right)_{\max}^n y^{n+1} dA \end{aligned} \quad (2.6)$$

$$\hat{M} = EI \frac{\partial^2 u}{\partial x^2} \mp \frac{EY}{n} \int_A \left[ \left( \frac{\partial^2 u}{\partial x^2} \right)_{\max} \pm \frac{\partial^2 u}{\partial x^2} \right]^n -$$

$$- 2^{n-1} \left( \frac{\partial^2 u}{\partial x^2} \right)_{\max}^n y^{n+1} dA \quad (2.7)$$

Comparing (2.7) with (2.1) we deduce that

$$\begin{aligned} \bar{\epsilon} \hat{\phi} = \mp \frac{EY}{n} \int_A \left[ \left( \frac{\partial^2 u}{\partial x^2} \right)_{\max} \pm \frac{\partial^2 u}{\partial x^2} \right]^n - \\ - 2^{n-1} \left( \frac{\partial^2 u}{\partial x^2} \right)_{\max}^n y^{n+1} dA \end{aligned} \quad (2.8)$$

Substituting the value for  $u$  from (2.3) into (2.8) and differentiating twice with respect to  $x$ , we get

$$\begin{aligned} \bar{\epsilon} \frac{\partial^2 \hat{\phi}}{\partial x^2} = \int_A \mp \frac{EY}{n} \left\{ \frac{\pi^2}{L^2} n [(n-1) \sin^{n-2} \frac{\pi x}{L} - \right. \\ \left. - n \sin^n \frac{\pi x}{L} \cdot [(-f(t))_m \mp f(t)]^n - \right. \\ \left. - 2^{n-1} (-1)^n f(t)_m^n] \right\} y^n \cdot y dA \end{aligned} \quad (2.9)$$

where  $f_m(t)$  is the maximum value of  $f(t)$ . It can be shown that the expression  $\mp EY/n \{ \dots \} y^n$  in (2.9) is always odd about  $y = 0$  regardless of the value of  $n$ . Thus the total integrand of (2.9) is always even. Due to this property we may integrate the above expression from zero to  $h/2$  and multiply by two instead of integrating from  $-h/2$  to  $+h/2$ . This removes the necessity to keep track of the signs of  $y$  and  $\epsilon$ . Thus

$$\begin{aligned} \bar{\epsilon} \frac{\partial^2 \hat{\phi}}{\partial x^2} = \mp \frac{2 EY}{n} \int_0^{h/2} \left\{ \frac{\pi^2}{L^2} n [(n-1) \sin^{n-2} \right. \\ \left. \frac{\pi x}{L} - n \sin^n \frac{\pi x}{L} \right\} \left( \frac{\pi}{L} \right)^{n+2} [(-f(t))_m \mp f(t)]^n - \\ - 2^{n-1} (-1)^n f(t)_m^n \} y^{n+1} dy \end{aligned}$$

where  $W$  indicates the width of the column. Integrating the above, we obtain

$$\begin{aligned} \bar{\epsilon} \frac{\partial^2 \hat{\phi}}{\partial x^2} = \mp \frac{2 EY W \pi^{n+4}}{L^{n+4}} \left\{ [(n-1) \sin^{n-2} \frac{\pi x}{L} - \right. \\ \left. - n \sin^n \frac{\pi x}{L} ] [(-f(t))_m \mp f(t)]^n - 2^{n-1} (-1)^n \right. \\ \left. f(t)_m^n \right\} \left( \frac{h}{2} \right)^{n+2} \frac{1}{n+2} \end{aligned} \quad (2.10)$$

We consider the special case where  $n = 2$

$$\bar{\epsilon} \frac{\partial^2 \ddot{f}}{\partial x^2} = \mp \frac{EY W h^6}{32 L^6} \left\{ [1 - 2 \sin \frac{2\pi x}{L}] \cdot \right. \\ \cdot [(f(t)_m^2 + 2 f(t)_m f(t) + f(t)^2 - \\ \left. - 2f(t)_m^2)] \quad (2.11)$$

Equation (2.11) represents the distributed lateral load due to dissipative material properties. We now substitute (2.11) into (2.4) and apply Galerkin's method by multiplying the resultant by  $\sin nx/L$  and integrating, we get

$$2EI \frac{\pi^4}{L^4} \frac{L}{\pi} f(t) - 2P(t) f(t) \frac{\pi^2 L}{L^2 \pi} + \\ + 2m \ddot{f}(t) \frac{L}{\pi} \mp \frac{EY W h^6 \pi^5}{48 L^5} \cdot [-f(t)_m^2 + \\ + 2 f(t)_m^2 f(t) + f(t)^2] = 0 \quad (2.12)$$

Remembering that  $P(t) = P_0 + P_1 \cos \theta$  and

$$P_E = EI \frac{\pi^2}{L^2}$$

is Eulers' buckling load and

$$\omega = \frac{\pi^2}{L^2} \frac{E\bar{I}}{m}$$

is the transverse natural frequency of the column without axial load and the transverse natural frequency of the column loaded by  $P_0$  is

$$\Omega = \omega \sqrt{1 - \frac{P_0}{P_E}}$$

We also denote the loading parameter  $\mu$  as

$$\mu = \frac{P_1(t)}{2(P_E - P_0)}$$

Substituting these relationships in (2.12) and rearranging, we get,

$$\ddot{f} + \Omega^2 (1 - 2\mu \cos \theta) f \mp \frac{EY W h^6 \pi^6}{96 L^6 m} \cdot \\ \cdot [f^2 + 2 f_m f - f_m^2] = 0 \quad (2.13)$$

Equation (2.13) represents the temporal equation of the motion of the column, and is the subject of the following asymptotic solution.

#### Asymptotic Solution

Only the first approximation will be sought in this analysis. We rearrange (2.13) in the

form

$$\ddot{f} + \Omega^2 f = \pm \bar{\epsilon}\beta [f^2 + 2f_m f - f_m^2] + \\ + \bar{\epsilon}2\Omega^2 \mu \cos \theta f \quad (2.14)$$

$$\text{where } \bar{\epsilon}\beta = \frac{EY W h^6 \pi^6}{96 L^6 m}$$

and the term  $2\Omega^2 \mu$  has been replaced by  $\bar{\epsilon}2\Omega^2 \mu$ . Note that if (2.14) were expanded we would get the term  $\pm \bar{\epsilon}\beta 2f_m f$ . It would appear at first glance that the coefficient  $\pm \bar{\epsilon}\beta 2f_m$  could be combined with  $\Omega^2$  on the left hand side of (2.14). It must be noted, however, that this term is actually a variable coefficient of  $f$  due to the alternating signs and we are thus justified in leaving it on the right hand side of the equation. We represent (2.14) in the form

$$\ddot{f} + \Omega^2 f = \bar{\epsilon}F(f, \theta, \tau) \quad (2.15)$$

where

$$F(f, \theta, \tau) \equiv F = \pm \beta [f^2 + 2f_m f - f_m^2] + \\ + 2\Omega^2 \mu f \cos \theta$$

We seek a solution to (2.15) in the form

$$f(t) \equiv f = a(t) \cos \left( \frac{\theta}{2} + \psi(t) \right) \quad (2.16)$$

We have assumed analysis of the first instability region only by using the angular displacement term  $\theta/2$  in (2.16). The terms  $a(t)$  and  $\psi(t)$  are to be determined from the usual relations,

$$\dot{a} = \bar{\epsilon}A_1(\tau, a, \psi) \quad (2.17)$$

$$\dot{\psi} = \Omega - \frac{v}{2} v(t) + \bar{\epsilon}B_1(\tau, a, \psi) \quad (2.18)$$

After some calculation we find:

$$\dot{a} = - \frac{E Y W h^6 \pi^6 (4a_m^2 - a^2)}{96 L^6 m 2\pi\Omega} - \frac{a\Omega^2 \mu}{v} \sin 2\psi \quad (2.19)$$

$$\dot{\psi} = \Omega - \frac{v}{2} - \frac{E Y W h^6 \pi^6 a_m}{96 L^6 m \Omega} - \frac{\Omega^2 \mu}{v} \cos 2\psi \quad (2.20)$$

#### Stationary Response

We now proceed to determine the stationary response of the column by investigating (2.19) and (2.20) in a special case. Stationary response is defined as the case where no system parameter changes with time. Explicitly we write  $v(t) = \text{constant}$ ,  $\mu(t) = \text{constant}$  which implies that  $\dot{a} = \dot{\psi} = 0$ . Under these conditions (2.19) and (2.20) become

$$-\frac{\beta_1}{2\pi\Omega} (4a_m^2 - a^2) - \frac{a\pi^2\mu}{v} \sin 2\psi = 0 \quad (2.21)$$

$$\Omega - \frac{v}{2} - \frac{\beta_1 a_m}{\Omega} - \frac{\Omega^2 \mu}{v} \cos 2\psi = 0 \quad (2.22)$$

where

$$\beta_1 = \frac{E\gamma Wh^4\pi^6}{96L^6m} \quad (2.23)$$

Eliminating  $\psi$  from these equations while noting that  $a_m = a = \text{constant}$  for the stationary case, we get the following

$$a = \frac{2\pi^2\Omega}{\beta_1(4\pi^2 + 9)} (2\Omega - v \pm [(2\Omega - v)^2 - \frac{(4\pi^2 + 9)((2\Omega - v)^2 - \Omega^2\mu^2)}{\pi^2}]^{\frac{1}{2}}) \quad (2.24)$$

The  $\pm$  sign denotes the possibility of two solutions for  $a$ .

We may now determine the stationary phase angle  $\psi$  from (2.21) a using the value of  $a$  from (2.24)

$$\begin{aligned} \psi = \frac{1}{2} \sin^{-1} \left( -\frac{3v\pi}{2\Omega\mu(4\pi^2 + 9)} [2\Omega - v \pm \right. \right. \\ \left. \left. [(2\Omega - v)^2 - \frac{(4\pi^2 + 9)((\Omega - \frac{v}{2})^2 - \Omega^2\mu^2)}{\pi^2}]^{\frac{1}{2}} \right) \right] \quad (2.25) \end{aligned}$$

The so-called "backbone curve" of the stationary response is that curve lying halfway between the two values of  $a$  obtained from (2.24). It is

$$a_B = \frac{2\pi^2\Omega(2\Omega - v)}{\beta_1(4\pi^2 + 9)}, \quad \beta_1 = \frac{E\gamma wh^4\pi^6}{96L^6m}$$

The boundaries of instability zone are:

$$v = \Omega [1 \pm \sqrt{1 \pm 2\mu}]$$

Applying well known steps in determination of stable or unstable branches, we obtain the following: For  $d a_0/dv > 0$  the solution is stable if

$$2\Omega - v + 2 \frac{\beta_1 a_0}{\Omega} - 4 \frac{\Omega^2 \mu^2}{v^3} > 0 \quad (2.26)$$

and for  $d a_0/dv < 0$  the solution is stable if

$$2\Omega - v - 2 \frac{\beta_1 a_0}{\Omega} - 4 \frac{\Omega^2 \mu^2}{v^3} < 0 \quad (2.27)$$

The region of stability is distinguished from the region of instability by the curve represented by

$$a = \frac{\Omega(2\Omega - v)}{2\beta_1} - \frac{2\Omega^5 \mu^2}{\beta_1 v^3} \quad (2.28)$$

called "stability curve". The stable and unstable branches of the phase angle  $\psi$  are found to be

$$(\Omega - v)/\frac{d\psi}{dv} < 0 \quad (2.29)$$

Hence the solution stable for  $v \neq 2\Omega$  and  $d\psi/dv > 0$ , otherwise it is unstable.

### 3. RESULTS AND CONCLUSIONS

#### Discussion of Material Properties and Stress Distributions.

The significance of the harmonic axial load on column response is demonstrated. Stress distributions in the column are also illustrated for the pointed loop hysteretic material.

Stationary response curves for the parametrically excited column whose material may be represented by the Davidenkov Model with the special assumption that the axial stresses are negligible are plotted in Figs. 6-10. Fig. 6 and Fig. 7 show the effect of varying the load parameter  $\mu$  on the column response, Fig. 8 shows the effect of varying the Davidenkov model parameter  $\gamma$ , while Fig. 9 shows the change of the first instability region with amplitude of response. Fig. 10 shows the instability region in three dimensions.

It is seen from Fig. 6 and Fig. 8 that the point defined by  $da/dv = 0$  separates the region for which non-trivial stable solution can exist to the right and the region for which no non-trivial stable solutions can exist to the left,  $n$ ,  $\mu$ ,  $P_0$  and  $\gamma$  being constant. This means that no non-trivial solutions exist for  $\gamma/2\Omega$  less than that at which  $da/dv = 0$ . This result has not been frequently observed in the literature, although it can be shown that the response curve of a parametrically excited column having nonlinear damping of the form  $df^2$  where  $d$  is the nonlinear damping coefficient and structural nonlinear elasticity does close at the backbone curve in a similar manner to the present case. It is further noted that as long as  $\gamma$  is positive the backbone curve leans toward decreasing frequencies, characterizing soft systems. (Negative  $\gamma$  implies that the material property is such that it generates energy over a cycle). Pisarenko [6] arrives at dynamic response curves for various problems using the Davidenkov relations which have also soft characteristics, but beyond this, comparison of results loses most of its meaning since Pisarenko analyzes systems near dynamic resonance, and the present work is concerned with systems near parametric resonance.

It is seen from Fig. 9 that the curve defining the region of instability for zero amplitude of vibration is the same as that for the perfectly elastic case. The authors believe that this is due to the fact that the axial stresses were considered small. The coupling of the bending and the axial stress probably would have provided a more significant dissipation term for  $a = 0$  and thus the curve would have been shifted slightly to the right from  $\mu = 0$ ;  $v/2\Omega = 1$  and would have been rounded somewhat, similar to the case where linear velocity dependent damping is included. In the case considered the energy dissipation per cycle is proportional to  $\gamma^3$  and so the curves in Fig. 9 defining the region of instability shift to the right and become rounded with increasing amplitude.

The downward shift in the curves defining the region of instability with increasing amplitude may be due to the nature of the maximum point locus curve for the Davidenkov model:

$$\omega_0 t = E \left( \frac{1}{n} \epsilon_0 + \frac{\gamma}{n} \epsilon_0^2 \right) \quad (3.1)$$

This equation contains a nonlinear component proportional to  $\epsilon_0^2$  which is symmetric, due to the alternating sign. Lazan [7] indicates that the maximum point locus curve may be an appropriate one to use for the calculation of stored energy in material. In our case this "nonlinear elastic" term is probably the most appropriate one to use in explaining the nonlinear character of the column response. From Fig. 9 one can further note that in the present case regions of instability exist for large values of  $a$  which do not exist in the linear elastic damped case. For example, in Fig. 9 let our system be described by state  $v/2\Omega = 0.9$  and  $\mu = 0.13$  (for the elastic case, our system is stable). Let the system now be perturbed such that  $zh/L > .0013$ . Under these conditions the system finds itself in a region of instability and a large amplitude results.

One must approach the problem of selecting a mathematical model to represent the real material of the parametrically excited column (or in fact any vibratory system) with extreme caution. If one attempts to use a strictly linear mathematical relationship to represent a material whose characteristics are essentially nonlinear, large errors may arise in the prediction of system vibratory response even though care is taken to see that energy dissipation per cycle is the same as the real material; see Mentel and Fu [8], for example.

Biot's linear hysteretic model is perhaps the best linear hysteretic model to extend for use with multi-frequency excitations as encountered in the parametrically excited column or plate. It possesses the characteristic of amplitude dependent damping found in most engineering materials and it results in a well defined mathematical problem at least for the single frequency case. If the addition of a

second frequency to the response of the model does not unduly complicate subsequent use in the governing equations then such work would constitute a valuable contribution. It may also be possible to incorporate into this model the nonlinear elastic effects without difficulty. Such nonlinear elasticity could be obtained from experimental data on the maximum point locus curve.

#### REFERENCES

1. K. K. Stevens, "On the Parametric Excitation of a Viscoelastic Column," A.I.A.A. Journal, Vol. 4, No. 12, Dec. 1966.
2. K. K. Stevens, R. M. Evan-Iwanowski, "Parametric Resonance of Viscoelastic Columns," Int. J. Solids Structures, Vol. 5, pp. 755-765, 1969.
3. V. V. Bolotin, The Dynamic Stability of Elastic Systems, Holden-Day, Inc., San Francisco, London, Amsterdam, 1964.
4. D. T. Mozer, "Parametrically Excited Column with Dissipative Material Properties," M.S. Thesis, Syracuse University, Syracuse, N.Y., 1969.
5. N. N. Davidenkov, "Energy Dissipation in Vibrations," J. Tech. Phys., 8, No. 6, p. 483, 1938.
6. G. S. Pisarenko, Dissipation of Energy in Mechanical Vibrations, (in Russian), Kiev, Izd-Vo Akad Nauk, USSR, 1962.
7. B. J. Lazan, Damping of Materials and Members in Structural Mechanics, Pergamon Press, Inc., 1968.
8. T. J. Mentel, C. C. Fu, "Analytical Formulation of Damped Stress-Strain Relations Based on Experimental Data with Applications to Vibrating Structures," ASD Technical Report, p. 61-63, 1961.

#### LIST OF SYMBOLS

A	Area of cross section of column
E	Young's Modulus
h	Depth of column in y direction
I	Moment of inertia about Z axis
K	Curvature 1/r
L	Length of column
m	Mass per unit length
n, σ	Material constants
P <sub>E</sub>	Euler's Load
P(t)	Axial load $P_0 + P_1(t) \cos \theta(t)$
P <sub>0</sub>	Static compressive load
P <sub>1</sub> (t)	Amplitude of dynamic load
W	Width of column
x	Axial coordinate end
y	Distance from neutral axis.
Z	Coordinate
ε, ε <sub>0</sub>	Total normal strain, Maximum strain
ε <sub>α</sub>	Normal strain due to $P_0 + P_1 \cos \theta$
ε̄	Small positive quantity

$\rho$  Radius of curvature  
 $\sigma$  Normal stress  
 $\omega$  Natural frequency of column  
 $\Omega$  Natural frequency of column with  $P_0$   
 $\theta(t)$  Angular displacement load  
 $v(t)$  Frequency load =  $\dot{\theta}(t)$   
 $\mu$  Load parameter  $P_1/2(P_E - P_0)$

### FIGURES

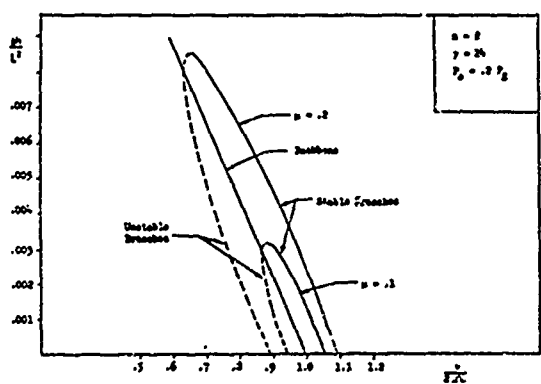


Fig. 6 - Effect of Varying  $\mu$  on Amplitude

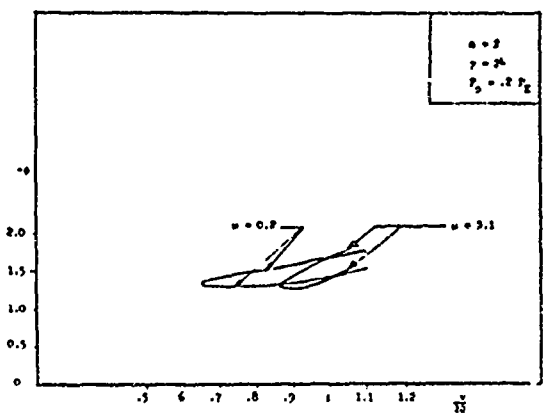


Fig. 7 - Effect of Varying  $\mu$  on Phase Shift  $\phi$

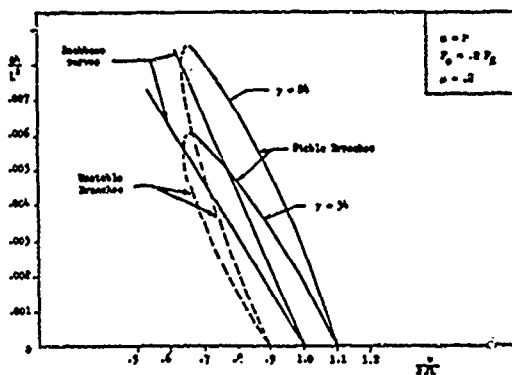


Fig. 8 - Effect of Varying  $\gamma$  on Amplitude

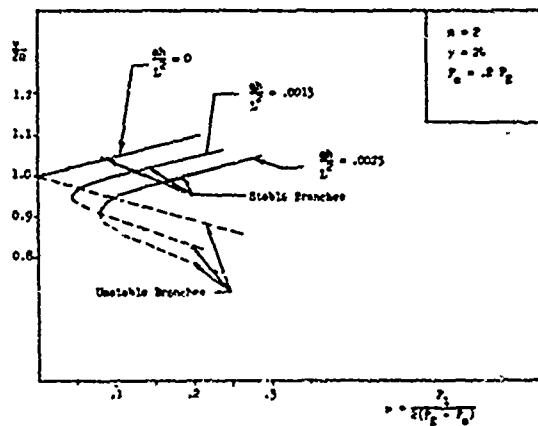


Fig. 9 - Change of Instability with Increasing Amplitude

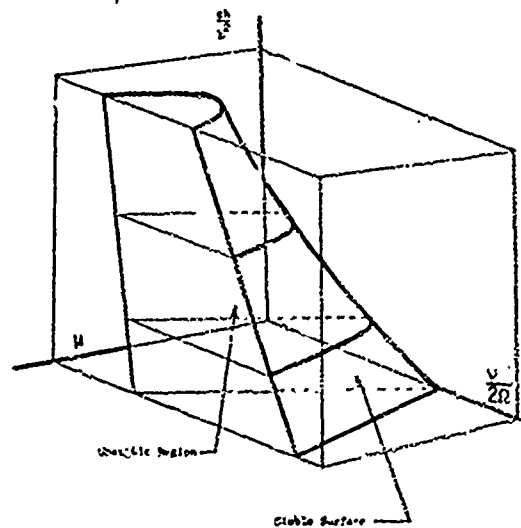


Fig. 10 - Three Dimensional Representation of Instability Region

## DISCUSSION

Mr. Zudans (Franklin Institute): You surprised me with very poor orthogonality. Was that mainly because of the use of experimental modes which had not been orthogonalized before their usage?

Mr. Stahle: The orthogonality referred to the abbreviated model test. The criterion that we had set up was that the measured experimental mode would check within 10 percent - not the analytical modes. The problem is the very limited amount of instrumentation used on the solar array panels. I think our main confidence was gained from the fact that the frequencies matched up very well, and that the main structural modes agreed relative to the modal admittance through the base shear.

Mr. Prause (Battelle Institute): What are some of the important frequencies? We saw a lot of natural frequencies in the presentation but what are the control system frequencies and what are the pogo frequencies for this type of space stations?

Mr. Stahle: This is the Earth Resources Technology Satellite which is a fairly small, 2,000 pound, space craft going up on the Thor Delta. The main pogo frequency varies somewhere between 17 and 23

Hertz. It was in this general frequency range that we were concerned. We had a number of modes which, through increased growth of the spacecraft, had gradually crept down into the pogo frequency range. We were also concerned with some of the large amplitude modes like the first longitudinal which actually went as high as 55 Hertz.

Mr. Schrantz (Comsat Labs): Did you couple your model with the Thor Delta to check out the responses?

Mr. Stahle: This is done by Douglas personnel. The model that we have been using is the model that I presented here. Essentially it is a modal model using modal coupling techniques to marry the spacecraft back to the launch vehicle. It follows the basic inertial coupling procedures of component synthesis discussed in the literature to couple this analytical representation of the spacecraft back to the launch vehicle.

\*The paper was presented and discussed by C. V. Stahle for the authors.

DYNAMIC INTERACTION BETWEEN  
VIBRATING CONVEYORS AND SUPPORTING STRUCTURE

Mario Paz  
Professor, Civil Engineering Department  
University of Louisville  
Louisville, Kentucky

and

Oscar Mathis  
Design Engineer, Rex Chainbelt Inc.  
Louisville, Kentucky

The dynamic analysis of the conveyor-structure system is presented using the stiffness method and an iterative scheme in which the structure and the vibrating conveyor are analyzed successively taking into account interacting effects. An example of a structural truss supporting a vibrating conveyor is given.

#### INTRODUCTION

Vibrating conveyors are widely used in industry for conveying granular-type material [1]. Depending on specific applications, these conveyors could weigh from a few hundred pounds to several tons. The main components are the pan or trough where the material is conveyed, a driving mechanism which produces rectilinear motion at an angle with regard to the horizontal direction, and a system of springs which connects the trough to a base, absorbers, or boosters, depending on the type of conveyor [2].

Usually the conveyors are supported to a rigid foundation through isolation springs, but, in some cases, they are suspended from or supported by a structural system. When vibrating conveyors are supported by a frame or truss, the dynamic forces which are transmitted to the supporting structure result in vibration of and interaction between the structure and the conveyors.

The dynamic analysis of the conveyor-structure system is presented using an iterative scheme where the three dimensional structure and the two dimensional conveyor are analyzed successively taking into account interacting effects. First, by assuming the

the supporting structure is rigid, the dynamic analysis of the conveyor is performed. Then the structure is analyzed under the effect of the reactive forces at the points of support of the conveyor. From this analysis the motion of the points of support is determined and used as boundary conditions in repeating the analysis of the conveyor. This iterative scheme continues, and the new reactive forces are applied in repeating the analysis of the structure, and after a few cycles, the final results are reached.

#### ANALYSIS

The vibrating conveyor and the supporting structure are analyzed independently by the dynamic stiffness method where the system is divided into a number of members, each having known elastic and inertial properties.

Dynamic forces and moments at the ends of each member are expressed in terms of the displacements and rotations at the ends, giving the so-called element dynamic stiffness matrix [3]. Basically, this result can be achieved by solving the appropriate equation of motion. The system dynamic stiffness matrix is assembled from element matrices using the conditions of continuity between elements and equilibrium at the

Preceding page blank

joints; the latter will include any applied external force and the forces from all the elements forming the joint. Equilibrium conditions at the joints result in n equations relating the applied external forces to the independent joint displacements of the system. The n equations may be written as

$$[S]\{u\} = \{F\} \quad (1)$$

$[S]$  is an  $n \times n$  symmetric matrix composed of terms derived from the dynamic stiffness matrices of the component elements of the system,  $\{u\}$  is a vector of the  $n$  independent joint displacement in the system, and  $\{F\}$  is a vector of the external forces which are exciting the structure at frequency  $w$ .

Vibrating conveyors are manufactured in a variety of types, ranging from a single moving deck to three or more vibrating masses. In this presentation the so-called "dynamic booster conveyor" is described in relation to the dynamic problem originated by the interaction between vibrating conveyors and supporting structures. As shown in Fig. 1, the dynamic booster conveyor consists of a trough supported by isolation springs, a drive unit connected through leaf springs to the trough, and a series of spring-mass assemblies known as dynamic boosters.

The drive unit houses two motors, one above the other, with double extended shafts to which eccentric masses are affixed. The motors rotate in opposite directions producing a horizontal harmonic force.

The dynamic boosters are tuned at a natural frequency in the neighborhood of the operating frequency of the motors. The boosters function as dynamic absorbers [4] for the component of the impressed force along the direction of the boosters. As a consequence of this absorbing action, the trough vibrates harmonically along a direction approximately normal to the orientation of the boosters.

In the analysis of the conveyor the boosters are treated as rigid bodies connected elastically to the trough. The trough is assumed to be composed of continuously connected beams with distributed and concentrated masses. The drive unit as well as the connecting leaf springs is considered to be a special beam element, and the isolation springs are treated as massless elastic members.

Diagrams for the basic elements of the booster conveyor are shown in Figs. 2 through 4, and the corresponding dynamic stiffness matrices are given in the appendix. The coordinates indicating joint displacements at the ends

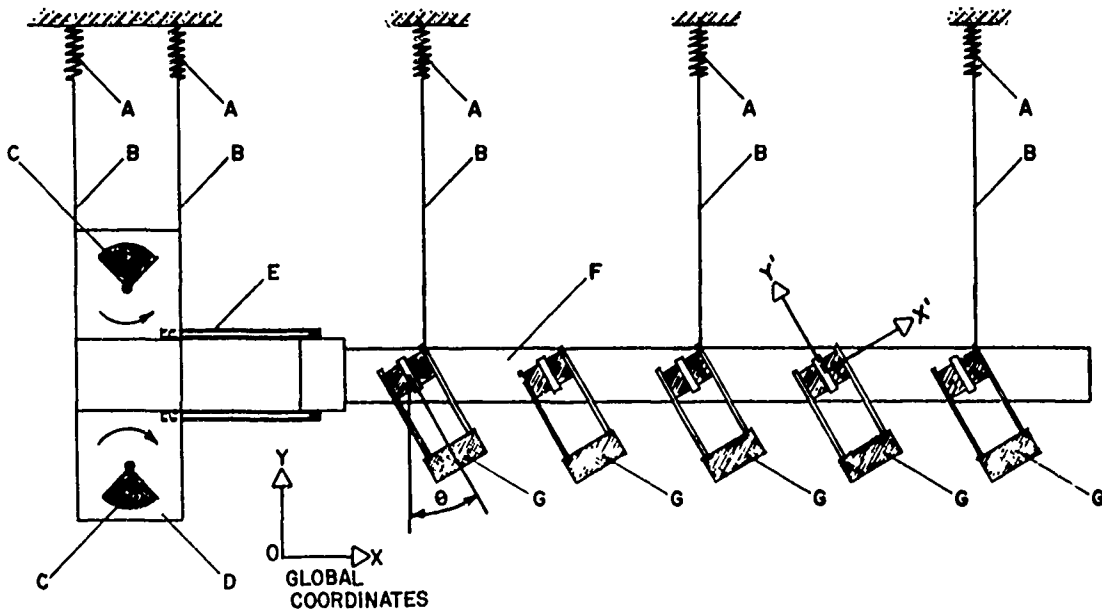


Fig. 1 - Dynamic booster conveyor

of the elements are numbered consecutively.

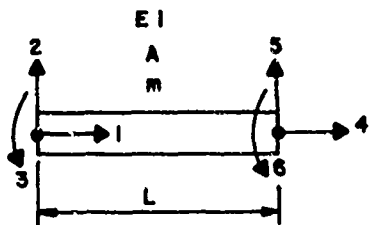


Fig.2 - Conveyor beam element

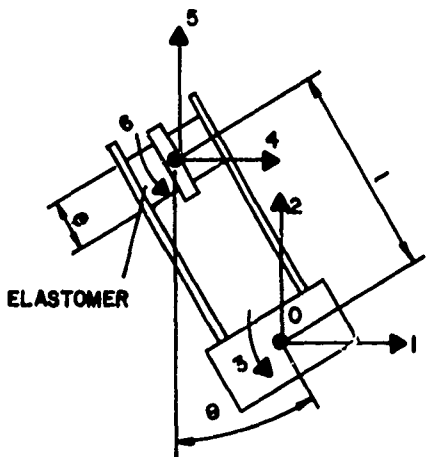


Fig.3 - Dynamic booster element

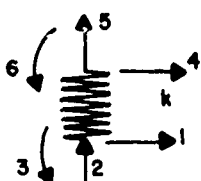


Fig.4 - Isolation spring element

#### SUPPORTING STRUCTURE

Installations of conveyor supporting structures vary from complex three dimensional frames and trusses to simple building floor systems. A space truss is used in the interaction example presented.

In general, any member of the truss, although assumed to be ideally pin connected at its ends, may undergo, under the action of inertial forces, flexural deformation in each of the two principal planes in addition to the extensional deformations along the longitudinal axis. It is assumed that for each individual element of the system these three deformations are uncoupled; thus, the dynamic stiffness matrix for the element of the truss is obtained independently for the two flexural deformations in each of the principal planes and for the axial deformations.

The dynamic stiffness matrix for a uniform pin-jointed bar element shown in Fig.5 is obtained by solving the corresponding Bernoulli-Euler differential equation for flexural deformation and the wave equation for the axial and by introducing the appropriate boundary conditions. The dynamic stiffness matrix for the pin-jointed bar element is given in the appendix.

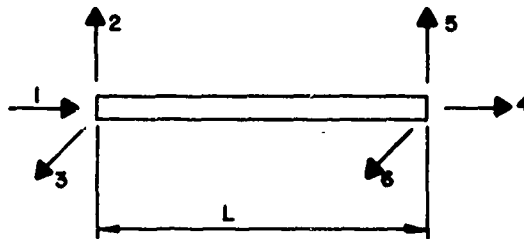


Fig.5 - Pin-jointed bar element

#### EXAMPLE

A dynamic booster conveyor supported by a truss type bridge between two buildings is presented to illustrate the interaction analysis.

Fig. 6 shows the schematic diagram of the space truss supporting the conveyor. As explained above, the conveyor is analyzed initially under the action of the driving force and the condition of zero displacements at the supporting points. Then, the reactive forces are applied in performing the analysis of the truss to obtain the first approximation for the displacements at the points of support of the conveyor. In the next cycle these dynamic displacements are imposed as external actions on the conveyor. The first four cycles of the interacting effects between the conveyor and the supporting structure are shown in Table I.

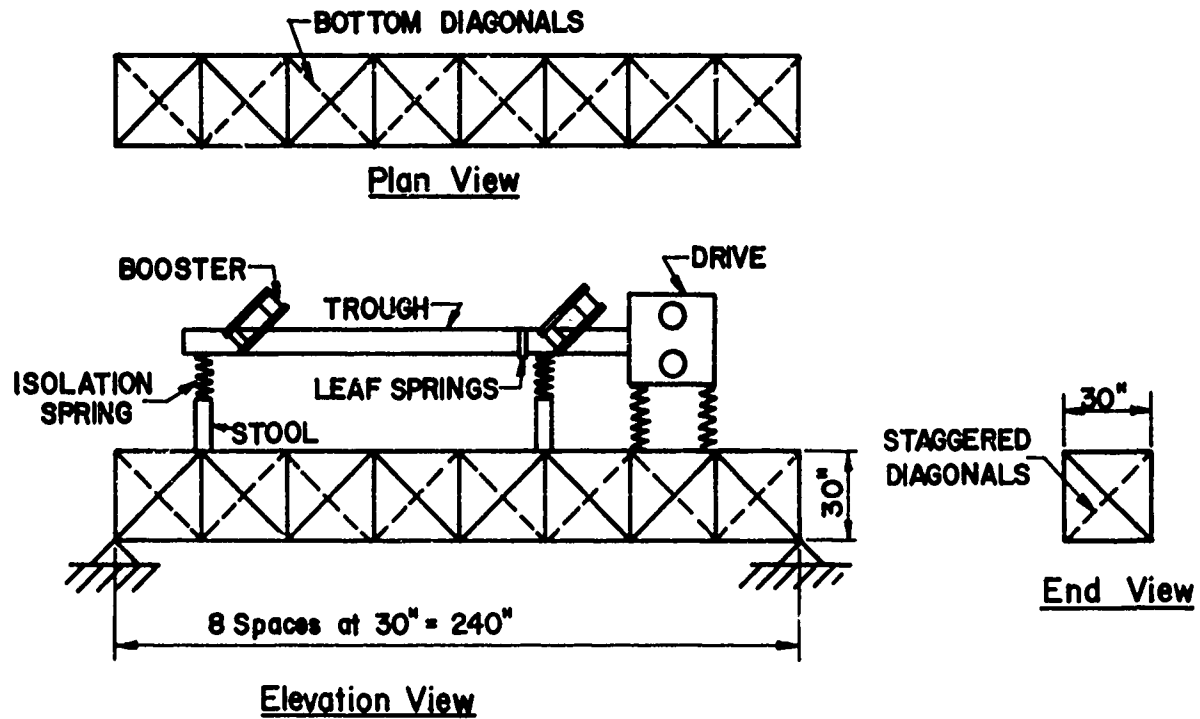


Fig.6 - Example space truss supporting vibrating conveyor

TABLE I  
Interaction Results

(a) Amplitude of truss vibration at conveyor supports (in.)

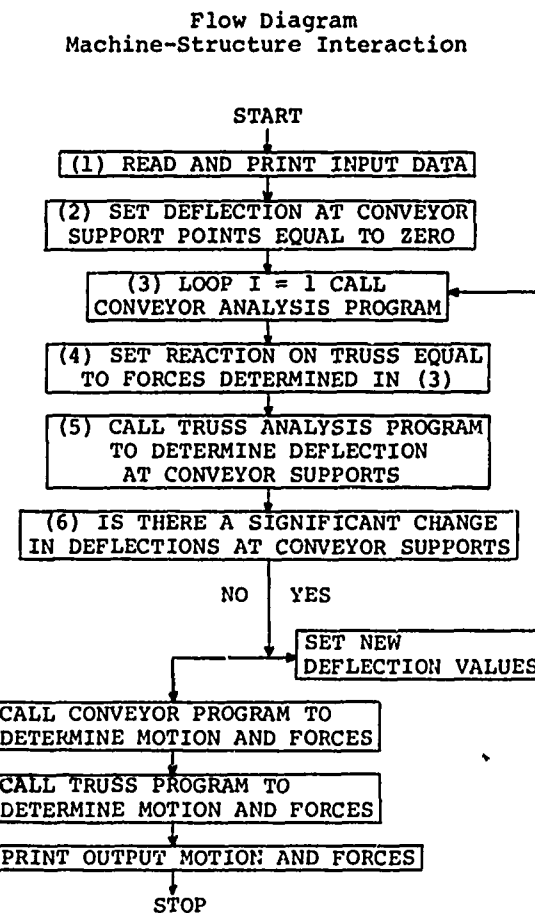
Cycle	Support 1		Support 2		Support 3		Support 4	
	Horizontal	Vertical	Horizontal	Vertical	Horizontal	Vertical	Horizontal	Vertical
1	0	0	0	0	0	0	0	0
2	-0.0077	-0.0370	0.0022	-0.0830	0.0082	-0.0998	0.0389	-0.0480
3	-0.0365	-0.0710	-0.0198	-0.1560	-0.0045	-0.1890	0.0600	-0.0770
4	-0.0390	-0.0730	-0.0200	-0.1590	-0.0053	-0.1940	0.0620	-0.0800
5	-0.0390	-0.0730	-0.0200	-0.1580	-0.0052	-0.1940	0.0620	-0.0800

(b) Amplitude of conveyor reactive forces at supports (lbs.)

Cycle	Support 1		Support 2		Support 3		Support 4	
	Horizontal	Vertical	Horizontal	Vertical	Horizontal	Vertical	Horizontal	Vertical
1	339	-172	203	-106	175	-33	139	-75
2	153	-123	162	-111	178	-62	204	-71
3	133	-132	153	-110	173	-48	237	-71
4	136	-132	153	-110	173	-48	239	-71

## NOTES ON COMPUTATIONAL METHOD

A computer program in Fortran IV is developed for the analysis of the space truss, the dynamic booster conveyor, and the iterative procedure as described in this paper. The flow diagram of the computer program follows.



The prescription of imposed displacements at the points of conveyor support may be programmed for a digital computer such that there results a reduction in the total number of equations to be solved. In order to avoid rearrangement of computer storage, however, it is often more convenient to proceed with the direct solution by implementing a computational device due to Payne and Iron and referred to by Zienkiewicz (5). The diagonal coefficient of the dynamic stiffness matrix corresponding to the equation with imposed displacement is multiplied by a very large number (say  $10^{20}$ ); at the same time the corresponding force term of this equation is replaced by the product of the newly formed diagonal element and the prescribed displacement.

## CONCLUSIONS

An iterative method for the analysis for vibrating conveyors mounted on supporting structure has been presented. The two systems are analyzed separately using as boundary conditions the deflections and forces developed at the points where the conveyor is supported by the structure.

Several testing problems as well as actual cases of installation of conveyors supported by structural systems were analyzed by the iterative method. This study of the interaction of a vibrating conveyor and the supporting structure indicates that the method presented requires four to eight cycles to converge to the final solution.

## APPENDIX

The dynamic stiffness matrices for the basic elements of the booster conveyor and for the pin-jointed bar element of the truss shown in Figs. 2 through 5 may be written as follows:

### a.- Isolation Spring

$$\begin{bmatrix} K_t & 0 & -K_v & -K_t & 0 & K_v \\ 0 & K_a & 0 & 0 & -K_a & 0 \\ -K_v & 0 & K_R & K_v & 0 & K_R/2 \\ -K_t & 0 & K_v & K_t & 0 & K_v \\ 0 & -K_a & 0 & 0 & -K_a & 0 \\ -K_v & 0 & K_R/2 & K_v & 0 & K_R \end{bmatrix}$$

where:

$$K_a = \text{Axial spring constant}$$

$$K_v = 1/2 K_t L$$

$$K_R = 1/3 K_t L^2$$

$$L = \text{Length of the spring}$$

$$K_t = \text{Transverse Spring Constant}$$

b.- Conveyor Beam Element

$$\begin{bmatrix} EABN_b - M_i \omega^2 & & & & \\ 0 & D_a^2 Q - M_i \omega^2 & & & \\ 0 & D_a S_a H_{sa} & DP - J_i \omega^2 & & \\ -EABU_b & 0 & 0 & EABN_b - M_f \omega^2 & \\ 0 & -D_a^2 (S_a + H_{sa}) & D_a (C_a - H_{ca}) & 0 & D_a^2 Q - M_f \omega^2 \\ 0 & D_a (H_{ca} - C_a) & D (H_{sa} - S_a) & 0 & -D_a S_a H_{sa} & DP - J_f \omega^2 \end{bmatrix}$$

Symmetric

where:

$E$  = Modulus of elasticity

$A$  = Cross-sectional area

$B = (m\omega^2/EA)^{1/2}$

$\omega$  = Angular velocity of forcing frequency

$m$  = Mass per unit length

$L$  = Length of beam

$N_b = \cot(BL)$

$M_i$  = Concentrated mass at left end of beam

$a = (m\omega^2/EI)^{1/4}$

$I$  = Cross-sectional moment of inertia

$C_a = \cos(aL)$

$S_a = \sin(aL)$

$H_{ca} = \cosh(aL)$

$H_{sa} = \sinh(aL)$

$D = EIa/(1-C_a H_{ca})$

$S_b = \sin(BL)$

$C_b = \cos(BL)$

$U_b = \text{CCSEC}(BL)$

$Q = C_a H_{sa} + S_a H_{ca}$

$P = S_a H_{ca} - C_a H_{sa}$

$M_f$  = Concentrated mass at right end of beam

$J_i$  = Concentrated mass moment of inertia at left end of beam

$J_f$  = Concentrated mass moment of inertia at right end of beam

c.- Booster Element

$$\begin{bmatrix} C^2 K_c + S^2 K_s - m\omega^2 & & & & \\ SC(K_c - K_s) & SSK_c + CCK_s - m\omega^2 & & & \\ -CK_c l & -SK_c l & K_c (l^2 + e/12) - j\omega^2 & & \\ -(C^2 K_c + S^2 K_s) & SC(K_s - K_c) & CK_c l & C^2 K_c + S^2 K_s & \\ SC(K_s - K_c) & -(S^2 K_c + C^2 K_s) & SK_c l & SC(K_c - K_s) & S^2 K_c + C^2 K_s \\ 0 & 0 & -e^2 K_c / 12 & 0 & 0 & e^2 K_c / 12 \end{bmatrix}$$

Symmetric

where:

$C = \cos\theta$

$S = \sin\theta$

$K_c$  = Spring modulus-compression

$K_s$  = Spring modulus-shear

$m$  = mass of booster

$j$  = mass moment of inertia about point 0 (Fig. 3)

$l, e, \theta$  = (See Fig. 3)

d.- Pin-jointed Bar

$A_1$	0	0	$A_2$	0	0
0	$Q(z)$	0	0	$P(z)$	0
0	0	$Q(y)$	0	0	$P(y)$
$A_2$	0	0	$A_1$	0	0
0	$P(z)$	0	0	$Q(z)$	0
0	0	$P(y)$	0	0	$Q(y)$

where:

$$A_1 = EA\beta \cot \beta L$$

$$A_2 = -EA\beta \operatorname{cosec} \beta L$$

$$Q(r) = \frac{\alpha^3 EI}{2} \left( \cot \alpha r L - \coth \alpha r L \right)$$

$$P(r) = \frac{\alpha^3 EI}{2} \left( \operatorname{cosech} \alpha r L - \operatorname{cosec} \alpha r L \right)$$

$$\alpha_r^4 = \frac{m\omega^2}{EI_r} \quad (r = y, z)$$

$$\beta^2 = \frac{m\omega^2}{AE}$$

NOMENCLATURE

$A$  = Area

$E$  = Modulus of elasticity

$L, l, e, h$  = dimension

$G$  = Modulus of elasticity in shear

$I, I_y, I_z$  = Cross-sectional moment of inertia

$J_i, J_f$  = Mass moment of inertia

$J, J_x$  = Polar moment of inertia

$k_a, k_c, k_s$  = Spring constant

$M, m_i, m_j$  = Mass

$m$  = Mass per unit length

$\theta$  = Angle

$\omega$  = Angular velocity

REFERENCES

- (1) Paz, M. - Conveying Speed of Vibrating Equipment Publication No. 64-WA/MH-1 - ASME 1965
- (2) Hinkle, T. Rolland - Design of Machines Prentice-Hall, Inc. New Jersey 1957
- (3) Przemieniecki, J. S. - Theory of Matrix-Structural Analysis McGraw-Hill, New York 1968
- (4) DenHartog, J. P. - Mechanical Vibrations McGraw-Hill Book Company, Inc. 1956
- (5) Zienkiewicz, O. C. and Cheung, Y.K. The Finite Element Method in Structural and Continuous Mechanics McGraw-Hill Company, London 1967

DISCUSSION

Mr. Zudans (Franklin Institute): I do not think I understand your model. My impression is that dynamically you only considered the conveyor and that the truss was taken as a simple static structure without any dynamics considered in the process of analysis. Is that correct?

Mr. Paz: No, sir. The forces coming from the conveyor to the truss were dynamic forces and the truss was analyzed as a dynamic problem. The truss members had distributed mass. The paper shows the dynamic stiffness matrix for a truss which, although it is pin-connected at the ends, still has bending due to the inertia effect.

Mr. Zudans: Did you have your truss represented as a lumped mass system with dynamic degrees of freedom and not only static degrees of freedom?

Mr. Paz: Actually this was done by the co-author, but this is not the case presented here. This is the distributed mass case. It has a finite number of degrees of freedom because of the masses of the matrix method of structural analysis. But the equation to determine the dynamic stiffness for each element takes into account the distributed mass and elasticity.

## RESPONSE OF A SIMPLY SUPPORTED CIRCULAR PLATE

EXPOSED TO THERMAL AND PRESSURE LOADING

J.E.Koch

North Eastern Research Associates, Upper Montclair,N.J.

and

M.L.Cohen

North Eastern Research Associates, Upper Montclair,N.J.,and  
Stevens Institute of Technology, Hoboken,N.J.

Using classical plate theory, equations are derived for the response of a simply supported circular plate exposed to time dependent pressure and thermal loading. Results based on these equations are presented for several loading conditions and plate geometries. One interesting effect is the presence of thermally induced vibrations having rather substantial amplitude in some cases. In addition it was observed that the thermal stresses may be compressive at both the front and rear surfaces, and tensile in the center.

### INTRODUCTION

There has been, in the recent past, a sustained interest in the consequences of exposing a structure to time-varying thermal as well as mechanical loading conditions. One may readily envision situations in which this type of loading might occur. For example, in the environment of a nuclear event, a period of rapid and intense heating would soon be followed by a shock wave. Whereas the effect of a shock wave on various structures has received considerable study, both analytical as well as experimental, the effect of rapid heating has been given less attention.

The object of this study is to determine the response induced in a circular plate simply supported on its boundary, when exposed to such loading conditions. The regimes in which the dynamic effect and the thermal loading become important may then be identified.

The analysis is based on the thermoelastic equation of motion for flexure of a circular plate subjected to time dependent lateral loads and temperature distribution. Classical modal series methods are used together with the Mindlin-Goodman procedure for treating time dependent boundary conditions. The elastic properties have been assumed to be uniform and not temperature dependent. The applied pressure loading and the temperatures within the plate

are time dependent but assumed not to vary in the in-plane directions. Regarding the heat conduction problem as uncoupled, the temperature distribution and history are computed using a finite difference technique.

Results computed on the basis of these equations are presented for several loading conditions and plate geometries. One interesting result is that in some cases the rapid heating of such a plate by exposure to thermal radiation induces vibrations of substantial amplitude compared to the quasi-static displacements. Another result of the computations is the observation that the thermal stresses may be compressive on both the front and rear surfaces and tensile at the center. In effect there appear to be two stress-free surfaces.

### GENERAL FORMULATION

We wish to determine the displacements in a simply supported circular plate subjected to a uniform time-dependent pressure  $p(t)$  and a time-dependent temperature field  $T(z,t)$  which varies depth-wise through the plate. The problem shall be formulated along classical plate-theory lines wherein, briefly, the displacement  $w$  must satisfy the well known [1] thermoelastic-dynamic plate equation together with the appropriate boundary and initial conditions.

Preceding page blank

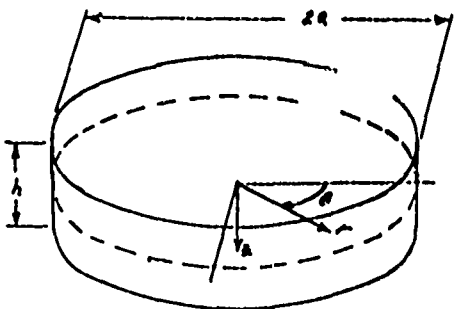


Figure 1 - Typical Circular Plate

Consider the thin circular plate of thickness  $h$  and radius  $a$ , as shown in Fig.1, with its median plane in the  $r-\theta$  plane and with  $z$  denoting the distance from this plane. Within this plate the displacement  $w$  must satisfy the governing differential equation

$$D\nabla^4 w + \rho h \frac{\partial^2 w}{\partial t^2} = p - \frac{1}{1-\nu} \nabla^2 M_r \quad (1)$$

where  $D = \frac{Ea^3}{12(1-\nu^2)}$

$$\nabla^2 = \frac{\partial^2}{\partial r^2} + \frac{1}{r} \frac{\partial}{\partial r} + \frac{1}{r^2} \frac{\partial^2}{\partial \theta^2}$$

$$M_r = \int_0^r \alpha E T z dz \quad (2)$$

Since the temperatures as well as the pressures are independent of  $r$  and  $\theta$ , this must be true of the thermal parameter  $M_r$  as well. Thus we may say that  $\nabla^2 M_r = 0$  in the above equation and omit derivatives with respect to  $\theta$ :

$$D\nabla^4 w + \rho h \frac{\partial^2 w}{\partial t^2} = p \quad (3)$$

$$\nabla^2 = \frac{\partial^2}{\partial r^2} + \frac{1}{r} \frac{\partial}{\partial r}$$

For the simply supported case we require that the moment  $M_r$  and the displacement  $w$  vanish on the boundary of the plate. Thus, on  $r=a$  for all  $t>0$ :

$$w = f_1(t) = 0 \quad (4)$$

$$M_r = -D \left[ \frac{\partial^2 w}{\partial r^2} + \frac{1}{r} \frac{\partial w}{\partial r} \right] - \frac{M_r}{1-\nu} = 0$$

or, alternatively:

$$\frac{\partial^2 w}{\partial r^2} + \frac{1}{r} \frac{\partial w}{\partial r} = -\frac{M_r}{1-\nu} = f_2(t) \quad (5)$$

Furthermore, we impose the condition that the resulting displacements and stresses be finite at  $r=0$ , the center of the plate.

Since no generality is lost if the effects of arbitrary initial conditions are not included, we choose the following conditions to apply at  $t=0$  for all values of  $r$ :

$$\begin{aligned} w &= 0 \\ \frac{\partial w}{\partial t} &= 0 \end{aligned} \quad (6)$$

#### DYNAMIC DISPLACEMENTS

We seek a solution to the governing equations together with the boundary and initial conditions in the following general form

$$w = \sum_{m=1}^{\infty} R_m(r) T_m(t) + \sum_{\lambda=1}^2 g_\lambda(r) f_\lambda(t) \quad (7)$$

in which  $R_m(r)$  are the normal functions arising from the free vibration problem, i.e.; the homogeneous solution.  $g_1(r)$  and  $g_2(r)$  are to be selected to satisfy the inhomogeneous boundary conditions.  $f_1(t)$  and  $f_2(t)$  represent the time dependency of the boundary conditions [2].

#### 1. Free Vibrations

The displacements of a plate vibrating freely satisfy the homogeneous form of the governing equation (3).

$$D\nabla^4 W_H + \rho h \frac{\partial^2 W_H}{\partial t^2} = 0 \quad (8)$$

Choosing a product solution of the form

$$W_H = R_n(r) e^{i\omega_n t}$$

we find that the normal function  $R_n(r)$  is composed of Bessel functions of the first and second kinds [3,4]:

$$\begin{aligned} R_n &= A_n J_0(\alpha_n r) + B_n I_0(\alpha_n r) \\ &\quad + C_n Y_0(\alpha_n r) + D_n Y_1(\alpha_n r) \end{aligned}$$

where:

$$\alpha_n = \alpha \sqrt{\frac{\rho h w_n^2}{D}} \quad (9)$$

The condition of finiteness of displacements at the center of the plate (at  $r=0$ ) requires that the coefficients  $C_n$  and  $D_n$  vanish. Applying the homogeneous form of boundary conditions (4) and (5) we obtain the normal function

$$R_n = I_0(\alpha_n r) J_0(\alpha_n r) - J_1(\alpha_n r) I_1(\alpha_n r) \quad (10)$$

and the frequency equation

$$\begin{aligned} & J_0(\alpha_n) I_0(\alpha_n) + I_0(\alpha_n) J_0(\alpha_n) \\ & = \frac{2\alpha_n}{1-\nu} J_0(\alpha_n) I_0(\alpha_n) \end{aligned} \quad (11)$$

$\alpha_n$  being the successive eigenvalues of this equation.

## 2. Orthogonality Of Normal Modes

The orthogonality condition among normal modes may be deduced from Clebsch's theorem [5], stated below for the  $r$ th and  $s$ th distinct normal modes:

$$\iiint_{V_0} \rho(u_r u_s + N_r N_s + w_r w_s) r dr d\theta dz = 0 \quad (12)$$

In the case of a circular plate, if  $u$ ,  $v$  and  $w$  are the radial, circumferential, and lateral displacements, respectively, then we may write

$$\begin{aligned} w_r &= R_r e^{iw_r t} \\ w_s &= R_s e^{iw_s t} \\ u_r &= -z \frac{\partial w_r}{\partial r} = -z \frac{\partial R_r}{\partial r} e^{iw_r t} \\ u_s &= -z \frac{\partial w_s}{\partial r} = -z \frac{\partial R_s}{\partial r} e^{iw_s t} \\ N_r &= N_s = 0 \end{aligned}$$

Substituting these displacements into equation (12) we obtain the desired condition of orthogonality among normal modes:

$$\int_a^a \left[ \frac{\partial^2}{\partial r^2} \left( R_s \frac{\partial R_r}{\partial r} \right) + R_s R_r \right] r dr = 0 \quad (13)$$

## 3. Response To Thermal And Mechanical Loads

Making use of the homogeneous solution and the orthogonality conditions we may now turn to the response of the plate to the actual time dependent thermal and mechanical loads. Substituting into the governing equation of motion (3) the modal series representation of the displacement  $w$  given by equation (7), we obtain:

$$\sum_{m=1}^{\infty} \left\{ D \nabla^4 R_m T_m + \rho h R_m \frac{\partial^2 T_m}{\partial t^2} \right\} = P - D \sum_{k=1}^{\infty} \nabla^4 g_k f_k - \rho h \sum_{k=1}^{\infty} g_k \frac{\partial^2 f_k}{\partial t^2} \quad (14)$$

From the homogeneous equation (8) we see that  $D \nabla^4 R_m = \rho h w_m^2 R_m$ . Making use of this to eliminate  $D \nabla^4 R_m$ , equation (14) becomes:

$$\sum_{m=1}^{\infty} \left\{ \frac{\partial^2 T_m}{\partial t^2} + w_m^2 T_m \right\} R_m = P - D \sum_{k=1}^{\infty} \nabla^4 g_k f_k - \sum_{k=1}^{\infty} g_k \frac{\partial^2 f_k}{\partial t^2} \quad (15)$$

The terms on the right side of this equation are expressed in infinite series form:

$$\begin{aligned} & \sum_{m=1}^{\infty} P_m(t) R_m(r) \\ & - \frac{D}{\rho h} \sum_{k=1}^{\infty} \nabla^4 g_k f_k = \sum_{m=1}^{\infty} G_m(t) R_m(r) \\ & - \sum_{k=1}^{\infty} g_k \frac{\partial^2 f_k}{\partial t^2} = \sum_{m=1}^{\infty} G_m^*(t) R_m(r) \end{aligned} \quad (16)$$

These series expressions may be substituted into equation (15) to obtain:

$$\sum_{m=1}^{\infty} R_m \left( \frac{\partial^2 T_m}{\partial t^2} + w_m^2 T_m \right) = \sum_{m=1}^{\infty} R_m Q_m(t)$$

where:  $Q_m(t) = P_m(t) + G_m(t) + G_m^*(t)$

Equating the coefficients of  $R_m$  on the left and right sides of this equation, we find that  $T_m$  must satisfy

$$\frac{\partial^2 T_m}{\partial t^2} + w_m^2 T_m = Q_m(t)$$

from which the solution for  $T_m$  is readily found to be

$$\begin{aligned} T_m &= A_m \cos w_m t + B_m \sin w_m t \\ &+ \frac{1}{w_m} \int_0^t Q_m(\tau) \sin w_m(t-\tau) d\tau \end{aligned} \quad (17)$$

## Boundary Conditions

The technique of Mindlin and Goodman [2] is used to treat the time dependent boundary conditions which appear in this case in connection with the thermal loading. This is done by selecting the arbitrary functions  $g_1(r)$  and  $g_2(r)$  in such a way as to transform them into homogeneous conditions.

Substituting equation (70) into the boundary conditions (4) and (5) yields, at  $r=a$ :

$$\begin{aligned} & \sum_{m=1}^{\infty} R_m T_m + \sum_{k=1}^{\infty} g_k f_k = f_1(t) = 0 \\ & \left[ \frac{\partial^2}{\partial r^2} + \frac{1}{r} \frac{\partial}{\partial r} \right] \left[ \sum_{m=1}^{\infty} R_m T_m + \sum_{k=1}^{\infty} g_k f_k \right] = f_2(t) \\ & = -\frac{M_T}{D(1-\nu)} \end{aligned}$$

Noting that the normal function  $R_m$  satisfies the homogeneous boundary conditions, these equations are equivalent to the following set of conditions on  $g_1$  and  $g_2$  at  $r=a$ :

$$g_1 = 1$$

$$g_2 = 0$$

$$\left( \frac{d^2}{dr^2} + \frac{1}{r} \frac{d}{dr} \right) g_1 = 0 \quad \text{or} \quad g_1(r) = \frac{r^2 - a^2}{2(1+\nu)}$$

$$\left( \frac{d^2}{dr^2} + \frac{1}{r} \frac{d}{dr} \right) g_2 = 1 \quad (18)$$

### Initial Conditions

Making use of the assumed displacement form (7) we find that the initial conditions (6) at  $t=0$ , for all values of  $r$ , become

$$\sum_{m=1}^{\infty} R_m T_m + \sum_{k=1}^2 g_k f_k = 0 \quad (19)$$

$$\sum_{m=1}^{\infty} R_m \frac{dT_m}{dt} + \sum_{k=1}^2 g_k \frac{df_k}{dt} = 0$$

The second term of each of these equations may be expanded in infinite series form, thereby simplifying these equations:

$$\sum_{k=1}^2 g_k f_k(0) = \sum_{m=1}^{\infty} E_m R_m \quad (20)$$

$$\sum_{k=1}^2 g_k \frac{df_k}{dt}(0) = \sum_{m=1}^{\infty} E_m^* R_m$$

Thus if we note from equation (17) that  $T_m(0)=A_m$  and  $\frac{dT_m}{dt}=w_m A_m$ , and substitute equations (20) into (19) we may equate to zero the coefficients of  $R_m$  to obtain the values of  $A_m$  and  $B_m$ :

$$A_m = E_m$$

$$B_m = \frac{1}{\omega_m} E_m^*$$

The formal solution for  $w$  may now be written:

$$W = \sum_{m=1}^{\infty} [I_c(\omega_m) J_c(\omega_m t) + J_c(\omega_m t) I_c(\omega_m t)] \cdot \\ \cdot [E_m \cos \omega_m t + \frac{1}{\omega_m} E_m^* \sin \omega_m t \\ + \frac{1}{\omega_m} \int_0^t Q_m(\tau) \sin \omega_m(t-\tau) d\tau] \\ + \sum_{k=1}^2 g_k f_k \quad (21)$$

### Evaluation Of Coefficients $E_m, E_m^*$ and $Q_m$ , etc.

The coefficients contained within equation (21) may be computed in detail by applying the orthogonality condition (13) to the infinite series expansions (16) and (19). For example, from the first of equations (16) the expression for  $p$  is

$$\frac{p}{rh} = \sum_{m=1}^{\infty} P_m(t) R_m$$

Applying the differential operator

$$Pr \left[ \frac{h^2}{12} \frac{dR_m}{dr} dr + h R_m \right]$$

to both sides of this equation, integrating with respect to  $r$  and making use of the orthogonality condition:

$$\int_0^a \left[ \frac{h^2}{12} \frac{dR_m}{dr} dr + R_m p \right] r dr =$$

$$= \sum_{m=1}^{\infty} P_m(t) \int_0^a \rho h \left[ \frac{h^2}{12} \frac{dR_m}{dr} dr + R_m p \right] r dr \\ = P_m(t) \int_0^a \rho h \left[ \frac{h^2}{12} \left( \frac{dR_m}{dr} \right)^2 + R_m^2 \right] r dr$$

Thus the coefficient may be computed according to the equation

$$P_m(t) = \frac{1}{I_n} \int_0^a \left[ \frac{h^2}{12} \frac{dR_m}{dr} dr + R_m p \right] r dr$$

Similarly

$$G_m(t) = -\frac{1}{I_n} \int_0^a \left[ \left( \frac{h^2}{12} \frac{dR_m}{dr} dr + R_m \right) \sum_{k=1}^2 g_k \frac{df_k}{dt} \right] r dr$$

$$G_m^*(t) = -\frac{1}{I_n} \int_0^a \left[ \left( \frac{h^2}{12} \frac{dR_m}{dr} dr + R_m \right) \sum_{k=1}^2 g_k \frac{df_k}{dt} \right] r dr$$

$$E_n = -\frac{1}{I_n} \int_0^a \left[ \left( \frac{h^2}{12} \frac{dR_m}{dr} dr + R_m \right) \sum_{k=1}^2 g_k f_k(0) \right] r dr$$

$$E_n^* = -\frac{1}{I_n} \int_0^a \left[ \left( \frac{h^2}{12} \frac{dR_m}{dr} dr + R_m \right) \sum_{k=1}^2 g_k \frac{df_k(0)}{dt} \right] r dr \quad (22)$$

where

$$I_n = \int_0^a \rho h \left[ \frac{h^2}{12} \left( \frac{dR_m}{dr} \right)^2 + R_m^2 \right] r dr$$

Finally, using the actual values  $p=p(t)$ ,  $f_1=0$ ,  $f_2=-M_r/(D(1-v))$ ,  $g_1=1$ , and  $g_2=(1+v)/(2(1-v))$  and carrying out the integrations these become:

$$P_m = \frac{a^2 p}{\rho h I_n} [I_c(\omega_m) J_c(\omega_m t) - J_c(\omega_m t) I_c(\omega_m t)]$$

$$G_m = 0$$

$$G_m^* = \frac{K_n}{2(1+v) I_n} \frac{\dot{M}_T}{D(1-v)}$$

$$E_n = \frac{K_n}{2(1+v) I_n} \frac{M_T(t)}{D(1-v)} \quad (23)$$

$$E_n^* = \frac{K_n}{2(1+v) I_n} \frac{\dot{M}_T(t)}{D(1-v)}$$

where

$$K_n = \int_0^a r \left[ \frac{h^2}{12} \frac{dR_m}{dr} dr + R_m \right] (r^2 a^2) dr$$

$$= -\frac{4a^4}{\omega_m^2} \left\{ \frac{11v}{1-v} I_c(\omega_m t) J_c(\omega_m t) \right\}$$

$$+ \frac{v h^2}{12 a^2} \left[ J_c(\omega_m t) I_c(\omega_m t) - I_c(\omega_m t) J_c(\omega_m t) \right]$$

$$I_n = J_c^2(\omega_m t) a^2 \left\{ \frac{v h^2}{24} \left( \frac{h}{\pi} \right)^2 \left[ \frac{J_c^2(\omega_m t)}{J_c^2(\omega_m t)} + \frac{J_c^2(\omega_m t)}{I_c^2(\omega_m t)} \right] \right. \\ \left. + \frac{1}{1-v} \left[ \omega_m \left( \frac{J_c^2(\omega_m t)}{J_c^2(\omega_m t)} + \frac{I_c^2(\omega_m t)}{I_c^2(\omega_m t)} \right) - (1+v) \right] \right\}$$

Using these displacements  $w$  may now be

written as:

$$W = \sum_{m=1}^{\infty} \left[ J_0(\omega_m r) I_c(\omega_m) - J_0(\omega_m) I_c(\omega_m r) \right] \cdot \\ \cdot \left\{ \frac{1}{4(1-\nu^2)} \frac{K_m}{I_m} \left[ M_T(t) \cos \omega_m t + \frac{\dot{M}_T(t)}{\omega_m} \sin \omega_m t \right. \right. \\ \left. \left. + \frac{1}{\omega_m} \int_0^t \ddot{M}_T(\tau) \sin \omega_m(t-\tau) d\tau \right] \right. \\ \left. + \frac{a^2}{r^2 \omega_m I_m} \left[ I_0(\omega_m) J_1(\omega_m) - J_0(\omega_m) I_1(\omega_m) \right] \right. \\ \left. \cdot \frac{1}{\omega_m} \int_0^t p(\tau) \sin \omega_m(t-\tau) d\tau \right\} \\ - \frac{r^2 a^2}{2(1+\nu)} \frac{M_T}{D(1-\nu)}$$

This may be further simplified by carrying out the integration of  $M_T$  and observing that

$$\sum_{m=1}^{\infty} \frac{K_m}{I_m} R_m(r)$$

is the series representation of  $(r^2 - a^2)$  deduced in the first of equations (20):

$$W = \sum_{m=1}^{\infty} \left[ J_0(\omega_m r) I_c(\omega_m) - J_0(\omega_m) I_c(\omega_m r) \right] \cdot \\ \cdot \left\{ - \frac{\omega_m}{2(1-\nu)D} \frac{K_m}{I_m} \int_0^t M_T(\tau) \sin \omega_m(t-\tau) d\tau \right. \\ \left. + \frac{a^2}{r^2 \omega_m I_m} \left[ I_0(\omega_m) J_1(\omega_m) - J_0(\omega_m) I_1(\omega_m) \right] \right. \\ \left. + \int_0^t p(\tau) \sin \omega_m(t-\tau) d\tau \right\}$$

#### QUASI-STATIC DISPLACEMENTS

The quasi-static counterpart of equation (24) in which inertia terms are neglected is readily shown to be:

$$W = \frac{a^2 r^2}{2(1+\nu)} \left[ \frac{M_T}{(1-\nu)D} + \frac{2(1-\nu)}{D} p a^2 \sum_{n=1}^{\infty} \frac{1}{\omega_n^2} \right] \\ + \frac{2 p a^4}{D} \sum_{n=1}^{\infty} \frac{J_0(\omega_n r)}{\omega_n^2 J_1(\omega_n)} \quad (25)$$

where  $\omega_n$  are the successive roots of the equation  $J_0(\omega_n) = 0$ .

#### STRESSES

The stresses may be computed from the displacements (24) or (25) by substituting into the thermo-elastic stress-displacement relations (1):

$$\sigma_r = -\frac{Ez}{1-\nu^2} \left[ \frac{\partial^2 w}{\partial r^2} + \frac{v}{r} \frac{\partial w}{\partial r} \right] r \frac{N_T}{4(1-\nu)} - \frac{\alpha ET}{1-\nu} \quad (26)$$

$$\sigma_\theta = -\frac{Ez}{1-\nu^2} \left[ \frac{1}{r} \frac{\partial w}{\partial r} + v \frac{\partial^2 w}{\partial r^2} \right] r \frac{N_T}{4(1-\nu)} - \frac{\alpha ET}{1-\nu}$$

Where

$$N_T = \int_{-a}^a \alpha ET dz / 2$$

#### RESULTS

Making use of equations (24) for the dynamic case and (25) for the static case, the displacements were computed for the center of an aluminum-magnesium alloy plate exposed to two radiant heating pulses. These pulses rapidly rose to peak intensities, which occurred at 0.1 seconds and 0.34 seconds. The total thermal exposures were 71 cal/cm<sup>2</sup> and 145 cal/cm<sup>2</sup> respectively. Plates of a number of thicknesses and diameters were studied.

The displacement-time history of those plates having the greatest fundamental periods (ranging from 0.62 seconds to 0.16 seconds) are presented in Figures 2 and 4, in which we may clearly see thermally induced vibrations of a substantial magnitude. Dynamic displacements were observed to range as high as 1.7 times the corresponding maximum static displacements. We see also that for pulses having a rise time fairly close to the fundamental period, the magnification is greatest.

Figures 3 and 5 summarize the results of these calculations as well as those for one other thickness. Strictly speaking, these other plates may not be compared simply on a fundamental period basis because the variation in thickness does not merely change the period, but renders the plates somewhat dissimilar in thermal response as well. Note, however, that for a given thickness, the dynamic effects diminish as the period becomes substantially smaller than the heating time.

On the basis of some preliminary stress calculations, another interesting phenomenon may be observed. The stresses within the plate may be compressive at both the front and rear surfaces, while they are tensile in the central region. This is clearly seen in Figure 6, which presents the static and dynamic stress distribution in a thin plate shortly after the thermal radiation peak has occurred. The static distribution is almost precisely that described above, and we see that there are now two "neutral" surfaces for stress. From the nearly symmetrical stress distribution in this case we also see that the static stresses induce no net moment in the plate. The dynamic case is somewhat different. While still satisfying the condition of no net axial force in the plate, a substantial moment is induced. Clearly this unusual stress distribution arises because of the sharp thermal gradients and should be expected when rapid heating is involved, or during the

early stages of the heating period.

#### ACKNOWLEDGEMENT

This work has been supported by the United States Navy under Contracts N00140-70-C-0019 and N60921-71-C-0197 monitored by the Naval Applied Science Laboratory, Brooklyn, New York, and the Naval Ordnance Laboratory, Silver Spring, Maryland.

#### REFERENCES

- 1 - Boley, B.A. and Weiner, J.H., Theory of Thermal Stresses, Wiley, New York, 1960
- 2 - Mindlin, R.D. and Goodman, L.E., "Beam Vibrations With Time Dependent Boundary Conditions", J. App. Mech., Vol. 72, 1950, p.377
- 3 - Jahnke, Emde, and Losch, Tables of Higher Functions, McGraw-Hill, New York, 1960
- 4 - Watson, G.N., Theory of Bessel Functions, Cambridge Univ. Press, London, 1966
- 5 - Love, A.E.H., Theory of Elasticity, Cambridge Univ.Press, London, 1927, p.189

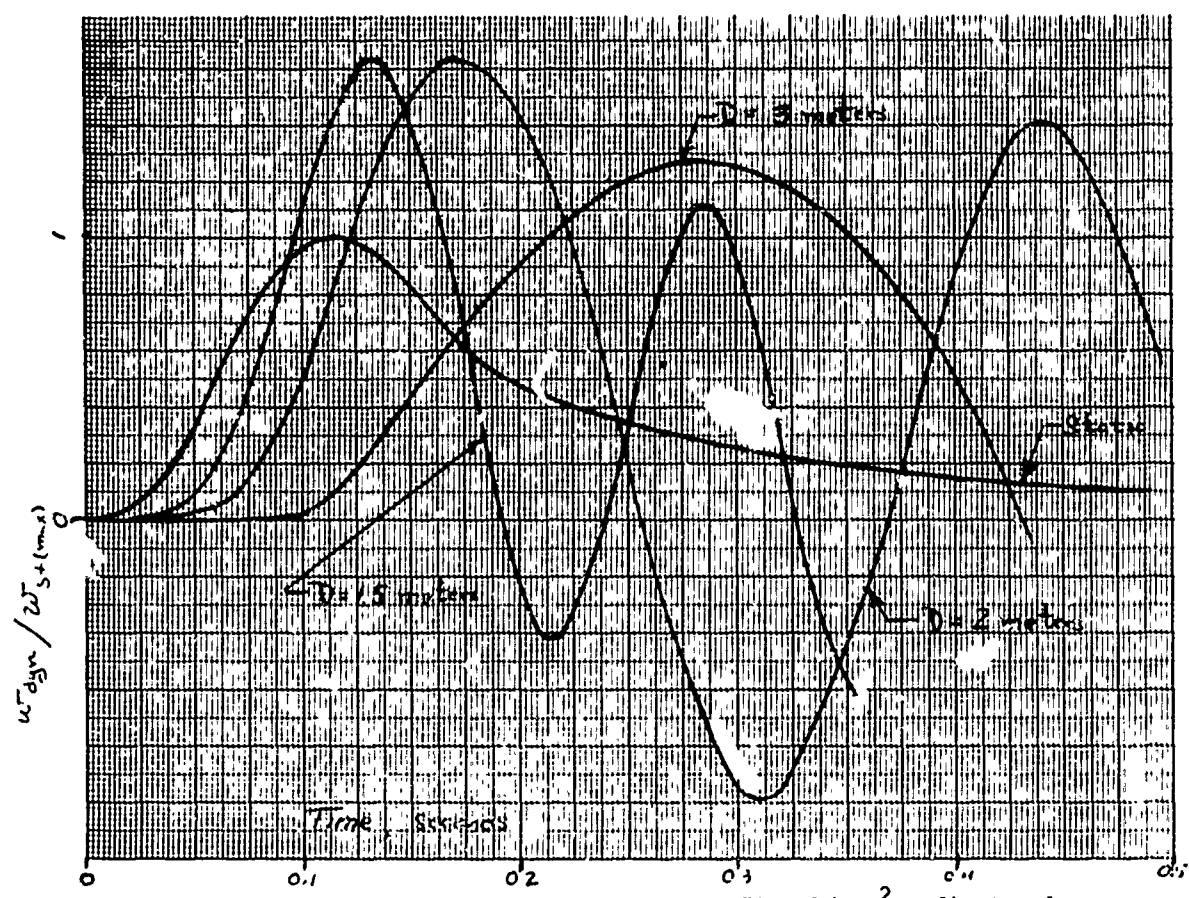


Figure 2 - Response of 1/8 in Thick Plates To A  $71 \text{ cal/cm}^2$  Radiant Pulse Having A Peak Intensity At 0.1 sec

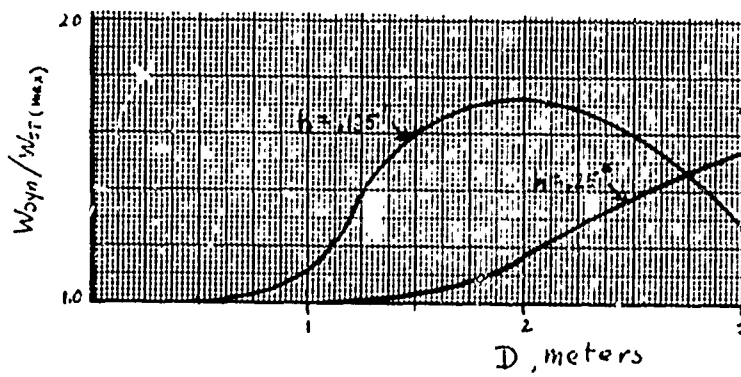


Figure 3 - Dynamic Magnification Of Displacements Of Plates Exposed to  $71 \text{ cal/cm}^2$  Radiant Pulse

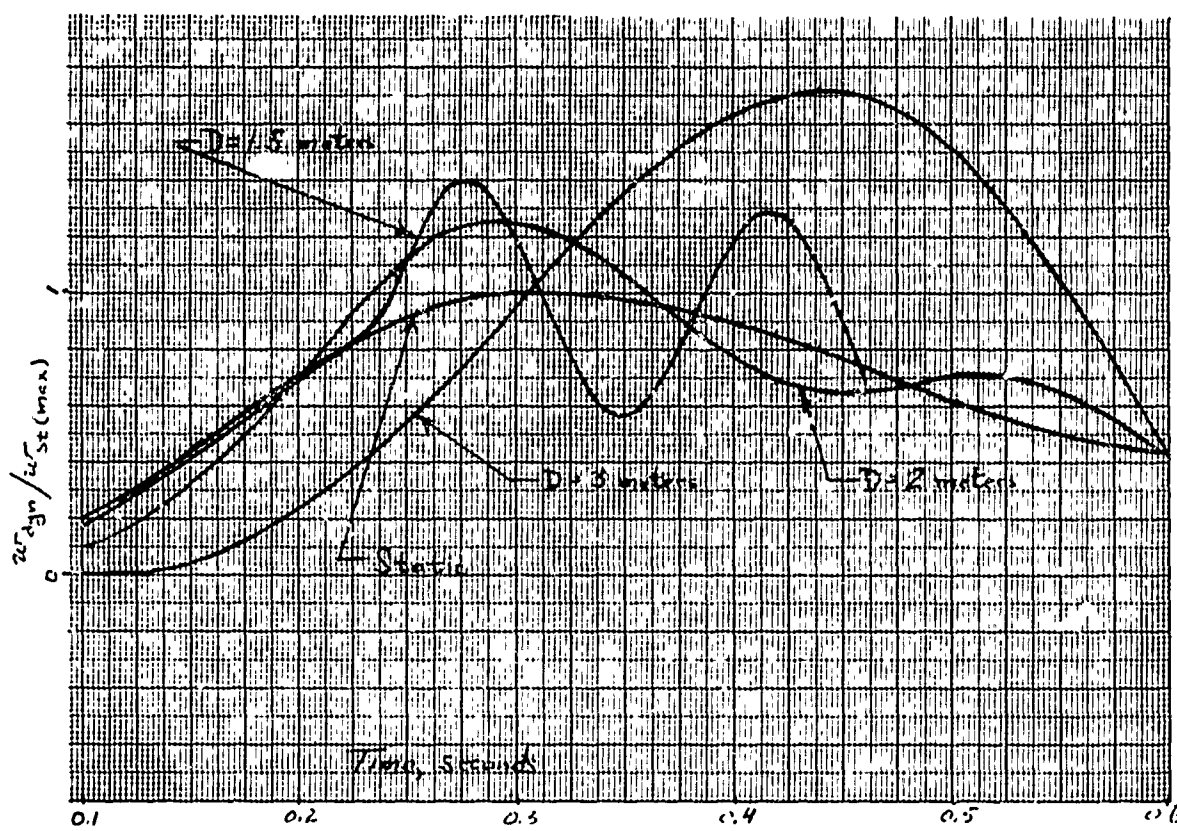


Figure 4 - Response Of 1/8 in Thick Plates To A  $145 \text{ cal/cm}^2$  Radiant Pulse Having A Peak Intensity At 0.34 sec

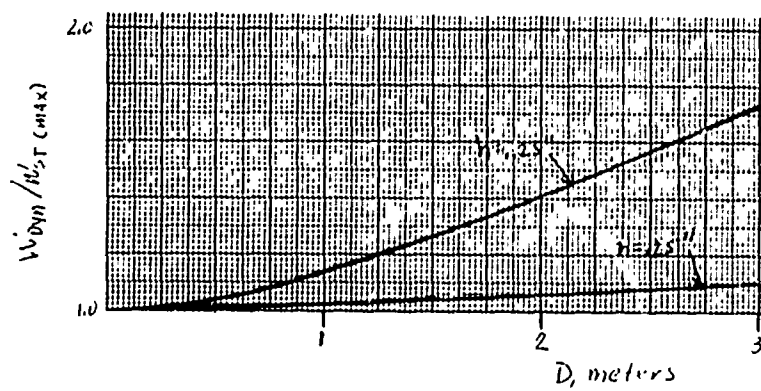
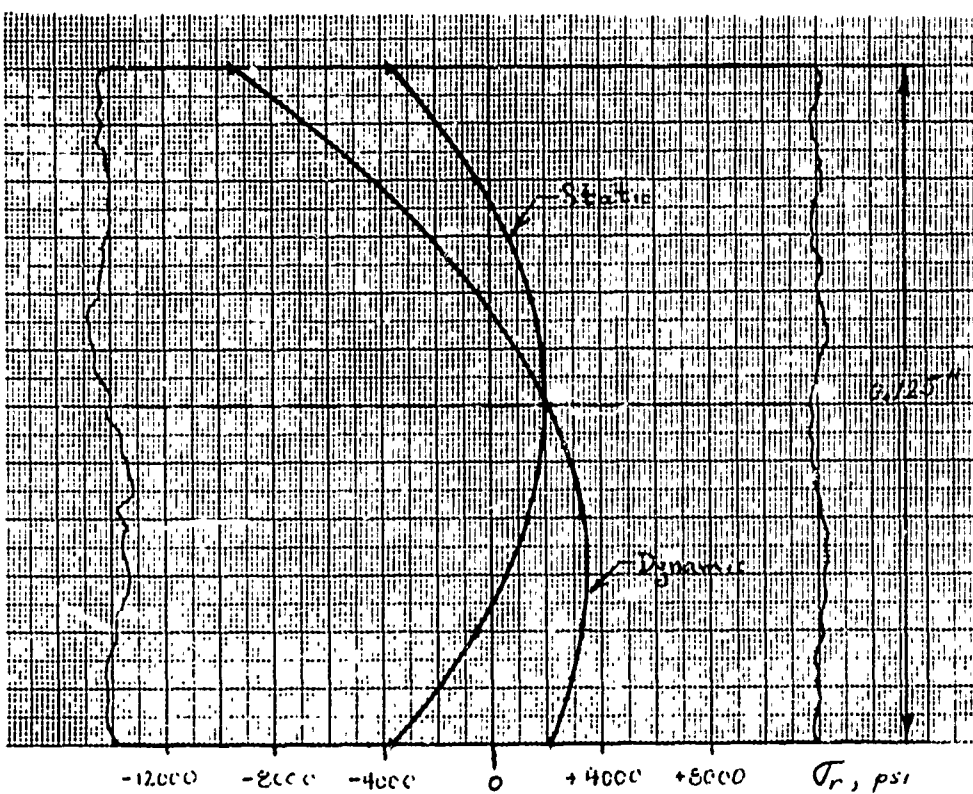


Figure 5 - Dynamic Magnification Of Displacements Of Plates Exposed To  $145 \text{ cal/cm}^2$  Radiant Pulse



**Figure 6** - Stress Distribution At Center Of 1/8 in Plate At Time = 0.105 sec  
After Exposure To A  $71 \text{ cal/cm}^2$  Radiant Pulse

## DISCUSSION

Mr. Mercurio (Sperry Gyroscope Company): I would like to commend you on a very interesting paper. I noticed that you had fluxes of 71, and I believe, and 145.

Mr. Koch: Yes, these happen to be particular weapon pulses.

Mr. Mercurio: What were the associated pressure loadings?

Mr. Koch: I think they were 10 psi. They would have wiped out these plates completely. I had to get rather flexible plates in order to show the dynamics, and I was constrained to use particular pulses by my contract.

Mr. Mercurio: You have not shown the pressure stresses on the plate. Is that correct?

Mr. Koch: Yes

Mr. Mercurio: Have you done any work in this area? I would like to know, because some of the common materials that we are dealing with get into problems when you apply both the thermal and pressure loads simultaneously.

Mr. Koch: We are getting into it right now. In fact in about a months time I am due to have a report on this subject. We are also attempting to answer the question: "What actually happens if the properties vary with temperature, let's say, through the thickness?" The frequency changes and the modulus changes, so the whole dynamic picture might change.

Mr. Mercurio: There is also the problem of the properties changing over very short time durations where very little information is available.

Mr. Koch: I have access to some data which is in a range less than one second -- perhaps in the millisecond range. I have not looked at it, but I was promised the data. I agree there is some lack of data on materials in the short time range.

Mr. Zudans (Franklin Institute): I would like to refer to your last slide. Something confused me, and I want to clarify it. You showed the static stresses as being perfectly symmetrical.

Mr. Koch: No, not quite --- almost.

Mr. Zudans: How can that be explained? Was the heat flux coming to one side of the plate or both sides of the plate?

Mr. Koch: One side of the plate only. It happened, I suspect, that the temperature distribution was such that, if you just turned the plate a bit, you get something that looked symmetrical. It was not actually, it just looked like it.

Mr. Zudans: How could the temperature distribution be anything near symmetrical if you had heat flux from one side only. This is what I do not understand.

Mr. Koch: If you shifted the distribution curve you would have something that would appear to be nearly symmetrical by coincidence. Accidentally this looked symmetrical, but the actual numerical value was such that it was not actually symmetrical.

Mr. Yang (University of Maryland): I have two questions. On one of your curves you show various diameters of 1.5, 2 and 3 meters. Since the rise time is dependent upon the diameter, I wonder why the rise time for a diameter of 3 meters is the slowest, whereas the time for 1.5 meters is in the middle and for 2 meters is the fastest?

Mr. Koch: I think I may have flashed the curve too fast. I do not think that actually happened. The 1.5 meter one was quickest.

Mr. Yang: The second question is, Have you done any work in the thermal stresses of composite materials?

Mr. Koch: No, however I have done some non-thermal work in the vibration of layered materials.

WHIRL FLUTTER ANALYSIS OF PROPELLER-NACELLE-PYLON  
SYSTEM ON LARGE SURFACE EFFECT VEHICLES

Yuan-Ning Liu

Naval Ship Research and Development Center  
Washington, D.C. 20034

A typical propeller-nacelle-pylon configuration installed on large surface effect vehicles is analyzed for dynamic stability in normal operations. A whirl-flutter theory developed by the aircraft industry for propeller-rotor dynamics is used to establish stability boundaries for variations of physical parameters of a propeller-nacelle-pylon system. The stability boundaries are presented in chart forms which can be used as design guides. The uppermost and lowest bounds for stability are shown on these charts. Classical whirl-flutter theory, which considers ideally rigid blades, defines the most conservative design and the uppermost bound. The lowest bound is found when the blade fundamental bending frequency is 4/10 of the propeller rotating speed. This is considered to be an optimum value in the sense of greatest freedom of choice of nacelle mounting stiffness for dynamic stability.

Although direct comparisons of experimental data with these analytical results are not possible in the present analysis, reported observations on the investigation of nacelle vibration on existing hovercrafts indicates that whirl-flutter could properly explain the results. Further studies are recommended.

## I. INTRODUCTION

In the aircraft industry, the possible occurrence of whirling-type instability on propeller-driven aircrafts was recognized as early as 1938 by Taylor and Browne [1]. This type of instability received a great deal of attention in 1960 with the impetus of two early failures on the Lockheed "Electra" aircrafts [2]. Subsequent investigations revealed that propeller whirl flutter could cause total destruction of the propeller-nacelle system if the nacelle was not mounted with sufficient rigidity. In the past decade, large helicopters and vertical and short takeoff and landing aircrafts (V/STOL) came into existence, at least partly, due to

the understanding of this phenomenon. This is attested to by the fact that on some V/STOL configurations, propeller whirl-flutter stability is one of the main considerations in design [3-10].

On a large existing surface effect vehicle (SEV) such as SR.N4 [11], the propeller-nacelle-pylon system is very similar to the propeller-rotor system on a typical V/S'TOL [3,10]. It seems logical then, for a future large SEV equipped with a similar propulsion unit, that studies be made to determine the controlling parameters of whirl-flutter to assure an adequate design.

The present analysis was undertaken for the purpose of gaining a general knowledge of the propeller

whirl-flutter phenomenon as related to the design of the propeller-rotor system for a SEV. Design criteria may be developed in order to define a stable propeller-nacelle-pylon system as functions of design parameters, such as nacelle mounting stiffness, nacelle inertias, etc., and blade vibration characteristics. The overall design for SEV must also consider the vibration characteristics of other machineries and the platform.

## II. NOMENCLATURE

$a_a$	Local lift curve slope of a blade section	$k_b$	Effective blade bending stiffness constant at hub-center
[C]	Equivalent damping matrix	[M]	Equivalent mass matrix
$c_d, c_l$	Sectional blade airfoil drag and lift coefficients, respectively	$m_b$	Blade mass per unit spanwise length
c	Blade chord	$m_s$	Nacelle (include shaft) mass per unit length
$c_{\phi_x}, c_{\phi_y}$	Effective viscous damping constants on nacelle pitching and yawing motions, respectively	N	Number of blades
D	Dissipating function	n	Blade designation number ( $n = 1, 2, 3, \dots, N$ )
$dD, dL$	Blade sectional drag and lift, respectively	R	Propeller radius
E	Potential energy	Re(s)	Real point of s
h	Nacelle length	r	Spanwise distance along the blade measured from hub-center to a blade section
$I_b$	Blade moment of inertia about hub-center	s	Laplace transform variable
$Im(s)$	Imaginary part of s	t	Time
$I_{\phi_x}, I_{\phi_y}$	Nacelle moment of inertia including the mass of propeller in pitch and yaw, respectively	T	Kinetic energy
i	$\sqrt{-1}$	U	Resultant air velocity on a blade element
[K]	Equivalent stiffness matrix	v	Propeller advance speed
$K_{d_0}, K_{d_1}, K_{d_2}$	Drag factors	x	Normalized spanwise distance, $r/R$
$k_{\phi_x}, k_{\phi_y}$	Effective nacelle spring constants in pitch and yaw, respectively	$x_b, x_s$	Position vectors for a blade section and a nacelle section, respectively
		$\alpha$	Instantaneous blade section angle of attack
		$\alpha_0$	Initial angle of attack at a blade section
		$\beta_n$	Effective flapping angle of the nth blade at its first bending mode, referred to the plane of rotation
		$\beta_c, \beta_s$	Propeller disc pitch and yaw angles, respectively, referred to the plane of rotation
		$\gamma$	Blade lock number, $\rho s_a c R^4 / I_b$
		$\delta$	Exponential decay factor

$\zeta$	Nacelle damping ratio
$\lambda$	Propeller inflow ratio, $V/R\Omega$
$\rho$	Air density
$\phi_x, \phi_y$	Nacelle instantaneous pitching and yawing angles, respectively
$\psi_n$	Azimuth position angle of the nth blade
$\Omega$	Propeller rotating speed
$\omega$	Nacelle natural frequency
$\omega_{\phi_x}, \omega_{\phi_y}$	Nacelle natural frequencies in pitch and yaw, respectively
$\omega_\beta$	Non-rotating blade fundamental bending frequency
$\eta_{\phi_x}, \eta_{\phi_y}$	Nacelle frequency ratios ( $\omega_{\phi_x}/\Omega$ ) and ( $\omega_{\phi_y}/\Omega$ ), respectively
$n_\beta$	Blade frequency ratio ( $\omega_\beta/\Omega$ )
(•)	Dot over a quantity indicates differentiation with respect to time $t$ , or, dot between two vector quantities indicates dot-product
(')	Superscript indicates differentiation with respect to the time variable $\Omega t$
(~)	Tilt over a quantity indicates Laplace transformation
(+)	Arrow over a quantity indicates a vector

### III. THEORETICAL CONSIDERATIONS

The classical whirl-flutter phenomenon, in which the propeller blades are considered infinitely stiff, is briefly explained as follows. The motion of the rigid-bladed propeller on a flexibly mounted nacelle consists of the pitching and yawing rotations of the nacelle combined with the corresponding motions of the propeller plane.

For a forward moving propeller-rotor in level flight, the resulting flow of air normal to the propeller plane is generally symmetrical and produces a symmetrically distributed propeller thrust. The pitching and yawing rotations of the propeller disc due to the nacelle flexibility destroy the central symmetry of the flow in a continuously varying manner and create additional undesirable moments which may lead to unstable nacelle circular motion in the direction opposite to that of the propeller rotation, i.e., the backward whirling. The aerodynamic source of this instability accounts for the usual designation "whirl flutter," which is to be distinguished from the purely mechanically-induced whirling motion in a rotating shaft system.

#### A. DYNAMIC STABILITY

When considering the dynamic stability of a propeller-rotor system a more realistic representation of the system would be to take into account the flexible motion of the blades as well as that of the rotor. The coupled motions of the blades and rotor form the theoretical background of this analysis.

Fig. 1 is a sketch which illustrates the configuration of the propeller-nacelle-pylon system on SR.N4. A schematic representation of this system or any other propeller-nacelle-pylon configuration for the mathematical model is shown in Fig. 2. The mathematical model used in this analysis is essentially that of a four-degree-of-freedom system. The steady aerodynamic loads and vibration theory used in this analysis are considered to be linear. It was demonstrated by

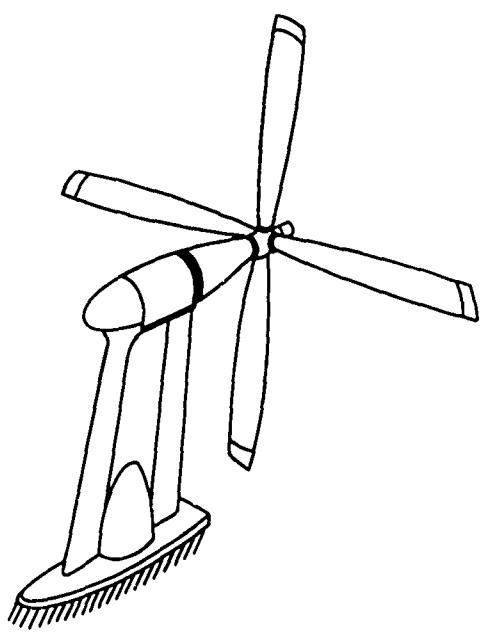


Fig. 1 - Propeller-Nacelle-Pylon System on the SR.N4 Hovercraft

Lytwyn [7] that the nonlinear effects were small on the variance of stability boundaries. It is felt that omitting higher order effects is justified and the stability boundaries resulting from this analysis are valid.

The nacelle is allowed to move in pitch and yaw directions and its flexibility is assumed to be concentrated at the root of the nacelle. The individual propeller blade is allowed to flap in its fundamental bending mode and an equivalent system is formed such that the blade is considered rigid but with an elastically restrained flapping hinge located at the center of propeller disk (see Fig. 2).

The variational principle was used to derive the governing differential equations. Hence, expressions for kinetic energy, potential energy and

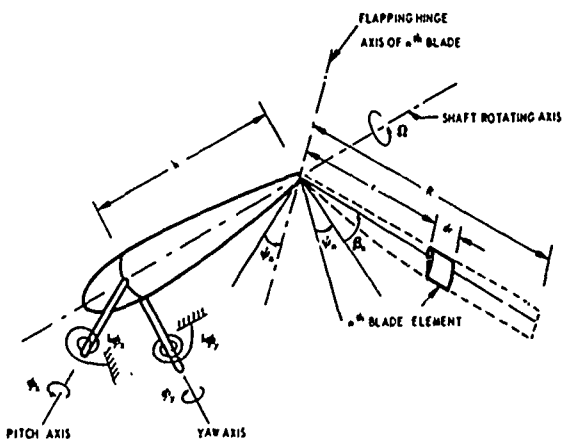


Fig. 2a - Propeller-Rotor Structural Model

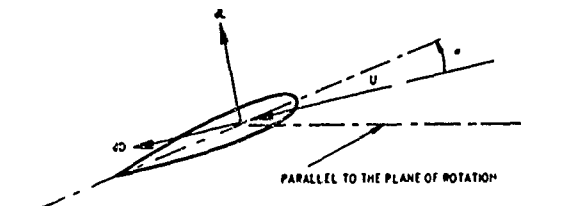


Fig. 2b - Aerodynamic Forces on a Blade Element

Fig. 2 - Schematic Representation of Mathematical Model for a Propeller-Rotor System

dissipation potential were needed and were formulated as follows.

$$T = T_{\text{blades}} + T_{\text{nacelle}} \quad (\text{shaft})$$

$$= \frac{1}{2} \sum_{n=1}^N \int_0^R (\dot{x}_b \cdot \dot{x}_b)_n dm_b \quad (1a)$$

$$+ \frac{1}{2} \int_0^h (\dot{x}_s \cdot \dot{x}_s) dm_s$$

$$E = \frac{1}{2} k_{\phi_x} \dot{\phi}_x^2 + \frac{1}{2} k_{\phi_y} \dot{\phi}_y^2$$

$$+ \frac{1}{2} \sum_{n=1}^N k_B \beta_n^2 \quad (1b)$$

$$D = \frac{1}{2} c_{\phi_x} \dot{\phi}_x^2 + \frac{1}{2} c_{\phi_y} \dot{\phi}_y^2 \quad (1c)$$

Utilizing the Lagrangian equations, the equations of motions of the dynamic system shown in Fig. 2 are given by

$$\frac{d}{dt} \left( \frac{\partial T}{\partial \dot{q}_i} \right) - \frac{\partial T}{\partial q_i} + \frac{\partial E}{\partial \dot{q}_i} + \frac{\partial D}{\partial \dot{q}_i} = \quad (2)$$

$$Q_i|_{\text{aerodynamic}} + Q_i|_{\text{external}}$$

$Q_i$  is the generalized aerodynamic or the external applied force associated with the generalized coordinates  $q_i$ . The generalized coordinates used in this analysis were  $\beta_c$ ,  $\beta_s$ ,  $\phi_x$ , and  $\phi_y$ . A constant rotating force is applied on the shaft so as to produce a constant driving torque and this was the base in the derivation of  $Q_i|_{\text{external}}$ . The aerodynamic forces  $Q_i|_{\text{aerodynamic}}$  involved in the above derivations were based on the quasi-static aerodynamics. The sectional lift and drag acting on the blade element are expressed in the form (see Fig. 2b)

$$dL = \frac{1}{2} \rho c U^2 C_L dr \quad (3a)$$

$$dD = \frac{1}{2} \rho c U^2 C_d dr \quad (3b)$$

where  $C_L$  and  $C_d$  are assumed in the form

$$C_L = a_\alpha \alpha \quad (4a)$$

$$C_d = K_{d_0} + K_{d_1} \alpha + K_{d_2} \alpha^2 \quad (4b)$$

The detailed analytical derivations for the mathematical model shown in Fig. 2 may be found in Ref. [7]. The governing equations from the derivations may be expressed in matrix forms.

$$[M] \begin{Bmatrix} \beta_c'' \\ \beta_s'' \\ \phi_x'' \\ \phi_y'' \end{Bmatrix} + [C] \begin{Bmatrix} \beta_c' \\ \beta_s' \\ \phi_x' \\ \phi_y' \end{Bmatrix} + [K] \begin{Bmatrix} \beta_c \\ \beta_s \\ \phi_x \\ \phi_y \end{Bmatrix} = \{0\} \quad (5)$$

The elements in the matrices  $[M]$ ,  $[C]$ , and  $[K]$  are formed from the coefficients in the governing differential equations of motions, again, they may be found in Ref. [7]. By taking Laplace transform on Eq. (5), it becomes

$$(s^2[M] + s[C] + [K]) \begin{Bmatrix} \tilde{\beta}_c \\ \tilde{\beta}_s \\ \tilde{\phi}_x \\ \tilde{\phi}_y \end{Bmatrix} = \{0\} \quad (6)$$

This represents a typical complex eigenvalue and eigenvector problem. The characteristic roots  $s$  are those which make the determinant of the coefficient matrix in Eq. (6) vanish. Each eigenvalue  $s$ , or the characteristic root, corresponds to a mode of oscillation and can be expressed in the form

$$s = Re(s) + i Im(s) \quad (7)$$

The variations of  $Re(s)$  and  $Im(s)$  of all the modes as a function of different configurations may be expressed in root-locus plots on a complex plane. Instability is considered to occur whenever any of the characteristic

roots enters the positive real axis plane. In physical terms, the damping value associated with a particular mode has become negative. The roots which are located on the imaginary axis are corresponding to neutral stable conditions. In practice, studying the variation of  $\text{Re}(s)$  alone as a function of different configurations is enough to define the stability boundaries. However, occasionally the variation of  $\text{Im}(s)$  is also needed in order to define whether the stability is a dynamic or a static divergence case, i.e., when both  $\text{Re}(s)$  and  $\text{Im}(s)$  become zero. Fig. 3 shows a typical root-locus plot for blade bending frequency ratio  $\eta_\beta = 1$ . Furthermore, sufficient variations in parameter for structural configurations are necessary in order to define accurate stability boundaries. These are shown in Figs. 4 and 5 for different  $\eta_\beta$  values for illustrating purpose. Any particular configuration then may be checked for stability in the preliminary design stage by utilizing these results.

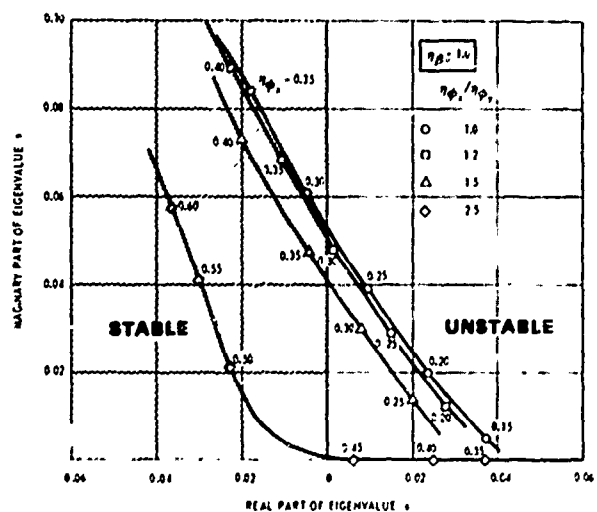


Fig. 3 - Root-Locus Plot for Blade Bending Frequency Ratio  $(\omega_\beta/\Omega) = 1.0$

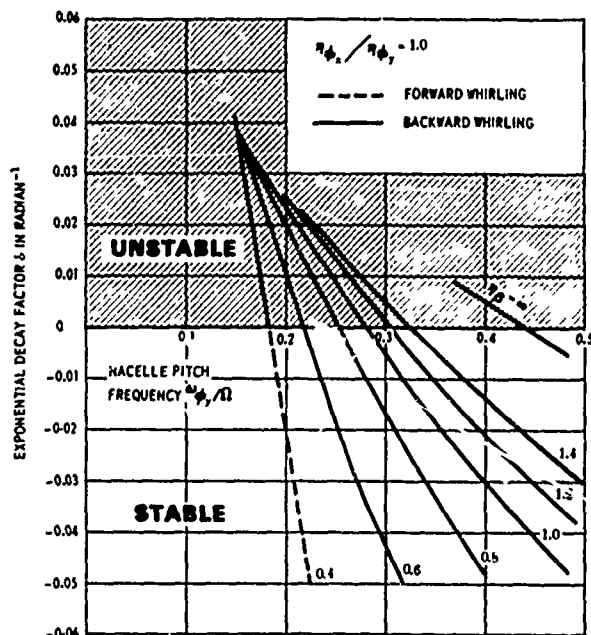


Fig. 4 - Exponential Decay Factor  $\delta$  as a Function of Nacelle Pitch Frequency for Various Blade Bending Frequencies

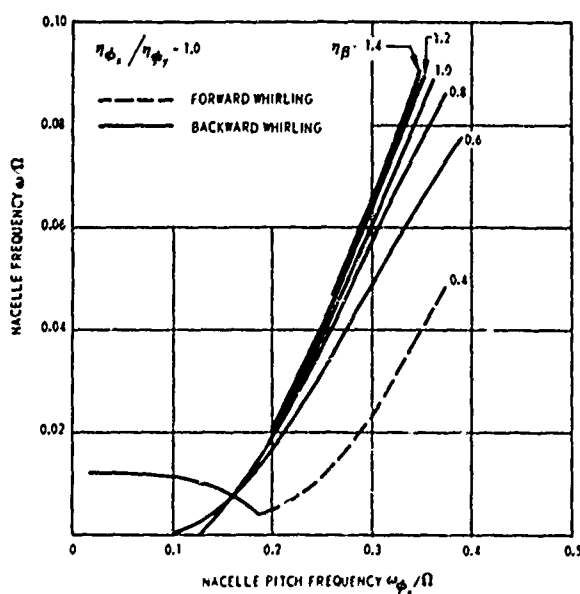


Fig. 5 - Nacelle Frequency as a Function of Nacelle Pitch Frequency for Various Blade Bending Frequencies

A digital computer program [12] developed for the Naval Ship Research and Development Center (NSRDC) was used to solve Eq. (6).

#### B. SPECIAL CASE - IDEALLY RIGID BLADES

Ideally speaking, an infinitely rigid blade is not possible in practice. However, this condition provides us the uppermost bound in defining whirl-flutter stability boundaries.

Referring to the set of governing differential Eq. (5) one may reduce these four equations to a special set of two equations for the case of ideally rigid blades. This may be accomplished by assuming that the blade root constraint stiffness or the blade fundamental bending frequency is infinite. These two equations of motion represent the "classical" whirl-flutter phenomenon of the two-degree-of-freedom propeller-nacelle combinations. By studying the characteristic roots of these equations, explicit expressions for stability boundaries may be obtained. This was done by assuming that the mass moment of inertia of nacelle was the same in both pitch and yaw directions.

#### C. STATIC DIVERGENCE

Static divergence of a propeller-rotor system may be considered as a limiting case of whirl-flutter phenomenon by considering only the static restoring ability from the structure. This may be visualized by letting the "natural frequency" of the system become

zero or by omitting time-dependent terms in Eq. (5). One obtains

$$[K] \begin{Bmatrix} \beta_c \\ \beta_s \\ \phi_x \\ \phi_y \end{Bmatrix} = \begin{Bmatrix} 0 \\ 0 \\ 0 \\ 0 \end{Bmatrix} \quad (8)$$

A necessary and sufficient condition to have a nontrivial solution for the above equation is that the determinant of the coefficient matrix  $[K]$  is identically equal to zero, i.e.,

$$| [K] | = 0 \quad (9)$$

Eq. (9) was utilized in the process of mapping the static divergence boundaries.

#### IV. PARAMETRIC STUDIES

A practical design for propeller-rotor systems would have physical properties such that their parameters were in the region bounded by the uppermost and lowest boundaries in the stability plot. The limiting boundaries have already been discussed as "Ideally Rigid Blades" and "Static Divergence." Therefore, as a design guide, parametric studies were made in order to define these whirl-flutter stability boundaries. The ratio of natural blade bending frequency to propeller rotational speed, i.e.,  $\eta_\beta$ , and its variations form a family of stability curves that are the results of such studies.

The propeller-rotor-system on SR.N4 represents a large high-speed SEV system, and its structural configuration will probably resemble one of an anticipated design. It is believed that design values for the propeller-nacelle-pylon system on a larger and faster vehicle would not vary too much from those of SR.N4. Therefore, a set of typical input values resembling the propeller-nacelle-pylon configuration on SR.N4 is used in this report to define whirl-flutter stability boundaries and are summarized in Table 1.

TABLE 1  
Nacelle and Blade Parameters Used in Defining Stability Boundaries

Parameter	Value
$n_\beta$	Variable
$n_{\phi_x}$	Variable
$n_{\phi_y}$	Variable
N	4
h/R	0.83
$I_b/I_\phi$	0.2
$\lambda$	0.3
$\gamma$	3
$K_{d_0}$	0.0087
$K_{d_1}$	-0.0216
$K_{d_2}$	0.4
$a_a$	5.73
$a_o$	4 deg
$\zeta$	0
Note: Assume $I_{\phi_x} = I_{\phi_y} = I_\phi$	

Using the input values from Table 1, one may form the matrix equation shown in Eq. (5). Solving this equation as functions of  $n_\beta$ ,  $n_{\phi_x}$ , and

$n_{\phi_y}$ , one can evaluate the variation of eigenvalues of different configurations and hence define the stability boundaries. The results are shown in Fig. 6.

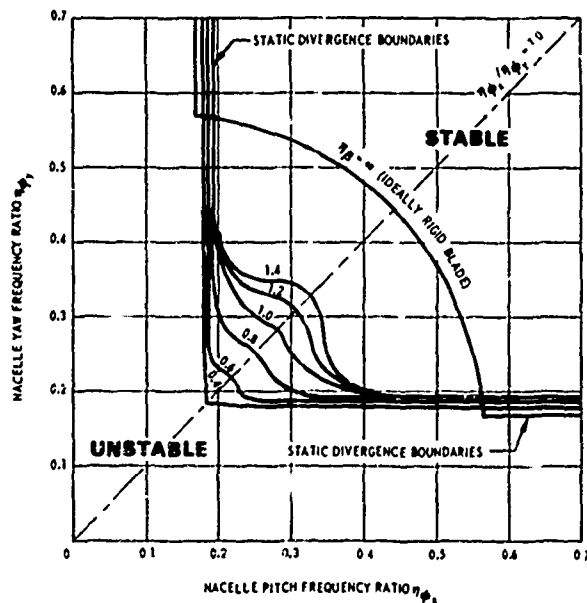


Fig. 6 - Propeller-Rotor Whirl Flutter Stability Boundaries for Various Blade Bending Frequencies

The stability boundaries for the case of ideally rigid blade and static divergence were also evaluated and presented in Fig. 6. By examining the results, an optimum value for blade bending frequency ratio  $n_\beta$  is found to be approximately 0.4. In a similar propeller-rotor configuration with a value of  $n_\beta$  less than 0.4, a sudden reversal from the backward whirl instability to a forward whirling would be developed. The stability boundary curve with  $n_\beta = 0.4$  encloses almost the largest stable region and allows a designer the maximum freedom to fulfill nacelle-suppling stiffness requirements.

## V. TRANSIENT RESPONSE ANALYSIS

A physical interpretation of a propeller-rotor configuration for dynamic stability is the transient response due to some initial disturbances. For a stable system, the amplitude of response would damp out in time, but in an unstable system the amplitude increases with time. A special case is the neutral stable condition, i.e., the response due to any initial disturbance could be represented by some harmonic functions with constant amplitudes. Numerical evaluations were performed on a PACE Model-231R active analog computer for five different propeller-rotor configurations to illustrate the above phenomena.

Referring to Fig. 6, use  $n_\beta = 1$  to define the stability boundary and pick five points along the  $n_{\phi_x}/n_{\phi_y} = 1$  line. In practice, this line represents an isotropic mounted nacelle. These five points correspond to  $n_{\phi_x}$  (or  $n_{\phi_y}$ ) = 0.4, 0.3, 0.2825, 0.25, and 0.2. The first two cases are in the stable region, the third one is on the neutral stable boundary, and the last two are in the unstable region. An initial angular velocity of 0.01 in the pitch direction was assumed throughout. The results were expressed through the usage of an X-Y plotter and are shown in Figs. 7a-7e. These figures clearly show the backward whirling phenomena as well as the degree of stability for each configuration. In these plots, the X-axis represents the pitch response and the Y-axis represents the yaw response. Hence, these figures actually represent the locus of the motion of a propeller hub.

## VI. COMPARISON OF THEORY WITH AVAILABLE EXPERIMENTAL INFORMATION ON SURFACE EFFECT VEHICLES

Since test results and structural information on existing SEV are not readily available, it is very difficult to make any rational precise experimental evaluation of the applicability of the theory to propeller-rotor systems. However, with the limited structural information available for SR.N2, SR.N3 and SK.5 air cushion vehicles, the following evaluations are made. The propeller-nacelle-pylon on SR.N2 is essentially the same as the one on SR.N3. The values of nacelle pitch and yaw natural frequencies, and the propeller blade fundamental bending frequency on SR.N2 or SR.N3 were obtained from Ref. [1]. The values of the same parameters on SK.5 were obtained from a vibration shake test performed by NSRDC.\*

The stability boundaries of the propeller-rotor configurations on SR.N2, SR.N3, and SK.5, shown in Fig. 8, were obtained from the interpolation of those shown in Fig. 6. This was based on the assumption that the nondimensional parameters used for stability analysis for SR.N2, SR.N3, and SK.5 were the same as those shown in Table 1. This may not necessarily be true; however, for the purposes of preliminary evaluation, the results should be close enough to give a designer a rough guidance. Nevertheless, experimental confirmation of the validity of the stability boundaries shown in Fig. 8 as well as those shown in Fig. 6 is still lacking. The only experimental

\* A. Hagen at NSRDC performed the SK-5 vibration shake test in March 1971.

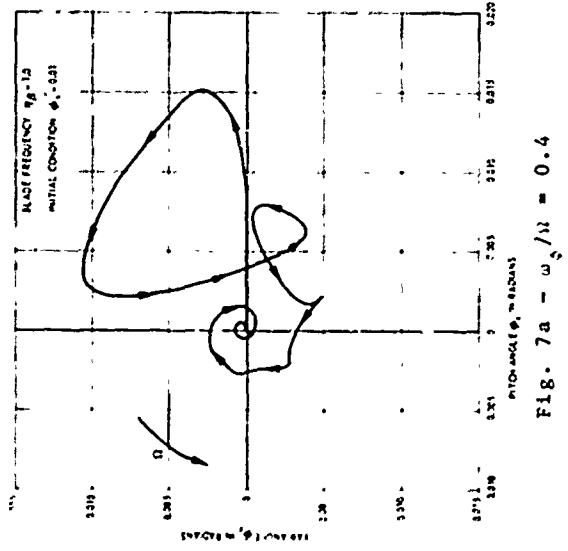


Fig. 7a -  $\omega_\phi/\Omega = 0.4$

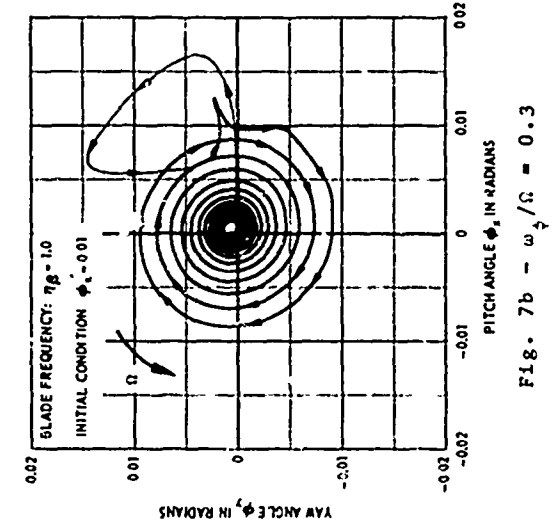


Fig. 7b -  $\omega_\phi/\Omega = 0.3$

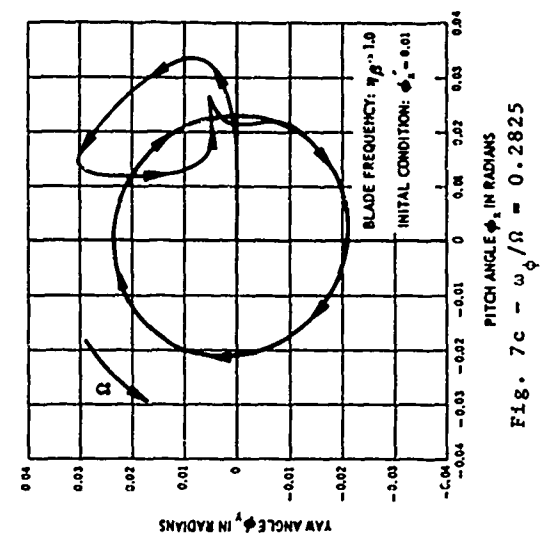


Fig. 7c -  $\omega_\phi/\Omega = 0.25$

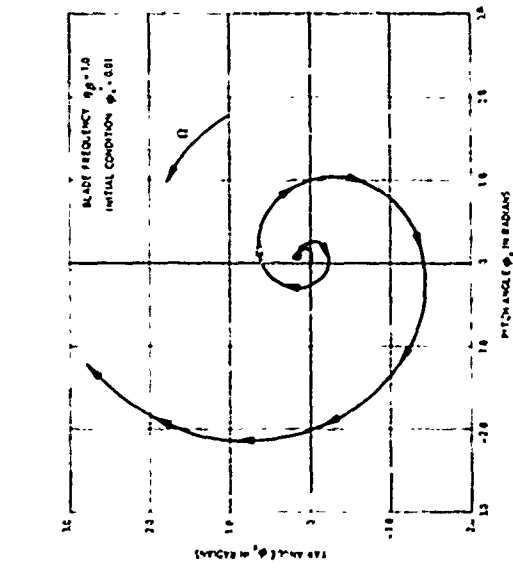


Fig. 7d -  $\omega_\phi/\Omega = 0.2$

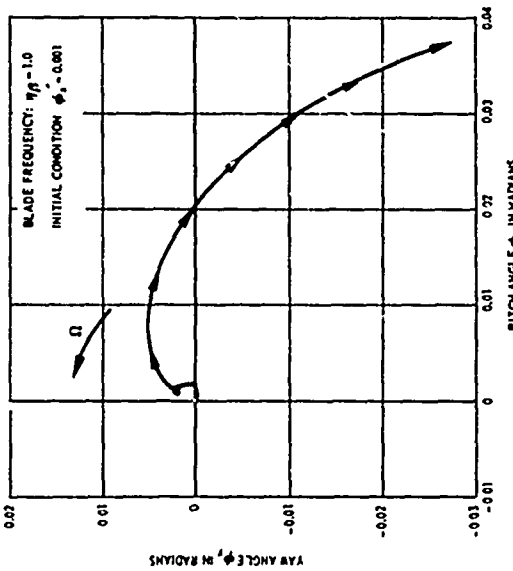


Fig. 7e -  $\omega_\phi/\Omega = 0.1$

Fig. 7 - Analog Simulation of Propeller Hub Motion for Various Nacelle Frequencies  $\omega_\phi/\Omega$  (Isotropic Nacelle Mounting)

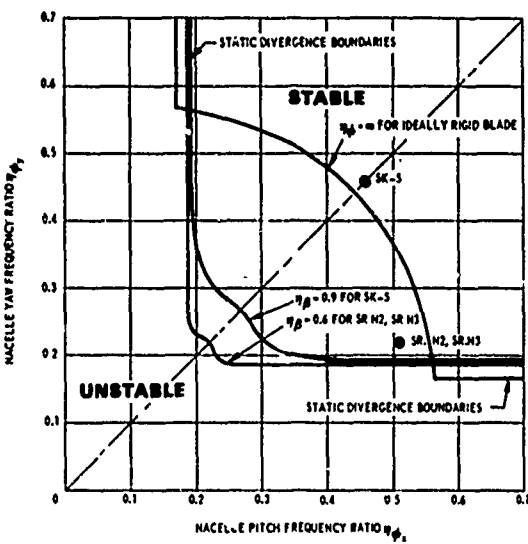


Fig. 8 - Propeller-Rotor Whirl Flutter Stability Boundaries for SK.5, SR.N2, and SR.N3 Air Cushion Vehicles

results the author could find were some observations on propeller-rotor vibration in Ref. [11].

" . . . The pylon situation is further complicated to the extent that not only will it have modes in the lateral plane but also in the vertical plane. In some of both the lateral and vertical modes the angular deflection at the propeller is considerable. As the propeller is rotating at high speed, angular motion, or precession, in one plane will induce a force in the plane at right angles, due to the gyroscope effect . . .

The propeller is obviously the main source of forcing in these modes . . .

Experience so far has disclosed appreciable vibration only in the lowest modes. Both SR.N2 and SR.N3 pylons can be seen to nod gently when running at idling conditions. The forcing at these conditions is very low, however,

and the condition is not serious . . ." (Ref. [11], p. 219.)

The above quoted statement clearly describes the propeller-rotor flutter whirling phenomenon and the actual occurrence on some SEV. Fig. 8 shows the same behavior, i.e., SK.5 has a very stable propeller-rotor configuration and SR.N2 or SR.N3 has a slightly stable one. How stable a system is can be judged by the distance between the data point and its corresponding stability boundary curve. As one can see from Fig. 8, the data point associated with SR.N2 or SR.N3 is very close to the neutral stable line and nacelle vibratory motion on SR.N2 and SR.N3 were observed.

In order to have a better feeling of the actual physical behavior of the propeller-rotor system on SR.N2 or SR.N3, an evaluation of transient responses due to an initial disturbance and the performance of a response analysis due to some random excitations were undertaken through the use of analog computer simulation. Fig. 9 shows the transient responses in both pitch and yaw directions due to an initial angular velocity 0.01. Fig. 10 shows the responses in the same directions due to some random excitations. Here the random excitations were generated by attaching a Gaussian noise generator to the analog circuit at the point associated with the nacelle pitching angular velocity. Fig. 10 also includes this particular noise output which has a rms value of 3.16, frequency range 0 to 50 Hz, and 3 JB cutoff. Fig. 9 shows the relatively small amount of damping in the system and Fig. 10 shows the actual response due to some random excitations

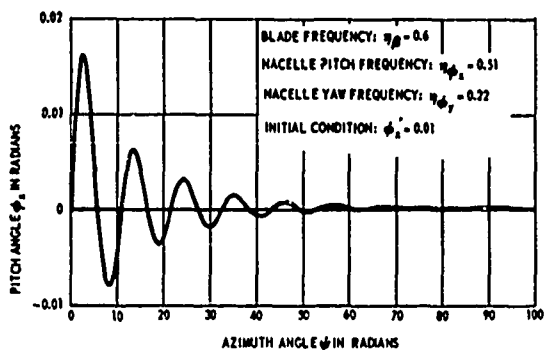


Fig. 9a - Nacelle Pitch Response

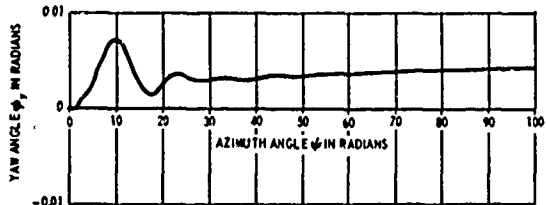


Fig. 9b - Nacelle Yaw Response

Fig. 9 - Analog Simulation of Propeller Hub Motion due to Initial Disturbance for SR.N2 and SR.N3 Air Cushion Vehicles

which always exist in reality. Both Figs. 9 and 10 clearly illustrate the relatively large oscillatory motion in the nacelle pitch direction in comparison with yaw. These results agree with the observations in Ref. [11] quoted above.

## VII. DISCUSSION

A propeller-rotor whirl flutter theory has been applied to pylon-nacelle-propeller configurations on surface effect vehicles. Stability boundaries based on a typical propeller-rotor system on large SEV were evaluated for the purpose of preliminary design and guidance. No experimental data were available to

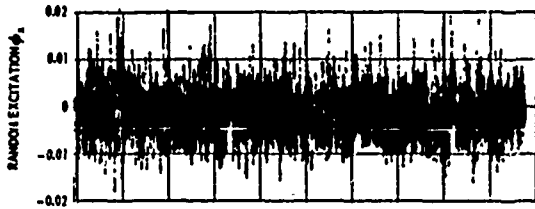


Fig. 10a - Random Exciting Forces

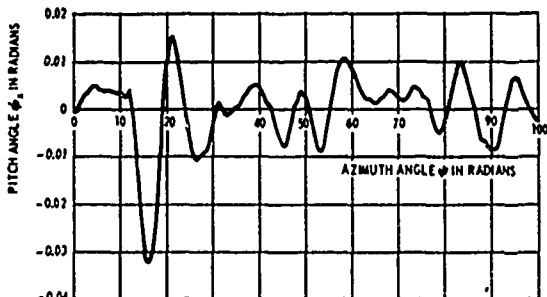


Fig. 10b - Nacelle Pitch Response

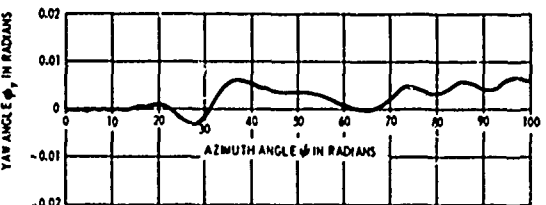


Fig. 10c - Nacelle Yaw Response

Fig. 10 - Analog Simulation of Propeller Hub Motion due to Random Excitation for SR.N2 and SR.N3 Air Cushion Vehicles

confirm the theoretical computations; however, some observations on SR.N2 and SR.N3 tend to agree with theoretical predictions.

As indicated in the evaluation of stability boundaries, blade fundamental bending frequency plays an important role since it affects the stability mapping. The classical whirl-flutter theory in which blades are assumed to be infinitely rigid gives the most rigid and

overly conservative stability criteria, leading to over-design and possibly uneconomical construction. An optimum value  $\eta_g = 0.4$  was found, and when the blade bending frequency is below this value, forward whirling as well as backward whirling could develop. However, the optimum value for blade bending frequency is restricted in the sense that it would allow a designer the most freedom to choose nacelle mounting stiffness in order to avoid whirl-flutter instability. Other dynamic considerations should be also included in overall design. As implemented in Fig. 6, increasing nacelle mounting stiffness to increase nacelle natural frequencies is another way to move a particular propeller-rotor configuration from the unstable region into the stable zone.

Transient analysis by analog computer simulation gives a direct physical interpretation of the actual whirl-flutter phenomenon. Transient responses due to initial disturbance and responses due to random excitations can be considered as the results of gusts and turbulence in the atmosphere or due to the irregularity in the ground/water surface. They are in connection with dynamic loads and fatigue failures. These loads may be significant for fatigue failure criteria even though the system is operating in the stable region. Observations on SR.N2 and SR.N3 tend to strengthen this consideration.

#### VIII. CONCLUSIONS

Analysis performed by applying the whirl-flutter theory on a typical propeller-rotor system of a large SEV resulted in a parametric chart for

design guidance. Direct experimental confirmation is not possible at this time, however, the following statements can be based on this analysis.

1. Observations of the nacelle motions on existing SEV tend to confirm the theoretical analysis used in this report.

2. Optimum fundamental blade bending frequency with respect to propeller rotating speed should have a value of 0.4 in order to impose the minimum requirements on nacelle supporting stiffness for a stable propeller-rotor configuration.

3. Classical whirl-flutter theory gives overconservative stability criteria which impose the most severe design requirements on the nacelle supporting stiffness.

4. Caution should be taken in the consideration of fatigue failure even when the propeller-rotor system is operating in the stable region.

#### IX. RECOMMENDATIONS

In view of the importance of a stable propeller-nacelle-pylon system on large high-speed SEV, and insufficient experimental data to substantiate the theoretical analysis of such a system, the following efforts are recommended.

1. Perform experimental evaluations by using a model with the same nondimensional parameters used in this report.

2. Perform a vibration shake test and underway test on a large SEV, and compare the test results with the theoretical computations in this report.

3. Extend the existing theory by including blade first torsion mode, blade second bending mode, and unsteady aerodynamic loadings.

4. Study the effects on the change of stability boundaries as functions of

important nondimensional parameters such as nacelle damping, nacelle length, blade inertia, propeller power setting, etc.

5. Study the effects on the change of stability boundaries due to the overall structural dynamic characteristics of surface effect vehicles.

#### REFERENCES

1. Taylor, E. S. and Browne, K. A., "Vibration Isolation of Aircraft Power Plants," J. Aero. Sci., Vol. 6, No. 2, pp. 43-49, Dec 1938
2. Houbolt, J.C. and Reed, W.H., III, "Propeller-Nacelle Whirl Flutter," I.A.S., pp. 333-347, Mar 1962
3. Reed, W. H., III and Bennett, R.M., "Propeller Whirl Considerations for V/STOL Aircraft," CAL-TRECOM Symposium on Dynamic Loads Problems Associated with the Helicopters and V/STOL Aircraft, Buffalo, N.Y., Jun 26-27, 1963
4. Reed, W. H., III, "Propeller Rotor Whirl Flutter: A State-of-the-Art Review," Symposium on the Noise and Loading Actions on Helicopter, V/STOL and Ground Effect Machines, Southampton, England, Aug 30 - Sep 3, 1965
5. Hall, W. E., Jr., "Prop-Rotor Stability at High Advance Ratios," J.A.H.S., Apr 1966

6. Niblett, T., "A Graphical Representation of the Binary Flutter Equations in Normal Coordinates," Royal Aircraft Establishment Tech. Rept. 66001, Jan 1966

7. Lytwyn, R. T., "Propeller-Rotor Dynamic Stability," The Boeing Co., Vertol Div., Tech. Rept. D8-0595, 1966

8. Edenborough, H. K., "Investigation of Tilt-Rotor VTOL Aircraft Rotor-Pylon Stability," Journal of Aircraft, Vol. 5, No. 6, Mar-Apr 1969

9. Brandt, E. E., "Aeroelastic Problems of Flexible V/STOL Rotors," paper presented at 34th AGARD Flight Mechanics Panel Meeting, 21-24 Apr 1969

10. Gaffey, T. M., Yen, J. G., and Kvaternik, R. G., "Analysis and Model Tests of the Proprotor Dynamics of a Tilt-Propotor VTOL Aircraft," Paper presented at the Air Force V/STOL Technology and Planning Conference, Las Vegas, Nevada, Sep 23-25, 1969

11. Elsley, G. H. and Devereus, A. J., Hovercraft Design and Construction, Cornell Maritime Press, Inc., 1968

12. Peterson, L., "SADSAM V User's Manual," MacNeal-Schwendler Corporation Project Report, 1970

#### DISCUSSION

Mr. Gayman (Jet Propulsion Laboratory): I ask for a point of clarification. Early in your presentation you discussed the degrees of freedom you were admitting to the problem in reference to blade bending. Did you not mean blade flapping as a rigid motion?

Mr. Liu: Yes, I meant the flapping motion of the blade, but only restricted to the first bending mode.

Mr. Gayman: That is associated with the oscillation of the plane of the propeller disk, is it not? The blades themselves are treated as rigid, are they not?

Mr. Liu: Perhaps I did not make the point very clear. We do consider the blade as an elastic blade but restrict it to the first bending mode. I made an equivalent system by considering the blade as rigid, but hinged at the hub. The system also included an equivalent rotation spring at the hub, and the bending or flexing frequency was the same frequency as the first bending mode.

Mr. Zudans (Franklin Institute): Because of the yaw and pitch of the nacelle, the blade plane moves as a rigid body. Was that motion included in your hydrodynamic forces?

Mr. Liu: Yes.

THE DYNAMIC RESPONSE OF STRUCTURES SUBJECTED TO TIME-DEPENDENT  
BOUNDARY CONDITIONS USING THE FINITE ELEMENT METHOD

George H. Workman  
Battelle, Columbus Laboratories  
Columbus, Ohio

The dynamic-matrix equation of motion characteristic of structures modeled by the finite element method of analysis is written in general form. This matrix equation is then rearranged and partitioned to separate constrained and unconstrained displacement degrees of freedom.

Once the general matrix equation has been properly partitioned, then by standard matrix manipulations, the original mixed boundary value problem is transformed to a modified force motion problem.

The dynamic response of a bellows subjected to dynamic edge displacements and internal pressure, as determined by this approach, is presented. This example is used as a vehicle to demonstrate the versatility and effectiveness of this solution technique.

#### INTRODUCTION

Over the past decade and a half, with the advent of high-capacity, high-speed digital computers and the increasing needs of the aerospace industry, the finite element method has emerged as a powerful tool for the structural analysis of large, complex structures. Evidence of this is the large number of general purpose finite element computer programs in use today.

The capability of this approach to obtain the dynamic response of complex structures to known forcing functions and base motion problems is well documented. This paper presents a straightforward extension of the finite element approach to solve dynamic response problems having time-dependent displacement.

#### METHOD OF ANALYSIS

In the finite element method, the continuum is separated by imaginary lines or surfaces into a number of "finite or discrete elements". These elements are assumed to be interconnected only at a discrete number of nodal points situated on their boundaries. The displacements of these nodal points are then the basic unknown parameters of the problem. The form that these discrete elements takes depends on the type of structural behavior assumed and the form of the approximation to that behavior.

Once nodal points and structural elements have been defined, the solution of this

discretized continuum elastic undamped dynamic problem becomes the solution of the matrix equation characterized as:

$$[M] \{ \ddot{\Delta}(t) \} + [K] \{ \Delta(t) \} = \{ F(t) \} \quad (1)$$

where

[M] = mass matrix

[K] = stiffness matrix

{F(t)} = nodal time-dependent forces

{\Delta(t)} = nodal displacements

\{ \ddot{\Delta}(t) \} = nodal accelerations.

The theoretical background and assumptions leading to the development of Matrix Equation (1) through the use of the finite element methodology is well known and not presented herein. Two excellent books describing the finite element method have been authored by Zienkiewicz<sup>(1)</sup> and Przemieniecki<sup>(2)</sup>.

Each row of Matrix Equation (1) represents a particular degree of freedom that, for this study, can be described as being associated with an unconstrained or constrained displacement. Displacements as used herein represent both translational and rotational motions. Constrained displacements are those degrees of freedom for which the motion is known as a function of time. This includes both zero and

nonzero motions. Therefore, accelerations and velocities of these constrained degrees of freedom are also known. Unconstrained displacements are those degrees of freedom for which the applied forces are known functions of time and whose resulting displacements are not prescribed.

Matrix Equation (1) can be rearranged such that those degrees of freedom associated with the unconstrained displacements and those associated with the constrained time-dependent displacements are partitioned as shown below:

$$\begin{bmatrix} M_{ii} & M_{ij} \\ M_{ji} & M_{jj} \end{bmatrix} \begin{Bmatrix} \ddot{\Delta}_i \\ \Delta_j \end{Bmatrix} + \begin{Bmatrix} F_i \\ F_j \end{Bmatrix} = \begin{Bmatrix} K_{ii} & K_{ij} \\ K_{ji} & K_{jj} \end{Bmatrix} \begin{Bmatrix} \Delta_i \\ \ddot{\Delta}_j \end{Bmatrix} \quad (2)$$

where subscript  $i$  is associated with the unconstrained displacements and subscript  $j$  is associated with the constrained displacements.

Matrix Equation (2) can then be expanded by rows and rearranged to yield

$$\begin{Bmatrix} M_{ii} & \ddot{\Delta}_i \\ F_i & \end{Bmatrix} + \begin{Bmatrix} K_{ii} & \Delta_i \\ M_{ij} & \ddot{\Delta}_j \end{Bmatrix} = \begin{Bmatrix} F_i \\ K_{ij} \Delta_j \end{Bmatrix} \quad (3)$$

and

$$\begin{Bmatrix} F_j \\ K_{ji} \Delta_i \end{Bmatrix} = \begin{Bmatrix} M_{ji} & \ddot{\Delta}_i \\ K_{ji} & \Delta_j \end{Bmatrix} + \begin{Bmatrix} M_{jj} & \ddot{\Delta}_j \\ K_{jj} & \Delta_j \end{Bmatrix} \quad (4)$$

Matrix Equation (3) is in the standard form associated with the elastic undamped multi-degree-of-freedom dynamic problem with a slightly modified right-hand side to include the effect of the constrained time-dependent displacements. This system of equations can be solved by a variety of methods depending on the requirements of the problem. Three excellent books giving a number of these techniques have been authored by Hurty and Rubinstein(3), Biggs(4), and Bisplinghoff, Ashley, and Halfman(5).

Matrix Equation (4) yields the reactive forces at the constrained displacement.

Once the time history solution of Matrix Equation (3) has been accomplished the nodal displacements of the discretized problem are known. The resulting time history of the stresses and strains in the individual elements can be determined from the assumed behavior pattern of the individual elements.

#### BELLOWS ANALYSIS

A dynamic analysis of a bellows was conducted utilizing the method of analysis given above. The bellows serves as a pressure seal between a vessel and a piston. The top edge of the bellows is attached to the stationary vessel and the bottom edge is attached to the moving piston used to generate a pressure pulsation in the vessel.

Figure 1 shows the bellows cross section. This shape was modeled by seven toroidal parts. Each part was described by its major and minor radii and the angular coordinates,  $\varphi$ , so that the exact shape of the bellows in its neutral position was reproduced quite accurately. The bellows is of uniform thickness,  $t = 0.062$  inch, and is constructed of steel sheet with  $E = 29 \times 10^6$  lb/in.<sup>2</sup> and poisson's ratio = 0.3.

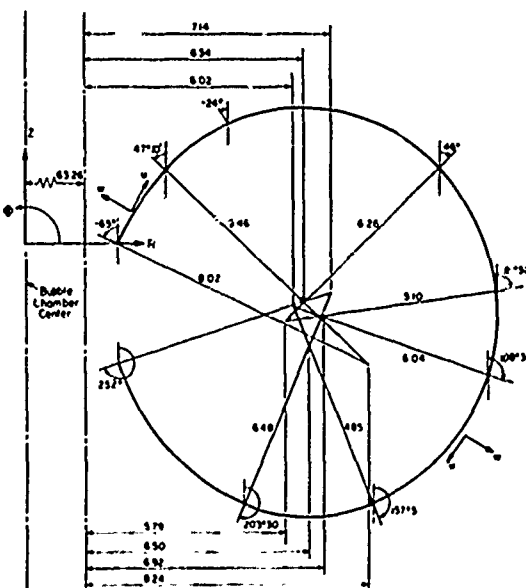


Fig. 1 - Cross section of bellows used for vibration analysis (neutral position)

Three finite element models of the bellows were created. These models contained 20, 30, and 40 conical elements, respectively. The basic conical element used in this analysis was similar to that developed by Grafton and Strome(6) except numerical integration was employed to generate the element stiffness matrix. An earlier study of this bellows was conducted utilizing a continuum axisymmetric shell program as the basic analysis tool. This program uti-

lized numerical integration of the governing continuum thin-shell equations. Unfortunately, the modulus of elasticity was taken to be  $27.4 \times 10^6$  lb/in.<sup>2</sup> for the bellows material and was assumed to  $29 \times 10^6$  lb/in.<sup>2</sup> for this study.

The mass of the bellows was lumped at the nodal points for the finite element model and was evenly distributed along the length for the continuum model. The two lowest axisymmetric natural frequencies of the bellows were calculated for the four models assuming both boundaries fixed. Table 1 gives the results of the natural frequency prediction along with the frequency determined experimentally for the first mode. The finite element models predicted natural frequencies slightly higher due to the difference in the assumed modulus of elasticity.

TABLE 2  
Natural Frequencies of the 30-Element Model

Mode No.	Frequency, cps
1	44.96
2	318.38
3	354.20
4	376.17
5	398.58
6	440.96

TABLE 1  
Natural Frequencies of Bellows Model

	Finite Element Model			Continuum Model	Experiment
	20-Element	30-Element	40-Element		
Mode 1	45.03	44.96	44.95	43.2	44.14
Mode 2	318.44	318.38	318.49	311	

Utilizing these natural frequency data it was decided to use the 30-element model for the dynamic analysis of the bellows. Figure 2 shows the node locations and elements for the 30-element model. Figures 3 and 4 give mode shapes for the first and second natural frequency, respectively. Also, the next four natural frequencies of the 30-element model were determined and are given in Table 2.

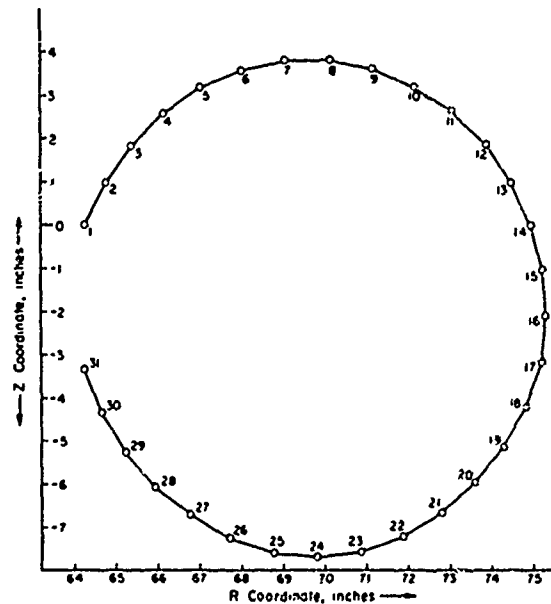


Fig. 2 - 30 element model of bellows

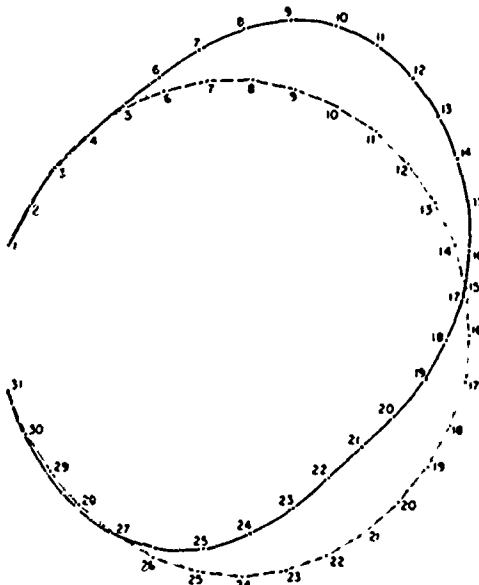


Fig. 3 - Modal deflection shape for first axisymmetric mode of bellows

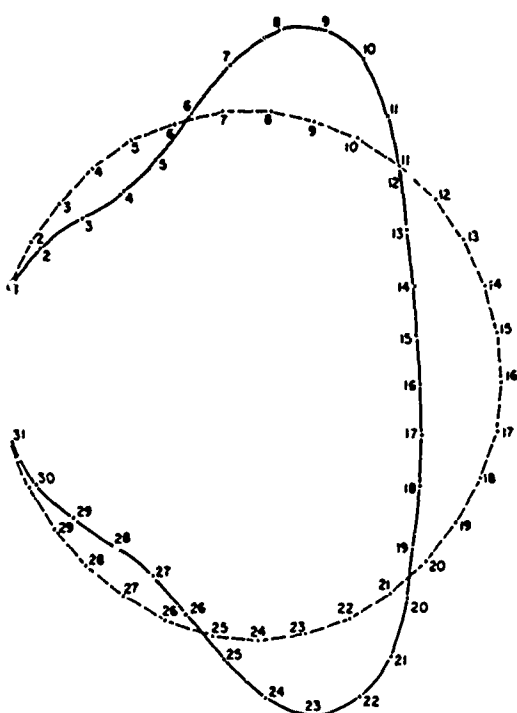


Fig. 4 - Modal deflection shape for second axisymmetric mode of bellows

The dynamic problem was formulated along standard finite element techniques for the forming of Matrix Equation (1). The constrained displacements are that the radial and vertical displacements and rotation of Node 1 are zero, the radial displacement and rotation of Node 31 are zero, and the vertical displacement of Node 31 is constrained to move downward as a versine with a period of 33 milliseconds and a maximum amplitude of 0.80 inch. The internal pressure of the bellows, initially at 80 psi, is in phase with the edge displacement, dropping to 10 psi as a versine. Figure 5 shows the internal pressure and edge displacement as a function of time. The matrix rearrangement and partitioning going from Matrix Equation (1) to Matrix Equation (3) is very straightforward when accomplished on the digital computer. The additional time, both engineering and computer, required to incorporate the dynamic mixed boundary value problem as formulated herein as compared with that for a typical force motion problem for a similar application is negligible.

One pulse of the piston was examined and no damping was included in this analysis. Experience has shown that, for analysis of this type, modal critical damping in the range of 0.5 to 1.0 percent gives realistic results. This small amount of damping has a minimal effect for the first few cycles and therefore was neglected in this preliminary study.

Two different techniques were employed for the solution of Matrix Equation (3). One was the straight numerical integration of Matrix Equation (3) by a fourth-order single-step Runge-Kutta method.<sup>(7)</sup> The other was the modal acceleration method.<sup>(5)</sup> Within the modal acceleration method only the first mode was employed. The static displacement component was determined utilizing standard static finite element techniques. By comparing the numerical integration solution and modal acceleration solution with only the first mode employed, it was clear that, for engineering purposes, only the first vibration mode makes any appreciable contribution to the dynamic solution.

Figure 6 shows the time history of the maximum stress occurring at the top side of the bellows; this stress occurred at Node 5 in the 30-element model. Figure 7 shows the time history of the maximum stress occurring at the bottom side of the bellows; that occurred at Node 27 of the model. The numerical integration solution is plotted in Figures 6 and 7 along with static stresses. The modal acceleration solution was not plotted because it would not be discernible from the numerical integration solution.

The dynamic magnification of the statically calculated stresses is quite clear when examining the plots given in Figures 6 and 7.

Figure 8 shows the time history of the vertical displacement of Nodes 8, 16, 24, and 31.

#### CONCLUSIONS

This paper has given and demonstrated a very straightforward and effective method of determining the dynamic response of structures subjected to time-dependent boundary conditions. This capability can be easily incorporated into an existing finite element computer program already programmed for dynamic force motion problems.

#### REFERENCES

1. Zienkiewicz, O. C., *The Finite Element Method in Structural and Continuum Mechanics*, McGraw-Hill, London, 1967.
2. Przemieniecki, J. S., *Theory of Matrix Structural Analysis*, McGraw-Hill, New York, 1968.
3. Hurty, W.C., and Rubinsteain, M. F., *Dynamics of Structures*, Prentice-Hall, Englewood Cliffs, New Jersey, 1965.
4. Biggs, J. M., *Introduction to Structural Dynamics*, McGraw-Hill, New York, 1964.
5. Bisplinghoff, R. L., Ashley, H., and Halfman, R. L., *Aeroelasticity*, Addison-

Wesley, Reading, Massachusetts, 1955.

6. Grafton, P. E., and Strome, D. R., "Analysis of Axi-Symmetric Shells by the Direct Stiffness Method", Journal A.I.A.A., Vol. 1, pp

2342-2347, 1963.

7. Ralston, A., A First Course in Numerical Analysis, pp 191-202, McGraw-Hill, New York, 1965.

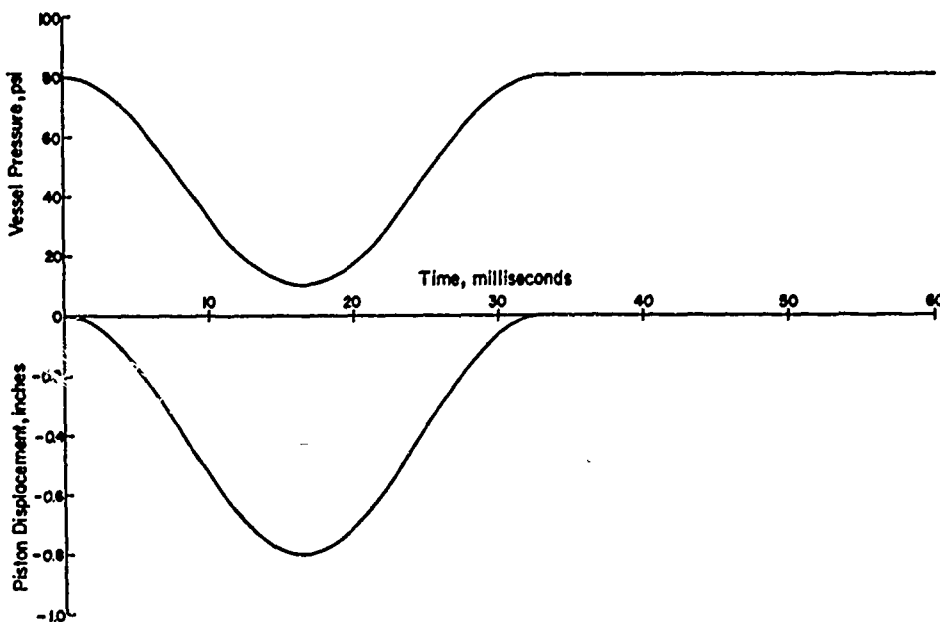


Fig. 5 - Time history of piston displacement and vessel pressure

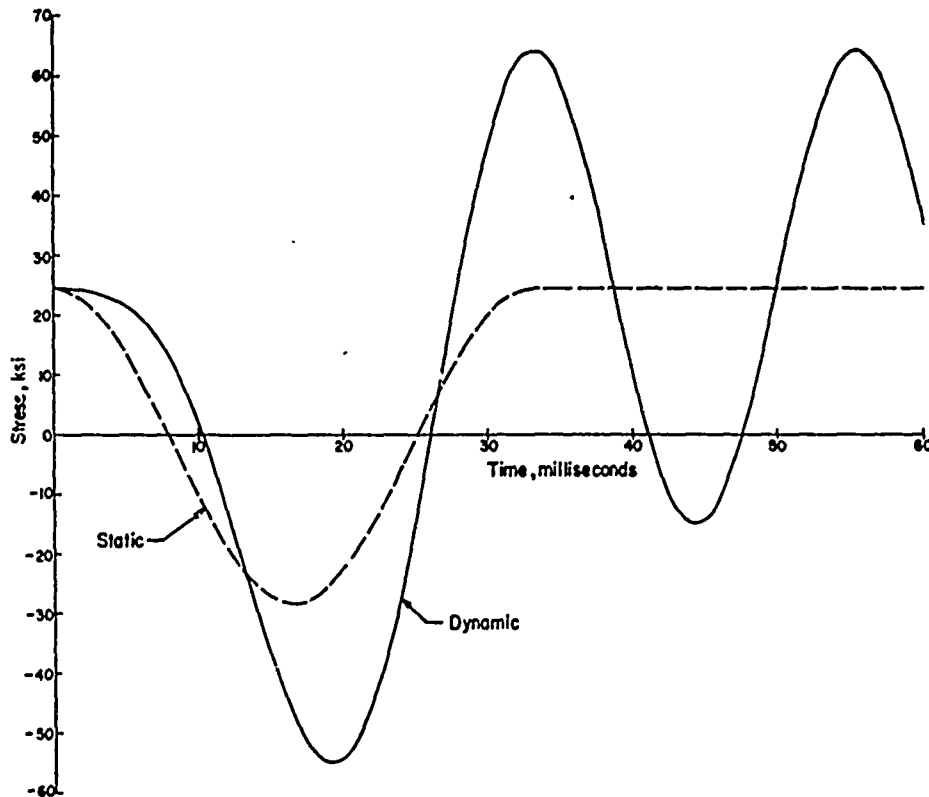


Fig. 6 - Time history of maximum stress at Node 5

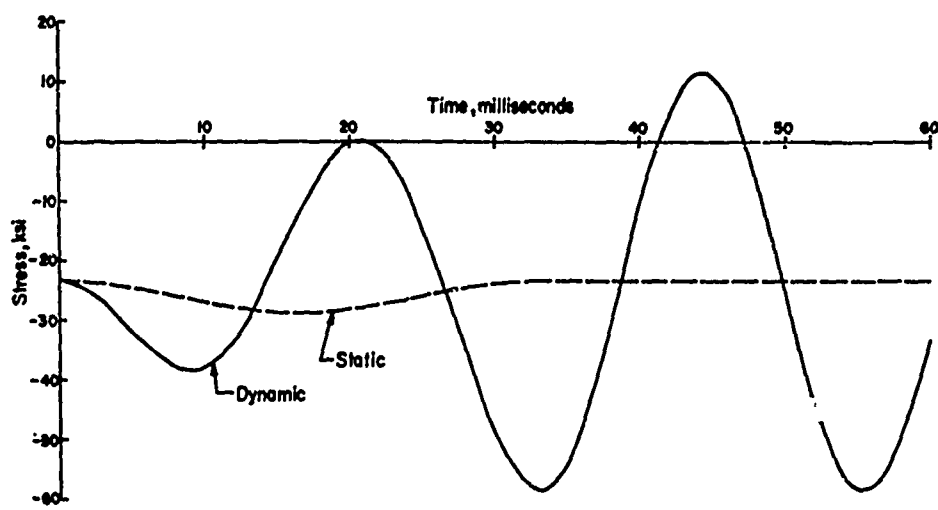


Fig. 7 - Time history of maximum stress at Node 27

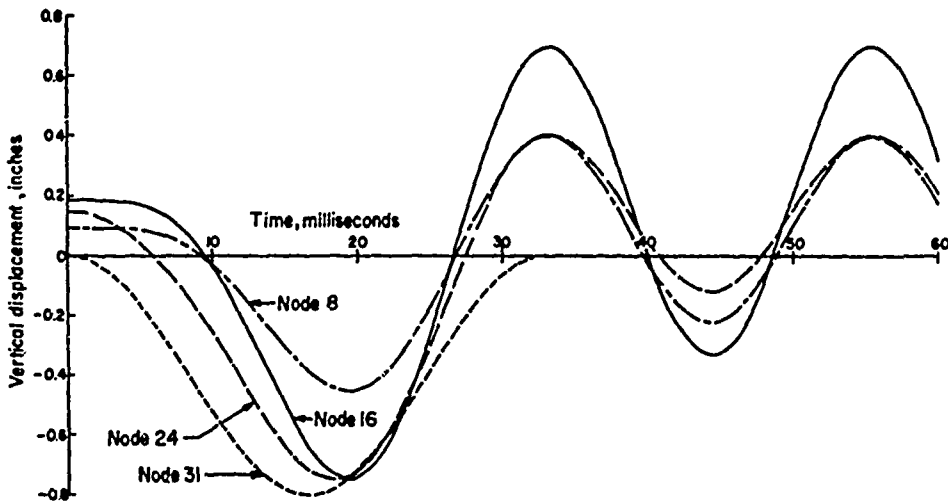


Fig. 8 - Time history of vertical displacement of Nodes 8, 16, 24 and 31

## DISCUSSION

Mr. Zudans (Franklin Institute): You mentioned comparison between modal solutions and you said that the response was entirely in the first mode. Yet the mode you showed was incompatible with boundary displacement, so you must have done something in addition to that.

Mr. Workman: No, the third slide showed the equation after it is rearranged to get it into the form that is solved. If you use the modal method on that equation, that boundary appears to be fixed. Then the displacement is used in the static solution. That mode finds the dynamic component, not the static displacement.

Mr. Schrantz (Comsat Laboratory): You said you used conical elements to define the bellows?

Mr. Workman: Right! I used a series of conical elements.

Voice: Is this a toroidal bellows? What form is it?

Mr. Workman: Yes, actually it is a toroid around a circular piston rather than a flat bellows. It is a shell of revolution.

## VIBRATION ANALYSIS AND TEST OF THE EARTH RESOURCES TECHNOLOGY SATELLITE

T. J. Cokonis and G. Sardella

General Electric Company  
Space Division  
Philadelphia, Pennsylvania

This paper presents a unique approach used for the launch vibration analysis of the Earth Resources Technology Satellite (ERTS) and compares the analytical results with experimental measurements. The ERTS is basically a modification of the Nimbus vehicle with solar array paddles unchanged. The complex paddle system could best be represented by measured data obtained from previous Nimbus modal testing. The successful extraction and subsequent re-coupling on ERTS of the solar array paddle modes from the original Nimbus experimental mode shapes is given. The analytical model is described along with its verification by an abbreviated modal test. Good correlation between test and analysis was evidenced by frequency and mode shape comparisons. Some areas of discrepancy in the analytical model were uncovered which were subsequently modified to improve the analytical representation of the spacecraft.

### INTRODUCTION

The Earth Resources Technology Satellite (ERTS) system (Figure 1) is being developed by the Goddard Space Flight Center (NASA) for obtaining data from near earth orbit immediately applicable to the determination of earth resources and their management. The spacecraft configuration will be launched on a Thor/Delta N-9 booster. The structural subsystem is based on the flight-proven Nimbus satellite using the same philosophy of design. The greater weight of the ERTS spacecraft and specific ERTS mission requirements necessitated structural modifications and some redesign.

The ERTS spacecraft structural segments are shown in Figure 2. These segments are: 1. The Attitude Control Subsystem (ACS); 2. The Solar Array Paddles; 3. The A-Truss Structure; 4. The Sensory Ring; and 5. The Launch Vehicle Adapter. Structural differences with respect to the Nimbus were primarily in the center section of the sensory ring assembly. New structure was designed to accommodate the ERTS payload and other new equipment. Sensory ring and truss structure was modified for increased stiffness and strength. In the launch configuration, the solar array is folded along its longitudinal axis to fit within the sensory ring envelope and is secured to the sensory ring structure by a latch mechanism. The spacecraft

is mounted on an adapter which is bolted to the launch vehicle adapter ring. Spacecraft adapter separation occurs at the lower ring flange of the sensory ring.

During the evolution of the Nimbus spacecraft from a 900-pound configuration to the 2000-pound ERTS configuration, the dynamic representation used for loads and clearance studies was based on an extrapolation of nodal test data on Nimbus A. Analytical comparisons with test results indicated that the extrapolated modal model no longer predicted the dynamic behavior of the spacecraft with the required degree of accuracy. This was evidenced in the flight loads analysis for the POGO condition using the extrapolated model which predicted extremely high loads due to high coupling between the lateral modes and the axial excitation. To overcome these deficiencies, a new analytical model was developed.

For an analytical model of the spacecraft the representation of the solar array becomes critical. This complex solar array was found to dominate all of the spacecraft modes. If finite element representation was used for the solar array, it would be difficult to derive and its accuracy would be questionable. This consideration was avoided, however, with a modal coupling approach using measured mode shapes. This required the extraction of 19 solar array

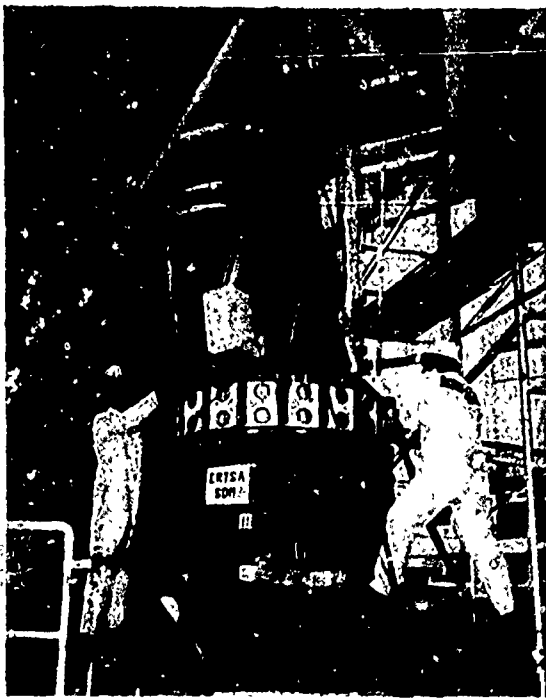


Figure 1. ERTS Spacecraft Vibration Test

normal vibration modes from Nimbus spacecraft modal data. Such an approach is valid since ERTS uses a solar array which is structurally unchanged from Nimbus. Paddle frequencies (starting at 13 hz.) and mode shapes having 154 coordinates were utilized for the new ERTS analytical model. Other major substructures were derived by a conventional finite element stiffness routine known as MASS (1). These substructures were then combined by modal coupling through a statically determinant interface in a manner similar to that used by Hurty and Hou (5, 8).

The following sections of the paper describe the formulation of the ERTS spacecraft analytical modal and its verification and evaluation by modal testing. Much of the modal dynamic analysis and testing activity conducted on ERTS/Nimbus programs parallels the well-documented Mariner Spacecraft Programs (5, 6, 7) and have had a similar degree of success.

#### DESCRIPTION OF ANALYTICAL MODEL

The analytical model of the spacecraft was developed by considering the major spacecraft segments separately. These structural segments are identified in Figure 2. Stiffness matrices were developed for the launch vehicle adapter, the sensory ring, truss, and ACS, and each segment was then combined to form the

complete spacecraft (less solar paddles) matrix. To complete the model, the paddles were added by the modal coupling technique. Nineteen paddle modes and 11 spacecraft modes (less paddles) were coupled to produce the final set of complete spacecraft modes and frequencies.

1. Spacecraft. The launch vehicle adapter structure was represented using over 160 internal joints in the MASS digital computer program (reference 1). These joints connected the beam and panel elements used to represent the adapter structure. The resulting stiffness matrix was reduced to nine external joints which were selected to coincide with the sensory ring external joints. The sensor ring structure in Figure 3 was modeled also using the MASS program. This representation consisted of over 250 joints connecting the beam and plate elements. The resulting stiffness matrix was reduced to 18 external joints common to the adapter, the truss, and other mass points of interest.

In a similar manner, the stiffness matrices of the truss and the ACS structures were also developed. The complete spacecraft structure, less paddles, was then assembled by the stiffness coupling of each segment. The fixed-free natural frequencies and mode shapes were calculated using this stiffness matrix and the mass matrix given by the distribution shown in Figure 4.

2. Solar Array. A very accurate representation of the solar array paddles was possible since measured mode shapes could be utilized. These measurements were taken from a previous modal survey of NIMBUS A (4) according to the pattern given in Figure 5. Since the ERTS spacecraft uses the NIMBUS solar array with minor modifications, these data were considered to be appropriate for the ERTS model.

The extraction of the 19 paddle modes from the NIMBUS modal survey started with the formulation of the characteristic matrix vibration equation:

$$\begin{matrix} n \times n & n \times m \\ [K] & [\Phi] \end{matrix} = \begin{matrix} n \times n & n \times m & m \times m \\ [M] & [\Phi] & [M] \end{matrix} \quad (1)$$

with  $[\Phi]$  normalized to,

$$[\Phi]^T [M] [\Phi] = [I]$$

where

- [K] is a  $n \times n$  square symmetric matrix of stiffness coefficients
- [M] is a  $n \times n$  square symmetric matrix of inertial mass items

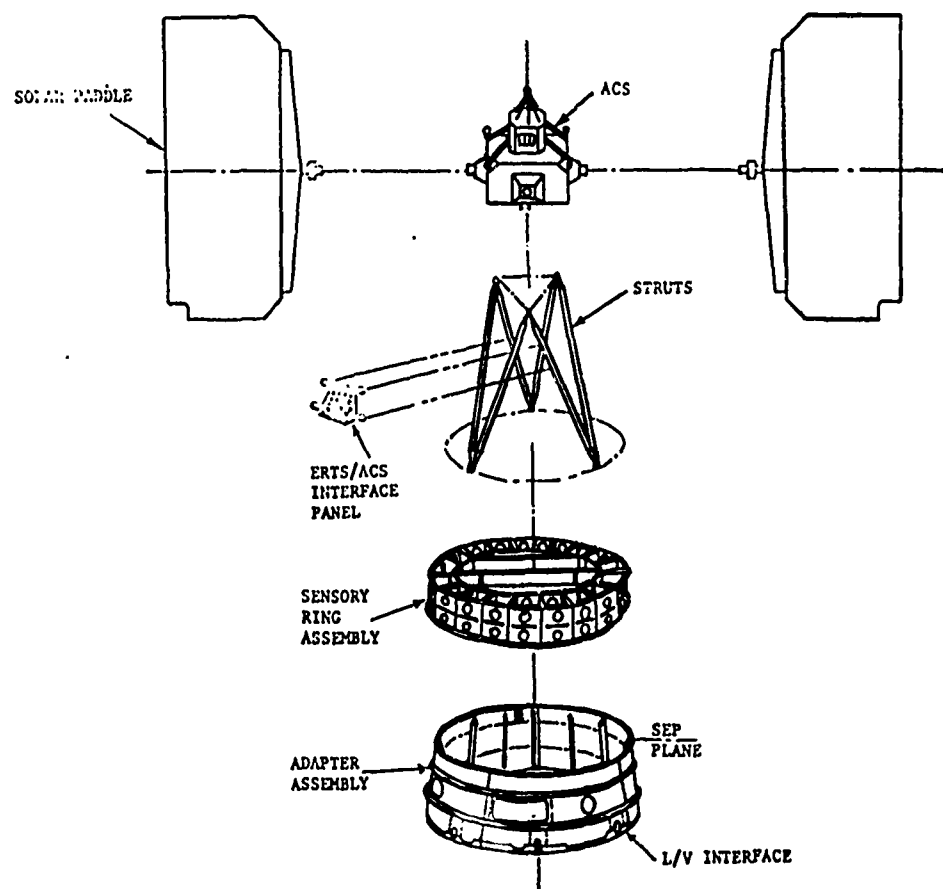


Figure 2 ERTS Structures Subsystem

$\lambda$  is a scalar of resonant frequency squared =  $\omega^2$   
 $[\Phi]$  is a  $n \times m$  modal matrix of eigenvectors (mode shapes) listed columnwise where  $m \leq n$   
 $[\Lambda]$  is a  $m \times m$  diagonal spectral matrix of eigenvalues ( $\lambda$ , resonant frequencies squared) listed diagonally where

$$[\Phi]^T [K] [\Phi] = [\Lambda]$$

$[I]$  is a  $m \times m$  identity matrix

$m$  refers to the number of modal degrees of freedom (modal coordinates)

$n$  refers to the number of generalized displacement coordinate degrees of freedom

Equation 1 can be manipulated to derive the stiffness matrix if the modal, spectral and inertial matrices are known (2, 3).

Post multiplying by:

$$[\Phi]^T [M]$$

$$[K] [\Phi] [\Phi]^T [M] = [M] [\Phi] [\Lambda] [\Phi]^T [M] \quad (2)$$

and utilizing the normalization

$$[\Phi] \left| [\Phi]^T [M] [\Phi] \right| = [\Phi] [I] \equiv [\Phi] \quad (3)$$

regrouping

$$[\Phi] [\Phi]^T [M] [\Phi] = [\Phi]$$

gives the identity

$$[\Phi] [\Phi]^T [M] \equiv [I]$$

which simplifies equation 2 to

$$\begin{matrix} n \times n & n \times n & n \times m & m \times m & m \times n & n \times n \\ [K] & = [M] & [\Phi] & [M] & [\Phi]^T & [M] \end{matrix} \quad (4)$$

Utilizing equation 4 nineteen constrained solar array paddle modes were determined from the original measured modes of the Nimbus Spacecraft by applying constraints at all non solar array coordinates.

The derived stiffness matrix was partitioned as follows:

$$\begin{bmatrix} K_{11} & K_{12} \\ K_{21} & K_{22} \end{bmatrix} \begin{Bmatrix} X_1 \\ X_2 \end{Bmatrix} = \begin{bmatrix} M_{11} & 0 \\ 0 & M_{22} \end{bmatrix} \begin{Bmatrix} X_1 \\ X_2 \end{Bmatrix} = \lambda \quad (5)$$

$$\text{Let } \begin{Bmatrix} X_1 \\ X_2 \end{Bmatrix} = \begin{bmatrix} \Phi_1 \\ 0 \end{bmatrix} \quad \begin{Bmatrix} Y_1 \\ Y_2 \end{Bmatrix}$$

where:  $K_{11}$  is the desired cantilevered paddle stiffness matrix

$X$  is the generalized physical displacement vector

( $\quad$ )<sub>1</sub> coordinates being retained; i.e., solar array

( $\quad$ )<sub>2</sub> coordinates being restrained, i.e., spacecraft

$$\begin{bmatrix} K_{11} & K_{12} \\ K_{21} & K_{22} \end{bmatrix} = \begin{bmatrix} M_1 & 0 \\ 0 & M_2 \end{bmatrix} \begin{bmatrix} \Phi_1 \\ \Phi_2 \end{bmatrix} \begin{bmatrix} Y_1 \\ Y_2 \end{bmatrix} = \begin{bmatrix} \Phi_1^T & \Phi_2^T \\ \Phi_2^T & M_2 \end{bmatrix} \begin{bmatrix} M_1 & 0 \\ 0 & M_2 \end{bmatrix} \quad (6)$$

$$= \begin{bmatrix} M_1 & 0 \\ 0 & M_2 \end{bmatrix} \begin{bmatrix} \Phi_1 & \Lambda & \Phi_1^T & \Lambda & \Phi_1 & \Lambda & \Phi_2^T \\ \Phi_2 & \Lambda & \Phi_2^T & \Lambda & \Phi_2 & \Lambda & \Phi_2^T \end{bmatrix} \begin{bmatrix} M_1 & 0 \\ 0 & M_2 \end{bmatrix} \quad (7)$$

$$= \begin{bmatrix} M_1 & \Phi_1 & \Lambda & \Phi_1^T & M_1 & M_1 & \Phi_1 & \Lambda & \Phi_2^T & M_2 \\ M_2 & \Phi_2 & \Lambda & \Phi_2^T & M_1 & M_2 & \Phi_2 & \Lambda & \Phi_2^T & M_2 \end{bmatrix} \quad (8)$$

Transforming Equation 5 in expanded form

$$\begin{bmatrix} \Phi_1 & 0 \\ M_1 & \Phi_1 & \Lambda & \Phi_1^T & M_1 & M_1 & \Phi_1 & \Lambda & \Phi_2^T & M_2 \\ M_2 & \Phi_2 & \Lambda & \Phi_2^T & M_1 & M_2 & \Phi_2 & \Lambda & \Phi_2^T & M_2 \end{bmatrix} \begin{bmatrix} \Phi_1 \\ 0 \\ Y_1 \\ Y_2 \end{bmatrix} = \begin{bmatrix} \Phi_1^T & M_1 & \Phi_1 \\ \Phi_2^T & M_1 & \Phi_1 \end{bmatrix} \begin{bmatrix} Y_1 \\ Y_2 \end{bmatrix} = \begin{bmatrix} \Phi_1^T & M_1 & \Phi_1 \\ \Phi_2^T & M_1 & \Phi_1 \end{bmatrix} \begin{bmatrix} Y_1 \\ Y_2 \end{bmatrix} = \lambda_p \quad (9)$$

solving the above eigenvalue problem yields  $\begin{bmatrix} Y_1 \\ Y_2 \end{bmatrix}$ ,  $\lambda_p$  and transforming

$$\text{back to obtain the paddle mode shapes } \begin{bmatrix} \Phi_{\text{Paddles}} \\ \Phi_i \\ 0 \end{bmatrix} = \begin{bmatrix} \Phi_1 \\ Y_1 \\ 0 \end{bmatrix} \quad (10)$$

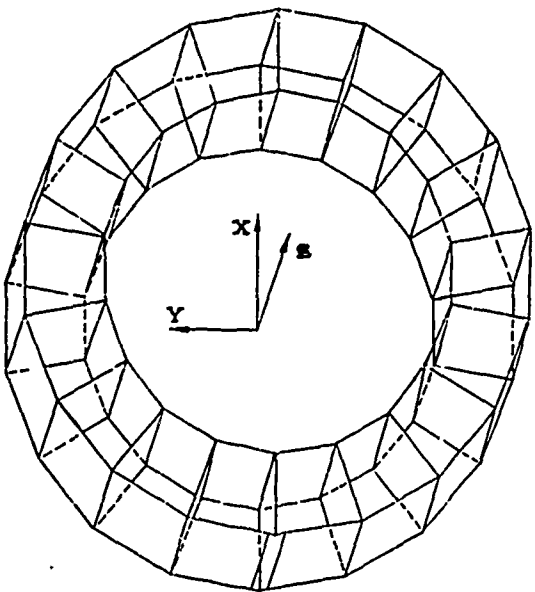


FIGURE 3 - MASS COMPUTER MODEL -  
SIMULATION OF SENSORY  
RING STRUCTURE (Cross-beam omitted for clarity)

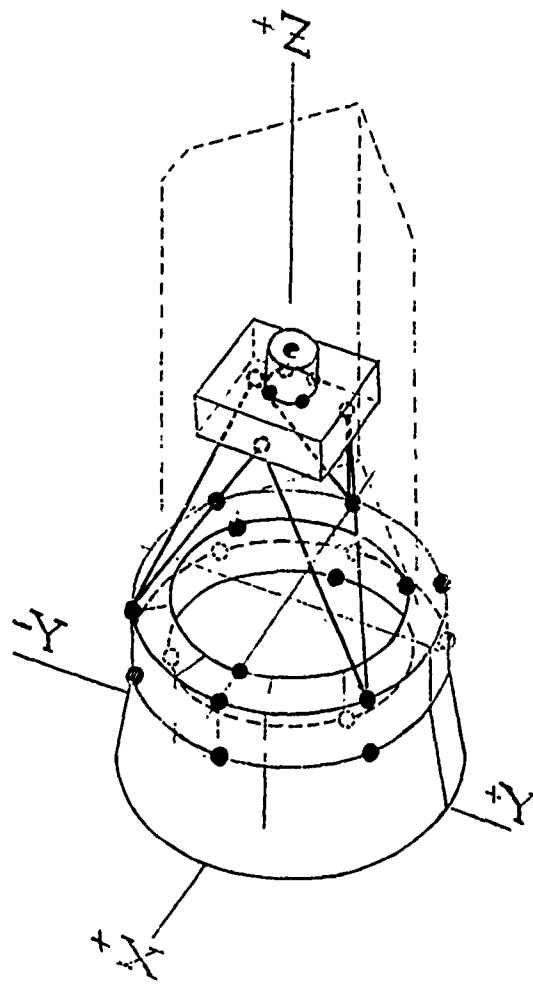


FIGURE 4 - SPACECRAFT ANALYTICAL MODEL

3. Modal Coupling. Having obtained the constrained modes, the statically determinant interface consisting of three translations and two angular reactions at the Solar Array Paddle Shaft and a latch line vertical tie to the sensory ring was released in the modal coordinate. This obtained the free modes. The free solar array and analytically derived ERTS spacecraft structures were then ready to be modally coupled to obtain the desired ERTS spacecraft vibration mode shapes and resonant frequencies.

Basically, a simplified Hurty (5, 8) attachment technique was used which entailed free mode coupling at statically determinate interfaces. The resulting eigenvalue equation form consisted of a coupled generalized mass matrix and diagonal generalized stiffness matrix with 30 degrees of freedom. Eleven modes of the structure and nineteen modes of the solar array were utilized in developing the complete system modes. The first twenty-four complete spacecraft modes ranging from 13 to 85 hz were subsequently correlated by vibration testing.

#### MODAL TEST DESCRIPTION

Modal testing of the ERTS full-scale structural dynamic model was performed as a

part of the structural verification test. The primary objective of this test was to obtain fixed-free modal vibration data suitable for evaluating the analytical model of the spacecraft for use in the flight loads analysis. This required the measurement of data sufficiently detailed to enable the response in the fundamental pitch, roll and yaw modes and the lateral modes in the frequency range of the POGO excitation to be evaluated.

Sine sweeps for modal definition were performed with low level base excitation at a rate of 8 minutes per octave. A total of ninety accelerometer channels were recorded during the resonant dwells. These were located on the spacecraft structure in triaxial and biaxial groups at points corresponding to mass points

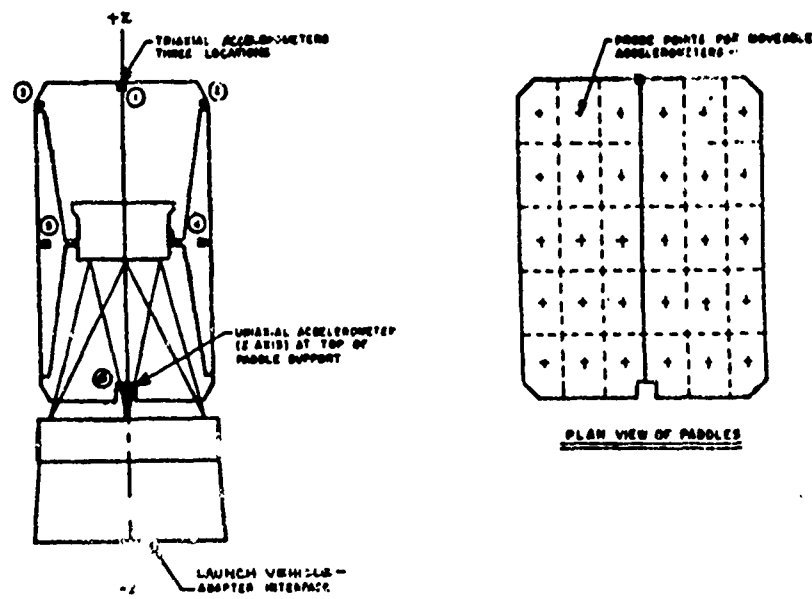


FIGURE 5 - ACCELEROMETER LOCATIONS FOR PADDLE MODAL SURVEY - NIMBUS

of the analytical model. The paddles were instrumented at its extremities only since modal data for this solar array had previously been obtained. (Previous Nimbus modal testing had recorded 200 channels of data with over 100 data points on the solar paddles). In-phase and quadrature response plots referenced to the input acceleration were obtained according to the phase separation technique of Reference (9) for particular accelerometer locations. These locations were selected based on analytical predictions of the paddle latch, ACS and sensory ring responses. Frequencies of interest were identified for resonant dwells. Since the testing was limited to the fundamental mode in each axis and the cross-axis modes in particular frequency ranges, not all resonances had modal dwells. Modal identification was established by plots of the quadrature component of acceleration. These plots were of the type given in Figure 6 and they were made for all of the dwell frequencies. From this group, nine significant mode shapes were determined. These modes were then used for direct comparison with the analytical mode shape.

The measured responses for the nine modes obtained were considered to behave as natural modes. This was based on reasonably good orthogonality shown by the evaluation of the generalized mass matrix which was calculated using the normalized experimental mode shapes. The average value of the off-diagonal

terms for the nine spacecraft modes was 9.4 percent. The test plan set a goal of  $\pm 10\%$  maximum coupling as evidenced by the off-diagonal terms for successful mode shape measurement. The greatest deviation from the criterion was found in the higher paddle modes. This result was anticipated since very few accelerometers were available for paddle response measurement. This became significant in the higher paddle modes where the necessary coarse mass distribution was inadequate.

A comparison of test and analytical resonant frequencies is given in Table 1. In general, the measured resonant frequencies are in good agreement with the corresponding calculated frequencies. This is particularly true for the fundamental pitch and yaw modes, the ACS roll mode, and the second paddle roll mode at 18.81 hz. Other frequencies were considered to be reasonably close to the corresponding calculated values. Resonant frequencies for which dwells were not made were estimated from total response plots and are noted with an asterisk in the tabulation.

Structural damping was determined by the method of Reference (9). This required the measurement of the frequency of the peak in-phase component of acceleration occurring just before and just after the resonance. The damping values obtained ranged from  $g = 0.032$  to 0.12. This corresponded to the range of magnification factors obtained in the high level vibration test.

A constant damping coefficient of  $g = 2 \text{ C/Cc} = 0.10$  was assumed for all modes in the analysis.

#### ANALYTICAL MODEL EVALUATION

The analytical model was evaluated on the basis of frequency, mode shape, and amplitude correlation with the analysis. Considering each area of comparison it was concluded that the analytical model was a good representation of the ERTS spacecraft. The basis of this conclusion is summarized in Table 2. Confidence in the model was supported by the good frequency agreement and the orthogonality checks.

In addition to frequency comparisons and orthogonality checks, another evaluation of mode shape was made. This was accomplished by the calculation of the modal shear for both test and analysis. The results here showed the agreement between test and analysis predictions to be within  $\pm 29$  percent for the primary response axis. There were larger deviations for those modes where the quantity of paddle measurements is critical. No criterion for this evaluation had been previously set, but the results were considered reasonable.

Improvements in the amplitude response were suggested by the damping evaluation where a range of values were measured for individual modes. A need for variation of the damping coefficient was indicated, especially in the lower frequency modes. Other possible areas of improvement considered as a result of the modal testing were in the mass distribution of the sensory ring and the representation of the launch vehicle adapter stiffness. Refinement of the analytical model was obtained without significant changes in the frequency correspondence. This resulted in better modal shear correlation with test within  $\pm 16$  percent. Also, better amplitude correlation was obtained by varying modal damping coefficients.

#### CONCLUSIONS

Analytically derived and test correlated mathematical models provide the most desirable data for use in ascertaining structural integrity of a spacecraft. Limitations in schedule and cost, however, frequently force the dynamicist to resort to abbreviated test and analysis procedures. The ERTS/NIMBUS experience has shown that satisfactory vibration models of subsystems or complete spacecraft can be established by analysis, test or a combination of both. The extraction technique was successfully demonstrated by the correlation with the modal test.

The limited quantity of measurements

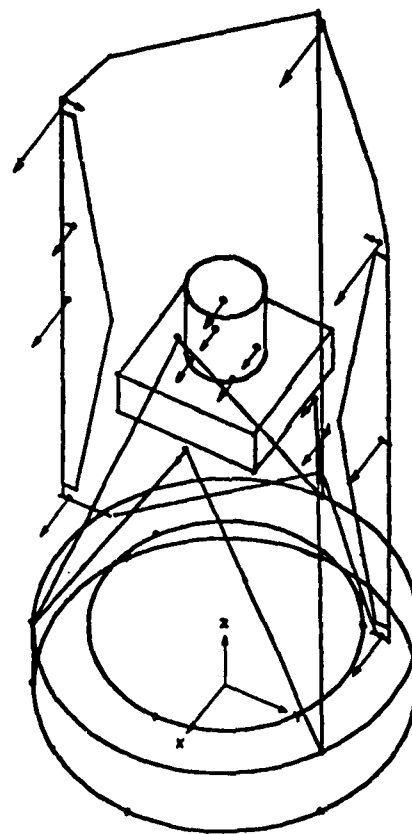


FIGURE 6 - ERTS MODAL TEST PLOT  
FREQUENCY: 15.29 Hz

made during the modal dwells restricted the scope of the analytical model evaluation. Where deviations from the criterion were large, as in the orthogonality check and modal shear comparison, they could be traced to lack of paddle measurements and not lack of validity of the mode. It was possible, however, to establish confidence in the model and to uncover some areas of discrepancy. This resulted in subsequent modification and improvements in the model. Improvement was made in the mode shapes which was reflected in better correlation of the modal shear. Also, better response amplitudes were obtained by the selection of damping for individual modes. The adjustments in the model were accomplished with insignificant changes in the frequency correspondence.

#### REFERENCES

1. Beitch, L., "MASS System - The Computer Program for General Redundant Structures With Vibratory and General Static Loading,"

TABLE 1.  
COMPARISON OF TEST AND CALCULATED NATURAL FREQUENCIES

NUMBER	CALCULATED NATURAL FREQUENCY CPS	MAJOR RESPONSE REGION	TEST NATURAL FREQUENCY CPS	
			X-AXIS	Z-AXIS
1	13.39	PADDLES	13.72	
2	14.13	PADDLES	15.29	
3	18.48	PADDLES	18.81	
4	19.57	ACS	17.47	
5	21.81	PADDLES	21.00*	
6	24.03	ACS	24.25	
7	29.29	ACS	28.50*	
8	31.09	PADDLES	30.22	
9	33.26	SENSORY, PADDLES	34.50*	
10	35.77	PADDLE, SENSORY	39.23	
11	38.53	PADDLE, TWIST	37.00*	
12	40.24	SENSORY, PADDLES	35.27	
13	43.71	SENSORY, PADDLES	39.00*	
14	47.42	SENSORY	41.00*	
15	48.92	SENSORY	42.50*	
16	53.57	PADDLES, SENSORY	50.00*	
17	55.34	SENSORY, PADDLES	53.00*	
18	58.24	PADDLES	55.00*	
19	58.76	ACS	59.35	
20	62.38	SENSORY, PADDLES	63.00*	
21	63.54	PADDLES, SENSORY	65.00*	
22	66.24	ACS	68.00*	
23	76.68	PNEUMATICS	79.50*	
24	85.29	PADDLES	90.00*	

\* APPROXIMATION FROM TOTAL RESPONSE PLOT; ALL OTHERS DETERMINED PRECISELY FROM QUADRATURE PLOTS.

TABLE 2 - ANALYTICAL MODEL EVALUATION

BASIS	ANAL. & TEST	REMARKS
a. Frequency	Very good	Correlation within less than 12% in most modes.
b. Orthogonality	Good	50% of all off-diagonal elements meet $\pm 10\%$ criterion; 80% meet $\pm 15\%$ criterion; overall average is 9.4%.
c. Modal Shear	Good	Primary axis of response less than 16% deviation. Those in excess lack paddle representation.
d. Amplitude	Fair	Measured damping ranges from 0.03 to 0.12 according to mode; analysis used 0.10 for all modes. Better correlation obtained by varying modal damping coefficients.

General Electric Co., TIS R66FPD172, September 13, 1966.

2. Cokonis, T. J., - "Structural Dynamics Modal Matrix Methods for the Coupling of Spacecraft/Launch Vehicle Systems," General Electric Company, TIS 68SD325, September, 1968.
3. Berman, A. and Flannelly, W. G. - "Theory of Incomplete Models of Dynamic Structures," AIAA Journal, Vol. 9, No. 8, pp. 1481-1487, August, 1971.
4. Smith, F., Freelin, T.R., Romano, R., and Hutton, F., - Nimbus Spacecraft Modal Survey Vibration Test Final Report, General Electric Company, TIS Report 68SD281, June, 1968.
5. Hurty, W. C. - "Dynamic Analysis of Structural Systems by Component Mode Synthesis," JPL Technical Report 32-530, Jan., 1964.
6. Holbeck, H. J., Arthurs, T. D., and Gaugh, J. J. - "Structural Dynamic Analysis of the Mariner Mars '69 Spacecraft," 38th Shock and Vibration Bulletin, Part 2, 1968.
7. Freeland, R. E. and Gaugh, W. J. - "Modal Survey Results from the Mariner Mars 1969 Spacecraft," Shock and Vibration Bulletin 39, February, 1969.
8. Hou, S., "Review of Modal Synthesis Techniques and a New Approach," Shock and Vibration Bulletin No. 40, Part 4, Dec., 1969.
9. Stahle, C. V., Jr., "Phase Separation Technique for Ground Vibration Testing," Aerospace Engineering, Vol. 21, No. 7, July, 1962.

## FINITE AMPLITUDE SHOCK WAVES IN INTERVERTEBRAL DISCS

William F. Hartman  
The Johns Hopkins University  
Baltimore, Maryland

The nonlinear deformation of intervertebral discs is discussed. The upward turning stress-strain curve implies that the discs will tend to shape pulses having sub-millisecond rise-times into shock waves and that shock inputs will propagate as shocks. These implications are explored for axial compressive impact of the spine, such as is incurred during aircraft-pilot ejection or during a fall onto the buttocks. Correlation with experimental results suggests that the application of finite amplitude wave theory to the shock loading of the spine should be further investigated.

### INTRODUCTION

A knowledge of the mechanical properties of human vertebrae and intervertebral discs is fundamental to understanding body mobility and spinal injuries and to designing protectors and prostheses for these spinal components. The dynamic response of an intervertebral disc must be studied in order to predict the vertebral stresses that are caused by rapid motions or impact. Most measurements of the dynamic mechanical properties of the disc have been restricted to small-amplitude deformations which are assumed appropriate for the perspective of linearized response. I here describe some of the large amplitude non-linear characteristics of the intervertebral discs and discuss the implication of these on the dynamic response of the spine.

The human spine is a nonuniformly curved column normally consisting of 7 cervical, 12 thoracic, 5 lumbar vertebrae and the sacrum-coccyx structure. Each vertebra has a cylindrical anterior part called the vertebral body and posterior arch-like parts called pedicles and facets. The latter guide and restrict relative displacements between the vertebrae for bending and torsion deformations but take up only 20% of axial loads[1]. The vertebrae are soft, cancellous bones, decreasing in height upwards, from about 1.2 in. for the fifth lumbar to about 0.5 in. for the third cervical vertebra. Adjacent vertebral bodies are separated by an intervertebral disc which in the lumbar region is approximately 0.4 the height of the vertebrae.

The intervertebral disc is a nonuniform

structure consisting of an elastic fibrocartilaginous envelope, the annulus fibrosus, and a fibroelastin core, the nucleus pulposus, which contains water in a mucopolysaccharide collagen framework[2]. The disc is capped above and below by bony end-plates which are distinct from the vertebral bodies. This structure of the disc suggests a possible appropriate mechanical model to be a sealed elastic cylinder containing a viscous fluid. However, not enough is known about the geometry or the material properties to warrant such modelling. The disc seems mechanically symmetrical about its vertical axis, as can be inferred from the compression measurements of Brown et al.[3]. Since the only data, which I shall discuss here, pertains to compressive loads and the resulting average strain, I shall assume the disc to be uniform, having the average mass and size of the actual disc-complex.

Herniation of the intervertebral disc results in a loss of material from the nucleus pulposus. This can be caused by trauma or disease and is one of the frequent etiological factors associated with back-pain and, in severe cases, sciatica[4,5]. Furthermore, 60% of all disc protrusions are caused by injury; one-third of these by a fall onto one's feet or buttocks, resulting mostly in injuries to the lumbar spine[6]. During static compression of the lumbar spine the vertebral endplate frequently fractures, allowing the nucleus pulposus to protrude into the spongiosa of the vertebral body[7]. Often this causes the cancellous bone to collapse and continued loading produces a comminuted fracture of the vertebral body.

Preceding page blank

Hypotheses about the type and mechanism of dynamically induced injuries could result from impact experiments or they may be formulated from an extension of the available static data. Of course, viscous effects are naturally anticipated for the deformation of a structure having the material composition of the disc. Although the viscous properties of vertebral bodies and intervertebral discs have not been documented for the large non-linear deformations which precede failures, the damping properties have been measured for small deformations. Fitzgerald and Freeland[8] have shown that the damping of fresh canine discs decreases with increasing frequency, while Markolf and Steidel[9] report the damping of the entire intervertebral joint is small for the compression-tension mode of deformation. These results suggest neglecting viscous effects in a first analysis of the stresses caused by compressive impact. It would be overly presumptuous to expect that accurate results could be obtained for a large range of impact speeds; but any analysis using only the data which is available is worthwhile if only to point out the necessity for specific additional experimental programs. In what follows I shall estimate the impact response of intervertebral discs using static stress-strain data obtained from the literature.

#### STRESS-STRAIN CURVES FOR INTERVERTEBRAL DISCS

Load-deflection data for the compression of lumbar intervertebral discs are given in [3,10, 11]. The compression tests of both Brown et al. [3] and Virgin[10] employed conventional testing machines and used specimens which had the posterior facets and pedicles removed. The dimensions of specimens were not reported, so I calculate stress by dividing axial load values by the average area of the appropriate lumbar disc as given by Perey[7]. Strain is calculated by dividing the deflection by the nominal height[12] of the corresponding disc. For the data of Virgin and Brown, this results in the stress-strain curve shown in Fig. 1. Virgin's data is reproduced from his "typical" load-deflection curve while Brown's is computed using the averaged values of four compression tests which are each described in [3]. The two curves are more than similar for both are proportional to the squared strain and the proportionality constant is the same for each. This suggests that the non-linear response of the disc can be well defined, for these two sources of data were obtained by different investigators in different countries using different testing machines and probably different loading rates. The tests of Virgin were conducted 20 years ago, those of Brown et al. 14 years ago and yet, to my best knowledge, I present here the first correlation of any independently performed tests of this

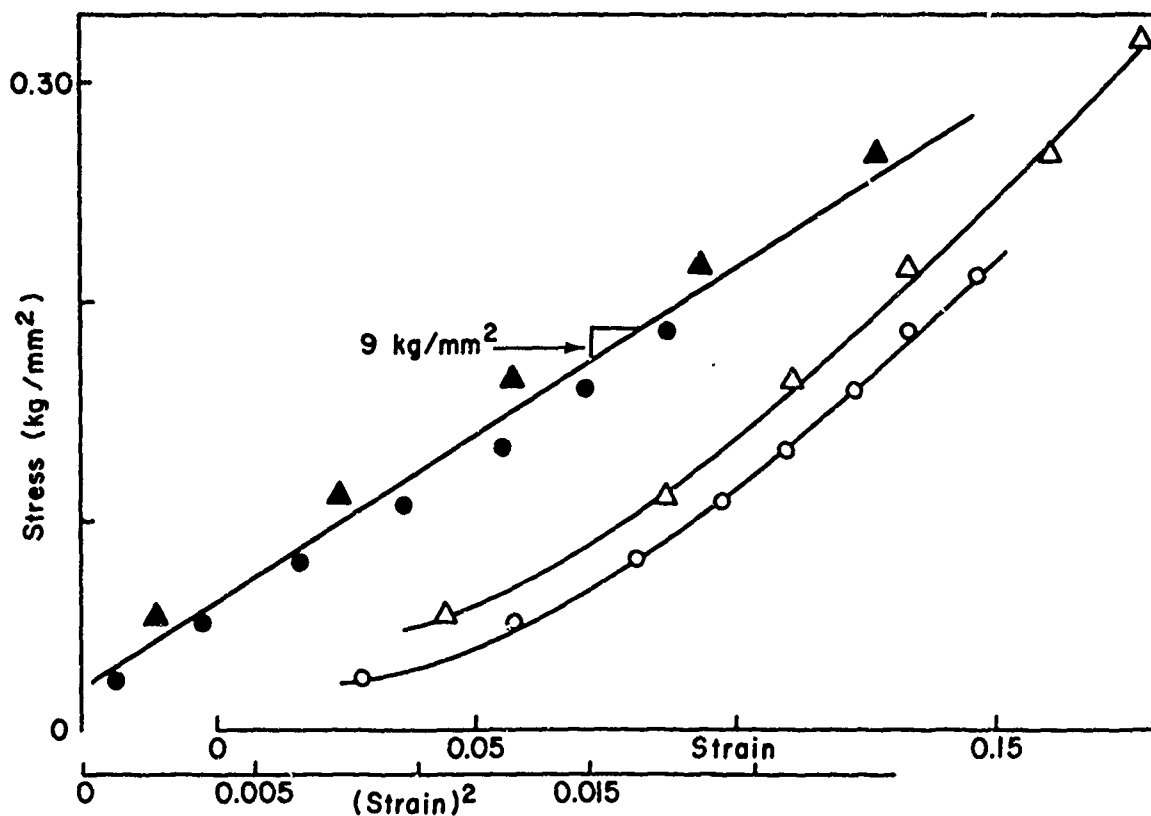


Fig. 1. Stress-strain curves for lumbar discs obtained from the data of Virgin, o, and Brown et al., ▲. Filled-in symbols are stress plotted against squared strain.

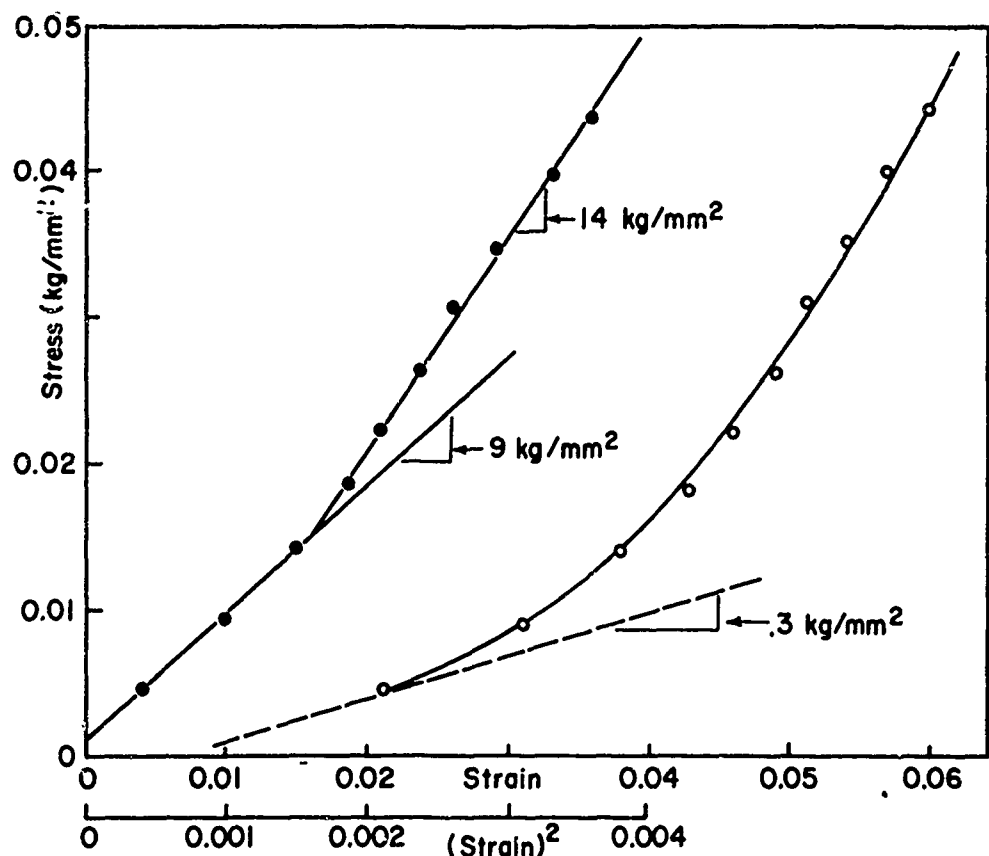


Fig. 2. Stress versus strain, o, and squared strain e - from fourth lumbar disc data of Hirsch[11]. The near-zero modulus for canine disc[8] is shown as ---.

kind. Furthermore, since neither [3] nor [10] report the cross-sectional areas of the specimens, the shift in the curves of Fig. 1 might be partially due to the use of inappropriate areas for one or both sets of data.

Reproducibility and consistency can be found in other mechanical properties of spinal components. For example, the average vertebral fracture stress calculated from the data of Perey[7] is .34 kg/mm<sup>2</sup>, which is the same value obtained from averaging compressive fracture strengths given in [3]. Of course, it is reasonable to assume that a general material description will apply to vertebrae and discs only for the averaged data of several specimens from several bodies. Variations are due to differences in age, size, sex, disease, injury, and specimen preservation. Normal deteriorations are not yet well documented and certain pathological disorders certainly go undetected. Nevertheless, the degree of consistency noted above suggests that gross material characterization is both sensible and ultimately useful.

The compressive deformation of intervertebral discs is also reported by Hirsch[11]. His

specimens contained half the upper and half the lower vertebral body and the corresponding intervertebral joints. The posterior pedicles and facets have been shown to take up approximately 20% of the axial load[1]. Therefore in calculating the stress on the disc from Hirsch's data, I use 80% of the load values. The longitudinal strain is calculated from the reported lateral bulge of the disc, assuming uniform incompressible deformation there. This is a poor assumption for large values of stress because Nachemson[13] has shown that the lateral bulging varies nonlinearly with axial strain and the disc's volume is known to decrease[3]. However, it should hold approximately for small values of stress and give at least an estimate for moderate stress. This procedure results in the stress-strain curve of Fig. 2. The initial nonlinearity is precisely the same as that of Fig. 1. The change in the slope of the stress-squared strain plot might correlate with the inapplicability of the incompressibility assumption. A qualitative correction, based on Nachemson's measurements, would increase the strains for increasing stress, thereby making the slope more akin to the initial behavior which agrees with the data of Fig. 1.

## WAVE PROPAGATION IN THE SPINE

A distinguishing feature of the stress-strain curve for the compression of intervertebral discs is its concavity away from the strain axis. Such material behavior is typical of many biological materials but here it has interesting implications regarding stress-wave propagation along the spine.

The one-dimensional finite amplitude wave theory as developed by Karman and Taylor is given in [14]. Some pertinent results of that theory, which is applicable for nonlinear strain-rate independent elastic or plastic deformations, are as follows. If the stress-strain relation is written as

$$\sigma = \phi(\epsilon) \quad (1)$$

where  $\sigma$  is the longitudinal stress,  $\epsilon$  the longitudinal strain, and  $\phi$  the response function, then the speed of propagation,  $C(\epsilon)$ , of any strain level is

$$C(\epsilon) = (\phi'/\rho)^{1/2} \quad (2)$$

where  $\rho$  is the density of the solid. The particle velocity,  $V(\epsilon)$ , associated with any  $\epsilon$  or  $\phi(\epsilon)$  can be written

$$V(\epsilon) = \frac{\epsilon}{t} C(\epsilon) d\epsilon \quad (3)$$

If  $\phi(\epsilon)$  is an upward turning function then  $\phi'(\epsilon)$  increases with strain and so the wave speeds given by Eq. (2) increase with strain. An interpretation of this result is that if a unit-step shock input is applied to the one-dimensional material then it will remain shock-like since the speed of the maximum stress is the greatest speed. On the other hand, if the material is subjected to a gradually rising pulse, then this pulse as it travels through the material will become continuously steeper since the larger strains propagate faster. If the material is sufficiently long, every pulse regardless of its shape will eventually develop into a shock.

Although the spine has the appearance of a curved rod, its axial dynamic response could be properly described as one-dimensional only if its major components, the vertebral bodies and the intervertebral discs, were dynamically similar. The vertebrae are sometimes assumed as rigid bodies in comparison with the discs for dynamic analysis[12]. Such an assumption does not square with the stress-strain relation shown in Fig. 3. This was constructed using the data on [7] for the compression of vertebral bodies. Both the deformation and the slope of this stress-strain curve are comparable with those of Figs. 1 and 2. Therefore, since the densities differ only by a factor of 2, the spinal components must be considered dynamically similar. Nevertheless, there are important subtle

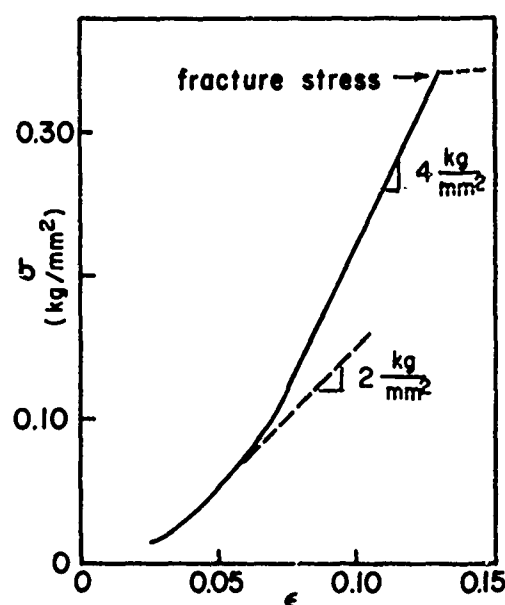


Fig. 3. Stress versus strain for a lumbar vertebral body - from the data of [7].

distinctions. The vertebrae, especially for large stresses, behave linearly. Also, the strength of the disc is generally assumed to be greater than that of the vertebrae. A perspective retaining the individual material properties of these components will result in a rather complicated picture for impact problems, especially since the sizes of the discs are such that individually they are not rods, their diameters being larger than their lengths. Since I have already indicated that I will ignore the nonuniform structure of the discs, I do not hesitate to assume that one-dimensional wave propagation can be used to obtain reasonable estimates.

Using the data described thus far, and Eqs. (2) and (3), I consider: (1) the pulse-shaping performed by the discs, (2) the prediction of the impact response of a preloaded vertebrae-disc-vertebrae specimen and a comparison with the experimental results given in (11), and (3) the prediction of the impact speed which would produce fracture in the fifth lumbar vertebra. In all cases only compressive axial deformations are considered, the spinal curvature, bending and viscosity are ignored.

The gross weights and dimensions of fresh canine intervertebral discs are given in [8]. Using these, a bulk density for the disc is calculated to be 2.22 g/cm³. Taking the average curve of Fig. 1 and the above value for  $\rho$ , Eqn. (2) results in the curve of Fig. 4. Nachemson and Morris[15] have reported *in vivo* measurements of intradiscal pressures for normal loads such as those occurring during standing and sitting. The corresponding axial stresses range from .04 to .08 kg/mm². The average

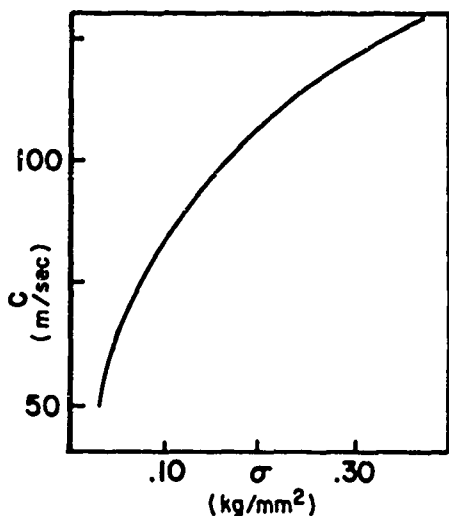


Fig. 4. Variation of wave speed with stress.

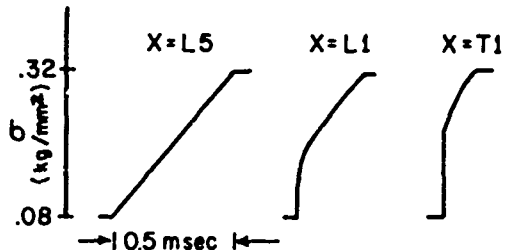


Fig. 5. Example of shock formation by discs.

vertebral fracture stress, which can be obtained from the data of [7], is  $.35 \text{ kg/mm}^2$ . Therefore, Fig. 4 shows that the wave speeds double over the range of probable dynamic stresses.

Fig. 5 illustrates the pulse shaping which can occur as a stress pulse propagates along the spine. In this case a linearly rising pulse increasing from the normal sitting stress to a value which is less than the fracture stress steepens from a 0.5 msec rise time at the fifth lumbar vertebra to a partial shock and 0.1 msec tail at the first thoracic vertebra. Of course any pulse whose initial rise time is less than 0.5 msec would become a more fully developed shock; while pulses whose rise times are longer than several msec would not be noticeably shaped. Rise times less than 1 msec seem plausible for dynamic stressing such as those occurring during aircraft-pilot ejection.

The porous structure of the soft cancellous bone of the vertebrae make them inherently weaker in tension than in compression. During sufficiently gradual application of compressive forces the deforming vertebrae uniformly distribute the load effectively over the entire cross section due to the collapse of voids and the reduction of porosity. However, if compressive

stress is applied sufficiently rapidly, such as a stress pulse whose length is less than the average pore size, then the effective cross-sectional area is reduced and failure will occur at a lower nominal stress. Thus the shock wave formation as described here could account for the fact that vertebral fractures occur in the thoracic vertebrae during pilot ejection even when no damage is sustained by the lumbar spine [12].

Some impact experiments on spinal segments were performed by Hirsch[11]. A lumbar disc and half of each adjacent vertebra including the posterior processes were preloaded in compression and then subjected to impact by allowing a weight to fall through a known height onto the loading lever of the testing machine. Since Hirsch did not report the dimensions or the materials of the testing apparatus, the effective impact speed at the vertebra cannot be calculated. Nevertheless, his recorded values of the dynamic bulging of the disc together with the stress strain curves of Figs. 2 and 3 and Eqn. (3) permit a check on the consistency of the present mechanical perspective. Assuming continuity of stress and particle velocity at the vertebra-disc interface the following jump equations apply for a shock input.

$$\begin{aligned} [\sigma_I] + [\sigma_R] &= [\sigma_T] \\ [v_I] + [v_R] &= [v_T] , \end{aligned} \quad (4)$$

where I, R label the incident and reflected shock in the vertebra and T labels the transmitted shock in the disc. Using a constant vertebrae impedance, the linear shock equations, the stress-strain curve of Fig. 2 and Eqn. (3), the response curve of Fig. 6 is obtained. The experimental points shown in the figure are plotted taking the equivalent impact speed to be twice that of the drop speed. The agreement with the theory further suggests that it might be rewarding to pursue experimental studies of wave propagation in the spine.

Using Eqns. (4), the speed sufficient to cause vertebral fracture from impact onto an infinite impedance may be calculated. The resulting expression is:

$$2[v_I] = [\sigma_0] + \frac{c}{Z_v} \int C(\epsilon') d\epsilon' , \quad (5)$$

where  $Z_v$  is the impedance of the vertebral body.

In the above, let  $[\sigma_0] = 0.26$  and  $c, c' = 0.17, 0.05$ , respectively. This corresponds to a dynamic jump from an initial stress of  $.04 \text{ kg/mm}^2$  to a value  $.30 \text{ kg/mm}^2$ . which is 90% of the fracture stress. The remaining stress is easily accomplished through the multiple reflections at the infinite impedance. Using the curve of Fig. 4, this gives

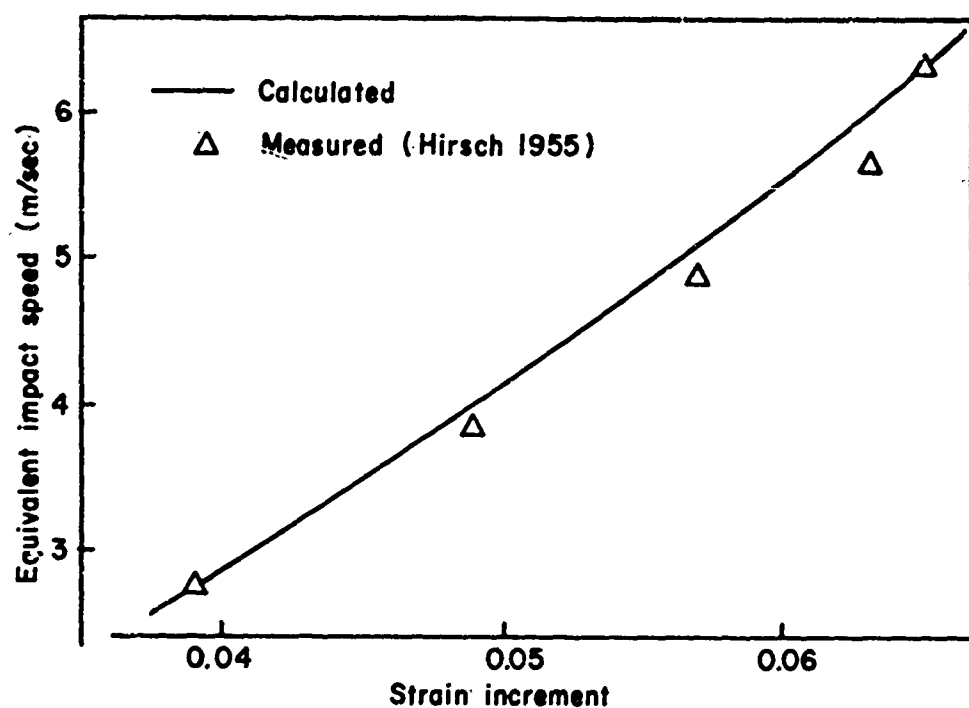


Fig. 6. The calculated additional strain increment due to impact is nonlinear with the speed. The case shown is for a lumbar disc-vertebrae segment prestressed  $0.005 \text{ kg/mm}^2$ .

an impact speed in the vertebra of 12.2 m/sec, which corresponds to a free terrestrial fall from approximately 7.5 meters. Since buttock and pelvic elasticity have been ignored, this value is surprisingly large and certainly does not seem to agree with ordinary experience. On the other hand, impacts which are truly axial are seldom achieved and the consideration of bending and shear would reduce the injury speed.

While much of what I have discussed will be considered speculative because it is based upon minimal appropriate data, the existence of finite amplitude shock waves in nonlinear intervertebral discs has been shown to be plausible and its study is potentially important in understanding dynamically induced spinal injuries.

#### REFERENCES

- [1] Alf. Nachemson, "Lumbar Intradiscal Pressure," *Acta Ortho. Scand., Suppl.* 43, 1960.
- [2] M. B. Coventry, "Anatomy of the Intervertebral Disk," *Clin. Ortho. and Rel. Res.*, Vol. 67, pp. 9-15, 1969.
- [3] Thornton Brown, R. J. Hansen, A. J. Yorra, "Some Mechanical Tests on the Lumbosacral Spine with Particular Reference to the Intervertebral Discs," *J. Bone and Joint Surg., Vol. 39-A, No. 5*, pp. 1135-1164, Oct., 1957.
- [4] D. C. Keyes and E. L. Compere, "The Normal and Pathological Physiology of the Nucleus Pulposus of the Intervertebral Disc," *J. Bone and Joint Surg., Vol. 14*, pp. 897-938, 1932.
- [5] S. Friberg, "Low Back and Sciatic Pain Caused by Intervertebral Disc Herniation," *Acta Ortho. Scand., Suppl.* 25, 1957.
- [6] J. E. A. O'Connell, "Protrusions of the Lumbar Intervertebral Discs," *J. Bone and Joint Surgery*, Vol. 33-B, pp. 8-30, 1951.
- [7] G. Perey, "Fracture of the Vertebral End Plate in the Lumbar Spine," *Acta Ortho. Scand., Suppl.* 25, 1957.
- [8] Edwin R. Fitzgerald and Alan E. Freeland, "Viscoelastic Response of intervertebral Disks at Audiotfrequencies," to appear in *J. Med. and Biol. Eng.*
- [9] Keith L. Markolf and Robert F. Steidel, "The Dynamic Characteristics of the Human Intervertebral Joint," ASME publication 70-WA/BHF-6, 1970.

- [10] W. J. Virgin, "Experimental Investigations into the Physical Properties of the Intervertebral Disc," *J. Bone and Joint Surg.*, Vol. 33-B, pp.607-611, 1951.
- [11] Carl Hirsch, "The Reaction of Intervertebral Discs to Compression Forces," *J. Bone and Joint Surg.*, Vol. 37-A, pp.1188-1196, 1955.
- [12] David Orne and Y. King Liu, "A Mathematical Model of Spinal Response to Impact," *J. Biomechanics*, Vol. 4, pp.49-71, 1971.
- [13] Alf Nachemson, "Some Mechanical Properties of the Lumbar Intervertebral Discs," *Bull. Hosp. Joint Disease*, Vol. 23, pp.130-143, 1962.
- [14] H. Kolsky, "Stress Waves in Solids," *Oxford University Press*, 1953.
- [15] Alf Nachemson and James M. Morris, "In Vivo Measurements of Intradiscal Pressure," *J. Bone and Joint Surg.*, Vol. 46-A, pp.1077-1092, 1964.

## ACCELERATION RESPONSE OF A BLAST-LOADED PLATE

Lawrence W. Fagel  
Bell Telephone Laboratories, Inc.  
Whippany, New Jersey

A solution for a simply supported plate loaded by a step-function pressure is closely examined to determine contributions to acceleration from the plate's higher modes of vibration. Plate dimensions are assumed to be such that classical bending equations apply, and it is established that the peak acceleration response can be as much as 2.6 times the peak response of a one-degree-of-freedom analog. When damping is incorporated in the solution, the peak values are attenuated and much of the very-high-frequency response appears to dissipate rapidly. In practical situations where the damping ratio will be at least 1 percent, nine modes should adequately represent the plate's true response; however, computed accelerations may be nonconservative by up to 40 percent if only four modes are considered and by more than 100 percent if only one mode is used.

### INTRODUCTION

A commonly used technique for calculating the approximate response of a plate subjected to blast loading is to consider the plate to be equivalent to a one-degree-of-freedom spring-mass system, the frequency of which corresponds to the fundamental frequency of the plate. A simply supported plate acted upon by a uniform step-function pressure is analyzed here to determine the validity of this approximation. Classical bending equations for plates, that is, plane-stress equations, are assumed to be applicable and these lead to a time-dependent, double infinite trigonometric series solution in which each term of the series represents the transverse vibrational response of a different mode. Comparison of the relative amplitudes of each modal response demonstrates that the first mode predominates for the dynamic responses of displacement and stress; hence the one-degree-of-freedom approximation is appropriate for these quantities. However, the amplitudes of some of the higher modes of acceleration response are significant compared to those of the first mode, indicating that these should not be ignored. Because the solution involves an infinite series in time, the maximum amplitude of response is not obvious from the solution expression. Acceleration responses are plotted as functions of time to determine the contributions associated with frequencies higher than the fundamental. Peak acceleration response for an undamped plate appears to be about 2.6 times the first mode response, i.e., what would be calculated using the one-degree-of-freedom analog.

### MOTIVATION

Structures which are designed to withstand nuclear-weapon effects are often either shell-like structures or are encapsulated within protective shell-like structures which, for design and analytical purposes, are sometimes regarded as composites of plate elements. Moreover, for structural-motion-response studies, it is a usual inherent requirement to consider these plate elements to be externally loaded by blast-induced overpressures\* which may in some cases be approximated by a step function for determining early-time responses. In this regard, a prevalent practice for analysts is to construct a mathematical model of the structure assuming that an entire panel can be represented by a single degree of freedom.† A direct consequence of this approach is that the calculated peak acceleration response at the center of a square plate element exposed to a step overpressure is

$$\text{Peak Acceleration} \approx 1.5 \frac{\text{Peak Overpressure}}{\text{Mass per Unit Area of Panel}} . \quad (1)$$

\*Pressures in excess of ambient.

†This practice is recommended in "Design of Structures to Resist the Effects of Atomic Weapons," U.S. Corps of Engineers Manual EM1110-345-410, 15 March 1957.

(1.5 is approximate to about  $\pm 10\%$ ; the value of this coefficient depends on edge-support conditions.) An examination of a plate-vibration-problem solution that includes modes which are higher than the fundamental, indicates that Eq. (1) characterizes the response in the first mode; however, the amplitudes of acceleration responses in modes other than the first, although also significant, have been ignored.

In situations where structural responses are computed for the sole purpose of specifying shock environments for acceleration-sensitive components within the structure, it is of course necessary that all modes which contribute significantly to acceleration response be accounted for. This apparently reasonable requirement is unfortunately somewhat ambiguous, and therefore there is perhaps a need for a more quantitative definition of the number of modes which, for the stated practical purpose, should be considered. The intentions of this study are to determine an upper limit of acceleration response values resulting from the consideration of higher modes, to ascertain the number of modes which significantly contribute to acceleration response, and to establish a quantitative comparison between one-mode and many-mode acceleration response solutions by considering a simply supported plate loaded by a step-function pressure.

#### ANALYSIS OF A SIMPLY SUPPORTED PLATE

The response solutions for an undamped simply supported plate acted upon by a step-function overpressure are directly derived as follows. Assuming that the classical bendings, i.e., plane stress equations apply, the governing differential equation [1] is

$$\frac{2h}{g} \ddot{w} + \frac{Eh^3}{12(1-\nu^2)} \nabla^4 w = q(x,y,t). \quad (2)$$

A deflection which conforms with the simple-support boundary conditions at  $x = 0$  and  $a, y = 0$  and  $b$  is

$$w = \sum_{i=1}^{\infty} \sum_{j=1}^{\infty} \phi_{ij}(t) \sin \frac{i\pi x}{a} \sin \frac{j\pi y}{b}. \quad (3)$$

The derivatives of  $w$  are

$$\ddot{w} = \sum_{i=1}^{\infty} \sum_{j=1}^{\infty} \ddot{\phi}_{ij}(t) \sin \frac{i\pi x}{a} \sin \frac{j\pi y}{b}, \quad (4a)$$

$$\begin{aligned} \nabla^4 w &= \frac{\partial^4 w}{\partial x^4} + \frac{2\partial^4 w}{\partial x^2 \partial y^2} + \frac{\partial^4 w}{\partial y^4} \\ &= \sum_{i=1}^{\infty} \sum_{j=1}^{\infty} \phi_{ij}(t) \left[ \left( \frac{i\pi}{a} \right)^2 + \left( \frac{j\pi}{b} \right)^2 \right]^2 \\ &\quad \sin \frac{i\pi x}{a} \sin \frac{j\pi y}{b} \end{aligned} \quad (4b)$$

Expanding  $q(x,y,t)$  in a double Fourier series involving  $x$  and  $y$ ,

$$q(x,y,t) = \sum_{i=1}^{\infty} \sum_{j=1}^{\infty} P_{ij}(t) \sin \frac{i\pi x}{a} \sin \frac{j\pi y}{b}.$$

The Fourier coefficient  $P_{ij}(t)$  is evaluated as

$$P_{ij}(t) = \frac{4}{ab} \int_0^b \int_0^a q(x,y,t) \sin \frac{i\pi x}{a} \sin \frac{j\pi y}{b} dx dy.$$

For uniform-loading cases where  $q(x,y,t)$  varies with time but is constant with respect to  $x$  and  $y$ , i.e.,  $q(x,y,t) = q(t)$ ,

$$P_{ij}(t) = \frac{4q(t)}{ab} \int_0^b \int_0^a \sin \frac{i\pi x}{a} \sin \frac{j\pi y}{b} dx dy.$$

$$P_{ij}(t) = \frac{4q(t)}{ab} \left( -\frac{a}{i\pi} \cos \frac{i\pi x}{a} \Big|_0^a \right) \left( -\frac{b}{j\pi} \cos \frac{j\pi y}{b} \Big|_0^b \right).$$

Therefore,

$$P_{ij}(t) = 0 \text{ for even values of } i \text{ or } j, \text{ and}$$

$$P_{ij}(t) = \frac{16}{ij\pi^2} q(t) \text{ for odd values of } i \text{ and } j.$$

If  $q(t)$  is a Heaviside step function of amplitude  $P_0$ , i.e.,  $q(t) = P_0 U(t)$ , then  $P_{ij}(t) = 16 P_0 U(t)/ij\pi^2$  for odd values of  $i$  and  $j$ . The expression for  $q(x,y,t)$  then becomes

$$q(x,y,t) = \frac{16P_0 U(t)}{\pi^2} \sum_{i=1}^{\infty} \sum_{j=1}^{\infty} \frac{\sin \frac{i\pi x}{a}}{i} \frac{\sin \frac{j\pi y}{b}}{j} \quad (5)$$

Eqs. (3), (4), and (5) substitute into Eq. (2) to form

$$\begin{aligned} & \frac{\gamma h}{g} \sum_{i=1}^{\infty} \sum_{j=1}^{\infty} \ddot{\phi}_{ij}(t) \sin \frac{i\pi x}{a} \sin \frac{j\pi y}{b} \\ & + \frac{Eh^3}{12(1-\nu^2)} \sum_{i=1}^{\infty} \sum_{j=1}^{\infty} \phi_{ij}(t) \left[ \left( \frac{i\pi}{a} \right)^2 + \left( \frac{j\pi}{b} \right)^2 \right]^2 \\ & \sin \frac{i\pi x}{a} \sin \frac{j\pi y}{b} \\ & = \begin{cases} 0 & \text{for even values of } i \text{ and } j, \\ \frac{16P_o U(t)}{\pi^2} \sum_{i=1}^{\infty} \sum_{j=1}^{\infty} \frac{1}{ij} \sin \frac{i\pi x}{a} \sin \frac{j\pi y}{b} & \text{for odd values of } i \text{ and } j, \end{cases} \end{aligned}$$

and each model differential equation becomes

$$\frac{\gamma h}{g} \ddot{\phi}_{ij} + \frac{Eh^3}{12(1-\nu^2)} \left[ \left( \frac{i\pi}{a} \right)^2 + \left( \frac{j\pi}{b} \right)^2 \right]^2 \phi_{ij}$$

$$= \begin{cases} 0 & \text{for even values of } i \text{ and } j, \\ \frac{16P_o U(t)}{ij\pi^2} & \text{for odd values of } i \text{ and } j, \end{cases} \quad (6a)$$

with all initial conditions being zero. Modal displacements  $\phi_{ij}$  for even values of  $i$  and  $j$  are trivially equal to zero by Eq. (6a). For odd values of  $i$  and  $j$  the equations are in the form

$$\ddot{\phi}_{ij} + \omega_{ij}^2 \phi_{ij} = \frac{16}{\pi^2} \frac{P_o}{W/g} \frac{U(t)}{ij} = A_{ij} U(t). \quad (7)$$

The Laplace transform of Eq. (7) is

$$S^2 \Phi_{ij}(S) - S \dot{\phi}_{ij}(0) - \dot{\phi}_{ij}(0) + \omega_{ij}^2 \Phi_{ij}(S) = \frac{A_{ij}}{S}. \quad (8)$$

The initial conditions are  $\phi_{ij}(0) = \dot{\phi}_{ij}(0) = 0$ . Solving Eq. (8),

$$\Phi_{ij}(S) = \frac{A_{ij}}{S(S^2 + \omega_{ij}^2)}, \quad (9)$$

$$\phi_{ij}(t) = \frac{A_{ij}}{\omega_{ij}^2} \left( 1 - \cos \omega_{ij} t \right),$$

Eq. (9) substituted into Eq. (3) yields

$$w = \frac{16}{\pi^2} \frac{P_o}{W/g} \sum_{i=1}^{\infty} \sum_{j=1}^{\infty} \sin \frac{i\pi x}{a} \sin \frac{j\pi y}{b} \left( 1 - \cos \omega_{ij} t \right). \quad (10)$$

Using the stress-strain relations for plates:

$$\begin{aligned} \sigma_{xx} &= - \frac{Ez}{1-\nu^2} \left( \frac{\partial^2 w}{\partial x^2} + \nu \frac{\partial^2 w}{\partial y^2} \right) \\ &= \frac{16}{\pi^2} \frac{P_o}{W/g} \frac{Ez}{1-\nu^2} \left\{ \sum_{i=1}^{\infty} \sum_{j=1}^{\infty} \left[ \left( \frac{i\pi}{a} \right)^2 + \nu \left( \frac{j\pi}{b} \right)^2 \right] \right. \\ &\quad \left. \cdot \frac{\sin \frac{i\pi x}{a}}{i} \frac{\sin \frac{j\pi y}{b}}{j} \frac{\left( 1 - \cos \omega_{ij} t \right)}{\omega_{ij}^2} \right\} \end{aligned} \quad (11)$$

$$\begin{aligned} \sigma_{yy} &= - \frac{Ez}{1-\nu^2} \left( \frac{\partial^2 w}{\partial y^2} + \nu \frac{\partial^2 w}{\partial x^2} \right) \\ &= \frac{16}{\pi^2} \frac{P_o}{W/g} \frac{Ez}{1-\nu^2} \left\{ \sum_{i=1}^{\infty} \sum_{j=1}^{\infty} \left[ \left( \frac{j\pi}{b} \right)^2 + \nu \left( \frac{i\pi}{a} \right)^2 \right] \right. \\ &\quad \left. \cdot \frac{\sin \frac{i\pi x}{a}}{i} \frac{\sin \frac{j\pi y}{b}}{j} \frac{\left( 1 - \cos \omega_{ij} t \right)}{\omega_{ij}^2} \right\} \end{aligned} \quad (12)$$

$$\begin{aligned}\tau_{xy} &= -\frac{Ez}{1-\nu} \frac{\partial^2 w}{\partial x \partial y} \\ &= \frac{16}{\pi^2} \frac{P_o}{W/g} \frac{Ez}{1+\nu} \left\{ \sum_{i=1}^{\infty} \sum_{j=1}^{\infty} \frac{\pi^2}{ab} \right. \\ &\quad \left. \cos \frac{i\pi x}{a} \cos \frac{j\pi y}{b} \frac{(1 - \cos \omega_{ij} t)}{\omega_{ij}^2} \right\}. \quad (13)\end{aligned}$$

The acceleration response is

$$\ddot{w} = \frac{16}{\pi^2 W/g} \sum_{i=1}^{\infty} \sum_{j=1}^{\infty} \frac{\sin \frac{i\pi x}{a} \sin \frac{j\pi y}{b}}{i j} \cos \omega_{ij} t. \quad (14)$$

In Eqs. (10) through (14)  $i$  and  $j$  are odd and

$$\omega_{ij} = \frac{\pi^2 h}{a^2} \sqrt{\frac{Eg}{3(1-\nu^2)\gamma}} \left( \frac{i^2 + j^2}{2} \right) = \omega_0 \left( \frac{i^2 + j^2}{2} \right).$$

Comparing higher-mode amplitudes to fundamental-mode amplitudes for displacement, stresses, and acceleration, we have:

**Displacement:**

$$\left| \frac{w_{ij}}{w(\text{first mode})} \right| = \frac{4}{ij(i^2 + j^2)^2},$$

**Stresses:**

$$\left| \frac{\sigma_{xx} ij}{\sigma_{xx}(\text{first mode})} \right| = \frac{4(i^2 + \nu j^2)}{ij(i^2 + j^2)^2 (1 + \nu)},$$

$$\left| \frac{\tau_{xy} ij}{\tau_{xy}(\text{first mode})} \right| = \frac{4}{(i^2 + j^2)^2},$$

**Acceleration:**

$$\left| \frac{\ddot{w}_{ij}}{\ddot{w}(\text{first mode})} \right| = \frac{1}{ij},$$

where  $i$  and  $j$  can only be odd values. The relative amplitudes of higher-modal values compared to the respective amplitudes associated with the fundamental mode are plotted on Fig. 1. Information from these graphs concurs with the philosophy that displacements and stresses resulting from mode shapes other than the fundamental are negligible compared to displacements and stresses associated with the fundamental mode. On the other hand, the contributions to acceleration from some higher modes appear to be significant. Just how the higher-mode acceleration amplitudes supplement the acceleration response of the first mode is not obvious from Fig. 1 nor from Eq. (14); therefore this phenomenon will now be more closely examined.

Interest is focused at the center of the plate where the single-degree-of-freedom analog had been presumed to be applicable. At the midpoint the acceleration is

$$\begin{aligned}\ddot{w}_{\text{midpoint}} &= \frac{16}{\pi^2 W/g} \sum_{i=1}^{\infty} \sum_{j=1}^{\infty} \frac{\sin \frac{i\pi}{2} \sin \frac{j\pi}{2}}{i j} \\ &\quad \cos \omega_{ij} t. \quad (15)\end{aligned}$$

where  $i$  and  $j$  are odd. At  $t = 0$ ,  $\cos \omega_{ij} t \approx 1$  for all  $i$  and  $j$ , and Eq. (15) degenerates to

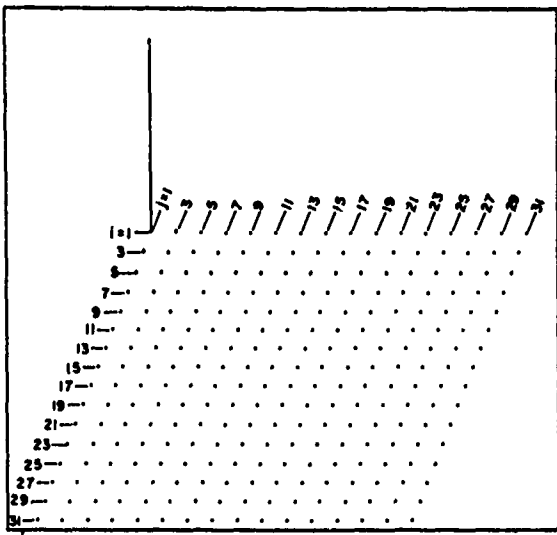
$$\ddot{w}_{\text{midpoint}} = \frac{16}{\pi^2 W/g} \sum_{i=1}^{\infty} \sum_{j=1}^{\infty} \frac{\sin \frac{i\pi}{2} \sin \frac{j\pi}{2}}{i j},$$

where  $i$  and  $j$  are odd. Note that

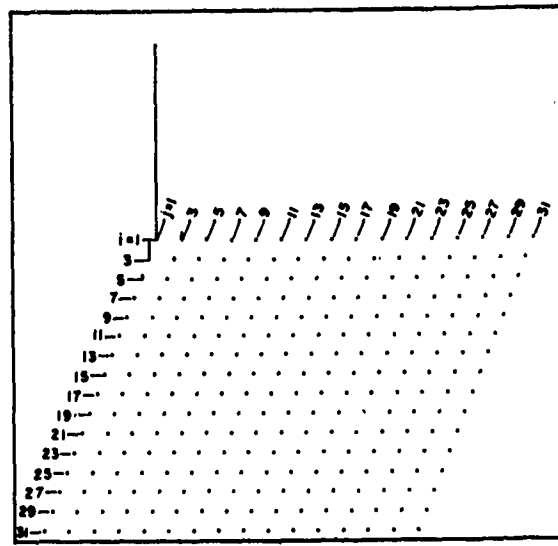
$$\begin{aligned}\sum_{i=1,3,5,\text{etc.}}^{\infty} \frac{\sin \frac{i\pi}{2}}{i} &= \sum_{k=0}^{\infty} (-1)^k \frac{1}{(2k+1)} \\ &= \tan^{-1} 1 = \frac{\pi}{4},\end{aligned}$$

so that at  $t = 0$ ,

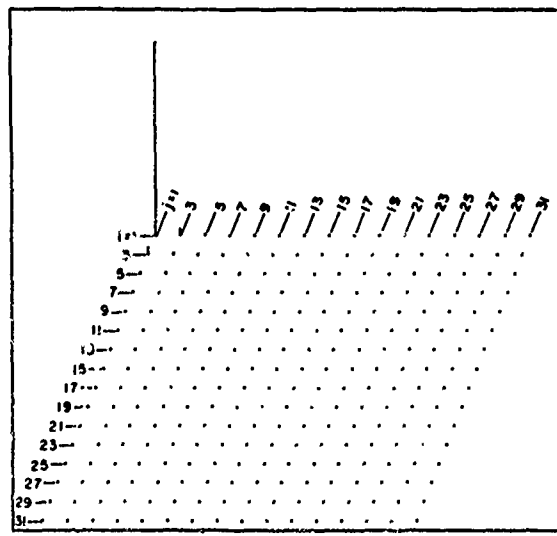
$$\begin{aligned}\ddot{w}_{\text{midpoint}} &= \frac{16}{\pi^2 W/g} \sum_{k=0}^{\infty} \sum_{r=0}^{\infty} \frac{(-1)^k}{(2k+1)} \frac{(-1)^r}{(2r+1)} \\ &= \frac{16}{\pi^2 W/g} \frac{\pi^2}{16} = \frac{P_o}{W/g}.\end{aligned}$$



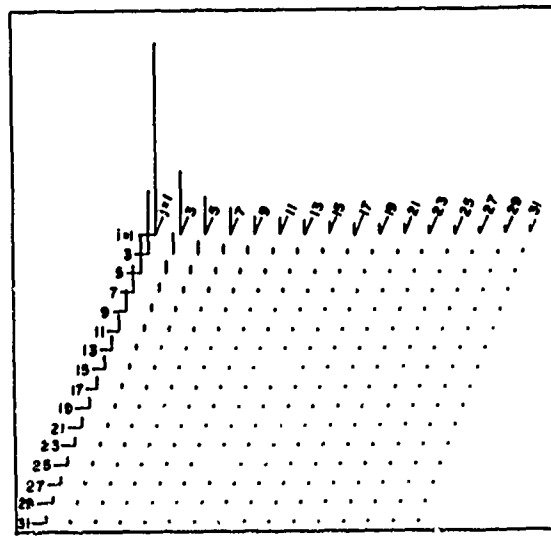
RELATIVE AMPLITUDES OF MODAL DISPLACEMENTS



RELATIVE AMPLITUDES OF MODAL NORMAL STRESSES



RELATIVE AMPLITUDES OF MODAL SHEAR STRESS



RELATIVE AMPLITUDES OF MODAL ACCELERATIONS

Fig. 1 - Comparisons of the Relative Amplitudes of Modal Responses

By comparing this with the first-mode contribution at  $t = 0$  [ $(16/\pi^2) P_0/(W/g) \approx 1.6 P_0/(W/g)$  which approximately agrees with Eq. (1)], it appears that the one-mode-only representation of response is reasonable and conservative for the initial value of acceleration. At  $t > 0$  however, it is not obvious that the absolute value of the sum of the contributions from all modes should remain bounded by the amplitude of the response of the first mode, and in fact, plots of normalized acceleration versus normalized time show a contrary trend. That is, the equation

$$\frac{\ddot{w}_{\text{midpoint}}}{P_0/(W/g)} = \frac{16}{\pi^2} \sum_{i=1}^m \sum_{j=1}^n \frac{\sin \frac{i\pi}{2}}{i} \frac{\sin \frac{j\pi}{2}}{j} \cos \omega_{ij} t \quad (\text{i and j are odd}) \quad (16)$$

plotted versus  $\omega_0 t / 2\pi$  on Fig. 2, indicates that the acceleration response increases substantially when higher modes are included in the calculation. These time-varying plots of Eq. (16) for increasingly larger values of  $m$  and  $n$  demonstrate the effect of considering higher frequencies in the acceleration response. The peak values from each of these graphs are plotted in Fig. 3 as a function of the number of modes, and this curve appears to be asymptotic to about  $4.12 P_0/(W/g)$  as  $m$  and  $n$  become

large, that is, about 2.6 times larger than the one-mode-only representation of response. Up to and including 225 modes are considered in computing these values even though it is recognized that Eq. (2), which neglects shear and rotary inertia is probably not appropriate for the very-high-frequency mode shapes. Nonetheless, this simplifying assumption permits the calculation of an approximate upper value, and as will be shown, the consideration of damping can greatly reduce the contributational effect of these very-high-frequency modes.

#### DAMPED RESPONSE

The previous discussion pertained only to undamped vibration; therefore, computed accelerations must be conservative since all mechanical vibrations, certainly all structural vibrations, are impeded by damping. An effort to consider structural damping is presented below; however, some discussion regarding this topic is appropriate.

The phenomena involved in damping of structural vibrations is complex and to the author's knowledge, no unified mathematical treatment of the problem exists which exactly defines the physics of such damping. It is generally conceded to be a combination of air damping and structural damping and although approximate solutions exist which incorporate these effects,

they are based on damping forces defined in a manner which preserves the linear nature of the modal differential equations of motion by introducing a viscous damping term. Damping is thereby defined so that Eq. (7) is replaced by

$$\ddot{\phi}_{ij} + 2\beta_{ij}\omega_{ij}\dot{\phi}_{ij} + \omega_{ij}^2\phi_{ij} = \frac{16}{\pi^2} \frac{P_0}{W/g} \frac{U(t)}{ij} = A_{ij} U(t) , \quad (17)$$

where  $2\beta_{ij}\omega_{ij}\dot{\phi}_{ij}$  is the modal viscous damping force, and  $\beta_{ij}$  is the percent-of-critical viscous damping ratio. When the governing partial differential equation is defined so that Eq. (17) results, the total response  $w$  and its time-derivatives are summations of the modal values  $\phi_{ij}$  and time-derivatives of  $\phi_{ij}$  respectively.

The solution to Eq. (17) is

$$\phi_{ij}(t) = \frac{A_{ij}}{\omega_{ij}} \left[ 1 - \frac{e^{-\beta_{ij}\omega_{ij}t}}{\sqrt{1 - \beta_{ij}^2}} \sin \left( \omega_{ij} \sqrt{1 - \beta_{ij}^2} t + \theta \right) \right],$$

$$\theta = \tan^{-1} \omega_{ij} \frac{\sqrt{1 - \beta_{ij}^2}}{\beta_{ij}},$$

and the modal acceleration is

$$\ddot{\phi}_{ij} = A_{ij} e^{-\beta_{ij}\omega_{ij}t} \left\{ \left( \sqrt{1 - \beta_{ij}^2} + \frac{\beta_{ij}^2}{\sqrt{1 - \beta_{ij}^2}} \right) \right. \\ \left. \left[ \sin \left( \omega_{ij} \sqrt{1 - \beta_{ij}^2} t + \theta \right) \right. \right. \\ \left. \left. - 2\beta_{ij} \cos \left( \omega_{ij} \sqrt{1 - \beta_{ij}^2} t + \theta \right) \right] \right\} .$$

For small values of  $\beta_{ij}$ ,  $\theta \approx \pi/2$  and the acceleration can be approximated by

$$\ddot{\phi}_{ij}(t) = A_{ij} e^{-\beta_{ij}\omega_{ij}t} \cos \omega_{ij} t = \frac{16}{\pi^2} \frac{P_0}{W/g} \frac{1}{ij} e^{-\beta_{ij}\omega_{ij}t} \cos \omega_{ij} t.$$

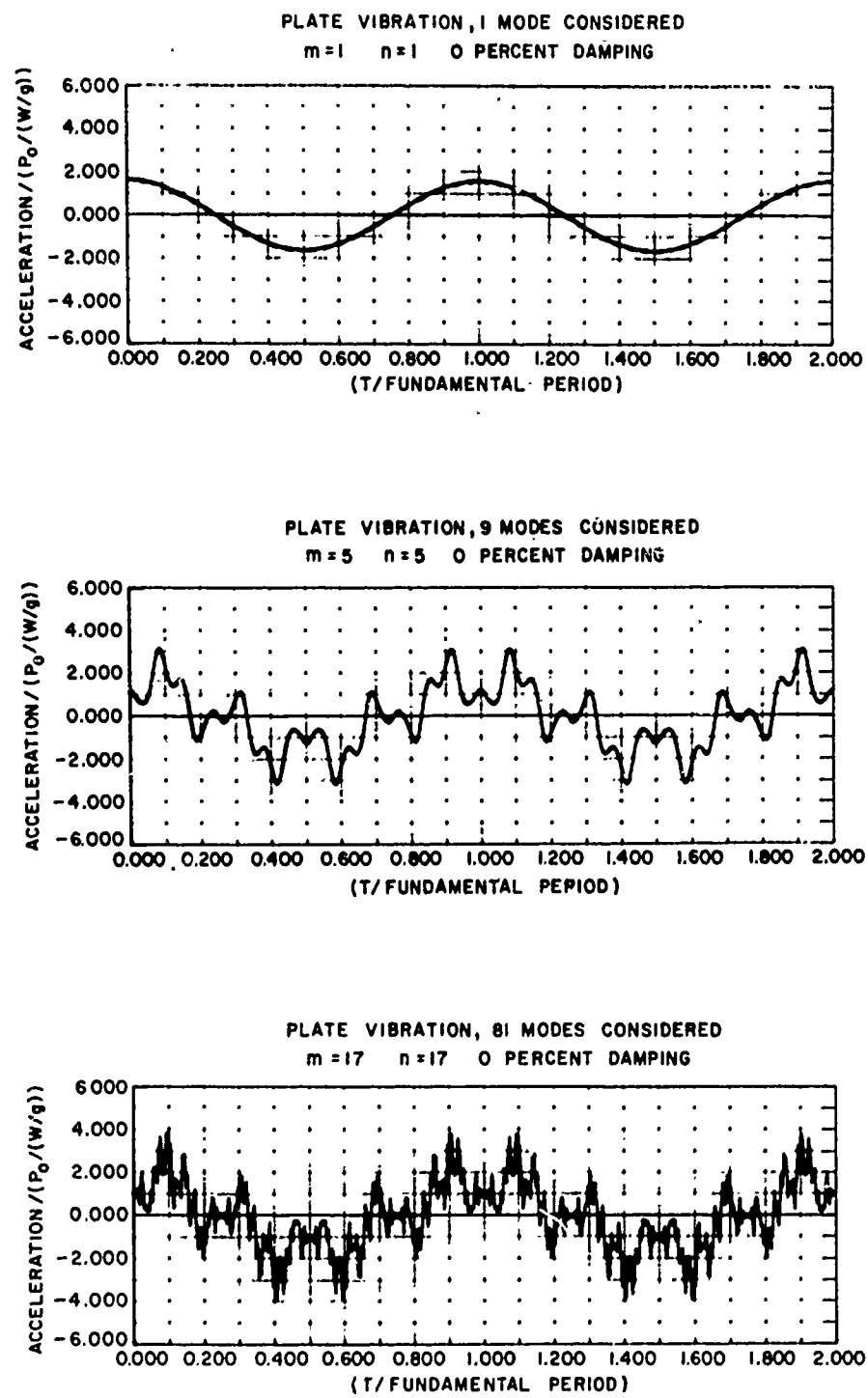


Fig. 2 - Comparison of Acceleration Response  
 Considering One and Many Modes

PEAK ACCELERATION AT THE MIDPOINT OF AN UNDAMPED SIMPLY-SUPPORTED PLATE SUBJECT TO A STEP-FUNCTION PRESSURE. VALUES ARE CALCULATED FROM THE EXACT SOLUTION:

$$\frac{\text{ACCELERATION}}{P_0/(Wg)} = \frac{16}{\pi^2} \sum_{i=1}^m \sum_{j=1}^n \frac{\sin \frac{i\pi}{2}}{i} \frac{\sin \frac{j\pi}{2}}{j} \cos \omega_{ij} t,$$

WHERE THE SUMMATION LIMITS ARE REPLACED BY FINITE VALUES OF  $m$  AND  $n$  FOR  $i$  AND  $j$  RESPECTIVELY.

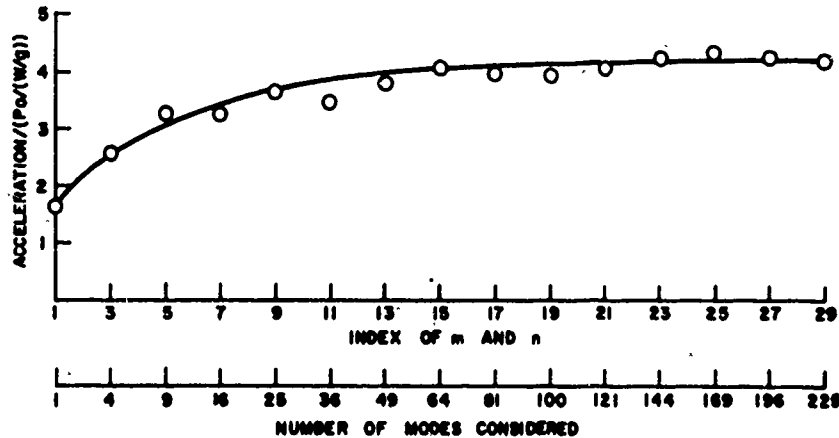


Fig. 3 - Peak Acceleration at the Midpoint of an Undamped Simply Supported Plate Subjected to a Step-Function Pressure

Thus a damped modal vibration can be considered the same as an undamped modal vibration except that it is enveloped by an exponential decay,  $e^{-\beta_{ij}\omega_{ij}t}$ . It is emphasized that this result is arrived at because of a desire for mathematical simplicity rather than from an exact definition of the physical phenomena for energy dissipation. The damping forces in structural vibrations are not, in fact, known to be viscous; however, this simplifying assumption provides a means to an end in that it yields approximately correct dynamic responses, and it is a standard method for evaluating damped multimodal vibration responses.

Regarding values for modal viscous damping ratio  $\beta_{ij}$ , the literature on structural damping contains different opinions regarding this subject. If the viscous-damped assumption were completely true, a Kelvin (also known as a Stokes) model could be assumed for the material (stress is proportional to strain rate as well as strain), the governing biharmonic equation would be modified by adding a  $(\partial/\partial t) \nabla^4 w$  term, and modal Eq. (17) would evolve where  $\beta_{ij}$  is proportional to  $\omega_{ij}$ . Whether or not the modal damping ratio is indeed proportional to

damping in real structural vibrations has been the subject of extensive experimentation, and there is apparent world-wide disagreement in the interpretations of results from such experiments as evidenced by a sample of some of the literature on the subject. While testing building structures Alford and Housner [2] found that the damping ratios for the higher modes were the same as for the fundamental mode; and Sesan, Crongradi, Diaconu and Strat [3] concurred with this finding in a separate study. On the other hand, Kawasumi and Kamai [4] claim to have experienced proportional damping by doing similar experiments. Nielson's [5] experiments showed that the same damping coefficient was evidenced at different modes during tests on one structure; however, proportional damping was experienced while testing a different structure. Kimball [6] found that internal damping is neither proportional to frequency nor constant, but rather that for most materials it increases to a maximum value at some frequency and then decreases for all subsequent frequencies. Mindlin, Stubner and Cooper [7] recommend using a constant damping ratio. Adamson's [8] observations are similar to Kimball's; however, Adamson has a compromise recommendation to use proportional damping if only a few modes are inherent but a

constant ratio if many modes of vibration exist in the response solution.

There exists, therefore, a variety of opinions regarding how equivalent modal viscous damping ratios vary as a function of modal frequency. The advice of Mindlin and others who recommend the use of a constant damping ratio, independent of frequency, is used in the investigation below to determine the effect that damping has on the acceleration response of a vibrating plate subjected to a step-function overpressure.

If  $\beta_{ij} = \beta$  for all values of  $i$  and  $j$  and  $\beta \ll 1$ , the acceleration response at the midpoint becomes

$$\frac{w_{\text{midpoint}}}{P_0/(W/g)} = \frac{16}{\pi^2} \sum_{i=1}^m \sum_{j=1}^n \frac{\sin \frac{i\pi}{2}}{i} \frac{\sin \frac{j\pi}{2}}{j}$$

$$e^{-\beta \omega_{ij} t} \cos \omega_{ij} t$$

where  $i$  and  $j$  are odd. The effect that  $\beta$  has on response is demonstrated in Fig. 4 which shows the midspan response considering 225 modes with and without damping. The very-high-frequency characteristics quickly disappear and the peak responses are attenuated. Of particular interest is the comparison of the amplitude of the damped-acceleration peak response considering few and many modes of vibration. This is shown on Fig. 5 where it is inferred from the asymptotic nature of the curve on Fig. 3 that the response considering 225 modes is equivalent to the response considering an infinite number of modes.

The curves on Fig. 5 suggest that larger values of critical damping ratio produce two desirable effects from a structural analysis viewpoint. They of course reduce the peak acceleration responses; however, the error introduced by using only a few rather than many modes to represent dynamic response is also reduced. For materials which have three or more percent damping, the difference between the peak responses using 9 and 225 modes is indistinguishable. From a practical standpoint, when both air and structural damping are con-

sidered, most materials (even steel plates) probably have minimum equivalent damping ratios of about 1 percent. The nine-mode curve on Fig. 5 indicates only about a 15 percent disagreement with the 225-mode response at 1 percent damping; therefore nine modes should, for practical purposes, usually be adequate for dynamic response calculations involving plates subjected to impulsive loads.

If fewer than nine modes are used to represent plate responses in a dynamic-analysis study, the calculated peak acceleration responses will possibly be nonconservative by an amount dependent on the percent of critical damping and the number of modes considered. If the excitation is impulsive (blast loading), the curves on Fig. 5 are indicative of the possible amount of nonconservatism which should be expected. For example, the peak acceleration response calculated for a 2-percent-of-critically damped plate that is approximated by using only one mode and considered to be subjected to an impulsive load, could be nonconservative by a factor of two.

If the excitation is oscillatory the above recommendation is not intended to apply. If dominant frequencies in the forcing function coincide with frequencies of the plate's higher modes, these frequencies will contribute more significantly to acceleration responses (displacements and stresses also) than if the structure were impulsively loaded. For these situations it most certainly would be prudent to have the mathematical model of the plate contain modes which at least include the dominant frequencies of the forcing function.

## CONCLUSIONS

The contribution to peak acceleration response of a blast-loaded plate from modes other than the fundamental can be significant; therefore modal values associated with frequencies above the fundamental should be incorporated in blast-response computations. For engineering purposes where at least 1 percent of critical damping may be assumed, it is recommended that the mathematical representation of the plate contain at least nine modes if blast-loading conditions exist and acceleration responses are desired. Computed accelerations may be nonconservative by up to 40 percent if only four modes are used and by more than 100 percent if only one mode is used.

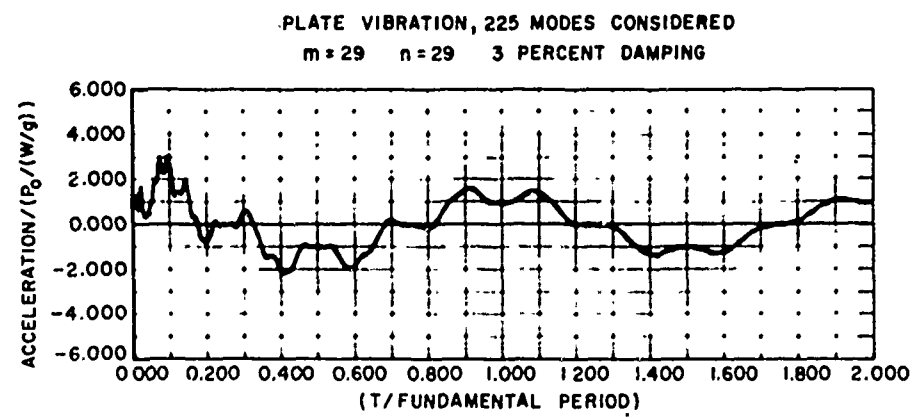
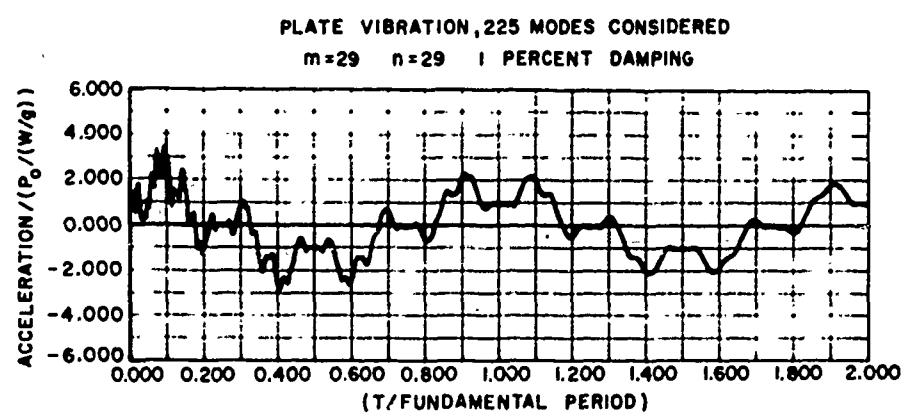
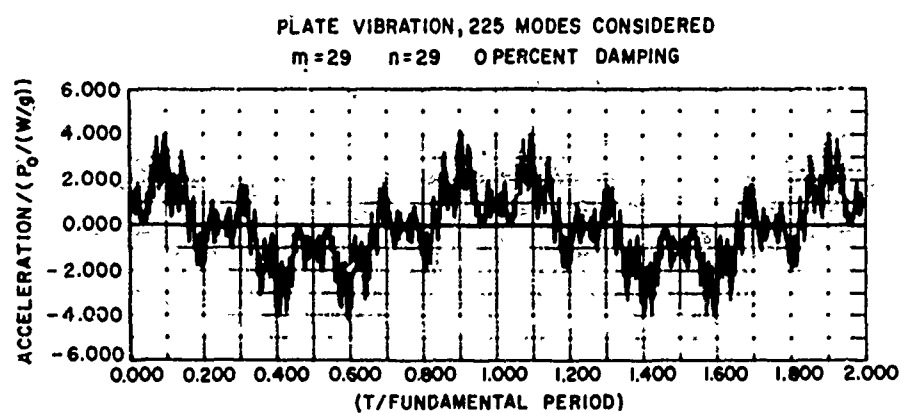


Fig. 4 - Comparison of Normalized Acceleration Response Without and With Damping

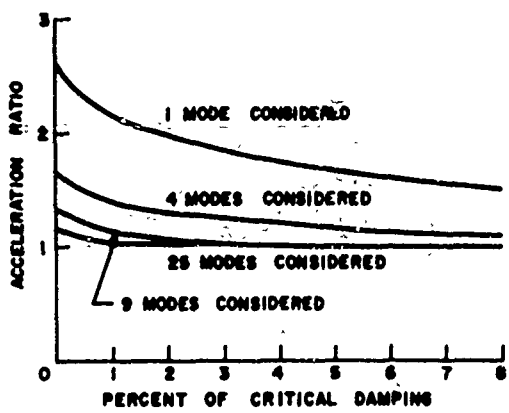


Fig. 5 - Ratio of Peak Acceleration Response Considering  
225 Modes to Peak Acceleration Response  
Considering Fewer Modes

## APPENDIX I - REFERENCES

1. Timoshenko, Vibration Problems in Engineering, Van Nostrand, January 1955.
2. B. J. Alford and G. W. Housner, "A Dynamic Test of a Four-Story Reinforced Concrete Building," Bulletin of Seismological Society, January 1953.
3. A. Sesan, I. Cronicadi, D. Diaconu, and L. Strat, "Experimental Determinations of Natural Periods and Damping in Buildings," Buletinul Institutului Politehnic, Tomul X (XIV), Fasc. 3-4, 1964.
4. H. Kawasumi and K. Kanai, "Small Amplitude Vibrations of Actual Buildings," Proceedings World Conference on Earthquake Engineering, 1956.
5. N. N. Nielson, "Damping in Multistory Buildings Determined from Steady-State Vibration Tests," ASCE Structural Engineering Conference, January 31, 1966.
6. A. L. Kimball, "Vibration Problems, Part V - Friction and Internal Damping," Journal of Applied Mechanics, Vol. 8, 1941.
7. R. D. Mindlin, F. W. Stubner, and H. L. Cooper, "Response of Damped Elastic Systems to Transient Disturbances," Proceedings of the Society for Experimental Stress Analysis, Vol. 5, No. 2, 1948.
8. B. Adamson, "A Method for Measuring Damping and Frequencies of High Modes of Vibration of Beams," Publication of International Association for Bridges and Structural Engineering, 1955.

## APPENDIX II - NOTATION

a,b = plate dimensions in x,y directions  
 $A_{ij}$  = modal coefficient of forcing function  
 $E$  = Young's modulus  
 $g$  = gravitational constant  
 $h$  = plate thickness  
 $i,j$  = modal indices  
 $P_{ij}(t)$  = Fourier coefficient  
 $P_o$  = overpressure  
 $q$  = pressure function  
 $S$  = Laplace transform variable  
 $t$  = time  
 $U(t)$  = Heaviside unit step function

w = transverse displacement  
 $\ddot{w}$  = transverse acceleration  
 $W$  = weight per unit area =  $\gamma h$   
x,y,z = plate coordinates  
 $\gamma$  = density  
 $\nabla$  = del operator  
 $\omega_{ij}$  =  $ij^{\text{th}}$  frequency  
 $\omega_0$  = fundamental frequency  
 $\nu$  = Poisson's ratio  
 $\sigma_{xx}, \sigma_{yy}$  = normal stresses  
 $\tau_{xy}$  = shear stress

EFFECT OF CORRELATION IN HIGH-INTENSITY  
NOISE TESTING AS INDICATED BY  
THE RESPONSE OF AN INFINITE STRIP (U)

Charles T. Morrow  
Advanced Technology Center, Inc.  
Dallas, Texas

(U) A narrow strip (bar or ribbon) is taken as a theoretical test case for the realism of high-intensity noise testing in much the same way that a simple mechanical resonator is commonly taken as a theoretical test case for more conventional shock and vibration testing. It is shown that in an effort to design a realistic test, one must consider the point-to-point correlation of the applied field as well as the sound pressure level, even when the damping of the strip is large enough to prevent significant return reflections from the ends. Three types of correlation are investigated in particular--complete correlation at the coincidence angle for the given frequency, and independent excitations at the different antinodal regions. With minor reinterpretation, the formulas remain applicable when, in addition, an exponential decay of correlation with distance in either direction along the strip is introduced.

(U) This type of analysis is also potentially useful in the prediction of responses. The prediction method that has received the most intensive development, Statistical Energy Analysis, is conceptually suited primarily to the reverberant field, since normal modes are assumed in the exciting field as well as in the structure. It may eventually be possible to calculate response corrections for reverberant versus flight fields.

#### INTRODUCTION

(U) Environmental testing is intended to provide an evaluation, with a minimum of computation, of whether a test item would survive and function as intended, in practical use. To accomplish this instead by theory, for an item of equipment subject to shock or vibration, would be time consuming and inaccurate, and some modes of failure might be overlooked. The same would be true for a complete space vehicle excited by turbulence or by high-intensity noise.

(U) No environmental simulation is ever completely realistic. Nevertheless, shock and vibration testing can be a useful engineering tool when it is planned intelligently on the basis of suitable criteria for realism. These criteria are obtained by calculation of the responses of a simple structure as a test case. The time-honored test case, more than any other, for vibration and shock, is the simple mechanical resonator. For vibration, the amount of damping is an important parameter. For shock, the damage potential is less critically dependent on damping and the resonator is frequently assumed to be undamped. It is not true that two shocks or two vibrations that produce practically identical responses in a simple resonator

will necessarily do the same in any item of more complicated internal dynamics. Yet, if the responses were not similar in the simple resonator, they would have almost no chance of being similar in the more complicated item of equipment. In spite of the limitations of the simple test case and the compromises that are necessary to achieve a practical environmental specification, it is generally possible to prescribe a useful test.

(U) Turbulence and rocket noise are distributed excitations. So is the high-intensity noise used frequently now to simulate them. It is not possible to obtain valid criteria for realism by a test case that involves only a single-point input. The simple mechanical resonator, even if the excitation is conceived as a force acting on the mass, is inadequate.

(U) The test case utilized in this paper is a simple strip of structure, narrow by comparison with the lateral correlation distances of the exciting field. The velocity of transverse vibration along the strip is assumed to vary with frequency, possibly according to the square root, but the precise relationship and the fundamental theory behind it are not critical to the discussion. The strip could be general-

ized to two dimensions, but the ultimate purpose is inference about practical situations. As with shock and vibration, the simplest test case yields much of the information one needs to know for this. For the present study the strip will be assumed infinite in both directions. Damping, or, more properly, attenuation with propagation distance, will be an important parameter. As we are concerned only with relative responses to different fields, the mechanical impedance of the strip on an absolute scale is unimportant. The important field characteristics will turn out to be not only the power spectral density of the sound pressure as a function of position and frequency but the point-to-point correlation as well.

#### EXCITATION ONLY AT THE ANTINODES

(U) At one time, I carried out a simplified analysis of the infinite strip by assuming that excitation took place only at the antinodes, as in Figure 1. This is a convenient simplified model to visualize and to use for inferences in advance of any calculation. For a completely correlated wave at normal incidence, the transverse waves propagating in either direction from alternate antinodes should be of opposite phase and tend to cancel each other. The lower the damping, the more complete the cancellation. At the other extreme, for a completely correlated wave incident at the coincidence angle so that its trace velocity equals the velocity of propagation of transverse waves in the strip, the transverse waves propagating from the antinodes should all be directly additive. The lower the damping, the more antinodes contribute significantly to the summation. For completely uncorrelated excitations exhibiting no dominant phase angle, the waves propagating from the antinodes should combine as the square root of the sum of the squares, producing an intermediate behaviour.

(U) Although the analysis based on this simplified model does not permit accurate prediction of the response of the strip to continuously distributed excitation, it does provide insights into the nature and effect of correlation. It is therefore worth summarizing here as a preliminary exercise.

(U) It is well known that the power spectral density for the sum or difference of two random signals is given by

$$w_{A+B} = w_A + w_B \pm 2w_{AB} = \\ w_A + w_B \pm 2(w_A w_B)^{1/2} c_{AB} \quad (1)$$

where  $w_A$  and  $w_B$  are the individual power spectral densities,  $w_{AB}$  is called variously the correlation density, co-spectrum or real part of the cross-power spectrum, and  $c_{AB}$  as the narrow-band correlation coefficient.

(U) That  $c_{AB}$  is of magnitude not greater than unity may be proved by squaring the sum and difference of two random signals A and B, normalized to unity variance by division by the respective standard deviations  $\sigma_A$  and  $\sigma_B$ , and averaging over time

$$(A/\sigma_A \pm B/\sigma_B)^2 = A^2/\sigma_A^2 \pm 2AB/\sigma_A\sigma_B + B^2/\sigma_B^2 = \\ 2(1 \pm c_{AB}) \geq 0. \quad (2)$$

Hence

$$|c_{AB}| \leq 1. \quad (3)$$

(U) In the analysis to follow, an expression analogous to equation (1) must be derived for the sum of an infinite number of random signals, subject to a phase reversal according to whether the integer numbering a particular antinode is even or odd, and subject to attenuation of the transverse waves on their way to the observation point, which will be chosen as the origin.

(U) Let a sinusoidal pressure  $p_i$  at the  $i^{\text{th}}$  antinode result in a transverse velocity

$$v_i = \beta_i p_i. \quad (4)$$

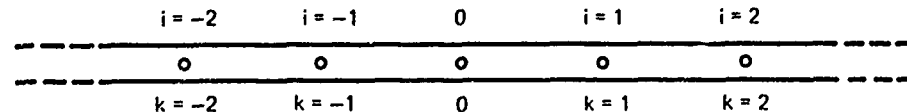


FIGURE 1 EXCITATION ONLY AT THE ANTINODES OF AN INFINITE STRIP.

at, the origin, with  $\beta_i$  a real quantity. Similarly, for the  $k$  in antinode,

$$v_k = \beta_k p_k. \quad (5)$$

(U) Now assume random pressures  $p_{i\Delta f}(t)$  and  $p_{k\Delta f}(t)$  within a narrow bandwidth  $\Delta f$ . The corresponding total velocity at the origin is

$$v_{\Delta f}(t) = \sum_{i=-\infty}^{\infty} \beta_i p_{i\Delta f}(t) = \sum_{k=-\infty}^{\infty} \beta_k p_{k\Delta f}(t) \quad (6)$$

(U) The square is

$$\begin{aligned} v_{\Delta f}^2(t) &= \sum_{i=-\infty}^{\infty} \beta_i p_{i\Delta f}(t) \cdot \sum_{k=-\infty}^{\infty} \beta_k p_{k\Delta f}(t) \\ &= \sum_{i=-\infty}^{\infty} \sum_{k=-\infty}^{\infty} \beta_i \beta_k p_{i\Delta f}(t) p_{k\Delta f}(t) \end{aligned} \quad (7)$$

(U) Average over time and let  $\Delta f$  approach zero to obtain the power spectral density of the total response

$$\begin{aligned} w_v(f) &= \sum_{i=-\infty}^{\infty} \sum_{k=-\infty}^{\infty} \beta_i \beta_k w_{pik}(f) \\ &= \sum_{i=-\infty}^{\infty} \sum_{k=-\infty}^{\infty} \beta_i \beta_k [w_{pi}(f) w_{pk}(f)]^{1/2} c_{pik}(f) \end{aligned} \quad (8)$$

at the origin. All possible power spectral densities ( $i=k$ ) appear in the summation, and all possible co-spectra. The latter are shown also as geometric means of all possible pairs of power spectral density, multiplied by the corresponding narrow band correlation coefficients.

(U) If all  $\beta_i = \beta_k = 1$ , this would be a direct generalization of Equation (1), taken with the positive sign for the power spectral density of a sum. If, for any pair of  $i$  and  $k$ ,  $\beta_i \beta_k = -1$ , indicating a phase reversal before combination at the origin, it would be a generalization of the power spectral density of a difference.

(U) For the problem at hand, we will assume a constant power spectral density  $w_p(f)$ , a phase reversal when the integer  $i$  or  $k$  is odd, indicating an odd number of half wavelengths spacing from the origin, and a transverse wave propagating in either direction from each antinode and decaying exponentially. In short,

$$w_{pi}(f) = w_{pk}(f) = w_p(f), \quad (9)$$

$$\beta_i = K (-1)^i e^{-\alpha|i|}, \quad (10)$$

and

$$\beta_k = K (-1)^{-k} e^{-\alpha|k|}, \quad (11)$$

where  $K$  is a constant of proportionality,  $\alpha$  is a decay constant, and the choice of sign for the exponents  $i$  and  $k$  has no numerical effect and will merely produce a form more similar to that of a derivation to come. Equation (6) becomes

$$w_v(f) = K^2 w_p(f) \sum_{i=-\infty}^{\infty} \sum_{k=-\infty}^{\infty} (-1)^{i-k} e^{-\alpha(|i|+|k|)} c_{pik}(f). \quad (12)$$

(U) For complete correlation at normal incidence, all  $c_{pik}(f) = 1$ . By expressing Equation (10) as the product of two summations in  $i$  and  $k$  and applying the expression for the sum of a binomial series and the definitions for the hyperbolic functions, we obtain

$$w_{vn}(f) = K^2 w_p(f) \tanh^2(\alpha/2) \quad (13)$$

(U) For incidence at the coincidence angle,  $c_{pik}(f) = (-1)^{i-k}$ , and we obtain

$$w_{vc}(f) = K^2 w_p(f) / \tanh^2(\alpha/2) \quad (14)$$

(U) Finally, if the excitations are uncorrelated, all terms for which  $i \neq k$  drop out, but  $c_{pik}(f) = 1$  when  $i = k$ . We obtain

$$w_{vv}(f) = K^2 w_p(f) \tanh \alpha \quad (15)$$

(U) These results are consistent with the trends predicted in advance but are not accurate for a strip excited all along its length.

#### EXCITATION AT ALL POSITIONS

(U) We will now turn our attention from this preliminary exercise to the analysis of a more realistic model excited continuously as a function of position. Except in special cases, the summations become integrals. As phase shifts in propagation are not limited to  $0^\circ$  and  $180^\circ$ , the quad spectrum or imaginary part of the cross-power spectrum of the sound pressure has an effect.

(U) In Appendix 1, the derivation of a general equation for the response of the continuous strip and expressions for three specific cases is carried out in detail.

(U) The equation corresponding to Equation (8) is

$$w_v(f) = \frac{\lambda^2 H^2 w_p(f)}{4} \int_{-\infty}^{\infty} dg \int_{-\infty}^{\infty} e^{-\alpha(|g|+|h|)} c_{ph}(f) \cos(|g|-|h|-\theta) dh, \quad (16)$$

where  $\theta$  and  $c_{ph}(f)$  describe the correlation characteristics of the incident field,  $H$  is a constant, and  $g$  and  $h$  are continuous variables along the strip, not confined to the integral values  $i$  and  $k$ , and  $\lambda$  is the wavelength of transverse vibration in the strip. The expression

$$(-1)^{i-k} c_{pik}(f)$$

is replaced by the continuous expression

$$c_{ph}(f) \cos(|g|-|h|-\theta),$$

again dependent on both the transmission characteristic and the correlation of the incident field.

(U) For a completely correlated field at normal incidence (e.g. incident normally from a single distant source), the final result is

$$w_{vn}(f) = \frac{\lambda^2 H^2 w_p(f)}{\alpha^2 + \pi^2}. \quad (17)$$

(U) For a completely correlated field incident at the coincidence angle such that the trace velocity equals the velocity of propagation of transverse vibration in the strip, the final result is

$$w_{vc}(f) = \lambda^2 H^2 w_p(f) \frac{\alpha^2 + \pi^2}{\alpha^2(\alpha^2 + 4\pi^2)} \quad (18)$$

(U) Up to this point, the fields considered have been completely correlated except for phase effects. We would like an indication of what happens to the response as the correlation distance of the pressure field approaches zero. Let  $C_{ph}(f) = +1$  and  $\theta = |g| - |h|$  for  $g - \Delta g \leq h \leq g + \Delta g$ , and  $C_{pxy}(f) = 0$  for all other pairs of  $x$  and  $y$ .

$$w_v(f) = \frac{\lambda^2 H^2 w_p(f)}{4} \int_{-\infty}^{\infty} dg \int_{g+\Delta g}^{g+\Delta g} -\alpha(|g|+|h|) dh, \quad (19)$$

which approaches zero as  $\Delta g$  approaches zero.

(U) On the other hand, if we take the antinodes to be the centers of half wavelength segments of the strip, as in Figure 2, and excite each segment by an independent normally incident wave so that the excitations of different segments are uncorrelated, the final result is

$$w_{vu}(f) = \frac{\lambda^2 H^2 w_p(f)}{\alpha^2 + \pi^2} \frac{2+3e^{-\alpha}-3e^{-2\alpha}}{1-e^{-2\alpha}} \quad (20)$$

Now, to weigh the realism of exciting a structure by a field of one characteristic as a simulation of the effect of a field of a different characteristic, we are particularly inter-

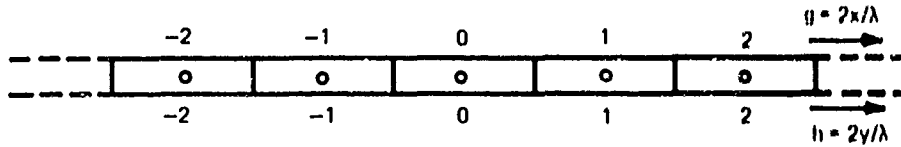


FIGURE 2 ANTINODES AS CENTERS OF HALF-WAVELENGTH SEGMENTS.

terested in ratios of response. It follows immediately that

$$R_n = \frac{w_{vn}(f)}{w_{vu}(f)} = 2 \frac{1-e^{-2a}}{2+3e^{-a}-e^{-3a}} \quad (21)$$

is the ratio of normal incidence to uncorrelated response. The ratio of coincidence to uncorrelated response is

$$R_c = \frac{w_{vc}(f)}{w_{vu}(f)} = 2 \frac{(a^2+\pi^2)^2}{a^2(a^2+4\pi^2)} \cdot \frac{1-e^{-2a}}{2+3e^{-a}-e^{-3a}}. \quad (22)$$

(U) We can find an equivalent Q corresponding to the decay constant  $a$  in the following way. Consider a finite strip starting at  $g=0$  and ending at  $g=n$ , an integer. The return wave from the  $m'$ th reflection at the far end, after stoppage of the excitation, is proportional to

$$e^{-2mn}$$

(U) The time of arrival of the  $m'$ th return wave is

$$t = mn/f,$$

so that

$$mn = ft.$$

(U) A simple resonant system decays according to

$$e^{-\pi ft/Q}$$

(U) Consequently, the equivalent Q is

$$Q = \pi/2a \quad (23)$$

(U) The two ratios are plotted against both  $a$  and  $Q$  in Figure 3, bracketing the possible responses of an infinite strip or a strip with enough internal attenuation to make returns from end reflections negligible. Quite large effects of the type of correlation occur for Q's that are typical of airframe structure.

## CONCLUSION

(U) The effect of the type of correlation of the correlation of the pressure field on structural response is by no means negligible even for infinite structures of typical Q's or structures long enough so that return reflections are negligible. Introducing an exponential decay of correlation along the strip has the same effect on response as increasing the internal attenuation. If the analysis given here were extended to cover a strip of finite length, it would also show a marked difference in response to the different fields according to whether the number of antinodes is odd or even.

(U) It follows that the correlation of the pressure field as well as its sound pressure level must be considered in establishing a simulation. As usual, however, realism must be a compromise limited by practical constraints. When it is not possible to control the correlation closely, it may be desirable to introduce corrections in the SPL to compensate. Analyses such as the one given here may be useful in suggesting the amount of correction to apply.

## ACKNOWLEDGMENT

I am indebted to my colleague, Warren A. Meyer, for verifying the derivation of Equation (20).

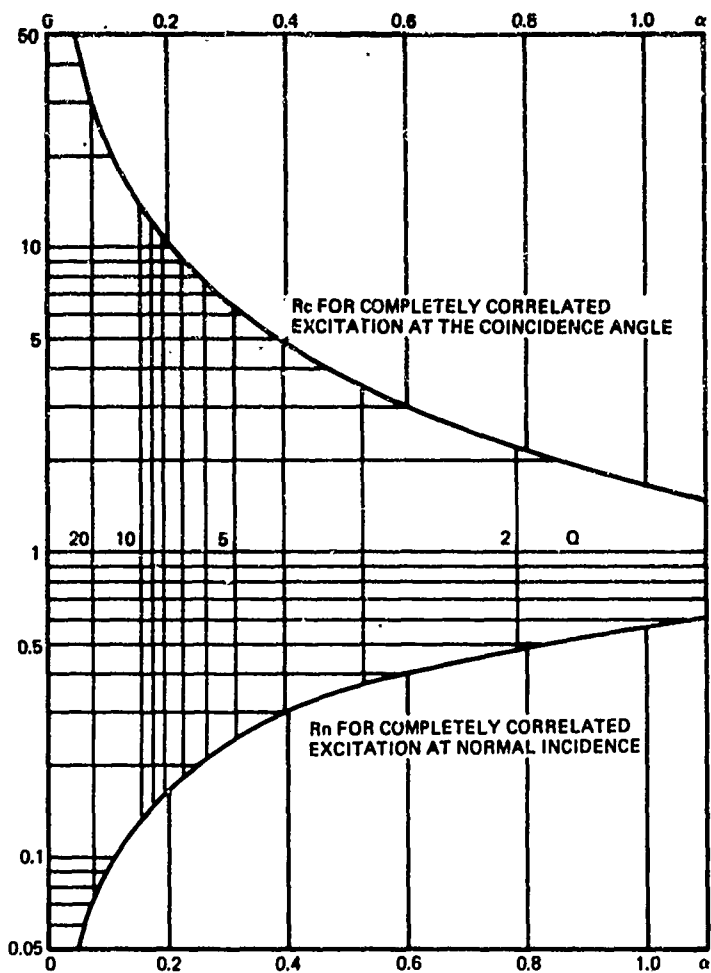


FIGURE 3 RATIO OF RESPONSE P.S.D. TO RESPONSE P.S.D. FOR EXCITATION CORRELATED ONLY WITHIN HALF WAVELENGTH SEGMENTS.

APPENDIX I  
ANALYSIS OF AN INFINITE STRIP  
EXCITED AT ALL POINTS

(U) The equation

$$e^{+j2\pi ft} = \cos 2\pi ft + j \sin 2\pi ft, \quad (24)$$

where  $j$  is a unit vector along the axis of imaginaries, expresses a rotating unit vector as a complex sum of projections along two orthogonal axes. The symbol  $e$  is the base of natural logarithms. It follows that

$$\cos 2\pi ft = \frac{e^{j2\pi ft} + e^{-j2\pi ft}}{2}, \quad (25)$$

or more simply, the cosine function can be extracted from Equation (24) by taking the real part.

(U) A phase shift  $\phi$  can be expressed as complex multiplier:

$$e^{-j\phi} e^{j2\pi ft} = e^{j(2\pi ft - \phi)} = \\ \cos(2\pi ft - \phi) + j \sin(2\pi ft - \phi) \quad (26)$$

or

$$e^{j\phi} e^{-j2\pi ft} = e^{-j(2\pi ft - \phi)} = \\ \cos(2\pi ft - \phi) - j \sin(2\pi ft - \phi) \quad (27)$$

so that

$$\cos(2\pi ft - \phi) = \frac{e^{j(2\pi ft - \phi)} + e^{-j(2\pi ft - \phi)}}{2}. \quad (28)$$

Note also that

$$\frac{d}{dt} e^{j2\pi ft} = j2\pi f e^{j2\pi ft}, \quad (29)$$

very simply.

(U) The analysis to follow will be expended by using the complex exponential.

(U) Imagine a loop of magnetic tape, with a sample of random pressure signal, played back continuously so as to generate an artificially periodic function, with energy at the fundamental frequency and at each harmonic. Let us examine the  $n$  th harmonic, which is among those within a small bandwidth  $\Delta f$ . Let the pressure at position  $x$

$$p_{xm} = p_{xm} e^{j(2\pi f_m - \phi_m)} \quad (30)$$

at the  $k$  th antinode result in a transverse velocity response

$$\Delta v_{xm} = \gamma_{xm} p_{xm} e^{j(2\pi f_m - \phi_{xm})} \Delta x \quad (31)$$

at the origin. The  $\gamma_{xm}$  is taken to be complex, for all possible phase shifts can occur in propagation from various  $x$  to the origin, but it is assumed constant over  $\Delta f$ , equal to  $\gamma_x(f)$ .

(U) The velocity produced by all  $p_{xn}$  within  $\Delta f$  is

$$\Delta v_{x\Delta f} = \sum_{\Delta f} \gamma_{xm} p_{xm} e^{j(2\pi f_m - \phi_{xm})} \Delta x \\ = \gamma_x(f) e^{j2\pi f} \sum_{\Delta f} p_{xm} e^{-2j\phi_{xm}} \Delta x \quad (32)$$

Let

$$\gamma_{xm} = G e^{-j\phi_{xm}} \quad (33)$$

(U) The total complex velocity at the origin is

$$v_{x\Delta f} = \int_{-\infty}^{\infty} \sum_{\Delta f} \gamma_{xm} p_{xm} e^{j(2\pi f_m - \theta_{xm}) dx}$$

$$= \int_{-\infty}^{\infty} \sum_{\Delta f} G_{xn} p_{xn} e^{j(2\pi f_m - \theta_{xm} - \theta_{xm}) dx} \quad (34)$$

(U) The total real velocity at the origin is

$$v_{\Delta f} = \int_{-\infty}^{\infty} \sum_{\Delta f} G_{xm} p_{xm} \cos(2\pi f_m - \theta_{xm} - \theta_{xm}) dx$$

$$= \frac{1}{2} \int_{-\infty}^{\infty} \sum_{\Delta f} G_{xm} p_{xm} [e^{j(2\pi f_m - \theta_{xm} - \theta_{xm})} + e^{-j(2\pi f_m - \theta_{xm} - \theta_{xm})}] dx, \quad (35)$$

which can be written in terms of  $y$  as the independent variable and  $n$  as the subscript. Obtain the square by multiplying the integrals in  $x$  and  $y$  together, and average over time

$$v_{\Delta f}^2 = \frac{1}{2} \int_{-\infty}^{\infty} dx \int_{-\infty}^{\infty} \sum_{\Delta f} G_{xm} G_{yn} p_{xm} p_{yn}$$

$$[e^{j(\theta_{xm} - \theta_{yn} + \theta_{xm} - \theta_{yn})} + e^{-j(\theta_{xm} - \theta_{yn} + \theta_{xm} - \theta_{yn})}] dy$$

$$= \int_{-\infty}^{\infty} dx \int_{-\infty}^{\infty} \sum_{\Delta f} G_{xn} G_{yn} p_{xn} p_{yn}$$

$$\cos(\theta_{xm} - \theta_{xn} + \theta_{xn} - \theta_{yn}) dy. \quad (36)$$

(U) Now, the  $p_{xn}$  and  $p_{yn}$  are random quantities. The  $\theta_{xn}$  and  $\theta_{yn}$  are also random, although their difference may or may not be a simple function of frequency and position, depending on the degree of correlation of the incident wave. However,  $G_{xm}$ ,  $G_{yn}$ ,  $\theta_{xn}$  and  $\theta_{yn}$ , characterizing the

the transmission characteristic of the strip, are always simple functions of frequency and position and may be assumed constant over  $\Delta f$  as follows:

$$G_{xm} = G_x \quad (37)$$

$$G_{yn} = G_y \quad (38)$$

$$\theta_{xm} = \theta_x \quad (39)$$

$$\theta_{yn} = \theta_y \quad (40)$$

$$\theta = \theta_x - \theta_y \quad (41)$$

$$v_{\Delta f}^2 = \frac{1}{2} \int_{-\infty}^{\infty} dx \int_{-\infty}^{\infty} G_x G_y \left\{ e^{j\theta} \sum_{\Delta f} p_{xn} p_{yn} e^{j(\theta_{xm} - \theta_{yn})} \right.$$

$$\left. + e^{-j\theta} \sum_{\Delta f} p_{xn} p_{yn} e^{-j(\theta_{xm} - \theta_{yn})} \right\} dy \quad (42)$$

$$= \frac{1}{2} \int_{-\infty}^{\infty} dx \int_{-\infty}^{\infty} G_x G_y \left\{ e^{j\theta} \left[ \sum_{\Delta f} \frac{p_{xm} p_{yn}}{2} \cos(\theta_{xm} - \theta_{yn}) \right. \right.$$

$$\left. \left. + j \sum_{\Delta f} \frac{p_{xm} p_{yn}}{2} \sin(\theta_{ym} - \theta_{yn}) \right] \right.$$

$$\left. + e^{-j\theta} \left[ \sum_{\Delta f} \frac{p_{xn} p_{yn}}{2} \cos(\theta_{xm} - \theta_{yn}) - j \sum_{\Delta f} \frac{p_{xm} p_{yn}}{2} \sin(\theta_{xm} - \theta_{yn}) \right] \right\} dy \quad (43)$$

(U) Now let the length of the sample increase beyond limit and  $\Delta f$  approach zero, more slowly so that the number of spectral lines within  $\Delta f$  also increases beyond limit. The power spectral density of transverse vibration at the origin is

$$w_v(f) = \int_{-\infty}^{\infty} dx \int_{-\infty}^{\infty} G_x G_y \left\{ e^{j\theta} [w_{pxy}(f) + j q_{pxy}(f)] \right. \quad (44)$$

$$+ e^{-j\theta} [w_{pxy}(f) - jq_{pxy}(f)] \Bigg\} dy, \quad (44)$$

where  $w_{pxy}$  is the co-spectrum or real part of the cross-power spectrum and  $q_{pxy}$  is the quad-spectrum or imaginary part. It follows that

$$w_{pxy}(f) \pm jq_{pxy}(f) = w_{pxy}(f) e^{\pm j\theta} \quad (45)$$

where

$$w_{pxy}(f) = [w_{pxy}^2(f) + q_{pxy}^2(f)]^{1/2} \quad (46)$$

and

$$\theta = \tan^{-1} \frac{q_{pxy}(f)}{w_{pxy}(f)}. \quad (47)$$

(U) Further, the magnitude  $w_{pxy}(f)$  is obtained by multiplying out the complex conjugates and taking the square root.

$$w_{pxy}(f) = \left\{ \sum_{\Delta f} \frac{P_{xm} P_{yn}}{2} \cos(\theta_{xm} - \theta_{yn}) \right. \\ \left. + \sum_{\Delta f} \frac{P_{xm} P_{yn}}{2} \sin(\theta_{xm} - \theta_{yn}) \sum_{\Delta f} \frac{P_{xm} P_{yn}}{2} \sin(\theta_{xm} - \theta_{yn}) \right\}^{1/2} \quad (48)$$

(U) It is important to note that within each product the m's and n's of one summation are independent of those of the other. Without actually assigning new symbols to one pair of subscripts and multiplying out, we can see that the result would reduce to a single summation of terms each involving four pressure amplitudes multiplied by the squared cosine of a compound difference angle, and, if all these difference angles should be zero, reaches a maximum value

$$\text{Max } w_{pxy}(f) = \left\{ w_{px}(f) w_{py}(f) w_{py}(f) \right\}^{1/2}, \quad (49)$$

when  $\Delta f$  approaches zero, which can also be inferred from Equation (3).

(U) If we define a new coefficient

$$c_{pxy}(f) = w_{pxy}(f) / \left\{ w_{px}(f) w_{py}(f) \right\}^{1/2}, \quad (50)$$

$$w_v(f) = \frac{1}{2} \int_{-\infty}^{\infty} dx \int_{-\infty}^{\infty} G_x G_y [w_{px}(f) w_{py}(f)]^{1/2} \\ [e^{j(\theta-\phi)} + e^{-j(\theta-\phi)}] dy = \int_{-\infty}^{\infty} dx \int_{-\infty}^{\infty} G_x G_y \\ [w_{px}(f) w_{py}(f)]^{1/2} c_{pxy}(f) \cos(\theta-\phi) dy \quad (51)$$

Now let

$$g = 2x/\lambda \quad (52)$$

and

$$h = 2y/\lambda \quad (53)$$

where  $\lambda$  is the wavelength of transverse vibration in the strip.

$$w_v(f) = \frac{\lambda^2}{4} \int_{-\infty}^{\infty} dg \int_{-\infty}^{\infty} G_g G_h [w_{pg}(f) w_{ph}(f)]^{1/2} c_{pxy}(f) \cos(\theta-\phi) dh \quad (54)$$

Let

$$G_g = He^{-\alpha|g|} \quad (55)$$

$$G_h = He^{-\alpha|h|} \quad (56)$$

$$\theta = \pi(|g| - |h|) \quad (57)$$

and

$$w_{pg}(f) = w_{ph}(f) = w_p(f), \quad (58)$$

a constant with distance.

$$w_v(f) = \frac{\lambda^2 H^2 w_p(f)}{4} \int_{-\infty}^{\infty} dg \int_{-\infty}^{\infty} e^{-\alpha(|g|+|h|)} \quad$$

$$c_{pgh}(f) \cos(\pi|g| - \pi|h| - \theta) dh,$$

which is the same as Equation (16).

(U) Consider first a field completely correlated so that  $c_{pxy}(f) = 1$  for all  $x$  and  $y$ , and normally incident so that  $\theta = 0$ .

$$w_{vn}(f) = \frac{\lambda^2 H^2 w_p(f)}{4} \int_{-\infty}^{\infty} \int_{-\infty}^{\infty} e^{-\alpha(|g|+|h|)}$$

$$\begin{aligned}
& \cos \pi(|g|-|h|) dh \\
&= \lambda^2 H^2 w_p(f) \int_0^\infty \int_0^\infty e^{-\alpha(g+h)} \cos \pi(g-h) dh \\
&= \frac{\lambda^2 H^2 w_p(f)}{2} \int_0^\infty \int_0^\infty \\
& \left[ e^{-\alpha(g+h)+j\pi(g-h)} e^{-\alpha(g+h)-j\pi(g-h)} \right] dh \\
&= \frac{\lambda^2 H^2 w_p(f)}{2} \left[ \int_0^\infty e^{-\alpha g - j\pi g} dg \int_0^\infty e^{-\alpha h + j\pi h} dh \right. \\
& \left. + \int_0^\infty e^{-\alpha g + j\pi g} dg \int_0^\infty e^{-\alpha h - j\pi h} dh \right] \\
&= \lambda^2 H^2 w_p(f) \int_0^\infty e^{-\alpha g + j\pi g} dg \int_0^\infty e^{-\alpha h - j\pi h} dh \\
&= \frac{\lambda^2 H^2 w_p(f)}{(a-j\pi)(a+j\pi)} = \frac{\lambda^2 H^2 w_p(f)}{a^2+\pi^2},
\end{aligned}$$

which is the same as Equation (17).

(U) Now consider a field completely correlated except for phase effects so that  $C_{pxy}(f) = 1$ , but incident at the coincidence angle corresponding to  $f$  so that  $\phi = \pm g-h$ . Choose the positive sign.

$$\begin{aligned}
w_v(f) &= \frac{\lambda^2 H^2 w_p(f)}{4} \int_{-\infty}^\infty dg \int_{-\infty}^\infty e^{-\alpha(|g|+|h|)} \\
&\cos(|g|-|g|-|h|+h) dh = \frac{\lambda^2 H^2 w_p(f)}{8} \\
& \int_{-\infty}^\infty dg \int_{-\infty}^\infty \left[ e^{-\alpha(|g|+|h|)+j\pi(|g|-g-|h|+h)} \right. \\
& \left. + e^{-\alpha(|g|+|h|)-j\pi(|g|-g-|h|+h)} \right] dh \\
&= \frac{\lambda^2 H^2 w_p(f)}{4} \int_{-\infty}^\infty e^{-\alpha|g|+j\pi(|g|-g)} dg \int_{-\infty}^\infty \\
& e^{-\alpha|h|-j\pi(|h|-h)} dh
\end{aligned}$$

$$\begin{aligned}
&= \frac{\lambda^2 H^2 w_p(f)}{4} \left[ \int_0^\infty e^{-\alpha g} dg + \int_0^\infty e^{-\alpha g + j2\pi g} dg \right] \\
& \left[ \int_0^\infty e^{-\alpha h} dh + \int_0^\infty e^{-\alpha h - j2\pi h} dh \right] \\
&= \frac{\lambda^2 H^2 w_p(f)}{4} \left[ \frac{1}{\alpha} + \frac{1}{\alpha-j2\pi} \right] \left[ \frac{1}{\alpha} + \frac{1}{\alpha+j2\pi} \right] \\
&= \frac{\lambda^2 H^2 w_p(f)}{4} \cdot \frac{2\alpha - j2\pi}{\alpha(\alpha-j2\pi)} \cdot \frac{2\alpha + j2\pi}{\alpha(\alpha+j2\pi)} \\
&= \lambda^2 H^2 w_p(f) \frac{\alpha^2 - \pi^2}{\alpha^2(\alpha^2 + 4\pi^2)},
\end{aligned}$$

which is the same as Equation (18).

(U) Finally, consider a sound field such that  $C_{pxy}(f) = 1$  for  $x$  and  $y$  within the same half wavelength segment,  $C_{pxy}(f) = 0$  for  $x$  and  $y$  in different segments and  $\phi = 0$  when  $C_{pxy}(f) = 1$ . Let the origin be at the center of one segment.

$$\begin{aligned}
w_p(f) &= \frac{\lambda^2 H^2 w_p(f)}{4} \\
& \sum_{k=-\infty}^{\infty} \int_{k-\frac{1}{2}}^{k+\frac{1}{2}} dg \int_{k-\frac{1}{2}}^{k+\frac{1}{2}} e^{-\alpha(|g|+|h|)} \cos \pi(|g|-|h|) \\
&= \frac{\lambda^2 H^2 w_p(f)}{8} \\
& \sum_{k=-\infty}^{\infty} \left[ \int_{k-\frac{1}{2}}^{k+\frac{1}{2}} dg \int_{k-\frac{1}{2}}^{k+\frac{1}{2}} e^{-\alpha(|g|+|h|)+j\pi(|g|-|h|)} dh \right. \\
& \left. + \int_{k-\frac{1}{2}}^{k+\frac{1}{2}} dg \int_{k-\frac{1}{2}}^{k+\frac{1}{2}} e^{-\alpha(|g|+|h|)-j\pi(|g|-|h|)} dh \right] \\
&= \frac{\lambda^2 H^2 w_p(f)}{8} \sum_{k=-\infty}^{\infty} \left\{ \int_{k-\frac{1}{2}}^{k+\frac{1}{2}} e^{-\alpha|g|+j\pi|g|} dg \int_{k-\frac{1}{2}}^{k+\frac{1}{2}} e^{-\alpha|h|-j\pi|h|} dh \right\}
\end{aligned}$$

$$+ \int_{k-\frac{1}{2}}^{k+\frac{1}{2}} e^{-\alpha|g|-j\pi|g|} dg \int_{k-\frac{1}{2}}^{k+\frac{1}{2}} e^{-\alpha|h|+j\pi|h|} dh \Bigg) = \frac{\lambda^2 H^2 w_p(f)}{\alpha^2 + \pi^2} \cdot \frac{2+2e^{-2\alpha}-2e^{-3\alpha}+2e^{-2\alpha}+e^{-\alpha}+e^{-3\alpha}}{2[1-e^{-2\alpha}]}$$

$$= \frac{\lambda^2 H^2 w_p(f)}{4}$$

$$\sum_{k=-\infty}^{\infty} \int_{k-\frac{1}{2}}^{k+\frac{1}{2}} e^{-\alpha|g|+j\pi|g|} dg \int_{k-\frac{1}{2}}^{k+\frac{1}{2}} e^{-\alpha|h|-j\pi|h|} dh$$

$$= \frac{\lambda^2 H^2 w_p(f)}{2(\alpha^2 + \pi^2)} \cdot \frac{2+3e^{-\alpha}-e^{-3\alpha}}{1-e^{-2\alpha}},$$

which is the same as Equation (20).

$$= \lambda^2 H^2 w_p(f) \left\{ \int_0^{\frac{1}{2}} e^{-\alpha g+j\pi g} dg \int_0^{\frac{1}{2}} e^{-\alpha h-j\pi h} dh \right\}$$

$$+ \frac{1}{2} \sum_{k=1}^{\infty} \int_{k-\frac{1}{2}}^{k+\frac{1}{2}} e^{-\alpha g+j\pi g} dg \int_{k-\frac{1}{2}}^{k+\frac{1}{2}} e^{-\alpha h-j\pi h} dh \Bigg\}$$

$$= \lambda^2 H^2 w_p(f) \left\{ \frac{1-e^{-\frac{\alpha}{2}+j\frac{\pi}{2}}}{\alpha-j\pi} \cdot \frac{1-e^{-\frac{\alpha}{2}-j\frac{\pi}{2}}}{\alpha+j\pi} \right\}$$

$$+ \frac{1}{2} \sum_{k=1}^{\infty} \left[ \frac{e^{-\alpha(k-\frac{1}{2})-j\pi(k-\frac{1}{2})} - e^{-\alpha(k+\frac{1}{2})-j(k+\frac{1}{2})}}{\alpha+j\pi} \right] \times \left[ \frac{e^{-\alpha(k-\frac{1}{2})-j\pi(k-\frac{1}{2})} - e^{-\alpha(k+\frac{1}{2})-j(k+\frac{1}{2})}}{\alpha+j\pi} \right]$$

$$= \frac{\lambda^2 H^2 w_p(f)}{\alpha^2 + \pi^2} \left\{ 1 + e^{-\alpha} - e^{-\alpha/2} [e^{j\pi/2} + e^{-j\pi/2}] \right\}$$

$$+ \frac{1}{2} \left[ e^{\alpha} + e^{-\alpha} - e^{-j\pi} - e^{j\pi} \right] \sum_{k=1}^{\infty} e^{-2\alpha k} \Bigg\}$$

$$= \frac{\lambda^2 H^2 w_p(f)}{\alpha^2 + \pi^2} \left\{ 1 + e^{-\alpha} + \left[ \frac{2 + e^{\alpha} + e^{-\alpha}}{2} \right] \right\}$$

$$\left[ \frac{-1 + \frac{1}{1 - e^{-2\alpha}}}{1 - e^{-2\alpha}} \right]$$

$$= \frac{\lambda^2 H^2 w_p(f)}{\alpha^2 + \pi^2} \left\{ 1 + e^{-\alpha} + \frac{[2 + e^{\alpha} + e^{-\alpha}] e^{-2\alpha}}{2[1 - e^{-2\alpha}]} \right\}$$